DESY 96-123D
June 1996

e^+e^- COLLISIONS AT TeV ENERGIES: THE PHYSICS POTENTIAL

PART D

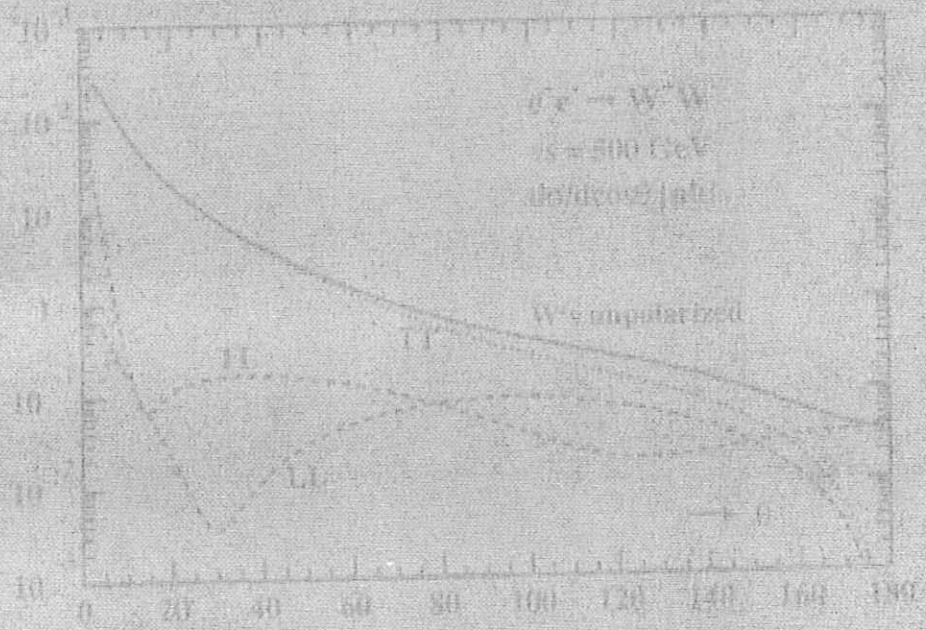

Proceedings of the Workshop Annecy, Gran Sasso, Hamburg
February 1995 to September 1995

edited by

P.M. Zerwas

DESY 96-123D
June 1996

e^+e^- COLLISIONS AT TeV ENERGIES: THE PHYSICS POTENTIAL

PART D

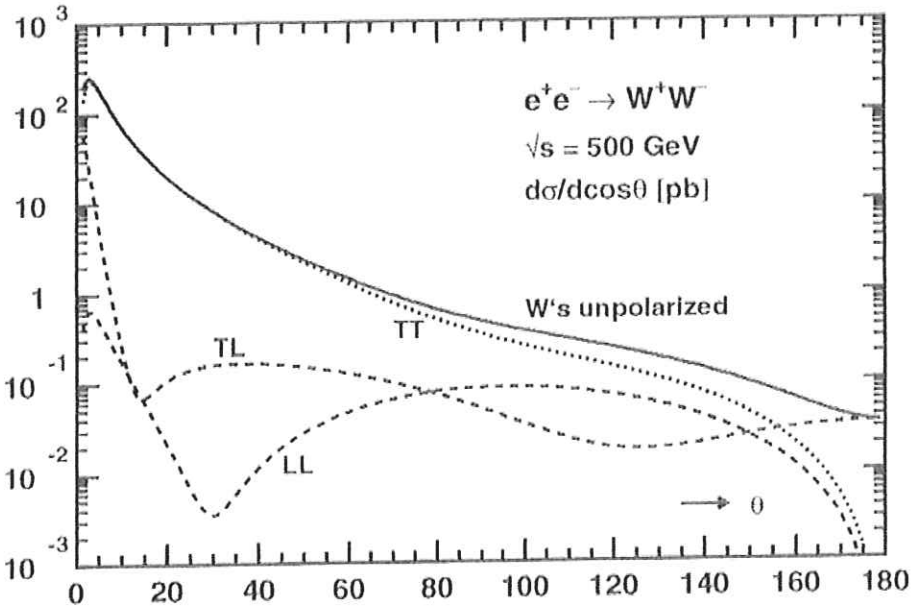

Proceedings of the Workshop – Annecy, Gran Sasso, Hamburg

February to September 1995

edited by

P.M. Zerwas

Workshop Sessions

1. **Laboratoire de Physique des Particules LAPP, Annecy-le-Vieux**
   February 1, 1995
   Organizing Committee: *P. Aurenche, G. Bélanger, F. Boudjema, G. Coignet*

2. **Laboratorio Nazionale del Gran Sasso, Assergi**
   June 2–3, 1995
   Organizing Committee: *M. Greco and P. Monacelli*

3. **Deutsches Elektronen–Synchrotron DESY, Hamburg**
   August 30 – September 1, 1995
   Organizing Committee: *A. Wagner and P.M. Zerwas*

This workshop has been a continuation of the 1991/92 and 1993 Munich Annecy Hamburg Workshops, elaborating on the physics with e^+e^- linear colliders in the extended energy range up to 2 TeV.

Organizing Committee of the Working Groups

G. Coignet, LAPP Annecy
M. Greco, Roma III and INFN Frascati
B. Sattler, MPI München
P. M. Zerwas, DESY Hamburg

Secretariate: S. Günther, DESY Hamburg

CONTENTS

Part D

2. HIGGS PARTICLES

Conveners: A. Djouadi, H. Haber, P. Igo-Kemenes, P. Janot and P.M. Zerwas

3. GAUGE THEORIES

Conveners: F. Boudjema, G. Gounaris, J.D. Hansen and K. Mönig C. Heusch, D. Schaile and C. Verzegnassi

TOP QUARK PHYSICS AND QCD: WORKSHOP SUMMARY

W. Bernreuther[1], S. Bethke[2], J.H. Kühn[3], M. Mangano[4], M. Martinez[5], R. Miquel[6], and P. Nason[7]

[1] Institut f. Theoretische Physik, RWTH Aachen, D-52056 Aachen, Germany
[2] III. Physikalisches Institut, RWTH Aachen, D-52056 Aachen, Germany
[3] Institut f. Theoretische Teilchenphysik, Universität Karlsruhe, D-76128 Karlsruhe, Germany
[4] Theory Division, CERN, CH-1211 Geneva 23, Switzerland
[5] I.F.A.E., Universitat Autònoma de Barcelona, E-08193 Bellaterra, Spain
[6] PPE Division, CERN, CH-1211 Geneva 23, Switzerland
[7] Theory Division, CERN, CH-1211 Geneva 23, Switzerland

In this overview we summarize the main results of the *Top Quark Physics and QCD* working group which are presented below as individual contributions. The aim of this working group was to supplement and to add some new features to the top quark and QCD studies which were made during the previous European workshops on e^+e^- linear colliders [1]. Several new issues were addressed under the following provisos: (a) option of longitudinally polarized electron beam, (b) a substantially higher integrated luminosity than the 10 fb^{-1}/year which was previously assumed for a 500 GeV collider, (c) the e^+e^- c.m. energy will eventually be extended into the TeV range.

The extremley high precision on the top mass, its width and its couplings which can be reached by experimental studies in the threshold region must be matched by the corresponding theoretical analysis. The basic aspects of top production have been detailed in the reports of the previous working groups [1]. The remnants of toponium merge into a sharply rising threshold enhancement. The precise prediction and combined analysis of the production cross section, the momentum and angular distribution and its polarization will constitute the basis for any precision measurement of m_t, α_s, and the effect of Higgs exchange on $t\bar{t}$ production. The following topics have been studied and were presented in the course of the workshop: Close to threshold sizable longitudinal quark polarization along the electron beam is predicted, about -0.4 for unpolarized beams and +1 for fully polarized (right handed) electrons. Small deviations from this prediction are present as a consequence of S-P-wave interference and rescattering which are studied in [2]. The former are present also for stable quarks, the latter are a consequence of the interplay between top production and decay due to the large width of the top quark. It is shown that the deviations from the lowest order predictions are negligible after integration over the angular distribution. The small angular dependent components of the polarization perpendicular to the beam direction are well under control. Their study may serve to obtain additional information and to further constrain the QCD potential in close analogy

with the study of the forward backward asymmetry. Rescattering corrections and S-P-wave interference are equally important. The former have been calculated up to now entirely on the basis of a purely perturbative one-gluon exchange potential. However, in the spirit of rescattering corrections with vanishing energy (but not momentum!) transfer this approximation can be improved by choosing the full QCD two loop potential instead. The resulting implications are also presented in [2].

Rescattering corrections are also studied and reviewed in [3]. Of particular importance are the formal proof that $\mathcal{O}(\alpha_s)$ corrections to the total cross section vanish and the explicit formulas for the influence of rescattering on the momentum distribution. It is shown [3] that these effects are indeed relevant for precision studies close to threshold and that they can, in contrast, be safely ignored in the continuum region.

Another fundamental issue is the precise computation of the $t\bar{t}$ cross section at very high c.m. energies. QCD corrections to the cross section of order α_s^2, including the full mass and energy dependence, are presented in ref. [4]. These results, which are for the moment still limited to vector current induced part, allow to predict unambiguously the cross section in the region above threshold where mass effects are still important.

In ref. [5] the weak corrections to the inclusive $t\bar{t}$ cross section and its behaviour at large $\sqrt{s}$ is investigated. The virtual corrections (without QED corrections) to $t\bar{t}$ production become large and negative: for instance at $\sqrt{s} = 2$ TeV the corrections amount to about 22 % of the Born cross section. On the other hand the Bremsstrahlung processes $e^+e^- \to t\bar{t}X$, $X = Z, H$ grow with increasing c.m. energy, and in the inclusive sum the cross sections of these channels compensate to a large extent the negative virtual corrections to $t\bar{t}$. The authors of ref. [5] conclude that in the 1 - 10 TeV energy range the electroweak corrections to the inclusive $t\bar{t}$ cross section are small, whereas the inclusive $t\bar{t}$ forward backward asymmetry deviates markedly from the Born result.

Exotic decays of the top quark with potentially sizable branching fractions are predicted by the Minimal Supersymmetric Extension of the Standard Model (MSSM). In ref. [6] the decay modes $t \to bH^+$ and $t \to \tilde{t} + neutralino$ are analyzed within the MSSM. A scan of the parameter space of the model was made, taking into account various phenomenological constraints. A new aspect of the analysis of [6] is the use of the full set of radiative corrections to the charged Higgs mass. The authors find that even if no supersymmetric signal would be found at LEP2 the MSSM can still accomodate a branching ratio $B(t \to bH^+) > 0.1$ for $m_{H^+} < 150$ GeV.

Top quark production and decay may also be probed for non-standard CP violation by means of appropriate angular correlations. The new features of the investigation of [7], as compared to previous workshop contributions, are: the use of optimized observables for c.m. energies up to the TeV range including the possibility of longitudinal beam polarization. On the basis of a model-independent computation of optimized correlations caused by CP-violating electric (EDM) and weak (WDM) dipole form factors of the top quark sensitivity estimates for these "couplings" are given for $\sqrt{s} = 500$ and 800 GeV. The sensitivity to $\mathrm{Re}d_t^V$ and to $\mathrm{Im}d_t^V$ drastically increases with beam polarization. This analysis is more specific than the one made in [9], where a deviation from the expected Standard Model (SM) production angular distribution was studied, which could be due to a $\gamma t\bar{t}$ anomalous magnetic moment and an EDM/WDM of the top quark. As to models

of CP violation: If a Higgs boson with mass below 200 GeV and sizable CP-violating couplings (i.e., somewhat larger than the SM Yukawa coupling) to top quarks exists then, with 30 fb^{-1}, there is a chance to see a signal above the $t\bar{t}$ threshold. Furthermore the "Compton collider" option was considered, too, and the prospects of probing Higgs sector CP violation in unpolarized $\gamma\gamma \to t\bar{t}$ was investigated. Once a Higgs boson φ will have been discovered a $\gamma\gamma$ collider could be tuned to resonantly produce φ. It turns out that the $t\bar{t}$ final state is a promising channel for studying the CP properties of Higgs bosons in the mass range between 300 GeVand 500 GeV.

During the 1995 workshop, several studies on the experimental feasibility of various measurements have been undertaken.

In an extension of the analysis initiated in 1991 and continued in 1993, the physics of the top-antitop threshold has been extensively studied [8] for a top mass of 180 GeV (150 GeV in the 1993 study) and including the effect of beamstrahlung and beam energy spread for the latest TESLA accelerator design. A new variable, the forward-backward charge asymmetry, has been added to the total cross section and the peak of the top momentum distribution, studied previously. It has been found that a fit of the three quantities in a nine-point centre-of-mass energy scan around 360 GeV leads to a determination of the top mass and $\alpha_s(M_Z)$ with overall uncertainties of 200 MeV and 0.005 respectively, for an overall integrated luminosity of 50 fb^{-1}.

Under the same circumstances, a one-parameter fit to the top quark width would result in its determination with an 18% precision. And a fit with only the top quark Yukawa coupling as a free parameter would measure it to within 30% of its value, for a Higgs mass of 100 GeV. A low-beamstrahlung accelerator design has also been tried leading to very similar results: the gain from having less beamstrahlung is compensated by the subsequent loss in luminosity.

An extensive study of the determination of top production and decay form-factors has been attempted for the first time, including realistic assumptions about experimental acceptance, resolution and backgrounds [9]. The analysis of the $t\bar{t}$ production vertex using a log-likelihood fit to the top quark production angle at $\sqrt{s} = 500$ GeV gives a precision of about 4% in the anomalous magnetic moment of the top quark, assuming 50 fb^{-1} of data.

As for the decay parameters, a study has been made measuring the amount of V+A structure present in the top decay vertex. In previous analyses only the energy spectrum of charged leptons in semileptonic top quark decays had been analysed. It has been shown that the use of the angular distribution of the charged leptons and the energy and angle of the neutrino (obtained through the missing momentum vector) improve the sensitivity to V+A couplings by about a factor two, to about 2% for 50 fb^{-1} at $\sqrt{s} = 362$ GeV.

Finally, the possible direct determination of the top quark Yukawa coupling by the detection of the $e^-e^- \to t\bar{t}H$ process has been analysed [10]. This process should provide the best way of determining directly such a coupling for a "light Higgs" ($m_H < 2m_t$). The dominant signature for this process, if the Higgs mass is below the WW threshold, consists in events with 8 jets out of which 4 would be originated by b quarks. Assuming a "perfect detector" the signal should be distinctive enough to have large efficiency and purity and, in this case, an expected precision of $\Delta\lambda_t/\lambda_t \sim 0.1$ could be obtained with an integrated luminosity of 50 fb^{-1} running at centre-of-mass energies of about 750 GeV.

Nevertheless, it is clear that several detector performance characteristics may limit

this sensitivity. For instance, by taking a sample of events simulated according to typical LEP detector performances, and assuming an almost ideal b-tagging capability, efficiencies smaller than 30% with a signal over background ratio below two are obtained. Therefore, this measurement seems to be at the limit of being possible and, if taken as a benchmark process for the detector design, it would impose strong constraints in several detector performances, very specially in invariant mass resolution and b tagging.

As for the QCD studies, ref. [11] concentrated on three main issues: *(i)* the separation of pure QCD events from the production and decay of W pairs and $t\bar{t}$ pairs, *(ii)* the feasibility of precise measurements of α_s at $\sqrt{s} = 2$ TeV and *(iii)* the detector specifications needed to accomplish the above. Point *(i)* is of interest because, contrary to what happens at 500 GeV, the final states of W- or t-pair production are highly collimated, and hardly distinguishable from the bulk of the $e^+e^- \to q\bar{q}$ events. The standard techniques used to extract the value of α_s from the structure of the hadronic final states cannot be therefore applied at 2 TeV in a straightforward manner. Measuring the value of α_s at this high energy, on the other hand, is one of the fundamental tasks of the QCD studies, because of the powerful lever arm which could allow to detect possible deviations from the SM QCD running. Measurements of α_s at the level of 3% of statistical accuracy should be possible. The extent to which the separation of QCD and $WW/t\bar{t}$ events will be possible will largely depend on the characteristics of the detectors. This will also be true of studies such as fragmentation functions, for both light and heavy quarks. Features like calorimeter granularity, tracking momentum resolution and tracking efficiency inside collimated jets, as well as the specifics of the micro-vertex detectors, will significantly influence the scope of QCD studies at a 2 TeV collider. In [11] some considerations and some suggestions are made for further exploration to be carried out by the groups developing the detector designs.

References

[1] Proceedings of the workshops on e^-e^- collisions at 500 GeV: The Physics Potential, P. Zerwas (Ed.), DESY 92-123 A,B (1992), DESY 93-123 C (1993).

[2] R. Harlander, M. Jeżabek, J.H. Kühn and M. Peter, these proceedings.

[3] K. Melnikov and O. Yakovlev, these proceedings.

[4] K.G. Chetyrkin, A.H. Hoang, J.H. Kühn, M. Steinhauser, T. Teubner, these proceedings.

[5] V. Driesen, W. Hollik and A. Kraft, these proceedings.

[6] F. Borzumati and N. Polonsky, these proceedings.

[7] W. Bernreuther, A. Brandenburg and P. Overmann, these proceedings.

[8] P. Comas, R. Miquel, M. Martinez and S. Orteu, these proceedings.

[9] M. Schmitt, these proceedings.

[10] M. Martinez and S. Orteu, these proceedings.

[11] S. Bethke, M. Mangano and P. Nason, these proceedings.

TOP QUARKS AT A POLARIZED LINEAR COLLIDER*

R. Harlander[a], M. Jeżabek[b,c], J.H. Kühn[a] and M. Peter[a]

[a] *Institut für Theoretische Teilchenphysik, Universität Karlsruhe, D-76128 Karlsruhe, Germany*

[b] *Institute of Nuclear Physics, Kawiory 26a, PL-30055 Cracow, Poland*

[c] *Institute of Physics, Silesian University, Katowice, Poland*

Abstract

Top quark polarization in e^+e^- annihilation into $t\bar{t}$ is calculated for linearly polarized beams. The Green function formalism is applied to this reaction near threshold. S-P-wave interference contributes to all components of the top quark polarization vector. Rescattering of the decay products is also considered. The mean values $\langle n\ell \rangle$ of the charged lepton four-momentum projections on appropriately chosen four-vectors n in semileptonic top decays are experimentally observable quantities sensitive to top quark polarization. It is demonstrated that for the longitudinally polarized electron beam a highly polarized sample of top quarks can be produced.

*Work supported in part by the Polish State Committee for Scientific Research (KBN) grants 2P30225205, by Graduiertenkolleg "Elementarteilchenphysik an Beschleunigern" and BMBF under contract 05-6KA93P(6) and by EEC contract ERBCIPDCT 940016

1 Introduction

The analysis of polarized top quarks and their decays has recently attracted considerable attention[1]. For nonrelativistic top quarks the polarization studies are free from hadronization ambiguities. This is due to the short lifetime of the top quark which competes favorably with the formation time of top mesons and toponium resonances. Threshold production of top quarks at a future electron-positron collider will allow to study their properties with extremely high precision. The analysis of the total cross section combined with the top quark momentum distribution will determine its mass m_t with an accuracy of at least 300 MeV and its width Γ_t to about 10%.

Additional constraints on these parameters can be derived from the forward-backward asymmetry of top quarks and from measurements of the top quark spin. Close to threshold, for $E = \sqrt{s} - 2m_t \ll m_t$, the total cross section and similarly the momentum distribution of the quarks are essentially governed by the S-wave amplitude, with P-waves suppressed $\sim \beta^2 \sim \sqrt{E^2 + \Gamma_t^2}/m_t \approx 10^{-2}$. The forward-backward asymmetry and, likewise, the transverse component of the top quark spin originate from the interference between S- and P-wave amplitudes and are, therefore, of order $\beta \approx 10^{-1}$ even close to threshold. Note that the expectation value of the momentum is always different from zero as a consequence of the large top width and the uncertainty principle, even for $E = 0$.

The Green function technique is particularly suited to calculate the total cross section and the top quark momentum distribution in the threshold region[2]. A further generalization then leads to the inclusion of P-waves and, as a consequence, allows to predict the forward-backward asymmetry. As long as final state rescattering is neglected the same function $\varphi_k(\mathbf{p}, E)$ which results from the S-P-wave interference governs the dynamical behaviour of the forward-backward asymmetry as well as the angular dependence of the transverse part of the top quark polarization. The close relation between this result and the tree level prediction, expanded up to linear terms in β, has been emphasized. The relative importance of Z versus γ and of axial versus vector couplings depend on the electron (and/or positron) beam polarization. All predictions can, therefore, be further tested by exploiting their dependence on beam polarization. In fact the reaction $e^+e^- \to t\bar{t}$ with longitudinally polarized beams is the most efficient and flexible source of polarized top quarks. At the same time the longitudinal polarization of the electron beam is an obvious option for a future linear collider.

In this contribution which is largely based on [4] predictions for the polarization dependent angular and momentum distributions of top quarks are presented and the results of [5] are expanded in three directions:

1. *Normal polarization.* The calculation of the polarization normal to the produc-

[1] For a recent review and an extensive list of references see e.g. [1, 2] and earlier papers in this series of DESY workshops [3].

[2] A comprehensive list of references can be found in [4].

tion plane is based on the same nonrelativistic Green function as in [5], involving, however, the imaginary part of the interference term $\mathcal{A}_1(\mathbf{p}, E)$. A component of the top quark polarization normal to the production plane may also be induced by time reversal odd components of the $\gamma t\bar{t}$- or $Zt\bar{t}$-coupling with an electric dipole moment as most prominent example. Such an effect would be a clear signal for physics beyond the standard model. The relative sign of particle versus antiparticle polarizations is opposite for the QCD-induced and the T-odd terms respectively which allows to discriminate between the two effects. Nevertheless it is clear that a complete understanding of the QCD-induced component is mandatory for a convincing analysis of the T-odd contribution.

2. *Rescattering of decay products.* Both t quark and $\bar{t}$ antiquark are unstable and decay into W^+b and $W^-\bar{b}$, respectively. Neither b nor $\bar{b}$ can be considered as freely propagating particles. Rescattering in the $t\bar{b}$ and $\bar{b}\bar{t}$ systems affects not only the momenta of the decay products but also the polarization of the top quark. Moreover, in the latter case, when the top quark decays first and its colored decay product b is rescattered in a Coulomb-like chromostatic potential of the spectator $\bar{t}$, the top polarization is not a well defined quantity. Instead one can consider other observables, like the angular momentum of the $W\bar{b}$ subsystem, which coincides with the spin of top quark if rescattering is absent. Rescattering corrections are suppressed by α_s. The resulting modifications of the momentum distribution are, therefore, minor and as far as the total cross section is concerned can even be shown to vanish. In contrast the forward-backward asymmetry as well as the transverse and normal parts of the top quark spin are suppressed by a factor $\sim \beta$. Hence they are relatively more sensitive towards rescattering corrections.

   The lifetime of the $t\bar{t}$ system is about $(2\Gamma_t)^{-1}$. At the time of the decay of the first constituent the typical potential energy of $t\bar{b}$ (or $b\bar{t}$) is about $\alpha_s^2 m_t \sim \alpha_s\sqrt{m_t\Gamma_t}$ where the approximate identity between the two quantities is a numerical coincidence valid for m_t of about 180 GeV. At the time of the second (spectator) decay the mean separation of b and $\bar{b}$ has increased to Γ_t and the corresponding potential energy is reduced to $\alpha_s\Gamma_t$. Thus, rescattering in the $b\bar{b}$ system is less important and will be neglected.

3. *Moments of the lepton angular distribution.* The direction of the charged lepton in semileptonic decays is optimally suited to analyze the polarization of the top quark [2]. The reason is that in the top quark rest frame the double differential energy-angular distribution of the charged lepton is a product of the energy and the angular dependent factors. The angular dependence is of the form $(1 - P\cos\theta)$, where P denotes the top quark polarization and θ is the angle between the polarization three-vector and the direction of the charged lepton. Gluon radiation and virtual corrections in the top quark decay practically do not affect these welcome properties. It is therefore quite natural to perform

polarization studies by measuring the inclusive distributions of say μ^+ in the process $e^+e^- \to t(\mu^+\nu_\mu b)\bar{t}(jets)$. This can be also convenient from the experimental point of view because there is no missing energy-momentum for the $\bar{t}$ subsystem. From the theoretical point of view the direction of the charged lepton is advantageous since it is equivalent to the top quark polarization when rescattering is absent and remains defined even after $b\bar{t}$ rescattering is included. However, the semi-analytic calculation of this effect is difficult because production and decay mechanisms are coupled. In this article moments of experimentally measurable distributions are proposed which are less difficult to calculate but still retain the important information on top quark polarization. These moments, the mean values $\langle nl\rangle$ of the charged lepton four-momentum projections in semileptonic top decays are calculated including S-P-wave interference and $\mathcal{O}(\alpha_s)$ rescattering corrections.

2 Green functions, angular distributions and quark polarization

2.1 Top production in electron positron annihilation

The differential cross section, summed over polarizations of quarks and including S-wave and S-P-interference contributions, is given by

$$\begin{aligned}\frac{d^3\sigma}{dp^3} &= \frac{3\alpha^2\Gamma_t}{4\pi m_t^3}(1 - P_+P_-)\left[(a_1 - \chi a_2)\left(1 - \frac{16\alpha_s}{3\pi}\right)|G(\mathbf{p}, E)|^2 + \right.\\ &\left. -(a_3 + \chi a_4)\left(1 - \frac{12\alpha_s}{3\pi}\right)\frac{\mathrm{p}}{m_t}\mathrm{Re}\left(G(\mathbf{p}, E)F^*(\mathbf{p}, E)\right)\cos\vartheta\right], \qquad (1)\end{aligned}$$

where the coefficients $a_1, \ldots, a_4$ are defined through

$$\begin{aligned} a_1 &= q_e^2q_t^2 + (v_e^2 + a_e^2)v_t^2d^2 + 2q_eq_tv_ev_td\\ a_2 &= 2v_ea_ev_t^2d^2 + 2q_eq_ta_ev_td\\ a_3 &= 4v_ea_ev_ta_td^2 + 2q_eq_ta_ea_td \qquad (2)\\ a_4 &= 2(v_e^2 + a_e^2)v_ta_td^2 + 2q_eq_tv_ea_td\\ d &= \frac{1}{16\sin^2\theta_W\cos^2\theta_W}\frac{s}{s - M_Z^2}, \end{aligned}$$

$$v_f = 2I_f^3 - 4q_f\sin^2\theta_W, \qquad a_f = 2I_f^3. \qquad (3)$$

$P_\pm$ denotes the longitudinal electron/positron polarization and $\chi = (P_+ - P_-)/(1 - P_+P_-)$ can be interpreted as effective longitudinal polarization of the virtual intermediate photon or Z boson.

The S- and P-wave Green's functions G and F are the solutions of the integral equations

$$G(\mathbf{p},E) = G_0(\mathbf{p},E) + G_0(\mathbf{p},E)\int\frac{d^3k}{(2\pi)^3}V(\mathbf{p}-\mathbf{k})G(\mathbf{k},E) \tag{4}$$

$$F(\mathbf{p},E) = G_0(\mathbf{p},E) + G_0(\mathbf{p},E)\int\frac{d^3k}{(2\pi)^3}\frac{\mathbf{p}\cdot\mathbf{k}}{\mathbf{p}^2}V(\mathbf{p}-\mathbf{k})F(\mathbf{k},E), \tag{5}$$

where

$$G_0(\mathbf{p},E) = \frac{1}{E - \frac{\mathbf{p}^2}{m_t} + i\Gamma_t} \tag{6}$$

and $V(\mathbf{p})$ is the chromostatic potential.

The vertex corrections from hard gluon exchange for S-wave and P-wave amplitudes are included in eq.(1). It leads to the following forward-backward asymmetry:

$$A_{FB}(\mathbf{p},E) = C_{FB}(\chi)\,\varphi_R(\mathbf{p},E), \tag{7}$$

with

$$C_{FB}(\chi) = \frac{1}{2}\,\frac{a_3+\chi a_4}{a_1+\chi a_2}, \tag{8}$$

$\varphi_R = \mathrm{Re}\,\varphi$, and

$$\varphi(\mathbf{p},E) = \frac{(1-4a_s/3\pi)}{(1-8a_s/3\pi)}\,\frac{\mathbf{p}}{m_t}\,\frac{F^*(\mathbf{p},E)}{G^*(\mathbf{p},E)}. \tag{9}$$

This result is still differential in the top quark momentum. Replacing $\varphi(\mathbf{p},E)$ by

$$\Phi(E) = \frac{(1-4a_s/3\pi)}{(1-8a_s/3\pi)}\,\frac{\int_0^{p_m}dp\,\frac{p^3}{m_t}F^*(\mathbf{p},E)G(\mathbf{p},E)}{\int_0^{p_m}dp\,p^2\,|G(\mathbf{p},E)|^2}, \tag{10}$$

one obtains the integrated forward-backward asymmetry. The cutoff p_m must be introduced to eliminate the logarithmic divergence of the integral. One may either choose a cutoff of order m_t or replace the nonrelativistic phase space element $p\,dp/m_t$ by $p\,dp/\sqrt{m_t^2-\mathbf{p}^2}$. In practical applications a cutoff will be introduced by the experimental procedure used to define $t\bar{t}$-events.

2.2 Polarization

To describe top quark production in the threshold region it is convenient to align the reference system with the beam direction and to define

$$\mathbf{s}_\parallel = \mathbf{n}_{e^-}, \qquad \mathbf{s}_N = (\mathbf{n}_{e^-}\times\mathbf{n}_t)/|\mathbf{n}_{e^-}\times\mathbf{n}_t|, \qquad \mathbf{s}_\perp = \mathbf{s}_N\times\mathbf{s}_\parallel. \tag{11}$$

In the limit of small β the quark spin is essentially aligned with the beam direction apart from small corrections proportional to β, which depend on the production angle.

The differential cross section for production of a top quark of three-momentum $\mathbf{p}$ and spin projection $-1/2$ on direction $\mathbf{s}_\perp$ reads

$$\frac{d^3\sigma(\mathbf{p},\mathbf{s}_\perp)}{dp^3} = \frac{1}{2}\,(1-\mathcal{P}\cdot\mathbf{s}_\perp)\,\frac{d^3\sigma}{dp^3}. \tag{12}$$

The three-vector $\mathcal{P}$ characterizes the polarization of the top quark. Its components $\mathcal{P}^i$ can be obtained from the formula

$$\mathcal{P}^i = \left[\frac{d^3\sigma(\mathbf{p},\mathbf{s}_\perp^{(i)})}{dp^3} - \frac{d^3\sigma(\mathbf{p},-\mathbf{s}_\perp^{(i)})}{dp^3}\right] \Big/ \left[\frac{d^3\sigma(\mathbf{p},\mathbf{s}_\perp^{(i)})}{dp^3} + \frac{d^3\sigma(\mathbf{p},-\mathbf{s}_\perp^{(i)})}{dp^3}\right], \tag{13}$$

where $\mathbf{s}_\perp^{(i)} = \mathbf{s}_\parallel$, $\mathbf{s}_\perp$ and $\mathbf{s}_N$. Including the QCD potential one obtains for the three components of the polarization

$$\mathcal{P}_\parallel(\mathbf{p},E,\chi) = C_\parallel^0(\chi) + C_\parallel^1(\chi)\,\varphi_R(\mathbf{p},E)\cos\vartheta \tag{14}$$

$$\mathcal{P}_\perp(\mathbf{p},E,\chi) = C_\perp(\chi)\,\varphi_R(\mathbf{p},E)\sin\vartheta \tag{15}$$

$$\mathcal{P}_N(\mathbf{p},E,\chi) = C_N(\chi)\varphi_I(\mathbf{p},E)\sin\vartheta, \tag{16}$$

$$\begin{aligned} C_\parallel^0(\chi) &= -\frac{a_2-\chi a_1}{a_1-\chi a_2}, & C_\parallel^1(\chi) &= \left(1-\chi^2\right)\frac{a_2a_3-a_1a_4}{(a_1+\chi a_2)^2},\\ C_\perp(\chi) &= -\frac{1}{2}\,\frac{a_4+\chi a_3}{a_1+\chi a_2}, & C_N(\chi) &= -\frac{1}{2}\,\frac{a_3+\chi a_4}{a_1+\chi a_2} = -C_{FB}(\chi), \end{aligned} \tag{17}$$

with $\varphi_I = \mathrm{Im}\,\varphi$, and $\varphi(\mathbf{p},E)$ as defined in (9). The momentum integrated quantities are obtained by the replacement $\varphi(\mathbf{p},E)\to\Phi(E)$. The case of non-interacting stable quarks is recovered by the replacement $\Phi\to\beta$, an obvious consequence of (10).
Let us emphasize the main qualitative features of the result:

- Top quarks in the threshold region are highly polarized. Even for unpolarized beams the longitudinal polarization amounts to about -0.41 and reaches ±1 for fully polarized electron beams. This later feature is of purely kinematical origin and independent of the structure of top quark couplings. Precision studies of polarized top decays are therefore feasible.

- Corrections to this idealized picture arise from the small admixture of P-waves. The transverse and the normal components of the polarization are of order 10%. The angular dependent part of the parallel polarization is even more suppressed. Moreover, as a consequence of the angular dependence its contribution vanishes upon angular integration.

- The QCD dynamics is solely contained in the functions φ or Φ which is the same for the angular distribution and the various components of the polarization. (However, this "universality" is affected by the rescattering corrections as

discussed in Sect. 3.) These functions which evidently depend on QCD dynamics can thus be studied in a variety of ways.

- The relative importance of P-waves increases with energy, $\Phi \sim \sqrt{E/m_t}$. This is expected from the close analogy between $\Phi_R = \mathrm{Re}\,\Phi$ and β. In fact, the order of magnitude of the various components of the polarization above, but close to threshold, can be estimated by replacing $\Phi_R \to p/m_t$.

The C_i are displayed in Fig. 1 as functions of the variable χ ($\sin^2\theta_W = 0.2317$, $m_t = 180$ GeV). As discussed before, $C_\parallel^0$ assumes its maximal value ± 1 for $\chi = \mp 1$ and the coefficient $C_\parallel^1$ is small throughout. The coefficient $C_\perp$ varies between -0.7 and -0.5 whereas C_N is typically around -0.5. The dynamical factors Φ are around 0.1 or larger, such that the P-wave induced effects should be observable experimentally.

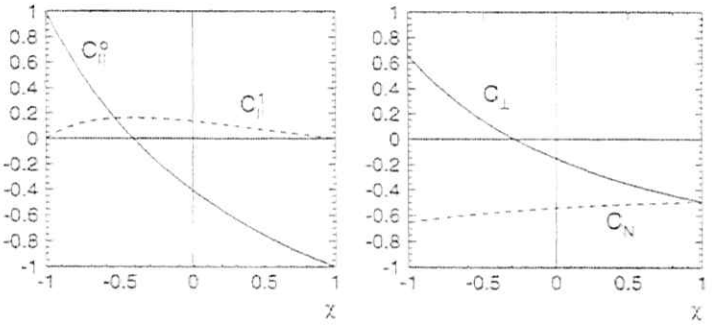

Figure 1: The coefficients (17) for $\sqrt{s}/2 = m_t = 180$ GeV.

The normal component of the polarization which is proportional to φ_1 has been predicted for stable quarks in the framework of perturbative QCD:

$$\varphi_1(p, E) \to \frac{2}{3}\alpha_s \frac{1 - 4\alpha_s/3\pi}{1 - 8\alpha_s/3\pi}. \tag{18}$$

The component of the polarization normal to the production plane is thus approximately independent of E and essentially measures the strong coupling constant. In fact one can argue that this is a unique way to get a handle on the scattering of heavy quarks through the QCD potential.

3 Rescattering corrections to the differential cross section

Close to threshold, the velocity β of the top quark is of the same order of magnitude as the strong coupling. To include only the $\mathcal{O}(\beta)$ contributions to the differential cross section and polarization and discard rescattering corrections is thus inconsistent. To obtain reliable predictions for the observables it is mandatory to calculate the $\mathcal{O}(\alpha_s)$ corrections. Some of these can be implemented without much effort as they are known since several years, and in fact they have already been taken into account in the preceding formulæ:

- the modification of the $t\bar{t}V$ and $t\bar{t}A$ vertices due to transverse gluon exchange
- corrections to t or $\bar{t}$ decay through the full 1-loop result for Γ_t

The differential cross section and polarization are affected through the diagrams shown in Figs. 2a and 2b (and a third diagram with gluon exchange between the two b-quarks, which can, however, be neglected), i.e. corrections caused by interactions between the decay products of one of the top quarks with the second top. They will also be called rescattering corrections.

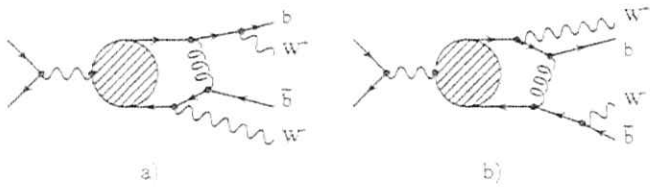

Figure 2: Lowest order rescattering diagrams.

The momentum distribution is affected by rescattering in the following way:

$$\frac{d\sigma^{(0)}}{dp} \to \frac{d\sigma^{(1)}}{dp} = \frac{d\sigma^{(0)}}{dp} \cdot \Big(1 + \omega_1(p, E)\Big), \tag{19}$$

where

$$\omega_1(p, E) = 2\,\mathrm{Im} \int \frac{d^3k}{(2\pi)^3} V(|k - p|) \frac{G(k, E)}{G(p, E)} \frac{\arctan \frac{|k-p|}{\Gamma_t}}{|k - p|}. \tag{20}$$

It follows that at order α_s the total cross section for $t\bar{t}$ production is unaffected by rescattering corrections.

4 Moments of the lepton spectrum

The optimal way to experimentally determine top quark polarization is based on the analysis of the charged lepton distribution in the process

$$e^+e^- \to t\bar{t} \to bl\nu\bar{b}W^-.$$

In [4] moments of this distributions have been proposed as measurable quantities which contain important information on top quark polarization.

Let l be the four-momentum of the charged lepton and n denote one of the following four-vectors, which in the $t\bar{t}$ rest frame read, c.f. (11):

$$n_\parallel = (0, \mathbf{s}_\parallel), \qquad n_\perp = (0, \mathbf{s}_\perp), \qquad n_N = (0, \mathbf{s}_N). \tag{21}$$

The moments are defined as the average values of the scalar products (nl). One can consider the moments $\langle nl\rangle$ for a fixed three-momentum of the top quark,

$$\langle nl\rangle \equiv \left(\frac{d^3\sigma}{dpd\Omega_p}\right)^{-1} \int dE_l d\Omega_l \frac{d\sigma(e^+e^- \to bl\nu\bar{b}W^-)}{dpd\Omega_p d\Omega_l dE_l}(nl) \tag{22}$$

or, integrating over the direction of the top quark, the moments

$$\langle\langle nl\rangle\rangle \equiv \left(\frac{d\sigma}{dp}\right)^{-1} \int dE_l d\Omega_l d\Omega_p \frac{d\sigma(e^+e^- \to bl\nu\bar{b}W^-)}{dpd\Omega_p d\Omega_l dE_l}(nl) \tag{23}$$

or, finally the moments $(\langle\langle nl\rangle\rangle)$ integrated also over p. Analytic results for these moments have been obtained in [4]:

$$(nl) = \mathrm{BR}(t \to bl\nu)\frac{1+2y-3y^2}{4(1-2y)}\left[(tn) + \frac{m_t}{3}n\mathcal{P} + \frac{m_t}{3}n\delta\mathcal{P}\right], \tag{24}$$

$$y = \frac{m_W^2}{m_t^2}, \qquad t^\mu = (m_t, \mathbf{p}). \tag{25}$$

The complete differential cross section as given by

$$\frac{d\sigma}{dpd\Omega_p} = \frac{d\sigma^{(0)}}{dp}\cdot\Big(1 + v_1(p,E)\Big)\frac{1 + 2\mathcal{A}_{FB}(p,E)\cos\vartheta}{4\pi} \tag{26}$$

with

$$\mathcal{A}_{FB}(p,E) = C_{FB}\,\varphi_R(p,E) + \frac{C_\parallel^e}{2}\kappa\, v_R(p,E) \tag{27}$$

should be used as normalization. $\mathcal{P}_\parallel$, $\mathcal{P}_\perp$ and $\mathcal{P}_N$ correspond to S-P-wave interference and are given by eqs.(14)–(16). The components of $\delta\mathcal{P}$ are due to the rescattering corrections. It is remarkable that

$$\delta\mathcal{P}_N = 0 \tag{28}$$

such that the normal component of the polarization vector is unaffected by rescattering corrections. The formulae describing the influence of rescattering corrections on the forward-backward asymmetry in the presence of longitudinally polarized beams can also be found in [4].

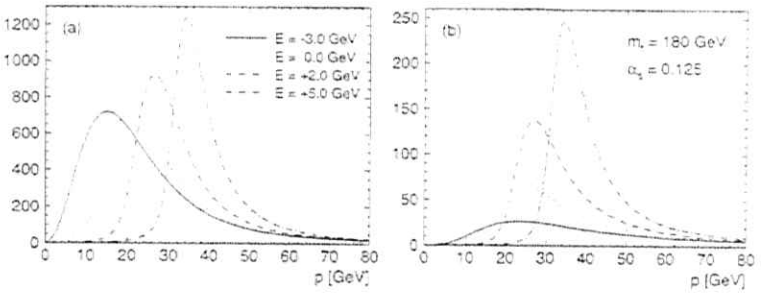

Figure 3: (a) $|pG(p,E)|^2$ and (b) the S-P-interference term $p^3/m_t \cdot \mathrm{Re}(G(p,E)F^*(p,E))$ for $m_t = 180$ GeV, $\alpha_s = 0.125$ and four different energies, where the solid line corresponds to the energy of the $1S$-Peak.

5 Numerical results

The QCD potential used in the numerical analysis has been described in [3]. If not stated otherwise $\alpha_{\overline{\mathrm{MS}}}(M_Z^2) = 0.125$ is adopted. For the top mass a value of 180 GeV is used and, correspondingly, Γ_t =1.55 GeV [6].

Momentum distribution

In Fig. 3 the squared S-wave Green function multiplied by p^2 and the S-P-interference term are displayed for four different energies. The former characterizes the shape of the momentum distribution $d\sigma/dp$, the latter is responsible for the forward-backward asymmetry and angular dependent spin effects, neglecting of course rescattering. The shift towards larger momenta and the narrowing of the distribution with increasing energy are clearly visible, as is the strong growth of the P-wave contribution.

In Fig. 4 we display real and imaginary parts of the function φ, which is essentially given by the ration between S-P-interference and the squared S-wave. In the limit of non-interacting quarks this corresponds to p/m_t. Fig. 5 shows the influence of the rescattering correction on the momentum distribution as given in (19). The attractive force of the $t\bar{t}$ spectator on the decay products from the primary decay leads to a shift towards smaller momenta. The dashed line corresponds to the Born result. Fig. 3(a), the other two include rescattering, implemented, however, in different ways. The solid line was calculated using the full potential. For the dotted line, which is hardly distinguishable from the solid curve, a pure Coulomb potential with fixed coupling constant $\alpha_s = 0.187$ was used.

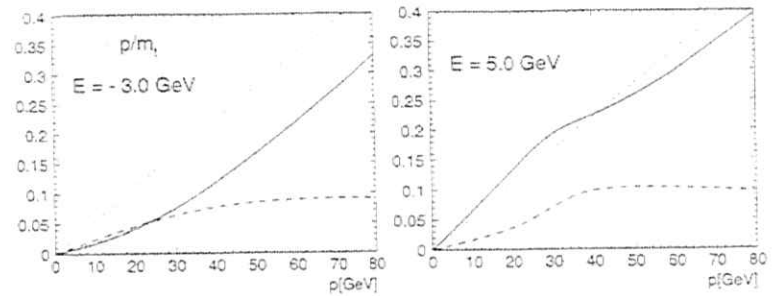

Figure 4: Real (solid) and imaginary (dashed) part of the function $\varphi(\mathrm{p}, E)$ for $m_t = 180$ GeV, $\alpha_s = 0.125$ and two different energies. The dotted line shows the free particle case $\mathrm{Re}\,\varphi = \mathrm{p}/m_t$.

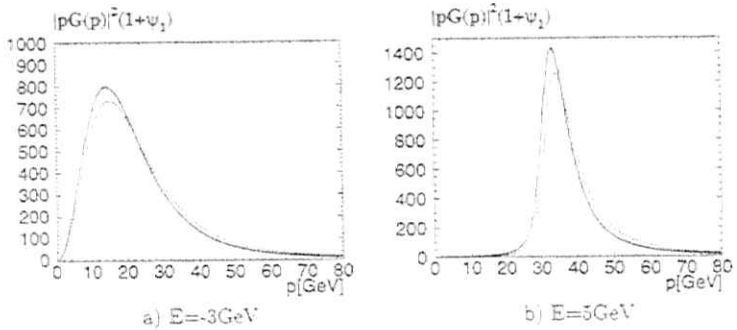

a) E=-3GeV b) E=5GeV

Figure 5: Modification of the momentum distribution through rescattering. Dashed line: no rescattering corrections included; Solid line: rescattering contribution with full potential included; dotted line: rescattering contribution with pure Coulomb potential and $\alpha_s = 0.187$ included.

Forward-backward asymmetry

Ignoring rescattering corrections for the moment the forward-backward asymmetry is governed by the relative magnitude of P- versus S-wave amplitudes. The ratio between the corresponding two distributions is shown in Fig. 4. For noninteracting stable quarks $\varphi(\mathrm{p}, E) = \mathrm{p}/m_t$, and this behaviour persists even in the presence of the QCD potential. The energy dependence of φ is not very strong even in the presence of the potential, and most of the energy variation of Φ visible in Fig. 6 is driven by the energy dependence of the Green function which through the averaging procedure samples different momentum regions.

It should be stressed that the rate and thus the experimental sensitivity varies strongly as a function of p (see Fig. 3) and thus only a limited momentum range will be explored for any given energy. In fact, given limited statistics only integrated quantities will be measured in a first round. These are characterized by the function $\Phi(E)$ whose real and imaginary parts are shown in Fig. 6. The result depends slightly on the cutoff procedure — in a real measurement the cutoff prescription will be dictated by experimental considerations. For definiteness all subsequent results will be given for the "relativistic" cutoff prescription where p/m_t is replaced by p/E.

The energy dependence of both the real and the imaginary parts of Φ can be understood as follows: Above threshold the interaction is of minor importance and Φ_R increases just like $\mathrm{p}/m_t = \sqrt{E/m_t}$. It reaches its minimum roughly in the region of the would-be-1S-resonance where the S wave is still fairly prominent and the P-wave is nearly absent. For lower energies Φ starts to increase, again roughly $\propto \sqrt{|E|/m_t}$, a consequence of the uncertainty principle (see also [7]). The imaginary part of Φ which will induce the normal component of the top quark polarization levels off at a constant value of around 0.09, well consistent with the perturbative prediction $\Phi_I = 2\alpha_s(\mathrm{p})/3$ with $\mathrm{p}^2 \approx m_t\sqrt{E^2 - \Gamma_t^2}$. It vanishes rapidly below $E = 0$: real intermediate $t\bar{t}$-states are no longer accessible, rescattering is absent and the imaginary part vanishes. Throughout most of the threshold region real and imaginary part of Φ are of comparable magnitude, and so are normal and transverse polarization.

The α_s dependence of Φ is displayed in Fig. 7. Above threshold the real part is practically independent of α_s and entirely determined by the kinematic relation. The minimum of the curve is lowered and shifted towards lower values of E, reflecting the decrease of the 1S peak and the larger separation between the "would be" S- and P-wave resonance. The imaginary part of Φ is essentially proportional to α_s, a result obvious from (18).

The influence of Higgs exchange on these predictions has also been studied in [8]. The modification of the cross section is quite sizeable, the influence on angular distribution and top polarization is negligible.

The forward-backward asymmetry $\mathcal{A}_{FB}$ depends on the beam polarization χ, the *cms* energy E and the top quark momentum p. The predictions without (dashed line) and with (solid line) rescattering are displayed in Fig. 8. The relative size and

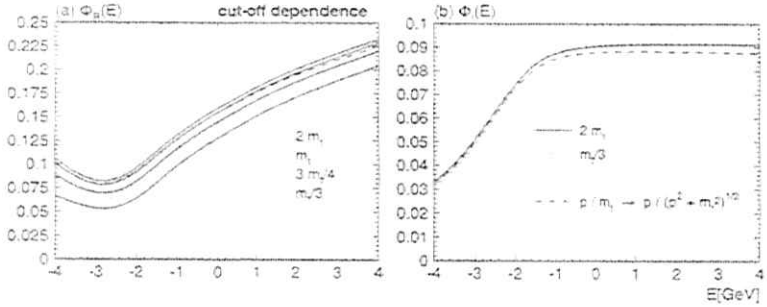

Figure 6: The integrated function $\Phi(E)$, (a) real part, (b) imaginary part. The different solid lines in (a) correspond to cutoffs of $p_m = 2m_t, m_t, 3m_t/4$ and $m_t/3$, with the highest curve for $p_m = 2m_t$. For the dashed lines in (a) and (b) the relativistic prescription was adopted.

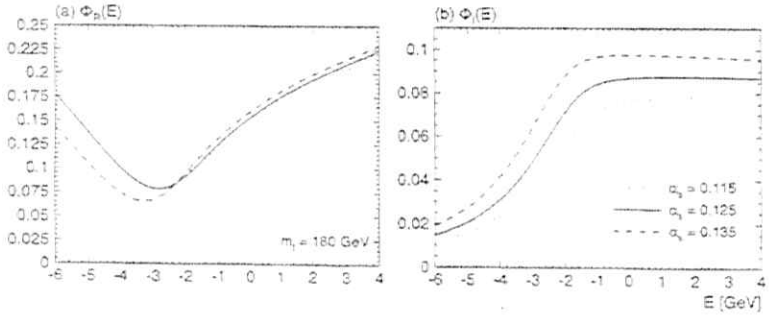

Figure 7: Real and imaginary part of $\Phi(E)$ for three different values of α_s.

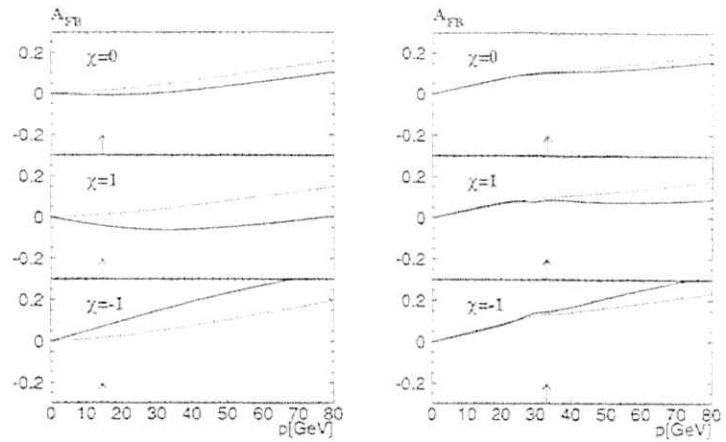

a) E=-3GeV b) E=5GeV

Figure 8: Rescattering corrections to the forward-backward asymmetry. Dashed line: S-P-wave interference contribution; solid line: full result. The little arrows indicate the position of the peak in the momentum distribution.

sign of the rescattering contribution also depend on momentum, energy and beam polarization. For precision studies rescattering may become important, in particular for polarized beams below the nominal threshold.

Top quark polarization

Three remarks are important regarding the effect of rescattering on the top quark polarization. First, what will be discussed in the following is the quantity that can be measured by the moments of the lepton spectrum, which should be understood as a practical way of defining top quark polarization. Second, an extremely useful result is that the normal component $\mathcal{P}_N$ is not affected by rescattering and can thus be obtained immediately from Figs. 1 and 4. As a rule of thumb one predicts $\mathcal{P}_N(p, E) \sim -0.07 \sin\vartheta$. Third, the angular dependence (see eqs.(14)–(16)) of the various spin components arising from S-P-interference seems to be spoilt by rescattering. However, the part of the correction modifying the angular dependence is always multiplied by a numerically small factor. Hence the form of the angular dependence for the longitudinal and transverse polarization remains essentially unchanged.

In contrast, the influence of rescattering on the longitudinal (Fig. 9) and transverse (Fig. 10) components of the "polarization vector" is dramatic. The subleading

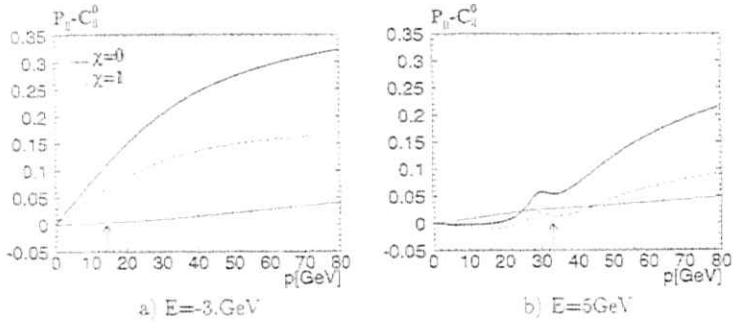

Figure 9: Subleading part of the longitudinal component of the polarization vector for $\vartheta = 0$. The solid line shows the complete result for unpolarized beams, the dotted line the S-P-interference contribution. The dash-dotted line shows the complete result for fully polarized beams, where the S-P-wave contribution vanishes. The arrows indicate the position of the peak in the momentum distribution.

piece of the longitudinal polarization, i.e. the coefficient of $\cos\vartheta$, is dominated by rescattering, essentially because the S-P-interference contribution is proportional to the small quantity C_1^1 and even vanishes for $|\chi| = 1$, a consequence of the normalization condition for the polarization vector. This condition does no longer hold once rescattering corrections are taken into account by calculating moments of the lepton spectrum. The dominant piece of the longitudinal polarization which is given by C_1^0 remains however unaffected and the subleading term which is shown in Fig. 9 vanishes after integration over the top direction. The transverse component is also dominated by the rescattering term. From Figs. 1 and 4 it is evident that S-P-interference alone would lead to a negative result for non-negative χ.

To summarize: Our analysis has shown that the forward-backward asymmetry and the normal component of the polarization vector are (relatively) stable against rescattering corrections. They determine the top couplings a_3 and a_4 via $C_{\rm FB}$ (or possibly some hints on non-standard CP-violating interactions) and both the real and imaginary part of the function Φ that contains important information on Γ_t (and thus on new physics or the existence of a fourth generation) and the strong coupling constant α_s. The longitudinal component of the polarization vector is split into two parts. The leading piece C_1^0 is independent of the production angle and measures the couplings a_1 and a_2. The subleading angular dependent part and the transverse component are small. They are sensitive to rescattering but vanish after angular integration.

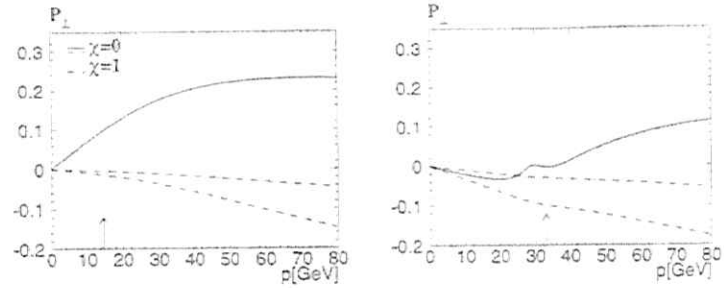

Figure 10: Transverse component of the polarization vector, for $\vartheta = \pi/2$. The solid and dotted lines correspond to unpolarized beams, the dash-dotted and dashed lines to fully polarized beams. The upper two curves show the full result, the lower two the S-P-interference contribution. The arrows indicate the position of the peak in the momentum distribution.

References

[1] J.H. Kühn, in: F.A. Harris et al. (eds.), *Physics and Experiments with Linear e^+e^- Colliders*, Singapore: World Scientific, 1993, p.72.

[2] M. Jeżabek, in: T. Riemann and J. Blümlein (eds.), *Physics at LEP200 and Beyond*, *Nucl. Phys.* **37 B** *(Proc.Suppl.)* (1994) 197.

[3] P.M. Zerwas (ed.), *e^+e^- Collisions at 500 GeV: The Physics Potential*, DESY Orange Report DESY 92-123A, DESY 92-123B and DESY 93-123C, Hamburg 1992–93.

[4] R. Harlander, M. Jeżabek, J.H. Kühn and M. Peter, Karlsruhe Preprint TTP95-48, hep-ph/9604328, to be published in *Zeitschrift für Physik C*.

[5] R. Harlander, M. Jeżabek, J.H. Kühn and T. Teubner, *Phys. Lett.* **B 346** (1995) 137.

[6] M. Jeżabek and J.H. Kühn, *Nucl. Phys.* **B 314** (1989) 1.

[7] M. Jeżabek, J.H. Kühn and T. Teubner, in Volume 3 of [3].

[8] R. Harlander, M. Jeżabek and J.H. Kühn, Karlsruhe Preprint TTP95-25, hep-ph/9506292.

Radiative Interference Effects in the Top production.

Kirill Melnikov and Oleg Yakovlev

Johannes Gutenberg Universität

Institut für Physik (THEP), Staudinger weg 7,

D-55099 Mainz, Germany

Introduction— When we discuss production of unstable particles we use to think in terms of *a narrow width approximation*. This approximation means that the process of the production of a resonance and subsequent decay of the resonance are independent. Hence the distribution over invariant mass of the resonance is described by the well known *Breit-Wigner* formulae:

$$\frac{d\sigma(m^2)}{dm^2} = \frac{\sigma_0(m_R)}{\pi} \frac{m\Gamma}{(m^2 - m_R^2)^2 + m^2\Gamma^2} \cdot Br(R \to X). \qquad (1)$$

Here m_R is the mass of the resonance, σ_0 is the on-shell cross section of the resonance production and $Br(R \to X)$ is a branching ratio of a particular decay channel of the resonance R. As a consequence we have a simple formula for the inclusive cross section (neglecting corrections of the order Γ/m_R):

$$\sigma = \sigma_0(m_R) \cdot Br(R \to X). \qquad (2)$$

In a similar way when we study radiative corrections we calculate them separately to the production cross-section σ_0, total widht Γ and the branching ratio $Br(R \to X)$ and then rewrite the eq.(1) through these one-loop quantities. For example, both QCD and electroweak corrections to the top production cross-section $e^+e^- \to t\bar{t}$ and to the top decay width $\Gamma(t \to Wb)$ are known [1], [2]. The question we address here is: do these corrections provide a complete set of the radiative corrections necessary to describe the process $e^+e^- \to t\bar{t} \to W^+W^-b\bar{b}$? To see that this question is not trivial, we emphasize that in calculating radiative corrections we meet the graphs which connect production and decay stages

of the complete processes. Consequently we have to take into account *radiative interference effects* which are a peculiarity of the physics of *unstable particles*. From the phenomenological point of view this problem is important for a precise measurement of the parameters of the top quark at the Next Linear Collider and for the study of the W-boson at the LEP-2. In this talk we review recent developments in this field.

In our opinion, the most important results here are:

- the theorem about the absence of the interference effects in the *total cross section* [3, 4, 5];
- results for the $O(\alpha_s)$ corrections to the differential cross section for the production of two unstable particles *far from the threshold* [6];
- results for the $O(\alpha_s)$ corrections to the distribution over the three momenta of the top quark for the process of the top quarks threshold production [7, 8].

In what follows we consider reaction $e^+e^- \to t\bar{t} \to W^+W^-b\bar{b}$ as a basis for our discussion. In the last section we also discuss the simplified model which highlights some special features of the processes with the unstable particles.

General features of the radiative interference effects in the production of two top quarks in the electron-positron collision— The basic features of this process in the threshold region were discussed in the non-relativistic approximation long ago [9]. The lowest order total cross-section reads:

$$\sigma(E) = \sigma(e^+e^- \to \mu^+\mu^-)\frac{6\pi Q_t^2}{m_t^2} \cdot ImG(0,0|E + i\Gamma_t), \qquad (3)$$

$$E = \sqrt{s} - 2m_t.$$

Here $G(x, y|E)$ is the non-relativistic Green- function for the top quark system which is defined through:

$$G(x, y|E) = < x|\frac{1}{\hat{H} - E - i\Gamma_t}|y >, \quad \hat{H} = \frac{\hat{p}^2}{m_t} + V(r) \qquad (4)$$

There are several sources of the QCD radiative corrections to the eq.(3): *(i)* hard corrections to the $\gamma t\bar{t}$ vertex [10]; *(ii)* corrections to the QCD potential $V(r)$ [11]; *(iii)* corrections to the top quark decay width Γ_t [2].

This corrections can be absorbed to the "master equation" (3) by substituting the one-loop quantities instead of the Born ones.

But there is also an additional source of the radiative corrections. We present them in the fig.1. Usually these corrections are called non-factorizable. It is clearly seen from the picture that production and decay chains of the two tops are now connected and hence there can be something in the final result which has to be attributed to the joint action of the whole system. Below we concentrate on the analyses of the contribution of the graphs in the fig.1 to the total and differential cross-sections.

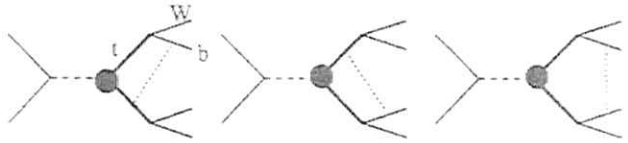

Figure 1: Non-factorizable contributions.

The basic observation concerning evaluation of this graphs is the following one: as we are interested in the α_s correction it is inevitable to consider virtual gluon momenta which are smaller than the width of the unstable particle. Larger values of the momentum shift the resonance propagator far from the pole. Hence the contributions of such momenta regions are suppressed as Γ_t/m_t. Note here that this also sets the scale for the coupling constant α_s and hence makes perturbative calculations sensible. General analyses of the corresponding problem was presented in Refs.[3-6].

The conclusion is: *there is no radiative corrections from the graphs of the fig.1 to the total cross section in order α_s, when virtual as well as real corrections are taken into account. The level of the suppression is*

$$\frac{\delta\sigma}{\sigma} \sim \alpha_s \frac{\Gamma_t}{m_t} \qquad (5)$$

or higher.

Being presented here for the particular reaction this conclusion holds in general [5]. Note that the level of suppression eq.(5) is sufficiently high to neglect these contributions in the total cross section.

On the other hand, the level of suppression crucially depends on the inclusiveness of the studied quantity. Hence, it is not evident that this level of suppression holds when one study differential distributions for the reaction in question.

Differential cross-section for $e^+e^- \to t\bar{t} \to W^+W^-b\bar{b}$ — The motivation to study differential distributions is twofold. First they are interesting on their own grounds as an additional check of the consistency of the theoretical predictions. Second, the study of an appropriate distribution can help to improve the accuracy of the determination of the basic parameters of the theory. For instance the measurement of the distribution in the three-momentum of the top-quark (i.e. three-momentum of W^+b) considerably improves the accuracy of the determination of m_t, Γ_t and α_s when combined with the measurement of the total cross section in the threshold region [12].

The lowest order cross section for this differential distribution reads:

$$\frac{d\sigma}{dp} = N_c Q_t^2 \alpha^2 \frac{p^2}{m_t^4} \Gamma_t |G(p|E + i\Gamma_t)|^2. \qquad (6)$$

Here $G(p|E+i\Gamma_t) = \int d^3x\, G(x, y=0|E+i\Gamma_t)\, e^{ipx}$.

The question is how this result is modified due to the contribution of the graphs shown in Fig.1. The details of the approach are described elsewhere [3, 7, 8]. Here we present the final result.

The next to leading order differential cross section reads:

$$\left(\frac{d\sigma}{dp}\right)_{NLO} = N_c Q_t^2 \alpha^2 \Gamma_t \frac{p^2}{m_t^4} \frac{4C_F\alpha_s}{3\pi} J, \qquad (7)$$

$$J = \int_0^\infty dq F(q) Im\{G^*(p|E+i\Gamma_t) G(q|E+i\Gamma_t)\}$$

where the function $F(q)$ is defined as following:

$$F(q) = \frac{q}{p}\left\{\frac{1}{2\Gamma_t}\log\frac{z_-^2(z_-^2+\Gamma_t^2)}{z_-^2(z_-^2+\Gamma_t^2)} - \frac{1}{z_-}\mathrm{arctg}\left(\frac{z_-}{\Gamma_t}\right) + \frac{1}{z_-}\mathrm{arctg}\left(\frac{z_-}{\Gamma_t}\right)\right\}. \qquad (8)$$

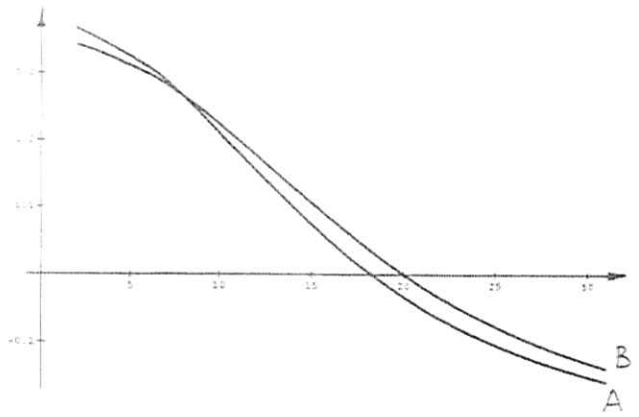

Figure 2: The ratio $(d\sigma/dp)_{NLO}/(d\sigma/dp)_{LO}$ as a function of the top quark three-momentum $|\vec{p}_t|$ in GeV . $E = \sqrt{s} - 2m_t$. $E = 0$. $\alpha_s = 0.1$; A-m_t=165 GeV; B-m_t=175 GeV

The quantities z_+ and z_- are defined through:

$$z_- = |p - q|, \quad z_+ = |p + q|.$$

On the base of the eq.(7) we perform numerical integration. The appropriate algorithms for calculating Green function $G(p|E + i\Gamma_t)$ can be found in the literature [12], [13]. For an illustration purposes we present some numerical results in the fig.2.

Generally, this correction shifts the position of the peak of the distribution to the region of the lower momenta. In the region where the leading order distribution is large the magnitude of the correction is no more than 10 percents.

Results for the simple model— So far we have discussed experimentally reliable situation. However, from the theoretical point of view, the threshold region is too complicated to be considered as a clean laboratory for various effects related to the interaction of unstable particles with the soft massless quanta. Hence, let us finally present some results for the simplest possible model [6] to gain more understanding of how corresponding behaviour of an amplitude is

organized.

We consider a model process $e^+e^- \to t\bar{t}$ with the stable $\bar{t}$- and the unstable t-quark. We are interested in the distribution over invariant mass of the t-quark. We describe it with the help of the parameter δ_t:

$$\delta_t = \frac{p_t^2 - m_t^2}{m_t} \tag{9}$$

where m_t is the pole mass of the top quark and $p_t^2 = m^2$ is the invariant mass of the final Wb system. The Born graph and non-factorizable corrections are shown in the fig.3.

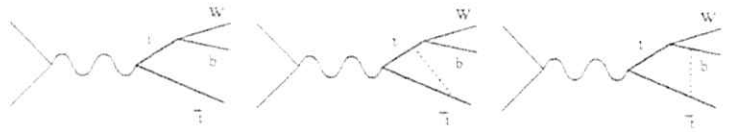

Figure 3: Feynman diagrams for the simple model. Dashed line represents a gluon.

To calculate these graphs we use soft photon approximation. As has already been mentioned the soft momentum region is the only one which gives $O(\alpha_s)$ corrections without additional power suppression [6]. The differential cross-section corrected due to the contribution of the graphs in the fig.3 and the corresponding interference terms in the real emission can be written as:

$$\frac{d\sigma}{dm^2} = \frac{\sigma_0(m_t)}{\pi} \frac{m_t\Gamma_t}{(m^2 - m_t^2)^2 + m_t^2\Gamma_t^2} \left\{1 - 2\,\eta\,\mathrm{arctg}\Big(\frac{\delta_t}{\Gamma_t}\Big)\right\}. \tag{10}$$

The quantity η reads:

$$\eta = \frac{4}{3}\alpha_s\,\frac{(1-\beta)^2}{2\beta}, \quad \beta = \sqrt{1 - \frac{4m_t^2}{s}}. \tag{11}$$

It is instructive to see how this correction disappears when we proceed to the total cross section [3, 5] : integrating previous equation over the range of the top quark invariant masses we get

$$\sigma = \sigma_0(1 - O\Big(\alpha_s\frac{\Gamma_t}{M_t}\Big)) \tag{12}$$

since the arctg δ_i/Γ_i is the odd function of the off-shellness while the usual Breit-Wigner is the even one. Therefore their convolution is zero.

However, this correction influences differential distributions in the invariant mass of the resonance eq.(10). We mention here two important points concerning eq.(10) and eq (11).

First, if the total energy grows the η-factor goes to zero very quickly. Hence, far from the threshold, this correction is not important even for the differential distributions.

Second, the position of the maximum of the distribution is changed. The position of the new maximum is approximately:

$$m_{max} - m_i \approx -\eta\ \Gamma_i. \tag{13}$$

Conclusion— We have briefly discussed the final state interaction in the reactions with the unstable particles. The effect is negligible for the total cross sections. For the differential cross sections the effect appears to be on the level of the other radiative corrections in the energy region slightly above threshold. We did not discuss here the influence of the hadronization on the precise measurement of the top quark line shape. We only note that the discussion of this important issue can be found in the ref. [14].

Acknowledgments— K.M. is grateful to the Graduiertenkolleg Teilchenphysik, Universität Mainz for support. O.Y. acknowledge support by Deutsche Forschungs Gemeinschaft.

References

[1] W. Hollik, W. Beenakker, Zeit. f. Phys. **C40** (1988), 141.

[2] M. Jezabek, J. H. Kühn, Nucl.Phys. **B314** (1989), 1.

[3] K. Melnikov, O. Yakovlev, Phys. Lett. **B324** (1994), 217.

[4] V. S. Fadin, V. A. Khoze, A. D. Martin, Phys. Rev. **D49** (1994), 2247.

[5] V. S. Fadin, V. A. Khoze, A. D. Martin, Phys. Lett. **B320** (1994), 141.

[6] K. Melnikov, O. Yakovlev, hep-ph **9501358**, submitted to Nucl. Phys. B.

[7] O. Yakovlev, Ph.D. Thesis, Novosibirsk, 1994.

[8] Y. Sumino, Ph.D. Thesis, Tokyo, 1993.

[9] V. S. Fadin, V. A. Khoze, JETP Lett. **46** (1987), 525; Sov. Journ. Nucl. Phys. **48** (1988), 309.

[10] W. Buchmuller, S. H. Tye, Phys. Rev. **D24** (1981), 132.

[11] M. J. Strassler, M. E. Peskin, Phys. Rev. **D43** (1991), 1500.

[12] Y.Sumino et al. Phys. Rev. **D47** (1992), 56; M. Jezabek, J. H. Kühn and T. Teubner, Zeit. f. Phys. **C56** (1992), 653.

[13] M. B. Voloshin, Sov. Journ. Nucl. Phys. **36** (1982), 365; M. Strassler, M. Peskin, Phys.Rev. **D43** (1991), 1500.

[14] V. A. Khoze, T. Stjöstrand, Phys. Lett. **B328** (1994), 466.

TOP QUARK PRODUCTION TO $\mathcal{O}(\alpha_s^2)$[‡]

K.G. Chetyrkin[a], A.H. Hoang[b§], J.H. Kühn[b], M. Steinhauser[b§], T. Teubner[c]

[a] *Max-Planck-Institut für Physik, Werner-Heisenberg-Institut, Föhringer Ring 6, D-80805 Munich, Germany and Institute for Nuclear Research, Russian Academy of Sciences, 60th October Anniversary Prospect 7a, Moscow 117312, Russia*

[b] *Institut für Theoretische Teilchenphysik, Universität Karlsruhe, D-76128 Karlsruhe, Germany*

[c] *Department of Physics, University of Durham, Durham, DH1 3LE, UK*

Abstract

The cross-section for the production of $t\bar{t}$ pairs in e^+e^--annihilation via a virtual photon is determined up to order α_s^2. For the cm-energies of interest the effect of the top mass may not be considered as small parameter and the full mass dependence must be included.

[‡]Work supported by BMFT under Contract 056KA93P6, DFG under Contract Ku502/6-1 and INTAS under Contract INTAS-93-0744.

[§]Supported by Graduiertenkolleg Elementarteilchenphysik, Karlsruhe.

Quark mass effects can often be considered as small perturbations in the analysis of the total cross sections for hadron production in e^+e^--annihilation. The approximation $m_q = 0$, supplemented by "mass corrections" of order m_q^2/s is adequate for most purposes and has lead to reliable predictions including terms of order α_s^3 [1]. The situation is drastically different for top quark production at a linear collider, where $2M_t$ and $E_{cm} = \sqrt{s}$ will be of comparable magnitude throughout. With this motivation in mind the QCD corrections to the vector current correlator have been calculated in [2, 3, 4] up to $\mathcal{O}(\alpha_s^2)$ including the full quark mass dependence. Since the corresponding results for the axial vector current are not yet available, the subsequent discussion is strictly applicable for the production through the virtual photon only. The results presented below should therefore not be considered as absolute predictions but rather as indicative for the magnitude and importance of the second order corrections. Our notation and conventions are based on [3]. The cross-section normalized to the point cross-section can be cast into the following form:

$$\begin{aligned} R &= \frac{\sigma(e^+e^- \to \gamma^* \to t\bar{t})}{\sigma_{point}} \\ &= Q_t^2 \left[R^{(0)} + \left(\frac{\alpha_s(M_t^2)}{\pi}\right) C_F R^{(1)} \right. \\ &\quad \left. + \left(\frac{\alpha_s(M_t^2)}{\pi}\right)^2 \left(C_F^2 R_A^{(2)} + C_F C_A R_{NA}^{(2)} + C_F T n_l R_l^{(2)} + C_F T R_F^{(2)} \right) \right] \\ &\quad + \sum_{q=u,d,s,c,b} Q_q^2 \left(\frac{\alpha_s(M_t^2)}{\pi}\right)^2 C_F T R_q^{(2)} . \end{aligned} \tag{1}$$

M_t denotes the top quark pole mass and $\alpha_s(M_t^2)$ the $\overline{\rm MS}$-renormalized strong coupling constant at the scale M_t with $n_l = 5$ light flavours. The abelian and non-abelian parts $R_A^{(2)}$ and $R_{NA}^{(2)}$ are taken from [3], where the Padé approximation method has been employed, whereas $R_l^{(2)}$ and $R_F^{(2)}$ originate from massless and top quark loop insertions, respectively, into the gluon propagator and are given in closed analytical form in [2]. The last term, $R_q^{(2)}$ originates from gluon splitting into $t\bar{t}$ and has been calculated in [5]. To fix our notation explicitely we note in passing that

$$R^{(0)} = \frac{3}{2}\beta(3-\beta^2),$$

$$\begin{aligned} R^{(1)} &= 3\left\{ \frac{(3-\beta^2)(1+\beta^2)}{2} \left[2\,{\rm Li}_2(p) - {\rm Li}_2(p^2) + \ln p \left(2\ln(1-p) + \ln(1+p) \right) \right] \right. \\ &\quad - \beta(3-\beta^2)\left(2\ln(1-p) + \ln(1+p)\right) \\ &\quad \left. - \frac{(1-\beta)(33-39\beta-17\beta^2+7\beta^3)}{16}\ln p + \frac{3\beta(5-3\beta^2)}{8} \right\}, \end{aligned} \tag{2}$$

where

$$p = \frac{1-\beta}{1+\beta}, \qquad \beta = \sqrt{1-4\frac{M_t^2}{s}}. \tag{3}$$

$\sqrt{s}$ [GeV]	400	500	600	700
β	0.48	0.71	0.81	0.87
$R^{(0)}$	2.0084	2.6673	2.8513	2.9228
$C_F R^{(1)}$	17.6874	10.7599	7.7942	6.2463
$C_F^2 R_A^{(2)}$	3.5(1)	-21.4(1)	-19.63(1)	-16.32(1)
$C_F C_A R_{NA}^{(2)}$	117.8(2)	31.9(1)	4.03(1)	-8.61(1)
$n_l C_F T R_l^{(2)}$	-32.4336	-6.8356	0.8496	4.1789
$C_F T R_F^{(2)}$	0.7044	1.0441	1.2375	1.3834
$\sum_q Q_q^2/Q_t^2 C_F T R_q^{(2)}$	$1.2\ 10^{-6}$	0.0005	0.0051	0.0209
$R^{(2)}$	89.5(3)	4.7(2)	-13.50(2)	-19.35(2)
$R^{(\alpha_s=0.115)}$	1.200	1.348	1.375	1.382
$R^{(\alpha_s=0.120)}$	1.213	1.354	1.380	1.385
$R^{(\alpha_s=0.125)}$	1.227	1.360	1.384	1.388

Table 1: Results for the different contributions to R for $M_t = 175$ GeV and the cm-energies $E_{cm} = 400, 500, 600, 700$ GeV. The total cross-section via photon exchange is given for the three different values of $\alpha_s(M_t^2)$ corresponding to $\alpha_s(M_Z^2) = 0.115, 0.120$ and 0.125.

β is the velocity of one of the produced top quarks in the $t\bar{t}$ cm frame. The result for the different contributions $R_q^{(2)}$ are presented in Table 1 for various energies, adopting a top mass value of 175 GeV. The error indicated for $R_A^{(2)}$ and $R_{NA}^{(2)}$ originates from the possible choice of different Padé approximants. As $R_l^{(2)}$, $R_F^{(2)}$ and $R_q^{(2)}$ are known analytically no error is specified in this case. $R^{(2)}$ denotes the sum of all second order correction functions. To arrive at the prediction for R, the correction functions have to be multiplied by the quark charge and the corresponding power of the strong coupling constant evaluated at the scale M_t. For $\alpha_s(M_Z^2) = 0.115$, 0.120 and 0.125 this corresponds to $\alpha_s(M_t^2) = 0.105$, 0.109 and 0.113, respectively. The complete predictions for the three values of α_s are also presented in Table 1. In Fig. 1a R is plotted against $\sqrt{s}$ including successively higher orders in α_s. The dependence on the choice of $\alpha_s(M_Z^2)$ is shown in Fig. 1b.

References

[1] K.G. Chetyrkin, J.H. Kühn and A. Kwiatkowski, *Phys. Reports* (in print), hep-ph/9503396 and references therein.

[2] A.H. Hoang, J.H. Kühn and T. Teubner, *Nucl. Phys.* B 452 (1995) 173.

[3] K.G. Chetyrkin, J.H. Kühn and M. Steinhauser, *Phys. Lett.* B 371 (1996) 93.

[4] K.G. Chetyrkin, A.H. Hoang, J.H. Kühn, M. Steinhauser and T. Teubner, Report Nos. DPT/96/12, MPI/PhT/96-10, TTP96-04, hep-ph/9603313.

[5] A.H. Hoang, M. Jeżabek, J.H. Kühn and T. Teubner, *Phys. Lett.* B 338 (1994) 330.

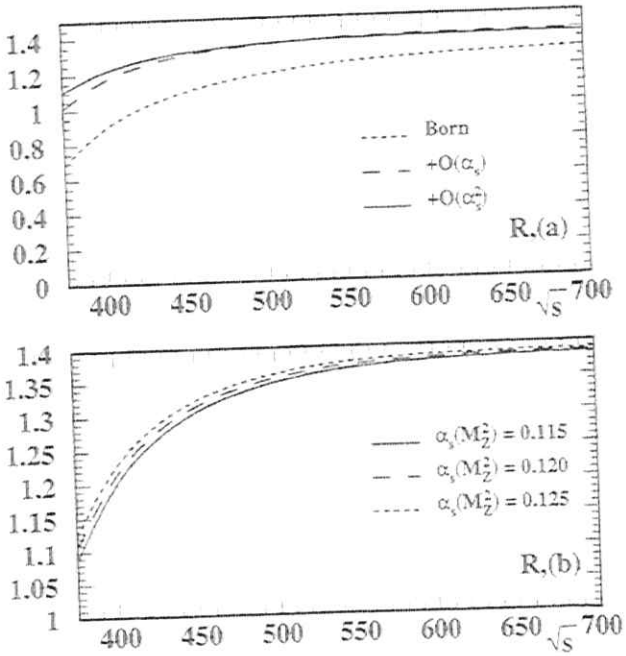

Figure 1: R as function of $\sqrt{s}$. In figure (b) the $O(\alpha_s^2)$ prediction to R is plotted for different choices of $\alpha_s(M_Z^2)$.

Top pair production in e^+e^- collisions with virtual and real electroweak radiative corrections.

V. Driesen, W. Hollik, A. Kraft

Institut für theoretische Physik
Universität Karlsruhe
D-76128 Karlsruhe, Germany

Abstract

The effect of virtual electroweak corrections to $e^+e^- \to t\bar{t}$ and the contribution of the radiation processes $e^+e^- \to t\bar{t}Z, t\bar{t}H$ to the inclusive top pair production cross section and forward-backward asymmetry are discussed in the high energy regime.

For an accurate prediction of top pair production cross sections at a high energy e^+e^- collider, various types of higher-order effects have to be taken into account:

- the QCD corrections, which are treated perturbatively far from the threshold region, but require refinements on threshold and finite width effects close to the production threshold [1],
- the electromagnetic bremsstrahlung corrections (QED corrections) with real and virtual photons inserted in the Born diagrams. They are complete at the 1-loop level in the virtual and soft photon part [2] as well as in the hard photon contribution [3],
- the genuine electroweak corrections, which consist of all electroweak 1-loop contributions to $e^+e^- \to t\bar{t}$, without virtual photons in the external charged fermion self energies and vertex corrections. These are also available as a complete set of 1-loop contribution [2, 4, 5].

An important feature of the electroweak corrections is that they are large and negative at high energies far above the $t\bar{t}$ threshold, and thus lead to a sizeable reduction of the production cross-section. At very high energies, on the other hand, there are also radiation processes besides the conventional photon radiation which contribute to inclusive top pair production $e^+e^- \to t\bar{t}X$: The radiation of Z bosons (Fig. 1) and the radiation of Higgs bosons (Fig. 2).

In previous work [7, 8] these radiation processes were studied with emphasis on searches for Higgs bosons and on investigating the Yukawa interaction. They may, however, also be considered as contributions to the (inclusive) $t\bar{t}$ cross section at 1-loop order. Since they constitute a positive contribution, they increase the production rate of $t\bar{t}$ pairs according to $e^+e^- \to t\bar{t}(X)$ and hence compensate at least partially the negative terms from the virtual corrections.

In this note we present the influence of the virtual electroweak 1-loop corrections on top pair production and the contribution of $e^+e^- \to t\bar{t}Z, t\bar{t}H$ to the inclusive cross section and forward-backward asymmetry. In a first subsection the structure and size of the virtual

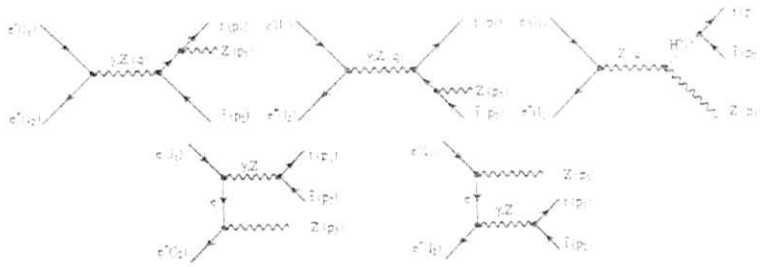

Figure 1: *Diagrams for* $e^+e^- \to t\bar{t}Z$.

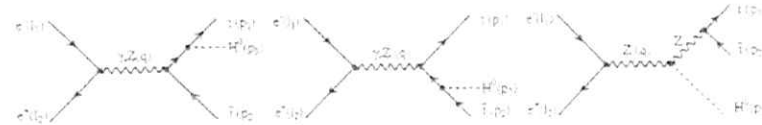

Figure 2: *Diagrams for* $e^+e^- \to t\bar{t}H$.

contributions are discussed. Subsequently, we include the Z and H radiation processes and show that the large and negative virtual contributions are sizeably compensated by including the Z, H bremsstrahlung processes.

Virtual contributions

The integrated cross section and the forward-backward asymmetry for the process $e^+(l_2) + e^-(l_1) \to t(p_1) + \bar{t}(p_2)$ with purely electroweak virtual corrections can be written in the form[1]

$$\begin{aligned} \sigma &= \frac{4\pi\alpha(s)^2}{3s} N_C \beta \left\{ \frac{1}{2}(3-\beta^2)\sigma_1(s) - \beta^2\sigma_2(s) - \Delta\sigma \right\} \\ A_{FB} &= \frac{3}{4}\beta \frac{\sigma_0 - \Delta\sigma'}{\frac{1}{2}(3-\beta^2)\sigma_1(s) - \beta^2\sigma_2(s) + \Delta\sigma} \end{aligned} \tag{1}$$

where

$$\begin{aligned} s &= (p_1 - p_2)^2, \\ \beta &= \sqrt{1 - \frac{4m_t^2}{s}} \quad , \quad \alpha(s) = \frac{\alpha}{1 - \hat{\Pi}^\gamma_{f\neq m_t}(s)} \equiv \frac{\alpha}{1 - \Delta\alpha(s)} \end{aligned} \tag{2}$$

With $\hat{\Pi}^\gamma_{f\neq m_t} = \hat{\Pi}^\gamma - \hat{\Pi}^\gamma_{t\bar{t}}$ we denote the fermionic part of the renormalized subtracted photon vacuum polarization. σ_1, σ_2, and σ_3 contain the lowest-order contribution and

[1] Up to $O(\alpha^4)$.

those one-loop corrections which can be incorporated in effective photon-fermion and Z-fermion couplings, i.e. the self-energies and the vertex corrections to the V, A couplings. The remaining terms, the top vertex corrections not of V, A structure and the contribution from the WW and ZZ box diagrams, are collected in $\Delta\sigma$ and $\Delta\sigma'$ for the symmetric and the antisymmetric cross section.

The σ_i can be written in the following way:

$$\begin{aligned}
\sigma_1 &= \left(Q_e^{V2}+Q_e^{A2}\right) Q_t^{V2} \\
&\quad -2\left(Q_e^V V_e + Q_e^A A_e\right) Q_t^V V_t \frac{s}{s-M_Z^2} \\
&\quad +\left(V_e^2+A_e^2\right) V_t^2 \left(\frac{s}{s-M_Z^2}\right)^2, \\
\sigma_2 &= Q_e^{V2} Q_t^{A2} \\
&\quad +2 Q_e^V V_e Q_t^A A_t \frac{s}{s-M_Z^2} \\
&\quad -\left(V_e^2+A_e^2\right) A_t^2 \left(\frac{s}{s-M_Z^2}\right)^2, \\
\sigma_3 &= 2 Q_e^V Q_t^V A_e A_t \frac{s}{s-M_Z^2} + 4 V_e V_t A_e A_t \left(\frac{s}{s-M_Z^2}\right)^2 .
\end{aligned} \tag{3}$$

The effective coupling constants in these formulae are ($f = e, t$)

$$\begin{aligned}
Q_f^V &= Q_f\left[1-\tfrac{1}{2}\hat{\Pi}'_{\rm had}(s)\right] - F_V^{\gamma f}(s), \\
Q_f^A &= -F_A^{\gamma f}(s), \\
V_f &= \bar{v}_f + F_V^{Zf}(s), \\
A_f &= \bar{a}_f + F_A^{Zf}(s)
\end{aligned} \tag{4}$$

with

$$\begin{aligned}
\bar{a}_f &= \left(\frac{\sqrt{2}G_\mu M_Z}{4\pi\alpha(s)}\right)^{1/2} \bar{\rho}^{1/2} I_3^f \\
\bar{v}_f &= \left(\frac{\sqrt{2}G_\mu M_Z}{4\pi\alpha(s)}\right)^{1/2} \bar{\rho}^{1/2} \left(I_3^f - 2Q_f \bar{s}^2\right)
\end{aligned} \tag{5}$$

They contain the propagator corrections

$$\begin{aligned}
\bar{\rho} &= 1-\Delta r - \hat{\Pi}^Z(s), \\
\bar{s}^2 &= s_W^2 - s_W c_W \hat{\Pi}^{\gamma Z}(s)
\end{aligned} \tag{6}$$

with the self-energies renormalized according to the on-shell scheme

$$\begin{aligned}
\hat{\Pi}^Z &= {\rm Re}\,\frac{\hat{\Sigma}^Z(s)}{s-M_Z}, \\
\hat{\Pi}^{\gamma Z} &= {\rm Re}\,\frac{\hat{\Sigma}^{\gamma Z}(s)}{s},
\end{aligned} \tag{7}$$

together with the V, A form factors $F_{V,A}$ from the vertex corrections (real part). Δr is the radiative correction to the Fermi coupling constant in the on-shell scheme. The explicit expressions can be found in [2, 6].

The Born cross section $\sigma^{(0)}$ can be obtained from the formulae above by setting all the self-energies, vertex corrections, $\Delta\sigma$, $\Delta\sigma'$ and Δr in Eqs. (4-6) equal to zero.

The effect of the virtual electroweak corrections on the cross section for $e^+e^- \to t\bar{t}$ is displayed in Fig. 3, where the relative deviation from the "Born" cross section is shown. Note that "Born" already includes the QED running of the effective charge in the γ-exchange amplitude. The results in Fig. 3 are thus the residual corrections which are specific for the electroweak standard model.

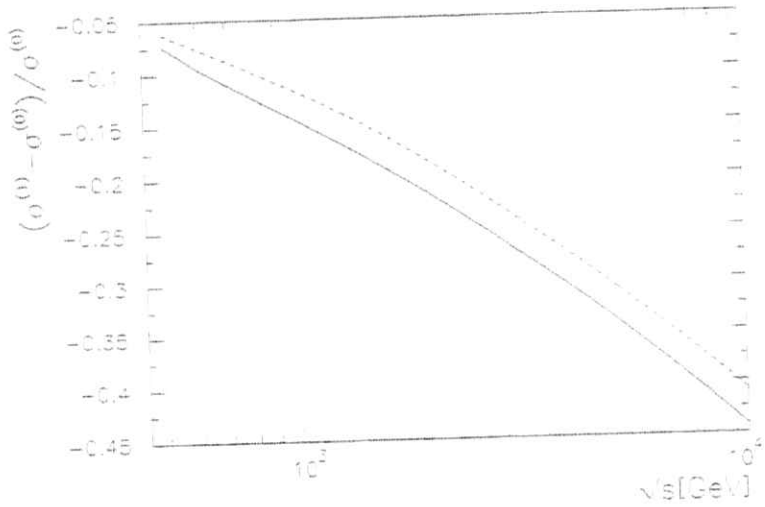

Figure 3: *Relative electroweak corrections to $e^+e^- \to t\bar{t}$ for $M_H = 100\,$GeV (solid line) and $M_H = 1000\,$GeV (dashed line).*

Real contributions

Next we consider the inclusive cross section for $t\bar{t}$ production in association with Higgs and Z bremsstrahlung. We thereby restrict our discussion to Higgs masses below $2m_t$, such that real Higgs production with subsequent decay into $t\bar{t}$ cannot occur. The latter case would be of specific interest for investigating the Higgs Yukawa interaction, and was explicitly studied in ref. [7].

The bremsstrahlung processes are of higher order in the coupling constants than the $2 \to 2$ process. The cross section at energies sufficiently above the threshold reach 10%

and more of the lowest order cross section. Their contribution to the $t\bar{t}$ final state hence becomes of the same order as the virtual electroweak corrections.

For the computation of the cross sections corresponding to the amplitudes in Figs. 1 and 2 the following set of couplings has been chosen:

$$\begin{aligned}
\gamma f\bar{f} &: -\sqrt{4\pi\,\alpha(s)}\,\gamma^\mu Q_f \\
Zf\bar{f} &: -\sqrt{\sqrt{2}\,G_\mu M_Z^2}\,\gamma^\mu\left[(I_3 - 2Q_f s_w^2) - I_3\gamma_5\right] \\
Hf\bar{f} &: -\sqrt{\sqrt{2}\,G_\mu}\,m_f \\
HZZ &: \sqrt{4\sqrt{2}\,G_\mu M_Z^2}\,M_Z
\end{aligned}$$

For s_w^2 the approximate expression

$$s_w^2 = \frac{1}{2} - \sqrt{\frac{1}{4} - \frac{\pi\,\alpha(M_Z)}{\sqrt{2}\,G_\mu M_Z^2}} = 0.2311 \tag{8}$$

is used.

In Fig. 4 we put together the integrated cross section for $e^+e^- \to t\bar{t}Z$ and $e^+e^- \to t\bar{t}H$ as function of the energy $\sqrt{s}$. The dominating contribution to the inclusive final state for $\sqrt{s} \geq 1$ TeV is from the "Z-strahlung", as can be seen from Fig. 4.

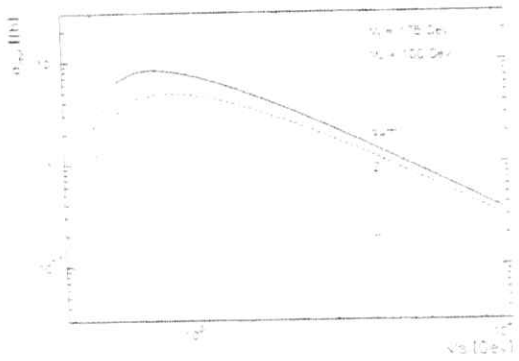

Figure 4: *Integrated cross section for $e^+e^- \to t\bar{t}Z$ and $e^+e^- \to t\bar{t}H$.*

We now can define an inclusive cross section for $t\bar{t}$ production in the following way:

$$\frac{d\sigma}{d\Omega}(t\bar{t}) = \frac{d\sigma_V}{d\Omega}(t\bar{t}) + \int d^3p_3 \frac{d\sigma(t\bar{t}H)}{d\Omega d^3p_3} + \int d^3p_3 \frac{d\sigma(t\bar{t}Z)}{d\Omega d^3p_3} \tag{9}$$

where $d\Omega = d\cos\theta_t\, d\phi$ is the solid angle of the outgoing top, and θ_t the scattering angle between e^- and t. $d\sigma_V$ denotes the 2-particle final states including the virtual contributions, and d^3p_3 is the phase space element for H and Z, respectively.

The integrated cross section is obtained as

$$\sigma_{t\bar{t}} = \sigma_V(t\bar{t}) + \sigma(e^+e^- \to t\bar{t}H) + \sigma(e^+e^- \to t\bar{t}Z). \tag{10}$$

The forward-backward asymmetry A_{FB} is given by

$$A_{FB} = \frac{1}{\sigma_{t\bar{t}}}\left(\int_0^1 d\cos\theta_t \frac{d\sigma(t\bar{t})}{d\cos\theta_t} - \int_{-1}^0 d\cos\theta_t \frac{d\sigma(t\bar{t})}{d\cos\theta_t}\right) \tag{11}$$

with

$$\frac{d\sigma(t\bar{t})}{d\cos\theta_t} = \int_0^{2\pi} d\phi\, \frac{d\sigma}{d\Omega}(t\bar{t}) \tag{12}$$

The results are displayed in Figs. 5, 6. As one can see from Fig. 5, the virtual and real contributions to the integrated cross section cancel each other to a large extent. For A_{FB}, however, the situation is different. Fig. 6 contains A_{FB} in Born order, with virtual corrections, and after including the real contributions. For A_{FB}, the totally inclusive $t\bar{t}$ asymmetry deviates more from the Born result than the one with only virtual corrections to $e^+e^- \to t\bar{t}$.

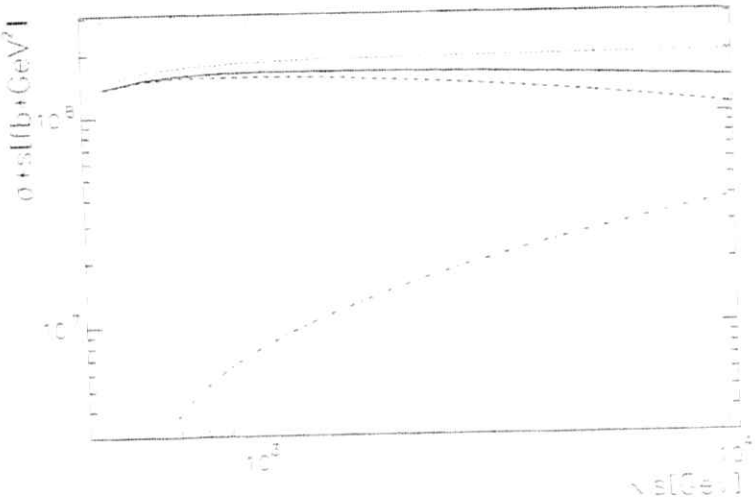

Figure 5: *Integrated cross section (times s). The dotted line shows the Born cross section $\sigma^{(0)}$, the dashed line contains all electroweak 1-loop virtual corrections, the dash-dotted line depicts the real contributions from $e^+e^- \to t\bar{t}H$ and $e^+e^- \to t\bar{t}Z$, and the solid line shows the inclusive cross section σ.*

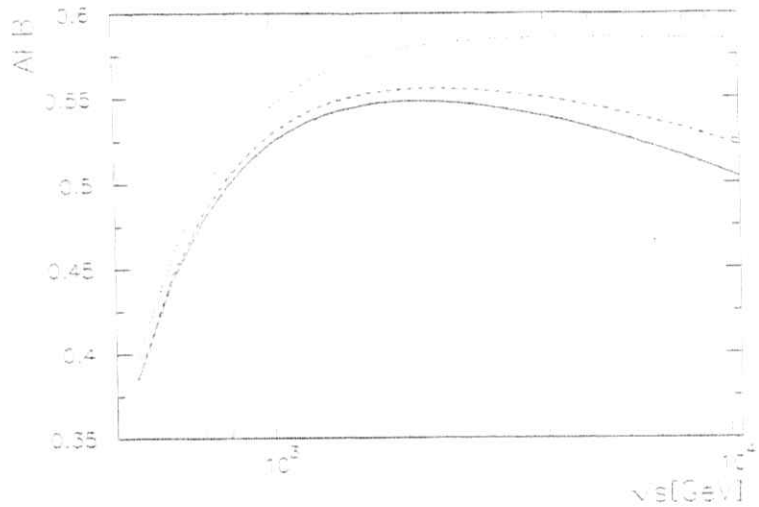

Figure 6: *Forward-backward asymmetry. The dotted line show the Born prediction, the dashed line contains also all electroweak 1-loop virtual corrections, and the solid line depicts the result for the inclusive production.*

Thereby, A_{FB} in Born approximation is obtained from Eq. (1) with expressions (3-6), where all self energies, vertex corrections, Δr and $\Delta\sigma$,$\Delta\sigma'$ are put to zero.

References

[1] J. Jersak, E. Laermann, P.M. Zerwas, *Phys. Rev.* **D25** (1980) 1218;
S. Güsken, J.H. Kühn, P.M. Zerwas, *Phys. Lett.* **B155** (1985) 185;
J.H. Kühn, P.M. Zerwas, *Phys. Rep.* **167** (1988) 321;
V.S. Fadin, V.A. Khoze, *Pi'sma v Zh. Eksp. Teor. Fiz.* **46** (1987) 417; *Yad. Fiz.* **48** (1988) 487;
V.S. Fadin, V.A. Khoze, T. Sjöstrand, *Z. Phys.* **C48** (1990) 613;
V.S. Fadin, O.I. Yakovlev, Novosibirsk preprint IYF 90-138 (1990);
W. Kwong, *Phys. Rev.* **D43** (1991) 1488;
H. Inazawa., T. Morii, J. Morishita, *Phys. Lett.* **B203** (1988) 279; *Z. Phys.* **C42** (1989) 569;
K. Hagiwara et al., *Nucl. Phys.* **B344** (1990) 1;
J. Feigenbaum, *Phys. Rev.* **D43** (1991) 264;
M.J. Strassler, M.E. Peskin, *Phys. Rev.* **D43** (1991) 1500;
J.H. Kühn, Proceedings of the *Workshop on on Physics and Experiments with Linear e^+e^- Colliders*, Waikoloa, Hawaii 1993, eds.: F.A. Harris, S.L. Olsen, S. Pakvasa, X. Tata

[2] W. Beenakker, W. Hollik and S.C. van der Marck, *Nucl. Phys.* **B365** (1991) 24.

[3] A.A. Akhundov, D.Y. Bardin and A. Leike, *Phys. Lett.* **B261** (1991) 321;
A. Arbuzov, D. Bardin, A. Leike, *Mod. Phys. Lett.* **A7** (1992) 2029; E: **A9** (1994) 1515.

[4] W. Beenakker and W. Hollik, *Phys. Lett.* **B269** (1991) 425.

[5] W. Beenakker, A. Denner and A. Kraft, *Nucl. Phys.* **B410** (1993) 219.

[6] W. Hollik, *Fortschr. Phys.* **38** (1990) 165;
M. Consoli, W. Hollik, F. Jegerlehner, in: *Z* Physics at LEP1, CERN 89-08(1989), eds. G. Altarelli, R. Kleiss, C. Verzegnassi.

[7] K. Hagiwara, H. Murayama, I. Watanabe, *Nucl. Phys.* **B367** (1991) 257.

[8] A. Djouadi, J. Kalinowski, P.M. Zerwas, *Z. Phys.* **C54** (1992) 255

SUPERSYMMETRIC DECAYS OF THE TOP QUARK: AN UPDATE *

Francesca M. Borzumati

Inst. Theoret. Physik. Techn. Universität München, Garching, Germany
Physics Department, Weizmann Institute, Rehovot, Israel

Nir Polonsky

Sekt. Physik Universität München, L.S. Prof. Wess, München, Germany

ABSTRACT

We analyze the two decays $t \to H^+ b$, $t \to \tilde{u}_1 \tilde{\chi}_1^0$ within the Minimal Supersymmetric Standard Model with radiative breaking of the electroweak sector. We discuss their detectability at present and in the eventuality that supersymmetry is not discovered at LEPII.

SUPERSYMMETRIC DECAYS OF THE TOP QUARK: AN UPDATE

FRANCESCA M. BORZUMATI[1,2], N. POLONSKY[3]

[1] *Inst. Theoret. Physik. Techn. Universität München, Garching, Germany*
[2] *Physics Department, Weizmann Institute, Rehovot, Israel*
[3] *Sekt. Physik Universität München, L.S. Prof. Wess, München, Germany*

ABSTRACT

We analyze the two decays $t \to H^+ b$, $t \to \tilde{u}_1 \tilde{\chi}_1^0$ within the Minimal Supersymmetric Standard Model with radiative breaking of the electroweak sector. We discuss their detectability at present and in the eventuality that supersymmetry is not discovered at LEPII.

1. Problem and Inputs

It is well known that in supersymmetric models the top quark can decay at the tree-level into a charged Higgs plus a bottom quark, $t \to H^+ b$, and into a stop $\tilde{u}_i$ plus the lightest neutralino $\tilde{\chi}_1^0$, $t \to \tilde{u}_i \tilde{\chi}_1^0$ (see for example [1] and references therein). Both decays can have sizable rates: $t \to H^+ b$ can easily reach the 10–30% level for large $\tan\beta$; $t \to \tilde{u}_i \tilde{\chi}_1^0$ has similarly large rates in some corners of the supersymmetric parameter space [1].

The agreement between the top production cross section measuread at the TEVATRON [2] and that which is predicted by the Standard Model (SM) still allows such large rates. Moreover, the measurement of the top mass (M_t) based on electron and muon tagging is not sensitive to these decay modes. For very large values of $\tan\beta$ which give large $t \to H^+ b$ rates, H^+ decays into third generation leptons $\tau\nu_\tau$ (more than 95% of the times), whereas, in general, the decay into the lightest chargino ($\tilde{\chi}_1^+$) and neutralino, $H^+ \to \tilde{\chi}_1^+ \tilde{\chi}_1^0$, may dominate. In the second mode $t \to \tilde{u}_i \tilde{\chi}_1^0$, $\tilde{u}_i$ can decay as $\tilde{u}_i \to \tilde{\chi}_1^+ b$ and $\tilde{u}_i \to c\tilde{\chi}_1^0$. In all these channels, a larger amount of missing energy than in the standard $t \to W^+ b$ is produced, which leads to softer spectra for the charged leptons.

By phase space suppression, the abovementioned rates can be progressively reduced to the level of "rare" ones when the masses of H^+, $\tilde{u}_i$, and $\tilde{\chi}_1^0$ increase. The question to be answered, therefore, is whether the Minimal Supersymmetric Standard Model (MSSM) can still support these two decay channels (and at which level), once all constraints coming from experiments are imposed. Independently, one should also consider how much information can be extracted for possible extensions of the MSSM by the observation (or non-observation) of these decay modes. In this contribution we provide an answer only to the first of these two questions.

The MSSM studied here is the most minimal realization of a supersymmetric version of the SM, with breaking of the electro-weak sector radiatively induced. We assume that the universal boundary conditions are given near the grand-unified scale of $M_G \sim 3 \cdot 10^{16}$ GeV. We do not make any assumptions regarding the details of the physics at the grand scale and we do not assume b–τ unification, which is affected by these details [4]. We fix the QCD coupling constant to its average value $\alpha_s(M_Z) = 0.12$ and the running mass

$m_b(M_Z)$ to be $m_b(M_Z) = 3\,\mathrm{GeV}$.

We include radiative corrections to the Higgs potential following the procedure described in [5] while we impose radiative breaking of the electroweak sector. We find that the spectrum of the Higgs mass parameters calculated using one-loop renormalization group equations and tree-level sum rules is slightly heavier than that which is described in [1, 7] where these corrections were not included.

Furthermore, we evaluate the mass-shifts for $H^\pm$ induced by these corrections as in [6]. We compare these results with those obtained following other calculations which make use, as [6], of the diagrammatic approch [9] and of the effective potential method [8, 10]. We find, in general, a rather good agreement (after replacing h_t with $-h_t$ in (5d) and (5e) of [10]). In generic supersymmetric models these mass corrections can be large for large left-right mixings in the squark mass matrices and can be positive and negative (this last possibility is in general observed for small values of $\tan\beta$). In our MSSM simulation, however, after radiative breaking of the electroweak sector is imposed, we find that the corrected masses hardly deviate from those obtained using the tree-level sum rules.

We come now to discuss the cuts imposed to the region of parameter space which we study. It is known that the decay $b \to c\tau\nu$ restricts the ratio $r = \tan\beta(\mathrm{GeV})/m_{H^\pm}$ to be $\lesssim 0.5$ in models containing two Higgs doublets with couplings of type II to the fermions (see [11] and related references therein). Although relevant for models of global realizations of supersymmetry and/or extensions of the MSSM [12], this decay is completely ineffective in our case. As we shall see, the experimental lower bounds on supersymmetric masses and the constraints coming from the requirement of radiative breaking of the electroweak gauge group push already $m_{H^\pm}$ to be larger than $\tan\beta$ (in GeV).

Similarly, the combined limit $m_{H^\pm}$-$\tan\beta$ recently set by CDF [3] by measuring energetic jets coming from b-quarks and hadronically decaying τ's (only the mode $H^- \to \tau^-\nu_\tau$ is considered), does not affect the regions of parameter space which we obtain in our MSSM simulation.

As in [1], also in this analysis, the only effective experimental bounds are those coming from direct searches of supersymmetric particles and from the decay $b \to s\gamma$.

In agreement with results coming from LEP I, LEP1.5 [13], and the TEVATRON, the cuts which we apply to the masses of gluinos $\tilde{g}$, charginos $\tilde{\chi}^\pm$, neutralinos $\tilde{\chi}^0$, charged and neutral sleptons $\tilde{l}$, $\tilde{\nu}$, up- and down-squarks $\tilde{u}$, $\tilde{d}$, and neutral Higgses (with h^0_s the lightest of the two CP-even states, h_3 the CP-odd state and $H^\pm$ the charged Higgs) are (in GeV): $m_{\tilde{g}} > 150$, $m_{\tilde{\chi}^\pm_{1,2}} > 150$, $m_{\tilde{u}_i} > 45$, $m_{\tilde{\chi}^0_2} > 60$, $m_{\tilde{\nu}_i} > 45$, $m_{\tilde{l}^\pm_i} > 45$, $m_{h^0_s} > 45$, $m_{h^0_3} > 20$, $m_{H^\pm} > 45$, $m_{\tilde{\chi}^0_1} > 20$. For the limit on the mass of the stop-squark we rely on searches at LEP since the decay $\tilde{u}_i \to t + \tilde{\chi}^0_1$ is forbidden or disfavoured at the TEVATRON. The limit on the mass of $\tilde{\chi}^0_1$, in general higher than the one obtained at LEP, is naturally induced in the MSSM by the limit on the $\tilde{\chi}^\pm_1$-mass. Finally, the inclusion of radiative corrections to the Higgs potential and the subsequent modification of the tree-level sum rules for the Higgs-masses force us to impose individual lower bounds for all Higgs particles.

The situation which the Next Linear e^+e^- Collider may have to face if supersymmetric particles remain undiscovered at LEP II can be mimicked by imposing the following

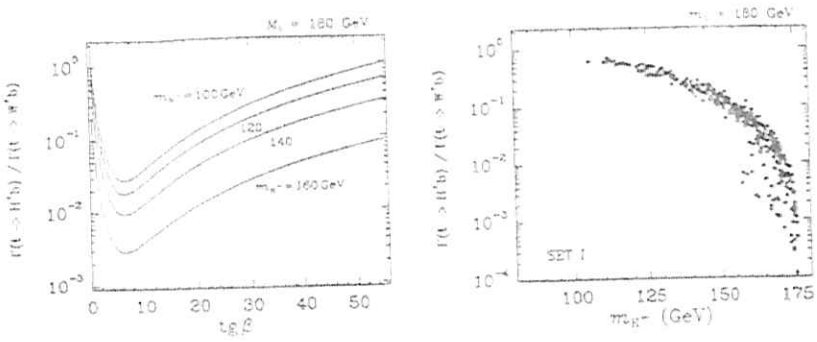

Figure 1: Rates for $t \to H^+b$ in a generic model with SUSY type of Higgs-couplings and in the MSSM

bounds [14] (in GeV): $m_{\tilde{g}} > 200$, $m_{\tilde{q}_{1,2,3}} > 200$, $m_{\tilde{\chi}^\pm_1} > 85$, $m_{\tilde{\chi}^0_2} > 85$, $m_{\tilde{\nu}_i} > 85$, $m_{\tilde{l}^\pm_i} > 85$, $m_{h^0_s} > 85$, $m_{h^0_3} > 40$, $m_{H^\pm} > 85$, $m_{\tilde{\chi}^0_1} > 40$. We assume that the TEVATRON limits on squarks and gluino masses will not increase more than 50 GeV. In the following we refer to these two choices of bounds as SET I and SET II.

Finally, we impose the constraints set by the CLEO Collaboration on $b \to s\gamma$: $1 \cdot 10^{-4} < BR(b \to s\gamma) < 4.2 \cdot 10^{-4}$ [15]. The evaluation of $BR(b \to s\gamma)$ is in accordance to [16]; the uncertainty associated to the theoretical prediction (due primarely to the ambiguity in the renormalization scale and to the experimental errors on parameters entering in the calculation) is estimated according to [17].

2. Results: phase spaces and widths

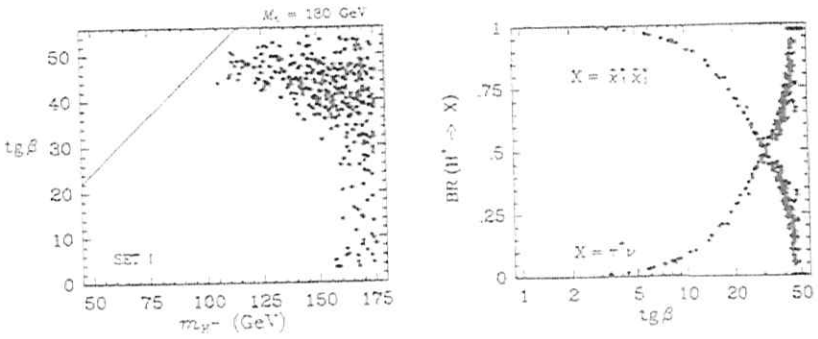

Figure 2: Allowed phase space for $t \to H^+b$ and branching ratios for the decays $H^+ \to \tilde{\chi}^\pm_2 \tilde{\chi}^0_1$, $H^+ \to \tau^+\nu_\tau$

We present in the following the results which we obtain in the MSSM for the two decay modes $t \to H^+b$ and $t \to \tilde{u}_1\tilde{\chi}^0_1$. No QCD or supersymmetric corrections are included

in the calculation of the rates. We show our results separetely before and after imposing the $b \to s\gamma$ constraints.

We show in the first frame of Fig. 1 the m_{H^+} and $\tan\beta$ dependence for the rate $\Gamma(t \to H^+ b)/\Gamma(t \to W^+ b)$ in a model with two Higgs doublets and type II Higgs couplings. The typical minimum for intermediate values of $\tan\beta$ ($2 < \tan\beta < 9$) is displayed, as well as the following steady increase for increasing $\tan\beta$. The second frame shows the rates obtained in our simulation when the experimental constraints SET I are imposed. The relative phase space for this decay is shown in the first frame of Fig. 2 where, for completness, we also display the line $\tan\beta(\mathrm{GeV})/m_{H^+} = 0.5$: the region excluded by the decay $b \to c\tau\nu_\tau$ lies above it. The H^+-masses shown in these figures correspond, in general, to values of $|\mu| \sim 150\,\mathrm{GeV}$ and $150 \lesssim |\mu| \lesssim 300\,\mathrm{GeV}$ for $\tan\beta \lesssim 30$.

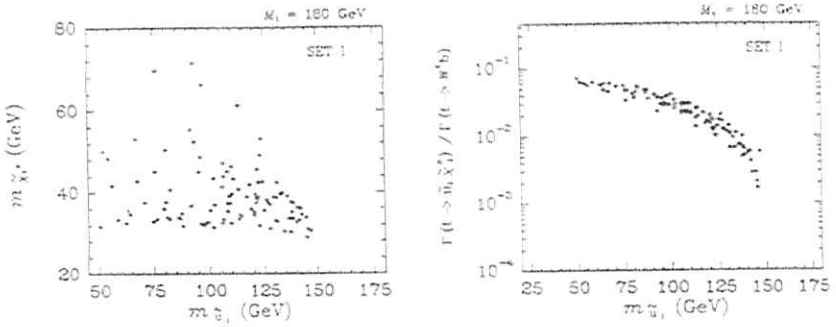

Figure 3: Region of parameter space where $t \to \tilde{u}_1\tilde{\chi}_1^0$ is kinematically accessible and relative rates

The shape of the phase space obtained has not been drastically affected by the inclusion of radiative corrections to the Higgs potential, with respect to the phase space shown in [1, 7]. The reduction in the size of this area is due to the increase of the experimental lower bounds imposed in this search and to the slightly heavier spectrum of the Higgs-mass parameters used here. As in [1], we find that the largest rates are obtained for the largest values of $\tan\beta$ where also the lightest H^+ are found. The second frame of Fig. 2 shows the branching ratios for the two possible decay modes of the produced H^+. The mode $\tau\nu_\tau$ saturates the total width for H^+ only for very large $\tan\beta$.

Wider regions of the supersymmetric parameter space need to be scanned to obtain the points where the decay $t \to \tilde{u}_1\tilde{\chi}_1^0$ is kinematically accessible. They correspond to large A and large $|\mu|$ and they are shown in Fig. 3, together with the relative widths. In the lower part of the region, the decay of $\tilde{u}_1$ into an on-shell chargino is still possible. The set of viable points in this figure is disjoint from that where $t \to H^+ b$ is allowed, i.e. the corresponding values of m_{H^+} in the points of Fig. 3 are large, in general above 250 GeV. Therefore, the non-observation of one of the two decay modes, in general, does not affect the possibility of observing the other one.

We show in Fig. 4 what is left for the rates of the two decays once we impose that the

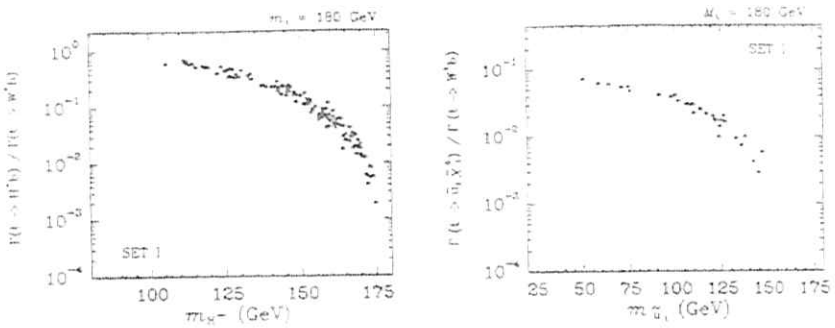

Figure 4: Rates still reachable after the present experimental constraint on $b \to s\gamma$ is imposed

lower theoretical estimate of $BR(b \to s\gamma)$ is $< 4.2 \cdot 10^{-4}$ and that the highest one is $> 1 \cdot 10^{-4}$, for each point of the MSSM parameter space (see for example discussion in [18]). This figure summarizes our prediction for these rates in the MSSM when all experimental constraints existing at present are imposed. We should warn the reader, however, that of the two, the prediction for $t \to H^+ b$ is the most "stable". It does not change very much if the band of allowed values for $b \to s\gamma$ is slightly restricted (see for example the band obtained at 95% c.l. from the measurement $BR(b \to s\gamma) = (2.32 \pm 0.57 \pm 0.35) \cdot 10^{-4}$ [15] when adding statistic and systematic errors in quadrature), whereas the allowed region for $t \to \tilde{u}_1\tilde{\chi}_1^0$ tends to shrink.

Our results for $t \to H^+ b$ are in qualitative agreement with those obtained in [19] where, however, milder lower bounds on supersymmetric particles are imposed.

3. Discussion and Future Prospects

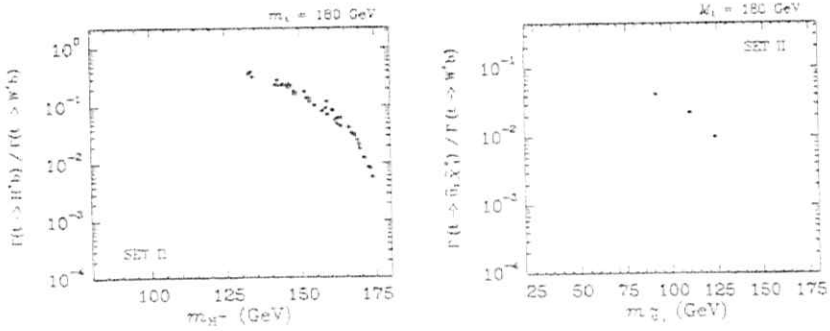

Figure 5: Same as in Fig. 4 when the lower bounds on supersymmetric masses SET II are imposed

As shown in the previous figures, rather large rates for $t \to H^+ b$ can be accomodated

within the MSSM at the moment. The largest values for $\Gamma(t \to H^+ b)/\Gamma(t \to \tilde{u}_1 \tilde{\chi}_1^0)$ may turn out to be excluded in future searches at the TEVATRON. More precision in the experimental measurement and in the theoretical calculation of $BR(b \to s\gamma)$ (through the inclusion of NLO QCD corrections) may completely close the second decay-mode $t \to \tilde{u}_1 \tilde{\chi}_1^0$. The same effect can be induced by an increase in the lower bounds on supersymmetric masses which LEP II and the TEVATRON will be able to put if no supersymmetric particle are detected in the meantime. We show in Fig. 5 our predictions for the two decays when the lower bounds SET II are imposed, together with the present limit on $b \to s\gamma$.

We conclude noticing that the consequences of the non-observation of $t \to H^+ b$ will not be drastic for the MSSM (since the regions of parameter space where $m_{H^+} < M_t$ are indeed not very large), whereas they may turn out to be interesting for models where the strong correlations of the MSSM parameter space are absent.

4. Acknowledgements

We acknowledge useful discussions with S. Bertolini, M. Carena, A. Djouadi, M. Drees, Y. Grossman, H. Haber, R. Hempfling, Y. Nir, and F. Vissani. We also thank G. Wolf, L. Lyons, E. Kovacs, K. Maeshima, and C. Couyoumtzelis for providing informations concerning charged Higgs searches.

References

[1] F.M. Borzumati, in Proceedings of the Workshop Munich, Annecy, Hamburg, November 1992 to April 1993, P.M. Zerwas (Ed.), DESY 93-123C, December 1993

[2] F. Abe et al., CDF Collaboration, *Phys. Rev. Lett.* **74** (1995) 2626
S. Abachi et al., D0 Collaboration, *Phys. Rev. Lett.* **74** (1995) 2632

[3] F. Abe et al., CDF Collaboration, FNAL preprint, FNAL-PUB-96/004-E (1996), **hep-ex/9601003**

[4] N. Polonsky, Munich University preprint, LMU-TPW-96-04 (1996), **hep-ph/9602206**

[5] P. Langacker and N. Polonsky, *Phys. Rev.* **D 50** (1994) 2199

[6] A. Brignole, *Phys. Lett.* **B 277** (1992) 313

[7] F.M. Borzumati, *Zeit. für Physik* **C 63** (1994) 291

[8] A. Brignole, J. Ellis, G. Ridolfi, and F. Zwirner, *Phys. Lett.* **B 271** (1991) 123

[9] H.E. Haber, R. Hempfling, and A.H. Hoang, CERN preprint, CERN-TH/95-216 (1995)

[10] M. Drees and M.M. Nojiri, *Phys. Rev.* **D 45** (1992) 2482

[11] Y. Grossman, H. Haber, and Y. Nir, *Phys. Lett.* **B 357** (1995) 630

[12] G.L. Kane and J.D. Wells, *Phys. Rev. Lett.* **76** (1996) 869

[13] G. Alexander et al., OPAL Collaboration, CERN preprint, CERN-PPE/96-020 to appear in *Phys. Lett.* B

[14] LEPII Physics Reports, G. Altarelli, T. Sjostrand and F. Zwirner (Eds.)

[15] M.S. Alam, CLEO Collaboration, *Phys. Rev. Lett.* **74** (1995) 2885

[16] S. Bertolini, F.M. Borzumati, A. Masiero, and G. Ridolfi, *Nucl. Phys.* **B 353** (1991) 591

[17] A.J. Buras, M. Misiak, M. Munz, and S. Pokorski, *Nucl. Phys.* **B 424** (1994) 374

[18] F.M. Borzumati, M. Drees, and M.M. Nojiri, *Phys. Rev.* **D 51** (1995) 27

[19] T. Goto and Y. Okada, KEK preprint, KEK-TH-468, TU-494 (1996), **hep-ph/9601368**

CP Nonconservation in Top Quark Production by (Un) Polarized e^-e^- and $\gamma\gamma$ Collisions

W. Bernreuther[a], A. Brandenburg[a], and P. Overmann[b]

[a]Institut f. Theoretische Physik, RWTH Aachen, D-52056 Aachen, Germany
[b]Institut f. Theoretische Physik, Universität Heidelberg, D-69120 Heidelberg, Germany

Abstract:
We report on an investigation of CP violation in (un)polarized $e^-e^- \to \bar{t}t$ resulting from an extended neutral Higgs sector or from the minimal SUSY extension of the Standard Model (SM). We consider c.m. energies from the $\bar{t}t$ threshold to the TeV range. In addition sensitivity estimates for CP-violating form factors of the top quark are made. Further we discuss the prospects of probing Higgs sector CP violation in $\gamma\gamma \to \bar{t}t$.

1 Introduction and Summary

In recent years quite a number of proposals have been made on how top quarks can serve as probes of CP-violating interactions beyond the Kobayashi-Maskawa (KM) mechanism ([1]-[17]). Model-independent analyses in terms of form factors can be found in [1, 2, 5, 7, 8, 10, 12]. Here we report on the results of an investigation of CP-violating interactions from an extended Higgs sector and from the minimal supersymmetric extension of the SM and their effects on $\bar{t}t$ production (and decay) at a linear collider. First we consider $e^-e^- \to \bar{t}t$. The new features of this study, as compared to previous work [1, 5], are: we take into account the possibility of longitudinally polarized electron beams which enhance some of the effects, and we propose and study optimized observables with maximal sensitivity to CP effects for "semileptonic" $t\bar{t}$ events. For the Higgs model we find: (a) The highest sensitivities are reached somewhat above the $t\bar{t}$ threshold. (b) Longitudinal electron polarization would be an asset; yet the sensitivity of our best observable depends only weakly on the electron polarization. In the above models the effects in $e^-e^- \to t\bar{t}$ are due to non-resonant radiative corrections and are therefore not easy to detect. If a light Higgs boson φ with mass $m_\varphi < 200$ GeV and sizable CP-violating couplings to top quarks exists then there is a chance to see a signal at a collider with 50 fb^{-1} integrated luminosity. It would obviously be more promising to check for CP violation directly in φ decays [14, 15]. Effects in $t\bar{t}$ production due to a CP phase in gluino exchange are too small to produce statistically significant signals.
In addition we have also investigated how well one could measure in the reactions (1), (2), (3) below the CP-violating form factors of the top quark with our optimized observables. Results are given in section 2. Of course, the sensitivity to the (dimensionful) form factors

increases considerably with the c.m. energy and with the availability of beam polarization. (See also [1, 12].)
High energetic photon-photon collisions [21], which are discussed in the context of a linear collider, may provide, among other things, an interesting possiblity to produce neutral Higgs bosons and study their quantum numbers. In the framework of two-Higgs doublet extensions we have investigated CP violation in unpolarized $\gamma\gamma \to \bar{t}t$ which includes resonant Higgs boson production and decay into $\bar{t}t$. Here the effects can be much larger than in e^-e^--annihilation. If one or more Higgs bosons of intermediate mass 300 GeV $\lesssim m_\varphi \lesssim$ 500 GeV exist we find that $\gamma\gamma \to \varphi \to \bar{t}t$ would be a promising channel to study its/their CP properties. Sensitivity estimates will be given in section 3. For a detailed exposition of our studies and further references see [6, 17].

2 $e^-e^- \to \bar{t}t$

In this section we consider the production of a top quark pair via the collision of an unpolarized positron beam and a longitudinally polarized electron beam:

$$e^-(\mathrm{e}_-) + e^-(\mathrm{e}_-, p) \quad \to \quad t(\mathrm{k}_t) + \bar{t}(\mathrm{k}_{\bar{t}}). \tag{1}$$

Here p is the longitudinal polarization of the electron beam ($p = 1$ refers to right handed electrons). For our purposes the most interesting final states are those from semileptonic t decay and non-leptonic $\bar{t}$ decay and vice versa:

$$t\,\bar{t} \quad \to \quad \ell^-(\mathrm{q}_-) + \nu_\ell + b + \overline{X}_{\mathrm{had}}(\mathrm{q}_X), \tag{2}$$

$$t\,\bar{t} \quad \to \quad X_{\mathrm{had}}(\mathrm{q}_X) + \ell^-(\mathrm{q}_-) + \bar{\nu}_\ell + \bar{b}\ , \tag{3}$$

where the 3-momenta in eqs. (1) - (3) refer to the e^-e^- c.m. frame.
CP-violating interactions can affect the $\bar{t}t$ production and decay vertices. Quantum mechanical interference of the CP-even and -odd parts of the amplitudes for the above reactions then lead to the correlations which we are after. For CP-nonconserving neutral Higgs boson couplings and for CP-nonconserving gluino-quark-squark couplings it has been shown [5] that these interactions lead to larger effects in $\bar{t}t$ production than in t (and $\bar{t}$) decay. Therefore we consider observables which are predominantly sensitive to CP effects in the production amplitude which, in these SM extensions, arise at 1-loop through induced electric and weak dipole form factors $\hat{d}^{\gamma,Z}(s)$. The real parts $\mathrm{Re}\hat{d}^{\gamma,Z}$ generate a difference in the t and $\bar{t}$ polarizations orthogonal to the scattering plane of reaction (1), whereas non-zero absorptive parts $\mathrm{Im}\hat{d}^{\gamma,Z}$ lead to a difference in the t and $\bar{t}$ polarizations along the top direction of flight. The class of events (2), (3) is highly suited to trace these spin-momentum correlations in the $\bar{t}t$ production vertex through final state momentum correlations: From the hadronic momentum in (2),(3) one can reconstruct the $\bar{t}$ and t momentum, respectively and hence the rest frames of these quarks. The extremely short life time of the top quark implies that the top polarization is essentially undisturbed by hadronization effects and can be analyzed by its parity-violating weak decay $t \to b + W$, which we assume to be the dominant decay mode. Further, the charged lepton from semileptonic top decay is known to be by far the best analyzer of the top spin [18]. Therefore our observables are chosen to be functions of the directions of the

hadronic system from top decay, of the charged lepton momentum, of the positron beam direction, and of the c.m. energy $\sqrt{s}$. In order to increase the statistical sensitivity of the observables we shall use the lepton unit momenta $\hat{q}^*_\pm$ in the corresponding top rest frames, which are directly accessible in the processes (2), (3).
The CP "asymmetries" which we discuss are differences of expectation values

$$\mathcal{A} \;=\; \langle \mathcal{O}_-(s, \hat{q}^*_-, \hat{q}_{\bar{X}}, \hat{e}_-)\rangle - \langle \mathcal{O}_-(s, \hat{q}^*_-, \hat{q}_X, \hat{e}_-)\rangle \quad , \tag{4}$$

where the mean values refer to events (2), (3) respectively. For instance, $\mathcal{O}_- = (\hat{q}^*_- \times \hat{q}_X)\cdot \hat{e}_-$. The observable $\mathcal{O}_-$ is defined to be the CP image of $\mathcal{O}_-$. It is obtained from $\mathcal{O}_-$ by the substitutions $\hat{q}_{\bar{X}} \to -\hat{q}_X$, $\hat{q}^*_- \to -\hat{q}^*_-$, $\hat{e}_- \to e_-$. The ratio

$$r \;=\; \frac{\langle \mathcal{O}_-\rangle - \langle \mathcal{O}_-\rangle}{\Delta \mathcal{O}_-} \tag{5}$$

is a measure of the statistical sensitivity of $\mathcal{O}$. Here $\Delta\mathcal{O} = \sqrt{\langle \mathcal{O}^2\rangle - \langle \mathcal{O}\rangle^2}$. For the observables used in this paper we have $\Delta\mathcal{O} \approx \sqrt{\langle \mathcal{O}^2\rangle}$ and $\Delta\mathcal{O}_- \simeq \Delta\mathcal{O}_+$. The signal-to-noise ratio of $\mathcal{A}$ is given by $S_{\mathcal{A}} = |r|\sqrt{N_{event}}/\sqrt{2}$, where N_{event} is the number of events of type (2) or (3).
In [6] explicit expressions are given for two observables $\mathcal{O}_\pm(1), \mathcal{O}_\pm(2)$ with optimized sensitivity $|r|$, and these observables pick up dispersive ($\mathrm{Re}\hat{d}_t^{\gamma\bar{Z}}$) and absorptive ($\mathrm{Im}\hat{d}_t^{\gamma\bar{Z}}$) CP effects, respectively. In addition to the functional dependence exhibited in (4) they depend also on the electron beam polarization p. As the expressions are somewhat lengthy we do not reproduce them here. Schematically an optimized observable is constructed as follows: Consider a differential cross section which is of the form $d\sigma = d\sigma_0 + \lambda d\sigma_1$ where λ is a small parameter. One can show [8, 19] that the observable with the highest statistical sensitivity is given by $\mathcal{O} = d\sigma_1/d\sigma_0$.
We shall consider phase space cuts which are CP-symmetric. When the e^-e^- beams are unpolarized (or transversely polarized) the asymmetries (4) can be classified as being odd under a CP transformation. This means that contributions to $\langle \mathcal{O}_\pm\rangle$ from CP-invariant interactions cancel in the difference. If the electron beam is longitudinally polarized the initial e^-e^- state is no longer CP-symmetric in its c.m. frame and the CP classification no longer applies. Contributions from CP-conserving interactions can, in principle, contaminate $\mathcal{A}$ if $p \neq 0$. However, in practice, this is not a problem because it can be argued that SM interactions induce contaminations at the per mill level [6]. On the other hand only ratios $|r| > 0.01$ have a chance to be detectable even at a high luminosity linear collider.
We now recall the salient features of neutral Higgs sector CP violation. For definiteness we consider two-doublet extensions of the SM with explicit CP violation in the Yukawa couplings (which leads to the Kobayashi-Maskawa phase) and in the Higgs potential. As a consequence the three physical neutral Higgs boson states $\varphi_{1,2,3}$ are in general states with indefinite CP parity; i.e. they couple both to scalar and pseudoscalar quark and lepton currents with strength $a_{jf}m_f/v$ and $\tilde{a}_{jf}m_f/v$, respectively, where m_f is the fermion mass and $v \simeq 246$ GeV. For the top quark we have $a_{jt} = d_{j2}/\sin\beta$, $\tilde{a}_{jt} = -d_{j3}\cot\beta$, where $\tan\beta = v_2/v_1$ is the ratio of the moduli of the vacuum expectation values of the two doublets, and d_{j2}, d_{j3} are the matrix elements of a 3×3 orthogonal matrix which describes the mixing of the neutral Higgs states of definite CP parity. Only the CP=+1 components of the mass eigenstates φ_j couple to the W, Z, and charged Higgs bosons at the Born level. (For notation and details, see [3].)

CP violation requires that the neutral Higgs bosons are not mass-degenerate. Only if one of the bosons, say φ_1, is rather light then there is a chance that effects are detectable in $e^+e^- \to t\bar{t}$. For the evaluation of the ratios r shown in Figs.1 we have put m_{φ_1}=100 GeV and have assumed that $m_{\varphi_{2,3}} >> m_{\varphi_1}$. Then the effect of $\varphi_{2,3}$ on the dipole form factors is negligible. The EDM form factor and, to a good approximation [3], the WDM form factor of the top are proportional to $\gamma_{CP} = -a_{1t}\tilde{a}_{1t}$ which is a measure of the strength of CP violation induced by φ_1 exchange. One may assume maximal CP violation in the neutral Higgs sector by putting $d_{i1} = 1/\sqrt{3}$ $(i = 1, 2, 3)$. The product γ_{CP} increases with decreasing $\tan\beta$. Phenomenologically the experimental upper bounds on the neutron and electron EDMs give the rough upper bound $|\gamma_{CP}| \leq 5$. Nevertheless it would be interesting to obtain from the top system direct information on γ_{CP}.
In Figs.1 we have plotted the ratios $r_{1,2}$ for the optimized dispersive and absorptive observables $\mathcal{O}_\pm(1), \mathcal{O}_\pm(2)$ defined in [6]. We have put $m_t = 180$ GeV, $m_{\varphi_1} = 100$ GeV, and $\gamma_{CP} = 1$. The ratios $r_{1,2}$ are directly proportional to γ_{CP}.

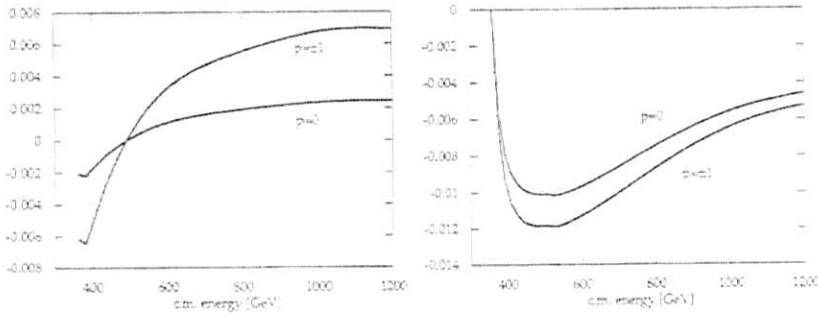

Fig 1: Ratios r_1 (left figure) and r_2 (right figure) for the optimized dispersive and absorptive observables $\mathcal{O}_\pm(i)$, $i = 1, 2$ defined in [6] for $m_t = 180$ GeV, $m_{\varphi_1} = 100$ GeV, and $\gamma_{CP} = 1$.

Figs.1 show that the absorptive asymmetry has the highest sensitivity to γ_{CP} and that it depends only weakly on the beam polarization. The maximal sensitivity is reached at $\sqrt{s} \simeq 450$ GeV where $|r_2| = 1.2\%$ (1%) if p=±1 (0). In order to detect this as a 3 s.d. effect one would need 125000 (180000) events of the type (2) and of (3). These event numbers are unrealistically large. If the CP-violating effect is larger, say γ_{CP}=4, then only 1/16 of these events would be needed for a 3 s.d. signal. In order to reach a sensitivity $\geq$ 3 s.d. to couplings $|\gamma_{CP}| \geq 4$ an integrated luminosity of 50 fb^{-1} must be collected.
In general the asymmetries become smaller with increasing Higgs mass. If we keep γ_{CP} fixed but change the Higgs mass to m_φ=200 GeV then the maximal value at $\sqrt{s} \approx 450$ GeV of the ratio r_2 in Fig.1 is reduced by about 30%.
In summary, for light Higgs masses m_φ <200 GeV and sizable CP-violating coupling γ_{CP} there is a chance to see Higgs sector CP violation as an induced dipole moment effect in $t\bar{t}$ production. A light Higgs particle φ would also be produced at a linear collider. A consequence of φ not being a CP eigenstate would be a CP violation effect in the φ fermion-antifermion amplitude at Born level which could be detected in $\varphi \to \tau^+\tau^-$ [14].

(For further tests of the CP properties of Higgs particles, see [9, 15, 20].)
In the minimal supersymmetric extension of the SM additional CP-violating phases (besides the KM phase) can be present in the Majorana mass terms, e.g. of the gluinos, and in the squark (and slepton) mass matrices. For mass eigenstates these phases then appear for instance in the $t\bar{t}$ – gluino couplings in the form (flavour mixing is ignored)

$$\mathcal{L}_{\tilde{g}t\bar{t}} = i\sqrt{2}\; g_{QCD}\left\{e^{i\phi_t}\,\bar{t}_L T^a(\bar{\lambda}^a t_R) - e^{-i\phi_t}\,\bar{t}_R T^a(\bar{\lambda}^a t_R)\right\} + h.c. \qquad (6)$$

with $\phi_t = \phi_\lambda - \phi_t$ and fields $\bar{t}_{R,L}$ which are related to the fields $\bar{t}_{1,2}$ corresponding to mass eigenstates by an orthogonal transformation. The 1-loop EDM and WDM form factors $d_t^{\gamma,Z}$ generated by (6) are proportional to $g^2_{\tilde{Q}CD}\sin(2\phi_t)$. We have computed these form factors and the resulting asymmetries (4) for the optimized observables $\mathcal{O}_\pm(1), \mathcal{O}_\pm(2)$ for maximal CP violation, $\sin(2\phi_t) = 1$, and a range of SUSY masses $m_\lambda, m_{\tilde{t}_{1,2}} \geq 150$ GeV. We have found [6] that the ratios $|r_{1,2}|\leq 0.01$. Hence it is unlikely that a statistically significant signal can be detected at a 50 fb^{-1} linear collider even for maximal SUSY CP violation. (Related studies were made in [13].)
Furthermore we also investigated how well one could measure $\mathrm{Re}d_t^{\gamma,Z}$ and $\mathrm{Im}d_t^{\gamma,Z}$ independent of any model. For this purpose we computed the corresponding ratios r for observables which, for a given polarization p, have optimized sensitivity to one of these form factors. Using an integrated luminosity of 20 fb^{-1} (50 fb^{-1}) at $\sqrt{s} = 500$ GeV (800 GeV) we estimate the 1 s.d. statistical errors given in Table 1. These numbers are to be multiplied with $1/\sqrt{\epsilon}$ where ϵ is the tagging efficiency for the channels (2), (3).

	20 fb^{-1}, $\sqrt{s} = 500$ GeV			50 fb^{-1}, $\sqrt{s} = 800$ GeV		
	$p = 0$	$p = -1$	$p = -1$	$p = 0$	$p = -1$	$p = -1$
$\delta\mathrm{Re}d_t^\gamma$	4.6	0.86	0.55	1.7	0.35	0.23
$\delta\mathrm{Re}d_t^Z$	1.6	1.6	1.0	0.91	0.85	0.55
$\delta\mathrm{Im}d_t^\gamma$	1.3	1.0	0.65	0.57	0.49	0.32
$\delta\mathrm{Im}d_t^Z$	7.3	2.0	1.3	4.0	0.89	0.58

Table 1: 1 s.d. sensitivities to the CP-violating form factors in units of 10^{-18} e cm.

Table 1 shows that the sensitivity to $\mathrm{Re}d_t^\gamma$ and to $\mathrm{Im}d_t^\gamma$ grows substantially with beam polarization. For a fixed number of $t\bar{t}$ events the sensitivity to the nonrenormalizable "couplings" $d_t^{\gamma,Z}$ obviously increases with increasing c.m. energy. However, one should keep in mind that the form factors vary with $\sqrt{s}$, and this variation is determined by thresholds which depend on the underlying dynamics of CP violation. If – like in the Higgs model – the relevant branch point where the form factors develop imaginary parts is set by the $t\bar{t}$ threshold then, as exemplified by Fig.1, there is no gain in going to very high energies. Needless to say: a priori one does not know.

3 $\gamma\gamma \to \bar{t}t$

After the discovery of a Higgs boson φ at some collider a high energetic "Compton collider" of high luminosity could be tuned to $\gamma\gamma \to \varphi$ in order to perform a detailed study of the φ quantum numbers (see,e.g.,[20]). If the photon polarizations are adjustable then one could check, as proposed in [16], for instance with the event asymmetry $(N(+,+1) - N(+,-1))/(N(+,+1) + N(+,-1))$ whether or not φ is a CP eigenstate. (Here $\pm$ refer to the photon helicities.) For unpolarized $\gamma\gamma \to \varphi$ the CP property of φ can be infered from the final states into which it decays. If φ is not a CP eigenstate then a CP-violating spin-spin correlation is induced in its fermionic decays already at the Born level, which can be as large as 0.5 [14]. It could be detectable in $\varphi \to \tau^+\tau^-$ and, for sufficiently heavy φ, in $\varphi \to \bar{t}t$. However, the narrow width approximation does not apply for a Higgs boson with mass in the vicinity or above the $t\bar{t}$ threshold and interference with the non-resonant $\gamma\gamma \to t\bar{t}$ amplitude decreases this spin-spin correlation significantly. In order to include also the case of light Higgs bosons φ below the $t\bar{t}$ threshold we have computed, for two-Higgs doublet extensions of the SM, the complete set of CP-nonconserving contributions to $\gamma\gamma \to t\bar{t}$ in one-loop approximation [17]. In the spin density matrix for $t\bar{t}$ production by unpolarized photon beams this leads to CP-violating dispersive contributions with the spin structure $\hat{\mathbf{k}}_t \cdot (\mathbf{s}_- \times \mathbf{s}_-)$ and to absorptive contributions which are of the form $\hat{\mathbf{k}}_t \cdot (\mathbf{s}_- - \mathbf{s}_-)$ and to similar terms where $\hat{\mathbf{k}}_t \to \hat{\mathbf{p}}_-$. Here $\mathbf{s}_-, \mathbf{s}_-$ are the spin operators of t and $\bar{t}$, respectively. The latter structures correspond to polarization asymmetries.
As in the case of $e^+e^- \to t\bar{t}$ these spin correlations and polarization asymmetries are most efficiently traced through the "semileptonic" $t\bar{t}$ decays (2) and the charge conjugated channels (3). The spin-spin correlation leads for events (2) to the triple product correlation $\mathcal{O}_- = (\mathbf{q}_- \times \hat{\mathbf{q}}^*_{b^-}) \cdot \hat{\mathbf{q}}_{\bar{X}}$. Here the asterisk denotes the $\bar{t}$ rest system. The CP-reflected observable $\mathcal{O}_-$ applies to the charge conjugated channels (3), and a non zero difference $\langle\mathcal{O}_-\rangle - \langle\mathcal{O}_-\rangle$ would be an unambiguous sign of CP violation. A CP asymmetry with a somewhat higher sensitivity to Higgs boson induced effects is

$$\mathcal{A}_{obs} = \langle\mathbf{q}_- \cdot \hat{\mathbf{q}}_{\bar{X}}\rangle - \langle\mathbf{q}_- \cdot \hat{\mathbf{q}}_X\rangle, \qquad (7)$$

which is a consequence of the single spin asymmetries.
For the calculation of these asymmetries we used the normalized photon distributions $N(x)$ with energy fraction $x = E_{photon}/E_{beam}$ as given, e.g. in [21, 22]. The maximal energy fraction of a photon x_{max} is determined by the laser energy $x_{max} = z/(1+z)$ with $z = 4E_{beam}E_{Laser}/m_e^2$. For a given beam energy the laser energy is chosen such that z reaches its maximal value. This value is determined by the threshold for unwanted e^+e^- pair production through annihilation of a backscattered photon with a laser photon. One gets $x_{max} \simeq 0.8284$.
Our result for the ratio r based on the asymmetry (7) is shown in Fig.2 for e^+e^- c.m. energy $\sqrt{s}$= 500 GeV and m_t=180 GeV as a function of the Higgs boson mass m_φ for two sets of parameters: $d_{11} = 1/\sqrt{3}$, $\tan\beta$=0.627 (set 1, solid line) and $d_{11} = 1/\sqrt{3}$, $\tan\beta$=0.3 (set 2, dashed line). These two sets correspond to γ_{CP}=1 and γ_{CP}=3.87, respectively. In contrast to $e^+e^- \to t\bar{t}$ we have here a complicated dependence of the asymmetries on the Higgs boson couplings, because the diagrams in which the φ propagator can become resonant contain also bosonic loops, and because in the resonant φ propagator the total width Γ_φ enters. The asymmetry $\mathcal{A}_{obs}$ has an extremum when the Higgs mass is close to the $t\bar{t}$ threshold due to large interference effects and an additional extremum when the Higgs mass is close to the maximal $\gamma\gamma$ energy. Even for a Higgs with mass above the maximal $\gamma\gamma$ energy there remains a significant interference effect that might be detectable.

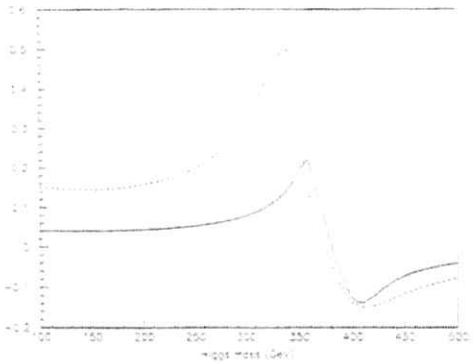

Fig 2: The ratio r for the asymmetry $\mathcal{A}_{obs}$ as a function of the Higgs mass m_φ at $\sqrt{s}$ = 500 GeV. The solid (dashed) line corresponds to the parameter set 1 (set 2).

One may also determine, for a given Higgs mass, the e^-e^- collider energy that maximizes the signal-to-noise ratio of an asymmetry. We have done this for $\mathcal{A}_{obs}$ and the parameter set 1. The results are listed in Table 2. In brackets we also give the numbers for set 2. (Note that S is not optimized with respect to this set.) In computing the number of events of the channels (2) or the charge conjugated channels (3) we use as in sect.1 semileptonic top decays into electrons, muons, and tauons.

m_φ [GeV]	$\sqrt{s_{opt}}$ [GeV]	$N_{events}/\left(\mathcal{L}/(100\ \mathrm{fb}^{-1})\right)$	$S/\sqrt{\mathcal{L}/(100\ \mathrm{fb}^{-1})}$
100	700	$5.97(5.35) \times 10^3$	1.8(5.4)
150	700	$5.96(5.31) \times 10^3$	1.8(5.3)
200	700	$5.93(5.21) \times 10^3$	1.9(5.5)
250	680	$5.44(4.70) \times 10^3$	2.1(6.1)
300	650	$4.67(3.84) \times 10^3$	2.6(7.5)
325	630	$4.10(3.30) \times 10^3$	3.0(8.9)
350	570	$2.39(2.32) \times 10^3$	4.0(11.4)
375	600	$3.41(4.27) \times 10^3$	4.4(8.8)
400	710	$6.18(6.42) \times 10^3$	3.6(7.7)
425	520	$1.87(2.31) \times 10^3$	3.7(4.7)
450	560	$3.02(3.39) \times 10^3$	3.4(4.5)
475	580	$3.58(3.85) \times 10^3$	3.3(4.2)
500	610	$4.38(4.58) \times 10^3$	2.9(3.7)

Table 2: Optimal collider energies, number of events of samples (2) or (3), and statistical significance S of $\mathcal{A}_{obs}$ for some Higgs masses and parameter set 1. The numbers in brackets are for set 2.

Table 2 tells us, for example, that if m_φ = 350 GeV (and if set 1 applies), one gets the largest sensitivity to the CP asymmetry $\mathcal{A}_{obs}$ at a collider energy of 570 GeV. For an integrated e^-e^- luminosity of 50 fb^{-1} (and an $e\gamma$ conversion rate of one) we then get

a statistical significance S of 2.8(5.0). By using an optimized observable instead of $\mathcal{A}_{obs}$ the sensitivity could still be enhanced. Should Higgs boson(s) of intermediate mass be discovered then, as our study shows, $e^-e^- \to \varphi \to t\bar{t}$ is a promising channel for probing Higgs sector CP violation.

References

[1] W. Bernreuther, O. Nachtmann, P. Overmann, T. Schröder: Nucl. Phys. B388 (1992) 53; ibid. B406 (1993) 516 (E)

[2] G.L. Kane, G. A. Ladinsky, C.-P. Yuan: Phys. Rev. D45 (1991) 124

[3] W. Bernreuther, T. Schröder, T.N. Pham: Phys. Lett. B279 (1992) 389

[4] C.R. Schmidt, M.E. Peskin: Phys. Rev. Lett. 69 (1992) 410

[5] W. Bernreuther, P. Overmann: Z. Phys. C61 (1994) 599

[6] W. Bernreuther, P. Overmann: preprint hep-ph/9511256, to appear in Z. Phys. C

[7] T. Arens, L.M. Sehgal: Phys. Rev. D50 (1994) 4372

[8] D. Atwood, A. Soni: Phys. Rev. D45 (1992) 2405

[9] S. Bar-Shalom et al.: preprint SLAC-PUB-95-6981 (1995)

[10] J.P. Ma, A. Brandenburg: Z. Phys. C56 (1992) 97; A. Brandenburg, J.P. Ma: Phys. Lett. B298 (1993) 211

[11] B. Grzadkowski: Phys. Lett. B305 (1993) 384

[12] F. Cuypers, S.D. Rindani: Phys. Lett. B343 (1995) 333; S. Poulose, S.D. Rindani: Phys. Lett. B349 (1995) 379; preprint hep-ph/9509299

[13] A. Bartl, E. Christova, W. Majerotto: Wien preprint HEPHY-PUB 624/95 (1995)

[14] W. Bernreuther, A. Brandenburg: Phys. Lett. B314 (1993) 104

[15] V. Barger, K. Cheung, A. Djouadi, B. Kniehl, P. Zerwas: Phys. Rev. D49 (1994) 79

[16] B. Grzadkowski, J.F. Gunion: Phys. Lett. B294 (1992) 361

[17] H. Anlauf, W. Bernreuther, A. Brandenburg: Phys. Rev. D52 (1995) 3803, Erratum to be published

[18] A. Czarnecki, M. Jezabek, J.H. Kühn: Nucl. Phys. B351 (1991) 70

[19] M. Diehl, O. Nachtmann: Z. Phys. C62 (1994) 397

[20] M. Kremer, J. Kühn, M. Stong, P. Zerwas: Z. Phys. C64 (1994) 21

[21] I.F. Ginzburg et al.: Nucl. Instrum. Meth. 205 (1983) 47; ibid. Vol. 219 (1984) 5; V.I. Telnov, Nucl. Instr. Meth. 294 (1990) 72

[22] J.H. Kühn, E. Mirkes, J. Steegborn: Z. Phys. C57 (1993) 615

The physics of the $e^+e^- \to t\bar{t}$ threshold scan*

Pere Comas, Ramon Miquel
CERN, PPE Division
CH-1211, Geneve 23

Manel Martinez, Salvador Orteu
IFAE, Universitat Autonoma de Barcelona
E-08193 Bellaterra (Barcelona)

Abstract

The physics of the top-antitop threshold is reexamined under the light of the new knowledge of the top mass. It is found that the combined measurement of the $t\bar{t}$ cross section, top momentum distribution and forward-backward charge asymmetry in a scan around the threshold region allows a simultaneous determination of the top quark mass and α_s with uncertainties 200 MeV and 0.005 respectively, for an integrated luminosity of 50 fb^{-1}. A one-parameter fit to the top quark width results in its determination with an 18% precision. Finally, the sensitivity of the $t\bar{t}$ cross section to the top Yukawa coupling has been found to be enough to measure it to $\pm 30\%$ of its value, for Higgs masses around 100 GeV.

1. Introduction

During the 1991 and 1993 Workshops on e^+e^- Collisions at 500 GeV, detailed studies of the physics capabilities of the measurements at the top-antitop threshold have been performed [1, 2], incorporating realistic detector and beam-related effects, experimental efficiencies and backgrounds. The studies were based on the measurement of both the total $t\bar{t}$ cross section and the top quark momentum distribution and focused on the determination of the top quark mass, m_t, and the strong coupling constant, α_s, appearing in the $t\bar{t}$ binding potential.

At that time most of the studies were done assuming a top quark mass of 150 GeV. After the discovery of the top quark at FNAL [3], one of the purposes of this work has been to update those results for the currently favoured value of the top mass, around 180 GeV. Also the continuous development of the accelerator designs leads to revised estimates for the luminosity available and for the specific beam parameters that affect the shape of the threshold region. The new design for the TESLA project [4] has been used here. The results of the updated analysis are presented in section 2.

Recently, several authors [5, 6] have presented calculations of the $t\bar{t}$ forward-backward charge asymmetry, A_{FB}, around the threshold region. The asymmetry comes from the overlap between the S- and P-wave $t\bar{t}$ states, and depends on the relative size of this overlap and the top decay width. Therefore, A_{FB} is expected to be sensitive to the $t\bar{t}$ potential and to the top quark width. An experimental study of the potential of the A_{FB} measurement is contained in section 3.

*Presented by P. Comas.

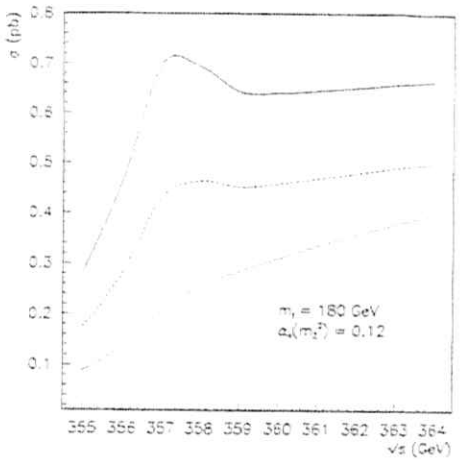

Figure 1: $t\bar{t}$ production cross section as a function of the centre-of-mass energy. Solid line: Born cross section; dashed line: with initial state radiation (ISR); dotted line: with ISR and beam effects, computed with the parameters of the TESLA accelerator design [4].

Apart from m_t and α_s, there are several parameters which influence the $t\bar{t}$ threshold region. Among them, the top quark width and the top Yukawa coupling are studied in sections 4 and 5, respectively.

2. Cross section and momentum distribution

The top quark decay width increases with the third power of the top quark mass:

$$\Gamma_t \sim 0.18 \text{ GeV} \left(\frac{m_t^3}{M_W^3} \right).$$

For a top mass of 180 GeV, Γ_t is about 2 GeV, to be compared to 1.2 GeV for m_t = 150 GeV. This increase in the top width will lead to a threshold excitation curve with less prominent features and a subsequent loss in sensitivity to the top mass and α_s.

The shape of the $t\bar{t}$ cross section near threshold for m_t = 180 GeV as predicted by the computer program TOPPIK [7] can be seen as the Born cross section in fig. 1. Also shown in fig. 1 is the effect of the inclusion of initial state radiation corrections. They lower the cross section significantly and smear the resonance peak. Finally, the effects of beamstrahlung and beam-energy spread according to the latest TESLA design [4] are also shown, washing out all remnants of structure at the threshold.

Figure 2 shows the distribution of the momentum of the top quarks produced at a centre-of-mass energy of 360 GeV, obtained also with TOPPIK. It can be seen that

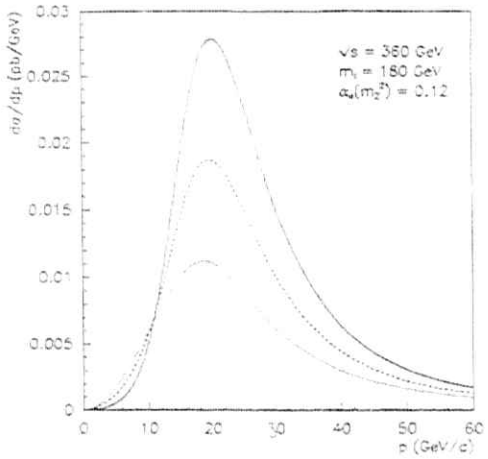

Figure 2: Top momentum distribution at $\sqrt{s} = 360$ GeV. Solid line: Born cross section; dashed line: with initial state radiation (ISR); dotted line: with ISR and beam effects, computed with the parameters of the TESLA accelerator design [4].

both initial state radiation and beam effects have a dramatic effect in the width of the distribution, while approximately preserving the position of its maximum. For this reason, the maximum is chosen as the variable that summarizes the information of the momentum distribution.

The simulated experimental analysis follows closely the line of the previous work [2]. The event selection used for the total cross section measurement is described in ref. [1]. The overall efficiency is 25% and the signal over background ratio is four. For the momentum measurement, the selection described in ref. [2] is used. It only uses events in which one of the Ws from a top decays leptonically, while the other decays hadronically. The lepton and missing energy are used to tag the event, while the hadronic top decay is used for the momentum determination. The efficiency relative to the total $t\bar{t}$ sample is 15%, with negligible background. The resolution in the top momentum is about 10%. The position of the peak of the momentum distribution can be obtained with a 5 GeV error for a luminosity of 5 fb^{-1}.

The total cross section and the maximum of the momentum distribution measured at nine equally-spaced centre-of-mass energy points between 356 and 364 GeV are used in a χ^2 fit with two free parameters: the top quark mass and $\alpha_s(M_Z)$. Systematic errors and correlations between measurements at different energies are included in the fit as explained in ref. [2]. Following the improvements in the accelerator designs, a luminosity of 5 fb^{-1} is assumed for each energy point, instead of the 1 fb^{-1} assumed

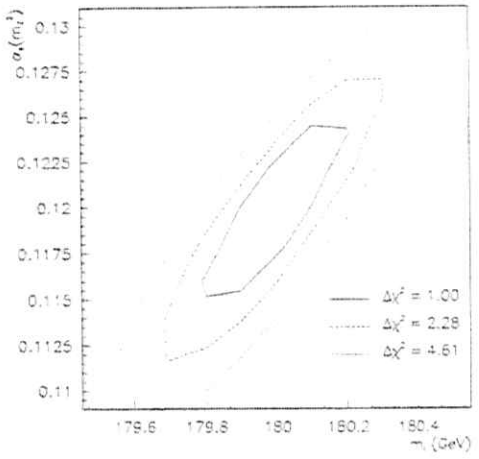

Figure 3: Results of the χ^2 fit using the total cross section and the momentum distribution.

previously [2]. Another 5 fb^{-1} are assumed to be taken below the threshold in order to measure the background. The statistical uncertainty in the background subtraction is taken into account in the fit.

The two-dimensional $\Delta\chi^2$ contours resulting from the fit are shown in fig. 3. The overall precision expected in the top quark mass is around 200 MeV. The strong coupling constant at the Z scale is determined with a ± 0.005 uncertainty. Most of the sensitivity comes from the total cross section measurement, although there is a non-negligible improvement coming from $d\sigma/dp$.

The extra degree of freedom represented by α_s can actually be viewed as a way to parametrize uncertainties in the binding QCD potential. For instance, in the scale at which the strong coupling constant has to be evaluated, or in the exact form of the long-distance part of the potential, although this has a limited impact due to the short top lifetime.

It is clear from fig. 1 that the effect of beamstrahlung in the total cross section leads to a big loss in sensitivity to the top mass. It has been proposed to use a particular accelerator design for the threshold scan run that would have reduced beamstrahlung. The price to pay is a subsequent loss in instantaneous luminosity. A set of accelerator parameters especially designed to minimize the beamstrahlung [4] has been used in the fit to m_t and α_s. The luminosity for each point has been reduced according to the loss in luminosity for the new design to 2.3 fb^{-1}. The result of the fit is very similar to the previous one, confirming that the loss in luminosity is compensated by the decrease in the amount of beamstrahlung. However, provided that the amount of beamstrahlung

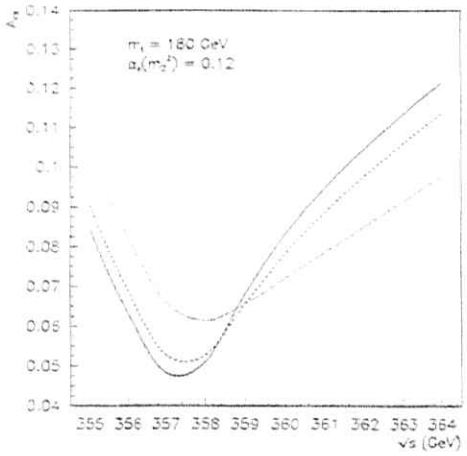

Figure 4: $t\bar{t}$ forward-backward asymmetry as a function of the centre-of-mass energy. Solid line: Born cross section; dashed line: with initial state radiation (ISR); dotted line: with ISR and beam effects, computed with the parameters of the TESLA accelerator design [4].

can be measured following the lines of ref. [8], then there is no real advantage in using the low-bremstrahlung, low-luminosity design.

3. Inclusion of forward-backward charge asymmetry

In refs. [5, 6] it was pointed out that the sizable overlap between the S- and P-wave top-antitop states near threshold would lead to a non-negligible amount of forward-backward charge asymmetry in the $t\bar{t}$ production near threshold. The amount of the overlap depends on the potential and, therefore, A_{FB} should be sensitive to the value of α_s in the potential. Since it is the large top width which makes the overlap possible, it is clear that A_{FB} will also be sensitive to the top quark width.

Figure 4 shows the TOPPIK prediction for the forward-backward asymmetry as a function of the centre-of-mass energy. Also shown is the asymmetry after including initial state radiation and beam effects. Both corrections are sizable but not as dramatic as in the case of the total cross section. The program MMO, described in [2], has been modified along the lines of [5] to compute A_{FB} as well. The prediction is in good agreement with that of TOPPIK. This is a powerful cross check of both calculations, which use very different techniques.

The selection of events for measuring A_{FB} is identical to that used to measure the momentum distribution. Again, only events with one W decaying leptonically and one decaying hadronically are used. This way, the charge of one of the top quarks is readily

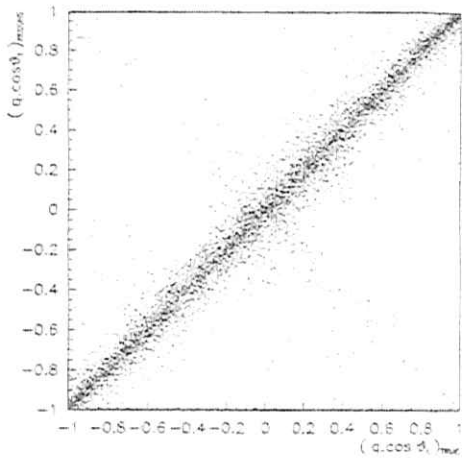

Figure 5: Correlation between true and measured values of $q\cos\vartheta$, where q is the charge of the primary lepton from top decay and ϑ the top polar angle.

obtained from the lepton charge. On the other hand, it was found to be very hard to use the fully hadronic events together with some kind of jet-charge determination.

Using simulated events generated with the PYTHIA program [9] and smeared according to the typical resolutions of a LEP detector, it is found that the charge of one of the quarks can be easily estimated from the charge of the highest energy lepton in the event. The simulation predicts a probability of charge confusion below 3%. Figure 5 shows the correlation between the true $q\cos\vartheta$ and the measured one, where q is the charge of the lepton from the (anti-)top quark and ϑ the (anti-)top angle relative to the beam direction. It is clear that the angular resolution is adequate for this measurement and that the charge confusion is small.

The expected sensitivity of A_{FB} to changes in the value of α_s can be seen in fig. 6 for energies around the threshold. The error bar shown corresponds to a 5 fb^{-1} luminosity at that energy point. The sensitivity is largest slightly below the nominal threshold, $\sqrt{s}$ = 360 GeV, but, even there, it is not very big, in view of the size of the expected error.

Nine measurements of the forward-backward asymmetry at centre-of-mass energies between 356 and 364 GeV have been included into the χ^2 fit presented in the previous section, that already includes the measurements of cross section and momentum distribution. The results for m_t and α_s change very little. The sensitivity of A_{FB} to α_s is not enough to have an impact in the two-dimensional fit, which is still dominated by the information coming from the total cross section. The sensitivity to the top quark

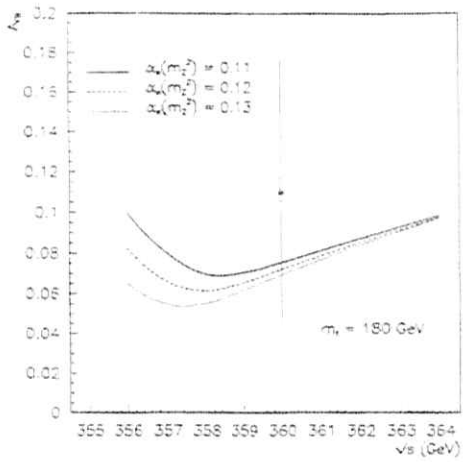

Figure 6: Sensitivity of A_{FB} to the value of $\alpha_s(M_Z)$. The dot represents a simulated data point at $\sqrt{s} = 2m_t$. The error bar includes the statistical error corresponding to a 5 fb^{-1} luminosity at that energy point.

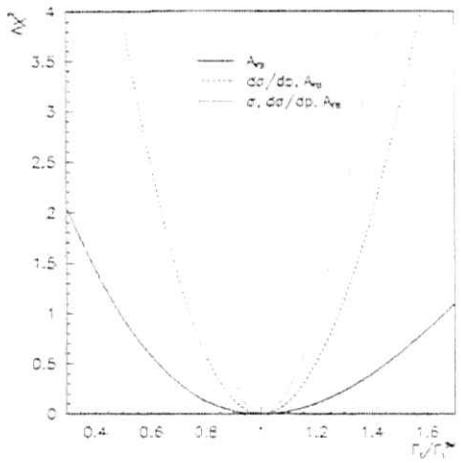

Figure 7: χ^2 increase as a function of the top width using only the forward-backward charge asymmetry (solid line), adding the top momentum information (dashed line) and adding as well the total cross section information (dotted line).

total width is discussed in the following section.

4. Top quark width

Since the top quark is so heavy, it is possible that it decays to heavy final states not predicted in the Minimal Standard Model. The top quark width is, therefore, an interesting parameter to measure. The deviation of the measurement from the Minimal Standard Model prediction could indicate the presence of new physics of several kinds. The existence of a fourth quark generation or of a relatively light charged Higgs are only two examples. A change in the top quark width modifies the shape of the $t\bar{t}$ threshold. The cross section, the top momentum distribution and the forward-backward charge asymmetry are all affected.

The nine-point centre-of-mass energy scan presented in section 2 is now used to determine the sensitivity to the top width. The nine measurements of cross section, peak of momentum distribution and A_{FB} are fit to the theoretical prediction with Γ_t as the only free parameter, that is, keeping m_t and α_s fixed. Figure 7 shows the increase of χ^2 for width values different from the Minimal Standard Model value, when including only A_{FB} in the fit and when adding to it, first, the peak of the momentum distribution and then also the total cross section. From the figure it can be seen that including all observables the precision of the width measurement would be around 18% of its value. In this case the forward-backward asymmetry indeed has a sizable sensitivity but it is still smaller than the sensitivity of σ and $d\sigma/dp$.

5. Top Yukawa coupling

Given the large mass of the top quark, its Yukawa coupling to the Higgs field, $\lambda_t = m_t/v$, with $v = (\sqrt{2}G_F)^{-1/2} \simeq 246$ GeV, is rather large, $\lambda_t^2 \sim 0.5$, and much larger than that of any other fermion (for instance, $\lambda_b^2 \sim 4 \times 10^{-4}$). Therefore, the top quark provides a unique opportunity to measure one of the Yukawa couplings.

Around the $t\bar{t}$ threshold the Higgs exchange between the two final state top quarks is proportional to λ_t^2 and can have measurable influence on the threshold observables. Jeżabek and Kühn have computed the Higgs exchange effects in ref. [10] and this calculation has been included into the TOPPIK program. They approximate the effect of the Higgs exchange by the addition of a static Yukawa potential,

$$V_Y(r) = -\frac{\lambda_t^2}{4\pi}\frac{e^{-M_H r}}{r},$$

to the standard QCD potential, and a remaining constant vertex correction. The vertex correction only affects the total cross section, while the change in the potential affects all observables.

It is clear from the previous equation that the effect will be larger for smaller Higgs masses. To see the sensitivity to λ_t a Higgs mass of 100 GeV has been assumed.

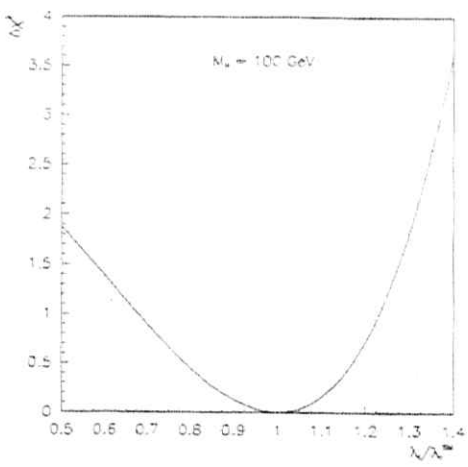

Figure 8: χ^2 increase as a function of the top Yukawa coupling using all information.

Then, in a similar way to what was done in the previous section, a χ^2 fit has been performed with λ_t as the only free parameter. The corresponding curve for $\Delta\chi^2$ is shown in fig. 8. The curve contains all information from cross section, momentum and A_{FB}. However, only the cross section contributes significantly to the sensitivity. The overall precision obtained for the determination of the top Yukawa coupling is around 30% of its value. This result holds for M_H = 100 GeV. For substantially higher Higgs masses (around 300 GeV) the sensitivity is too small to perform a measurement of λ_t.

Assuming the Minimal Standard Model value for λ_t, the same Higgs effect can be used to try to measure the Higgs mass, which appears in the Yukawa potential and in the vertex correction. The sensitivity is only large enough for low Higgs masses (below 200 GeV). However, such a Higgs boson would have already been found directly in the same linear collider and its mass measured with an adequate precision.

6. Conclusions

A study of the physics potential of the top-antitop production threshold has been presented, assuming m_t = 180 GeV and using the latest TESLA accelerator parameters. The feasibility of measuring the forward-backward charged asymmetry at threshold has been studied. It has been found that it can be measured rather precisely by using semileptonic top decays.

With all the information from σ, $d\sigma/dp$ and A_{FB} put together, it has been found that the top mass and $\alpha_s(M_Z)$ can be measured simultaneously to about 200 MeV and 0.005 respectively. Fixing the values of m_t and α_s, the top quark width can be

determined with an 18% uncertainty and the top Yukawa coupling, λ_t, to about 30% of its value for Higgs masses around 100 GeV. In all cases, most of the sensitivity comes from the measurement of the total cross section.

Acknowledgements

We would like to thank Mokhtar Chmeissani for his help in the early stages of this analysis. We are indebted to Marek Jeżabek and his collaborators for making their program TOPPIK available to us, as well as for many discussions.

Bibliography

1. G. Bagliesi *et al.* in *Proceedings of the Workshop on e^+e^- Collisions at 500 GeV: The Physics Potential (Munich, Annecy, Hamburg, February 1991–September 1991)*, ed. P. M. Zerwas, DESY report 92-123A, pp. 327–377.
2. P. Igo-Kemenes, M. Martinez, R. Miquel and S. Orteu in *Proceedings of the 1992 Workshop on e^+e^- Physics at 500 GeV: The Physics Potential (Munich, Annecy, Hamburg, November 1992–April 1992)*, ed. P. M. Zerwas, DESY report 93-123C, pp. 319–329.
3. F. Abe *et al.*, CDF Collaboration, Phys. Rev. D50 (1994) 2966; Phys. Rev. Lett. 73 (1994) 225;
   S. Abachi *et al.*, D0 Collaboration, Phys. Rev. Lett. 74 (1995) 2422.
4. R. Bacher *et al.*, TESLA Collaboration, DESY-TESLA 94-24 (1994) 83 and D. Schulte, private communication.
5. R. Harlander, M. Jeżabek, J. H. Kühn and T. Teubner, Phys. Lett. B346 (1995) 137.
6. K. Fujii, T. Matsui and Y. Sumino, Phys. Rev. D50 (1994) 4341.
7. TOPPIK computer program written by R. Harlander, M. Jeżabek and T. Teubner, based on refs. [5], [10] and
   M. Jeżabek, J. H. Kühn and T. Teubner, Z. Phys. C56 (1992) 653;
   M. Jeżabek and T. Teubner, Z. Phys. C59 (1993) 669.
8. M. N. Frary and D. J. Miller in *Proceedings of the Workshop on e^+e^- Collisions at 500 GeV: The Physics Potential (Munich, Annecy, Hamburg, February 1991–September 1991)*, ed. P. M. Zerwas, DESY report 92-123A, pp. 379–391.
9. T. Sjostrand, CERN preprint CERN-TH-6488-92.
10. M. Jeżabek and J. H. Kühn, Phys. Lett. B316 (1993) 360.

Top Production and Decay Form Factors

Michael Schmitt*
Department of Physics, University of Wisconsin, Madison, WI 53706, USA

Abstract: The production and decay of top quarks at a future linear collider provides opportunities to detect physics beyond the Standard Model. Experimental studies show that a deviation from the expected production angular distribution can be detected at a level of 4%. Such a deviation could be caused by an anomalous magnetic dipole moment, or by an electric dipole moment. Further studies show that an admixture of $V-A$ in the decay of top quarks is observable at a level of 2%. These studies are described in this note.

1 Production and Decay Form Factors

The production and decay of top quarks at a future linear collider provides opportunities to detect physics beyond the Standard Model (SM). There can be anomalous form factors associated to the production vertex which modify the $t\bar{t}$ coupling to the neutral electroweak current, and to the decay vertex which modify coupling to the weak charged current. The presence of such anomalous couplings, if large enough, would be observable in the angular and energy distributions of the $t\bar{t}$ final state.

Top quarks are produced in e^+e^- collisions with a high degree of longitudinal polarization. In contrast to lighter quarks, this polarization is not obscured during hadronization, and the initial top helicity is transferred efficiently to the final state.

The current operator can be written

$$j^a_\mu \propto \gamma_\mu (F^a_{1L} P_L + F^a_{1R} P_R) - \frac{i\sigma_{\mu\nu}q^\nu}{2m_t}(F^a_{2L} P_L + F^a_{2R} P_R)\,, \qquad (1)$$

where F^a ($a = \gamma$, Z, W) are form factors. To lowest order in the SM, $F^\gamma_{1L} = F^\gamma_{1R} = F^W_{1L} = 1$, $F^Z_{1L} = g_L$, $F^Z_{1R} = g_R$, and $F^\gamma_{2L} = F^\gamma_{2R} = F^W_{1R} = 0$. A nonzero value for $F^{\gamma,Z}_{2L} - F^{\gamma,Z}_{2R}$ would be caused by a magnetic (weak for "Z") dipole moment, and nonzero value for the CP-violating combination $F^{\gamma,Z}_{2L} - F^{\gamma,Z}_{2R}$ by an electric (weak) dipole moment. These would influence the production distributions for top quarks. If $F^W_{1R} \neq 0$, then there might be a $V+A$ admixture to the top charged current, or a W_R boson, or charged Higgs. F^W_{1R} is tested in the study of decay distributions of top quarks.

We have performed simple investigations of the production and decay distributions to estimate the statistical precision attainable at a future linear collider. The results are presented in the next two sections.

*Supported by the US Department of Energy, grant number DE-FG0295ER40896.

1.1 Production Vertex

The polar angle distribution of the $t\bar{t}$ pair contains, in addition to the usual $1+\cos^2\theta$ terms, a term proportional to $\sin^2\theta$:

$$\frac{d\sigma}{d\cos\theta} \propto \left[\frac{m_t}{E}(F_{1L} - F_{1R}) + \frac{E}{m_t}(F_{2L} + F_{2R})\right]^2 \cdot \sin^2\theta. \qquad (2)$$

The normal spin-flip probability, proportional to $1/s^2$, is augmented by a anomalous term which grows with energy [1, 2].

The extra piece $(F_{2L} + F_{2R}$ in Eq. 2) increases the total cross section as well as changes the differential distribution. In order to extract information which is not already included in the cross section measurement, we chose to perform a maximum likelihood fit to the polar angle distribution to detect an anomalous $\sin^2\theta$ piece:

$$\mathcal{P}_{\rm obs} = (1-\delta)\cdot\mathcal{P}_{\rm SM} + \delta\cdot\mathcal{P}_{\rm anom} \qquad (3)$$

where δ is a single free parameter [3]. The probability density for the standard model $\mathcal{P}_{\rm SM}$ is assumed known (see for example Ref. [3]); the anomalous piece is simply $\frac{3}{2}\sin^2\theta$. A value for δ significantly greater than zero signals new physics.

An event selection was developed using events simulated with PYTHIA [4]. The top mass was 180 GeV, and $\sqrt{s} = 500$ GeV. It was found that the event thrust axis approximates the top line of flight rather well, and that leptonic decays of the top can be used to differentiate t from $\bar{\rm t}$. Close to threshold the direction of the top was difficult to measure inclusively, and at much higher $\sqrt{s}$ the separation of prompt leptons (from $\rm t \to b\ell^+\nu_\ell$) from secondary leptons (from $\rm b \to c\ell^-\bar{\nu}_\ell$) was difficult due to the boost of the decaying b quark. The performance of the detector was assumed to be similar to that of the ALEPH detector.

Several cuts reduced the backgrounds sufficiently: (*i*) the value of the thrust $T < 0.9$; (*ii*) visible energy $E_{\rm vis} > 0.2\sqrt{s}$; (*iii*) missing momentum $P_{\rm miss} > 0.03\sqrt{s}$ (recall that leptonic decays will be used); (*iv*) thrust direction $|\cos\theta_T| < 0.95$, where θ_T is the angle the thrust axis makes with the beam; (*v*) direction of the missing momentum $|\cos\theta_{\rm miss}| < 0.8$, and; (*vi*) at least three jets, clustering with the JADE algorithm with $y_{\rm cut} = (30\ {\rm GeV}/\sqrt{s})^2$. These cuts also select a subset of top events which are well contained in the detector. Approximately 50% of the top events pass these requirements.

Kinematic criteria were applied to select prompt leptons (electrons and muons): (*i*) lepton momentum $P_\ell > 30$ GeV; (*ii*) $|\cos\theta_\ell| < 0.9$; (*iii*) invariant mass of all particles in the hemisphere, excepting the lepton, $M_h < 100$ GeV; (*iv*) at least ten charged particles in the hemisphere; (*v*) transverse momentum with respect to the thrust axis $P_{T\,\rm thrust} > 10$ GeV; (*vi*) transverse momentum with respect to the closest jet $P_{T\,\rm jet} > 3$ GeV, *or* $E_{\rm jet} - E_\ell > 10$ GeV. Assuming a selection efficiency of 90% for the lepton candidate selection, the net acceptance for all these criteria is 60% for prompt leptons. The net acceptance for top decays is 30%, not including semileptonic branching ratios (about 11% each for e and μ).

process	production (pb)	acceptance (%)	accepted (pb)
$t\bar{t}$	0.6	14	0.086
W^+W^-	8.0	0.15%	0.012
$q\bar{q}\gamma$	25	<0.03	<0.008
$W\bar{w}$	3.2	<0.03	<0.001
$Ze\nu$	0.5	<0.03	negl.

Table 1: *Cross sections (pb), for major hadronic processes, before and after the selection for the analysis of the production angular distribution.*

Accepted cross sections for major processes are summarized in Table 1. The signal-to-background ratio is about 4, and could be improved by applying an impact parameter b tag.

The resolution on the top quark direction ($\Delta\theta$) was estimated from the PYTHIA simulation. It can be parameterized as a sum of two gaussians: the core distribution (80%) has an rms of 0.16 radians, and the tail of 0.48 radians.

The direction of the top quark is inferred from the lepton, and is defined to be:

$$\cos\theta_t = \cos\theta_T \times Q_\ell \times \mathrm{sign}(\cos\alpha_{\ell T})$$

where $\alpha_{\ell T}$ is the angle between the lepton and the thrust axis. At $\sqrt{s} = 500$ GeV, the sign can be wrong for two reasons. 1) The lepton comes from a b decay, and has the "wrong" sign. 2) The lepton goes backward with respect to the top direction (in the lab frame). According to the simulation, 82% of the leptons are prompt. A higher fraction, 92%, give the "right" sign, because leptons from c quark decays have the same sign as prompt leptons. Of the right sign leptons, 93% are forward; of the wrong sign, 100% are forward. All together, the thrust axis is given the wrong sign (is "flipped") 15% of the time.

The acceptance as a function of $\cos\theta_t$ is parameterized by a simple function $A(\cos\theta_t) = A \cdot (1 - |\cos\theta_t|^\epsilon)$, with $\epsilon = 4.4$. The background distribution as a function of $\cos\theta_T$ is represented by an exponential for W^+W^- and by a polynomial for $q\bar{q}$.

All of these parametrizations, properly normalized and including the 15% wrong signing of the thrust axis for top events, are employed in a toy MC program. An illustration of the reconstructed polar angle distribution is shown in Figure 1. The clear asymmetry from the top quark is evident despite the contamination, dominated by W pairs and $b\bar{b}$, which peaks in the opposite direction.

Samples generated with this toy Monte Carlo program were fit to Expression 3, and the distribution of δ examined to determine the statistical uncertainty. The result is given in Table 2, showing how it decreases as each "realistic" effect is included. Assuming an integrated luminosity of 50 fb^{-1}, the expected statistical uncertainty is $\Delta\delta = 0.04$.

[3] It is not the same symbol δ as used in Ref. [1, 2].

case	$\Delta\delta$
ideal	0.015
selection efficiency	0.026
acceptance (as function of θ)	0.033
resolution	0.034
flip (15% probability)	0.038
backgrounds (20% contamination)	0.041

Table 2: *Statistical sensitivity to an anomalous $\sin^2\theta$ term in the production cross section, as each realistic effect is included in a toy Monte Carlo simulation. $m_t = 180$ GeV, $\sqrt{s} = 500$ GeV, $\mathcal{L} = 50$ fb^{-1}.*

The dependence on the beam polarization was considered. For $\rho = 1$ (ie. left-handed beam electrons) the error on is $\Delta\delta = 0.041$. It drops to 0.038 for $\rho = -1$, if the number of events is kept constant. However, the total cross section changes by a factor of two, thus giving *fewer* events per fb^{-1}, so $\rho = 1$ is optimal.

The parameters were varied to assess sensitivity to systematic effects. In order to keep the contribution to δ below $\Delta\delta = 0.020$, the acceptance must be forward-backward symmetric to 3%, the tail of the resolution function must be known to 50%, the 'flip rate' must be known to 20% relative, and the the background must be known to 20% relative. None of these requirements is severe.

1.2 Decay Vertex

The charged weak current in the SM is pure $V - A$, leading to unambiguous predictions for the energy and angular decay distributions of leptons. A small admixture of $V - A$ interaction modifies these distributions; the difference between pure $V - A$ and pure $V - A$ is large for neutrinos in decays of down-type fermions, and for leptons in up-type fermions. The L3 Collaboration has used this difference to constrain the charged current in b decays [5].

The theoretical work has been carried out by Jezabek and others [6]; the decay distributions are known including first order QCD corrections. They can be written in terms of a parameter κ, such that $g_V = (1 + \kappa)/\sqrt{1 - \kappa^2}$ and $g_A = (-1 + \kappa)/\sqrt{1 - \kappa^2}$, so $\kappa^2 = 0$ is the SM and $\kappa^2 \to \infty$ is pure $V + A$. (See Ref. [6] for complete expressions.) Given the lepton direction θ (with respect to the top polarization vector of magnitude P) and its scaled energy x, the double-differential distributions have the simple form

$$D(x, \cos\theta; \kappa) \equiv \frac{d^2N}{dx\, d\cos\theta} = A(x) + B(x) \cdot P \cdot \cos\theta$$

where the functions $A(x)$ and $B(x)$ are different for charged leptons and neutrinos. They depend on κ.

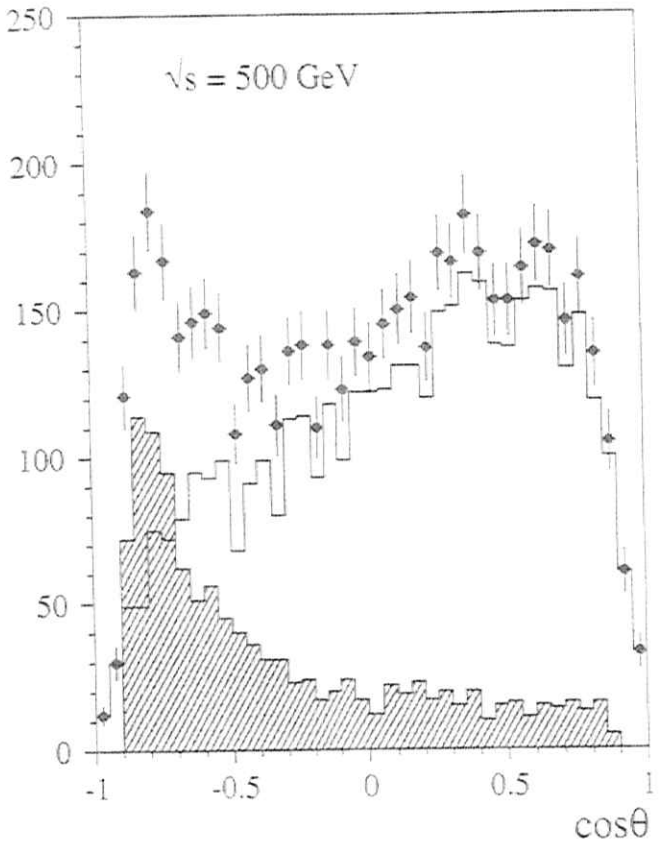

Figure 1: *Simulated thrust axis polar angle distribution, signed by an energetic, isolated lepton. The contributions of $t\bar{t}$ (solid line) and background (shaded histogram) are shown separately, $m_t = 180$ GeV and $\sqrt{s} = 500$ GeV.*

quantities used	figure-of-merit	gain wrt x_ℓ only
x_ℓ	35	1
x_ℓ, $\cos\theta_\ell$	48	1.4
x_ν	35	1
x_ν, $\cos\theta_\nu$	42	1.2
x_ℓ, $\cos\theta_\ell$, x_ν	58	1.7
x_ℓ, $\cos\theta_\ell$, x_ν, $\cos\theta_\ell$	63	1.8

Table 3: *Ideal relative statistical sensitivity to an admixture of $V-A$ in top decays. The figure-of-merit improves substantially as more information is included.*

The experimental task is to constrain κ^2 using as much information as possible from the lepton energy and direction, and if possible, from the neutrino. Studies were performed using top decays simulated at threshold, since in this case the top spin points along the beam direction, and the energy and angle of the lepton in the lab frame are essentially the same as those in the top rest frame. An integrated luminosity of 50 fb^{-1} was assumed.

The lepton energy and angular resolution is good enough so as to have little impact on the measurement. The neutrino measurement, approximated by the missing momentum vector, is less certain, due to unknown and variable losses to ISR, and detector acceptance. Nonetheless, a resolution of about 10% was obtained from a simulation using PYTHIA.

The energy and angular distributions for the lepton were condensed into a single "optimal" variable ω_ℓ, and for the neutrino, a separate variable ω_ν. The technique of statistically optimal variables has been applied in tau physics at LEP [7]. It can be derived from the likelihood function, and amounts to

$$\omega = \omega(x, \cos\theta) \equiv \left\{ \frac{1}{D(x, \cos\theta; \kappa)} \frac{\partial D(x, \cos\theta; \kappa)}{\partial \kappa^2} \right\}_{\kappa^2=0}$$

The mean ω changes monotonically as a function of κ^2; the significance of a shift in terms of the variance of ω is the statistical sensitivity of a measurement. The x_ℓ and corresponding ω distributions are shown in Figure 2 as an illustration. Several versions of ω were calculated, corresponding to the charged lepton and neutrino, their energy, and their direction. The correlation between the lepton and the neutrino was not taken into account.

A toy Monte Carlo was used to generate distributions of $D(x, \cos\theta; \kappa)$ for various values of κ^2. The shift in $\langle\omega\rangle$ as a function of κ^2 was obtained, and normalized to σ_ω. A figure-of-merit was defined as the slope of $\langle\Delta\langle\omega\rangle/\sigma_\omega\rangle$ as a function of κ^2, assuming that 4000 leptonic top decays are observed under ideal conditions. A comparison of these figures-of-merit is given in Table 3. Almost a factor of two can be obtained by taking into account all the available information. The simplest ω calculated using only the lepton energy is 25% more sensitive that the $n = -1$ moment as suggested in Ref. [3].

The significance $\langle\Delta\langle\omega\rangle/\sigma_\omega\rangle$ is plotted as a function of κ^2 in Figure 3. The increase in sensitivity as more information is taken into account is manifested as a steeper line: the

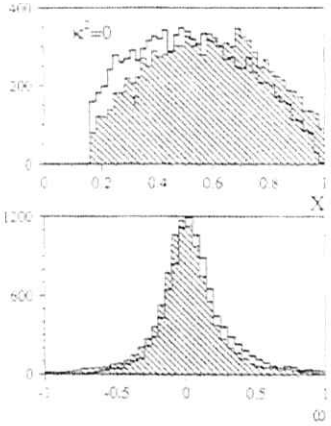

Figure 2: *Comparison of the x_l and ω distributions.*

shift passes three sigma for a twice smaller value of κ^2 when all information from the lepton and neutrino are used compared to the lepton energy alone. (A single optimized variable incorporating the lepton and neutrino information was not constructed explicitly; rather, the significances for the lepton and the neutrino were added together in quadrature.)

The effects of realistic energy and direction resolution, and of acceptance have been estimated using the simulation. Most important is the lower cutoff on momenta and the resolution on the neutrino direction (rms = 0.3 radians). These effects degrade the sensitivity by about 25%. Backgrounds have not been taken into account, but they should be small at threshold. For an integrated luminosity of 50 fb^{-1}, the statistical uncertainty would be approximately $\Delta\kappa^2 \approx 0.02$.

2 Conclusion

The top production and decay distributions can be sensitive probes of new physics. Straightforward analyses based on techniques currently employed at LEP and SLD allow interesting limits to be placed on anomalies due to non-standard top form factors. They could easily be improved once details of the detector and accelerator are better known.

Acknowledgement

This work has benefitted from discussions with Ramon Miquel. The assistance of Marek Jezabek is also acknowledged.

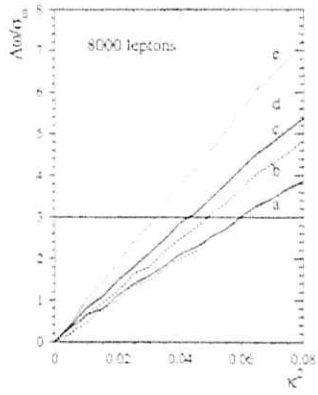

Figure 3: *Increase in significance $\Delta\omega/\sigma_\omega$ as κ^2 is increased. The inclusion of more information results in a steeper line: a) lepton or neutrino energy alone, b) neutrino energy and angle, c) lepton energy and angle, d) lepton energy and angle, and neutrino energy, e) lepton and neutrino energies and angles.*

References

[1] M. Peskin, proceedings of the Linear Collider workshop held in Saariselkä, Finland, 9-14. Sept. 1991, pp. 1-50.

[2] C. Schmidt, SCIPP 95/14, hep-ph/9504434.

[3] M. Jezabek, Nucl. Phys. B (Proc. Suppl.) 37B (1994) 197.

[4] T. Sjöstrand, CERN-TH 7112/93
T. Sjöstrand, Comput. Phys. Commun. 39 (1986) 347;
T. Sjöstrand and M. Bengtsson, Comput. Phys. Commun. 43 (1987) 367;
H.-U. Bengtsson and T. Sjöstrand, Comput. Phys. Commun. 46 (1987) 43.

[5] L3 Collaboration, Phys. Lett. B 351 (1995) 375.

[6] M. Jezabek, TTP 95-12 (March, 1995)
M. Jezabek and J.H. Kühn, Phys. Lett. B329 (1994) 317.
M. Jezabek and J.H. Kühn, Nucl. Phys. B320 (1989) 20.

[7] ALEPH Coll., Zeit. Phys. C59 (1993) 369-386.
OPAL Coll., Zeit. Phys. C66 (1995) 31-41.

Direct measurement of the top quark Yukawa coupling *

Manel Martinez and Salvador Orteu
IFAE. Universitat Autònoma de Barcelona
E-08193 Bellaterra (Barcelona)

Abstract

The direct measurement of the top quark Yukawa coupling, in a light Higgs scenario, by using the process $e^+e^- \to t\bar{t}H$ is analyzed. Although, the signature of the process is rather singular and, in ideal conditions, should allow a determination of the top Yukawa coupling at the level of $\Delta\lambda_t/\lambda_t \sim 0.1$ with 50 fb^{-1} for $M_H < 240$ GeV, our simulation shows that, taking into account detector effects and background processes, in practice the measurement seems to be at the limit of being possible.

1. Introduction

Even if the MSM Higgs is found, the coupling to the other fundamental particles must be measured to check the Higgs mechanism. Since the Higgs coupling to fermions is proportional to the fermion mass squared, $\lambda_f^2 = (m_f/v)^2$ being $v = (\sqrt{2}G_F)^{1/2} \simeq 246$ GeV, the Yukawa coupling for the top quark is much larger than for any other fermion:$\lambda_t^2 \sim 0.5$ whereas, for instance $\lambda_b^2 \sim 0.0004$. Therefore, the top quark provides a unique opportunity to measure the Yukawa coupling.

The top Yukawa coupling might show its effects in several observables. It has some effect, for instance, in the interquark potential near the top production threshold and hence, indirectly affects the threshold observables [1]. Rather than these sort of measurements, in this study we wanted to concentrate in the feasibility of a more direct measurement of this coupling.

For the direct measurement of the top Yukawa coupling, two different scenarios should be distinguished:

(1) "Heavy Higgs" ($M_H > 2m_t$). In this case, the fermionic Higgs decays would predominantly be into $t\bar{t}$, which would compete with the bosonic Higgs decays. The Higgs could predominantly be produced either through the "standard" Bjorken mechanism $e^+e^- \to ZH$ or through the W fusion mechanism in $e^+e^- \to \nu\bar{\nu}H$ (see fig.1) and afterwards decay into $t\bar{t}$. The first mechanism is predominant for energies below 1 TeV whereas the second one is mostly relevant for even higher energies. These processes constitute the basic mechanism for Higgs searches and hence, have already been studied in that context by several authors.

(2) "Light Higgs" ($M_H < 2m_t$). In this case, the fermionic Higgs decays would predominantly be into $b\bar{b}$. If the Higgs is heavier than twice the W or the Z mass they would compete with the bosonic decays. The Higgs could be produced thorough

*Presented by S. Orteu.

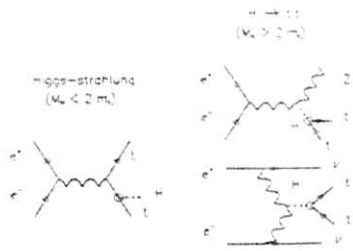

Figure 1: Feynman diagrams for the processes that can be used to directly measure the top Yukawa coupling.

"radiation" off a top ("Higgs-strahlung", see fig. 1). Since the detectability of this process had not been studied, that is the process that we want to discuss in detail.

In section 2 we present the basic features of the theoretical predictions for the process $e^+e^- \to t\bar{t}H$. We also compute the sensitivity to the top Yukawa coupling theoretically attainable. In section 3 we discuss the detectability of the signal and its possible backgrounds and we present the analysis used to select the events in which both top decay hadronically. Finally in section 4 we present the results of our analysis and we draw some conclusions.

2. Theoretical aspects

At the lowest order the process $e^+e^- \to t\bar{t}H$ is described by three Feynman diagrams (see fig. 2). For a light higgs, the contribution due to the radiation of the Higgs out of the Z line is just an small correction with respect to the rest. Therefore, the cross section is, in very good approximation, proportional to λ_t^2.

The calculation for the "Higgs-strahlung" with only γ-exchange existed since long time ago [2] and few years ago the complete calculation was also finished [3]. Since at the NLC energies the γ-exchange contribution dominates by far, both calculations are in good agreement.

The total cross section, for any given value of M_H decreases at low $\sqrt{s}$ due to phase space and also decreases at high $\sqrt{s}$ due to unitarity. For the range of $M_H < 2m_t$ the cross section is maximal around 750 GeV but reaches only O(1-10 fb) as can be gleaned from fig. 3.

Assuming "ideal" detection conditions (100% acceptance and 0% background) figure 4 shows for three different $\sqrt{s}$ the sensitivity S to λ_t^2 as a function of the Higgs mass, defined in such a way that

$$\Delta\lambda_t^2 = \frac{1}{S\sqrt{L}} \qquad (1)$$

where L stands for the luminosity in fb^{-1}. Therefore, ideally one could make a mea-

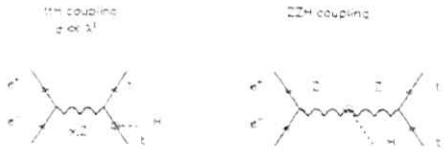

Figure 2: Feynman diagrams for $e^+e^- \to t\bar{t}H$.

surement at the level of $\Delta\lambda_t/\lambda_t \sim 0.1$ with 50 fb^{-1} for $M_H < 240$ GeV.

3. Experimental aspects

Using the complete calculation by Djouadi et al. [3] we have written a M.C. event generator to make an experimental simulation of this process. The events have been processed with PYTHIA and smeared to simulate "standard detector" conditions [4].

Assuming that the Higgs decays with a 100% branching ratio into $b\bar{b}$ (which is a good approximation for $M_H < 160$ GeV) the signal consists in $e^+e^- \to t\bar{t}H \to W^+bW^-\bar{b}b\bar{b}$.

The W can decay either hadronically or leptonically. In the second case, the existence of an energetic neutrino prevents the direct reconstruction of the W mass. Nevertheless, if at least one of the W decays hadronically, then the requirement of total energy-momentum conservation allows to recover the missing neutrino information. Therefore, two different cases can be studied:

- one $W \to q\bar{q}'$ and the other $W \to l\nu$ which amounts to about 38 % of the cases, and
- both $W \to q\bar{q}'$ which amounts to about 37 % of the cases.

In the first case, we have $l\nu b\ jj\bar{b}\ b\bar{b}$ so that the basic signature are events with a prompt lepton plus 6 jets out of which 4 jets come from b quarks. Given the fact that prompt leptons come also from b decays, in practice the signature might not be very clear. So far we have decided to leave aside the analysis of this configuration and the study of the actual feasibility of the analysis of the 4 jet plus 2 lepton configuration.

By taking only hadronic W decays, then we have $jjb\ jj\bar{b}\ b\bar{b}$ so that the basic signature consists in a 8 jet event which has 4 b plus 4 non-b jets which can be selected using b-tagging plus 2 M_W, 2 m_t and the M_H constraints. We have simulated specifically the case in which $M_H = 100$ GeV and our selection procedure had the following steps:

- Require ≥ 7 jets (where a jet can be also an isolated lepton) but force the event afterwards to have 8 jets

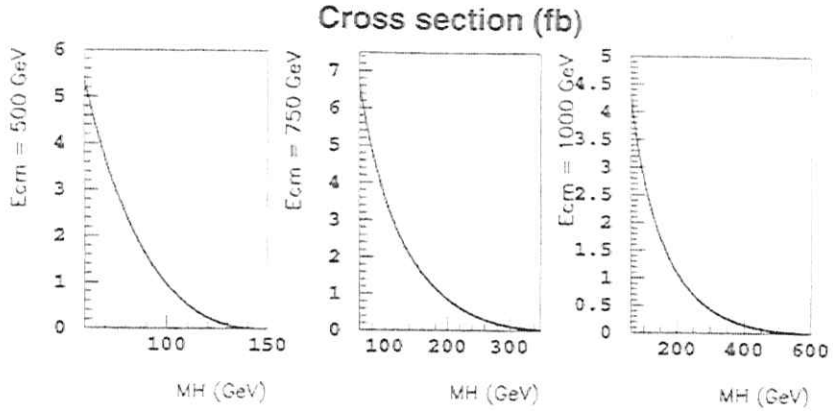

Figure 3: Total cross section for the "Higgs-strahlung" process as a function of M_H for different E_{cm}.

- Discard events with jets being just one lepton
- Apply b-tagging to the jets to classify them into b and non-b jets. In this step we have assumed that b hadrons can be identified with very high efficiency (we actually take 100%) and a jet is assumed to be a b jet if, at least, half of its energy comes from b hadrons. Therefore the actual b tagging efficiency that we assume is not 100% but it is still very high.
- Require the event to have 4 identified b jets.
- Find best W-mass combination for non-b jets.
- Find best H-mass combination for b jets and require 80 GeV $< M_H <$ 110 GeV.
- Check best t-mass combination for W and remaining b jets.

Figure 5 shows the W, top and Higgs invariant mass distributions obtained in this analysis for the simulated signal events. The resolution in the Higgs invariant mass that we get is of about 10 GeV.

Concerning backgrounds, there are, for the signature that we have chosen to identify our signal, at least two potentially dangerous channels:

(1) $e^+e^- \to t\bar{t}Z$. The cross section turns out to be very similar to the one of the signal for $M_H = 100$ GeV, but the requirement of $Z \to b\bar{b}$ introduces an additional factor ~ 10 decrease. The Higgs invariant mass cut could reduce in addition the background if the Higgs mass is sensibly different from the Z mass, which is not the case for $M_H =$

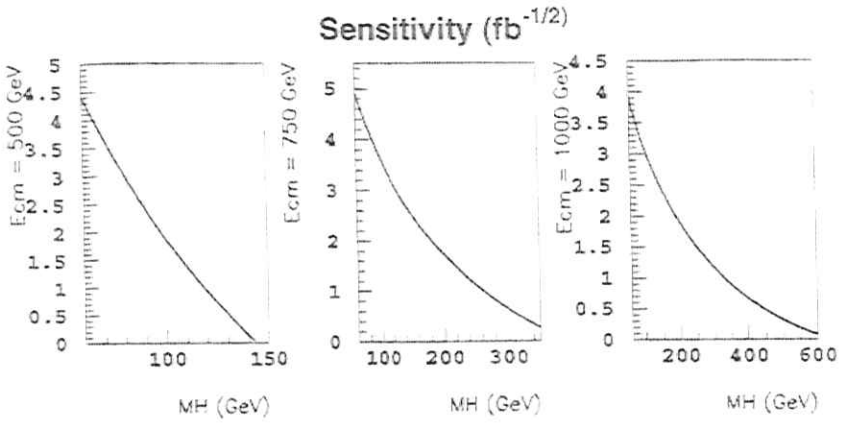

Figure 4: Ideal sensitivity function S to λ_t^2 as a function of of M_H for different E_{cm} (see text for the precise definition).

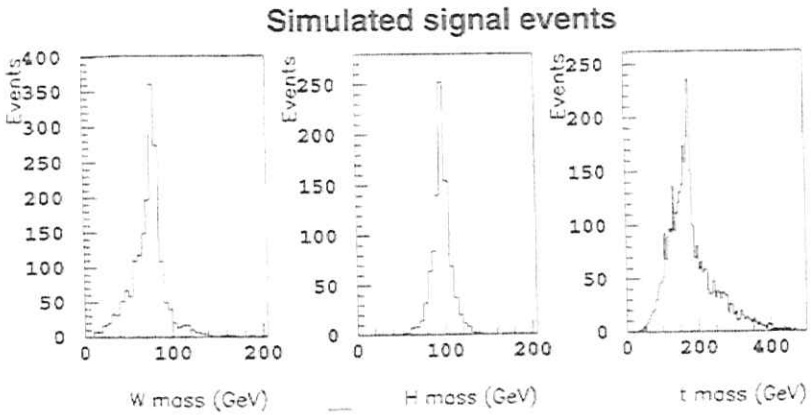

Figure 5: Reconstructed invariant mass distributions for the "Higgs-strahlung" signal events. In the top mass distribution, the combinatorial background is also shown.

100 GeV, our choice for the simulation. In our case, the signature of this process is irreducibly mixed with the one of the signal and hence, we have not directly simulated it but rather considered that it would contribute unavoidably to about 10% of the signal. Nevertheless, since the cross section for this process can be predicted with even better accuracy as the one of the signal, handling this small background, in our opinion, should not be a problem.

(2) $e^+e^- \to t\bar{t}$ where, due to confusion in the jet assignment or due to the actual production of additional $b\bar{b}$ pairs (for instance coming from virtual giuon emission $e^+e^- \to t\bar{t}g^* \to t\bar{t}b\bar{b}$) the signal signature is emulated. In spite of the a priori low probability of such a background, the fact is that, since the cross section for $e^+e^- \to t\bar{t}$ is of about two orders of magnitude larger than the one for the signal, some background might still be expected. We have simulated this process by using a complete JETSET simulation.

4. Results

The results of the selection for the signal and the background are shown in table 1. For the signal, the requierement on the number of jets cuts about 50% of the events and the b tagging keeps about 65 % of the remaining events leading to a final efficiency after the Higgs invariant mass cut of $\epsilon_{tHZ} \sim 26\%$. For an integrated luminosity of 50 fb^{-1} that represents about 50 events at $E_{cm} = 750$ GeV.

For the $t\bar{t}$ background, table 1 shows that the b tagging cut is the main responsible for the rejection. In fact, what happens is that having so many jets, the probability of wrong assignment of a b tag is large and hence, many events surviving the selection are just $t\bar{t}$ events with no additionnal $b\bar{b}$ pair, in which the actual b jets have been splitted by the jet algorithm mimicking the required 4 b jets.

Since we think that our analysis is optimistical concerning b tagging, this rejection could, in practice, be rather worse. The final efficiency is of just few permille but, since the cross section is a couple of orders of magnitude larger than the one for the signal, the actual number of background events expected is of the same order of magnitude as the one expected for the $t\bar{t}H$ events. On the contrary to what happens with the $t\bar{t}Z$ background, this background estimation might not be reliable for, at least, the following reasons:

- it comes from the tails of distributions which might not be well simulated by PYTHIA (we may have a large systematical uncertainty in the background subtraction) and
- its actual size depends very strongly on the detector performance (specially concerning b tagging).

Therefore, even though we get a signal over background ratio of about 2, we are not confident, at this stage, about just applying a simple subtraction of this background.

As can be seen in table 1, for the optimal energy ($E_{cm} = 750$ GeV) even assuming a 100% b hadron tagging efficiency, the total selection efficiency is smaller than 30 % and the signal to noise ratio is below 2. Therefore, our preliminary conclusion, is that the measurement seems to be at the limit of being possible and, in any case, it is clear that a detailed simulation of the b-tagging is crucial to make a quantitative statement

Table 1: Results of the experimental simulation for the Yukawa coupling measurement assuming an integrated luminosity of 50 fb^{-1}

Energy (GeV)	500	750	1000
$t\bar{t}H$(signal)			
Generated events	10000	10000	10000
$\geq$ 7 jets	4978	5244	5216
4 b jets	3209	3299	3331
$80 < M_H < 110$ GeV	2754	2637	2538
x-section (fb)	.95	3.6	2.8
Events (50 fb^{-1})	13.1	47.5	22.6
$t\bar{t}$(background)			
Generated events	10000	10000	10000
$\geq$ 7 jets	917	1232	1676
4 b jets	7	31	45
$80 < M_H < 110$ GeV	4	19	32
x-section (fb)	550	300	175
Events (50 fb^{-1})	11.0	28.5	28.0
Signal/noise	1.2	1.7	1.3

about the actual sensitivity that can be obtained in the measurement of the top Yukawa coupling.

Acknowledgements

We are indebted to Ramon Miquel for several discussions concerning this analysis. We would like to thank also Peter Zerwas and Ron Settles for their interest.

Bibliography

1. " The physics of the $e^+e^- \to t\bar{t}$ threshold scan ", P. Comas, R. Miquel, M. Martinez and S. Orteu, in this report.
2. K. J. F. Gaemers and G. J. Gounaris, Phys. Lett. 77B (1978) 379.
3. A. Djouadi, J. Kalinowski and P. M. Zerwas, Z. Phys. C54 (1992) 255.
4. G. Bagliesi et al. in *Proceedings of the Workshop on e^+e^- Collisions at 500 GeV: The Physics Potential (Munich, Annecy, Hamburg, February 1992–September 1992)*, ed. P. M. Zerwas, DESY report 92-123A, pp. 327–377.

QCD in e^+e^- Collisions at 2 TeV

Sigfried Bethke[a], Michelangelo L. Mangano[b,1] and Paolo Nason[b,2]

[a] III. Phys. Inst. RWTH, D-52074 Aachen, Germany
[b] CERN TH-Division, CH-1211 Geneva 23, Switzerland

Abstract

We discuss some topics in QCD studies at 2 TeV. Particular emphasis is given to the separation of pure QCD events from the WW and the $t\bar{t}$ backgrounds.

[1] On leave of absence from INFN, Sezione di Pisa, Pisa, Italy.
[2] On leave of absence from INFN, Sezione di Milano, Milano, Italy.

1 Introduction

QCD studies in e^+e^- colliders at 2 TeV will be similar in many respects to QCD studies at lower energy (for a review of studies in e^+e^- collisions at 500 GeV, see *e.g.* ref. [1]). One will attempt to measure the strong coupling constant, scaling violation in fragmentation functions, detailed studies of multi-jet distributions, and the like. In this short study we concentrate of features which are novel to collisions at this high energy. The general theoretical and experimental framework for QCD studies in e^+e^- collisions can be found in previous reviews [1].

The main problem at this energy, is how to disantangle the $t\bar{t}$ and W^+W^- backgrounds from the pure QCD di-jet or multi-jet events. The W^+W^- cross section is particularly high and when the W's decay into hadrons one will be unable to distinguish the final state from that of two ordinary high energy jets. A typical 1 TeV QCD jet will in fact have an invariant mass of the order of α_S times 1 TeV, which is roughly 90 GeV, of the same order of the W mass. In fig. 1 we show the

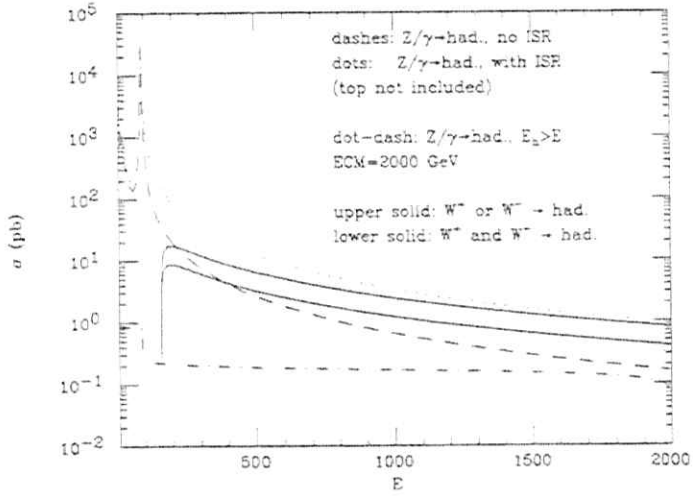

Figure 1: *Cross sections for e^+e^- into light hadrons and into WW pairs, as a function of $\sqrt{s}$. The solid lines represent the WW cross section (upper curve: at least one W hadronic decay; lower curve: both W hadronic decays). The light hadrons cross section is given by the dotted line (no initial state radiation), and by the dashed line (ISR included). The dash-dotted line is the integral of the light hadron cross section at $\sqrt{s} = 2$ TeV, integrated above a given value of the energy of the final hadronic state, in presence of ISR.*

cross section for e^+e^- into light hadrons (from now on, by "hadronic events" we will mean e^+e^- into light hadrons, *i.e.* top contribution excluded), and the WW cross

section. Initial state radiation causes a loss of cross section around a factor of two, depending on the cuts one imposes. In the figure the ISR effect is only shown for hadronic events, but we should expect something similar for the W. It is therefore reasonable to assume that the Born cross sections give a good indication of the relative magnitudes of the WW and hadronic cross sections. We should therefore compare 0.16 pb for the hadronic cross section to 0.4 pb for the WW fully hadronic events. Fortunately, the WW events are concentrated in the forward region, because of their t-channel nature. This is shown in fig. 2, where the cross section is shown

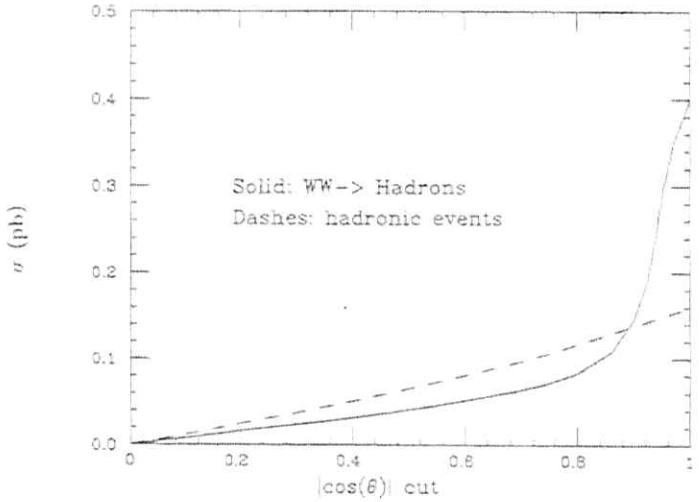

Figure 2: *Cross section at 2 TeV as a function of the cut on the direction of the thrust axis.*

as a function of an angular cut on the thrust axis. We see that requiring $\cos\theta < 0.8$ leaves us with a 60% of the hadronic events and 40% of WW events. Further work is needed to clean the sample in a better way. For example, one expects in general that WW events will always have high thrust. Conversely, one can assume that the WW events are well understood (W decays will be similar to Z decays, a fact that can be verified at LEP2), and subtract them from the measured distributions.

The separation of $t\bar{t}$ events will also require some work. The relative fraction of each flavour is given in fig. 3. At 2 TeV the top quark production represents 22% of the total.

In the following sections we will study some simple variables which allow to separate the various contributions, and will discuss to which extent a separation is indeed necessary. A complete study of the potential for QCD studies at 2 TeV would require some detailed knowledge of the detector specifications. In what follows, we

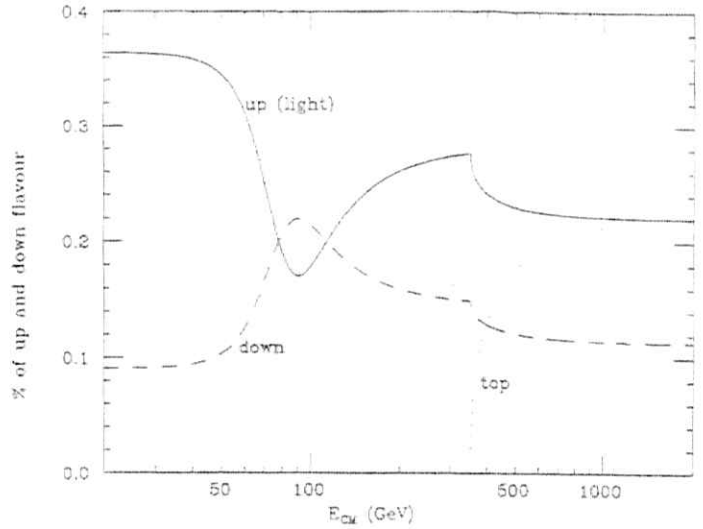

Figure 3: *Flavour composition for $Z/\gamma \to q\bar{q}$ as a function of $\sqrt{s}$.*

will therefore briefly comment on which detector parameters have an impact on this physics.

2 Conventions

We will define jets using the Durham algorithm [2], in the E recombination scheme. Unless otherwise stated, the MC studies are done using HERWIG [3] version 5.8, and use partons as opposed to hadrons. Namely, jets are reconstructed out of the partons after the full shower evolution and gluon splitting, and before being clustered and hadronized.

No QED ISR nor beamstrahlung have been included, as our assigned goal was to study QCD at *exactly* (or very close to) 2 TeV.

A word of caution must be added, however, before we present the results of our case study: here, we are extrapolating our current knowledge to c.m. energies which are about *twenty times larger* than those energies which are presently available. This is equivalent to a hypthetical attempt to predict the physics at LEP-I based on the knowledge of the early data from SPEAR ($\sqrt{s} \sim 5$ GeV).

3 Separation of QCD and WW events

It is hard to separate the two samples without significantly biasing the properties of the jets. The typical property of a WW event is that no hard emission at large angle is possible. In fact the W's will decay in flight into $q\bar{q}'$ pairs, and the mass of the hadronic system resulting will never exceed M_W. Since the W's are boosted to 1 TeV, the two or more jets from their decay will coalesce into a single thin jet, with angular aperture of the order of $M_W/1\ \mathrm{TeV} \sim 5°$. Particles emitted outside this cone cannot be too energetic, or else they would form together with the leading jet an object of invariant mass higher than M_W. We tried to use this property to separate WW events from QCD events. In fig. 4 we plot the multiplicity distribution of

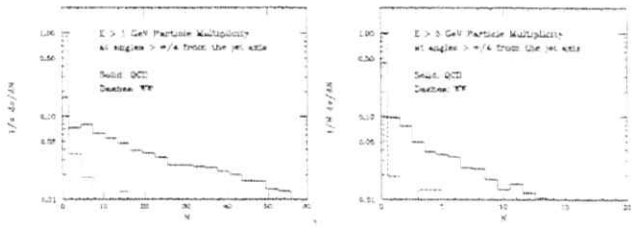

Figure 4: *Multiplicity distribution for particles above 1 GeV (left) and 5 GeV (right) found in the region outside cones of radius 45° centered around the axis of the two leading jets. QCD events (solid) vs. WW events (dashed).*

particles above 1 and 5 GeV found in the region outside cones of radius 45° centered around the axis of the two leading jets. The continuous lines are for QCD events, the dashed lines for WW events. From the figures we learn the following:

- The area outside the jet cores is indeed much quieter in WW events.
- Only a fraction of the order of 10% of the WW events would survive the request that particles above 1 GeV be present outside the 45° cones. More than 80% of the QCD sample would survive this cut.
- If we require the 5 GeV cut, only a fraction of the order of 10^{-2} of the WW events would survive. Approximately 50% of the QCD sample would be left.
- It is not clear how this request would bias the jets, and whether the extraction of α_S from the properties of jets selected in this way would have a significant systematic uncertainty. This issue can however be studied using shower Montecarlo programs.

4 Jet Production Rates and $t\bar{t}$ Events

For the studies presented in this section we generated hadronic final states at $\sqrt{s} = 2$ TeV using PYTHIA version 5.7 [4] with QCD- and hadronisation parameters as optimised to describe the data from LEP1. As before, effects due to initial state radiation, beamstrahlung and detector acceptance are not taken into account. The Durham ($k_\perp$) jet algorithm [2] is used to study jet multiplic-

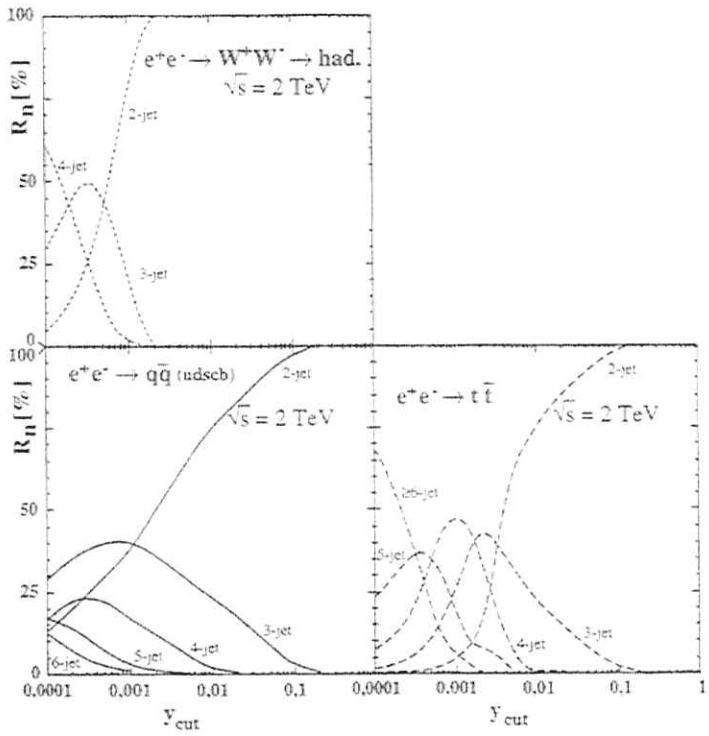

Figure 5: *Integral relative production rates of n-jet events ($n = 2, 3, 4, 5, \geq 6$), as a function of the jet resolution parameter y_{cut}.*

ities for different event classes, namely for hadronically decaying W-pair events ($e^+e^- \to W^+W^- \to$ hadrons), for hadronic events from primary 'light' quark pairs ($e^+e^- \to q\bar{q}$; where q may be a u, d, s, c or b-quark) and for top quark events ($e^+e^- \to t\bar{t}$). The results are shown in Fig. 5, where the integral, relative production rates of n-jet events ($n = 2, 3, 4, 5, \geq 6$) are plotted as a function of the jet resolution parameter y_{cut}. The following observations can be made:

- for $y_{cut} > 0.002$, all W^+W^- events are classified as 2-jet ($\sqrt{0.002} \times 2000$ GeV $= 98.4$ GeV $> M_W$).

- $t\bar{t}$-events have a markedly enhanced and clear 6-jet signal around $y_{cut} \sim 0.0001$. This allows to select top-quark events and study e.g. the decay $t \rightarrow 3$ jets in detail. Of course, the reconstruction of jets at such small values of y_{cut} might require particular granularity in the calorimeter. The accuracy with which the top mass will be measured from the reconstruction of these high energy jets could significantly depend on this parameter.

- for $y_{cut} > 0.01$, the 3-jet production rates of $t\bar{t}$ and $q\bar{q}$ events are almost identical - which is intuitively clear since $\sqrt{0.01} \times 2000$ GeV $\geq M_t$.

From these observations and other studies we conclude:

- At c.m. energies of 2000 GeV, the separation of $t\bar{t}$ events from light-quark QCD events for a typical QCD analysis, like e.g. the determination of α_S from 3-jet rates, seems not to be necessary: these event classes show similar QCD properties in regions where the jet resolution is coarser than the mass of the top quark. The situation is similar as for b-quark events at e.g. TRISTAN energies ($\sqrt{s} \leq 60$ GeV), where the mass of the heaviest quark also was about 10% of the c.m. energy.

- In fact we tried to separate $t\bar{t}$ events from light quark QCD events using kinematic variables, similarly to the separation of W^+W^- events described in the previous section. While the algorithms which we devised are good in extracting a sample of top events with good purity, they are not very good at providing a pure sample of light quark QCD events which is not too biased. The same is true when selecting $t\bar{t}$ events by requiring 6 jets at $y_{cut} = 0.0001$; see Fig. 5.

- Determination of α_S from 3-jet event rates will be possible by analysing *relative* production rates or by analysing *absolute* cross sections of 3-jet events. In the first case, one has to correct the measurement according to the large production of W^+W^- events, which all end up as 2-jets for decent values of y_{cut} and therefore spoil the relative number of 3-jets by the overall normalisation. The absolute normalization of the WW rate is well known within the SM, this being a purely EW process. If we allow for possible new phenomena, we could still determine the WW rate from the data, by counting the number of events where one of the W's decays leptonically. The statistical error of this measurement is comparable to the statistical error on the QCD 2-jet production rate. The use of the *absolute* 3-jet event production rate is not influenced by the production of W^+W^- pairs, provided one works with $y_{cut} > 0.002$. This method however relies on a good knowledge of luminosities, acceptances and theoretical expectations. The uncertainty on these last ones is in principle correlated to that at LEP1 and LEP2, and should not constitute a major source of systematics for comparisons between results at LEP1/LEP2 and NLC.

- With 5000 selected hadronic ($q\bar{q}$ and $t\bar{t}$) events (i.e. after about 2-3 years of data taking with luminosities around $10^{33} s^{-1} cm^{-2}$), we expect about 750 3-jet events at $y_{cut} = 0.02$, leading to a statistical precision in α_S of about 3%. Including the systematic sources mentioned in the previous point, we would estimate the final uncertainty on α_S not to exceed 5%. Starting with $\alpha_S(M_Z) = 0.123 \pm 0.002$ we evaluate an expected $\alpha_S(2\text{ TeV}) = 0.085 \pm 0.004$. The evidence for running would therefore be a clear 7 σ effect. On the contrary, with the value preferred by DIS ($\alpha_S(M_Z) = 0.111$) as a boundary condition one should expect $\alpha_S(2\text{ TeV}) = 0.078 \pm 0.004$. The difference between the two values at 2 TeV is less than 2 σ. As expected, operations at 2 TeV will not enable any improvement in the measurement of Λ_{QCD}.

5 Fragmentation Functions

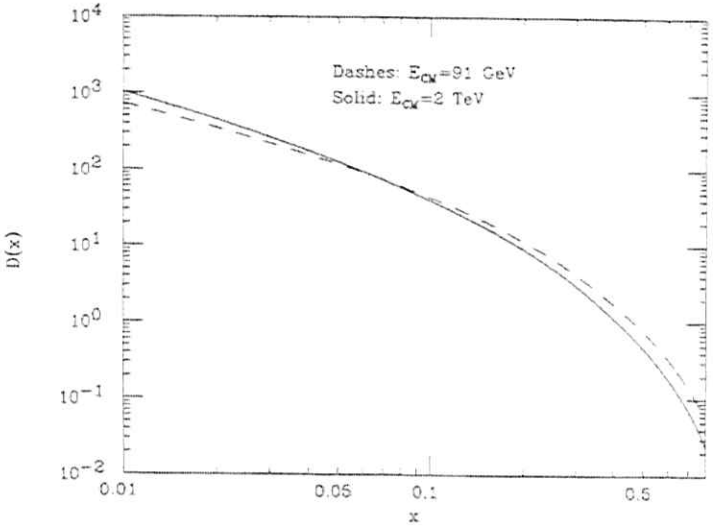

Figure 6: *Inclusive charged particle fragmentation function at $\sqrt{s} = M(Z)$ (dashed) and 2 TeV (solid).*

The study of the evolution of fragmentation functions provides another interesting test of perturbative QCD. In fig. 6 we show the expected evolution of the inclusive fragmentation functions from $\sqrt{s} = M_Z$ to 2 TeV. Although the differences are quite noticeable (the fragmentation function is softer by almost a factor of 2 at $z > 0.5$ because of the larger amount of radiation given off), it is not clear to which extent such effects can be measured. The highest energy jets will be extremely collimated.

and fundamental parameters such as track reconstruction efficiency, fake track rates and momentum resolution will depend very strongly on the detector parameters: magnetic field, tracking resolution etc. It is therefore impossible at this stage to formulate a potential for a physics measurement based on fragmentation functions.

In fig. 7 we plot the b fragmentation function, separated between non-$t\bar{t}$ events and $t\bar{t}$ events. We point out the following features:

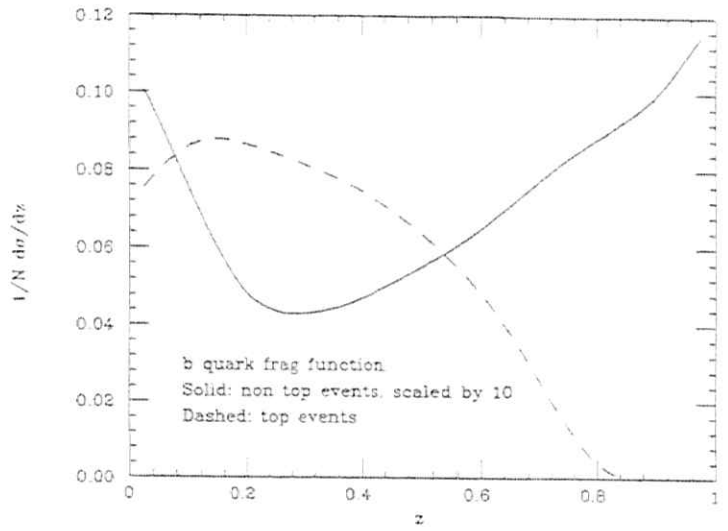

Figure 7: *Inclusive b quark fragmentation function at 2 TeV. Non-$t\bar{t}$ events (solid) and $t\bar{t}$ events scaled by 10 (dashed).*

- The high tail at small-z in non-$t\bar{t}$ events comes from the splitting of gluons emitted during the evolution of light $q\bar{q}$ events.
- A large fraction of inclusive b's therefore comes from non-b events. Measurements of the direct $Zb\bar{b}$ vertex at 2 TeV will therefore be severely biased by our capability to predict the precise contamination due to events initiated by light quarks. The requirement of double tagging on opposite jets would significantly reduce the non-$Zb\bar{b}$ signal, but at the expense of a loss in statistics.
- In addition, the only region of z in which a pure sample of non-$t\bar{t}$ events can be selected is for $z > 0.8$. Below this value, the two fragmentation functions do not differ enough to allow an event-by-event separation of the two components.
- The average momentum of a b is of the order of $z = 1/2$, i.e. 500 GeV, both in $t\bar{t}$ and in non-$t\bar{t}$ events. This is more than ten times the momentum of b's produced at LEP1, and corresponds to decay lenghts of the order of 4 cm. The secondary-vertex tagging detectors should therefore be optimized accordingly. In particular, the radius should be such as to guarantee that the acceptance for the decay taking place *before* the tracking device be large enough. Furthermore, in comparison with LEP1 b's at 2 TeV will be softer relative to the remaining tracks of the jet, and surrounded by larger hadronic activity.

Altogether, it is therefore very difficult to estimate the impact of the detector design on the physics potential. Simple extrapolations from LEP1 values could be seriously misleading, and realistic designs and tracking reconstruction algorithms will have to be used before numbers such as b-tagging efficiency can be estimated.

References

[1] S Bethke et al., in "e^+e^- Collisions at 500 GeV: the Physics Potential", P. Zerwas ed., DESY 92-123A, Vol. A, p.393-463;
G. Cowan, in "e^+e^- Collisions at 500 GeV: the Physics Potential", P. Zerwas ed., DESY 93-123C, Vol. C, p.331.

[2] S. Catani et al., *Phys. Lett.* **269B** (1991) 432.

[3] G. Marchesini and B.R. Webber, *Nucl. Phys.* **B310** (1988) 461.

[4] T. Sjöstrand, *Comput. Phys. Commun.* **82** (1994) 74.

HIGGS PARTICLES

Introduction and Summary

A. DJOUADI[1,2] and P.M. ZERWAS[1]

[1] Deutsches Elektronen-Synchrotron DESY, D-22603 Hamburg, FRG.

[2] Institut für Theoretische Physik, Universität Karlsruhe, D-76128 Karlsruhe, FRG.

The search for scalar Higgs particles and the exploration of the mechanism which breaks the electroweak symmetry, will be one of the major tasks at future high-energy e^+e^- colliders. In previous studies it has been shown that e^+e^- linear colliders operating in the energy range $\sqrt{s} \sim 300$ to 500 GeV with a luminosity of $\int \mathcal{L} \sim 20$ fb^{-1} are ideal machines to search for light Higgs particles.

In the Standard Model (SM) the Higgs mass range $M_H \lesssim 200$ GeV is easy to cover at these energies. This intermediate Higgs mass range is one of the theoretically most favored ranges, allowing the particles to remain weakly interacting up to the GUT scale $\Lambda \sim 10^{16}$ GeV [a prerequisite for the perturbative renormalization of the electroweak mixing angle from the GUT symmetry value 3/8 down to the experimentally observed value at low energies]. The search of intermediate-mass Higgs bosons can be carried out in three different channels: the Higgs-strahlung process $e^+e^- \to ZH$ and the fusion mechanisms $WW/ZZ \to H$. The cross sections are large and the properties of the Higgs boson, in particular spin-parity quantum numbers and couplings to gauge bosons and fermions, can be thoroughly investigated, allowing for crucial tests of the Higgs mechanism.

In the Minimal Supersymmetric Standard Model (MSSM) the Higgs sector is extended to three neutral scalar and pseudoscalar particles h/H, A and a pair of charged particles $H^\pm$. The lightest Higgs boson h has a mass $M_h \lesssim 140$ GeV and can be detected in the entire MSSM parameter space either in the Higgs-strahlung process, $e^+e^- \to hZ$, or by the complementary mechanism of associated production with the pseudoscalar particle, $e^+e^- \to hA$. Moreover, there is a substantial area in the MSSM parameter space where the heavy Higgs bosons can be also found: for a total energy of 500 GeV this is possible if the H, A and $H^\pm$ masses are less than 230 GeV. Similar to the SM, various properties of these Higgs bosons can be investigated.

Higher energies are required to sweep the entire mass range of the SM Higgs particle, $M_H \lesssim 1$ TeV. The high energies will also be needed to produce and to study the heavy scalar particles in extensions of the SM, such as the MSSM, if their masses are larger than ~ 250 GeV. Masses of the heavy Higgs bosons in this range are suggested by grand unified supersymmetric theories. In e^+e^- collisions, these experiments can be performed in the second phase of the colliders with a c.m. energy up to 1.5 to 2 TeV. In this report, we analyze the potential of a 1.5 TeV e^+e^- linear collider, with an integrated luminosity of $\int \mathcal{L} \sim 200$ fb^{-1} *per annum* to compensate for the drop of the cross sections at high

energies. We will study the heavy Higgs particles in the Standard Model, in the minimal supersymmetric extension and in other more speculative scenarios.

In the Standard Model, the main production mechanisms of Higgs particles, $e^+e^- \to HZ$ and $e^+e^- \to \nu\bar{\nu}H/e^+e^-H$, will be discussed and the cross sections, including the interference between the Higgs-strahlung and the fusion processes, will be given [2]. The double Higgs production process, in which the trilinear Higgs coupling can be determined [therefore leading to the first non-trivial test of the Higgs potential], will be discussed in Ref.[3]. Finally, possible effects of New Physics beyond the SM on production cross sections and angular distributions of Higgs bosons, will be summarized in Ref.[4]. Consequences of a model in which the Higgs boson interacts strongly with scalar singlet fields in a hidden sector, are described in Ref.[5].

Subsequently, we will investigate the properties of the heavy Higgs particles in supersymmetric extensions of the SM. We will restrict ourselves first to the minimal extension which is highly constrained, parameterized by only two free parameters at the tree-level: a Higgs mass parameter [generally the mass the pseudoscalar Higgs boson M_A] and the ratio of the vacuum expectation values of the two doublet fields responsible for the symmetry breaking, $\tan\beta$, which in grand unified supersymmetric models with Yukawa coupling unification is forced to be either small, $\tan\beta \sim 1.5$, or large, $\tan\beta \sim 50$.

The various decay modes of the heavy CP-even Higgs boson H, the pseudoscalar boson A and the charged Higgs particles $H^\pm$ will be analyzed in Ref.[6], in particular the decays into supersymmetric particles, charginos, neutralinos, squarks and sleptons. The production of the heavy Higgs particles, primarily through the channels $e^+e^- \to HA$ and H^+H^-, will be also discussed in Ref.[6] and the complete one-loop electroweak radiative corrections of the cross sections will be summarized [7,8]. We will finally discuss the multiple production of the SM and the light MSSM Higgs bosons in Refs.[9,10]. Some of these processes will allow us to determine the fundamental Higgs trilinear couplings.

A brief discussion of the Higgs sector in the next-to-minimal supersymmetric extension of the Standard Model, Ref.[11], concludes this report.

References

[1] Proceedings of the Workshop e^+e^- *Collisions at 500 GeV: The Physics Potential*, DESY Reports 92-123 A+B, and 93-123 C, P.M. Zerwas ed.

[2] W. Kilian, M. Krämer and P.M. Zerwas, *Anomalous Couplings in the Higgs-Strahlung Process*.

[3] E. Chopin, *Associated Pair Production of the SM Higgs and the Probing of the Higgs Self-Coupling*.

[4] W. Kilian, M. Krämer and P.M. Zerwas, *Higgs-Strahlung and Vector Boson Fusion in e^+e^- Collisions.*

[5] E. T. Binoth and J.J. van der Bij, *The Hidden Higgs Model at the NLC.*

[6] A. Djouadi, J. Kalinowski, P. Ohmann and P. M. Zerwas, *Heavy SUSY Higgs Bosons at e^+e^- Linear Colliders.*

[7] V. Driesen, W. Hollik and J. Rosiek, *Production of Heavy Neutral MSSM Higgs Bosons: a Complete 1-loop Calculation.*

[8] A. Arhrib and G. Moultaka, *Radiative Corrections to $e^+e^- \to H^+H^-$.*

[9] A. Djouadi, H.E. Haber and P.M. Zerwas, *Multiple Production of MSSM Neutral Higgs Bosons at High-Energy e^+e^- Colliders.*

[10] A. Djouadi, V. Driesen and C. Jünger, *Loop Induced Higgs Boson Pair Production.*

[11] B.R. Kim, G. Kreyerhoff and S.K. Oh, *Search for Higgs Bosons of the NMSSM at Linear Colliders.*

Higgs-strahlung and Vector Boson Fusion in e^-e^- Collisions

W. KILIAN, M. KRÄMER, AND P.M. ZERWAS
Deutsches Elektronen-Synchrotron DESY, D-22603 Hamburg/FRG

Abstract

Higgs-strahlung $e^+e^- \to ZH$ and WW (ZZ) fusion $e^+e^- \to \bar{\nu}_e\nu_e H$ (e^-e^-H) are the most important mechanisms for the production of Higgs bosons at future e^-e^- linear colliders. We have calculated the cross sections and energy/angular distributions of the Higgs boson for these production mechanisms. When the Z boson decays into (electron-)neutrinos or e^+e^-, the two production amplitudes interfere. In the cross-over region between the two mechanisms the interference term is positive (negative) for $\bar{\nu}_e\nu_e$ (e^-e^-) decays, respectively, thus enhancing (reducing) the production rate.

1. The analysis of the mechanism which breaks the electroweak gauge symmetry $SU(2)_L \times U(1)_Y$ down to $U(1)_{EM}$, is one of the key problems in particle physics. If the gauge fields involved remain weakly interacting up to high energies – a prerequisite for the (perturbative) renormalization of $\sin^2\theta_W$ from the symmetry value 3/8 of grand-unified theories down to a value near 0.2 at low energies – fundamental scalar Higgs bosons [1] must exist which damp the rise of the scattering amplitudes of massive gauge particles at high energies. In the Standard Model (SM) an isoscalar doublet field is introduced to accomodate the electroweak data, leading to the prediction of a single Higgs boson. Supersymmetric extensions of the Standard Model expand the scalar sector to a spectrum of Higgs particles [2]. The Higgs particles have been searched for, unsuccessfully so far, at LEP1, setting a lower limit on the SM Higgs mass of $m_H > 65.2$ GeV [3]. The search for these particles and, if found, the exploration of their profile, will continue at LEP2 [4], the LHC [5], and future e^-e^- linear colliders [6].

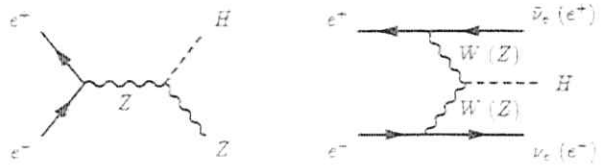

Figure 1: *Higgs-strahlung and vector boson fusion of (CP-even) Higgs bosons in e^-e^- collisions.*

In this note (see also [7]) we will focus on the production of scalar Higgs bosons in e^-e^- collisions. The main production mechanisms for these particles are Higgs-strahlung [8] and WW (ZZ) fusion [9–11] [supplemented in supersymmetric theories by associated scalar/pseudoscalar Higgs pair production]. In particular, we will present a comprehensive analysis of the interplay between the production mechanisms[1] (Fig.1)

$$\begin{aligned} &\text{Higgs-strahlung:} && e^-e^- \to ZH \to \bar{\nu}\nu H \quad (e^-e^-H) \\ &WW \text{ fusion} && : e^-e^- \to \bar{\nu}_e\nu_e H \\ &ZZ \text{ fusion} && : e^-e^- \to e^-e^- H \end{aligned} \tag{1}$$

For $\bar{\nu}_e\nu_e$ and e^-e^- decays of the Z bosons, the two production amplitudes interfere. It turns out that the interference term is positive for $\bar{\nu}_e\nu_e$ and negative for e^-e^- decays, respectively, in the cross-over region between the two mechanisms. The interference effect had been noticed earlier [9,13]; however, we improve on these calculations by deriving analytic results for the energy and polar angular distribution of the Higgs particle (E_H, θ) in the final states of $e^-e^- \to H +$ neutrinos and $e^-e^- \to He^-e^-$. This representation can comfortably serve as input for Monte Carlo generators like PYTHIA/JETSET [14] and HZHA [15] which include the leading QED bremsstrahlung corrections and the important background processes.

2. Total cross sections. The cross section for the Higgs-strahlung process can be written in the following compact form:

$$\sigma(e^-e^- \to ZH) = \frac{G_F^2 m_Z^4}{96\pi s}\left(v_e^2 + a_e^2\right)\lambda^{\frac{1}{2}}\frac{\lambda - 12m_Z^2/s}{(1-m_Z^2/s)^2} \tag{2}$$

where $\sqrt{s}$ is the center-of-mass energy, and $a_e = -1$, $v_e = -1 + 4\sin^2\theta_W$ are the Z charges of the electron; $\lambda = (1-(m_H+m_Z)^2/s)(1-(m_H-m_Z)^2/s)$ is the usual two-particle phase space function. So long as the non-zero width of the Z boson[2] is not taken into account, the cross section rises steeply at threshold $\sim (s-(m_H+m_Z)^2)^{1/2}$. After reaching a maximum [about 25 GeV above threshold in the LEP2 energy range], the cross section falls off at high energies, according to the scaling law $\sim g_W^4/s$ asymptotically. Thus, Higgs-strahlung is the dominant production process for moderate values of the energy. The cross section (2) for Higgs-strahlung is reduced by a factor $3 \times \mathrm{BR}_\nu = 20\%$ if the final state of Z decays is restricted to neutrino pairs.

The total cross section for the WW (ZZ) fusion of Higgs particles can be cast into a similarly compact form[3] [17]:

$$\sigma = \frac{G_F^3 m_V^4}{64\sqrt{2}\pi^3}\int_{z_H}^1 dx \int_x^1 \frac{dy}{[1+(y-x)/x_V]^2}\left[(v^2+a^2)^2 f(x,y) + 4v^2a^2 g(x,y)\right] \tag{3}$$

[1] We will concentrate first on the Standard Model (SM); the extension to the Minimal Supersymmetric Standard Model (MSSM) is trivial as will be demonstrated in the last section of this note.

[2] The results presented in this note are insensitive to non-zero width effects of the Higgs boson [16]. For SM Higgs masses below 100 GeV, Γ_H is at least three orders of magnitude smaller than Γ_Z; for larger Higgs masses, m_H can be reinterpreted as the effective invariant mass of the Higgs decay products.

[3] The variable x is the invariant mass squared of ν_e plus H, $(x-y)$ the 4-momentum transfer squared from e^+ to $\bar{\nu}_e$ (all momenta in units of the total energy).

where V denotes either W or Z, the charges are $v = c = \sqrt{2}$ ($v = v_e$ and $c = a_e$) for WW (ZZ) fusion, respectively, and

$$f(x,y) = \left(\frac{2x}{y^2} - \frac{1+2x}{y^2} + \frac{2+x}{2y} - \frac{1}{2}\right)\left[\frac{z}{1+z} - \log(1+z)\right] + \frac{x}{y^2}\frac{z^2(1-y)}{1+z}$$

$$g(x,y) = \left(-\frac{z}{y^2} + \frac{2+z}{2y} - \frac{1}{2}\right)\left[\frac{z}{1+z} - \log(1+z)\right]$$

with $x_H = m_H^2/s$, $x_V = m_V^2/s$ and $z = y(x - x_H)/(xx_V)$. For moderate Higgs masses and energies, the cross section, being $\mathcal{O}(g_W^6)$, is suppressed with respect to Higgs-strahlung by the additional electroweak coupling. The smaller value of the Z-electron coupling suppresses the ZZ fusion process by an additional order of magnitude compared to WW fusion. At high energies, the WW fusion process becomes leading, nevertheless, since the size of the cross section is determined by the W mass, in contrast to the scale-invariant Higgs-strahlung process,

$$\sigma(e^-e^- \to \bar{\nu}_e\nu_e H) \approx \frac{G_F^3 m_W^4}{4\sqrt{2}\pi^3}\left[\left(1 + \frac{m_H^2}{s}\right)\log\frac{s}{m_H^2} - 2\left(1 - \frac{m_H^2}{s}\right)\right]$$
$$\to \frac{G_F^3 m_W^4}{4\sqrt{2}\pi^3}\log\frac{s}{m_H^2} \qquad (4)$$

The cross section rises logarithmically at high energies, as to be anticipated for this t-channel exchange process.

3. Differential cross section and interference for WW fusion. The compact form (3) for the fusion cross section cannot be maintained once the interference term between vector boson fusion and Higgs-strahlung is included. Moreover, since in the case of WW fusion the integration variables x and y do not correspond to observable quantities, the formula is useful only for calculating the total cross section without experimental cuts. Nevertheless, similarly compact expressions can be derived in this general case by choosing the energy E_H and the polar angle θ of the Higgs particle as the basic variables in the e^-e^- c.m. frame. The overall cross section that will be observed experimentally for the process

$$e^-e^- \to H + \bar{\nu}\nu$$

receives contributions $3 \times \mathcal{G}_S$ from Higgs-strahlung with Z decays into three types of neutrinos, $\mathcal{G}_W$ from WW fusion, and $\mathcal{G}_I$ from the interference term between fusion and Higgs-strahlung for $\bar{\nu}_e\nu_e$ final states. We find[4] for energies $\sqrt{s}$ above the Z resonance:

$$\frac{d\sigma(H\bar{\nu}\nu)}{dE_H\, d\cos\theta} = \frac{G_F^2 m_Z^6 p}{\sqrt{2}\pi^5 s}\left(3\mathcal{G}_S + \mathcal{G}_I + \mathcal{G}_W\right) \qquad (5)$$

[4]The analytic result for $\mathcal{G}_W$ had first been obtained in Ref.[11].

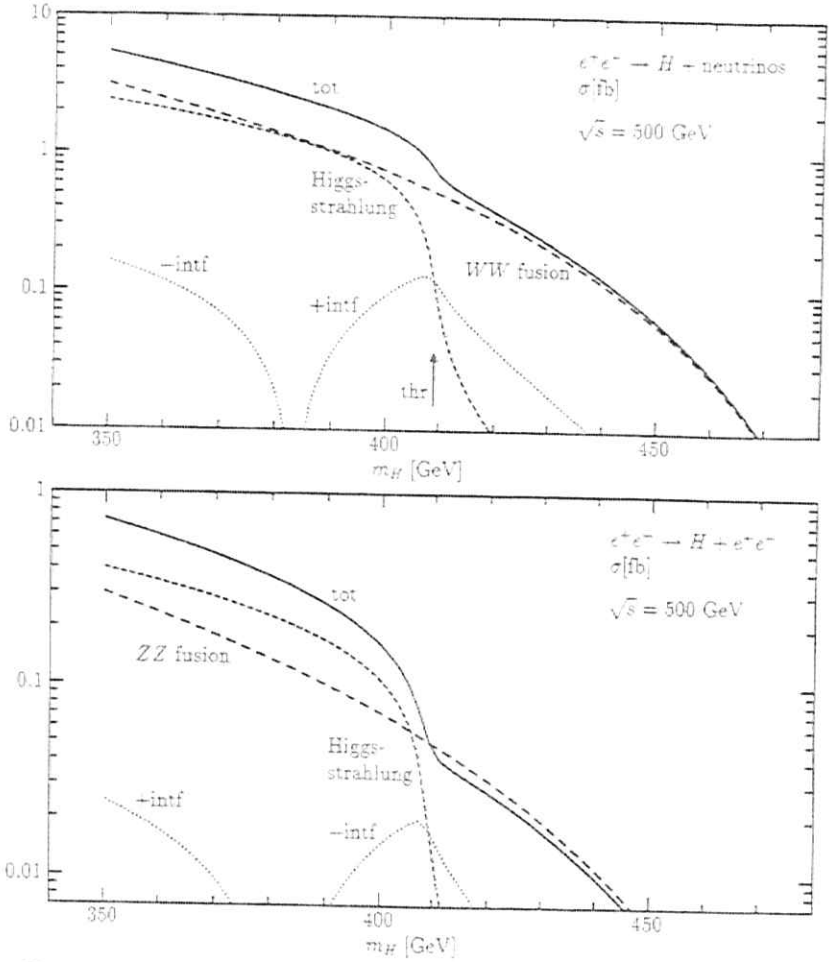

Figure 2: *Total cross sections for the processes $e^-e^- \to H\bar{\nu}\nu$ and $e^-e^- \to He^-e^-$ as a function of the Higgs mass. The cross sections are broken down to the three components Higgs-strahlung, vector boson fusion, and the interference term. "thr" denotes the maximum Higgs mass for on-shell ZH production, "tot" is the total cross section. In $e^-e^- \to H\bar{\nu}\nu$ (above) the interference term is negative for small Higgs masses, for large Higgs masses positive. In $e^-e^- \to He^-e^-$ (below), the interference term is of opposite sign.*

with

$$\mathcal{G}_S = \frac{v_e^2+a_e^2}{96}\,\frac{ss_\nu+s_1s_2}{(s-m_Z^2)^2[(s_\nu-m_Z^2)^2+m_Z^2\Gamma_Z^2]} \tag{6}$$

$$\mathcal{G}_I = \frac{(v_e-a_e)\cos^4\theta_W}{8}\,\frac{s_\nu-m_Z^2}{(s-m_Z^2)[(s_\nu-m_Z^2)^2+m_Z^2\Gamma_Z^2]} \times\left[2-(h_1-1)\log\frac{h_1+1}{h_1-1}-(h_2-1)\log\frac{h_2+1}{h_2-1}+(h_1+1)(h_2-1)\frac{\mathcal{L}}{\sqrt{r}}\right] \tag{7}$$

$$\mathcal{G}_W = \frac{\cos^6\theta_W}{s_1s_2r}\left\{(h_1+1)(h_2-1)\left[\frac{2}{h_1^2-1}+\frac{2}{h_2^2-1}-\frac{6s_\chi^2}{r}-\left(\frac{3t_1t_2}{r}-c_\chi\right)\frac{\mathcal{L}}{\sqrt{r}}\right] -\left[\frac{2t_1}{h_2-1}+\frac{2t_2}{h_1-1}+\left(t_1+t_2+s_\chi^2\right)\frac{\mathcal{L}}{\sqrt{r}}\right]\right\} \tag{8}$$

The cross section is written explicitly in terms of the Higgs momentum $p=\sqrt{E_H^2-m_H^2}$, and the energy $\epsilon_\nu=\sqrt{s}-E_H$ and invariant mass squared $s_\nu=\epsilon_\nu^2-p^2$ of the neutrino pair. In addition, the following abbreviations have been adopted from Ref.[11].

$$\begin{aligned} s_{1,2} &= \sqrt{s}(\epsilon_\nu \pm p\cos\theta) & t_{1,2} &= h_{1,2}+c_\chi h_{2,1}\\ h_{1,2} &= 1+2m_W^2/s_{1,2} & r &= h_1^2+h_2^2-2c_\chi h_1h_2-s_\chi^2\\ c_\chi &= 1-2ss_\nu/(s_1s_2) & \mathcal{L} &= \log\frac{h_1h_2-c_\chi+\sqrt{r}}{h_1h_2-c_\chi-\sqrt{r}}\\ s_\chi^2 &= 1-c_\chi^2 \end{aligned}$$

To derive the total cross section $\sigma(e^+e^-\to H\bar\nu\nu)$, the differential cross section must be integrated over the region

$$-1<\cos\theta<1 \quad\text{and}\quad m_H<E_H<\frac{\sqrt{s}}{2}\left(1+\frac{m_H^2}{s}\right) \tag{9}$$

4. Differential cross section and interference for ZZ fusion. Similarly, the overall cross section for the process

$$e^+e^-\to H+e^-e^-$$

receives contributions $\mathcal{G}_S$ from Higgs-strahlung with Z decays into electron-positron pairs, $\mathcal{G}_Z$ from ZZ fusion, and $\mathcal{G}_I$ from the interference term between fusion and Higgs-strahlung:

$$\frac{d\sigma(He^+e^-)}{dE_H\,d\cos\theta}=\frac{G_F^3m_Z^2p}{\sqrt{2}\pi^3}\left(\mathcal{G}_S+\mathcal{G}_I+\mathcal{G}_{Z1}+\mathcal{G}_{Z2}\right) \tag{10}$$

with

$$\mathcal{G}_S = \frac{\left(v_e^2+a_e^2\right)^2}{192}\,\frac{ss_\nu+s_1s_2}{(s-m_Z^2)^2[(s_\nu-m_Z^2)^2+m_Z^2\Gamma_Z^2]} \tag{11}$$

$$\mathcal{G}_I = \frac{\left(v_e^2-a_e^2\right)^2+4v_e^2a_e^2}{64}\,\frac{s_\nu-m_Z^2}{(s-m_Z^2)[(s_\nu-m_Z^2)^2+m_Z^2\Gamma_Z^2]} \times\left[2-(h_1-1)\log\frac{h_1+1}{h_1-1}-(h_2+1)\log\frac{h_2-1}{h_2+1}+(h_1-1)(h_2+1)\frac{\mathcal{L}}{\sqrt{r}}\right] \tag{12}$$

$$\mathcal{G}_{Z1} = \frac{\left(v_e^2-a_e^2\right)^2+4v_e^2a_e^2}{32\,s_1s_2r}\left\{(h_1-1)(h_2+1)\left[\frac{2}{h_1^2-1}+\frac{2}{h_2^2-1}-\frac{6s_\chi^2}{r}+\left(\frac{3t_1t_2}{r}-c_\chi\right)\frac{\mathcal{L}}{\sqrt{r}}\right] -\left[\frac{2t_1}{h_2-1}+\frac{2t_2}{h_1-1}-\left(t_1+t_2+s_\chi^2\right)\frac{\mathcal{L}}{\sqrt{r}}\right]\right\} \tag{13}$$

$$\mathcal{G}_{Z2} = \frac{\left(v_e^2-a_e^2\right)^2}{16\,s_1s_2r}(1-c_\chi)\left[\frac{2}{h_1^2-1}+\frac{2}{h_2^2-1}-\frac{6s_\chi^2}{r}+\left(\frac{3t_1t_2}{r}-c_\chi\right)\frac{\mathcal{L}}{\sqrt{r}}\right] \tag{14}$$

where the same abbreviations as in the formulae following Eq.(5), with the appropriate replacements $\nu\to e$ and $W\to Z$, have been used.

5. To interpret the results, we display the three components of the total cross sections $\sigma(e^-e^-\to H\bar\nu\nu)$ and $\sigma(e^+e^-\to He^-e^-)$ in Fig.2 for the linear collider energy $\sqrt{s}=500$ GeV in the cross-over region.[5]

While the energy distribution of the Higgs particle peaks at $E_H\sim(s+m_H^2-m_Z^2)/2\sqrt{s}$ for Higgs-strahlung, it is nearly flat for WW fusion (Fig.3, left). Only with rising total energy the lower part of the Higgs spectrum becomes more pronounced. The angular distribution for Higgs-strahlung is almost isotropic at threshold while the standard $\sin^2\theta$ law is approached, in accordance with the equivalence principle, at asymptotic energies (Fig.3, right). The angular distribution peaks, by contrast, in the WW fusion process at $\theta\to0$ and π for high energies as expected for t-channel exchange processes.

6. Polarized beams. At linear colliders the incoming electron and positron beams can be polarized longitudinally. Higgs-strahlung and WW fusion both require opposite helicities of the electrons and positrons. If $\sigma_{UI,RL}$ denote the cross sections in $e^-e^-\to H\bar\nu\nu$ for unpolarized electrons/positrons, left-handed electrons/right-handed positrons, and right-handed electrons/left-handed positrons, respectively, we can easily derive, in the notation of Eq.(5):

$$\sigma_U \propto 3\mathcal{G}_S+\mathcal{G}_I+\mathcal{G}_W \tag{15}$$

$$\sigma_{LR} \propto 6\mathcal{G}_S+4\mathcal{G}_I+4\mathcal{G}_W \tag{16}$$

$$\sigma_{RL} \propto 6\mathcal{G}_S \tag{17}$$

The cross section for WW fusion of Higgs particles increases by a factor four, compared with unpolarized beams, if left-handed electrons and right-handed positrons are used. By using right-handed electrons, the WW fusion mechanism is switched off. [The interference term cannot be separated from the WW fusion cross section.]

[5] Note that Higgs-strahlung dominates WW fusion at 500 GeV for moderate Higgs masses only if the total ZH cross section is considered.

For the process $e^+e^- \to He^+e^-$, the pattern is slightly more complicated:

$$\sigma \propto \mathcal{G}_S + \mathcal{G}_I + \mathcal{G}_{ZI} + \mathcal{G}_{ZZ} \quad (18)$$

$$\sigma_{LR} \propto 2\frac{(v_e+a_e)^2}{(v_e^2+a_e^2)^2}\mathcal{G}_S + 2\frac{(v_e-a_e)^4}{(v_e^2-a_e^2)^2+4v_e^2a_e^2}(\mathcal{G}_I+\mathcal{G}_{ZI}) \quad (19)$$

$$\sigma_{RL} \propto 2\frac{(v_e-a_e)^2}{(v_e^2+a_e^2)^2}\mathcal{G}_S + 2\frac{(v_e-a_e)^4}{(v_e^2-a_e^2)^2+4v_e^2a_e^2}(\mathcal{G}_I+\mathcal{G}_{ZI}) \quad (20)$$

$$\sigma_{LL} = \sigma_{RR} \propto 2\mathcal{G}_{ZZ}. \quad (21)$$

However, since $v_e \ll a_e$, the difference between σ_{RL} and σ_{LR} is suppressed.

7. Supersymmetric CP-even Higgs bosons. It is trivial to transfer all these results from the Standard Model to the Minimal Supersymmetric Standard Model (MSSM). Since the couplings to Z/W gauge bosons in the MSSM are shared [20] by the CP-even light and heavy scalar Higgs bosons, h and H, respectively, only the overall normalization of the cross sections is modified with respect to the Standard Model:

$$\sigma(h)_{\rm MSSM} = \sin^2(\beta-\alpha) \times \sigma(H)_{\rm SM} \quad (22)$$

$$\sigma(H)_{\rm MSSM} = \cos^2(\beta-\alpha) \times \sigma(H)_{\rm SM} \quad (23)$$

Higgs-strahlung, vector boson fusion, and the interference term are affected in the same way. [The angle α is the mixing angle in the CP-even Higgs sector while the mixing angle β is determined by the ratio of the vacuum expectation values of the two neutral Higgs fields in the MSSM. A recent discussion of the size of the coefficients $\sin^2$ / $\cos^2(\beta-\alpha)$ may be found in Ref.[21].]

References

[1] P.W. Higgs, Phys. Rev. Lett. 12 (1964) 132, and Phys. Rev. D145 (1966) 1156; F. Englert and R. Brout, Phys. Rev. Lett. 13 (1964) 321; G.S. Guralnik, C.R. Hagen, and T.W. Kibble, Phys. Rev. Lett. 13 (1964) 585.

[2] P. Fayet, Nucl. Phys. B90 (1975) 104.

[3] J.-F. Grivaz, Proceedings of the *International EPS Conference on High-Energy Physics*, Bruxelles 1995.

[4] M. Carena et al., *Higgs Physics*, in: Proceedings of the Workshop *Physics with LEP2*, eds. G. Altarelli and F. Zwirner, CERN 1995.

[5] G. Altarelli, Proceedings of the *ECFA LHC-Workshop*, eds. G. Jarlskog and D. Rein, Aachen 1990, CERN 90/10.

[6] Proceedings of the Workshop *e^+e^- Collisions at 500 GeV: The Physics Potential*, Munich–Annecy–Hamburg, ed. P.M. Zerwas, Reports DESY 92-123A,B; 93-123C.

[7] W. Kilian, M. Krämer, and P.M. Zerwas, Phys. Lett. B373 (1996) 135.

[8] J. Ellis, M.K. Gaillard, and D.V. Nanopoulos, Nucl. Phys. B106 (191976) 292; B.L. Ioffe and V.A. Khoze, Sov. J. Part. Nucl. 9 (1978) 50; B.W. Lee, C. Quigg, and H.B. Thacker, Phys. Rev. D16 (1977) 1519; J.D. Bjorken, Proc. *Summer Institute on Particle Physics*, SLAC Report 198 (1976).

[9] D.R.T. Jones and S.T. Petcov, Phys. Lett. B84 (1979) 440.

[10] R.N. Cahn and S. Dawson, Phys. Lett. B136 (1984) 96; G.L. Kane, W.W. Repko, and W.B. Rolnick, Phys. Lett. B148 (1984) 367; R.N. Cahn, Nucl. Phys. B255 (1985) 341; B.A. Kniehl, Z. Phys. C55 (1992) 605.

[11] G. Altarelli, B. Mele, and F. Pitolli, Nucl. Phys. B287 (1987) 205.

[12] S. Katsanevas et al., in preparation.

[13] E. Boos, M. Sachwitz, H. Schreiber, and S. Shichanin, Int. J. Mod. Phys. A10 (1995) 2067.

[14] T. Sjöstrand, *The PYTHIA 5.7 and JETSET 7.4 Manual*, LU–TP 95/20 and CERN–TH 112/93, and Comput. Phys. Commun. 82 (1994) 74.

[15] P. Janot, *The HZHA Generator Program*, in preparation.

[16] A. Djouadi, M. Spira, and P.M. Zerwas, DESY 95-210 and Z. Phys. C in print.

[17] A. Djouadi, D. Haidt, B.A. Kniehl, B. Mele, and P.M. Zerwas, in Ref.[6].

[18] V.N. Baĭer, V.S. Fadin, and V.A. Khoze, Sov. Phys. JETP 23 (1966) 104.

[19] E. Boos et al., Report SNUTP-94-116.

[20] J.F. Gunion and H.E. Haber, Nucl. Phys. B272 (1986) 1; B278 (1986) 449; B307 (1988) 445; Erratum *ibid.* B402 (1993) 567; A. Djouadi, J. Kalinowski, and P.M. Zerwas, Z. Phys. C57 (1993) 569.

[21] A. Djouadi, J. Kalinowski, and P.M. Zerwas, DESY 95-211 and Z. Phys. C in print.

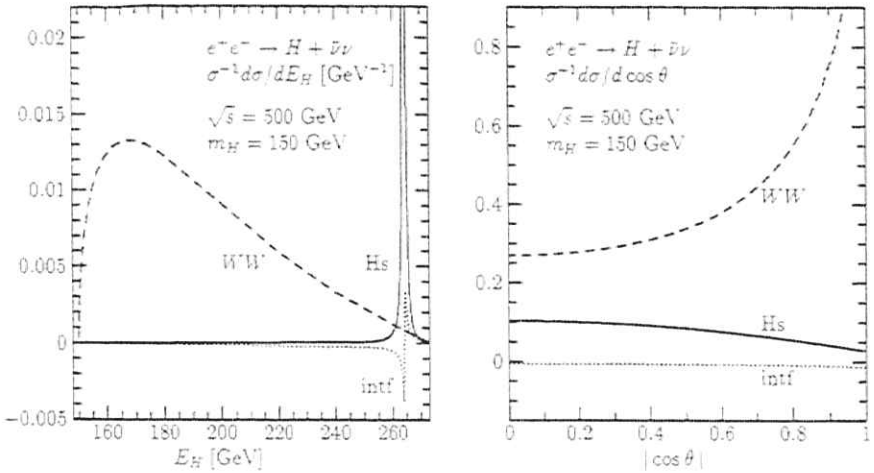

Figure 3: *Energy distribution (left) and angular distribution (right) of the Higgs bosons for the three components of the cross section [*Hs *= Higgs-strahlung;* WW *= fusion:* intf *= interference term]. The individual curves are normalized to the total cross section. The* Hs *peak extends up to maximal values of* 0.22 GeV^{-1}. *The total cross section is* 69.4 fb.

Associated Pair Production of the $\mathcal{SM}$ Higgs and the Probing of the Higgs Self-Coupling

E. CHOPIN

Laboratoire de Physique Théorique ENSLAPP *
B.P.110, 74941 Annecy-Le-Vieux Cedex, France
E-mail: chopin@lappnp0.in2p3.fr

1 Associated Higgs Pair Production

The interest in double Higgs production is the probing of the triple Higgs self coupling. It has been considered in e^+e^- sometime ago[1]. The most efficient means for double Higgs production is $e^+e^- \to \nu_e\bar{\nu}_e HH$ (see fig. 1). Double Higgs bremstrahlung ($e^+e^- \to ZHH$) is only competing at relatively low energies where the event sample is too low to be useful. The equivalent loop-induced double Higgs production in e^+e^- has been found to be much too small[4] and is not sensitive to the H^3 coupling. However, the $\gamma\gamma$ mode can form a $J_Z = 0$ state and therefore $\gamma\gamma \to HH$ is a candidate for testing the H^3 coupling[3]. It has been pointed out recently that another interesting process is $\gamma\gamma \to W^+W^-HH$ [2] that is expected to compete with double Higgs production in e^+e^- . The reason is that in the TeV range, W fusion processes are very much enhanced. The sub-process involved is $W^+W^- \to HH$, where the dominant helicity amplitude is:

$$\begin{aligned}\bar{\mathcal{M}}_{LL} &= \frac{g^2}{2}\left\{\frac{1}{\beta_H\beta_W^3}\left(\frac{1}{x-x_0}-\frac{1}{x-x_0}\right)(\tau\frac{M_H^2}{s}+\beta_H^2+\beta_W^4)\right.\\ &- \left.\frac{1}{\beta_W^2}(2-\beta_W^2-\tau)+\frac{3h_3\tau}{4}\left(\frac{1+\beta_W^2}{1-M_H^2/s}\right)\right\} \to \frac{g^2}{4}\tau(3h_3-2)+\ldots \qquad (1)\end{aligned}$$

Where h_3 is the anomaly in the triple Higgs coupling g, *i.e.* $g = h_3 g_{sm}$ where g_{sm} is the minimal standard model coupling of H^3. We also denote $\beta_{W,H} = \sqrt{1-4M_{W,H}^2/s}$, $\tau = M_H^2/M_W^2$, $z_0 = (1+\beta_H^2)/2\beta_W\beta_H$, $x = \cos\theta$.

Figure 2 shows that at 2TeV, the cross sections drops precipitously with increasing Higgs mass. One can also notice that in $\gamma\gamma \to W^+W^-HH$ the external outgoing W (mainly transverse) are produced at small angle and take a large amount of energy. For the fusion diagrams of this process, the internal W triggers $W^+W^- \to HH$, which implies that these diagrams dominate for a heavy Higgs. When convoluting with the much advertised photon spectra of[5] and for $M_H = 100GeV$ the cross section of $\gamma\gamma \to W^+W^-HH$ drops by about at least a factor of 2 compared with the result without convolution. For W-fusion-like processes, the internal W's are almost on shell and one may wonder if some structure functions could reproduce the exact results.

*URA 14-36 du CNRS, associée à l'E.N.S de Lyon et à l'Université de Savoie.

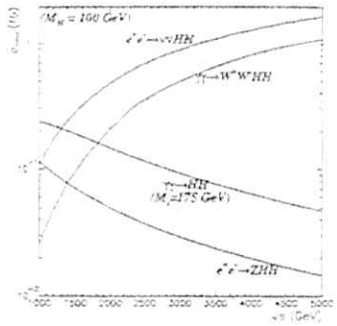

Figure 1: Comparison of cross sections for double Higgs production at e^+e^- and $\gamma\gamma$ reactions for a light Higgs $M_H = 100GeV$.

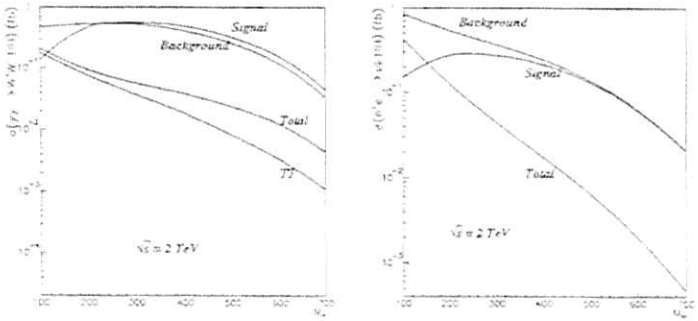

Figure 2: Higgs mass dependence of the $\gamma\gamma \to W^+W^-HH$ cross section at 2TeV. The contribution of the diagrams involving the triple Higgs vertex (Signal) and the rest (Background) is shown separetely. Note the strong interference that occurs in the $\mathcal{SM}$ especially for large M_H.

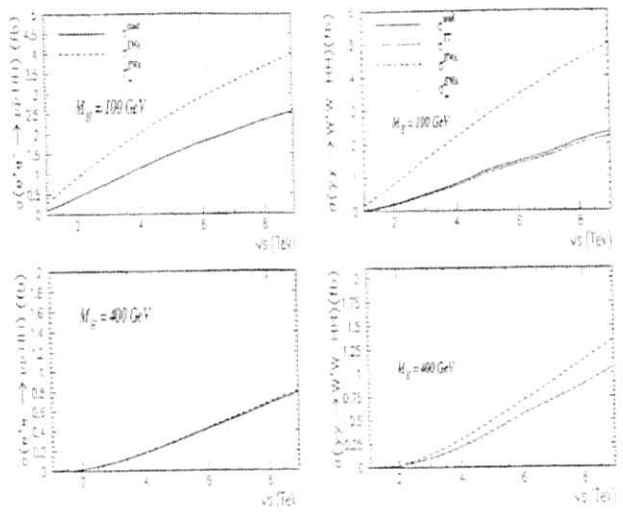

Figure 3: Comparing the result of the W_L effective approximation (σ^{EWA}) to the exact result σ^{exact} for $e^+e^- \to \nu_e\bar{\nu}_e HH$ (left) and $\gamma\gamma \to W^+W^-HH$ (right) for a light Higgs and a heavy Higgs. Also shown is the asymptotic analytical cross section σ_∞^{EWA}. σ^{TT} is the cross section with both outgoing W's transverse.

2 The structure function approach

There have been numerous derivations of the distribution (or structure function) of the W inside the light fermions (quarks and electrons) [6]. For the effective W approximation, the most interesting aspect concerns the W_L content, which has been used to investigate manifestations of models of symmetry breaking and Higgs production. The W_L distribution inside the photon has only very recently been studied [7]. For the case of the heavy Higgs the approximation is excellent, already at 2TeV. However, for a light Higgs, the approximation is not good and reproduce only the energy behaviour. If one makes the further approximation that the hard process cross section is independent of the energy, this additional "asymptotic" approximation only reproduces the energy behaviour as well as the order of magnitude (even for a heavy Higgs, see figs. 3).

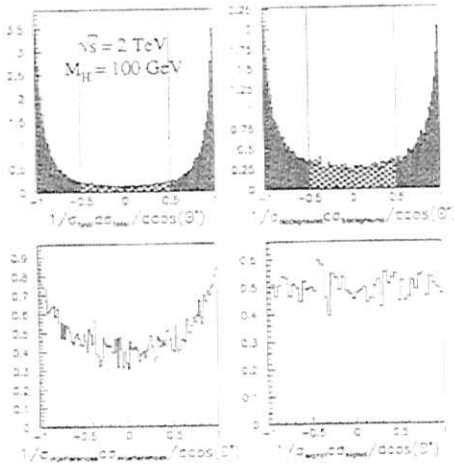

Figure 4: The distribution in the reconstructed angle ϑ^* for the signal, background and the interference in the case of $\gamma\gamma \to W^+W^-HH$ without convolution with photon spectra.

3 Identifying and measuring the Higgs triple vertex

There is a specific signature of the H^3 coupling in all processes that we have studied. Once we note that the two Higgses that originate from this vertex can be regarded as produced by a scalar H^* then in the centre of mass system of the pair, the angular distribution of the Higgses is flat. Therefore, we suggest to reconstruct the angle, ϑ^*, measured in the centre-of-mass of the pair, between the Higgs direction and the boost axis or the direction of the beam. For the "signal"[†] the distribution is flat, while the "background" is peaked in the forward/backward direction (see fig. 4). We therefore consider the ratio R of events that verify $|\cos(\vartheta^*)| < \cos(\vartheta_0^*)$[‡], over the number of events outside this region. Assuming a total integrated luminosity of $300 fb^{-1}$, and a 50% efficiency for the reconstruction of the double Higgs events one obtain ~ 68 $e^+e^- \to \nu_e\bar{\nu}_e HH$ events for $M_H = 100GeV$. Here the criterion for detection of an anomaly in h_3 is a 50% deviation in the expected number of events, provided one has at least 30 events. We conclude that with the total cross section one would only be able to claim New Physics if $\delta h_3 < -0.75$ or $\delta h_3 > 2$.

[†] We call "signal" the part of the amplitude that include the H^3 vertex. The rest is called "background".
[‡] $\cos\vartheta_0^* = 0.5$ is taken in the following.

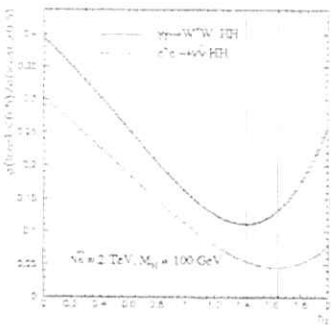

Figure 5: Dependence of the ratio R on h_3.

For $M_H = 400GeV$, $S\mathcal{M}$ values will not lead to a measurement, however if $|\delta h_3| > 1$ a signal will be recorded (with more than 30 events) and would be a clear indication for an anomalous h_3 coupling. For $M_H = 100GeV$ where one has enough events for a $S\mathcal{M}$ value, the ratio R is much more powerful in constraining the coupling. First the event sample within $|\cos\theta^*| < 0.5$ is about 7 out of 60 outside this region. Assuming that the ratio can be measured at 20%, we find $-.10 < |\delta h_3| < .15$ (see fig. 5) which means a precision of about 10% on h_3. For $\gamma\gamma \to W^+W^-HH$ and considering the effective $\gamma\gamma$ luminosity, for $M_H = 100GeV$, one can hope to collect 15 events. In view of this number the criterion for detection of non-standard values is 100% deviation in the number of events. However, for a Higgs mass of 400GeV the effect of an anomalous H^3 coupling are dramatic and, by far, much more interesting than in e^+e^-. Requiring observation of at least 15 events for $M_H = 400$GeV (within the $S\mathcal{M}$ one expects only 3) useful constraints on the coupling can be set: $-.7 < \delta h_3 < 0.5$. There is thus a complementarity between the e^+e^- and the $\gamma\gamma$ depending on the Higgs mass in probing the Higgs triple vertex. As for the ratio R, taking $M_H = 100GeV$ it is unlikely that with the number of total $WWHH$ events at $\gamma\gamma$ one would be able to make such a measurement, nonetheless even if this ratio were measured with the same precision as in e^+e^- one would not constrain the couplings further than what is achieved in the classic e^+e^- mode. For $M_H > 600GeV$, $\gamma\gamma \to HH$ is the only reaction where useful limits can be set. Thus, there is at a 2TeV collider a very nice coverage of the h_3 sensitivity by all three reactions.

4 Conclusions

We have seen that a 2TeV e^+e^- collider with the realistic luminosities expected for this machine one may hope to achieve a measurement of the tri-linear couplings at the level of 10% (for a light Higgs). The results are also encouraging in the sense that the e^+e^- and the $\gamma\gamma$ modes can cover different ranges of the Higgs mass. We find that for a light Higgs (up to 250GeV) the best limits on the H^3 couplings come from $e^+e^- \to \nu_e\bar{\nu}_e HH$. However, for heavier Higgses up to mass of $500GeV$, the best channel is the associated double Higgs production in $\gamma\gamma$. For still heavier masses, the one-loop induced $\gamma\gamma \to HH$ is by far better. The variable R clearly helps in discriminating the triple Higgs vertex. As a by-product we have verified the validity of the distribution function describing the longitudinal W content of the photon. We should also insist on the complementarity of the e^+e^- and the $\gamma\gamma$ modes of the linear collider for these studies.

References

[1] V. Barger, T. Han and R. J. N Phillips, Phys. Rev. **D38** (1988) 2766.
V. Barger, T. Han, *Mod. Phys. Lett.* **A5** (1990) 667.

[2] F. Boudjema, E. Chopin, *HEP-PH/9507396*, submitted to Z. Phys.

[3] G.V. Jikia and Yu.F. Pirogov, *Phys. Let.* B283 (1992) 135.
G.V. Jikia, Nucl. Phys. **B412** (1994) 57.

[4] K.J.F. Gaemers, F. Hoogeveen, Z. Phys. C26 (1984) 249.
A. Djouadi, V. Driesen, C. Jünger, *HEP-PH/9602341*, KA-TP-02-96 (Feb. 96).

[5] I.F. Ginzburg *et al.*, *Nucl. Instrum. Meth.* **205** (1983) 47.
I.F. Ginzburg *et al.*, *Nucl. Instrum. Meth.* **219** (1984) 5.
V.I. Telnov, *Nucl Instrum. Meth.* **A294** (1990) 72.

[6] S. Dawson, Nucl. Phys. **B249** (1984) 42.
W.B. Rolnick, Nucl. Phys. **B274** (1986) 171.
Z. Kunszt and D.E. Soper, Nucl. Phys. **B296** (1988) 253.

[7] M. Baillargeon, G. Bélanger and F. Boudjema, in *Proceedings of Two-Photon Physics from DAΦNE to LEP200 and Beyond*, Paris, 1994, edited by F. Kapusta and J. Parisi (world Scientific, Singapore, 1995), p.267.

Anomalous Couplings in the Higgs-strahlung Process

W. KILIAN, M. KRÄMER, AND P.M. ZERWAS
Deutsches Elektronen-Synchrotron DESY, D-22603 Hamburg, FRG

Abstract

The angular distributions in the Higgs-strahlung process $e^+e^- \to HZ \to Hff$ are uniquely determined in the Standard Model. We study how these predictions are modified if non-standard couplings are present in the ZZH vertex, as well as lepton-boson contact terms. We restrict ourselves to the set of operators which are singlets under standard $SU_3 \times SU_2 \times U_1$ transformations, CP conserving, dimension 6, helicity conserving, and custodial SU_2 conserving.

1. The Higgs-strahlung process [1]

$$e^+e^- \to HZ \to Hff \tag{1}$$

together with the WW fusion process, are the most important mechanisms for the production of Higgs bosons in e^+e^- collisions [2,3]. Since the ZZH vertex is uniquely determined in the Standard Model (SM), the production cross section of the Higgs-strahlung process, the angular distribution of the HZ final state as well as the fermion distribution in the Z decays can be predicted if the mass of the Higgs boson is fixed [4]. These predictions may be modified when deviations from the pointlike coupling are present, which can occur in models with non-pointlike character of the Higgs boson itself or through interactions beyond the SM at high energy scales. Since the effective energy scale of the Higgs-strahlung process is set by the c.m. energy $\sqrt{s}$, while the fusion processes are essentially low-energy processes with an effective scale of the order M_W, new interactions manifest themselves more clearly in the total cross section and angular distributions for the Higgs-strahlung process (see also [5]).

2. Operator basis. Deviations from the pointlike coupling can occur in models with non-pointlike character of the Higgs boson itself or through interactions beyond the SM at high energy scales. We need not specify the underlying theory but instead we will adopt the usual assumption that these effects can globally be parameterized by introducing a set of dimension-6 operators

$$\mathcal{L} = \mathcal{L}_{\rm SM} + \sum_i \frac{a_i}{\Lambda^2} O_i \tag{2}$$

The coefficients are in general expected to be of the order $1/\Lambda^2$, where Λ denotes the energy scale of the new interactions. However, if the underlying theory is weakly interacting, the a_i can be significantly smaller than unity, in particular for loop-induced operators. [It is assumed *a priori* that the ratio of the available c.m. energy to Λ is small enough for the expansion in powers of $1/\Lambda$ to be meaningful.]

If we restrict ourselves to operators O_i which are singlets under $SU_3 \times SU_2 \times U_1$ transformations of the SM gauge group, CP conserving, and conserving the custodial SU_2 symmetry, the following bosonic operators are relevant for the Higgs-strahlung process:

$$O_{\Phi 1} = \frac{1}{2}\partial_\mu(\varphi^\dagger\varphi)\partial^\mu(\varphi^\dagger\varphi) \tag{3}$$

$$O_{\varphi W} = \frac{1}{2}\varphi^\dagger \hat{W}^2_{\mu\nu}\varphi \tag{4}$$

$$O_{\varphi B} = \frac{1}{2}\varphi^\dagger B^2_{\mu\nu}\varphi \tag{5}$$

where the gauge fields W^3, B are given by the Z, γ fields. This set of operators is particularly interesting because it does not affect, at tree level, observables which do not involve the Higgs particle explicitly. [It is understood that the fields and parameters are (re-)normalized in the Lagrangian $\mathcal{L}$ in such a way that the particle masses and the electromagnetic coupling retain their physical values.]

In addition, we consider the following helicity-conserving fermionic operators which induce contact terms contributing to $e^+e^- \to ZH$:

$$O_{L1} = (\varphi^\dagger i D_\mu \varphi)(\bar{\ell}_L \gamma^\mu \ell_L) + \text{h.c.} \tag{6}$$

$$O_{L3} = (\varphi^\dagger \tau^3 i D_\mu \varphi)(\bar{\ell}_L \tau^3 \gamma^\mu \ell_L) + \text{h.c.} \tag{7}$$

$$O_R = (\varphi^\dagger i D_\mu \varphi)(\bar{e}_R \gamma^\mu e_R) + \text{h.c.} \tag{8}$$

[ℓ_L and e_R denote the left-handed lepton doublet and the right-handed singlet, respectively. The vacuum expectation value of the Higgs field is given by $\langle\varphi\rangle = (0, v/\sqrt{2})$ with $v = 246\,\text{GeV}$, and the covariant derivative acts on the Higgs doublet as $D_\mu = \partial_\mu - \frac{1}{2}g\tau^a W^a_\mu - \frac{1}{2}g' B_\mu$.] Helicity-violating fermionic operators do not interfere with the SM amplitude, so that their contribution to the cross section is suppressed by another power of Λ^2. The helicity-conserving fermionic operators modify the SM Zee couplings and are therefore constrained by the measurements at LEP1; however, it is possible to improve on the existing limits by measuring the Higgs-strahlung process at a high-energy e^+e^- collider since the impact on this process increases with energy [7].

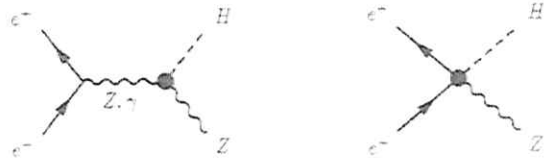

Figure 1: *Anomalous $ZZH/\gamma ZH$ couplings and e^+e^-ZH contact terms in the Higgs-strahlung process.*

The effective ZZH and the induced γZH interactions (Fig.1, left diagram) may be written

$$\mathcal{L}_{ZZH} = g_Z M_Z \left(\frac{1+a_0}{2} Z_\mu Z^\mu H - \frac{a_1}{4} Z_{\mu\nu} Z^{\mu\nu} H \right) \tag{9}$$

$$\mathcal{L}_{eZH} = g_Z M_Z \frac{b_1}{2} Z_\mu A^{\mu\nu} H \tag{10}$$

where $g_Z = M_Z \sqrt{4\sqrt{2}G_F}$. Additional operators $Z_\mu Z^{\mu\nu}\partial_\nu H$ and $Z_\mu A^{\mu\nu}\partial_\nu H$ are redundant in this basis: They may be eliminated in favor of the other operators and the contact terms by applying the equations of motion. The remaining coefficients are given by

$$a_0 = -\frac{1}{2} a_{eW} v^2/\Lambda^2 \tag{11}$$

$$a_1 = 4 g_Z^{-2} \left(c_W^2 a_{eW} + s_W^2 a_{eB} \right)/\Lambda^2 \tag{12}$$

$$b_1 = 4 g_Z^{-2} c_W s_W \left(-a_{eW} + a_{eB} \right)/\Lambda^2 \tag{13}$$

where s_W and c_W are the sine and cosine of the weak mixing angle, respectively.

In the same way the $e\bar{e}HZ$ contact interactions (Fig.1, right diagram) can be defined for left-/right-handed electrons and right-/left-handed positrons

$$\mathcal{L}_{eeZH} = g_Z M_Z \left[c_L \bar{e}_L Z e_L H + c_R \bar{e}_R Z e_R H \right] \tag{14}$$

with

$$c_L = -2 g_Z^{-1} \left(a_{L1} - a_{L3} \right)/\Lambda^2 \tag{15}$$

$$c_R = -2 g_Z^{-1} a_R/\Lambda^2 \tag{16}$$

Some consequences of these operators for Higgs production in e^+e^- collisions have been investigated in the past. Most recently, the effect of novel ZZH vertex operators and $\ell\ell ZH$ contact terms on the total cross sections for Higgs production has been studied in Ref.[7]. The impact of vertex operators on angular distributions has been analyzed in Refs.[8] and [9]. We expand on these analyses by studying the angular distributions for the more general case where both novel vertex operators and contact interactions are present. The analysis of angular distributions in the Higgs-strahlung process (1) allows us to discriminate between various novel interactions. In fact, the entire set of parameters a_0, a_1, b_1 and c_L, c_R can be determined by measuring the polar and azimuthal angular distributions as a function of the beam energy if the electron/positron beams are unpolarized. As expected, the energy dependence of the polar angular distribution is sufficient to provide a complete set of measurements if longitudinally polarized electron beams are available[1].

3. Total cross section and polar angular distribution. Denoting the polar angle between the Z boson and the e^+e^- beam axis by θ, the differential cross section for the process $e^+e^-_{L,R} \to ZH$ may be written as

$$\frac{d\sigma^{L,R}}{d\cos\theta} = \frac{G_F^2 M_Z^4}{96\pi s} \left(v_e \pm a_e \right)^2 \lambda^{3/2} \frac{\frac{3}{4}\lambda \sin^2\theta \left(1 + \alpha^{L,R} \right) + 6 \left(1 + \beta^{L,R} \right) M_Z^2/s}{\left(1 - M_Z^2/s \right)^2} \tag{17}$$

[1] Since we can restrict ourselves to helicity-conserving couplings, as argued before, additional positron polarization need not be required.

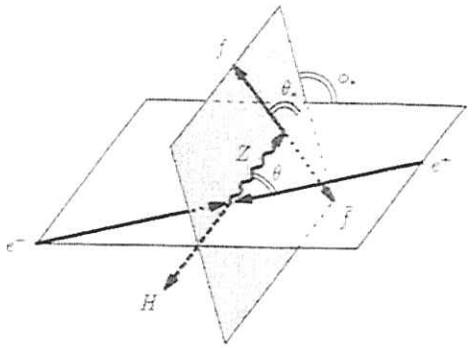

Figure 2: *Polar and azimuthal angles in the Higgs-strahlung process. [The polar angle θ_* is defined in the Z rest frame.]*

and the integrated cross section

$$\sigma = \frac{G_F^2 M_Z^4}{96\pi s} \left(v_e \pm a_e \right)^2 \lambda^{3/2} \frac{\lambda \left(1 + \alpha^{L,R} \right) + 12 \left(1 + \beta^{L,R} \right) M_Z^2/s}{\left(1 - M_Z^2/s \right)^2} \tag{18}$$

The Z charges of the electron are defined as usual by $a_e = -1$ and $v_e = -1 + 4s_W^2$. s is the c.m. energy squared, and λ the two-particle phase space coefficient $\lambda = [1 - (m_H + m_Z)^2/s] \times [1 - (m_H - m_Z)^2/s]$. The coefficients $\alpha(s)^{L,R}$ and $\beta(s)^{L,R}$ can easily be determined for the interactions in Eqs.(9) and (14):

$$\alpha(s)^{L,R} = 2a_0 - (s - M_Z^2) \frac{2 c_W s_W}{v_e \pm a_e} c_{L,R} \tag{19}$$

$$\beta(s)^{L,R} = \alpha(s)^{L,R} + 2\gamma\sqrt{s} M_Z \left[a_1 - \frac{4 c_W s_W}{v_e \pm a_e} \left(1 - \frac{M_Z^2}{s} \right) b_1 \right] \tag{20}$$

where the boost of the Z boson is given by $\gamma = (s - M_Z^2 - M_H^2)/2M_Z\sqrt{s}$.

The modification of the cross section by the new interaction terms has a simple structure. The coefficient a_0 just renormalizes the SM cross section. By contrast, the contact interactions grow with s. [The ratio s/Λ^2 is assumed to be small enough for the restriction to dimension-6 operators to be meaningful.] The operators $\mathcal{O}_{eW}$, $\mathcal{O}_{eB}$ affect the coefficient in the cross section which is independent of θ. They damp the fall-off of this term, changing the $1/s^2$ to a $1/s$ behavior; however, these contributions remain subleading since they are associated with transversely polarized Z bosons which are suppressed at high energies compared with the longitudinal components. To illustrate the size of the modifications $\alpha(s)^{L,R}$ and $\beta(s)^{L,R}$, we have depicted these functions in Fig.3(a) for the special choice $a_i = 1$.

4. Azimuthal distributions. The azimuthal angle ϕ_* of the fermion f is defined as the angle between the $[e^-, Z]$ production plane and the $[Z, f]$ decay plane (Fig.2). It corresponds to the azimuthal angle of f in the Z rest frame with respect to the $[e^-, Z]$ plane. On general grounds, the ϕ_* distribution must be a linear function of $\cos\phi_*$, $\cos 2\phi_*$, and $\sin\phi_*$, $\sin 2\phi_*$, measuring the helicity components of the decaying spin-1 Z state. The coefficients of the sine terms vanish for CP invariant theories. The $\cos\phi_*$ and $\cos 2\phi_*$ terms correspond to P-odd and P-even combinations of the fermion currents. The general azimuthal distributions are quite involved [4,8,9]. We therefore restrict ourselves to the simplified case in which all polar angles are integrated out, i.e., the polar angle θ of the Z boson in the laboratory frame and the polar angle θ_* of f in the Z rest frame. In this way we find for the azimuthal ϕ_* distribution:

$$\frac{d\sigma^{L,R}}{d\phi_*} \sim 1 + \frac{9\pi^2}{32}\frac{2\,v_f a_f}{v_f^2+a_f^2}\frac{\gamma}{\gamma^2+2}\left(1+f_1^{L,R}\right)\cos\phi_* + \frac{1}{2(\gamma^2+2)}\left(1+f_2^{L,R}\right)\cos 2\phi_* \quad (21)$$

with

$$f_1(s)^{L,R} = M_Z\sqrt{s}\,\frac{(\gamma^2-1)(\gamma^2-2)}{\gamma(\gamma^2+2)}\left[a_1 - \frac{4s_W c_W}{v_e \pm a_e}\left(1-\frac{M_Z^2}{s}\right)b_1\right] \quad (22)$$

$$f_2(s)^{L,R} = 2M_Z\sqrt{s}\,\frac{\gamma(\gamma^2-1)}{\gamma^2+2}\left[a_1 - \frac{4s_W c_W}{v_e \pm a_e}\left(1-\frac{M_Z^2}{s}\right)b_1\right] \quad (23)$$

The cross section flattens with increasing c.m. energy in the Standard Model, i.e. the coefficients of $\cos\phi_*$ and $\cos 2\phi_*$ decrease asymptotically proportional to $1/\sqrt{s}$ and $1/s$, respectively. The anomalous contributions modify this behavior: The $\cos\phi_*$ term receives contributions which increase proportional to $\sqrt{s}$ with respect to the total cross section, while the $\cos 2\phi_*$ term receive contributions from the transversal couplings that approaches a constant value asymptotically. The size of the new terms in $f_{1,2}^{L,R}$ is shown in Fig.3(b) as a function of the energy. [The special choice $\alpha_i = 1$ we have adopted for illustration, implies $f_{1,2}^L = f_{1,2}^R$.]

5. High-energy limit. It is instructive to study the high-energy behavior of the coefficients in the limit $M_Z^2 \ll s \ll \Lambda^2$. In this case we obtain the simplified relations:

$$\alpha(s)^{L,R} \simeq -s\cdot 8 s_W c_W\, c_{L,R} + \mathcal{O}(v_e) \quad (24)$$

$$\beta(s)^{L,R} \simeq \alpha(s)^{L,R} + s\,(a_1 - 4 s_W c_W\, b_1) + \mathcal{O}(v_e) \quad (25)$$

and

$$f_1(s)^{L,R} \simeq \frac{s}{2}\,(a_1 - 4 s_W c_W\, b_1) + \mathcal{O}(v_e) \quad (26)$$

$$f_2(s)^{L,R} \simeq s\,(a_1 - 4 s_W c_W\, b_1) + \mathcal{O}(v_e) \quad (27)$$

Terms which are proportional to $v_e = -1 + 4s_W^2$ are suppressed by an order of magnitude. If longitudinally polarized electrons are available, the asymptotic value of the coefficients

a_1, b_1, c_L and c_R can be determined by measuring the polar angular distribution without varying the beam energy. The analysis of the azimuthal ϕ_* distribution provides two additional independent measurements of the coefficients a_1 and b_1. On the other hand, the set of measurements remains incomplete for fixed energy if only unpolarized electron/positron beams are used at high energies; in this case the coefficients cannot be disentangled completely without varying the beam energy within the preasymptotic region.

References

[1] J. Ellis, M.K. Gaillard, and D.V. Nanopoulos, Nucl. Phys. B106 (1976) 292; B.L. Ioffe and V.A. Khoze, Sov. J. Part. Nucl. 9 (1978) 50; B.W. Lee, C. Quigg, and H.B. Thacker, Phys. Rev. D16 (1977) 1519; J.D. Bjorken, Proc. *Summer Institute on Particle Physics*, SLAC Report 198 (1976).

[2] M. Carena, P.M. Zerwas (conv.) et al., *Higgs Physics*, in: Proceedings of the Workshop *Physics with LEP2*, eds. G. Altarelli, T. Sjöstrand, and F. Zwirner, CERN Yellow Report 96-01.

[3] Proceedings of the Workshop e^+e^- *Collisions at 500 GeV: The Physics Potential*, Munich-Annecy-Hamburg, ed. P.M. Zerwas, Reports DESY 92-123A,B; 93-123C.

[4] V. Barger, K. Cheung, A. Djouadi, B. Kniehl, and P.M. Zerwas, Phys. Rev. D49 (1994) 79.

[5] W. Kilian, M. Krämer, and P.M. Zerwas, Report DESY-95-217, to appear in Phys. Lett. B.

[6] W. Buchmüller and D. Wyler, Nucl. Phys. B268 (1986) 621.

[7] B. Grzadkowski and J. Wudka, Phys. Lett. B364 (1995) 49.

[8] K. Hagiwara and M.L. Stong, Z. Phys. C62 (1994) 99.

[9] G.J. Gounaris, F.M. Renard, and N.D. Vlachos, Nucl. Phys. B459 (1996) 51; G.J. Gounaris, J. Layssac, J.E. Paschalis, F.M. Renard, and N.D. Vlachos, Preprint PM/96-08.

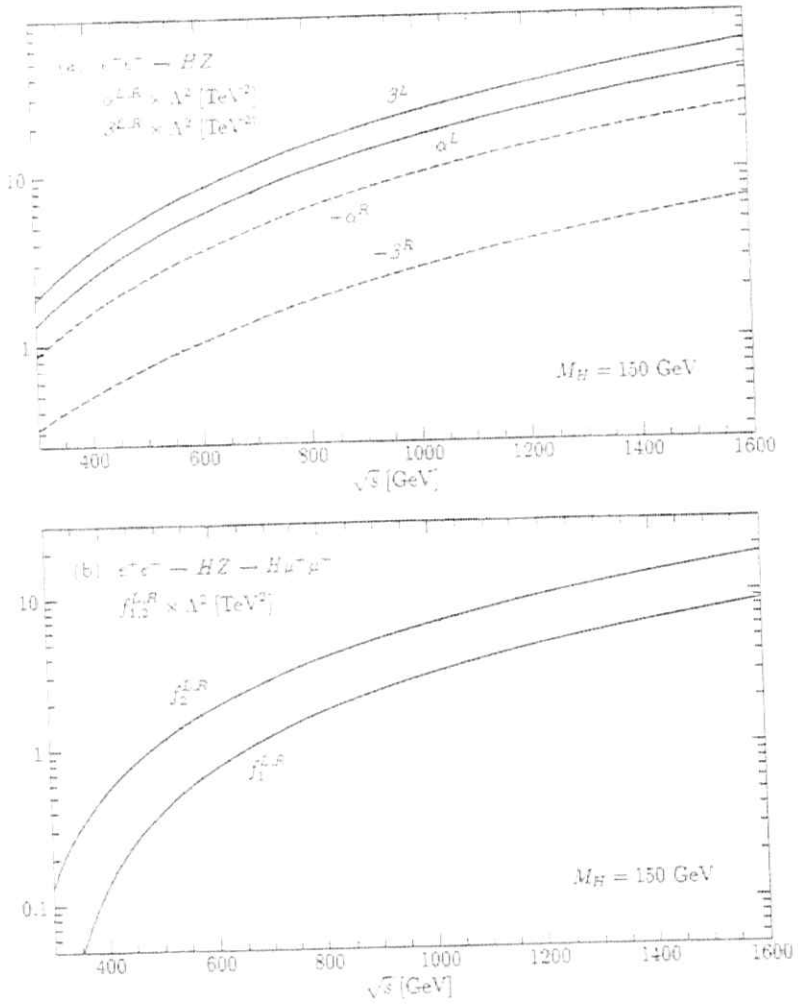

Figure 3: *Coefficients of the angular distributions as a function of the beam energy. Parameters are described in the text; in particular, $\alpha_i = 1$ has ben chosen in the effective Lagrangian Eq.(2). [The L,R coefficients of the azimuthal distribution coincide for the special choice $\alpha_i = 1$.]*

The hidden Higgs model at the NLC.

T. Binoth and J. J. van der Bij
Albert-Ludwigs-Universität Freiburg, Fakultät für Physik
Hermann-Herder-Strasse 3 79104 Freiburg, Germany

Abstract

We investigate the influence of massless scalar singlets on Higgs signals at the NLC. An exclusion bound is presented which restricts large regions of the parameter space but on the other hand implies that for strong interactions between the Higgs boson and the singlet fields of the hidden sector, detection of such a non standard Higgs signal can become impossible.

1. Introduction

Understanding of the electroweak symmetry breaking mechanism is one of the main tasks in particle physics. The determination of its nature would be a break-through in our knowledge about matter. So it is important to think about alternatives to the Standard Model Higgs sector. Various such extensions are available. Maybe the best motivated one is the supersymmetrized Standard Model with its important phenomenological implication of a light Higgs boson and which allows a consistent frame for grand unified theories. Another well understood extension – though in its minimal version disfavoured by the precision experiments at LEP – are technicolor theories. Though these theories avoid fundamental scalars, a rich bosonic spectrum of techniquark condensates may exist. Thus in both theories, as long as they do not occur in their minimal form, light bosonic matter could be present modifying the standard Higgs signals we are looking for at present and future colliders. If such bosons appear as singlets under the Standard Model gauge group, they do not feel the color or electroweak forces, but they can couple to the Higgs particle. As a consequence radiative corrections to weak processes are not sensitive to the presence of singlets in the theory, because no Feynman graphs containing singlets appear at the one–loop level. Since effects at the two–loop level are below the experimental precision, the presence of a singlet sector is not ruled out by any of the LEP1 precision data. The only connection to such a hidden sector is a possible Higgs–singlet coupling, leading to a nonstandard invisible Higgs decay. The invisible decay of the Higgs boson with a narrow width leads to relatively sharp missing energy signals, well known from discussions on Majoron models [2]. However a strongly coupled hidden sector could lead to fast Higgs decay and thereby to wide resonances. This would disturb the signal to background ratio if necessary cuts are imposed.

To check the influence of a hidden sector we will study the coupling of a Higgs boson to an O(N) symmetric set of scalars, which is one of the simplest possibilities, introducing only a few extra parameters in the theory. The effect of the extra scalars is practically the presence of a possibly large invisible decay width of the Higgs particle. When the coupling is large enough the Higgs resonance can become wide even for a light Higgs boson. It was shown earlier that there will be a range of parameters, where such a Higgs boson can be seen neither at LEP nor at the LHC [1, 2].

In the next section we will introduce the model together with its theoretical constraints and in the last section we will discuss exclusion limits at the NLC.

2. The model

The scalar sector of the model consists of the usual Higgs sector coupled to a real N–component vector $\vec{\varphi}$ of scalar fields, denoted by phions in the following. The Lagrangian density is given by,

$$\begin{aligned}\mathcal{L} &= -\partial_\mu\phi^\dagger\partial^\mu\phi - \lambda(\phi^\dagger\phi - v^2/2)^2 - 1/2\,\partial_\mu\vec{\varphi}\partial^\mu\vec{\varphi} - 1/2\,m^2\,\vec{\varphi}^2 \\ &\quad -\kappa/(8N)\,(\vec{\varphi}^2)^2 - \omega/(2\sqrt{N})\;\vec{\varphi}^2\,\phi^\dagger\phi\end{aligned}$$

where ϕ is the standard Higgs doublet. Couplings to fermions and vector bosons are the same as in the Standard Model. The ordinary Higgs field acquires the vacuum expectation value $v/\sqrt{2}$. For positive ω the $\vec{\varphi}$–field acquires no vacuum expectation value. After spontaneous symmetry breaking one is left with the ordinary Higgs boson, coupled to the phions into which it decays. Also the phions receive an induced mass from the spontaneous symmetry breaking which is suppressed by a factor $1/\sqrt{N}$. If the factor N is taken to be large, the model can be analysed with $1/N$–expansion techniques. By taking this limit the phion mass remains small, but as there are many phions, the decay width of the Higgs boson can become large. Therefore the main effect of the presence of the phions is to give a large invisible decay rate to the Higgs boson. The invisible decay width is given by

$$\Gamma_H = \frac{\omega^2 v^2}{32\pi M_H} = \frac{\omega^2(\sin\theta_W\cos\theta_W M_Z)^2}{32\pi^2\alpha_{em}M_H}\,.$$

The Higgs width is compared with the width in the Standard Model for various choices of the coupling ω in Fig. 1. The model is different from Majoron models [2], since the width is not necessarily small. The model is similar to the technicolor–like model of Ref. [4].

Consistency of the model requires two conditions. One condition is the absence of a Landau pole below a certain scale Λ. The other follows from the stability of the vacuum up to a certain scale. An example of such limits is given in Fig. 2, where $\kappa = 0$ was taken at the scale $2m_Z$, which allows for the widest parameter range. The regions of validity up to a given scale Λ are sandwiched between the lower–left and the upper–right contour lines in the figure. The first stem from instability of the vacuum, the second from the presence of a Landau pole at that scale.

To search for the Higgs boson there are basically two channels, one is the standard decay, which is reduced in branching ratio due to the decay into phions. The other is the invisible decay, which rapidly becomes dominant, eventually making the Higgs resonance wide (see Fig. 1). In order to give the bounds we neglect the coupling κ as this is a small effect. We also neglect the phion mass. For other values of the phion mass the bounds can be found by rescaling the decay widths with the appropriate phase space factor. Now we confront this two dimensional parameter space with the experimental potential of the NLC.

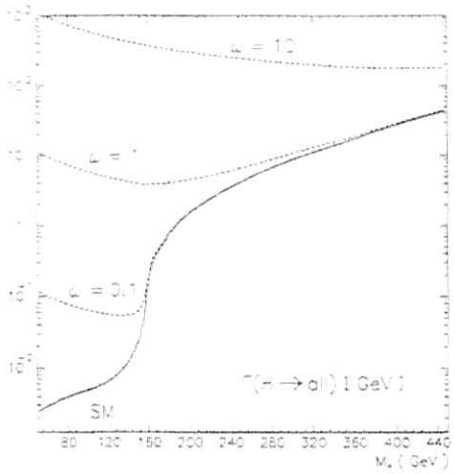

Figure 1: *Higgs width in comparison with the Standard Model.*

3. NLC bounds

At the NLC the upper limits on the couplings in the present model come essentially from the invisible decay, as the branching ratio into visible particles drops with increasing φ-Higgs coupling (ω), whereas for small ω one has to consider visible Higgs decays, too. Since the main source for Higgs production, the WW-fusion process, can not be used to look for invisible Higgs decay, one is in principle left with the Higgsstrahlung und ZZ-fusion reaction. For energies up to 500 GeV the Higgsstrahlungs cross section is dominant and is of comparable size to the ZZ-fusion process even if one is folding in the branching ratio $B(Z \to e^+e^-, \mu^+\mu^-)$. The possibility to tag an on-shell Z boson via a leptonic system which is extremely useful for the discrimination of possible backgrounds makes Higgsstrahlung to be the preferred production mechanism. Thus we only have considered reactions containing an on shell Z boson with its decay into e^+e^- or $\mu^+\mu^-$. One should be aware that a few events from the huge WW background may survive [3], but that the $Z\nu\nu$ background is dominant after imposing the cuts defined below. Then the signal cross section is the well known Higgsstrahlungs cross section modified by the non standard Higgs width due to phion decay. With the invariant mass of the invisible phion system, s_I, it has the form:

$$\sigma_{(e^+e^- \to Z+B)} = \int ds_I \, \sigma_{(e^+e^- \to ZH)}(s_I) \, \frac{\sqrt{s_I}\ \ \Gamma(H \to B)}{\pi((M_H^2 - s_I)^2 + s_I \Gamma(H \to \mathrm{All})^2)}$$

We calculated the $Z\nu\nu$ background with the standard set of graphs for Z production (ZZ-production, WW-fusion and Z initial, final state radiation) by a Monte Carlo program

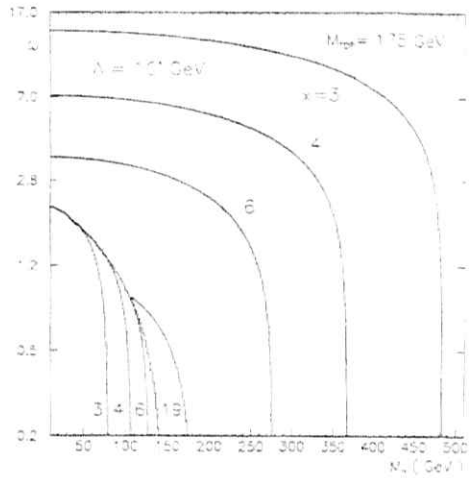

Figure 2: *Theoretical limits on the parameters of the model in the ω vs. M_H plane. The contour lines correspond to the cutoff scales $\Lambda = 10^{19}$, 10^6, 10^4 and 10^3 GeV.*

(see Ref. [5]). To reduce the background we used the fact that the angular distribution of the Z-boson for the signal peaks for small values of $|\cos\theta_Z|$ in contrast to the background. Thus we imposed the cut $|\cos\theta_Z| < 0.7$. Because we assume the reconstruction of the on-shell Z-boson we use the kinematical relation $E_Z = (s + M_Z^2 - s_I)/(2\sqrt{s})$ between the Z energy and the invariant mass of the invisible system to define a second cut. Since the differential cross section $d\sigma/ds_I$ contains the Higgs resonance at $s_I = M_H^2$, we impose the following condition on the Z energy:

$$\frac{s + M_Z^2 - (M_H + \Delta_H)^2}{2\sqrt{s}} < E_Z < \frac{s + M_Z^2 - (M_H - \Delta_H)^2}{2\sqrt{s}}$$

For the choice of Δ_H a comment is in order. As long as the Higgs width is small, one is allowed to use small Δ_H, which reduces the background considerably keeping most of the signal events. But in the case of large φ-Higgs coupling, ω, one looses valuable events. To compromise between both effects we took $\Delta_H = 30$ GeV.

For the exclusion limits we assumed an integrated luminosity of $20\,fb^{-1}$. To define the 95% confidence level we used Poisson statistics similar to the description of Ref. [2]. The result is given in Fig. 3. One notices the somewhat reduced sensitivity for $M_H \simeq M_Z$ due to a resonating Z boson in the ZZ background. For larger values of M_H the limit stems from the other $Z\nu\nu$ backgrounds with W bosons in the t-channel and kinematical constrains. For large ω the signal ceases to dominate over the background because the Higgs peak is smeared out to an almost flat distribution.

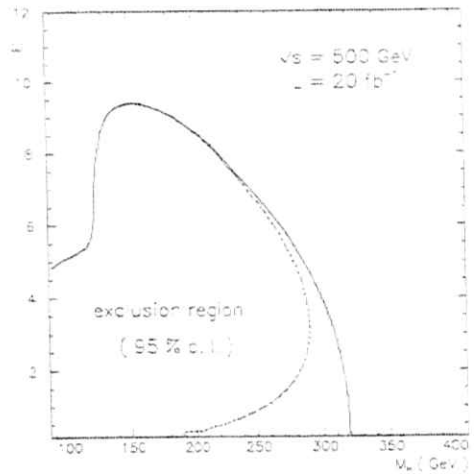

Figure 3: *Exclusion limits at the NLC due to Higgs searches. The dashed line corresponds to the invisible, the full line to all Higgs decay modes.*

We conclude from this analysis that the NLC can put further limits on the parameter space of our invisible Higgs model. Note that within the kinematic range very strong limits on ω can be set. Again there is a range where the Higgs boson will not be discovered, even if it does exist in this mass range. This has already been shown for the Higgs search at LEP and also holds true for the heavy Higgs search at LHC. We see that a sufficiently wide nonstandard Higgs resonance would make it very difficult to test the mechanism of electroweak symmetry breaking at future colliders.

References

[1] T. Binoth, J. J. van der Bij, Quarks 94, Vladimir, Freiburg-THEP-94/26, hep-ph/9409332.

[2] M. Carena, P.M. Zerwas (conv) et al., Higgs Physics, Proceedings of the Workshop Physics at LEP2, CERN Yellow Report 96-01.

[3] O. J. P. Eboli et al., e^+e^--collisions at 500 GeV, part C, DESY 93-123C, 55 (1993).

[4] R. S. Chivukula, M. Golden, Phys. Lett. B267, 233 (1991).

[5] Ambrosanio S., Mele B., Nucl. Phys. B374, 3 (1992).

Heavy SUSY Higgs Bosons at e^+e^- Linear Colliders

A. DJOUADI[1,2], J. KALINOWSKI[3], P. OHMANN[1,4] AND P.M. ZERWAS[1]

[1] Deutsches Elektronen–Synchrotron DESY, D-22603 Hamburg, FRG.

[2] Institut für Theoretische Physik, Universität Karlsruhe, D-76128 Karlsruhe, FRG.

[3] Institute of Theoretical Physics, Warsaw University, PL-00681 Warsaw, Poland.

[4] Department of Theoretical Physics, Oxford University, OX1 3NP, Oxford, UK.

Abstract

The production mechanisms and decay modes of the heavy neutral and charged Higgs bosons in the Minimal Supersymmetric Standard Model are investigated at future e^+e^- colliders in the TeV energy regime. We generate supersymmetric particle spectra by requiring the MSSM Higgs potential to produce correct radiative electroweak symmetry breaking, and we assume a common scalar mass m_0, gaugino mass $m_{1/2}$ and trilinear coupling A, as well as gauge and Yukawa coupling unification at the Grand Unification scale. Particular emphasis is put on the low $\tan\beta$ solution in this scenario where decays of the Higgs bosons to Standard Model particles compete with decays to supersymmetric charginos/neutralinos as well as sfermions. In the high $\tan\beta$ case, the supersymmetric spectrum is either too heavy or the supersymmetric decay modes are suppressed, since the Higgs bosons decay almost exclusively into b and τ pairs. The main production mechanisms for the heavy Higgs particles are the associated AH production and H^+H^- pair production with cross sections of the order of a few fb.

1. Introduction

Supersymmetric theories [1, 2] are generally considered to be the most natural extensions of the Standard Model (SM). This proposition is based on several points. In these theories, fundamental scalar Higgs bosons [3, 4] with low masses can be retained in the context of high unification scales. Moreover, the prediction [5] of the renormalized electroweak mixing angle $\sin^2\theta_W = 0.2336 \pm 0.0017$, based on the spectrum of the Minimal Supersymmetric Standard Model (MSSM) [6], is in striking agreement with the electroweak precision data which yield $\sin^2\theta_W = 0.2314(3)$ [7]. An additional attractive feature is provided by the opportunity to generate the electroweak symmetry breaking radiatively [8]. If the top quark mass is in the range between ~ 150 and ~ 200 GeV, the universal squared Higgs mass parameter at the unification scale decreases with decreasing energy and becomes negative at the electroweak scale, thereby breaking the $SU(2)_L \times U(1)_Y$ gauge symmetry while leaving the U(1) electromagnetic and SU(3) color gauge symmetries intact [8]. The analysis of the electroweak data prefers a light Higgs mass [7, 9] as

predicted in supersymmetric theories; however since the radiative corrections depend only logarithmically on the Higgs mass [10], the dependence is weak and no firm conclusions can yet be drawn.

The more than doubling the spectrum of states in the MSSM gives rise to a rather large proliferation of parameters. This number of parameters is however reduced drastically by embedding the low–energy supersymmetric theory into a grand unified (GUT) framework. This can be achieved in supergravity models [8], in which the effective low–energy supersymmetric theory [including the interactions which break supersymmetry] is described by the following parameters: the common scalar mass m_0, the common gaugino mass $m_{1/2}$, the trilinear coupling A, the bilinear coupling B, and the Higgs–higgsino mass parameter μ. In addition, two parameters are needed to describe the Higgs sector: one Higgs mass parameter [in general the mass of the pseudoscalar Higgs boson, M_A] and the ratio of the vacuum expectation values, $\tan\beta = v_2/v_1$, of the two Higgs doublet fields which break the electroweak symmetry.

The number of parameters can be further reduced by introducing additional constraints which are based on physically rather natural assumptions:

(*i*) Unification of the b and τ Yukawa couplings at the GUT scale [11] leads to a correlation between the top quark mass and $\tan\beta$ [12, 13, 14]. Adopting the central value of the top mass as measured at the Tevatron [15], $\tan\beta$ is restricted to two narrow ranges around $\tan\beta \sim 1.7$ and $\tan\beta \sim 50$, with the low $\tan\beta$ solution theoretically somewhat favored [14].

(*ii*) If the electroweak symmetry is broken radiatively, then the bilinear coupling B and the Higgs–higgsino mass parameter μ are determined up to the sign of μ. [The sign of μ might be determined by future precision measurements of the radiative b decay amplitude.]

(*iii*) It turns out *a posteriori* that the physical observables are nearly independent of the GUT scale value of the trilinear coupling A_G, for $|A_G| \lesssim 500$ GeV.

Mass spectra and couplings of all supersymmetric particles and Higgs bosons are determined after these steps by just two mass parameters along with the sign of μ; we shall choose to express our results in terms of the pseudoscalar Higgs boson A mass M_A and the common GUT gaugino mass $m_{1/2}$.

In this paper we focus on heavy Higgs particles A, H and $H^\pm$ with masses of a few hundred GeV, and therefore close to the decoupling limit [16]. The pattern of Higgs masses is quite regular in this limit. While the upper limit on the mass of the lightest CP–even Higgs boson h is a function of $\tan\beta$ [17],

$$M_h \lesssim 100 \text{ to } 150 \text{ GeV} \quad [\text{for low to high } \tan\beta] \tag{1.1}$$

the heavy Higgs bosons are nearly mass degenerate [c.f. Fig.1]

$$M_A \simeq M_H \simeq M_{H^\pm} \tag{1.2}$$

Moreover, the properties of the lightest CP–even Higgs boson h become SM–like in this limit. The production of the heavy Higgs bosons becomes particularly simple in e^+e^- collisions; the heavy Higgs bosons can only be pair–produced,

$$e^+e^- \;\to\; A\,H \tag{1.3}$$
$$e^+e^- \;\to\; H^+H^- \tag{1.4}$$

Close to this decoupling limit, the cross section for H Higgs–strahlung $e^+e^- \to ZH$ is very small and the cross section for the WW fusion mechanism $e^+e^- \to \nu_e\bar{\nu}_e H$ is appreciable only for small values of $\tan\beta$, $\tan\beta \sim 1$, and relatively small H masses, $M_H \lesssim 350$ GeV. The cross section for ZZ fusion of the H is suppressed by an order of magnitude compared to WW fusion. The pseudoscalar A particle does not couple to W/Z boson pairs at the tree level.

The decay pattern for heavy Higgs bosons is rather complicated in general. For large $\tan\beta$ the SM fermion decays prevail. For small $\tan\beta$ this is true above the $t\bar{t}$ threshold of $M_{H,A} \gtrsim 350$ GeV for the neutral Higgs bosons and above the $t\bar{b}$ threshold of $M_{H^\pm} \gtrsim 180$ GeV for the charged Higgs particles. Below these mass values many decay channels compete with each other: decays to SM fermions $f\bar{f}$ [and for H to gauge bosons VV], Higgs cascade decays, chargino/neutralino $\chi_i\chi_j$ decays and decays to supersymmetric sfermions $\tilde{f}\bar{\tilde{f}}$

$$H \;\to\; f\bar{f}\;,\; VV\;,\; hh\;,\; \chi_i\chi_j\;,\; \tilde{f}\bar{\tilde{f}} \tag{1.5}$$
$$A \;\to\; f\bar{f}\;,\; hZ\;,\; \chi_i\chi_j\;,\; \tilde{f}\bar{\tilde{f}} \tag{1.6}$$
$$H^\pm \;\to\; f\bar{f}'\;,\; hW^\pm\;,\; \chi_i\chi_j\;,\; \tilde{f}\bar{\tilde{f}}' \tag{1.7}$$

In this paper, we analyze in detail the decay modes of the heavy Higgs particles and their production at e^+e^- linear colliders. The analysis will focus on heavy particles for which machines in the TeV energy range are needed. The paper is organized in the following way. In the next section we define the physical set–up of our analysis in the framework of the MSSM embedded into a minimal supergravity theory. In section 3, we discuss the production cross sections of the heavy Higgs bosons. In the subsequent sections, we discuss the widths of the various decay channels and the final Higgs decay products.

2. The Physical Set–Up

The Higgs sector of the Minimal Supersymmetric Standard Model is described at tree-level by the following potential

$$\begin{aligned} V_0 \;=\; & (m_{H_1}^2+\mu^2)|H_1|^2 + (m_{H_2}^2+\mu^2)|H_2|^2 - m_3^2(\epsilon_{ij}H_1^iH_2^j + \text{h.c.}) \\ & + \frac{1}{8}(g^2+g'^2)\left[|H_1|^2 - |H_2|^2\right]^2 + \frac{1}{2}g^2|H_1^\dagger H_2|^2 \end{aligned} \tag{2.1}$$

The quadratic Higgs terms associated with μ and the quartic Higgs terms coming with the electroweak gauge couplings g and g' are invariant under supersymmetric transformations. m_{H_1}, m_{H_2} and m_3 are soft–supersymmetry breaking parameters with $m_3^2 = B\mu$. ϵ_{ij} [$i,j = 1,2$ and $\epsilon_{12} = 1$] is the antisymmetric tensor in two dimensions and $H_1 \equiv (H_1^1, H_1^2) = (H_1^0, H_1^-)$, $H_2 \equiv (H_2^1, H_2^2) = (H_2^+, H_2^0)$ are the two Higgs-doublet fields. After the symmetry breaking, three out of the initially eight degrees of freedom will be absorbed to generate the $W^\pm$ and Z masses, leaving a quintet of scalar Higgs particles: two CP–even Higgs bosons h and H, a CP–odd [pseudoscalar] boson A and two charged Higgs particles $H^\pm$.

Retaining only the [leading] Yukawa couplings of the third generation

$$\lambda_t = \frac{\sqrt{2}m_t}{v\sin\beta}\;,\quad \lambda_b = \frac{\sqrt{2}m_b}{v\cos\beta} \;\text{ and }\; \lambda_\tau = \frac{\sqrt{2}m_\tau}{v\cos\beta} \tag{2.2}$$

where $\tan\beta = v_2/v_1$ [with $v^2 = v_1^2 + v_2^2$ fixed by the W mass, $v = 246$ GeV] is the ratio of the vacuum expectation values of the fields H_2^0 and H_1^0, the superpotential is given in terms of the superfields $Q = (t,b)$ and $L = (\tau,\nu_\tau)$ by[1]

$$W = \epsilon_{ij}\left[\lambda_t H_2^i Q^j t^c - \lambda_b H_1^i Q^j b^c - \lambda_\tau H_1^i L^j \tau^c - \mu H_1^i H_2^j\right] \tag{2.3}$$

Supersymmetry is broken by introducing the soft–supersymmetry breaking bino $\tilde{B}$, wino $\tilde{W}^a$ [a =1–3] and gluino $\tilde{g}^a$ [a =1–8] mass terms,

$$\frac{1}{2}M_1\,\overline{\tilde{B}}\,\tilde{B} \;+\; \frac{1}{2}M_2\,\overline{\tilde{W}}^a\,\tilde{W}^a \;+\; \frac{1}{2}M_3\,\overline{\tilde{g}}^a\,\tilde{g}^a\;, \tag{2.4}$$

soft–supersymmetry breaking trilinear couplings,

$$\epsilon_{ij}\left[\lambda_t A_t H_2^i \tilde{Q}^j \tilde{t}^c + \lambda_b A_b H_1^i \tilde{Q}^j \tilde{b}^c + \lambda_\tau A_\tau H_1^i \tilde{L}^j \tilde{\tau}^c - \mu B H_1^i H_2^j\right] \tag{2.5}$$

and soft–supersymmetry breaking squark and slepton mass terms

$$M_Q^2[\tilde{t}_L^*\tilde{t}_L + \tilde{b}_L^*\tilde{b}_L] + M_U^2\tilde{t}_R^*\tilde{t}_R + M_D^2\tilde{b}_R^*\tilde{b}_R + M_L^2[\tilde{\tau}_L^*\tilde{\tau}_L + \tilde{\nu}_{\tau L}^*\tilde{\nu}_{\tau L}] + M_E^2\tilde{\tau}_R^*\tilde{\tau}_R \;+\; \cdots \tag{2.6}$$

where the ellipses stand for the soft mass terms corresponding to the first and second generation sfermions.

The minimal SUSY–GUT model emerges by requiring at the GUT scale M_G:

(i) the unification of the U(1), SU(2) and SU(3) coupling constants $\alpha_i = g_i^2/4\pi$ [i = 1–3],

$$\alpha_3(M_G) = \alpha_2(M_G) = \alpha_1(M_G) = \alpha_G \tag{2.7}$$

[1] Note that our convention for the sign of μ is consistent with Ref.[18], which is opposite to the one adopted in Ref.[19].

(*ii*) a common gaugino mass, the M_i with $i = 1$–3 at the electroweak scale are then related through renormalization group equations (RGEs) to the gauge couplings,

$$M_i = \frac{\alpha_i(M_Z)}{\alpha_G} m_{1/2} \longrightarrow M_3(M_Z) = \frac{\alpha_3(M_Z)}{\alpha_2(M_Z)} M_2(M_Z) = \frac{\alpha_3(M_Z)}{\alpha_1(M_Z)} M_1(M_Z) \tag{2.8}$$

(*iii*) a universal trilinear coupling A

$$A_G = A_t(M_G) = A_b(M_G) = A_\tau(M_G) \tag{2.9}$$

(*iii*) a universal scalar mass m_0

$$\begin{aligned} m_0 &= M_Q = M_U = M_D = M_L = M_E \\ &= m_{H_1}(M_G) = m_{H_2}(M_G) \end{aligned} \tag{2.10}$$

Besides the three parameters $m_{1/2}, A_G$ and m_0 the supersymmetric sector is described at the GUT scale by the bilinear coupling B_G and the Higgs–higgsino mass parameter μ_G. The theoretically attractive assumption that the electroweak symmetry is broken radiatively constrains the latter two parameters. Indeed, radiative electroweak symmetry breaking results in two minimization conditions [see Ref.[19] for details] of the Higgs potential; at the low–energy scale in the tree approximation, they are given by

$$\frac{1}{2} M_Z^2 = \frac{m_{H_1}^2 - m_{H_2}^2 \tan^2\beta}{\tan^2\beta - 1} - \mu^2 \tag{2.11}$$

$$B\mu = \frac{1}{2}(m_{H_1}^2 + m_{H_2}^2 - 2\mu^2) \sin 2\beta \tag{2.12}$$

For given values of the GUT parameters $m_{1/2}, m_0, A_G$ as well as $\tan\beta$, the first minimization equation can be solved for μ [to within a sign]; the second equation can then be solved for B. Since $m_{H_1}^2$ and $m_{H_2}^2$ are related to M_A through the RGEs, the solution for μ and B can be approximately expressed as a function of M_A and $\tan\beta$. The power of supergravity models with radiative electroweak symmetry breaking becomes apparent when one includes the one-loop contributions to the Higgs potential. It is through these one–loop terms that most of the supersymmetric particle masses are determined; the minimization conditions [which are also solved for μ to within a sign and B] *fix* the masses in order that the electroweak symmetry is broken correctly, i.e. with the correct value of M_Z. [U(1)$_{\rm EM}$ and SU(3) remain unbroken of course]. The one–loop contributions and the minimization equations are given in Ref. [19] to which we refer for details.

A heavy top quark is required to break the electroweak symmetry radiatively, since it is the large top Yukawa coupling which will drive one of the Higgs mass parameters squared to a negative value. As emphasized before, the additional condition of unification of the b–τ Yukawa couplings gives rise to stringent constraints on $\tan\beta$. The attractive idea of explaining the large top Yukawa coupling as a result of a fixed point solution of the RGEs leads to a relationship between M_t and the angle β, $M_t \simeq (200\ \text{GeV}) \sin\beta$ for $\tan\beta \lesssim 10$, giving a further constraint on the model.

To limit the parameter space further, one could require that the SUGRA model is not fine–tuned and the SUSY breaking scale should not be too high, a constraint which can be particularly restrictive in the small $\tan\beta$ region. However, the degree of fine–tuning which can be considered acceptable is largely a matter of taste, so we disregard this issue in our analysis.

We now detail the calculations of the supersymmetric particle spectrum more precisely. We incorporate boundary conditions at both electroweak and GUT scales, adopting the ambidextrous approach of Ref.[19]. We specify the values of the gauge and Yukawa couplings at the electroweak scale, in particular M_t, $\tan\beta$ and α_s. The gauge and Yukawa couplings are then evolved to the GUT scale M_G [defined to be the scale $\tilde{\mu}$ for which $\alpha_1(\tilde{\mu}) = \alpha_2(\tilde{\mu})$] using the two–loop RGEs [13]. At M_G we specify the soft supersymmetry breaking parameters $m_{1/2}$, m_0 and A_G. We then evolve parameters down to the electroweak scale where we apply the one–loop minimization conditions derived from the one–loop effective Higgs potential and solve for μ to within a sign and B [we then can integrate the RGEs back to M_G and obtain μ_G and B_G]. By this procedure, the supersymmetric spectrum is completely specified; that is, we generate a unique spectrum corresponding to particular values of $m_{1/2}$, m_0, A_G, $\tan\beta$ and the sign of μ. It turns out that the spectrum is nearly independent of A_G, for $|A_G| \lesssim 500$ GeV. In most of our calculations, we substitute a particular value of M_A for m_0 in order to introduce a mass parameter which can be measured directly.

We discuss the SUSY spectrum and its phenomenological implications for two representative points in the M_t–$\tan\beta$ plane[2]. We choose $M_t^{\rm pole} = 175$ GeV, consistent with the most recent Tevatron analyses [15] throughout our calculations, and values of $\tan\beta = 1.75$ and 50, which are required (within uncertainties) by b–τ unification at M_G. In particular, we emphasize the low $\tan\beta$ solutions; they are theoretically favored from considerations such as $b \to s\gamma$ [21] and cosmological constraints [22]. The low $\tan\beta$ solutions generate much lighter SUSY spectra, more likely to be seen at future e^+e^- colliders. In both the low and high $\tan\beta$ regions we take[3] $\alpha_s(M_Z) = 0.118$ [23] and $A_G = 0$, though the qualitative behavior in each region should not depend greatly on these parameters.

(a) Low $\tan\beta$

As a typical example of the low $\tan\beta$ region we consider the point $M_t^{\rm pole} = 175$ GeV and $\tan\beta = 1.75$ for which $\lambda_t(M_G)$ lies in its "fixed-point" region [12, 14]. If M_A is fixed, the scalar mass parameter m_0 can be calculated as a function of the common gaugino mass parameter $m_{1/2}$ so that all Higgs and supersymmetric particle masses can in principle be parameterized by $m_{1/2}$. The correlation between m_0 and $m_{1/2}$ is shown in Fig.2 for three

[2] Our numerical analysis is consistent with the numbers obtained in Ref.[20], once their value of A_τ in Tab.X is corrected. We thank W. de Boer for a discussion on this point.

[3] This corresponds to the $\sin^2\theta_W$ value quoted and compared with the high–precision electroweak analyses in the Introduction.

values of $M_A = 300, 600$ and 900 GeV in the low $\tan\beta$ region.

Some of the parameter space is already eliminated by experimental bounds on the light Higgs mass, the chargino/neutralino masses, the light stop mass, the slepton masses and the squark/gluino masses from LEP1/1.5 and the Tevatron [24]. The lower limits are indicated by the non-solid lines in Fig.2. Low values of $m_{1/2} \lesssim 60$ GeV are excluded by the lower bound on the gaugino masses. For $\mu > 0$, the bound from the negative search of charginos at LEP1.5 almost rules out completely the scenario with $M_A \lesssim 300$ GeV. If the h boson is not discovered at LEP2, i.e. if $M_h \gtrsim 95$ GeV, the whole $\mu < 0$ scenario [for $m_{1/2}, m_0 < 500$ GeV] can be excluded, while for $\mu > 0$ only the $m_{1/2} > 200$ GeV range [which implies very large values of M_A] would survive. The requirement that the lightest neutralino is the LSP, and therefore its mass is larger than the lightest $\tilde{\tau}$ mass, excludes a small edge of the parameter space [dotted line] at small m_0 with $m_{1/2} > 200$ GeV in the $\mu < 0$ case.

The masses of the Higgs bosons are shown in Fig.3a as a function of $m_{1/2}$ for $\tan\beta = 1.75$, both signs of μ and for two representative values of $m_0 = 100$ and 500 GeV. The lightest Higgs boson has a rather small tree-level mass and M_h comes mainly from radiative corrections; the maximal values [for $m_{1/2} \sim 400$ GeV] are $M_h^{\rm max} \sim 90$ GeV for $\mu < 0$ and ~ 100 for $\mu > 0$. Because the pseudoscalar mass is approximately given by $M_A^2 \sim B\mu/\sin 2\beta \sim B\mu$ [at the tree-level] and since $B\mu$ turns out to be large in this scenario, the pseudoscalar A is rather heavy especially for large values of m_0, and thus is almost mass degenerate with the heavy CP-even and charged Higgs bosons, $M_A \sim M_H \simeq M_{H^\pm}$. Note that M_A is below the $t\bar{t}$ threshold, $M_A \lesssim 350$ GeV, only if m_0 and $m_{1/2}$ are both of $\mathcal{O}(100)$ GeV.

The chargino/neutralino and sfermion masses are shown Fig.3b-d as a function of $m_{1/2}$ for the two values $M_A = 300$ and 600 GeV and for both signs of μ. In the case of charginos and neutralinos, the masses are related through RGEs by the same ratios that describe the gauge couplings at the electroweak scale. The LSP is almost bino-like [with a mass $m_{\chi_1^0} \sim M_1$] while the next-to-lightest neutralino and the lightest chargino are wino-like [with masses $m_{\chi_2^0} \sim m_{\chi_1^\pm} \sim M_2 \sim 2m_{\chi_1^0}$]. The heavier neutralinos and chargino are primarily higgsinos with masses $m_{\chi_3^0} \sim m_{\chi_4^0} \sim m_{\chi_2^\pm} \sim |\mu|$. Note that the masses approximately scale as M_A and that the decay of the heavy scalar and pseudoscalar Higgs bosons into pairs of the heaviest charginos and neutralinos is kinematically not allowed.

The left- and right-handed charged sleptons and sneutrinos are almost mass degenerate, the mass differences not exceeding $\mathcal{O}(10)$ GeV; the mixing in the τ sector is rather small for small $\tan\beta$, allowing one to treat all three generations of sleptons on the same footing. In the case of squarks, only the first two generations are degenerate, with left- and right-handed squarks having approximately the same mass. The mixing in the stop as well as in the sbottom sector leads to a rather substantial splitting between the two stop or sbottom mass eigenstates. Only for small values of M_A and for $\mu < 0$ is $\tilde{b}_1$ the lightest squark; otherwise $\tilde{t}_1$ is the lightest squark state. Note that the squark masses increase with $m_{1/2}$ and that they scale as M_A i.e. as $|\mu|$. The slepton masses decrease

with increasing $m_{1/2}$: this is due to the fact that when $m_{1/2}$ increases and M_A is held constant, m_0 decreases [see Fig.2], and the dependence of the slepton masses on m_0 is stronger [for fixed m_0, the slepton masses would increase with increasing $m_{1/2}$].

(b) High $\tan\beta$

In this region we take $\tan\beta = 50$ as a representative example, a value consistent with the unification of the t, b and τ Yukawa couplings. The set of possible solutions in the parameter space $[m_{1/2}, m_0]$ for $M_A = 300$ and 600 GeV is shown in Fig.4. At $\tan\beta = 50$ and $M_t^{\rm pole} = 175$ GeV, we find solutions only for $\mu < 0$; this is a result of the large one-loop contribution to M_A, the sign of which depends on μ [25]. The boundary contours given in the figure correspond to tachyonic solutions in the parameter space: $m_{\tilde{\tau}_1}^2 < 0$, $M_A^2 < 0$ or $M_h^2 < 0$ at the tree-level. The latter constraint is important for algorithmic reasons: M_h^2 at the tree-level enters into the minimization equations in the form of a logarithm [19]. Also the requirement of the lightest neutralino to be the LSP excludes a small edge of the parameter space at small values of m_0; this explains why the curves for $M_A = 300$ and 600 GeV do not terminate for low m_0 values.

Particle	Mass (GeV)	Mass (GeV)	Mass (GeV)	Mass (GeV)
M_A	300	300	600	600
$(m_{1/2}, m_0)$	(364,250)	(352,800)	(603,300)	(590,800)
$\tilde{g}$	940	910	1557	1524
$\tilde{t}_1,\tilde{t}_2$	662,817	753,896	1115,1285	1156,1325
$\tilde{b}_1,\tilde{b}_2$	689,787	804,894	1159,1260	1220,1312
$\tilde{u}_1,\tilde{u}_2$	881,909	1144,1164	1431,1479	1586,1628
$\tilde{d}_1,\tilde{d}_2$	878,912	1142,1167	1425,1481	1582,1630
$\tilde{\tau}_1,\tilde{\tau}_2,\tilde{\nu}_\tau$	165,365; 325	567,740; 729	255,517; 485	586,812; 799
$\tilde{e}_1,\tilde{e}_2,\tilde{\nu}_e$	290,360; 351	813,838; 835	381,519; 513	833,901; 898
$\chi_1^\pm$	268,498	261,536	452,764	443,779
χ_1^0	144,268,485,496	139,261,526,534	239,452,754,763	234,443,771,778
$M_A, M_{H^\pm}, M_H, M_h$	300,315,300,124	300,315,300,124	600,608,600,131	600,608,600,131

Tab.1: Particle spectra for $M_t^{\rm pole} = 175$ GeV, $\tan\beta = 50$ for selected M_A, $m_{1/2}$ and m_0 values.

The sparticle spectra for $M_A = 300$ and 600 GeV and two sets of $m_{1/2}$ and (extreme) m_0 values are shown in Table 1. In all these cases, the particle spectrum is very heavy; hence most of the SUSY decay channels of the Higgs particles are shut for large $\tan\beta$.

The only allowed decay channels are $H, A \to \tilde{\tau}_1\tilde{\tau}_1, \chi_1^0\chi_1^0$ and $H^\pm \to \tilde{\tau}_1\tilde{\nu}$ [for large M_A values]. However, the branching ratios of these decay channels are suppressed by large $b\bar{b}$ and $t\bar{t}$ widths of the Higgs particles for large $\tan\beta$: while the supersymmetric decay widths are of the order $\mathcal{O}(0.1$ GeV), the decays involving b quarks have widths $\mathcal{O}(10$ GeV) and dominate by 2 orders of magnitude.

(c) Additional Constraints

There are additional experimental constraints on the parameter space for both high and low $\tan\beta$: the most important of these are the $b \to s\gamma$, $Z \to b\bar{b}$, and dark matter [relic LSP abundance] constraints. These constraints are much more restrictive in the high $\tan\beta$ case.

Recent studies [21] have indicated that the combination of $b \to s\gamma$, dark matter and m_b constraints disfavor the high $\tan\beta$ solution for which the t, b and τ Yukawa couplings are equal, in particular the minimal SUSY-SO(10) model with universal soft-supersymmetry breaking terms at M_G. This model can, however, be saved if the soft terms are not universal [implying a higgsino–like lightest neutralino], and there exist theoretical motivations for non–universal soft terms at M_G [26]. The presently favored $Z \to b\bar{b}$ decay width would favor a very low A mass for large $\tan\beta$.

For low $\tan\beta$, these additional constraints do not endanger the model, yet they can significantly reduce the available parameter space. In particular the $Z \to b\bar{b}$ constraint favors a light chargino and light stop for small to moderate values of $\tan\beta$ [27, 28] so that they could be detected at LEP2 [28]. The dark matter constraint essentially places an upper limit on m_0 and $m_{1/2}$ [29]. The $b \to s\gamma$ constraint [30], on the other hand, is plagued with large theoretical uncertainties mainly stemming from the unknown next-to-leading QCD corrections and uncertainties in the measurement of $\alpha_s(M_Z)$. However, it is consistent with the low $\tan\beta$ solution and may in the future be useful in determining the sign of μ [31].

3. Production Mechanisms

The main production mechanisms of neutral Higgs bosons at e^+e^- colliders are the Higgs-strahlung process and pair production,

$$\begin{array}{lll} (a)\ \text{Higgs-strahlung} & e^+e^- \to (Z) \to Z + h/H \\ (b)\ \text{pair production} & e^+e^- \to (Z) \to A + h/H \end{array}$$

as well as the WW and ZZ fusion processes,

$$\begin{array}{lll} (c)\ \text{fusion processes} & e^+e^- \to \bar{\nu}\nu\,(WW) \to \bar{\nu}\nu\ + h/H \\ & e^+e^- \to e^+e^-(ZZ) \to e^+e^- + h/H \end{array}$$

[The $C\!P$–odd Higgs boson A cannot be produced in the Higgs–strahlung and fusion processes to leading order since it does not couple to VV pairs.] The charged Higgs particle

can be pair produced through virtual photon and Z boson exchange,

$$(d)\ \text{charged Higgs} \qquad e^+e^- \to (\gamma, Z^*) \to H^+H^-$$

[For masses smaller than ~ 170 GeV, the charged Higgs boson is also accessible in top decays, $e^+e^- \to t\bar{t}$ with $t \to H^+b$.]

The production cross sections[4] for the neutral Higgs bosons are suppressed by mixing angle factors compared to the SM Higgs production,

$$\sigma(e^+e^- \to Zh)\ ,\ \sigma(VV \to h)\ ,\ \sigma(e^+e^- \to AH) \ \sim\ \sin^2(\beta-\alpha) \tag{3.1}$$
$$\sigma(e^+e^- \to ZH)\ ,\ \sigma(VV \to H)\ ,\ \sigma(e^+e^- \to Ah) \ \sim\ \cos^2(\beta-\alpha) \tag{3.2}$$

while the cross section for the charged Higgs particle does not depend on any parameter other than $M_{H^\pm}$.

In the decoupling limit, $M_A \gg M_Z$, the HVV coupling vanishes, while the hVV coupling approaches the SM Higgs value

$$g_{HVV} \ =\ \cos(\beta-\alpha) \to M_Z^2 \sin 4\beta/2M_A^2 \to 0 \tag{3.3}$$
$$g_{hVV} \ =\ \sin(\beta-\alpha) \to 1 - \mathcal{O}(M_Z^4/M_A^4) \ \to 1 \tag{3.4}$$

Hence, the only relevant mechanisms for the production of the heavy Higgs bosons in this limit will be the associated pair production (b) and the pair production of the charged Higgs particles (d). The cross sections, in the decoupling limit and for $\sqrt{s} \gg M_Z$, are given by [we use $M_H \sim M_A$]

$$\sigma(e^+e^- \to AH) \ =\ \frac{G_F^2 M_Z^4}{96\pi s}(v_e^2+a_e^2)\beta_A^3 \tag{3.5}$$
$$\sigma(e^+e^- \to H^+H^-) \ =\ \frac{2G_F^2 M_W^4 s_W^4}{3\pi s}\left[1 + \frac{v_e v_H}{8 s_W^2 c_W^2} + \frac{(a_e^2+v_e^2)v_H^2}{256 c_W^4 s_W^4}\right]\beta_{H^\pm}^3 \tag{3.6}$$

where $\beta_i = (1-4M_i^2/s)^{1/2}$ is the velocity of Higgs bosons, the Z couplings to electrons are given by $a_e = -1, v_e = -1 + 4\sin^2\theta_W$, and to the charged Higgs boson by $v_H = -2 + 4\sin^2\theta_W$. The cross sections for hA and HZ production vanish in the decoupling limit since they are proportional to $\cos^2(\beta-\alpha)$.

The cross section for the fusion process, $e^+e^- \to \bar{\nu}_e\nu_e H$, is enhanced at high energies since it scales like $M_W^2 \log s/M_H^2$. This mechanism provides therefore a useful channel for H production in the mass range of a few hundred GeV below the decoupling limit and small values of $\tan\beta$, where $\cos^2(\beta-\alpha)$ is not prohibitively small; the cross section, though, becomes gradually less important for increasing M_H and vanishes in the decoupling limit.

[4] The complete analytical expressions of the cross sections can be found, e.g., in Ref.[32]. Note that in this paper there are a few typos that we correct here: in eq.(20), the factor 92 should replaced by 96; in the argument of the λ function of the denominator in eq.(21), the parameter M_Z^2 should be replaced by M_H^2; finally, the minus sign in the interference term in eq.(25) should be replaced by a plus sign.

In the high energy regime, the $WW \to H$ fusion cross section is well approximated by the expression

$$\sigma(e^+e^- \to \bar{\nu}_e\nu_e H) = \frac{G_F^3 M_W^4}{4\sqrt{2}\pi^3}\left[\left(1-\frac{M_H^2}{s}\right)\log\frac{s}{M_H^2} - 2\left(1-\frac{M_H^2}{s}\right)\right]\cos^2(\beta-\alpha) \quad (3.7)$$

obtained in the effective longitudinal W approximation. Since the NC couplings are small compared to the CC couplings, the cross section for the ZZ fusion process is $\sim 16\cos^4\theta_W$, i.e. one order of magnitude smaller than for WW fusion.

Numerical results for the cross sections are shown in Fig.5 at high-energy e^+e^- colliders as a function of $\sqrt{s}$ TeV for the two values $\tan\beta = 1.75$ and 50, and for pseudoscalar masses $M_A = 300$, 600 and 900 GeV [note that $M_H \simeq M_{H^\pm} \simeq M_A$ as evident from Figs. 1 and 3a]. For a luminosity of $\int \mathcal{L} = 200$ fb^{-1}, typically a sample of about 1000 HA and H^+H^- pairs are predicted for heavy Higgs masses of ~ 500 GeV at $\sqrt{s} = 1.5$ TeV. For small $\tan\beta$ values, $\tan\beta \lesssim 2$, a few hundred events are predicted in the $WW \to H$ fusion process for H masses ~ 300 GeV. The cross sections for the hA and HZ processes are too low, less than ~ 0.1 fb, to be useful for $M_H \gtrsim 300$ GeV; Fig.5b.

Note that the cross sections for the production of the lightest Higgs boson h in the decoupling limit and for $\sqrt{s} \gg M_Z, M_h$ are simply given by

$$\sigma(e^+e^- \to ZZ) \simeq \frac{G_F^2 M_Z^4}{96\pi s}(v_e^2 + a_e^2) \quad (3.8)$$

$$\sigma(e^+e^- \to \bar{\nu}_e\nu_e h) \simeq \frac{G_F^2 M_W^4}{4\sqrt{2}\pi^3}\log\frac{s}{M_h^2} \quad (3.9)$$

The cross sections are the same as for the SM Higgs particle and are very large ~ 100 fb, especially for the WW fusion mechanism.

4. Decay Modes

4.1 Decays to standard particles

For large $\tan\beta$ the Higgs couplings to down-type fermions dominate over all other couplings. As a result, the decay pattern is in general very simple. The neutral Higgs bosons will decay into $b\bar{b}$ and $\tau^+\tau^-$ pairs for which the branching ratios are close to ~ 90 % and ~ 10 %, respectively. The charged Higgs particles decay into $\tau\nu_\tau$ pairs below and into $t\bar{b}$ pairs above the top-bottom threshold.

The partial decay widths of the neutral Higgs bosons[5], $\Phi = H$ and A, to fermions are given by [4]

$$\Gamma(\Phi \to \bar{f}f) = N_c\frac{G_F M_\Phi}{4\sqrt{2}\pi} g^2_{\Phi ff} m_f^2 \beta_f^p \quad (4.1)$$

[5]We refrain from a discussion of the h decays which become SM-like in the decoupling limit. In addition, we discuss only the dominant two-body decay modes of the heavy Higgs bosons; for an updated and more detailed discussion, including also three-body decays, see Ref.[33].

with $p = 3(1)$ for the CP-even (odd) Higgs bosons; $\beta_f = (1 - 4m_f^2/M_\Phi^2)^{1/2}$ is the velocity of the fermions in the final state, N_c the color factor. For the decay widths to quark pairs, the QCD radiative corrections are large and must be included: for a recent update and a more detailed discussion, see Ref.[34].

The couplings of the MSSM neutral Higgs bosons [normalized to the SM Higgs coupling $g_{H_{\rm SM}ff} = \left[\sqrt{2}G_F\right]^{1/2} m_f$ and $g_{H_{\rm SM}VV} = 2\left[\sqrt{2}G_F\right]^{1/2} M_V^2$] are given in Table 2.

Φ	$g_{\Phi bb}$	$g_{\Phi tt}$	$g_{\Phi VV}$
h	$\cos\alpha/\sin\beta$	$-\sin\alpha/\cos\beta$	$\sin(\beta-\alpha)$
H	$\sin\alpha/\sin\beta$	$\cos\alpha/\cos\beta$	$\cos(\beta-\alpha)$
A	$1/\tan\beta$	$\tan\beta$	0

Tab. 2: Higgs boson couplings in the MSSM to fermions and gauge bosons relative to the SM Higgs couplings.

In the decoupling limit, $M_A \gg M_Z$, we have

$$\cos\alpha \sim \sin\beta - \cos\beta\frac{M_Z^2}{2M_A^2}\sin 4\beta \to \sin\beta \quad (4.2)$$

$$\sin\alpha \sim -\cos\beta - \sin\beta\frac{M_Z^2}{2M_A^2}\sin 4\beta \to -\cos\beta \quad (4.3)$$

Therefore the hff couplings reduce to the SM Higgs couplings, while the Hff couplings become equal to those of the pseudoscalar boson A,

$$\begin{aligned} \cos\alpha/\sin\beta &\to 1 \\ -\sin\alpha/\cos\beta &\to 1 \\ -\sin\alpha/\sin\beta &\to 1/\tan\beta \\ \cos\alpha/\cos\beta &\to \tan\beta \end{aligned} \quad (4.4)$$

The partial width of the decay mode $H^- \to u\bar{d}$ is given by

$$\Gamma(H^- \to u\bar{d}) = \frac{N_c G_F}{4\sqrt{2}\pi}\frac{\lambda^{1/2}_{ud,H^\pm}}{M_{H^\pm}}|V_{ud}|^2 \times \left[(M^2_{H^\pm} - m_u^2 - m_d^2)\left(m_d^2\tan^2\beta + m_u^2\,{\rm ctg}^2\beta\right) - 4m_u^2 m_d^2\right] \quad (4.5)$$

with V_{ud} the CKM-type matrix element for quarks and λ is the two-body phase space function defined by

$$\lambda_{i,jk} = (1 - M_i^2/M_k^2 - M_j^2/M_k^2)^2 - 4M_i^2M_j^2/M_k^4 \quad (4.6)$$

For decays into quark pairs, the QCD corrections must be also included.

Below the $\bar{t}t$ threshold, a variety of channels is open for the decays of the heavy CP-even Higgs bosons, the most important being the cascade decays $H \to \Phi\Phi$ with $\Phi = h$ or A, with a partial width [for real light Higgs bosons]

$$\Gamma(H \to \Phi\Phi) = \frac{G_F}{16\sqrt{2}\pi} \frac{M_Z^3}{M_H} g^2_{H\Phi\Phi} \beta_\Phi \tag{4.7}$$

where $\beta_\Phi = (1 - 4M_\Phi^2/M_H^2)^{1/2}$ and the radiatively corrected three-boson self-couplings [to leading order], in units of $g_Z' = (\sqrt{2}G_F)^{1/2} M_Z^2$, are given by

$$\begin{aligned} g_{Hhh} &= 2\sin 2\alpha \sin(\beta+\alpha) - \cos 2\alpha \cos(\beta+\alpha) - 3\frac{\epsilon}{M_Z^2} \frac{\sin\alpha \cos^2\alpha}{\sin\beta} \\ g_{HAA} &= -\cos 2\beta \cos(\beta+\alpha) + \frac{\epsilon}{M_Z^2} \frac{\sin\alpha \cos^2\beta}{\sin\beta} \end{aligned} \tag{4.8}$$

In contrast to the previous couplings, the leading m_t^4 radiative corrections cannot be absorbed entirely in the redefinition of the mixing angle α, but they are renormalized by an explicit term depending on the parameter ϵ given by [M_S is the common squark mass at the electroweak scale]

$$\epsilon = \frac{3G_F}{\sqrt{2}\pi^2} \frac{m_t^4}{\sin^2\beta} \log\left(1 + \frac{M_S^2}{m_t^2}\right) \tag{4.9}$$

In the decoupling limit, these couplings approach the values

$$\begin{aligned} g_{Hhh} &\to \frac{3}{2}\sin 4\beta \\ g_{HAA} &\to -\frac{1}{2}\sin 4\beta \end{aligned} \tag{4.10}$$

In the mass range above the WW and ZZ thresholds, where the HVV couplings are not strongly suppressed for small values of $\tan\beta$, the partial widths of the H particle into massive gauge bosons can also be substantial; they are given by

$$\Gamma(H \to VV) = \frac{\sqrt{2}G_F \cos^2(\alpha-\beta)}{32\pi} M_H^3 (1 - 4\kappa_V + 12\kappa_V^2)(1 - 4\kappa_V)^{1/2}\, \delta_V' \tag{4.11}$$

with $\kappa_V = M_V^2/M_H^2$ and $\delta_V' = 2(1)$ for $V = W(Z)$.

For small values of $\tan\beta$ and below the $\bar{t}t$ and the $t\bar{b}$ thresholds, the pseudoscalar and charged Higgs bosons can decay into the lightest Higgs boson h and a gauge boson; however these decays are suppressed by $\cos^2(\beta-\alpha)$ and therefore are very rare for large A masses. The partial decay widths are given by

$$\begin{aligned} \Gamma(A \to hZ) &= \frac{G_F \cos^2(\beta-\alpha)}{8\sqrt{2}\pi} \frac{M_Z^4}{M_A} \lambda^{1/2}_{Zh,A} \lambda_{Ah,Z} \\ \Gamma(H^- \to hW^-) &= \frac{G_F \cos^2(\beta-\alpha)}{8\sqrt{2}\pi} \frac{M_W^4}{M_{H^-}} \lambda^{\frac{1}{2}}_{Wh,H^-} \lambda_{H^-h,W} \end{aligned} \tag{4.12}$$

In the decoupling limit, the partial widths of all decays of the heavy CP-even, CP-odd and charged Higgs bosons involving gauge bosons vanish since $\cos^2(\beta-\alpha) \to 0$. In addition, the $H \to hh$ decay width is very small since it is inversely proportional to M_H, and $H \to AA$ is not allowed kinematically. Therefore, the only relevant channels are the decays into $b\bar{b}/\bar{t}t$ for the neutral and $t\bar{b}$ for the charged Higgs bosons. The total decay widths of the three bosons H, A and $H^\pm$, into standard particles can be approximated in this limit by

$$\Gamma(H_k \to \text{all}) = \frac{3G_F}{4\sqrt{2}\pi} M_{H_k} \left[m_t^2 \tan^2\beta + m_b^2 \text{ctg}^2\beta\right] \tag{4.13}$$

[We have neglected the small contribution of the decays into τ leptons for large $\tan\beta$.]

4.2 Decays to charginos and neutralinos

The decay widths of the Higgs bosons H_k [$k = (1,2,3,4)$ correspond to $(H, h, A, H^\pm)$] into neutralino and chargino pairs are given by [35]

$$\begin{aligned} \Gamma(H_k \to \chi_i\chi_j) = \frac{G_F M_W^2}{2\sqrt{2}\pi} \frac{M_{H_k} \lambda_{ijk}^{1/2}}{1+\delta_{ij}} \Big[&(F_{ijk}^2 + F_{jik}^2)\left(1 - \frac{m_{\chi_i}^2}{M_{H_k}^2} - \frac{m_{\chi_j}^2}{M_{H_k}^2}\right) \\ &- 4\eta_k \epsilon_i \epsilon_j F_{ijk} F_{jik} \frac{m_{\chi_i} m_{\chi_j}}{M_{H_k}^2} \Big] \end{aligned} \tag{4.14}$$

where $\eta_{1,2,4} = -1$, $\eta_3 = -1$ and $\delta_{ij} = 0$ unless the final state consists of two identical (Majorana) neutralinos in which case $\delta_{ij} = 1$; $\epsilon_i = \pm 1$ stands for the sign of the i'th eigenvalue of the neutralino mass matrix [the matrix Z is defined in the convention of Ref.[18], and the eigenvalues of the mass matrix can be either positive or negative] while $\epsilon_i = 1$ for charginos; λ_{ijk} is the usual two-body phase space function given in eq.(4.4).

In the case of neutral Higgs boson decays, the coefficients F_{ijk} are related to the elements of the matrices U, V for charginos and Z for neutralinos,

$$H_k \to \chi_i^+ \chi_j^- \quad : \quad F_{ijk} = \frac{1}{\sqrt{2}} \left[e_k V_{i1} U_{j2} - d_k V_{i2} U_{j1}\right] \tag{4.15}$$

$$H_k \to \chi_i^0 \chi_j^0 \quad : \quad F_{ijk} = \frac{1}{2}\left(Z_{j3} - \tan\theta_W Z_{j1}\right)\left(e_k Z_{i2} - d_k Z_{i1}\right) \; + \; i \leftrightarrow j \tag{4.16}$$

with the coefficients e_k and d_k given by

$$e_1/d_1 = \cos\alpha \; , \; -\sin\alpha \; , \; e_2/d_2 = \sin\alpha \; , \; \cos\alpha \; , \; e_3/d_3 = -\sin\beta \; , \; \cos\beta \tag{4.17}$$

For the charged Higgs boson, the coupling to neutralino/chargino pairs are given by

$$\begin{aligned} F_{ij4} &= \cos\beta \left[Z_{j4} V_{i1} - \frac{1}{\sqrt{2}}\left(Z_{j2} + \tan\theta_W Z_{j1}\right) V_{i2}\right] \\ F_{ji4} &= \sin\beta \left[Z_{j3} U_{i1} - \frac{1}{\sqrt{2}}\left(Z_{j2} + \tan\theta_W Z_{j1}\right) U_{i2}\right] \end{aligned} \tag{4.18}$$

The matrices U, V for charginos and Z for neutralinos can be found in Ref.[18].

Since in most of the parameter space discussed in Section 2, the Higgs–higgsino mass parameter $|\mu|$ turned out to be very large, $|\mu| \gg M_1, M_2, M_Z$, it is worth discussing the Higgs decay widths into charginos and neutralinos in this limit. First, the decays of the neutral Higgs bosons into pairs of [identical] neutralinos and charginos $H_k \to \chi_i \chi_j$ will be suppressed by powers of M_Z^2/μ^2. This is due to the fact that neutral Higgs bosons mainly couple to *mixtures* of higgsino and gaugino components, and in the large μ limit, neutralinos and charginos are either pure higgsino– or pure gaugino–like. For the same reason, decays $H^- \to \chi_{1,2}^0 \chi_1^-$ and $\chi_{3,4}^0 \chi_2^-$ of the charged Higgs bosons will be suppressed. Furthermore, since in this case M_A is of the same order as $|\mu|$, decays into pairs of heavy charginos and neutralinos will be kinematically forbidden. Therefore, the channels

$$\begin{aligned} H, A &\to \chi_1^0 \chi_{3,4}^0 \,,\; \chi_2^0 \chi_{3,4}^0 \text{ and } \chi_1^+ \chi_1^- \\ H^+ &\to \chi_1^+ \chi_{3,4}^0 \text{ and } \chi_2^+ \chi_{1,2}^0 \end{aligned} \tag{4.19}$$

will be the dominant decay channels of the heavy Higgs particles. Up to the phase space suppression [i.e. for M_A sufficiently larger than $|\mu|$], the partial widths of these decay channels, in units of $G_F M_W^2 M_{H_k}/(4\sqrt{2}\pi)$, are given by [35]

$$\begin{aligned} \Gamma(H \to \chi_1^0 \chi_{3,4}^0) &= \frac{1}{2}\tan^2\theta_W (1 \pm \sin 2\beta) \\ \Gamma(H \to \chi_2^0 \chi_{3,4}^0) &= \frac{1}{2}(1 \pm \sin 2\beta) \\ \Gamma(H \to \chi_1^+ \chi_1^-) &= 1 \end{aligned} \tag{4.20}$$

$$\begin{aligned} \Gamma(A \to \chi_1^0 \chi_{4,3}^0) &= \frac{1}{2}\tan^2\theta_W (1 \pm \sin 2\beta) \\ \Gamma(A \to \chi_2^0 \chi_{4,3}^0) &= \frac{1}{2}(1 \pm \sin 2\beta) \\ \Gamma(A \to \chi_1^+ \chi_2^-) &= 1 \end{aligned} \tag{4.21}$$

$$\begin{aligned} \Gamma(H^- \to \chi_1^- \chi_{3,4}^0) &= 1 \\ \Gamma(H^- \to \chi_2^- \chi_1^0) &= 1 \\ \Gamma(H^- \to \chi_2^- \chi_2^0) &= \tan^2\theta_W \end{aligned} \tag{4.22}$$

[We have used the fact that in the decoupling limit $\sin 2\alpha = -\sin 2\beta$.] If all these channels are kinematically allowed, the total decay widths of the heavy Higgs bosons to chargino and neutralino pairs will be given by the expression

$$\Gamma(H_k \to \sum \chi_i \chi_j) = \frac{3 G_F M_W^2}{4\sqrt{2}\pi} M_{H_k} \left(1 + \frac{1}{3}\tan^2\theta_W\right) \tag{4.23}$$

which holds universally for all the three Higgs bosons $H, A, H^\pm$.

4.3 Decays to squarks and sleptons

Decays of the neutral and charged Higgs bosons, $H_k = h, H, A, H^\pm$, to sfermion pairs can be written as

$$\Gamma(H_k \to \tilde{f}_i \tilde{f}_j) = \frac{N_C G_F}{2\sqrt{2}\pi M_{H_k}} \lambda_{\tilde{f}_i \tilde{f}_j H_k}^{1/2} g_{H_k \tilde{f}_i \tilde{f}_j}^2 \tag{4.24}$$

$\tilde{f}_i$ with $i = 1, 2$ are the sfermion mass eigenstates which are related to the current eigenstates $\tilde{f}_L, \tilde{f}_R$ by

$$\begin{aligned} \tilde{f}_1 &= \tilde{f}_L \cos\theta_f + \tilde{f}_R \sin\theta_f \\ \tilde{f}_2 &= -\tilde{f}_L \sin\theta_f + \tilde{f}_R \cos\theta_f \end{aligned} \tag{4.25}$$

The mixing angles θ_f are proportional to the masses of the partner fermions and they are important only in the case of third generation sfermions. The couplings $g_{H_k \tilde{f}_i \tilde{f}_j}$ of the neutral and charged Higgs bosons H_k to sfermion mass eigenstates are superpositions of the couplings of the current eigenstates,

$$g_{H_k \tilde{f}_i \tilde{f}_j} = \sum_{\alpha,\beta = L,R} T_{ij\alpha\beta}\, g_{\Phi \tilde{f}_\alpha \tilde{f}_\beta} \tag{4.26}$$

The elements of the 4×4 matrix T are given in Tab.3a. The couplings $g_{H_k \tilde{f}_\alpha \tilde{f}_\beta}$ in the current eigenstate basis $\tilde{f}_{\alpha,\beta} = \tilde{f}_{L,R}$ [normalized to $2(\sqrt{2}G_F)^{1/2}$] may be written as [4, 35]

$$\begin{aligned} g_{H_k \tilde{f}_L \tilde{f}_L} &= m_f^2 g_1^\Phi + M_Z^2 (T_3^f - e_f s_W^2) g_2^\Phi \\ g_{H_k \tilde{f}_R \tilde{f}_R} &= m_f^2 g_1^\Phi + M_Z^2 e_f s_W^2 g_2^\Phi \\ g_{H_k \tilde{f}_L \tilde{f}_R} &= -\frac{1}{2} m_f \left[\mu g_3^\Phi - A_f g_4^\Phi\right] \end{aligned} \tag{4.27}$$

for the neutral Higgs bosons, $H_k = h, H, A$. $T_3 = \pm 1/2$ is the isospin of the [left–handed] sfermion and e_f its electric charge. The coefficients g_i^Φ are given in Tab.3b; in the decoupling limit, the coefficients g_2^Φ reduce to

$$\begin{aligned} \cos(\beta - \alpha) &\to \sin 2\beta \\ \sin(\beta + \alpha) &\to -\cos 2\beta \end{aligned} \tag{4.28}$$

[for the other coefficients, see eqs.(4.2)]. For the charged Higgs bosons, the couplings [also normalized to $2(\sqrt{2}G_F)^{1/2}$] are

$$g_{H^+ \tilde{u}_\alpha \tilde{d}_\beta} = -\frac{1}{\sqrt{2}} \left[g_1^{\alpha\beta} + M_W^2 g_2^{\alpha\beta}\right] \tag{4.29}$$

with the coefficients $g_{1/2}^{\alpha\beta}$ with $\alpha, \beta = L, R$ listed in Table 3c.

i,j / α,β	LL	RR	LR	RL
11	$\cos\theta_f\cos\theta_{f'}$	$\sin\theta_f\sin\theta_{f'}$	$\cos\theta_f\sin\theta_{f'}$	$\sin\theta_f\cos\theta_{f'}$
12	$-\cos\theta_f\sin\theta_{f'}$	$\sin\theta_f\cos\theta_{f'}$	$\cos\theta_f\cos\theta_{f'}$	$-\sin\theta_f\sin\theta_{f'}$
21	$-\sin\theta_f\cos\theta_{f'}$	$\cos\theta_f\sin\theta_{f'}$	$-\sin\theta_f\sin\theta_{f'}$	$\cos\theta_f\cos\theta_{f'}$
22	$\sin\theta_f\sin\theta_{f'}$	$\cos\theta_f\cos\theta_{f'}$	$-\sin\theta_f\cos\theta_{f'}$	$-\cos\theta_f\sin\theta_{f'}$

Tab. 3a: Transformation matrix for the Higgs couplings to sfermions in the presence of mixing.

$\tilde{f}$	Φ	g_1^Φ	g_2^Φ	g_3^Φ	g_4^Φ
$\tilde{u}$	h	$\cos\alpha/\sin\beta$	$-\sin(\alpha+\beta)$	$-\sin\alpha/\sin\beta$	$\cos\alpha/\sin\beta$
	H	$\sin\alpha/\sin\beta$	$\cos(\alpha+\beta)$	$\cos\alpha/\sin\beta$	$\sin\alpha/\sin\beta$
	A	0	0	1	$-1/\tan\beta$
$\tilde{d}$	h	$-\sin\alpha/\cos\beta$	$-\sin(\alpha+\beta)$	$\cos\alpha/\cos\beta$	$-\sin\alpha/\cos\beta$
	H	$\cos\alpha/\cos\beta$	$\cos(\alpha+\beta)$	$\sin\alpha/\cos\beta$	$\cos\alpha/\cos\beta$
	A	0	0	1	$-\tan\beta$

Tab. 3b: Coefficients in the couplings of neutral Higgs bosons to sfermion pairs.

$g_{1/2}^{LL}$	$g_{1/2}^{RR}$	$g_{1/2}^{LR}$	$g_{1/2}^{RL}$
$m_u^2/\tan\beta + m_Z^2\tan\beta$ $-\sin 2\beta$	$m_u m_d(\tan\beta + 1/\tan\beta)$ 0	$m_d(\mu - A_d\tan\beta)$ 0	$m_u(\mu + A_u/\tan\beta)$ 0

Tab. 3c: Coefficients in the couplings of charged Higgs bosons to sfermion pairs.

Mixing between sfermions occurs only in the third-generation sector. For the first two generations the decay pattern is rather simple. In the limit of massless fermions, the pseudoscalar Higgs boson does not decay into sfermions since by virtue of CP-invariance it couples only to pairs of left- and right-handed sfermions with the coupling proportional to m_f. In the asymptotic regime, where the masses $M_{H,H^\pm}$ are large, the decay widths of the heavy CP-even and charged [36] Higgs bosons into sfermions are proportional to

$$\Gamma(H, H^+ \to \tilde{f}\bar{\tilde{f}}) \sim \frac{G_F M_W^4}{M_H}\sin^2 2\beta \tag{4.30}$$

These decay modes can be significant only for low values $\tan\beta$ [which implies $\sin^2 2\beta \sim 1$]. However, in this regime the decay widths are inversely proportional to M_H, and thus cannot compete with the decay widths into charginos/neutralinos and ordinary fermions which increase with increasing Higgs mass. Therefore, the decays into first and second generations are unlikely to be important.

In the case of the third generation squarks, the Higgs decay widths can be larger by more than an order of magnitude. For instance the decay widths of the heavy neutral Higgs boson into top squarks of the same helicity is proportional to

$$\Gamma(H \to \tilde{t}\bar{\tilde{t}}) \sim \frac{G_F m_t^4}{M_H \tan^2\beta} \tag{4.31}$$

in the asymptotic region, and it will be enhanced by large coefficients [for small $\tan\beta$] compared to first/second generation squarks. Conversely, the decay widths into sbottom quarks can be very large for large $\tan\beta$. Furthermore, the decays of heavy neutral CP-even and CP-odd Higgs bosons to top squarks of different helicities will be proportional in the asymptotic region [and for the CP-even, up to the suppression by mixing angle] to

$$\Gamma(H, A \to \tilde{t}\bar{\tilde{t}}) \sim \frac{G_F m_t^2}{M_H}[\mu - A_t/\tan\beta]^2 \tag{4.32}$$

For μ and A_t values of the order of the Higgs boson masses, these decay widths will be competitive with the chargino/neutralino and standard fermion decays. Therefore, if kinematically allowed, these decay modes have to be taken into account.

4.4 Numerical results

The decay widths of the H, A and $H^\pm$ Higgs bosons into the sum of charginos and neutralinos, squark or slepton final states, as well as the standard and the total decay widths are shown in Figs.6a, 7a and 8a as a function of $m_{1/2}$ for two values of the pseudoscalar Higgs boson mass $M_A = 300$ and 600 GeV, and for positive and negative μ values; $\tan\beta$ is fixed to 1.75.

Fig.6a shows the various decay widths for the heavy CP-even Higgs boson. For $M_A = 300$ GeV, the $H \to t\bar{t}$ channel is still closed and the decay width into standard particles is rather small, being of $\mathcal{O}(250)$ MeV. In this case, the decays into the lightest stop squarks which are kinematically allowed for small values of $m_{1/2}$ will be by far the dominant decay channels. This occurs in most of the $m_{1/2}$ range if $\mu > 0$, but if $\mu < 0$ only for $m_{1/2} \lesssim 50$ GeV which is already ruled out by CDF and LEP1.5 data.

The decays into charginos and neutralinos, although one order of magnitude smaller than stop decays when allowed kinematically, are also very important. They exceed the standard decays in most of the $m_{1/2}$ range, except for large values of $m_{1/2}$ and $\mu < 0$ where no more phase space is available for the Higgs boson to decay into combinations of the heavy and light chargino/neutralino states. For small $m_{1/2}$ values, chargino and

neutralino decays can be larger than the standard decays by up to an order of magnitude.

As expected, the decay widths into sleptons are rather small and they never exceed the widths into standard particles, except for large values of $m_{1/2}$. Note that due to the isospin and charge assignments, the coupling of the H boson to sneutrinos is approximately a factor of two larger than the coupling to the charged sleptons. Since all the sleptons of the three generations are approximately mass degenerate [the mixing in the $\tilde{\tau}$ sector is very small for low values of $\tan\beta$], the small decay widths into sleptons are given by the approximate relation: $\Gamma(H \to \tilde{\nu}\bar{\tilde{\nu}}) \simeq 4\Gamma(H \to \tilde{l}_L\bar{\tilde{l}}_L) \simeq 4\Gamma(H \to \tilde{l}_R\bar{\tilde{l}}_R)$.

For larger values of M_H, $M_H \gtrsim 350$ GeV, the decay widths into supersymmetric particles have practically the same size as discussed previously. However, since the $H \to t\bar{t}$ channel opens up, the decay width into standard model particles becomes rather large, $\mathcal{O}(10$ GeV), and the supersymmetric decays are no longer dominant. For $M_H \simeq 600$ GeV, Fig.6a, only the $H \to \tilde{q}\bar{\tilde{q}}$ decay width can be larger than the decay width to standard particles; this occurs in the lower range of the $m_{1/2}$ values. The chargino/neutralino decays have a branching ratio of $\sim 20\%$, while the branching ratios of the decays into sleptons are below the 1% level.

Fig.6b and 6c show the individual decay widths of the heavy H boson with a mass $M_H \simeq 600$ GeV into charginos, neutralinos, stop quarks and sleptons for the set of parameters introduced previously. For decays into squarks, only the channels $H \to \tilde{t}_1\bar{\tilde{t}}_1, \tilde{t}_1\bar{\tilde{t}}_2$, and in a very small range of $m_{1/2}$ values the channel $H \to \tilde{b}_1\bar{\tilde{b}}_1$ are allowed kinematically [see Fig.3c]. The decay into two different stop states is suppressed by the [small] mixing angle, and due to the larger phase space the decay $H \to \tilde{t}_1\bar{\tilde{t}}_1$ is always dominating.

For the decays into chargino and neutralinos, the dominant channels are decays into mixtures of light and heavy neutralinos and charginos, in particular $H \to \chi_1^+\chi_2^-$ and $H \to \chi_1^0\chi_3^0$ or $\chi_2^0\chi_3^0$. This can be qualitatively explained, up to phase space suppression factors, by recalling the approximate values of the relative branching ratios in the large $|\mu|$ limit given in eqs.(4.18–20): $\Gamma(H \to \chi_1^+\chi_2^-) \sim 1$, while $\Gamma(H \to \chi_2^0\chi_3^0) \sim 1$ and $\Gamma(H \to \chi_1^0\chi_3^0) \sim \tan^2\theta_W$ because $\sin 2\beta$ is close to one. The mixed decays involving χ_4^0 are suppressed since they are proportional to $(1 - \sin 2\beta)$, and all other decay channels are suppressed by powers of M_Z^2/μ^2 for large $|\mu|$ values.

The decay widths for the pseudoscalar Higgs boson are shown in Fig.7a. There are no decays into sleptons, since the only decay allowed by CP–invariance, $A \to \tilde{\tau}_1\bar{\tilde{\tau}}_2$, is strongly suppressed by the very small $\tilde{\tau}$ mixing angle. For $M_A = 300$ GeV, the decay into the two stop squark eigenstates, $A \to \tilde{t}_1\bar{\tilde{t}}_2$, is not allowed kinematically and the only possible supersymmetric decays are the decays into charginos and neutralinos. The sum of the decay widths into these states can be two orders of magnitude larger than the decay width into standard particles.

For values of M_A above the $t\bar{t}$ threshold, the decay width into charginos and neutralinos is still of the same order as for low M_A, but because of the opening of the $A \to t\bar{t}$ mode, the total decay width increases dramatically and the chargino/neutralino decay branching

ratio drops to the level of 20%. As in the case of the heavy CP–even Higgs boson H, the relative decay widths of the pseudoscalar boson into charginos and neutralinos, Fig.7b, are larger for the channels involving mixtures of light and heavy neutralinos or charginos: the dominant decay modes are, roughly, $A \to \chi_1^+\chi_2^-$ and $A \to \chi_1^0\chi_4^0$ or $\chi_2^0\chi_4^0$. Again, this can be qualitatively explained, up to phase space suppression factors, by recalling the approximate formulae of eqs.(4.18–19), since the situation is the same as for H, with the two neutralino states χ_3^0 and χ_4^0 being interchanged.

For small values of the common gaugino mass, $m_{1/2} \lesssim 100$ GeV, the decay mode of the pseudoscalar Higgs boson into stop squarks, $A \to \tilde{t}_1\bar{\tilde{t}}_2$, is phase space allowed. In this case, it is competitive with the top–antitop decay mode. As discussed previously, the $1/M_A^2$ suppression [and to a lesser extent the suppression due to the mixing angle] of the $A \to \tilde{t}_1\bar{\tilde{t}}_2$ decay width compared to $\Gamma(A \to t\bar{t})$ will be compensated by the enhancement of the $At_1\bar{t}_2$ coupling for large values of μ and A_t.

Fig.8a shows the decay widths for the charged Higgs boson. Since the dominant decay channel $H^- \to t\bar{b}$ is already open for $M_{H^\pm} \simeq 300$ GeV [although still slightly suppressed by phase space], the charged Higgs decay width into standard particles is rather large and it increases only by a factor of ~ 4 when increasing the pseudoscalar mass to $M_A = 600$ GeV. The situation for the supersymmetric decays is quite similar for the two masses: the chargino/neutralinos decay modes have branching ratios of the order of a few ten percent, while the branching ratios for the decays into sleptons, when kinematically allowed, do not exceed the level of a few percent, as expected. Only the decay $H^- \to \tilde{t}_1\bar{\tilde{b}}_1$, the only squark decay mode allowed by phase space [see Fig.3c] for relatively low values of $m_{1/2}$, is competitive with the $t\bar{b}$ decay mode.

The decay widths of the charged Higgs into the various combinations of charginos and neutralinos are shown in Fig.8b for $M_{H^\pm} \sim 600$ GeV. The dominant channels are again decays into mixtures of gauginos and higgsinos, since $|\mu|$ is large. The pattern follows approximately the rules of eq.(4.22), modulo phase suppression.

As discussed in section 2, since the chargino, neutralino and sfermion masses scale as M_A, the situation for even larger values of the pseudoscalar Higgs boson mass, $M_A \sim 1$ TeV, will be qualitatively similar to what has been discussed for $M_A \sim 600$ GeV. The only exception is that there will be slightly more phase space available for the supersymmetric decays to occur.

5. Final Decay Products of the Higgs Bosons

In this section, we will qualitatively describe the final decay products of the produced Higgs bosons. Assuming that M_A is large, $M_A \gtrsim 500$ GeV, the decays into standard particles [and more precisely, the $t\bar{t}$ for the neutral and the $t\bar{b}$ decays for the charged Higgs bosons] always have substantial branching ratios, even for the value $\tan\beta = 1.75$ which will be chosen for the discussion. Therefore, to investigate decays into SUSY particles in the main production processes, $e^+e^- \to HA$ and H^+H^-, one has to look for

final states where one of the Higgs bosons decays into standard modes while the other Higgs boson decays into charginos, neutralinos or stop squarks. As discussed previously, the decays into the other squarks are disfavored by phase space, while the branching ratios into sleptons are always small and can be neglected.

Let us first discuss the case where one of the Higgs bosons decays into chargino and neutralino pairs,

$$\begin{aligned} e^+e^- &\to H\,A \to [t\bar{t}]\,[\chi^+\chi^-] \text{ and } [t\bar{t}]\,[\chi^0\chi^0] \\ e^+e^- &\to H^+H^- \to [t\bar{b}]\,[\chi^-\chi^0] \end{aligned} \tag{5.1}$$

The lightest chargino $\chi_1^\pm$ and next-to-lightest neutralino χ_2^0 decay into [possibly virtual] W, Z and the lightest Higgs boson h, assuming that decays into sleptons and squarks are kinematically disfavored. In the limit of large $|\mu|$, the decay widths [in the decoupling limit] are proportional to [37]

$$\Gamma(\chi_1^\pm \to \chi_1^0 W^\pm) \sim \sin^2 2\beta \tag{5.2}$$

$$\begin{aligned} \Gamma(\chi_2^0 \to \chi_1^0 Z) &\sim \cos^2 2\beta\,[(M_2 - M_1)/2\mu]^2 \\ \Gamma(\chi_2^0 \to \chi_1^0 h) &\sim \sin^2 2\beta \end{aligned} \tag{5.3}$$

In most of the parameter space, the $W/Z/h$ are virtual [in addition to the three-body phase space factors, the decay widths are suppressed by powers of $M_2 M_Z/\mu^2$] except near the upper values of $m_{1/2}$. In the case of χ_2^0, the channel $\chi_2^0 \to \chi_1^0 Z$ mode is always dominant although suppressed by additional powers of M_Z^2/μ^2 compared to the $\chi_2^0 \to h\chi_1^0$ mode, since both h and Z are off-shell, and the Z boson width is much larger than the width of the h boson for small values of $\tan\beta$. The radiative decay $\chi_2^0 \to \chi_1^0\gamma$ should play a marginal role except for very small values of $m_{1/2}$ where the difference between the χ_2^0 and Z boson masses becomes too large.

For large values of $m_{1/2}$, the sleptons become rather light compared to the gauginos and the decays of the light chargino and neutralino into leptons+sleptons are kinematically possible. In this case, these cascade decays become dominant since the partial widths for large $|\mu|$ are given by

$$\sum_l \Gamma(\chi_2^0 \to l\tilde{l}) = \sum_l 2\Gamma(\chi_1^\pm \to l\tilde{\nu}) = \frac{3G_F^2 M_W^2}{\sqrt{2}\pi} M_2 \tag{5.4}$$

and therefore not suppressed by powers of $M_Z M_2/\mu^2$, unlike the previous decay modes [we assume of course that there is no suppression by phase-space]. The sleptons will then decay into the LSP and massless leptons, leading to multi-lepton final states.

The heavier chargino, in the absence of squark and slepton decay modes, will decay preferentially into the lightest chargino and neutralinos plus gauge or light Higgs bosons. The decay widths, in units of $G_F M_W^2 |\mu|/(8\sqrt{2}\pi)$ may be approximated in the decoupling limit by [37]

$$\chi_2^\pm \to \chi_1^\pm Z \;:\; \Gamma = 1$$

$$\begin{aligned} &\to \chi_1^\pm h \;:\; \Gamma = 1 \\ &\to \chi_1^0 W^\pm \;:\; \Gamma = \tan^2\theta_W \\ &\to \chi_2^0 W^\pm \;:\; \Gamma = 1 \end{aligned} \tag{5.5}$$

The branching ratios for the various final states are roughly equal. Since $\chi_2^\pm$ is almost higgsino-like, the decay widths into sleptons and partners of the light quarks, when kinematically allowed, are extremely small since they are suppressed by powers of m_f^2/M_W^2. Because of the large m_t value, only the decays into stop squarks and bottom quarks will be very important. This decay is allowed in most of the parameter space for $M_A \gtrsim 600$ GeV and, up to suppression by mixing angles, it is enhanced by a power m_t^2 [37]

$$\frac{\Gamma(\chi_2^\pm \to \tilde{t}\tilde{b})}{\Gamma(\chi_2^\pm \to W, Z, h)} \sim \frac{3m_t^2}{M_W^2} \frac{1}{\sin^2\beta(3 + \tan^2\theta_W)} \sim 4 \tag{5.6}$$

compared to the other decays. Therefore, when kinematically possible, this decay will be the dominant decay mode of the heavy charginos.

For the heavier neutralinos, $\chi_{3,4}^0$, the decay widths into $W/Z/h$ bosons, again in units of $G_F M_W^2 |\mu|/(8\sqrt{2}\pi)$ may be be written in the decoupling limit as [37]

$$\begin{aligned} \chi_{3/4}^0 &\to \chi_1^0 Z \;:\; \Gamma = \frac{1}{2}\tan^2\theta_W(1 \mp \sin 2\beta) \\ &\to \chi_1^0 h \;:\; \Gamma = \frac{1}{2}\tan^2\theta_W(1 \mp \sin 2\beta) \\ &\to \chi_2^0 Z \;:\; \Gamma = \frac{1}{2}(1 \pm \sin 2\beta) \\ &\to \chi_2^0 h \;:\; \Gamma = \frac{1}{2}(1 \pm \sin 2\beta) \\ &\to \chi_1^\pm W^\mp \;:\; \Gamma = 2 \end{aligned} \tag{5.7}$$

The dominant mode is the charged decay, $\chi_{3,4}^0 \to \chi_1^\pm W^\mp$, followed by the modes involving the $h(Z)$ boson for $\chi_4^0(\chi_3^0)$. Because $\sin 2\beta \sim 1$, only one of the h or Z decay channels is important. Here again, because of the higgsino nature of the two heavy neutralinos, the decay widths into sleptons and the scalar partners of the light quarks are negligible; the only important decays are the stop decays, $\chi_{3,4}^0 \to t\tilde{t}_1$, when they are allowed kinematically [i.e. for not too large values of $m_{1/2}$]. The ratio between stop and $W/Z/h$ decay widths, up to suppression by mixing angles, is also given by eq.(5.6), and the stop decays will therefore dominate.

We now turn to the case where one of the produced Higgs particles decays into stop squarks

$$\begin{aligned} e^+e^- &\to H\,A \to [t\bar{t}]\,[\tilde{t}_1\tilde{t}_1^*] \text{ and } [t\bar{t}]\,[\tilde{t}_1\tilde{t}_2^*] \\ e^+e^- &\to H^+H^- \to [t\bar{b}]\,[\tilde{t}_1\tilde{b}_1^*] \end{aligned} \tag{5.8}$$

From the squark mass plots, Fig. 3c, the only decay modes of the lightest stop squark allowed by phase space are

$$\tilde{t}_1 \to t\chi_1^0 \quad , \quad t\chi_2^0 \quad , \quad b\chi_1^+ \tag{5.9}$$

Only the last decay mode occurs for relatively small values of $m_{1/2}$, since $m_{\tilde{t}_1} < m_t + m_{\chi^0_{1,2}}$ in this case. For larger values of $m_{1/2}$, $\tilde{t}_1$ is heavy enough to decay into top quarks plus the lightest neutralinos. For these $m_{1/2}$ values, the three decay modes of eq.(5.9) will have approximately the same magnitude since the chargino and the neutralinos are gaugino-like and there is no enhancement due to the top mass for the $\tilde{t}_1 \to t\chi^0$ decays.

The heavier stop squark, in addition to the previous modes, has decay channels with $\tilde{t}_1$ and Z/h bosons in the final state

$$\tilde{t}_2 \to \tilde{t}_1 Z \quad , \quad \tilde{t}_1 h \tag{5.10}$$

These decays, in particular the decay into the lightest Higgs boson h, will be dominant in the large $|\mu|$ limit, since they will be enhanced by powers of μ^2.

Appendix A: Chargino and Neutralino Masses and Couplings

In this Appendix we collect the analytical expressions of the chargino and neutralino masses and couplings, and we discuss the limit in which the Higgs-higgsino mass parameter $|\mu|$ is large.

The general chargino mass matrix [18],

$$\mathcal{M}_C = \begin{bmatrix} M_2 & \sqrt{2}M_W \sin\beta \\ \sqrt{2}M_W \cos\beta & \mu \end{bmatrix} \tag{A1}$$

is diagonalized by two real matrices U and V,

$$U^* \mathcal{M}_C V^{-1} \;\to\; U = \mathcal{O}_- \text{ and } V = \begin{cases} \mathcal{O}_+ & \text{if } \det\mathcal{M}_C > 0 \\ \sigma\mathcal{O}_- & \text{if } \det\mathcal{M}_C < 0 \end{cases} \tag{A2}$$

where σ is the matrix

$$\sigma = \begin{bmatrix} \pm 1 & 0 \\ 0 & \pm 1 \end{bmatrix} \tag{A3}$$

with the appropriate signs depending upon the values of M_2, μ, and $\tan\beta$ in the chargino mass matrix. $\mathcal{O}_\pm$ is given by:

$$\mathcal{O}_\pm = \begin{bmatrix} \cos\theta_\pm & \sin\theta_\pm \\ -\sin\theta_\pm & \cos\theta_\pm \end{bmatrix} \tag{A4}$$

with

$$\begin{aligned} \tan 2\theta_- &= \frac{2\sqrt{2}M_W(M_2\cos\beta + \mu\sin\beta)}{M_2^2 - \mu^2 - 2M_W^2\cos\beta} \\ \tan 2\theta_+ &= \frac{2\sqrt{2}M_W(M_2\sin\beta - \mu\cos\beta)}{M_2^2 - \mu^2 + 2M_W^2\cos\beta} \end{aligned} \tag{A5}$$

This leads to the two chargino masses, the $\chi_{1,2}^\pm$ masses

$$\begin{aligned} m_{\chi^\pm_{1,2}} = \; & \frac{1}{\sqrt{2}}\Big[M_2^2 + \mu^2 - 2M_W^2 \\ & \mp \Big\{(M_2^2 - \mu^2)^2 + 4M_W^4\cos^2 2\beta + 4M_W^2(M_2^2 + \mu^2 - 2M_2\mu\sin 2\beta)\Big\}^{\frac{1}{2}}\Big]^{\frac{1}{2}} \end{aligned} \tag{A6}$$

In the limit $|\mu| \gg M_2, M_Z$, the masses of the two charginos reduce to

$$\begin{aligned} m_{\chi_1^\pm} &\simeq M_2 - \frac{M_W^2}{\mu^2}(M_2 - \mu\sin 2\beta) \\ m_{\chi_2^\pm} &\simeq |\mu| - \frac{M_W^2}{\mu^2}\epsilon_\mu(M_2\sin 2\beta + \mu) \end{aligned} \tag{A7}$$

where ϵ_μ is for the sign of μ. For $|\mu| \to \infty$, the lightest chargino corresponds to a pure wino state with mass $m_{\chi_1^\pm} \simeq M_2$, while the heavier chargino corresponds to a pure higgsino state with a mass $m_{\chi_2^\pm} = |\mu|$.

In the case of the neutralinos, the four-dimensional neutralino mass matrix depends on the same two mass parameters μ and M_2, if the GUT relation $M_1 = \frac{5}{3}\tan^2\theta_W M_2 \simeq \frac{1}{2}M_2$ [18] is used. In the $(-i\tilde{B}, -i\tilde{W}_3, \tilde{H}_1^0, \tilde{H}_2^0)$ basis, it has the form

$$\mathcal{M}_N = \begin{bmatrix} M_1 & 0 & -M_Z s_W \cos\beta & M_Z s_W \sin\beta \\ 0 & M_2 & M_Z c_W \cos\beta & -M_Z c_W \sin\beta \\ -M_Z s_W \cos\beta & M_Z c_W \cos\beta & 0 & -\mu \\ M_Z s_W \sin\beta & -M_Z c_W \sin\beta & -\mu & 0 \end{bmatrix} \tag{A8}$$

It can be diagonalized analytically [38] by a single real matrix Z; the [positive] masses of the neutralino states $m_{\chi_i^0}$ are given by

$$\begin{aligned} \epsilon_1 m_{\chi_1^0} &= C_1 - \left(\frac{1}{2}a - \frac{1}{6}C_2\right)^{1/2} + \left[-\frac{1}{2}a - \frac{1}{3}C_2 + \frac{C_3}{(8a - 8C_2/3)^{1/2}}\right]^{1/2} \\ \epsilon_2 m_{\chi_2^0} &= C_1 + \left(\frac{1}{2}a - \frac{1}{6}C_2\right)^{1/2} - \left[-\frac{1}{2}a - \frac{1}{3}C_2 - \frac{C_3}{(8a - 8C_2/3)^{1/2}}\right]^{1/2} \\ \epsilon_3 m_{\chi_3^0} &= C_1 - \left(\frac{1}{2}a - \frac{1}{6}C_2\right)^{1/2} - \left[-\frac{1}{2}a - \frac{1}{3}C_2 - \frac{C_3}{(8a - 8C_2/3)^{1/2}}\right]^{1/2} \\ \epsilon_4 m_{\chi_4^0} &= C_1 + \left(\frac{1}{2}a - \frac{1}{6}C_2\right)^{1/2} + \left[-\frac{1}{2}a - \frac{1}{3}C_2 - \frac{C_3}{(8a - 8C_2/3)^{1/2}}\right]^{1/2} \end{aligned} \tag{A9}$$

where $\epsilon_i = \pm 1$; the coefficients C_i and a are given by

$$\begin{aligned} C_1 &= (M_1 + M_2)/4 \\ C_2 &= M_1 M_2 - M_Z^2 - \mu^2 - 6C_1^2 \\ C_3 &= 2C_1\left[C_2 - 2C_1^2 + 2\mu^2\right] - M_Z^2(M_1 c_W^2 + M_2 s_W^2) - \mu M_Z^2 \sin 2\beta \\ C_4 &= C_1 C_3 - C_1^2 C_2 - C_1^4 - M_1 M_2 \mu^2 - (M_1 c_W^2 + M_2 s_W^2) M_Z^2 \mu \sin 2\beta \end{aligned} \tag{A10}$$

and

$$a = \frac{1}{2^{1/3}} \mathrm{Re}\left[S - i\left(\frac{D}{27}\right)^{1/2}\right]^{1/3} \tag{A11}$$

with

$$\begin{aligned} S &= C_3^2 + \frac{2}{27}C_2^3 - \frac{8}{3}C_2 C_4 \\ D &= \frac{4}{27}(C_2^2 - 12C_4)^3 - 27S^2 \end{aligned} \tag{A12}$$

In the limit of large $|\mu|$ values, the masses of the neutralino states simplify to

$$\begin{aligned} m_{\chi_1^0} &\simeq M_1 - \frac{M_Z^2}{\mu^2}(M_1 + \mu \sin 2\beta)\, s_W^2 \\ m_{\chi_2^0} &\simeq M_2 - \frac{M_Z^2}{\mu^2}(M_2 + \mu \sin 2\beta)\, c_W^2 \\ m_{\chi_3^0} &\simeq |\mu| + \frac{1}{2}\frac{M_Z^2}{\mu^2}\epsilon_\mu(1 - \sin 2\beta)\left(\mu + M_2 s_W^2 - M_1 c_W^2\right) \\ m_{\chi_4^0} &\simeq |\mu| + \frac{1}{2}\frac{M_Z^2}{\mu^2}\epsilon_\mu(1 - \sin 2\beta)\left(\mu - M_2 s_W^2 - M_1 c_W^2\right) \end{aligned} \tag{A13}$$

Again, for $|\mu| \to \infty$, two neutralinos are pure gaugino states with masses $m_{\chi_1^0} \simeq M_1$, $m_{\chi_2^0} = M_2$, while the two others are pure higgsino states, with masses $m_{\chi_3^0} \simeq m_{\chi_4^0} \simeq |\mu|$.

The matrix elements of the diagonalizing matrix, Z_{ij} with $i, j = 1, .4$, are given by

$$Z_{i1} = \left[1 - \left(\frac{Z_{i2}}{Z_{i1}}\right)^2 - \left(\frac{Z_{i3}}{Z_{i1}}\right)^2 - \left(\frac{Z_{i4}}{Z_{i1}}\right)^2\right]^{-1/2} \tag{A14}$$

$$\frac{Z_{i2}}{Z_{i1}} = -\frac{1}{\tan\theta_W}\frac{M_1 - \epsilon_i m_{\chi_i^0}}{M_2 - \epsilon_i m_{\chi_i^0}}$$

$$\frac{Z_{i3}}{Z_{i1}} = \frac{\mu(M_1 - \epsilon_i m_{\chi_i^0})(M_2 - \epsilon_i m_{\chi_i^0}) - M_Z^2 \sin\beta\cos\beta[(M_1 - M_2)c_W^2 - M_2 - \epsilon_i m_{\chi_i^0}]}{M_Z(M_2 - \epsilon_i m_{\chi_i^0})s_W(\mu\cos\beta - \epsilon_i m_{\chi_i^0}\sin\beta)}$$

$$\frac{Z_{i4}}{Z_{i1}} = \frac{-\epsilon_i m_{\chi_i^0}(M_1 - \epsilon_i m_{\chi_i^0})(M_2 - \epsilon_i m_{\chi_i^0}) - M_Z^2 \cos^2\beta[(M_1 - M_2)c_W^2 + M_2 - \epsilon_i m_{\chi_i^0}]}{M_Z(M_2 - \epsilon_i m_{\chi_i^0})s_W(\mu\cos\beta - \epsilon_i m_{\chi_i^0}\sin\beta)}$$

where ϵ_i is the sign of the ith eigenvalue of the neutralino mass matrix, which in the large $|\mu|$ limit are: $\epsilon_1 = \epsilon_2 = 1$ and $\epsilon_4 = -\epsilon_3 = \epsilon_\mu$.

Appendix B: Sfermion Masses and Mixing

We now present the explicit expressions of the squark and slepton masses. We will assume a universal scalar mass m_0 and gaugino mass $m_{1/2}$ at the GUT scale, and we will neglect the Yukawa couplings in the RGE's [see Appendix C]. For third generation squarks this is a poor approximation since these couplings can be large; these have been taken into account in the numerical analysis.

By performing the RGE evolution to the electroweak scale, one obtains for the left- and right-handed sfermion masses at one-loop order [we include the full two-loop evolution of the masses in the numerical analysis]

$$m_{\tilde{f}_{L,R}}^2 = m_0^2 - \sum_{i=1}^{3} F_i(f) m_{1/2}^2 \pm (T_{3f} - e_f s_W^2) M_Z^2 \cos 2\beta \tag{B1}$$

T_{3f} and e_f are the weak isospin and the electric charge of the corresponding fermion f, and F_i are the RGE coefficients for the three gauge couplings at the scale $Q \sim M_Z$, given by

$$F_i = \frac{c_i(f)}{b_i}\left[1 - \left(1 - \frac{\alpha_G}{4\pi} b_i \log\frac{Q^2}{M_G^2}\right)^{-2}\right] \tag{B2}$$

The coefficients b_i, assuming that all the MSSM particle spectrum contributes to the evolution from Q to the GUT scale M_G, are

$$b_1 = 33/5 \quad , \quad b_2 = 1 \quad , \quad b_3 = -3 \tag{B3}$$

The coefficients $c(\tilde{f}) = (c_1, c_2, c_3)(\tilde{f})$ depend on the hypercharge and color of the sfermions [$F_L = L_L$ or Q_L is the slepton or squark doublet]

$$c(\tilde{L}_L) = \begin{pmatrix} 3/10 \\ 3/2 \\ 0 \end{pmatrix} \quad , \quad c(\tilde{E}_R) = \begin{pmatrix} 6/5 \\ 0 \\ 0 \end{pmatrix}$$

$$c(\tilde{Q}_L) = \begin{pmatrix} 1/30 \\ 3/2 \\ 8/3 \end{pmatrix} \quad , \quad c(\tilde{U}_R) = \begin{pmatrix} 8/15 \\ 0 \\ 8/3 \end{pmatrix} \quad , \quad c(\tilde{D}_R) = \begin{pmatrix} 2/15 \\ 0 \\ 8/3 \end{pmatrix} \tag{B4}$$

With the input gauge coupling constants at the scale of the Z boson mass

$$\alpha_1(M_Z) \simeq 0.01 \quad , \quad \alpha_2(M_Z) \simeq 0.033 \quad , \quad \alpha_3(M_Z) \simeq 0.118 \tag{B5}$$

one obtains for the GUT scale M_G and for the coupling constant α_G

$$M_G \sim 1.9 \times 10^{16}\ \mathrm{GeV} \quad \text{and} \quad \alpha_G = 0.041 \tag{B6}$$

Using these values, and including only gauge loops in the one–loop RGE's, one obtains for the left– and right–handed sfermion masses [39]

$$\begin{aligned}
m^2_{\tilde{u}_L} &= m_0^2 + 6.28 m^2_{1/2} - 0.35 M_Z^2 \cos(2\beta) \\
m^2_{\tilde{d}_L} &= m_0^2 + 6.28 m^2_{1/2} - 0.42 M_Z^2 \cos(2\beta) \\
m^2_{\tilde{u}_R} &= m_0^2 + 5.87 m^2_{1/2} - 0.16 M_Z^2 \cos(2\beta) \\
m^2_{\tilde{d}_R} &= m_0^2 + 5.82 m^2_{1/2} - 0.08 M_Z^2 \cos(2\beta) \\
m^2_{\tilde{\nu}_L} &= m_0^2 + 0.52 m^2_{1/2} - 0.50 M_Z^2 \cos(2\beta) \\
m^2_{\tilde{e}_L} &= m_0^2 + 0.52 m^2_{1/2} - 0.27 M_Z^2 \cos(2\beta) \\
m^2_{\tilde{e}_R} &= m_0^2 + 0.15 m^2_{1/2} - 0.23 M_Z^2 \cos(2\beta)
\end{aligned} \tag{B7}$$

In the case of the third generation sparticles, left– and right–handed sfermions will mix; for a given sfermion $\tilde{f} = \tilde{t}, \tilde{b}$ and $\tilde{\tau}$, the mass matrices which determine the mixing are

$$\begin{bmatrix} m^2_{\tilde{f}_L} + m_f^2 & m_f(A_f - \mu r_f) \\ m_f(A_f - \mu r_f) & m^2_{\tilde{f}_R} + m_f^2 \end{bmatrix} \tag{B8}$$

where the sfermion masses $m_{\tilde{f}_{L,R}}$ are given above, m_f are the masses of the partner fermions and $r_b = r_\tau = 1/r_t = \tan\beta$. These matrices are diagonalized by orthogonal matrices with mixing angles θ_f defined by

$$\sin 2\theta_f = \frac{2 m_f (A_f - \mu r_f)}{m^2_{\tilde{f}_1} - m^2_{\tilde{f}_2}} \quad , \quad \cos 2\theta_f = \frac{m^2_{\tilde{f}_L} - m^2_{\tilde{f}_R}}{m^2_{\tilde{f}_1} - m^2_{\tilde{f}_2}} \tag{B9}$$

and the masses of the squark eigenstates given by

$$m^2_{\tilde{f}_{1,2}} = m_f^2 - \frac{1}{2}\left[m^2_{\tilde{f}_L} - m^2_{\tilde{f}_R} \mp \sqrt{(m^2_{\tilde{f}_L} - m^2_{\tilde{f}_R})^2 + 4 m_f^2 (A_f - \mu r_f)^2} \right] . \tag{B10}$$

Appendix C: Renormalization Group Equations

Finally, we collect for completeness the renormalization group equations for the soft–SUSY breaking parameters [the trilinear couplings, scalar masses as well as for μ and B], including the dependence on A_t, A_b and A_τ. We restrict ourselves to the one–loop RGE's and we keep only the leading terms in the mass hierarchy in the MSSM with three fermion generations. The complete expressions for the RGE's can be found in Refs.[13, 19].

For the trilinear couplings of the third generation sfermions, the RGE's are given by

$$\begin{aligned}
\frac{dA_t}{dt} &= \frac{2}{16\pi^2}\Big(\sum c_i g_i^2 M_i + 6\lambda_t^2 A_t + \lambda_b^2 A_b \Big) \\
\frac{dA_b}{dt} &= \frac{2}{16\pi^2}\Big(\sum c'_i g_i^2 M_i + 6\lambda_b^2 A_b + \lambda_t^2 A_t + \lambda_\tau^2 A_\tau \Big) \\
\frac{dA_\tau}{dt} &= \frac{2}{16\pi^2}\Big(\sum c''_i g_i^2 M_i - 3\lambda_b^2 A_b + 4\lambda_\tau^2 A_\tau \Big)
\end{aligned} \tag{C1}$$

while for the scalar masses of the third generation sfermions, one has

$$\begin{aligned}
\frac{dM^2_{\tilde{Q}_L}}{dt} &= \frac{2}{16\pi^2}\Big(-\frac{1}{15} g_1^2 M_1^2 - 3 g_2^2 M_2^2 - \frac{16}{3} g_3^2 M_3^2 + \lambda_t^2 X_t + \lambda_b^2 X_b \Big) \\
\frac{dM^2_{\tilde{t}_R}}{dt} &= \frac{2}{16\pi^2}\Big(-\frac{16}{15} g_1^2 M_1^2 - \frac{16}{3} g_3^2 M_3^2 + 2\lambda_t^2 X_t \Big) \\
\frac{dM^2_{\tilde{b}_R}}{dt} &= \frac{2}{16\pi^2}\Big(-\frac{4}{15} g_1^2 M_1^2 - \frac{16}{3} g_3^2 M_3^2 + 2\lambda_b^2 X_b \Big) \\
\frac{dM^2_{\tilde{L}_L}}{dt} &= \frac{2}{16\pi^2}\Big(-\frac{3}{5} g_1^2 M_1^2 - 3 g_2^2 M_2^2 + \lambda_\tau^2 X_\tau \Big) \\
\frac{dM^2_{\tilde{\tau}_R}}{dt} &= \frac{2}{16\pi^2}\Big(-\frac{12}{5} g_1^2 M_1^2 + 2\lambda_\tau^2 X_\tau \Big)
\end{aligned} \tag{C2}$$

The evolution parameter is defined by $t = \log(Q/M_G)$,

$$\begin{aligned}
b_i &= (33/5\,,\ 1\,,\ -3) \\
c_i &= (13/15\,,\ 3\,,\ 16/3) \\
c'_i &= (7/15\,,\ 3\,,\ 16/3) \\
c''_i &= (9/5\,,\ 3\,,\ 0)
\end{aligned} \tag{C3}$$

and

$$\begin{aligned}
X_t &= M^2_{Q_L} + M^2_{t_R} - M^2_{H_2} - A_t^2 \\
X_b &= M^2_{Q_L} + M^2_{b_R} + M^2_{H_1} + A_b^2 \\
X_\tau &= M^2_{L_L} + M^2_{\tau_R} + M^2_{H_1} + A_\tau^2
\end{aligned} \tag{C4}$$

For the first and second generation sfermions, these expressions reduce to

$$\begin{aligned}
\frac{dA_u}{dt} &= \frac{2}{16\pi^2}\Big(\sum c_i g_i^2 M_i + \lambda_t^2 A_t \Big) \\
\frac{dA_d}{dt} &= \frac{2}{16\pi^2}\Big(\sum c'_i g_i^2 M_i + \lambda_b^2 A_b + \frac{1}{3}\lambda_\tau^2 A_\tau \Big) \\
\frac{dA_e}{dt} &= \frac{2}{16\pi^2}\Big(\sum c''_i g_i^2 M_i + \lambda_b^2 A_b + \frac{1}{3}\lambda_\tau^2 A_\tau \Big)
\end{aligned} \tag{C5}$$

and

$$\begin{aligned}
\frac{dM^2_{q_L}}{dt} &= \frac{2}{16\pi^2}\Big(-\frac{1}{15} g_1^2 M_1^2 - 3 g_2^2 M_2^2 - \frac{16}{3} g_3^2 M_3^2 \Big) \\
\frac{dM^2_{u_R}}{dt} &= \frac{2}{16\pi^2}\Big(-\frac{16}{15} g_1^2 M_1^2 - \frac{16}{3} g_3^2 M_3^2 \Big) \\
\frac{dM^2_{d_R}}{dt} &= \frac{2}{16\pi^2}\Big(-\frac{4}{15} g_1^2 M_1^2 - \frac{16}{3} g_3^2 M_3^2 \Big) \\
\frac{dM^2_{l_L}}{dt} &= \frac{2}{16\pi^2}\Big(-\frac{3}{5} g_1^2 M_1^2 - 3 g_2^2 M_2^2 \Big) \\
\frac{dM^2_{e_R}}{dt} &= \frac{2}{16\pi^2}\Big(-\frac{12}{5} g_1^2 M_1^2 \Big)
\end{aligned} \tag{C6}$$

For the gauge coupling constants and the other soft-SUSY breaking parameters, the RGE's are given by

$$\frac{dg_i}{dt} = \frac{1}{16\pi^2} b_i g_i^3 \tag{C7}$$

$$\frac{dM_i}{dt} = \frac{2}{16\pi^2} b_i g_i^2 M_i \tag{C8}$$

$$\frac{dB}{dt} = \frac{2}{16\pi^2}\left(\frac{3}{5}g_1^2 M_1 + 3g_2^2 M_2 + 3\lambda_b^2 A_b - 3\lambda_t^2 A_t - \lambda_\tau^2 A_\tau\right) \tag{C9}$$

$$\frac{d\mu}{dt} = \frac{\mu}{16\pi^2}\left(-\frac{3}{5}g_1^2 - 3g_2^2 + 3\lambda_t^2 + 3\lambda_b^2 - \lambda_\tau^2\right) \tag{C10}$$

$$\frac{dm_{H_1}^2}{dt} = \frac{2}{16\pi^2}\left(-\frac{3}{5}g_1^2 M_1^2 - 3g_2^2 M_2^2 + 3\lambda_b^2 X_b + \lambda_\tau^2 X_\tau\right) \tag{C11}$$

$$\frac{dm_{H_2}^2}{dt} = \frac{2}{16\pi^2}\left(-\frac{3}{5}g_1^2 M_1^2 - 3g_2^2 M_2^2 - 3\lambda_t^2 X_t\right) \tag{C12}$$

References

[1] J. Wess and B. Zumino, Phys. Lett. B49 (1974) 52.

[2] For reviews on supersymmetric theories, see P. Fayet and S. Ferarra, Phys. Rep. 32 (1977) 249; H. P. Nilles, Phys. Rep. 110 (1984) 1. R. Barbieri, Riv. Nuovo Cimento 11 (1988) 1; H. Haber and G. Kane, Phys. Rep. 117 (1985) 75.

[3] P. W. Higgs, Phys. Rev. Lett. 12 (1964) 132 and Phys. Rev. 145 (1966) 1156; F. Englert and R. Brout, Phys. Rev. Lett. 13 (1964) 321; G. S. Guralnik, C. R. Hagen and T. W. Kibble, Phys. Rev. Lett. 13 (1964) 585.

[4] For a review on the Higgs sector in the MSSM, see J.F. Gunion, H.E. Haber, G. Kane and S. Dawson, The Higgs Hunter's Guide, Addison-Wesley, Reading 1990.

[5] H. Georgi, H. Quinn and S. Weinberg, Phys. Rev. Lett. 33 (1974) 451.

[6] J. Ellis, S. Kelley and D. V. Nanopoulos, Phys. Lett. 260B (1991) 131; U. Amaldi, W. de Boer and H. Fürstenau, Phys. Lett. 260B (1991) 447; P. Langacker and M. Luo, Phys. Rev. D44 (1991) 817; G. G. Ross and R. G. Roberts, Nucl. Phys. B377 (1992) 571.

[7] The LEP Electroweak Working Group, Report CERN-PPE/95-172.

[8] K. Inoue, A. Kakuto, H. Komatsu and S. Takeshita, Prog. Theor. Phys. **68** (1982) 927; **71** (1984) 413. L. E. Ibañez and G. G. Ross, Phys. Lett. **B110** (1982) 215; L. Alvarez-Gaumé, M. Claudson and M. B. Wise, Nucl. Phys. **B207** (1982) 96; J. Ellis, D. V. Nanopoulos, and K. Tamvakis, Phys. Lett. **B121** (1983) 123; M. Drees, Phys. Rev. **D33** (1986) 62; J. Ellis, J. Hagelin, D. V. Nanopoulos, K. Olive and M. Srednicki, Nucl. Phys. **B238** (1984) 453; M. Drees and M. M. Nojiri, Phys. Rev. **D47** (1993) 376; H. Baer, R. Barbieri and M. Tata, Phys. Rev. **D41** (1990) 906; R. Barbieri and M. Frigeni, Phys. Lett. **B258** (1991) 395; G. F. Giudice and A. Pomarol, Phys. Lett. **B287** (1992) 164; H. Baer, M. Brhlik, M. A. Diaz, J. Ferrandis, P. Mercadante, P. Quintana and X. Tata, Phys. Rev. **D63** (2001) 015007.

[9] J. Ellis, L. Fogli and M. Lisi, Z. Phys. **C69** (1996) 627; P. Chankowski and S. Pokorski, Phys. Lett. *B356* (1995) 307.

[10] M. Veltman, Nucl. Phys. **B123** (1977) 89.

[11] M. Chanowitz, J. Ellis and M. Gaillard, Nucl. Phys. 128 (1977) 506.

[12] B. Pendleton and G. G. Ross, Phys. Lett. **98B** (1981) 291; C. T. Hill, Phys. Rev. **D24** (1981) 691.

[13] V. Barger, M.S. Berger, and P. Ohmann, Phys. Rev. **D47**, (1993) 1093.

[14] V. Barger, M.S. Berger, P. Ohmann, and R.J.N. Phillips, Phys. Lett. **B314** (1993) 351; M. Carena, S. Pokorski, and C. E. M. Wagner, Nucl. Phys. **B406** (1993) 59.

[15] F. Abe et al., CDF Coll., Phys. Rev. Lett. **74** (1995) 2626; S. Abachi et al., DO Coll., Phys. Rev. Lett. **74** (1995) 2632; F. Abe et al., CDF Coll., FNAL-PUB-96/004.

[16] H.E. Haber, Report CERN-TH/95-109, Proceedings *Conference on Beyond the Standard Model IV*, Lake Tahoe CA 1994; World Sci., J.F. Gunion et al., eds.

[17] Y. Okada, M. Yamaguchi and T. Yanagida, Prog. Theor. Phys. **85** (1991) 1; H.E. Haber and R. Hempfling, Phys. Rev. Lett. **66** (1991) 1815; J. Ellis, G. Ridolfi and F. Zwirner, Phys. Lett. **257B** (1991) 83; R. Barbieri, F. Caravaglios and M. Frigeni, Phys. Lett. **258B** (1991) 167.

[18] H.E. Haber and G. Kane in Ref.[2].

[19] V. Barger, M. S. Berger, and P. Ohmann, Phys. Rev. **D49**, (1994) 4908.

[20] W. de Boer et al., IEKP-KA/96-04, hep-ph/9603350.

[21] F. M. Borzumati, M. Olechowski, and S. Pokorski, Phys. Lett. **B349**, 311 (1995); H. Murayama, M. Olechowski, and S. Pokorski, UCB-PTH-95/34, hep-ph/9510327.

[22] M. Drees and M. Nojiri, Nucl. Phys. **B369** (1992) 54.

[23] S. Bethke, Proceedings of the *QCD 1994*, Montpellier 1994.

[24] J.-F. Grivaz, Proc. *Europhysics Conference on High Energy Physics*, Brussels 1995; for the recent limits including LEP1.5 data, see: D. Buskulic et al., Aleph Collab. CERN-PPE-96-010; G. Alexander et al., OPAL Collab. CERN-PPE-019, 020; M. Acciarri et al., L3 Collab. CERN-PPE-96-029.

[25] J. Ellis, G. Ridolfi, and F. Zwirner, Phys. Lett. **B262**, 477 (1991); A. Brignole, J. Ellis, G. Ridolfi, and F. Zwirner, Phys. Lett. **B271**, 123 (1991).

[26] M. Drees, Phys. Lett. **B181**, (1986) 279; J. S. Hagelin and S. Kelley, Nucl. Phys. **B342**, (1990) 95.

[27] A. Djouadi, G. Girardi, W. Hollik, F. Renard and C. Verzegnassi, Nucl. Phys. **B349** (1991) 48; M. Boulware and D. Finnell, Phys. Rev. **D44** (1991) 2054.

[28] See for instance W. Hollik, Proc. *Europhysics Conference on High Energy Physics*, Brussels 1995; J. D. Wells, C. Kolda, and G. L. Kane Phys. Lett. **B338** (1994) 219.

[29] G. Kane, C. Kolda, L. Roszkowski, and J. D. Wells, Phys. Rev. **D49**, (1994) 6173.

[30] A. J. Buras, M. Misiak, M. Münz, and S. Pokorski, Nucl. Phys. **B424**, (1994) 374.

[31] V. Barger, M. S. Berger, P. Ohmann and R. J. N. Phillips, Phys. Rev. **D51**, (1995) 2438; B. de Carlos and J. A. Casas, Phys. Lett. **B349**, (1995) 300, erratum – *ibid.* **351**, (1995) 604.

[32] A. Djouadi, J. Kalinowski and P. M. Zerwas, Z. Phys. **C57**, (1993) 569.

[33] A. Djouadi, J. Kalinowski and P. M. Zerwas, Z. Phys. **C70** (1996) 435.

[34] A. Djouadi, M. Spira and P. M. Zerwas, Z. Phys. **C70** (1996) 427.

[35] J.F. Gunion and H.E. Haber, Nucl. Phys. **B272** (1986) 1; **B278** (1986) 449; **B307** (1988) 445; erratum hep-ph/9301201.

[36] A. Bartl et al., Phys. Lett. **B373** (1996) 117.

[37] J.F. Gunion and H.E. Haber, Phys. Rev. **D37** (1988) 2515.

[38] M. El Kheishen, A. Shafik and A. Aboshousha, Phys. Rev. **D45** (1992) 4345.

[39] L. E. Ibañez and and C. Lopez, Nucl. Phys. **B233** (1984) 511.

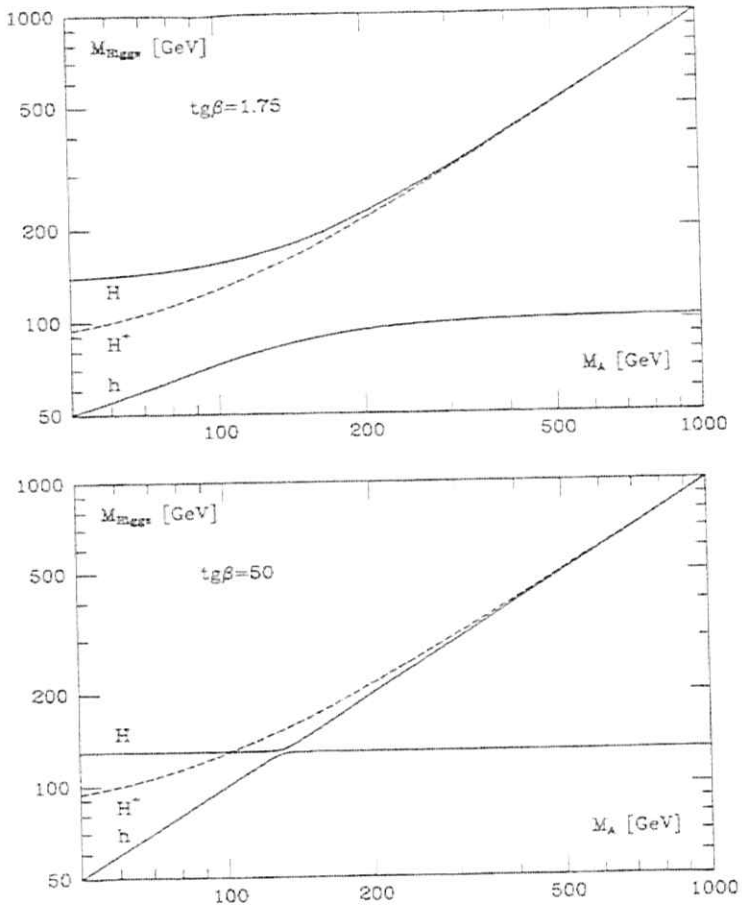

Fig. 1: Masses of the CP–even Higgs bosons h, H and of the charged Higgs particles $H^\pm$ as a function of M_A for two values of $\tan\beta = 1.75$ and 50; the common squark mass M_S at the weak scale is fixed to $M_S = 1$ TeV and we take $\mu = A_t = 0$.

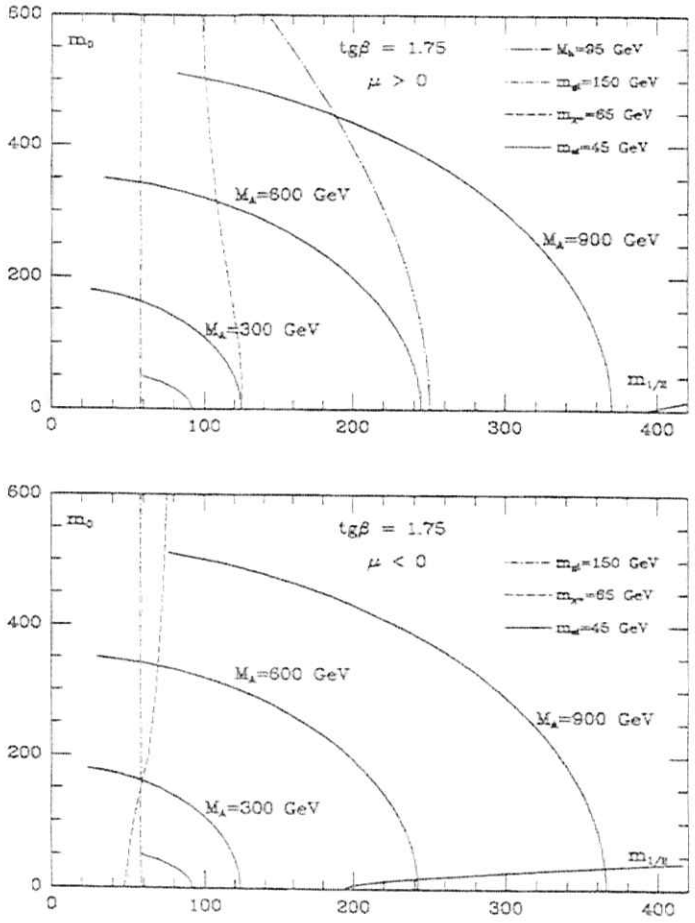

Fig. 2: The correlation between m_0 and $m_{1/2}$ for $\tan\beta$ = 1.75 and three values of M_A = 300, 600 and 900 GeV. The non-solid lines show the boundaries which can be excluded by including the experimental bounds from LEP1.5 and Tevatron.

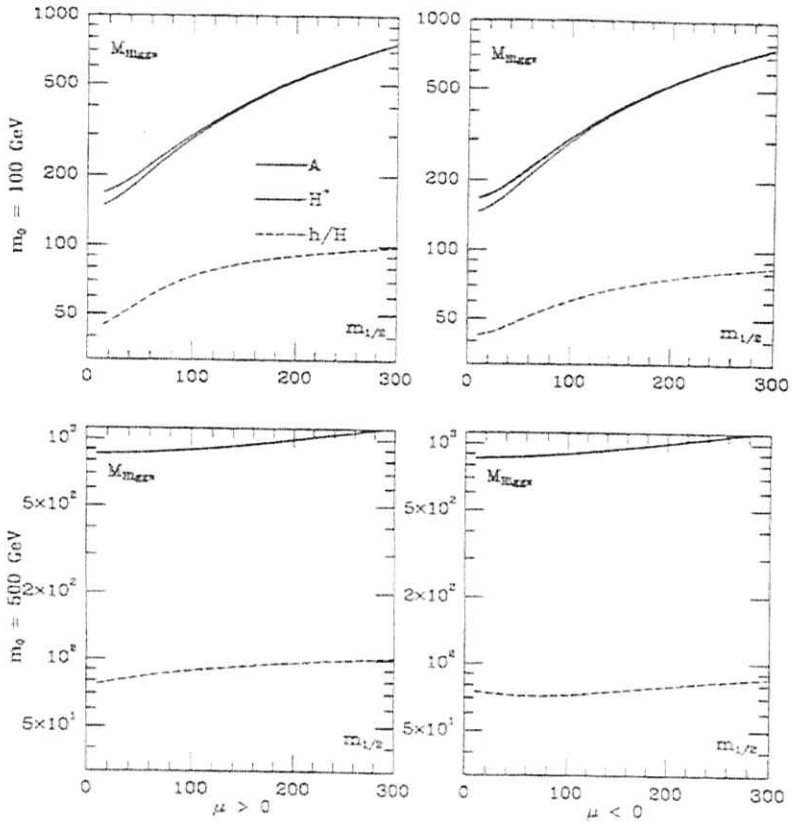

Fig. 3a: The masses of the Higgs bosons as a function of $m_{1/2}$ for $\tan\beta$ = 1.75, for the two values m_0 = 100 and 500 GeV and both signs of μ.

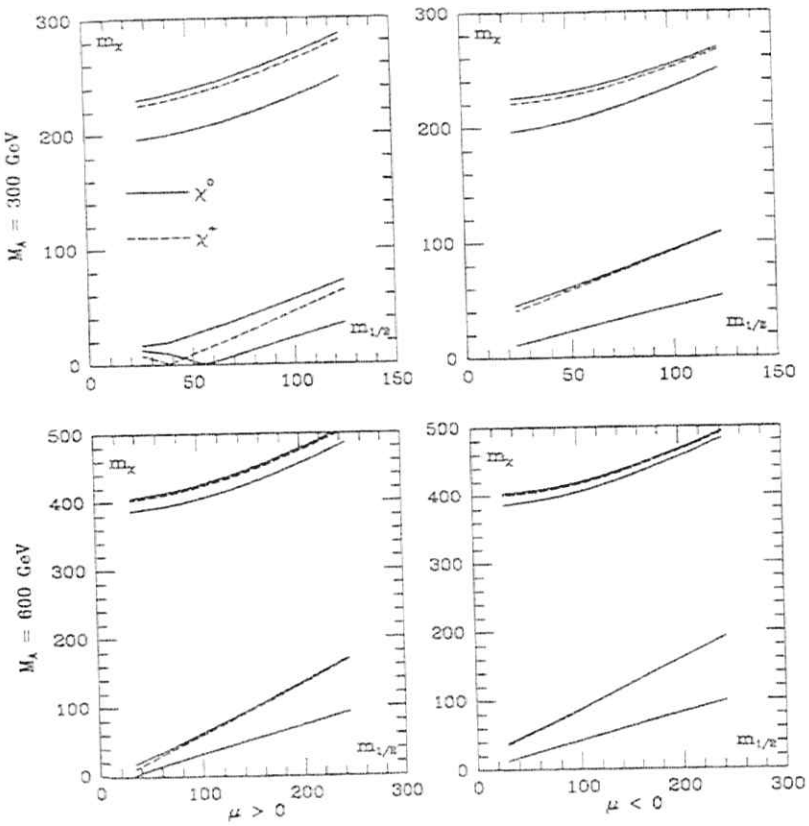

Fig. 3b: The masses of the two charginos (dashed lines) and the four neutralinos (solid lines) as a function of $m_{1/2}$ for $\tan\beta = 1.75$, $M_A = 300$ and 600 GeV and for both signs of μ. The chargins/neutralinos are ordered with increasing masses.

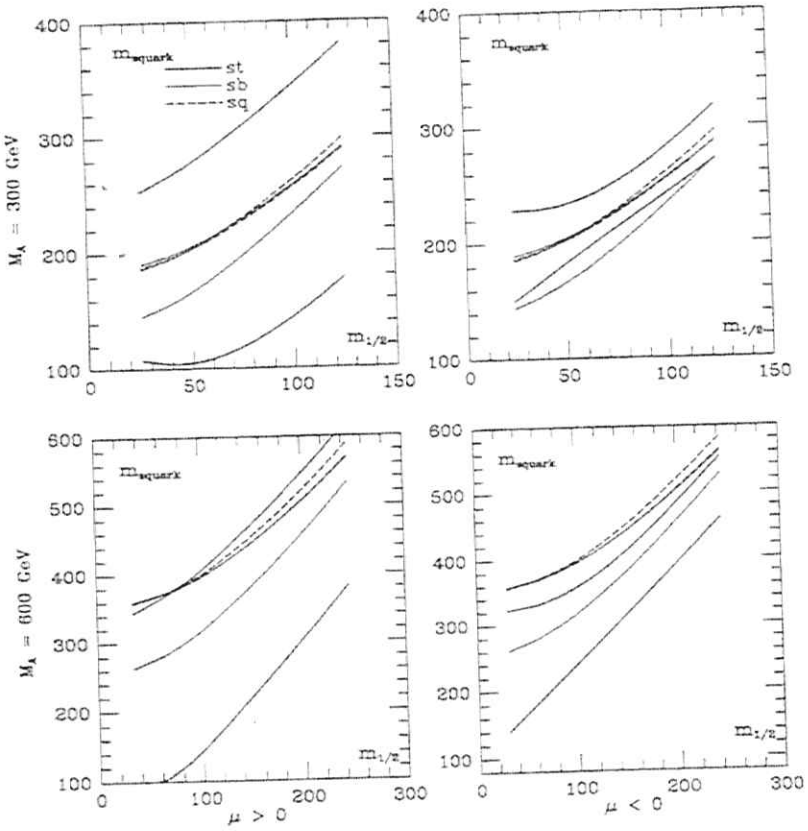

Fig. 3c: The masses of the two stop (solid lines), sbottom (dotted lines) and first/second generation squark (dashed lines) eigenstates as a function of $m_{1/2}$ for $\tan\beta = 1.75$, $M_A = 300$ and 600 GeV and for both signs of μ.

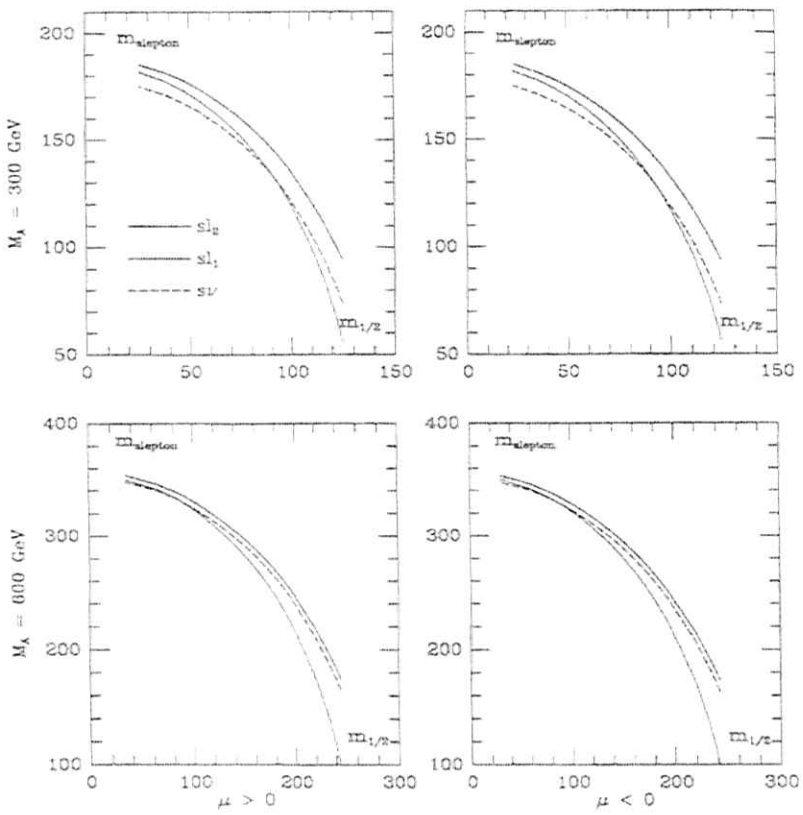

Fig. 3d: The masses of the charged sleptons (solid and dotted lines) and the sneutrino (dashed lines) of the three generations as a function of $m_{1/2}$ for $\tan\beta = 1.75$, $M_A = 300$ and 600 GeV and for both signs of μ.

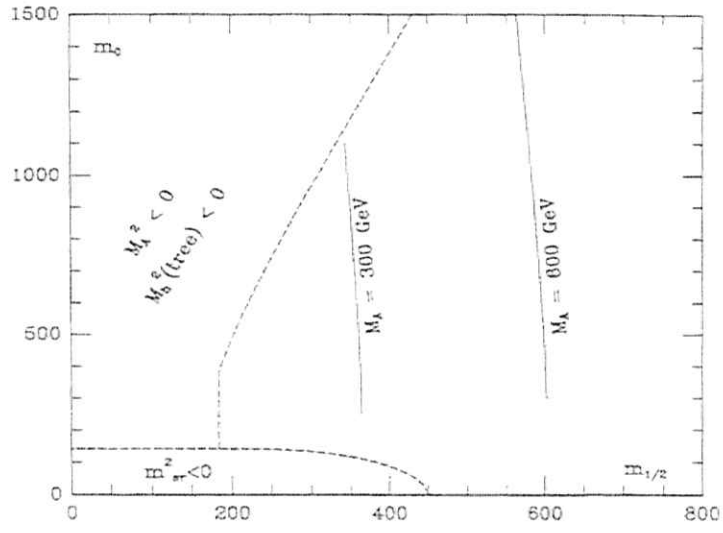

Fig. 4: The correlation between m_0 and $m_{1/2}$ for $\tan\beta \simeq 50$, $\mu < 0$, and two values of $M_A = 300$ and 600 GeV. The boundary contours correspond to tachyonic solutions, $m_0^2 < 0$, $M_A^2 < 0$ and $M_h^2 < 0$ at the tree–level.

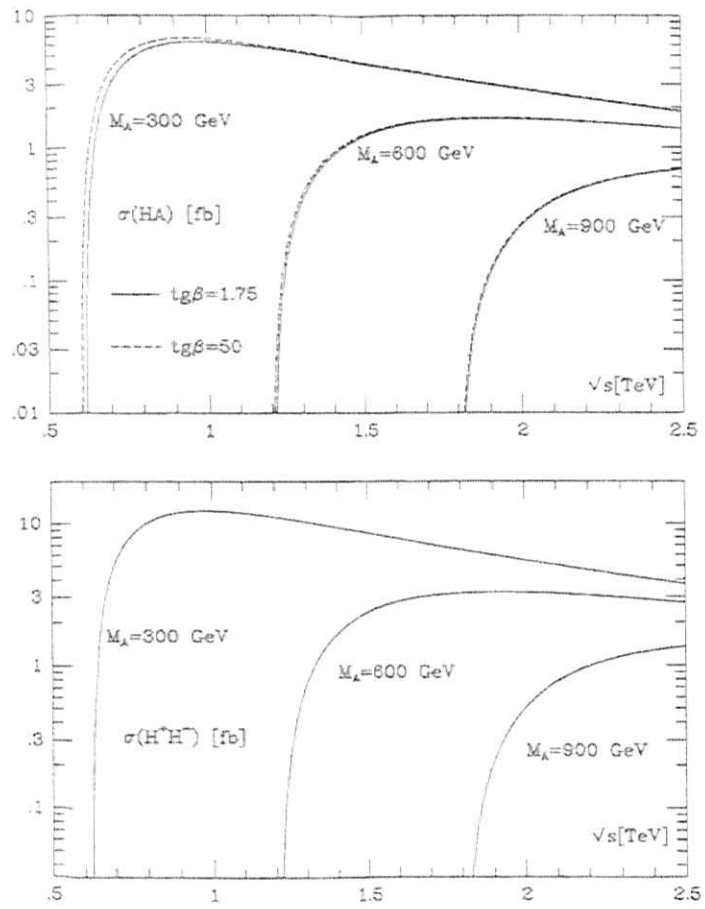

Fig. 5a: Cross sections for the pair production processes $e^+e^- \to HA$ and $e^+e^- \to H^+H^-$ as a function of $\sqrt{s}$ for $\tan\beta = 1.75$ (solid lines) and $\tan\beta = 50$ (dashed lines) and three values of $M_A = 300, 600$ and 900 GeV.

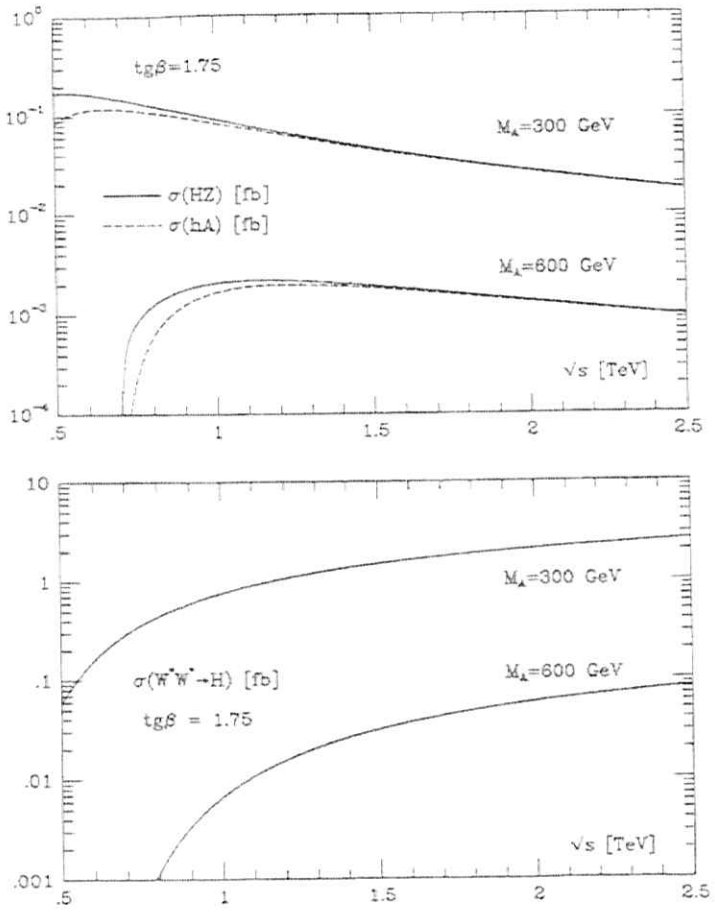

Fig. 5b: Cross sections for the production processes $e^+e^- \to HZ$, $e^+e^- \to hA$ and $e^+e^- \to H\nu\bar{\nu}$ as a function of $\sqrt{s}$ for $\tan\beta = 1.75$ and the values $M_A = 300$ and 600 GeV.

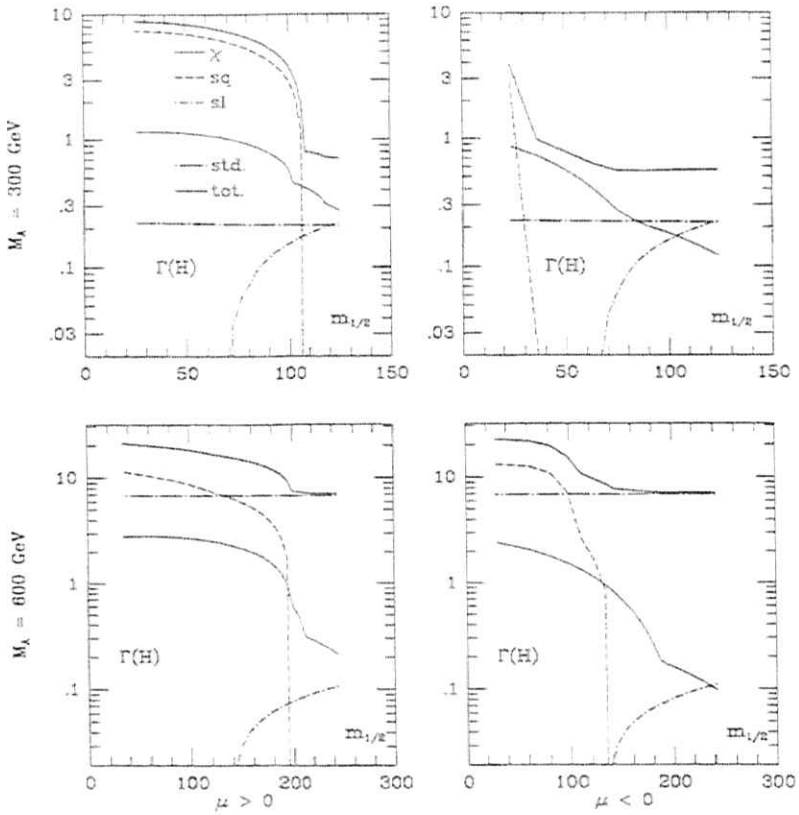

Fig. 6a: Decay widths (in GeV) of the heavy CP–even Higgs boson H into charginos and neutralinos (dotted lines), squarks (dashed lines), sleptons (dash–dotted lines), standard particles (dott–long–dashed lines) and the total decay widths (solid lines) as a function of $m_{1/2}$ for $\tan\beta = 1.75$, $M_A = 300$ and 600 GeV and for both signs of μ.

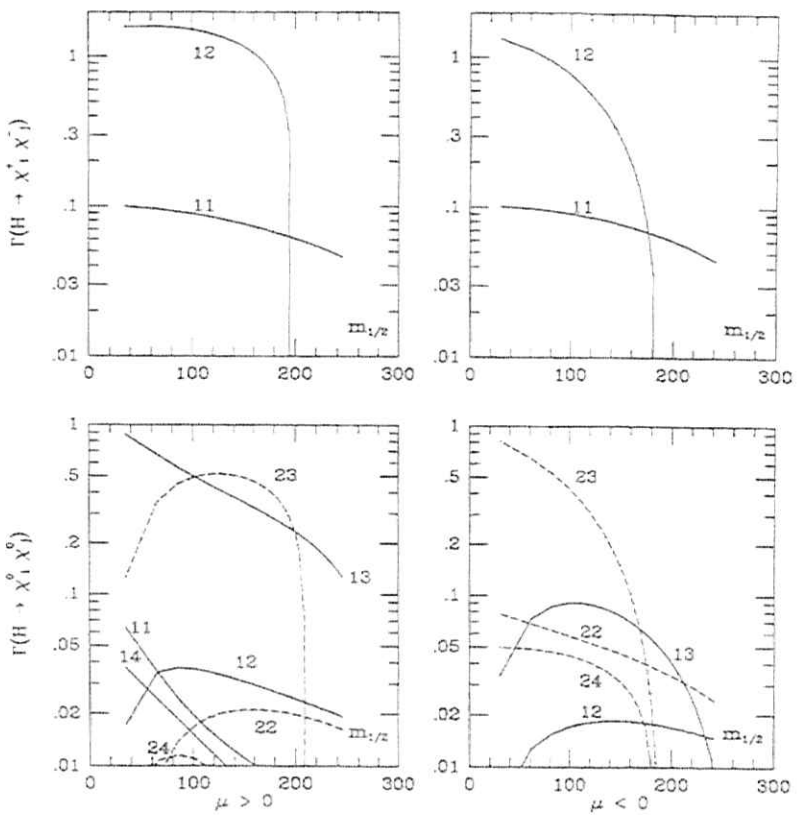

Fig. 6b: Partial decay widths (in GeV) of the heavy CP–even Higgs boson H into all combinations of chargino and neutralino pairs $[ij \equiv \chi_i\chi_j]$ as a function of $m_{1/2}$ for $\tan\beta = 1.75$, $M_A = 600$ GeV and for both signs of μ.

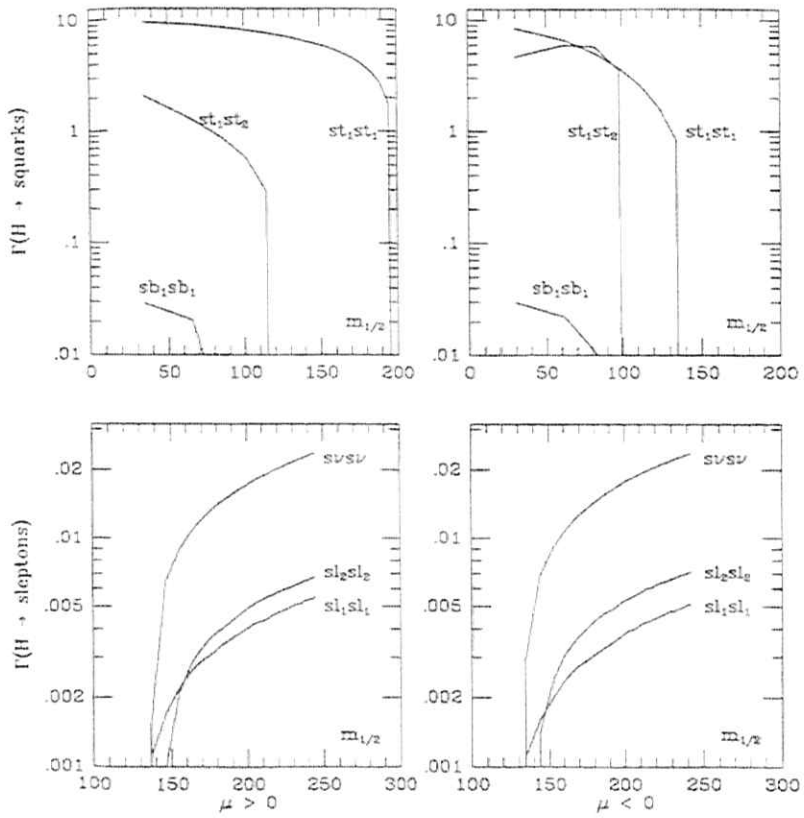

Fig. 6c: Partial decay widths (in GeV) of the heavy CP–even Higgs boson H into stop and sbottom squarks and into slepton pairs as a function of $m_{1/2}$ for $\tan\beta = 1.75$, $M_A = 600$ GeV and for both signs of μ.

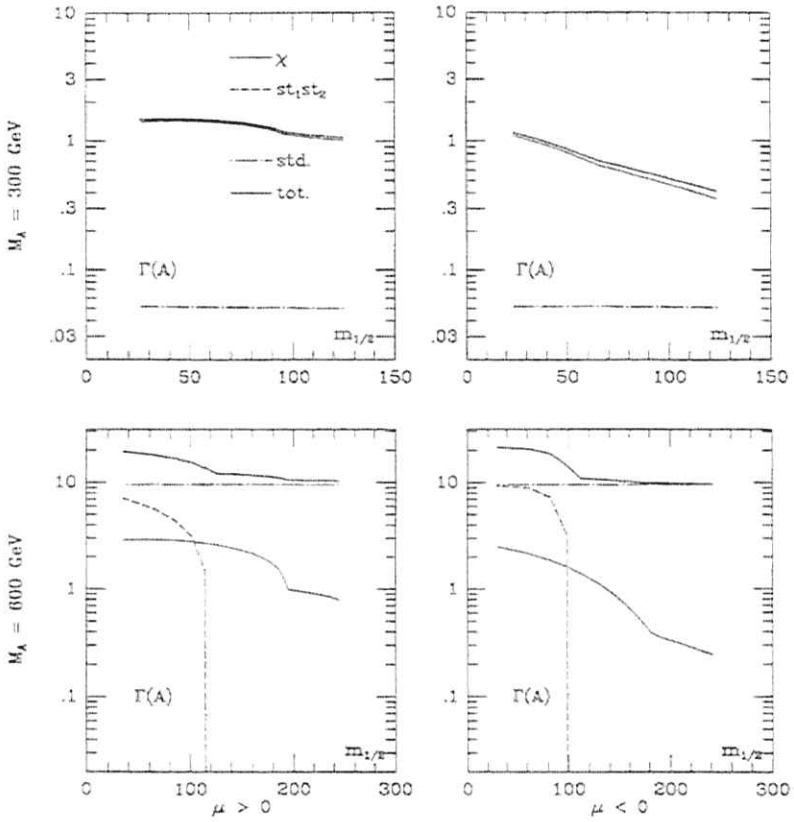

Fig. 7a: Decay widths (in GeV) of the pseudoscalar Higgs boson A into charginos and neutralinos (dotted lines), stop squarks (dashed lines), standard particles (dott–long–dashed lines) and the total decay widths (solid lines) as a function of $m_{1/2}$ for $\tan\beta = 1.75$, $M_A = 300$ and 600 GeV and for both signs of μ.

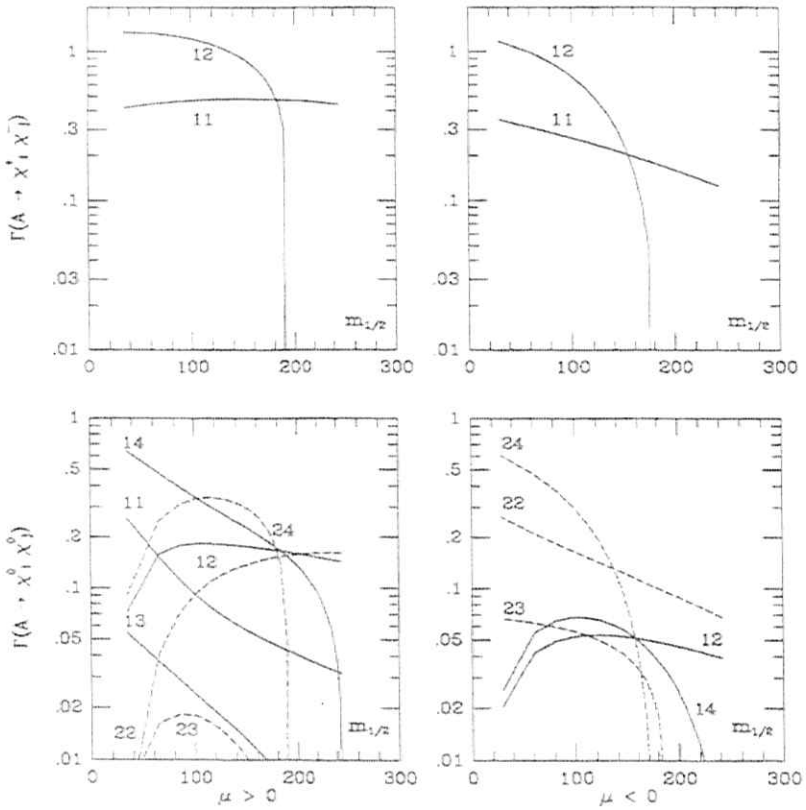

Fig. 7b: Partial decay widths (in GeV) of the pseudoscalar Higgs boson A into all combinations of chargino and neutralino pairs [$ij \equiv \chi_i\chi_j$] as a function of $m_{1/2}$ for $\tan\beta = 1.75$, $M_A = 600$ GeV and for both signs of μ.

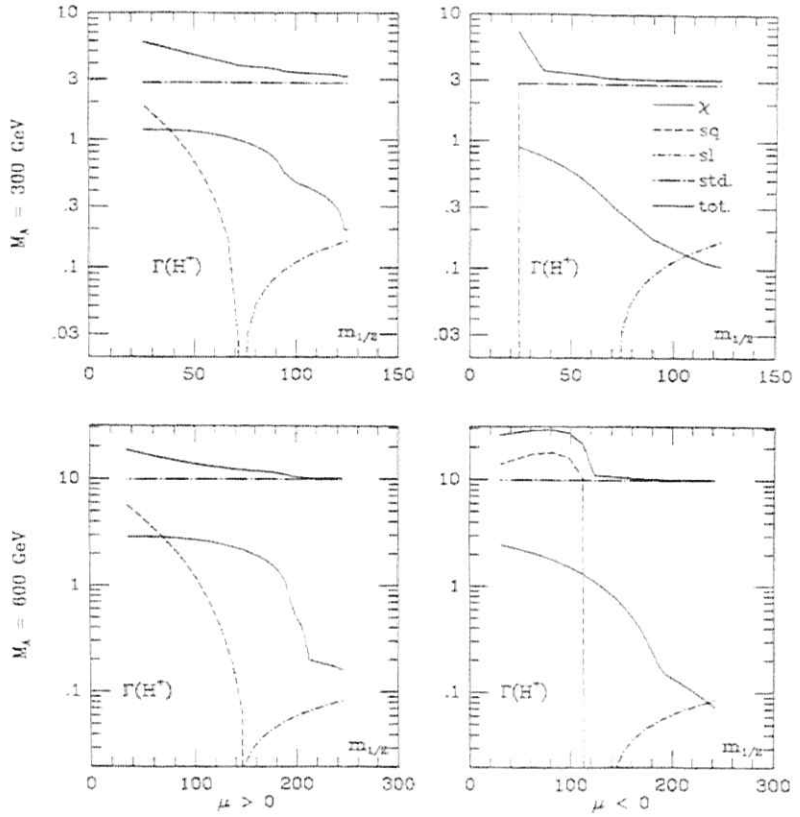

Fig. 8a: Decay widths (in GeV) of the charged Higgs bosons into charginos and neutralinos (dotted lines), squarks (dashed lines), sleptons (dash-dotted lines), standard particles (dott-long-dashed lines) and the total decay widths (solid lines) as a function of $m_{1/2}$ for $\tan\beta = 1.75$, $M_A = 300$ and 600 GeV and for both signs of μ.

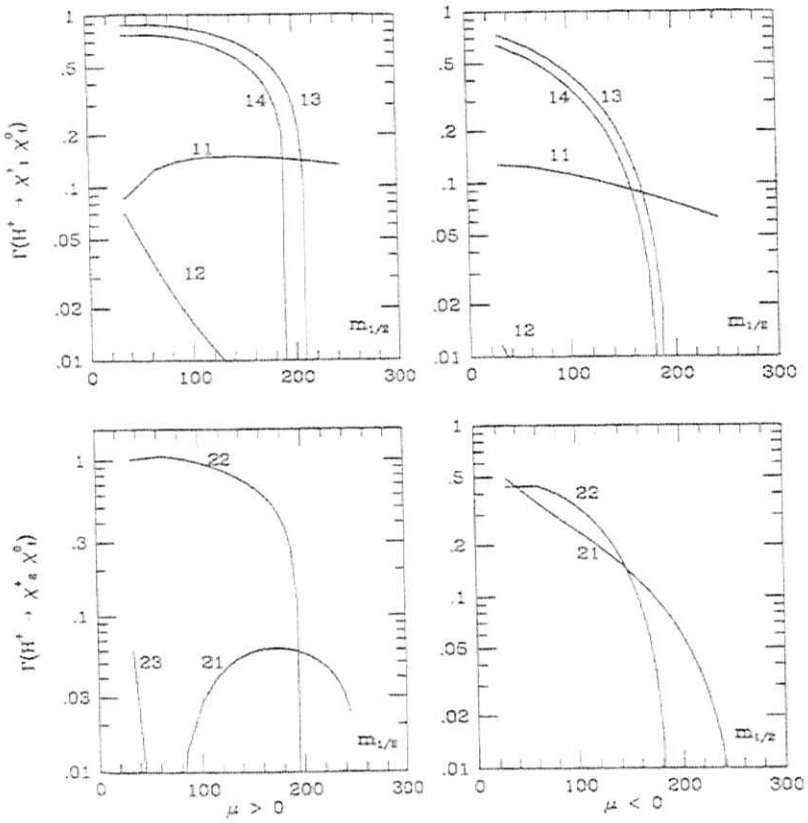

Fig. 8b: Partial decay widths (in GeV) of the charged Higgs boson H^+ into all combinations of charginos and neutralinos [$ij \equiv \chi_i^+ \chi_j^0$] as a function of $m_{1/2}$ for $\tan\beta = 1.75$, $M_A = 600$ GeV and for both signs of μ.

Production of Heavy Neutral MSSM Higgs Bosons a complete 1-loop calculation.

V. Driesen, W. Hollik and J. Rosiek*

Institut für Theoretische Physik, Universität Karlsruhe, D-76128 Karlsruhe, Germany

Abstract

The complete 1-loop diagrammatic calculations of the cross sections for the neutral Higgs production processes $e^+e^- \to Z^0H^0(Z^0h^0)$ and $e^+e^- \to A^0H^0(A^0h^0)$ in the MSSM are presented and compared the with the corresponding results of the simpler and compact effective potential approximation.

1. Introduction

In order to experimentally detect possible signals of the neutral MSSM Higgs bosons, detailed studies for the decay and production processes of Higgs boson are required. As has been discovered several years ago [1-3], radiative corrections in the MSSM Higgs sector are large and have to be taken into account for phenomenological studies. Three main approaches have been developed to calculate the 1-loop radiative corrections to the MSSM Higgs boson masses, production and decay rates:

a) The Effective Potential Approach (EPA) [2].

b) The Renormalization Group approach (RGE) [3].

c) The diagrammatic calculation in the on-shell renormalization scheme (Feynman Diagram Calculation, FDC) [4, 5]: The masses are calculated from the pole positions of the Higgs propagators, and the cross sections are obtained from the full set of 1-loop diagrams contributing to the amplitudes, including [4]:
   - the most general form of the MSSM lagrangian with soft breaking terms,
   - the virtual contributions from all the particles of the MSSM spectrum,
   - all 2-, 3- and 4-point Green's functions for a given process with Higgs particles,
   - the momentum dependence of the Green's functions,
   - the leading reducible diagrams of higher orders corrections.

The experimental searches for Higgs bosons at LEP1 [6] and studies for the future searches at higher energies [7] conventionally make use of the most compact effective potential approximation. We present the complete 1-loop diagrammatic results for the cross sections for the neutral Higgs production processes $e^+e^- \to Z^0H^0(Z^0h^0)$ and $e^+e^- \to A^0H^0(A^0h^0)$, compare them with the corresponding ones of the simpler and compact EPA approximation and discuss the typical size of the differences.

*Supported in part by the Alexander von Humboldt Stiftung and by the Polish Committee for Scientific Research.

2. Outline of the calculations

The tree level potential for the neutral MSSM Higgs bosons can be written as:

$$V^{(0)} = m_1^2 H_1^2 + m_2^2 H_2^2 + \epsilon_{ij}(m_{12}^2 H_1^i H_2^j + H.c.) + \frac{g^2 - g'^2}{8}(H_1^2 - H_2^2)^2 + \frac{g^2}{4}(H_1 H_2)^2 \quad (1)$$

Diagonalization of the mass matrices following from the potential (1) leads to three physical particles: two CP-even Higgs bosons H^0, h^0 and one CP-odd Higgs boson A^0, and defines their tree-level masses m_H, m_h and m_A, with $m_H > m_h$, and the mixing angles α, β. The way of calculating the radiative corrections in the EPA and FDC methods is briefly described as follows:

In the EPA, the tree level potential $V^{(0)}$ is improved by adding the 1-loop terms [2]:

$$V^{(1)}(Q^2) = V^{(0)}(Q^2) + \frac{1}{64\pi^2} \sum_{\substack{\text{quarks,} \\ \text{squarks}}} \mathrm{Str}\mathcal{M}^4 \left(\log \frac{\mathcal{M}^2}{Q^2} - \frac{3}{2} \right) \quad (2)$$

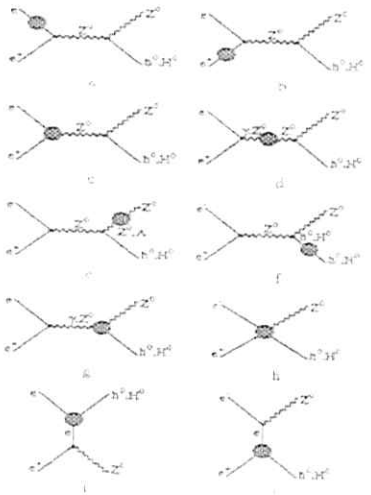

Figure 1: Classes of diagrams contributing to the $e^+e^- \to Z^0h^0(H^0)$ process in the FDC approach.

where $V^{(0)}(Q^2)$ is the tree level potential evaluated with couplings renormalized at the scale Q^2, and Str denotes the supertrace over the third generation of quark and squark fields contributing to the generalized mass matrix $\mathcal{M}^2$. The 1-loop potential $V^{(1)}$ is rediagonalized yielding the 1-loop corrected physical masses M_H, M_h and the effective mixing angle α_{eff} (for explicit formulae see [2]).

In the FDC the 1-loop physical Higgs boson masses are obtained as the pole positions of the dressed scalar propagators. M_H^2 and M_h^2 are given by the solution of the equation (3). For the calculations of the cross sections we need the full set of 2-, 3- and 4-point functions. In Fig. 1 the diagrams contributing to the $e^+e^- \to Z^0h^0(H^0)$ process are collected. The diagrams contributing to the $e^+e^- \to A^0h^0(H^0)$ process can be obtained by changing Z^0 into A^0 on the external line and skipping the diagrams i), j)

$$\mathrm{Re}\left[\left(p^2 - m_h^2 - \Sigma_{hh}(p^2)\right)\left(p^2 - m_H^2 - \Sigma_{HH}(p^2)\right) - \Sigma_{hH}^2(p^2) \right] = 0 \quad (3)$$

The formulae for the cross sections obtained in the FDC differ from the Born expressions, because not only the effective masses are corrected but also new form factors and momentum dependent effects are considered (see [4] for a detailed description).

3. Results on production cross sections

In this section we present the results for $Z^0H^0(Z^0h^0)$ and $A^0H^0(A^0h^0)$ production from the FDC and discuss the quality of simpler EPA approximation. In all figures we use as an example the set of parameters listed in Table 1. μ is the parameter describing the Higgs doublet mixing in the MSSM superpotential. M_2 denotes the SU(2) gaugino mass parameter. For the U(1) gaugino mass we use the value $M_1 = \frac{5}{3}\tan^2\theta_W M_2$, suggested by GUT constraints. M_{sq}, M_{sl}, A_t and A_b are the parameters entering the sfermion mass matrices (for the detailed expressions see e.g. [8]). For simplicity we assume a common value M_{sq} for all generations of squarks, and a common M_{sl} for sleptons.

Parameter	m_t	M_A	M_{sq}	M_{sl}	M_2	μ	$A_t = A_b$
Value (GeV)	175	200	1000	300	1000	500	1000

Table 1: Parameters used for the numerical analysis.

From the theoretical point of view, the most convenient parameters for the Higgs sector are the mass M_A of the CP-odd Higgs boson and the ratio $\tan\beta = \frac{v_2}{v_1}$. From the experimental point of view it is more natural to use, depending on the process considered, the masses M_h or M_H of the CP-even Higgs instead of the formal quantity $\tan\beta$.

As a first step, we apply the conventional M_A , $\tan\beta$ parameterization. Figs. 2 and 3 show the production cross sections for the processes $\sigma(e^+e^- \to Z^0h^0, A^0h^0)$ and $\sigma(e^+e^- \to Z^0H^0, A^0H^0)$ for $\sqrt{s}$ = 500 GeV. For the chosen set of parameters the numerical differences can reach 30% at $\sqrt{s}$ = 500 GeV. They become more important with

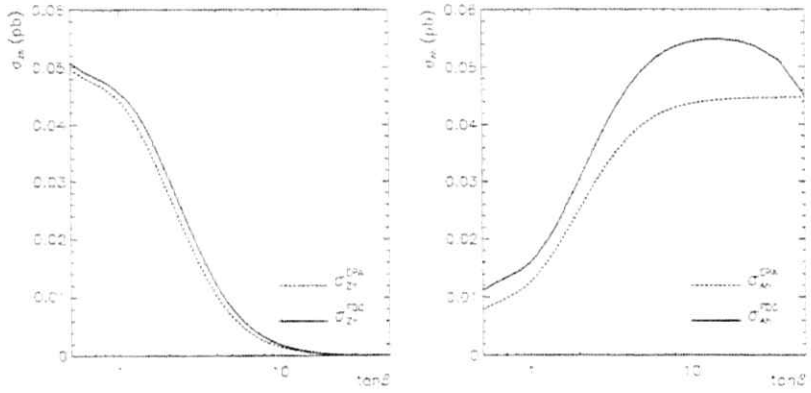

Figure 2: Comparison of the cross sections $\sigma(e^+e^- \to Z^0h^0, A^0h^0)$ obtained in the EPA and FDC. Parameters as given in Table 1, $\sqrt{s} = 500$ GeV.

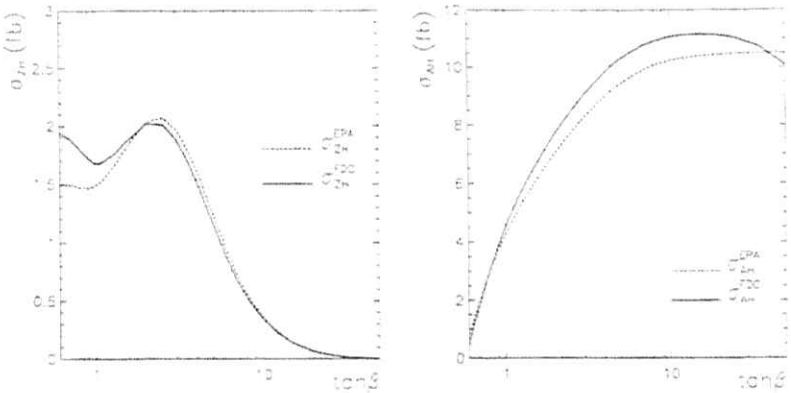

Figure 3: Comparison of the cross sections $\sigma(e^+e^- \to Z^0H^0, A^0H^0)$ obtained in the EPA and FDC. Parameters as given in Table 1, $\sqrt{s} = 500$ GeV.

increasing energies, exceeding 40% at 1 TeV. Note, however, that in the region of large cross sections the EPA accuracy is better (20% at 500 GeV). More detailed discussion of the lighter CP-even Higgs boson production can be found in ref. [9].

Fig. 4 shows the production cross sections for the processes $\sigma(e^+e^- \to Z^0H^0, A^0H^0)$ as a function of $\sqrt{s}$. The effect of the additional form factors included in the FDC grows when center-of-mass energy increases. For $\sqrt{s}$ = 1.5 TeV the differences between FDC and EPA can reach 50% for the $\sigma(e^+e^- \to Z^0H^0)$ production channel. In addition, the

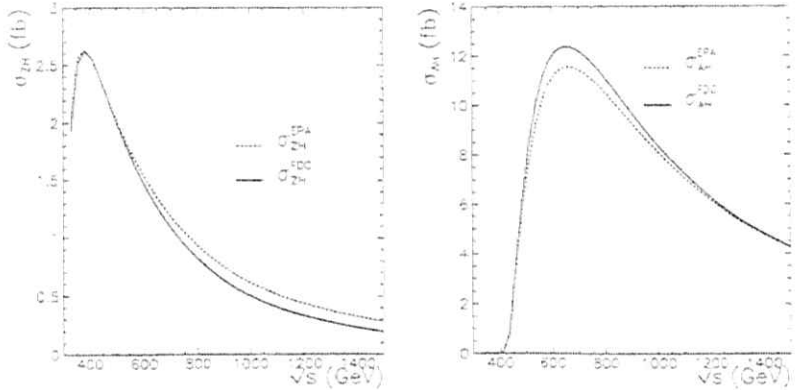

Figure 4: Comparison of the cross sections $\sigma(e^+e^- \to Z^0H^0, A^0H^0)$ as a function of $\sqrt{s}$ obtained in the EPA and FDC. $\tan\beta$ = 2, other parameters as given in Table 1

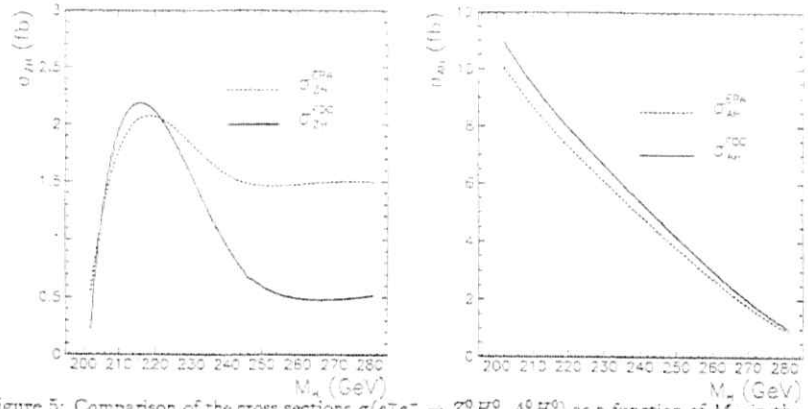

Figure 5: Comparison of the cross sections $\sigma(e^+e^- \to Z^0H^0, A^0H^0)$ as a function of M_H in the EPA and FDC. Parameters as given in Table 1, $\sqrt{s} = 500$ GeV.

angular dependence of the cross section given by the FDC is modified in compare to the effective Born approximation.

We now turn to the more physical parameterization of the cross sections in terms of the two Higgs boson masses M_A and M_h or M_H . This parameterization is more clumsy in the calculations, but it has the advantage of physically well defined input quantities avoiding possible confusions from different renormalization schemes. Varying M_H (M_A and other input quantities fixed) we obtain $\tan\beta$ and σ_{ZH}, σ_{AH} as functions of M_H . For the parameter values given in Table 1, the differences between the $\tan\beta$ values obtained in the EPA and FDC can reach 10% (up to 20% for smaller $M_A \approx 100$ GeV). Also significant differences can occur for the cross sections, as displayed in Fig. 5 where the predictions of EPA and FDC for the σ_{ZH} and σ_{AH} are plotted as functions of M_H . The typical size of differences between the methods is 10-20% for $\sqrt{s} = 500$ GeV, but they may became as large as 60% in case of the process $\sigma(e^+e^- \to Z^0H^0)$. This particularly large deviation occurs for large M_H values, corresponding to small $\tan\beta \leq 1$ (compare Fig. 2).

We have analyzed also the dependence of the differences between the EPA and the FDC predictions on the SUSY parameters: sfermion and gaugino masses, μ parameter and sfermion mixing parameters. In most cases the variation of those parameters does not have a large effect on the size of the differences between the EPA and FDC (a more detailed discussion can be found in ref. [10]).

To give a more global impression of the typical size of the differences between the EPA and FDC results, we have chosen 1000 random points (for each $\sqrt{s}$ value in Table 2) from the hypercube in the MSSM parameters space with the following bounds:

$0.5 < \tan\beta < 50$ — $50\ \text{GeV} < M_A < 250\ \text{GeV}$
$-500\ \text{GeV} < \mu < 500\ \text{GeV}$ — $200\ \text{GeV} < M_2 < 1000\ \text{GeV}$
$200\ \text{GeV} < M_{\tilde{q}} = 2M_{\tilde{u}} < 1000\ \text{GeV}$ — $-M_{\tilde{q}} < A_t = A_b < M_{\tilde{q}}$

We define the relative differences for the masses and cross sections as follows:

$$\delta X^{EPA} = \frac{X^{FDC} - X^{EPA}}{X^{FDC}}. \tag{4}$$

where X can be chosen as M_h , M_H , σ_{ZH}, σ_{Zh}, σ_{AH} or σ_{Ah}.

We calculated the quantities δM_h^{EPA}, δM_H^{EPA}, $\delta\sigma_{Zh}^{EPA}$, $\delta\sigma_{Ah}^{EPA}$, $\delta\sigma_{ZH}^{EPA}$and $\delta\sigma_{AH}^{EPA}$and averaged them (and also their absolute values) arithmetically over all generated points of the parameter space. The average mass differences are small and equal $|\delta M_h^{EPA}| = 2\%$ and $|\delta M_H^{EPA}| = 1\%$. The results for the cross sections are summarized in Table 2. It shows that the predictions of both methods deviate in particular for σ_{ZH}.

$\sqrt{s}$ (GeV)	$\delta\sigma_{Zh}^{EPA}$	$\delta\sigma_{Ah}^{EPA}$	$\delta\sigma_{ZH}^{EPA}$	$\delta\sigma_{AH}^{EPA}$	$\lvert\delta\sigma_{Zh}^{EPA}\rvert$	$\lvert\delta\sigma_{Ah}^{EPA}\rvert$	$\lvert\delta\sigma_{ZH}^{EPA}\rvert$	$\lvert\delta\sigma_{AH}^{EPA}\rvert$
500	16.4%	-2.4%	57%	4.4%	21%	31%	62%	14%
1000	10.3%	1.1%	56%	-3.0%	15%	31%	62%	14%
1500	4.2%	4.9%	53%	-9.0%	17%	32%	63%	18%

Table 2: Differences between the EPA and FDC predictions averaged over a random sample of parameters.

Summarizing, comparisons between the FDC predictions with the simpler EPA approximation have shown that at $\sqrt{s} = 500$ GeV the EPA has an accuracy of typically 10-20% in the parameter regions where the cross sections are large. The differences become larger with increasing energy, where also modifications of the Born-like angular distributions are more visible. The use of the physical input variables M_A, M_h or M_A, M_H avoids ambiguities from the definition of $\tan\beta$ in higher order, but the observed differences remain of the same size. For a better accuracy, the full FDC would be required.

Recently some papers on the leading 2-loop corrections to the CP-even MSSM Higgs boson masses have been published [11]. The main conclusion is that 2-loop corrections are also significant and tend to compensate partially the effects of 1-loop corrections. The calculations are based on the EPA and RG methods. Since the main emphasis of this study is to figure out the difference between complete and approximate results in a given order, we have not implemented the 2-loop terms. They would improve the 1-loop FDC results in the same way as the approximations and thus do not influence the remaining differences which can only be obtained by an explicit diagrammatic calculation.

The library of FORTRAN codes for the calculation of the 1-loop radiative corrections in the on-shell renormalization scheme to the MSSM neutral Higgs production and decay rates [4] can be found at the URL address:
http://itpaxp1.physik.uni-karlsruhe.de/~rosiek/neutral_higgs.html

References

1. S. P. Li, M. Sher, *Phys. Lett.* **B140** (1984), 339; J. Gunion, A. Turski, *Phys. Rev.* **D39** (1989) 2701; **D40** (1989) 2325, 2333; M. Berger, *Phys. Rev.* **D41** (1990) 225.
2. J. Ellis, G. Ridolfi, F. Zwirner, *Phys. Lett.* **262B** (1991) 477; R. Barbieri, M. Frigeni, *Phys. Lett.* **258B** (1991) 395; A. Brignole, J. Ellis, G. Ridolfi, F. Zwirner *Phys. Lett.* **271B** (1991) 123.
3. M. Carena, K. Sasaki, C.E.M. Wagner, *Nucl. Phys.* **381B** (1992) 66; H.E. Haber, R. Hempfling, *Phys. Rev.* **D48** (1993) 4280; P.H. Chankowski, S. Pokorski, J. Rosiek, *Phys. Lett.* **281B** (1992) 100.
4. P. Chankowski, S. Pokorski, J. Rosiek *Nucl. Phys.* **B423** (1994) 437; **B423** (1994) 497; V. Driesen, W. Hollik, *Z. Phys.* **C68** (1995) 485.
5. A. Brignole, *Phys. Lett.* **281B** (1992) 284.
6. ALEPH Collab., D. Buskulic et al., *Phys. Lett.* **313B** (1993), 312; DELPHI Collab., P. Abreu et al., *Nucl. Phys.* **373B** (1992), 3; L3 Collab., O. Adriani et al., *Z. Phys.* **57C** (1993), 355; OPAL Collab., R. Akers et al., Preprint CERN, PPE/94-104 (1994); J. F. Grivaz, Proc. of the International Europhysics Conference on High Energies, Brussels, July 27 - August 2, 1995; preprint LAL-95-83.
7. *Higgs Physics*, M. Carena, P. Zerwas et al., to appear in the Proceedings of LEP2 Workshop, CERN Yellow Report, eds. G. Altarelli et al.; *Higgs Particles*, in: e^+e^- Collisions at 500 GeV, DESY 92-123A,B,C, ed. P. Zerwas.
8. J. Rosiek, *Phys. Rev.* **D41** (1990) 3464; erratum hep-ph/9511250.
9. V. Driesen, W. Hollik, J. Rosiek, hep-ph/9512441, in print in *Z. Phys.* **C**.
10. J. Rosiek, A. Sopczak, *Phys. Lett.* **B341** (1994) 419.
11. R. Hempfling, A. Hoang, *Phys. Lett.* **B331** (1994) 99; M. Carena, J.R. Espinosa, M. Quiros, C.E.M. Wagner, *Phys. Lett.* **B355** (1995) 209; M. Carena, M. Quiros, C.E.M. Wagner, preprint CERN-TH-95-157, hep-ph/9508343.

Radiative corrections to $e^+e^- \to H^+H^-$

A. Arhrib[a,b] and G. Moultaka[a]

[a] Physique Mathematique et Theorique, E.S.A du CNRS N° 5032,
Université Montpellier II, F-34095 Montpellier France

[b] L.P.T.N., Faculté des Sciences Semlalia, B.P. S15, Marrakesh, Morocco

Abstract

We study the 1-loop corrections to the charged Higgs production both in the Minimal Supersymmetric Standard Model (MSSM) and in a more general type II two-Higgs-doublet model (THDM-II). We consider the full set of corrections (including soft photon contributions as well as box diagrams), and define a parametrization that allows a comparison between the two models. Besides the soft photon radiation there can be prominent model-dependent effects.

1 Introduction

In contrast to hadronic machines, a high energy e^+e^- collider in the TeV range will be a rather unique place to discover and study charged higgses in a clean environment. These would be produced either in pairs [1], our main concern here, or in (rare) production in association with $W^\mp$. It was first found in [2] that loop corrections from matter fermions and their susy partners (mainly the $(t,b),(\tilde{b},\tilde{t})$ sector), are likely to change the tree-level result at $\sqrt{s} = 500$ GeV [1, 4], by as much as 10% dip in the cross-section. The effect could even lie between -25% and 25% and perhaps grow out of perturbative control, though in a realistic range of the model-parameters. Such a sensitivity to loop effects appears to be related to the fact that at tree-level the γ and Z mediated process is exclusively controlled by $U_{\rm EM}(1) \times U_{W_3}(1)$ gauge invariance and thus knows nothing about the structure of the non-standard extension whatsoever.

It is thus important in a first step to go beyond [2] and study the full 1-loop structure, in order to understand the sensitivity to the various model-parameters and the origin of large effects, whether in the MSSM or in a general THDM-II. In a second step one should perform a renormalization group analyses, eventually taking into account constraints from SUGRA-GUT models, and ask whether the allowed regions of the model-parameters could still lead to large or even uncontrollable loop effects in charged Higgs pair production.

In the present study we resume the first of these steps and improve upon the results of ref [2] by including:

a) the complete Higgs sector contributions (self-energies, vertices and boxes);

b) the infrared part, including initial and final soft photon radiation as well as $\gamma\gamma$ and γZ boxes;

c) The complete set of charginos/neutralinos/$\tilde{e}/\tilde{\nu}$ box diagrams.

We performed the analysis in the on-shell renormalization scheme defined in [3]. Since at tree-level only standard model couplings appear in $e^+e^- \to H^+H^-$, we need only to supplement the above scheme with the wave function and mass renormalization conditions of the charged Higgs field. It is also convenient to take the charged Higgs mass $M_{H^\pm}$, rather than that of the CP-odd scalar M_{A^0}, as the input on-shell physical mass (see [2] for more details). It will turn out that besides the sensitivity to the heavy quark-squark sector, there are on one hand model-independent large effects from the soft photon radiation, and on the other possibly important effects in the vertex corrections involving the purely Higgs sector. The latter case occurs when deviations from the tree-level MSSM triple-self-couplings are allowed. One of the issues will be the possibility of signing a clear difference between the MSSM and a non-supersymmetric THDM-II.

2 Effective Parametrization

In this section we outline a general parametrization describing deviations from the tree-level Higgs self-couplings as given in the MSSM. Let us recall first that the most general gauge invariant scalar potential (corresponding to CP-invariant THDM-II) is given by (see for instance ref. [5]):

$$V(\Phi_1,\Phi_2) = \lambda_1(\Phi_1^\dagger\Phi_1 - v_1^2)^2 + \lambda_2(\Phi_2^\dagger\Phi_2 - v_2^2)^2 - \lambda_3((\Phi_1^\dagger\Phi_1 - v_1^2) + (\Phi_2^\dagger\Phi_2 - v_2^2))^2$$
$$+\lambda_4((\Phi_1^\dagger\Phi_1)(\Phi_2^\dagger\Phi_2) - (\Phi_1^\dagger\Phi_2)(\Phi_2^\dagger\Phi_1)) + \lambda_5(Re(\Phi_1^\dagger\Phi_2) - v_1v_2)^2 + \lambda_6 Im(\Phi_1^\dagger\Phi_2)^2 \quad (1)$$

where all λ_i are real and v_1, v_2 denote the vacuum expectation values of the two Higgs fields. We have also omitted an additive constant in eq. (1). Thus one has in general 7 free parameters, i.e. the λ_i's and $\tan\beta(= v_2/v_1)$, v being $\overline{v_1^2 + v_2^2}$ being fixed by the electroweak scale. Let us now define

$$\lambda_1 = \lambda_2 - \delta_{12} \qquad , \qquad \lambda_3 = \frac{1}{2}(g^2 + g'^2) - \lambda_1 - \delta_{32}$$
$$\lambda_4 = 2\lambda_1 - \frac{1}{2}g'^2 - \delta_{42} \qquad , \qquad \lambda_5 = -\frac{1}{2}(g^2 + g'^2) - 2\lambda_1 + \delta_{52} \quad (2)$$
$$\lambda_6 = -\frac{1}{2}(g^2 + g'^2) - 2\lambda_1 + \delta_{62}$$

where the δ_i's $\neq 0$ in general. It is well known [5] that (softly broken) supersymmetry forces the δ_i's to zero. From this follow the usual tree-level relations among the Higgs masses, $\tan 2\alpha$ and $\tan\beta$, as well as the negative sign of $\sin 2\alpha$. In this case the triple scalar couplings read (here we only show those entering the 1-loop corrections in $e^+e^- \to H^+H^-$):

$$
\begin{aligned}
g^{MSSM}_{H^0H^+H^-} &= -ig(m_W\cos(\beta-\alpha) - \frac{m_Z}{2c_w}\cos 2\beta\cos(\beta+\alpha)) \\
g^{MSSM}_{h^0H^+H^-} &= -ig(m_W\sin(\beta-\alpha) + \frac{m_Z}{2c_w}\cos 2\beta\sin(\beta+\alpha)) \\
g_{H^0H^\pm G^\mp} &= \frac{-ig\sin(\beta-\alpha)(m^2_{H^\pm}-m^2_H)}{2m_W} \\
g_{h^0H^\pm G^\mp} &= \frac{ig\cos(\beta-\alpha)(m^2_{H^\pm}-m^2_h)}{2m_W} \\
g_{A^0H^\pm G^\mp} &= \pm\frac{m^2_{H^\pm}-m^2_A}{2m_W}
\end{aligned}
\tag{3}
$$

As one can easily see, none of the couplings in eq. (3) can be enhanced at tree-level in the supersymmetric case. In the non supersymmetric case however, $\delta_i \neq 0$, there is an important difference between $g_{H^0H^+H^-}$ and $g_{h^0H^+H^-}$ on one side, and the three remaining couplings of eq. (3) on the other. The couplings involving the charged goldstone bosons $G^\pm$ retain their initial form, so that a possible enhancement is due only to deviations from the supersymmetric Higgs-boson-mass sum rules. In contrast $g_{H^0H^+H^-}$ and $g_{h^0H^+H^-}$ will deviate from their forms in eq. (3) through a non trivial dependence on $\tan\beta$, $m_{H^\pm}$, λ_3, etc... . These aspects will be of importance in what follows.

Starting from eq.(2) it is possible to express all couplings and mass relations in terms of the non-vanishing δ_i's, $\tan\beta$ and one of the λ_i's. (The general expressions are somewhat involved and will be given elsewhere). Here we would like to insist on a physically interesting special case: It is possible to define a deviation from the MSSM in such a way that *all* the MSSM tree-level relations[1] among the higgs masses, $\tan 2\alpha$ and $\tan\beta$ remain valid. This occurs provided we require the δ_i's to satisfy

$$
\begin{aligned}
\delta_{51} &= \frac{2tan^2\beta}{1-tan^2\beta}\delta_{12} \\
\delta_{61} = \delta_{41} &= -2\sin^2(\beta)\delta_{12} \\
\delta_{31} &= \frac{1}{2}\sin^2(\beta)(1-\frac{1}{\cos 2\beta})\delta_{12}
\end{aligned}
\tag{4}
$$

[1] Strictly speaking one should include the known radiative corrections to these relations, however due to our Higgs mass renormalization condition they would correspond to higher order effects in $e^+e^- \to H^+H^-$

Under such conditions we have only three free parameters which we can choose as $\tan\beta$, $M^2_{\tilde{H}}$ and λ_3. The MSSM corresponds then to a particular value of λ_3, λ_3^{MSSM} which is a function of $\tan\beta$ and $M^2_{\tilde{H}}$ and leads to $\delta_i = 0$ as a special case of eq. (4). For this reason eq. (4) will be dubbed quasi-supersymmetric. It can be thought of as corresponding to the situation where all the two-Higgs doublet spectrum has been experimentally unraveled and found to be consistent with the MSSM Higgs mass sum rules but with no other direct evidence for supersymmetry. Although not generic, the quasi-supersymmetric parametrization would then be a very useful device in terms of which the tests of the Higgs self-couplings can be expressed. As far as the charged Higgs sector is concerned only $g_{H^0H^+H^-}$ and $g_{h^0H^+H^-}$ can deviate from their supersymmetric values given in eq.(3). We give here for illustration their behavior in the large $\tan\beta$ limit (with $\lambda_3 \neq \lambda_3^{MSSM}$ and $m_A > m_Z$)

$$
\begin{aligned}
g_{H^0H^+H^-} &\sim g^{MSSM}_{H^0H^+H^-} - igm_W(\frac{1}{2c_w^2} - \frac{m_A^2}{m_W^2} + \frac{s_w^2}{\pi\alpha}\lambda_3)\tan\beta \\
g_{h^0H^+H^-} &\sim g^{MSSM}_{h^0H^+H^-} - igm_W\frac{2m_A^2}{m_A^2-m_Z^2}(\frac{1}{2c_w^2} + \frac{m_A^2}{m_W^2} - \frac{s_w^2}{\pi\alpha}\lambda_3)
\end{aligned}
\tag{5}
$$

where $g^{MSSM}_{H^0H^+H^-}$, $g^{MSSM}_{h^0H^+H^-}$, $g_{H^0H^\pm G^\mp}$, $g_{h^0H^\pm G^\mp}$ and $g_{A^0H^\pm G^\mp}$ are given in eq.(3). Note that triple couplings of gauge bosons to Higgses are never enhanced, and quartic couplings enter exclusively one-loop diagrams that vanish with m_e. It is thus interesting to note that the sensitivity to large $\tan\beta$ resides exclusively in $g_{H^0H^+H^-}$ of eq. (5), while $g_{h^0H^+H^-}$ is more sensitive to m_A in this limit. A more general investigation of the full Higgs sector can be persued along the same lines.

3 Numerical Results

We now present some numerical results, using the exact expressions for the Higgs self-couplings in terms of the 3 free quasi-susy parameters, $\tan\beta$, $m_{H^\pm}$ and λ_3.

In fig.1 we show the percentage contribution to the integrated cross section, for each sector separately, as a function of $\sqrt{s}$. One finds that the Higgs sector contributions can counterbalance those of the heavy quarks found in [2] for large $\tan(\beta)$, but only near threshold and for $\lambda_3 \neq \lambda_3^{MSSM}$. Far from threshold all of the effects, except for WW boxes, become negative. Furthermore the "neutral" model-independent contributions, including soft bremsstrahlung, obtained by adding one photon (or Z) line to the tree diagrams depend loosely on $M_{H^\pm}$ or $\sqrt{s}$ and contribute at the level of -17% for a soft photon cut $\Delta E_\gamma \sim 0.1E_{beam}$. In fig.2 we show (excluding those "neutral" contributions)

the integrated cross-section for two values of $M_{H^\pm}$ and $\tan(\beta)$. In THDM-II the total loop effect increases (negatively) with increasing $\tan(\beta)$, the farther one goes from production threshold. In the MSSM ($\lambda_5 = \lambda_5{}^{MSSM}$) the leading effects come exclusively from the heavy quark-squark sector and the conclusions of [2] remain unaltered in this case. The $\chi^\pm\chi^0\bar{c}'\bar{b}$ contributions do not exceed a few percent despite the large number of diagrams. For instance we evaluated the full set of supersymmetric boxes, (taking into account fermion-number violation through the rules of ref. [6]), and found that they largely cancel among each other, leading at most to $1-3\%$ (negative) effect for a wide range of sparticle masses. Finally we should stress that the large effects in THDM-II are not an artifact of the quasi-susy parametrization, they are also present even if the tree-level Higgs mass sum rules are relaxed. This raises the question of whether such effects would appear in the MSSM as a result of the running of the λ_i's [7].

We conclude that the charged Higgs sector seems to offer a non-trivial structure beyond the tree-level, which can complement the information gained from the neutral sector. Yet a more elaborate strategy involving the full-fledged Higgs sector still needs to be worked out.

References

[1] S. Komamiya, Phys.Rev. D38 (1988) 2158;

[2] A. Arhrib, M. Capdequi Peyranere, G. Moultaka Phys.Lett. B 341 (1995) 313;

[3] M.Böhm, W.Hollik and H.Spiesberger, Fortschr.Phys.34 (1986) 11;

[4] A.Brignole et al., in Proceedings of the Workshop on e^+e^- Collisions at 500 GeV : The Physics Potential, ed. P.M.Zerwas, DESY 92-123, p.613;
A.Djouadi, J.Kalinowski, P.M.Zerwas, *ibid.* p.83 and Z.Phys.C57 (1993) 569;

[5] J.F.Gunion and H.E.Haber, Nucl. Phys. B272 (1986) 1;

[6] A.Denner, H.Eck, O.Hahn and J.Kübelbeck Nucl. Phys. B387 (1992) 467;

[7] H.E. Haber and R. Hempfling, Phys.Rev. D48 (1993) 4280;

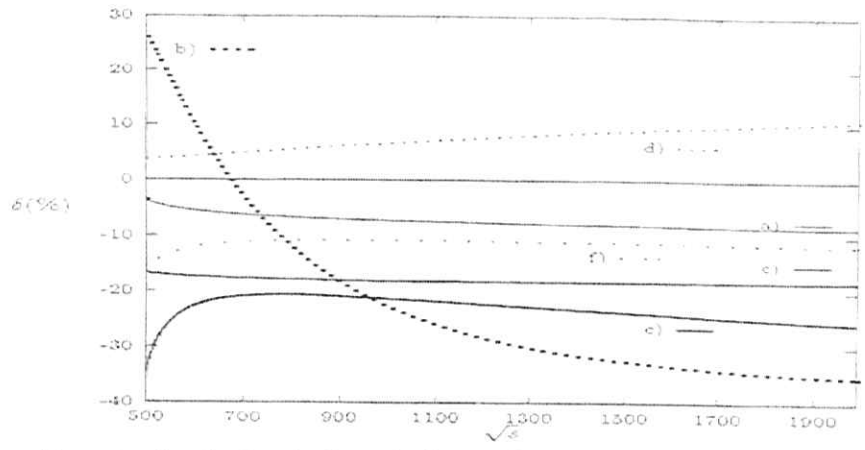

Figure 1: Contributions in % to the integrated cross-section in quasi-susy, $\lambda_2 = -0.61$, $M_{H^\pm} = 220$: a) Higgs sector, $\tan\beta = 2$; b) Higgs sector, $\tan\beta = 30$; c) virtual Z, γ and soft bremsstrahlung; d) virtual W boxes; e) matter fermion sector, $m_{top} = 180GeV$, $\tan\beta = 30$; f) same as e) but with $\tan\beta = 2$.

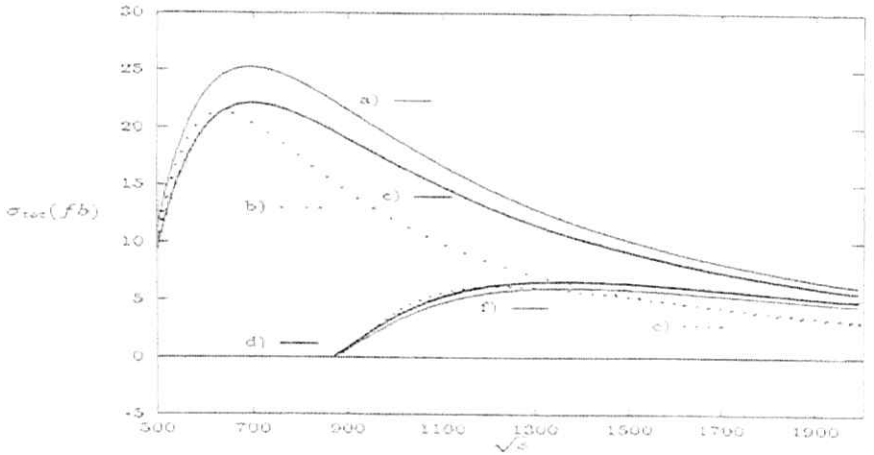

Figure 2: a) Tree-level, $M_{H^\pm} = 220GeV$; b) quasi-susy, $\lambda_2 = -0.61$ (MSSM value -0.71), $\tan\beta = 30$; c) quasi-susy, $\lambda_2 = -0.61$, $\tan\beta = 2$; d) Tree-level, $M_{H^\pm} = 430GeV$; e) quasi-susy, $\lambda_2 = -2.6$ (MSSM value -2.84), $\tan\beta = 30$; f) same as e) but with $\tan\beta = 2$; $m_{top} = 180GeV$.

Multiple Production of $\mathcal{MSSM}$ Neutral Higgs Bosons at High-Energy e^-e^- Colliders

A. DJOUADI[1,2*], H.E. HABER[3], AND P.M. ZERWAS[2]

[1] Institute für Theoretische Physik, Universität Karlsruhe, D-76128 Karlsruhe, FRG.

[2] Deutsches Elektronen-Synchrotron DESY, D-22603 Hamburg, FRG.

[3] Santa Cruz Institute for Particle Physics, University of California, Santa Cruz, CA 95064, USA.

Abstract

The cross sections for the multiple production of the lightest neutral Higgs boson at high-energy e^-e^- colliders are presented in the framework of the Minimal Supersymmetric extension of the Standard Model ($\mathcal{MSSM}$). We consider production through Higgs-strahlung, associated production of the scalar and the pseudoscalar bosons, and the fusion mechanisms for which we use the effective longitudinal vector-boson approximation. These cross sections allow one to determine trilinear Higgs couplings λ_{Hhh} and λ_{hhh}, which are theoretically determined by the Higgs potential.

1. Introduction

The only unknown parameter in the Standard Model ($\mathcal{SM}$) is the quartic coupling of the Higgs field in the potential, which determines the value of the Higgs mass. If the Higgs mass is known, the potential is uniquely fixed. Since the form of the Higgs potential is crucial for the mechanism of spontaneous symmetry breaking, *i.e.* for the Higgs mechanism *per se*, it will be very important to measure the coefficients in the potential once Higgs particles have been discovered.

If the mass of the scalar particle is less than about 150 GeV, it very likely belongs to the quintet of Higgs bosons, $h, H, A, H^\pm$ predicted in the two-doublet Higgs sector of supersymmetric theories [1] [h and H are the light and heavy CP-even Higgs bosons, A is the CP-odd (pseudoscalar) Higgs boson, and $H^\pm$ is the charged Higgs pair]. The potential of the two doublet Higgs fields, even in the Minimal Supersymmetric Standard Model ($\mathcal{MSSM}$), is much more involved than in the Standard Model [2]. If CP is conserved by the potential, the most general two-doublet model contains three mass parameters and seven real self-couplings. In the $\mathcal{MSSM}$, the potential automatically conserves CP; in addition, supersymmetry fixes all the Higgs self-couplings in terms of gauge couplings. The remaining three free mass parameters can be traded in for the two vacuum expectation values (VEV's) of the neutral Higgs fields and one of the physical Higgs masses. The sum of the squares of the VEV's is fixed by the W mass, while the ratio of VEV's is a free parameter of the model called $\tan\beta$. It is theoretically convenient to choose the free parameters of the $\mathcal{MSSM}$ Higgs sector to be $\tan\beta$ and M_A, the mass of the CP-odd Higgs boson A. The other Higgs masses and the mixing angle α of the CP-even neutral sector are then determined. Moreover, since all coefficients in the Higgs potential are also determined, the trilinear and quartic self-couplings of the physical Higgs particles can be predicted theoretically. By measuring these couplings, the Higgs potential can be reconstructed - an experimental *prima facie* task to establish the Higgs mechanism as the basic mechanism for generating the masses of the fundamental particles.

The endeavor of measuring all Higgs self-couplings in the $\mathcal{MSSM}$ is a daunting task. We will therefore discuss a first step by analyzing theoretically the production of two light Higgs particles of the $\mathcal{MSSM}$. These processes may be studied at the proton collider LHC [3] and at a high-energy e^-e^- linear collider. In this paper we will focus on the e^-e^- accelerators that are expected to operate in the first phase at an energy of 500 GeV with a luminosity of about $\int\mathcal{L} = 20$ fb^{-1}, and in a second phase at an energy of about 1.5 TeV with a luminosity of order $\int\mathcal{L} = 200$ fb^{-1} *per annum* [4]. They will allow us to eventually study the couplings λ_{Hhh} and λ_{hhh}. The measurement of the coupling λ_{hhh} will be very difficult.

Multiple light Higgs bosons h can [in principle] be generated in the $\mathcal{MSSM}$ by four mechanisms[1]:

(i) Decay of the heavy CP-even neutral Higgs boson, produced either by H-strahlung and associated AH pair production, or in the WW fusion mechanisms, Fig. 1a,

$$\left.\begin{array}{l} e^+e^- \to ZH,\ AH \\ e^+e^- \to \nu_e\bar{\nu}_e H \end{array}\right\} \quad H \to hh \tag{1}$$

Associated production $e^-e^- \to hA$ followed by $A \to hZ$ decays leads to hhZ background final states.

(ii) Double Higgs-strahlung in the continuum, with a final state Z boson, Fig. 1b,

$$e^-e^- \to Z^* \to hhZ \tag{2}$$

(iii) Associated production with the pseudoscalar A in the continuum, Fig. 1c,

$$e^-e^- \to Z^* \to hhA \tag{3}$$

(iv) Non-resonant $WW(ZZ)$ fusion in the continuum, Fig. 1d,

$$e^-e^- \to \bar{\nu}_e\nu_e W^*W^* \to \bar{\nu}_e\nu_e hh \tag{4}$$

*Supported by Deutsche Forschungsgemeinschaft DFG (Bonn).

[1] The production of two light Higgs bosons, $e^-e^- \to hh$, through loop diagrams does not involve any trilinear Higgs coupling; the production rates are rather small [5].

The cross sections for ZZ fusion in (1) and (4) are suppressed by an order of magnitude. The largest cross sections can be anticipated for the processes (1), where heavy on–shell H Higgs bosons decay into pairs of the light Higgs bosons. [Cross sections of similar size are expected for the backgrounds involving the pseudoscalar Higgs bosons.] We have derived the cross sections for the four processes analytically; the fusion process has been treated in the equivalent particle approximation for longitudinal vector bosons.

We will carry out the analysis in the $\mathcal{MSSM}$ for the value $\mathrm{tg}\beta = 1.5$. [A summary will be given in the last section for all values of $\mathrm{tg}\beta$]. In the present exploratory study, squark mixing will be neglected, *i.e.* the supersymmetric Higgs mass parameter μ and the parameter A_t in the soft symmetry breaking interaction will be set to zero, and the radiative corrections will be included in the leading m_t^4 one–loop approximation parameterized by [6]

$$\epsilon = \frac{3G_F}{\sqrt{2}\pi^2}\frac{m_t^4}{\sin^2\beta}\log\left(1+\frac{M_S^2}{m_t^2}\right) \tag{5}$$

with the common squark mass fixed to $M_S = 1$ TeV. In terms of $\mathrm{tg}\beta$ and M_A, the trilinear Higgs couplings relevant for our analysis are given in this approximation by

$$\begin{aligned}
\lambda_{hhh} &= 3\cos 2\alpha \sin(\beta+\alpha) + 3\frac{\epsilon}{M_Z^2}\frac{\cos^3\alpha}{\sin\beta} \\
\lambda_{Hhh} &= 2\sin 2\alpha \sin(\beta+\alpha) - \cos 2\alpha\cos(\beta+\alpha) - 3\frac{\epsilon}{M_Z^2}\frac{\sin\alpha}{\sin\beta}\cos^2\alpha
\end{aligned} \tag{6}$$

In addition, the coupling

$$\lambda_{hAA} = \cos 2\beta \sin(\beta+\alpha) + \frac{\epsilon}{M_Z^2}\frac{\cos\alpha}{\sin\beta}\cos^2\beta \tag{7}$$

will be needed even though it turned out – *a posteriori* – that it cannot be measured using the experimental methods discussed in this note[2]. As usual, these couplings are defined in units of $(2\sqrt{2}G_F)^{1/2}M_Z^2$; the $h, H, H^\pm$ masses and the mixing angle α can be expressed in terms of M_A and $\mathrm{tg}\beta$ [see e.g. Ref. [8] for a recent discussion].

In the decoupling limit [9] for large A, H and $H^\pm$ masses, the lightest Higgs particle becomes $\mathcal{SM}$–like and the trilinear hhh coupling approaches the $\mathcal{SM}$ value $\lambda_{hhh} \to M_h^2/M_Z^2$. In this limit, only the first three diagrams of Fig. 1b and 1d contribute and the cross-sections for the processes $e^+e^- \to hhZ$ and $WW \to hh$ approach the corresponding cross sections of the $\mathcal{SM}$ [10, 11].

2. H Production and hh Decays

If kinematically allowed, the most copious source of multiple h final states are cascade decays $H \to hh$, with H produced either by Higgs–strahlung or associated pair production

[2] For small masses the decay $h \to AA$ could have provided an experimental opportunity to measure this coupling. However, for $\mathrm{tg}\beta > 1$, this area of the $\mathcal{MSSM}$ parameter space has been excluded by LEP [7].

[1],

$$\sigma(e^+e^- \to ZH) = \frac{G_F^2 M_Z^4}{96\pi s}(v_e^2+a_e^2)\cos^2(\beta-\alpha)\frac{\lambda_Z^{1/2}[\lambda_Z + 12M_Z^2/s]}{(1-M_Z^2/s)^2} \tag{8}$$

$$\sigma(e^+e^- \to AH) = \frac{G_F^2 M_Z^4}{96\pi s}(v_e^2+a_e^2)\sin^2(\beta-\alpha)\frac{\lambda_A^{3/2}}{(1-M_Z^2/s)^2} \tag{9}$$

The Z couplings to electrons are given by $a_e = -1, v_e = -1 + 4\sin^2\theta_W$ and λ_j is the usual two–body phase space function $\lambda_j = (1 - M_j^2/s - M_H^2/s)^2 - 4M_j^2M_H^2/s^2$. The cross sections (8) and (9) are shown in Fig. 2 for the total e^+e^- energies $\sqrt{s} = 500$ GeV and 1.5 TeV as a function of the Higgs mass M_H for a small value of $\mathrm{tg}\beta = 1.5$ where the H cascade decays are significant over a large mass range. As a consequence of the decoupling theorem, associated AH production is dominant for large Higgs masses.

The trilinear Hhh coupling can be measured in the decay process $H \to hh$

$$\Gamma(H \to hh) = \frac{G_F\lambda_{Hhh}^2}{16\sqrt{2}\pi}\frac{M_Z^4}{M_H}\left(1-\frac{4M_h^2}{M_H^2}\right)^{1/2} \tag{10}$$

if the branching ratio is neither too small nor too close to unity. This is indeed the case, as shown in Fig. 3a, for H masses between 180 and 350 GeV and small to moderate $\mathrm{tg}\beta$ values. The other important decay modes are WW^*/ZZ^* decays. Since the H couplings to the gauge bosons can be measured through the production cross sections of the fusion and Higgs–strahlung processes, the branching ratio $\mathrm{BR}(H \to hh)$ can be exploited to measure the coupling λ_{Hhh}.

The ZH final state gives rise to resonant two–Higgs $[hh]$ final states. The AH final state typically yields three Higgs $h[hh]$ final states since the channel $A \to hZ$ is the dominant decay mode in most of the mass range we consider. This is shown in Fig. 3b where the branching ratios of the pseudoscalar A are displayed for $\mathrm{tg}\beta = 1.5$.

Another type of two–Higgs hh final states is generated in the chain $e^+e^- \to Ah \to [Zh]h$, which does not involve any of the Higgs self–couplings. However, in this case, the two h bosons do not resonate while $[Zh]$ does, so that the topology of these background events is very different from the signal events. The size of the $e^+e^- \to hA$ background cross section is shown in Fig. 2 together with the signal cross sections; for sufficiently large M_A, it becomes small, in line with the decoupling theorem [9].

A second large signal cross section is provided by the WW fusion mechanism. [Since the NC couplings are smaller compared to the CC couplings, the cross section for the ZZ fusion processes in (1) and (4) is $\sim 16\cos^4\theta_W$, *i.e.* one order of magnitude smaller than for WW fusion.] In the effective longitudinal W approximation [12] one obtains

$$\sigma(e^+e^- \to H\bar{\nu}_e\nu_e) = \frac{G_F^3 M_W^4}{4\sqrt{2}\pi}\left[\left(1-\frac{M_H^2}{s}\right)\log\frac{s}{M_H^2} - 2\left(1-\frac{M_H^2}{s}\right)\right]\cos^2(\beta-\alpha) \tag{11}$$

The magnitude of the cross section[3] $e^+e^- \to H\nu_e\bar{\nu}_e$ is also shown in Fig. 2 for the two energies $\sqrt{s} = 500$ GeV and 1.5 TeV as a function of the Higgs mass M_H and for $\mathrm{tg}\beta = 1.5$. The signals in $e^+e^- \to [hh]$ + missing energy are very clear, competing only with H-strahlung and subsequent neutrino decays of the Z boson. Since the lightest Higgs boson will decay mainly into $b\bar{b}$ pairs, the final states will predominantly include four and six b quarks.

At $\sqrt{s} = 500$ GeV, about 500 signal events are predicted in the mass range of $M_H \sim 200$ GeV for an integrated luminosity of $\int \mathcal{L} = 20$ fb^{-1} *per annum*; and at $\sqrt{s} = 1.5$ TeV, about 8,000 to 1,000 signal events for the prospective integrated luminosity of $\int \mathcal{L} = 200$ fb^{-1} *per annum* in the interesting mass range between 180 and 350 GeV. Note that for both energies, the Ah background cross section is significantly smaller.

3. Non-Resonant Double hh Production

The double Higgs-strahlung $e^+e^- \to Zhh$, the triple Higgs production process $e^+e^- \to Ahh$ and the WW fusion mechanism $e^+e^- \to \nu_e\bar{\nu}_e hh$ outside the resonant $H \to hh$ range are disfavored by an additional power of the electroweak coupling compared to the resonance processes. Nevertheless, these processes must be analyzed carefully in order to measure the value of the hhh coupling.

3.1 $e^+e^- \to Zhh$

The double differential cross section of the process $e^+e^- \to hhZ$, Fig. 1b, is given by

$$\frac{d\sigma(e^+e^- \to hhZ)}{dx_1 dx_2} = \frac{G_F^3 M_Z^6}{384\sqrt{2}\pi^3 s}\,(a_e^2 + v_e^2)\;\frac{\mathcal{A}}{(1-\mu_Z)^2} \tag{12}$$

The couplings have been defined in the previous section. $x_{1,2} = 2E_{1,2}/\sqrt{s}$ are the scaled energies of the Higgs particles, $x_3 = 2 - x_1 - x_2$ is the scaled energy of the Z boson; $y_k = 1 - x_k$. The scaled masses squared are denoted by $\mu_i = M_i^2/s$. In terms of these variables, the coefficient $\mathcal{A}$ in the cross section may be written as:

$$\begin{aligned}\mathcal{A} \;=\; & \left\{ \frac{a^2}{2} f_0 + \frac{\sin^4(\beta-\alpha)}{4\mu_Z^2(y_1+\mu_h-\mu_Z)}\left[\frac{f_1}{y_1-\mu_h-\mu_Z} + \frac{f_2}{y_2+\mu_h-\mu_Z}\right] + \frac{\cos^4(\beta-\alpha)}{4\mu_Z^2(y_1-\mu_h-\mu_A)} \right. \\ & \times \left[\frac{f_3}{y_1+\mu_h-\mu_A} + \frac{f_4}{y_2+\mu_h-\mu_A}\right] + \frac{a}{\mu_Z}\left[\frac{\sin^2(\beta-\alpha) f_5}{y_1+\mu_h-\mu_Z} + \frac{\cos^2(\beta-\alpha) f_6}{y_1+\mu_h-\mu_A}\right] \\ & \left. + \frac{\sin^2 2(\beta-\alpha)}{8\mu_Z^2(y_1+\mu_h-\mu_Z)}\left[\frac{f_7}{y_1+\mu_h-\mu_Z} + \frac{f_8}{y_2-\mu_h-\mu_Z}\right]\right\} + \{y_1 \leftrightarrow y_2\} \end{aligned} \tag{13}$$

with

$$a = \frac{1}{2}\left[\frac{\sin(\beta-\alpha)\lambda_{hhh}}{y_3+\mu_Z-\mu_h} - \frac{\cos(\beta-\alpha)\lambda_{HHh}}{y_3+\mu_Z-\mu_H}\right] + \frac{\sin^2(\beta-\alpha)}{y_1+\mu_h-\mu_Z} + \frac{\sin^2(\beta-\alpha)}{y_2+\mu_h-\mu_Z} + \frac{1}{2\mu_Z} \tag{14}$$

[3] In the effective W approximation, the cross section may be overestimated by as much as a factor of 2 for small masses and/or small c.m. energies. Therefore we display the exact cross sections [13] in Fig.2.

[omitting the small decay widths of the Higgs bosons]. Only the coefficient a includes the Higgs self-couplings λ_{HHh} and λ_{hhh}. Introducing the notation $y_0 = (y_1 - y_2)/2$, the coefficients f_i which do not involve any Higgs couplings, are defined by

$$\begin{aligned}
f_0 &= (y_1-y_2)^2 - 4\mu_Z(1-3\mu_Z) \\
f_1 &= \left[(1+y_1)^2 - 4\mu_Z(y_1-\mu_h)\right]\left[y_1^2 + \mu_Z^2 - 2\mu_Z(y_1-2\mu_h)\right] \\
f_2 &= \left[2\mu_Z(\mu_Z - 2\mu_h + 1) - (1+y_1)(1-y_2)\right]\left[\mu_Z(\mu_Z - y_1 - y_2 - 4\mu_h - 2) - y_1 y_2\right] \\
f_3 &= \left[y_0^2 + \mu_Z(1 - y_1 - y_2 - \mu_Z - 4\mu_h)\right]\left[1 - y_1 + y_2 - y_0^2 - \mu_Z(\mu_Z - 4\mu_h - 2y_1)\right] \\
f_4 &= \left[y_0^2 + \mu_Z(1 - y_1 - y_2 + \mu_Z - 4\mu_h)\right]\left[y_0^2 - 1 + \mu_Z(\mu_Z - y_1 - y_2 - 4\mu_h - 2)\right] \\
f_5 &= 2\mu_Z^3 - 4\mu_Z^2(y_1 + 2\mu_h) + \mu_Z\left[(1-y_1)(3y_1 - y_2) + 2\right] - y_1^2(1 - y_1 - y_2) - y_1 y_2 \\
f_6 &= 2\mu_Z^3 - \mu_Z^2(y_2 - 3y_1 + 8\mu_h - 2) + 2\mu_Z y_0(1 - y_1 - y_0) + 2y_1 y_0 - y_0^2(y_1 - y_2 - 2) \\
f_7 &= \left[\mu_Z(4\mu_h - \mu_Z - 1 + 2y_1 - y_0) - y_1 y_0\right]\left[\mu_Z(4\mu_h - \mu_Z - 1 + 3y_1) - (1-y_0)(1+y_1)\right] \\
f_8 &= \left[\mu_Z(4\mu_h - \mu_Z - 1 + 2y_1 - y_0) - y_1 y_0\right]\left[\mu_Z(4\mu_h - \mu_Z - 2 + y_1) + (1-y_0)(1-y_1)\right]
\end{aligned} \tag{15}$$

In the decoupling limit, the cross section is reduced to the $S\mathcal{M}$ cross section for which

$$\mathcal{A} = \frac{a^2}{2} f_0 + \frac{1}{4\mu_Z^2(y_1+\mu_h-\mu_Z)}\left[\frac{f_1}{y_1+\mu_h-\mu_Z} + \frac{f_2}{y_2+\mu_h-\mu_Z} + 4a\mu_Z f_5\right] + \{y_1 \leftrightarrow y_2\}$$

with the f_i's as given above, and

$$a = \frac{1}{2}\frac{\lambda_{hhh}}{y_3+\mu_Z-\mu_h} + \frac{1}{y_1+\mu_h-\mu_Z} + \frac{1}{y_2+\mu_h-\mu_Z} + \frac{1}{2\mu_Z}$$

The cross section $\sigma(e^+e^- \to hhZ)$ is shown for $\sqrt{s} = 500$ GeV at $\mathrm{tg}\beta = 1.5$ as a function of the Higgs mass M_h in Fig. 4a. For small masses, the cross section is built up almost exclusively by $H \to hh$ decays [dashed curve], except close to the point where the λ_{HHh} coupling accidentally vanishes (cf. Ref.[8]) and for masses around ~ 90 GeV where additional contributions come from the decay $A \to hZ$ [this range of M_h corresponds to M_A values where $\mathrm{BR}(A \to hZ)$ is large; c.f. Fig.3]. For intermediate masses, the resonance contribution is reduced and, in particular above 90 GeV where the decoupling limit is approached, the continuum hh production becomes dominant, falling finally down to the cross section for double Higgs production in the Standard Model [dashed line]. After subtracting the $H \to hh$ decays [which of course is very difficult], the continuum cross section is about 0.5 fb, and is of the same order as the $S\mathcal{M}$ cross section at $\sqrt{s} = 500$ GeV. Very high luminosity is therefore needed to measure the trilinear hhh coupling. At higher energies, since the cross section for double Higgs-strahlung scales like $1/s$, the rates are correspondingly smaller, c.f. Fig.4b.

Prospects are similar for large $\mathrm{tg}\beta$ values. The cascade decay $H \to hh$ is restricted to a small M_h range of less than 70 GeV, with a production cross section of ~ 20 fb at $\sqrt{s} = 500$ GeV and ~ 3 fb at 1.5 TeV. The continuum cross sections are of the order of 0.1 fb at both energies, so that very high luminosities will be needed to measure the

continuum cross sections in this case if the background problems can be mastered at all.

We have repeated the analysis for the continuum process $e^+e^- \to Ahh$ (cf. Fig.1c). However, it turned out that the cross section is built up almost exclusively by resonant $AH \to Ahh$ final states, with a very small continuum contribution, so that the measurement of the coupling λ_{hAA} is extremely difficult in this process.

3.2 $W_LW_L \to hh$

In the effective longitudinal W approximation[4], the total cross section for the subprocess $W_LW_L \to hh$, Fig. 1d, is given by

$$\begin{aligned}\hat{\sigma}_{LL} &= \frac{G_F^2\hat{s}}{64\pi}\frac{\beta_h}{\beta_W}\left\{(1+\beta_W^2)^2\left[\frac{\mu_Z\sin(\beta-\alpha)}{1-\mu_h}\lambda_{hhh}+\frac{\mu_Z\cos(\beta-\alpha)}{1-\mu_H}\lambda_{Hhh}+1\right]^2\right. \qquad (16)\\ &- \frac{\beta_W^2}{\beta_W\beta_h}\left[\frac{\mu_Z\sin(\beta-\alpha)}{1-\mu_h}\lambda_{hhh}-\frac{\mu_Z\cos(\beta-\alpha)}{1-\mu_H}\lambda_{Hhh}-1\right][\sin^2(\beta-\alpha)g_1\\ &- \left.\cos^2(\beta-\alpha)g_2]+\frac{1}{\beta_W^2\beta_h^2}\left[\sin^4(\beta-\alpha)g_3+\cos^4(\beta-\alpha)g_4+\sin^2 2(\beta-\alpha)g_5\right]\right\}\end{aligned}$$

with

$$\begin{aligned}g_1 &= 2[(\beta_W-x_W\beta_h)^2+1-\beta_W^4]l_W-4\beta_h(2\beta_W-x_W\beta_h)\\ g_2 &= 2(x_C\beta_h-\beta_W)^2l_C+4\beta_h(x_C\beta_h-2\beta_W)\\ g_3 &= \beta_h[\beta_hx_W(3\beta_h^2x_W^2+14\beta_W^2+2-2\beta_W^4)-4\beta_W(3\beta_h^2x_W^2+\beta_W^2+1-\beta_W^4)][l_W+x_Wy_W]\\ &\quad -[\beta_W^4+(1-\beta_W^4)(1+2\beta_W^2-\beta_W^4)][l_W/x_W-y_W]-2\beta_h^2y_W(2\beta_W-\beta_hx_W)^2\\ g_4 &= \beta_h[\beta_hx_C(3\beta_h^2x_C^2+14\beta_W^2)-4\beta_W(3\beta_h^2x_C^2+\beta_W^2)][l_C+x_Cy_C]\\ &\quad -\beta_W^4[l_C/x_C-y_C]-2y_C\beta_h^2(2\beta_W-\beta_hx_C)^2\\ g_5 &= \frac{\beta_h\beta_Wl_W}{x_W^2-x_C^2}[2x_W(2x_W^2\beta_h\beta_W-x_Cx_W^2\beta_h^2-x_C\beta_W^2)-2x_W^2(\beta_h^2x_W^2+\beta_W^2+1-\beta_W^4)\\ &\quad +\frac{x_C}{\beta_W\beta_h}((\beta_h^2x_W^2+\beta_W^2)(1-\beta_W^4)+(\beta_h^2x_W^2+\beta_W^2)^2)]-4\beta_h^2\beta_W(x_W+x_C)\\ &\quad +\frac{\beta_h\beta_Wl_C}{x_C^2-x_W^2}[4x_C^2\beta_h\beta_W-2x_Cx_W(\beta_h^2x_C^2+\beta_W^2+1-\beta_W^4)-2x_C^2(\beta_h^2x_C^2-\beta_W^2)\\ &\quad +\frac{x_W}{\beta_W\beta_h}((\beta_W^2-\beta_h^2x_C^2)(1-\beta_W^4)+(\beta_h^2x_C^2-\beta_W^2)^2)]-2\beta_H^2(x_Cx_W\beta_H^2+4\beta_W^2) \qquad (17)\end{aligned}$$

The scaling variables are defined in the same way as before. $\hat{s}^{1/2}$ is the c.m. energy of the subprocess. $\beta_W = (1-4M_W^2/\hat{s})^{1/2}$ and $\beta_h = (1-4M_h^2/\hat{s})^{1/2}$ are the velocities of the W and h bosons, and

$$\begin{aligned}x_W = (1-2\mu_h)/(\beta_W\beta_h) \quad , \quad x_C = (1-2\mu_h+2\mu_{H^\pm}-2\mu_W)/(\beta_W\beta_h)\\ l_i = \log(x_i-1)/(x_i+1) \quad , \quad y_i = 2/(x_i^2-1) \qquad (18)\end{aligned}$$

[4]For qualifying comments see footnote 3.

The value of the charged Higgs boson mass $M_{H^\pm}$ in the $H^\pm$ t-channel exchange diagram of Fig.1d is given by $M_{H^\pm}^2 = M_A^2 + M_W^2$.

In the decoupling limit, the cross section reduces again to the $\mathcal{SM}$ cross section which in terms of g_1 and g_2, defined above, is given by:

$$\hat{\sigma}_{LL} = \frac{G_F^2\hat{s}}{64\pi}\frac{\beta_h}{\beta_W}\left\{(1+\beta_W^2)^2\left[\frac{\mu_Z\lambda_{hhh}}{1-\mu_h}+1\right]^2+\frac{1+\beta_W^2}{\beta_W\beta_h}\left[\frac{\mu_Z\lambda_{hhh}}{1-h_i}+1\right]g_1+\frac{g_2}{\beta_W^2\beta_h^2}\right\} \qquad (19)$$

After folding $\hat{\sigma}_{LL}$ with the longitudinal W_LW_L luminosity [12], one obtains the total cross section $\sigma(e^+e^- \to \nu_e\bar{\nu}_ehh)$ shown in Fig. 4b as a function of the light Higgs mass M_h for $\mathrm{tg}\beta = 1.5$ at $\sqrt{s} = 1.5$ TeV. It is significantly larger than for double Higgs–strahlung in the continuum. Again, for very light Higgs masses, most of the events are $H \to hh$ decays [dashed line]. The continuum hh production is of the same size as pair production of $\mathcal{SM}$ Higgs bosons [dotted line] which, as anticipated, is being approached near the upper limit of the h mass in the decoupling limit. The size of the continuum hh fusion cross section renders this channel more promising than double Higgs–strahlung for the measurement of the trilinear hhh coupling.

For large $\mathrm{tg}\beta$ values, strong destructive interference effects reduce the cross section in the continuum to very small values, of order 10^{-2} fb, before the $\mathcal{SM}$ cross section is reached again in the decoupling limit. As before, the hh final state is almost exclusively built up by the resonance $H \to hh$ decays.

4. Summa

It is convenient to summarize our results by presenting Fig.5, which displays the areas of the $[M_A, \mathrm{tg}\beta]$ plane in which λ_{Hhh} [solid lines, 135° hatching] and λ_{hhh} [dashed lines, 45° hatching] could eventually be accessible by experiment. The size of these areas is based on purely theoretical cuts so that they are expected to shrink if background processes and detector effects are taken into account.

(i) In the case of $H \to hh$, we require a lower limit of the cross section $\sigma(H)\times\mathrm{BR}(H \to hh) > 0.5$ fb and at the same time for the decay branching ratio $0.1 < \mathrm{BR}(H \to hh) < 0.9$, as discussed earlier. Based on these definitions, λ_{Hhh} may become accessible in two disconnected regions denoted by I and II [135° hatched] in Fig.5. For low $\mathrm{tg}\beta$, the left boundary of Region I is set by LEP1 data. The gap between Regions I and II is a result of the nearly vanishing λ_{Hhh} coupling in this strip. The right boundary of Region II is due to the overwhelming $t\bar{t}$ decay mode for heavy H masses, as well as due to the small H production cross section. For moderate values of $\mathrm{tg}\beta$, the left boundary of Region I is defined by $\mathrm{BR}(H \to hh) > 0.9$. In the area between Regions I and II, H cannot decay into two h bosons, i.e. $M_H < 2M_h$. For large $\mathrm{tg}\beta \gtrsim 10$, $\mathrm{BR}[H \to hh(AA)]$ is either too large or too small, except in a very small strip, $M_A \simeq 55$ GeV, towards the top of Region I. [Note that h and A are nearly mass-degenerate in this area.]

(ii) The dashed line in Fig.5 describes the left boundary of the area [45° hatched] in

which λ_{hhh} may become accessible; it is defined by the requirement that the continuum $W_L W_L \to hh$ cross section, σ_{cont}, is larger than 0.5 fb. Note that the resonant $H \to hh$ events in Region II must be subtracted in order to extract the λ_{hhh} coupling.

In conclusion, we have derived the cross sections for the double production of the lightest neutral Higgs boson in the $\mathcal{MSSM}$ at e^-e^- colliders: in the Higgs-strahlung process $e^-e^- \to Zhh$, [in the triple Higgs production process $e^-e^- \to Ahh$], and in the WW fusion mechanism. These cross sections are large for resonant $H \to hh$ decays so that the measurement of the triple Higgs coupling λ_{Hhh} is expected to be fairly easy for $H \to hh$ decays in the M_H mass range between 150 and 350 GeV for small tgβ values. The continuum processes must be exploited to measure the triple Higgs coupling λ_{hhh}. These continuum cross sections, which are of the same size as in the $\mathcal{SM}$, are rather small so that high luminosities are needed for the measurement of the triple Higgs coupling λ_{hhh}.

Acknowledgements:

Discussions with G. Moultaka and technical help by T. Plehn are gratefully acknowledged. A.D. thanks the Theory Group for the warm hospitality extended to him at DESY, and H.E.H. acknowledges the partial support of the U.S. Department of Energy.

References

[1] For reviews on the Higgs sector in the $\mathcal{SM}$ and $\mathcal{MSSM}$, see J.F. Gunion, H.E. Haber, G. Kane and S. Dawson, *The Higgs Hunter's Guide*, Addison-Wesley 1990; A. Djouadi, Int. J. Mod. Phys A10 (1995) 1.

[2] J.F. Gunion and H.E. Haber, Nucl. Phys. B272 (1986) 1; B278 (1986) 449.

[3] T. Plehn, M. Spira and P. M. Zerwas, DESY 95-215 and Z. Phys. C (in press).

[4] See *e.g.* P.M. Zerwas, Proceedings, *Les Rencontres de Physique de la Vallée d'Aoste*, La Thuile 1994 and DESY 94-001.

[5] K. Gaemers and F. Hoogeveen, Z. Phys. C26 (1984) 249; A. Djouadi, V. Driesen and C. Jünger, Report KA-TP-02-96.

[6] H.E. Haber and R. Hempfling, Phys. Rev. Lett. 66 (1991) 1815; Y. Okada, M. Yamaguchi and T. Yanagida, Prog. Theor. Phys. 85 (1991) 1; J. Ellis, G. Ridolfi and F. Zwirner, Phys. Lett. 257B (1991) 83.

[7] J.-F. Grivaz, Proceedings, *Int. Conference on High-Energy Physics*, Brussels 1995.

[8] A. Djouadi, J. Kalinowski and P. M. Zerwas, DESY 95-211 (hep-ph 9511342) and Z. Phys. C (in press).

[9] H.E. Haber, CERN-TH/95-109 and SCIPP-95/15, Proceedings, *Conference on Physics Beyond the Standard Model IV*, Lake Tahoe CA 1994; and *Perspectives for Electroweak Interactions in e^-e^- Collisions*, Ringberg Castle, Tegernsee 1995.

[10] G. Gounaris, D. Schildknecht and F. Renard, Phys. Lett. B83 (1979) 191 and (E) 89B (1980) 437.

[11] V. Barger and T. Han, Mod. Phys. Lett. A5 (1990) 667; V. Barger, T. Han and R.J. Phillips, Phys. Rev. D38 (1988) 2766; J. F. Gunion et al., Phys. Rev. D38 (1988) 3444; D. Dicus, K. Kallianpur and S. Willenbrock, Phys. Lett. B200 (1988) 187; K. Kallianpur, Phys. Lett. B215 (1988) 392; A. Abbasabadi, W. Repko, D. Dicus and R. Vega, Phys. Rev. D38 (1988) 2770; V. Ilyin, A. Pukhov, Y. Kurihara, Y. Shimitzu and T. Kaneko, KEK CP-030; F. Boudjema and E. Chopin, ENSLAPP-A534/95.

[12] R.N. Cahn and S. Dawson, Phys. Lett. B136 (1984) 196; S. Dawson, Nucl. Phys. B249 (1984) 42; S. Chanowitz and M.K. Gaillard, Phys. Lett. B142 (1984) 85; I. Kuss and H. Spiesberger, Report BI-TP-95/25.

[13] A. Djouadi, D. Haidt, B. Kniehl, B. Mele and P.M. Zerwas, Proceedings, *e^-e^- collisions at 500 GeV: The Physics Potential*, Munich-Annecy-Hamburg, DESY 92-123A.

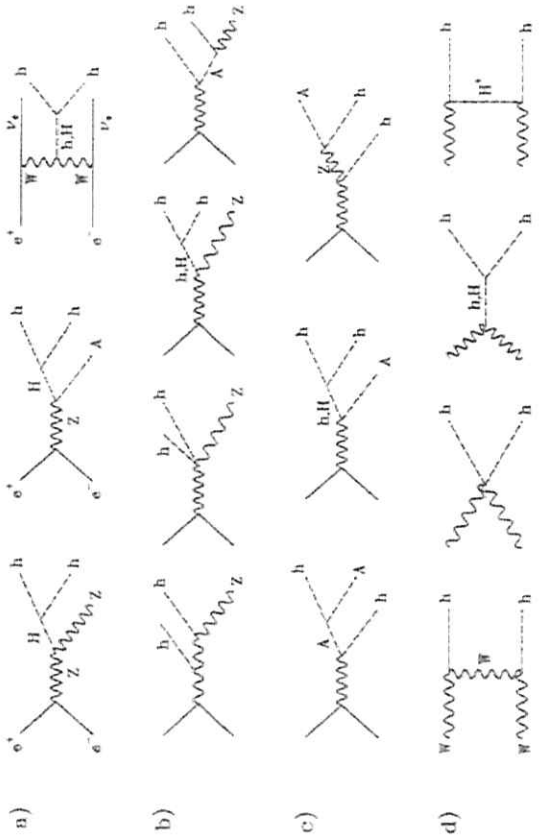

Fig. 1

Fig.1: Main mechanisms for the double production of the light MSSM Higgs boson in e^+e^- collisions: a) $e^+e^- \to ZH$, $e^+e^- \to AH$ and $WW \to H$ followed by $H \to hh$; (b) $e^+e^- \to hhZ$, (c) $e^+e^- \to hhA$ and (d) $WW \to hh$.

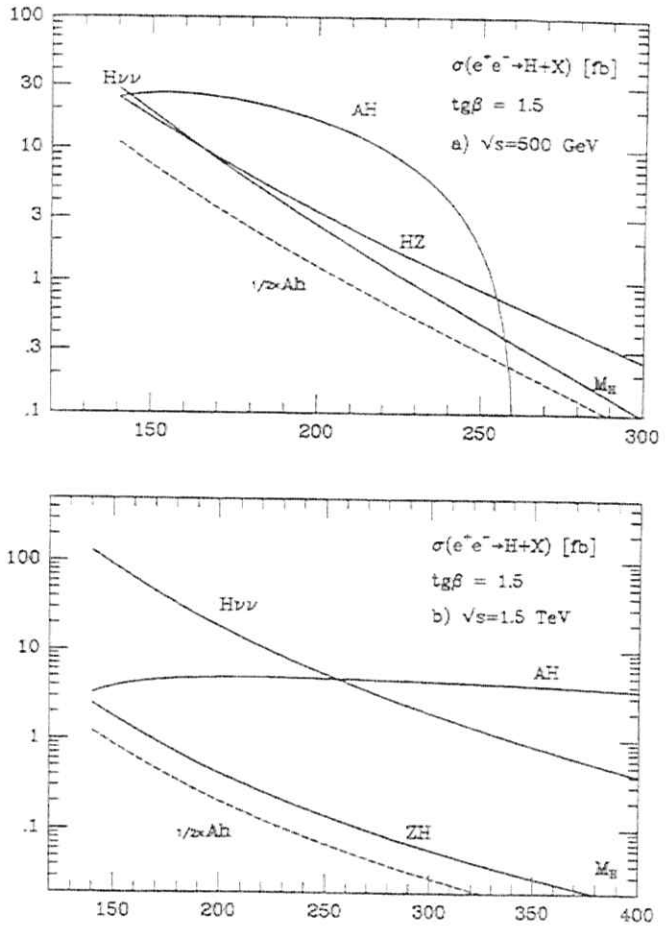

Fig. 2: Cross sections for the production of the heavy CP-even Higgs boson H in e^+e^- collisions, $e^+e^- \to ZH/AH$ and $e^+e^- \to H\nu_e\bar{\nu}_e$, and for the background process $e^+e^- \to Ah$ [the dashed curve shows $\frac{1}{2} \times \sigma(Ah)$ for clarity of the figures]. The c.m. energies are chosen $\sqrt{s} = 500$ GeV in (a), and 1.5 TeV in (b).

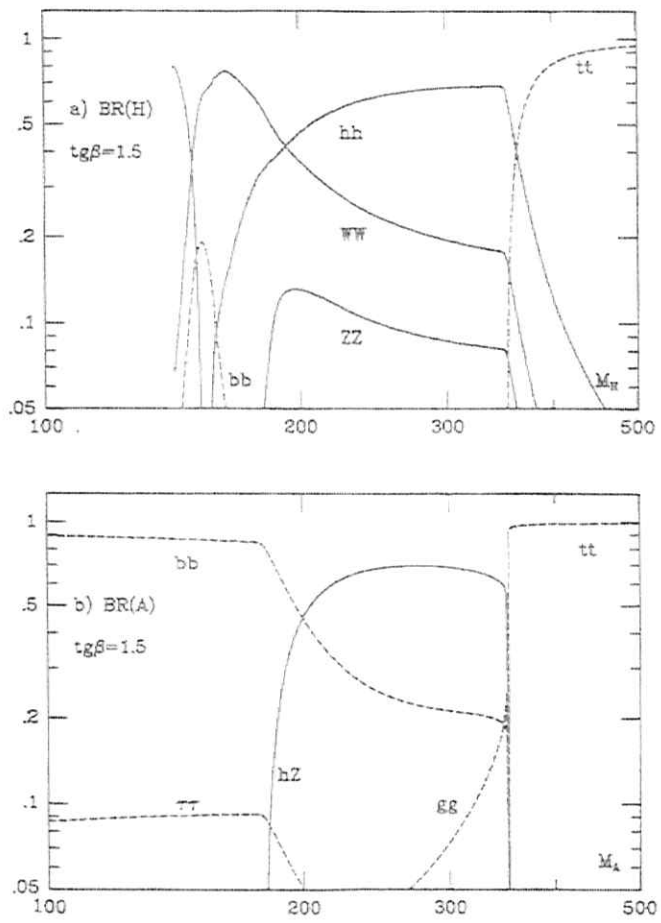

Fig. 3: The branching ratios of the main decays modes of the heavy CP–even neutral Higgs boson H in (a), and of the pseudoscalar Higgs boson A in (b).

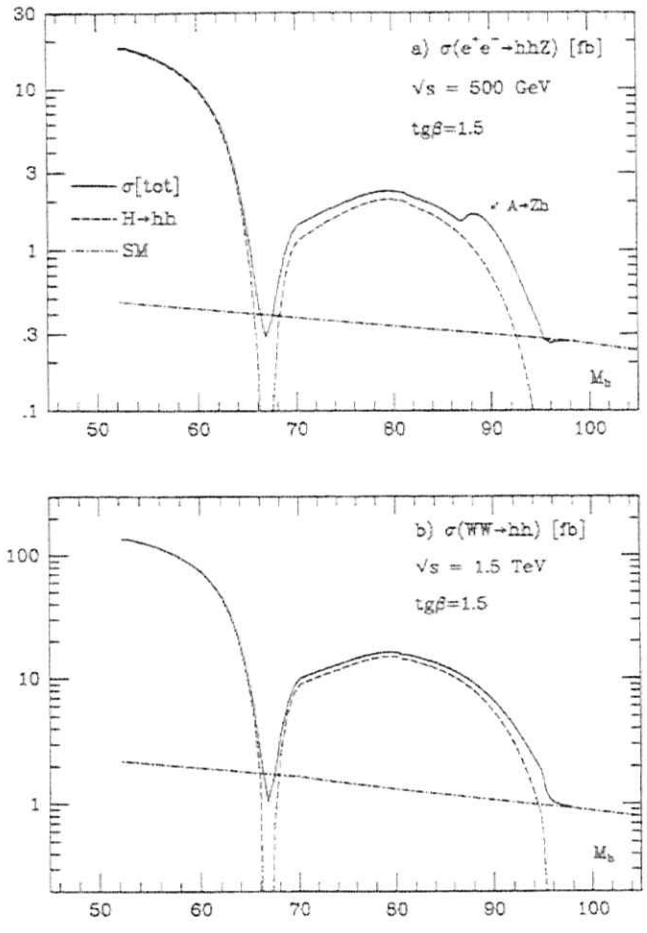

Fig. 4: The cross sections for hh production in the continuum for $\mathrm{tg}\beta = 1.5$: $e^+e^- \to hhZ$ at a c.m. energy of $\sqrt{s} = 500$ GeV (a) and $W_L W_L \to hh$ at $\sqrt{s} = 1.5$ TeV (b).

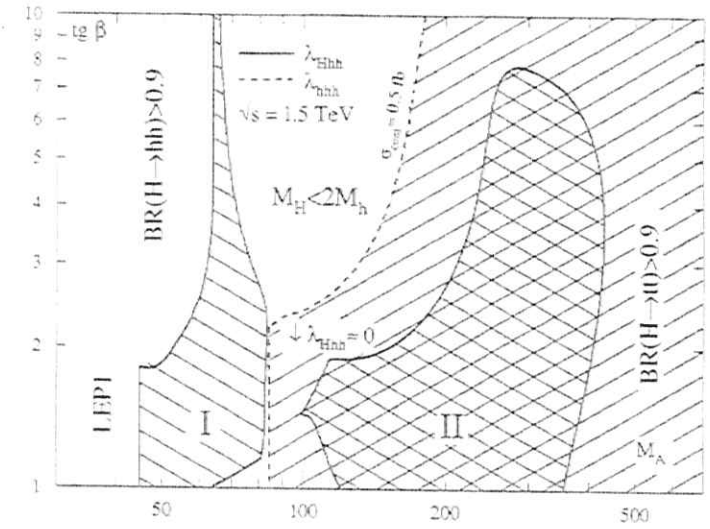

Fig. 5: The areas of the $[M_A, \mathrm{tg}\beta]$ plane in which the Higgs self-couplings λ_{HAA} and λ_{hAA} could eventually be accessible by experiment at $\sqrt{s} = 1.5$ TeV [see text for further discussions].

Loop Induced Higgs Boson Pair Production

A. Djouadi, V. Driesen and C. Jünger
Institut für Theoretische Physik, Universität Karlsruhe, D–76128 Karlsruhe, Germany.

Abstract

We discuss the loop induced production of Higgs boson pairs at high–energy e^+e^- colliders, both in the Standard Model and in its minimal supersymmetric extension. The cross sections are rather small, but these processes could be visible with high-enough luminosities and if longitudinal polarization is available.

1. Introduction

If the genuine supersymmetric particles were too heavy to be kinematically accessible in collider experiments, the only way to distinguish between the Standard Model (SM) and the lightest Higgs boson of its minimal extension (MSSM) in the decoupling limit [where all the other MSSM Higgs bosons are heavy, and the lightest Higgs boson h has exactly the same properties [1] as the SM Higgs boson except that its mass is restricted to be smaller than $M_h \lesssim 140$ GeV], is to search for loop induced contributions of the supersymmetric particles, which could give rise to sizeable deviations from the predictions of the SM. Well known examples of this loop induced processes are the $\gamma\gamma$ widths of the Higgs particles [2] or the process $e^+e^- \to Z$+Higgs which in the MSSM receive extra contributions from supersymmetric gaugino and sfermion loops [3].

Another type of such discriminating processes is the pair production of Higgs bosons which will be analyzed here. In the SM, where it has been first discussed in Ref.[4], the process $e^+e^- \to H^0H^0$ is mediated only by W and Z boson loops, Fig.1a, while in the Minimal Supersymmetric extension, additional contributions to the corresponding process $e^+e^- \to hh$ will originate from chargino, neutralino, selectron and sneutrino loops, as well as loops built up by the associated A and $H^\pm$ bosons; Fig.1b. The cross sections for these two processes [as well as for the production of the heavy MSSM Higgs bosons, $e^+e^- \to HH, AA$ and hH] have been derived in [5] and here we will summarize the results.

2. SM Higgs Pair Production

In the SM, non–zero contributions to the process $e^+e^- \to H^0H^0$ can only come from one–loop diagrams, in the limit of vanishing electron mass. Among these, the diagrams involving the one–loop He^+e^- vertex [because $m_e \simeq 0$] and those with γ and Z boson s–channel exchanges [because of CP invariance] give zero–contribution; additional contributions from vertex diagrams involving the quartic WWH^0H^0/ZZH^0H^0 couplings are proportional m_e and also negligible. The only contribution to Higgs pair production in the SM will therefore come from W and Z box diagrams, Fig.1a. The expressions of the cross sections, allowing for longitudinal polarization of the initial beams are given in [5].

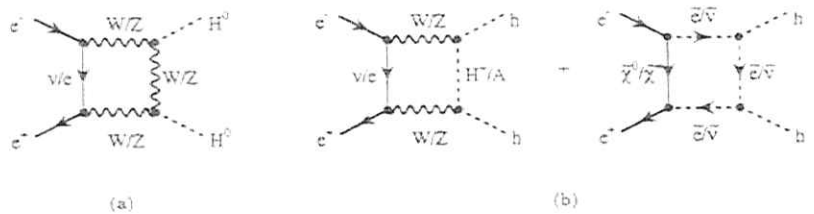

Fig. 1: Feynman diagrams contributing to the Higgs boson pair production process in e^+e^- collisions in the SM (a) and in the MSSM (b).

The cross sections are shown in Fig.2 as a function of the Higgs boson mass for two center–of–mass energies, $\sqrt{s} = 500$ GeV and 1.5 TeV. Except when approaching the $2M_H$ threshold [and the small dip near the WW threshold], the cross sections are practically constant for a given value of the c.m. energy, and amount to $\sigma \sim 0.2$ fb at $\sqrt{s} = 500$ GeV in the unpolarized case. The decrease of the cross sections with increasing center–of–mass energy is very mild: at $\sqrt{s} = 1.5$ TeV, the cross section is still at the level of $\sigma \sim 0.15$ fb for Higgs boson masses less than $M_H \lesssim 350$ GeV.

With left–handed polarized electrons, the cross section $e^-_L e^+ \to H^0H^0$ is larger by a factor of two, while for left–handed electrons and right–handed positrons, the cross section $e^-_L e^+_R \to H^0H^0$ is larger by a factor of four, compared to the unpolarized case. Therefore, the availability of longitudinal polarization of the initial beams is very important. With integrated luminosities of the order of $\int \mathcal{L} \sim 100$ fb^{-1} which are expected to be available for future high–energy linear colliders, one could expect a few hundred events in the course of a few years, if both initial beams can be longitudinally polarized.

For $M_H \lesssim 140$ GeV, the signal will mainly consist of four b quarks in the final state, $e^+e^- \to H^0H^0 \to b\bar{b}b\bar{b}$, since the dominant decay mode of the Higgs boson in this mass range is $H^0 \to b\bar{b}$. This calls for very efficient μ–vertex detectors to tag the b jets. Since these rare events will be searched for only after the discovery of the Higgs boson in the main production processes [5], M_H will be precisely known and the two mass constraints $m(b\bar{b}) = M_H$, together with the large number of final b quarks, give a reasonable hope to experimentally isolate the signals despite of the low rates. For $M_H \gtrsim 140$ GeV, since $H^0 \to W^+W^-$ and $H^0 \to ZZ$ will be the dominant decay modes of the Higgs boson, the signals will consist of four gauge bosons in the final state, $e^+e^- \to H^0H^0 \to VVVV$, leading to eight final fermions. These rather spectacular events should also help to experimentally isolate the signal.

3. MSSM Higgs Pair Production

For the pair production of the light CP–even Higgs boson of the MSSM, $e^+e^- \to hh$,

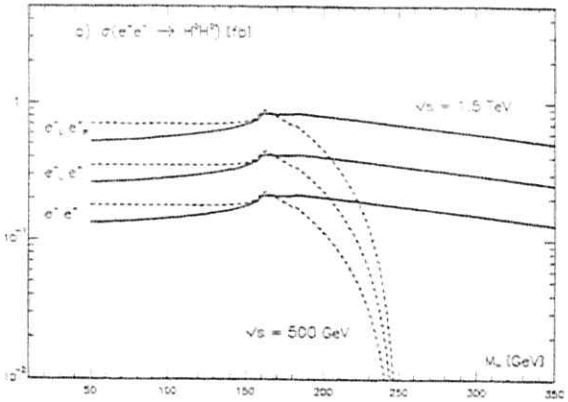

Fig. 2: The cross sections for, $e^+e^- \to H^0H^0$, as a function of M_H for $\sqrt{s} = 500$ GeV [dashed lines] and $\sqrt{s} = 1.5$ TeV [solid lines]. The lower, middle and upper curves correspond to the cross sections with unpolarized, e_L^- and $e_R^-e_L^-$ beams respectively.

several additional diagrams will contribute to the process; Fig.1b. Besides the W and Z boson box diagrams, one has the box diagrams with the exchange of the pseudoscalar and the charged Higgs bosons, A and $H^\pm$ and the box diagrams built up by chargino/sneutrino and neutralino/selectron loops. The analytical expressions of the cross sections, allowing for longitudinal polarization of the initial beams are also given in [5].

In Fig.3, we show the cross section for the process $e^+e^- \to hh$ as a function of M_h for two c.m. energies $\sqrt{s} = 500$ GeV and 1.5 TeV and two values of $\tan\beta = 1.5$ and 50. The solid lines are for the full cross sections, while the dashed lines are for the cross sections without the SUSY contributions. To include the latter we have chosen the parameters $M_2 = -\mu = 150$ GeV, while the common slepton and squark masses are taken to be $M_L = 300$ GeV and $M_S = 500$ GeV; the parameter A_t and A_b are set to zero. Only the unpolarized cross sections are discussed: as mentioned previously, they are simply increased by a factor of 2(4) when the initial beam(s) are longitudinally polarized.

Let us first discuss the case where the supersymmetric contributions are not included. for small $\tan\beta$ the cross section is of the same order as the SM cross section and does not strongly depend on M_h especially at very high-energies. Although the WWh/Zhh couplings are suppressed by $\sin(\beta-\alpha)$ factors, the suppression is not very strong and the W/Z box contributions are not much smaller than in the SM; the diagrams where $A/H^\pm$ are exchanged will give compensating contributions since the $hAZ/hH^\pm W$ couplings are proportional to the complementary factor $\cos(\beta-\alpha)$. As in the SM case, the cross sections slightly decrease with increasing energy. For large $\tan\beta$ values, the factors $\sin/\cos(\beta-\alpha)$ vary widely when M_h is varied. For small M_h, the factor $\sin(\beta-\alpha) \to 0$, and the

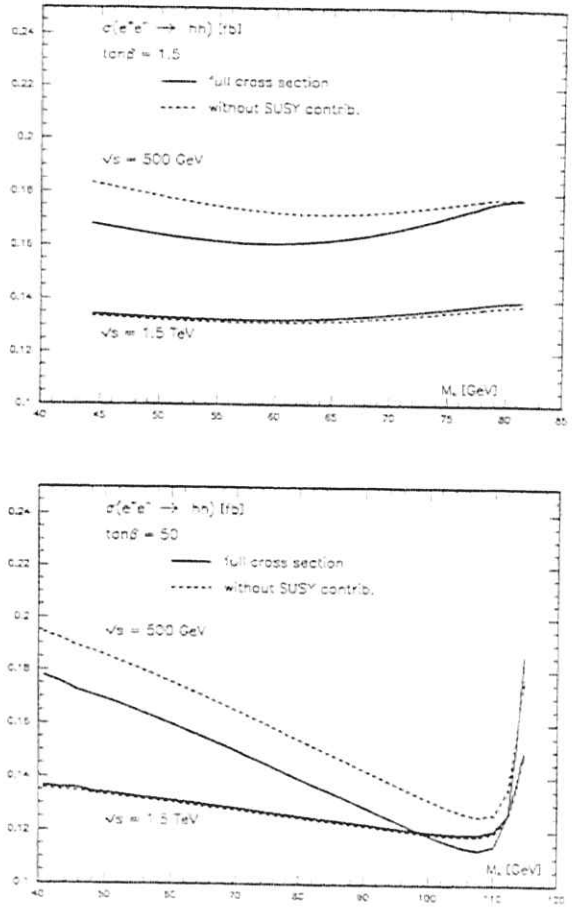

Fig. 3: The cross sections for $e^+e^- \to hh$ in the MSSM, as a function of M_h for $\sqrt{s} = 500$ GeV and $\sqrt{s} = 1.5$ TeV and for $\tan\beta = 1.5$ and 50. The solid curves correspond to the full cross sections, while the dashed curves correspond to the cross sections without the SUSY contributions.

contribution of the diagrams with $A/H^{\pm}$ exchange dominates. The latter contribution decreases with increasing M_h [i.e. with decreasing $\cos(\beta-\alpha)$], until the decoupling limit is reached for $M_h \simeq 110$ GeV. In this case, the factor $\sin(\beta-\alpha) \to 1$ and the W/Z boson loops are not suppressed anymore: one then obtains the SM cross section.

The contributions of the chargino/selectron and neutralino/sneutrino loops lead to a destructive interference. At high–energies, the supersymmetric boxes practically do not contribute; but at low energies, and especially below the decoupling limit, the SUSY contributions can be of the order of $\sim 10\%$. We have scanned the SUSY parameter space, and the maximum contribution of the SUSY loops that we have found was about $\sim -15\%$. In the decoupling limit, the SUSY contributions are, at most, of the order of a few percent. Because of the rather low production rates, it will therefore be difficult to experimentally see this effect.

4. Summary

We have discussed the one–loop induced production of Higgs boson pairs at future high–energy e^+e^- colliders in the SM and the MSSM. In the SM, the unpolarized cross section is rather small, of the order 0.1–0.2 fb. The longitudinal polarization of both the e^- and e^+ beams will increase the cross section by a factor of 4. With integrated luminosities $\int \mathcal{L} \gtrsim 100$ fb^{-1} as expected to be the case for future high–energy linear colliders, one could expect a few hundred events in the course of a few years if longitudinal polarization is available. The final states are rather clean, giving a reasonable hope to isolate the signals experimentally. In the MSSM, additional contributions to the processes $e^+e^- \to hh$ come from chargino/ neutralino and slepton loops. For hh production, the contributions of the supersymmetric loops are in general rather small, being of the order of a few percent; the cross sections are therefore of the same order as in the SM. For the processes involving heavy Higgs bosons, the cross sections are even smaller than for $e^+e^- \to hh$, and the signals will be hard to be detected experimentally.

References

[1] For reviews see, J. Gunion, H. Haber, G. Kane and S. Dawson, *The Higgs Hunter's Guide*. Addison–Wesley, Reading 1990; D. Haidt, P. Zerwas et al., Proceedings of the workshop e^+e^- *collisions at 500 GeV: The Physics Potential*, Munich–Annecy–Hamburg, DESY 92–123A+C, P.M. Zerwas (ed.); A. Djouadi, Int. J. Mod. Phys. A10 (1995)1.

[2] J. Ellis, M.K. Gaillard and D.V. Nanopoulos, Nucl. Phys. B106 (1976) 292; for recent discussions of the Higgs–$\gamma\gamma$ coupling in the MSSM see: G.L. Kane, G.D. Kribs, S.P. Martin and J.D. Wells, Phys. Rev. D53 (1996) 213; B. Kileng, P. Osland and P.N. Pandita, NORDITA-95-48-P (1995).

[3] For a discussion of the radiative corrections to the process $e^+e^- \to hZ$, see V. Driesen, W. Hollik and J. Rosiek, Report KA-TP-16-1995, hep-ph/9512441.

[4] K. Gaemers and F. Hoogeveen, Z. Phys. C26 (1984) 249.

[5] A. Djouadi, V. Driesen and C. Jünger, hep-ph/9602341. Phys. Rev. D (in press).

Search for the Higgs Bosons of the NMSSM at Linear Colliders

B. R. Kim[1], G. Kreyerhoff[1] and S. K. Oh[2]

[1] III. Physikalisches Institut A, RWTH Aachen, D-52056 Aachen, Germany

[2] Department of Physics, Kon-Kuk University, Seoul, Korea

Abstract

We show that at least one of the Higgs bosons of the Next to Minimal Supersymmetric Standard Model can be detected at future Linear Colliders of 500, 1000 and 2000 GeV c.m. energies.

1. Introduction

The Next to Minimal Supersymmetric Standard Model (NMSSM) [1–3] is a minimal extension to the Minimal Supersymmetric Standard Model [4]. The NMSSM provides the most economic solution of the so called μ-problem of the MSSM by introducing an additional Higgs singlet superfield $\mathcal{N} = (N, \psi_N, F_N)$ with a Higgs singlet N, a higgsino singlet ψ_N and an auxiliary field F_N. Together with the two Higgs doublets superfields $\mathcal{H}_{1,2} = (H_{1,2}, \psi_{1,2}, F_{1,2})$ the superpotential of the NMSSM is given by

$$W = \lambda \mathcal{H}_1^T \epsilon \mathcal{H}_2 \mathcal{N} - \frac{1}{3} k \Lambda^3 \tag{1}$$

The soft breaking part of the Higgs sector is given by

$$V_{soft} = -\lambda A_\lambda H_1^T \epsilon H_2 N - \frac{1}{3} k A_k N^3 - h.c. \tag{2}$$

where A_λ and A_k are soft breaking mass parameters.

H_1, H_2 and N develop vacuum expectation values v_1, v_2 and x respectively. The NMSSM contains three scalar Higgs bosons S_1, S_2 and S_3 with masses $m_{S_1} \leq m_{S_2} \leq m_{S_3}$, two pseudoscalar Higgs bosons P_1 and P_2 with masses $m_{P_1} \leq m_{P_2}$ and a charged one $H^\pm$ with mass m_C.

The Higgs sector has 6 free parameters $\lambda, k, \tan\beta = v_1/v_2, x, A_\lambda$ and A_k.

2. Constraints on parameters

A remarkable result of the MSSM is the tree level bound of $m_{S_1} \leq m_Z \cos 2\beta$. This is due to the fact that all quartic terms have gauge coupling constants. In case of the NMSSM there is a quartic term with the coupling constant λ. It turns out that the upper bound of λ may be relevant for m_{S_1}. An effective way of determining this bound is RG-analysis [1–8].

The one loop RG-equation of λ is coupled with that of k and h_t, the Yukawa coupling constant of the top quark (neglecting other quarks) and is given by

$$\begin{aligned}
\frac{d\lambda}{dt} &= \frac{1}{8\pi^2}\left(k^2 - 2\lambda^2 + \frac{3}{2}h_t^2 - \frac{3}{2}g_2^2 - \frac{1}{2}g_1^2\right)\lambda \\
\frac{dk}{dt} &= \frac{3}{8\pi^2}\left(k^2 + \lambda^2\right)k \\
\frac{dh_t}{dt} &= \frac{1}{8\pi^2}\left(\frac{1}{2}\lambda^2 + 3h_t^2 - \frac{8}{3}g_3^2 - \frac{3}{2}g_2^2 - \frac{13}{18}g_1^2\right)h_t
\end{aligned} \tag{3}$$

where $t = \ln\mu$ and μ being the renormalization scale. By demanding no Landau pole up to the GUT scale one can determine from eq. (4) the upper bound of λ and k and the lower bound of $\tan\beta$ at the electroweak scale. We plot our results in Fig. 1 (Fig. 2) for $m_t = 175$ GeV (190 GeV). They show that λ_{max} decreases with increasing k*. The lower bound of $\tan\beta$ is about 1.24 for $m_t = 175$GeV and 2.6 for $m_t = 190$GeV. For $\tan\beta \geq 3$ λ_{max} is almost independent on $\tan\beta$. The upper bound of k is about 0.7.

3. Mass upper bounds

The tree level bound of m_{S_i} is given by [3]

$$m_{S_i}^2 \leq m_Z^2\left(\cos^2 2\beta + \frac{2\lambda^2}{g_1^2 + g_2^2}\sin^2 2\beta\right) = m_{S_i^{max}}^2 \tag{4}$$

The upper bound of m_{S_2} and m_{S_3} can be expressed in terms of $m_{S_1^{max}}$ and m_{S_i}

$$\begin{aligned}
m_{S_2}^2 &\leq m_{S_2^{max}}^2 = \frac{m_{S_1^{max}}^2 - R_1^2 m_{S_1}^2}{1 - R_1^2} \\
m_{S_3}^2 &\leq m_{S_3^{max}}^2 = \frac{m_{S_1^{max}}^2 - (R_1^2 + R_2^2)m_{S_1}^2}{1 - (R_1^2 + R_2^2)}
\end{aligned} \tag{5}$$

where $R_i = U_{i1}\cos\beta - U_{i2}\sin\beta$ and U_{ij} is the 3×3 orthogonal matrix which diagonalizes the scalar mass matrix.

R_1 and R_2 satisfy the unitarity condition $0 \leq R_1^2 + R_2^2 \leq 1$. The tree level upper bound (4) yields $m_{S_1} \leq m_Z$ for $\lambda^2 \leq (g_1^2 - g_2^2)/2 = (0.52)^2$ and $m_{S_1} \leq \sqrt{2/(g_1^2 + g_2^2)}\lambda m_Z = 1.92\lambda m_Z$ for $\lambda^2 > (0.52)^2$. Using $\lambda_{max} = 0.64 - 0.74$ from section 2 the tree level relation yields $m_{S_1} \leq 113$GeV $- 131$GeV.

As in the case of the MSSM the contributions of radiative corrections may change this result considerably. Several groups calculated higher order contributions to the mass matrices using the one loop effective potential and determined the corrected upper bound [8–11].

*We obtain $\lambda_{max} = 0.64 - 0.74$ for $m_t = 175 - 190$ GeV.

The result in our notation [8] is given by

$$m_{S_1}^2 \leq m_Z^2 \left(\cos^2 2\beta + \frac{2\lambda^2}{g_1^2 - g_2^2} \sin^2 2\beta \right) + \alpha \cos^2 \beta + \beta \sin 2\beta + \gamma \sin^2 \beta \qquad (6)$$

with ($A_T = -A_t + \lambda x \cot \beta$)

$$\begin{aligned} \alpha &= -\frac{1}{16\pi^2} \left(\frac{\lambda x A_T}{v_1} \right)^2 \left(\frac{m_t}{m_t} \right)^4 \\ \beta &= \frac{3}{8\pi} \lambda x A_T \left(\frac{m_t^2}{m_t v_1} \right)^2 \left(1 + \frac{A_t A_T}{6 m_t^2} \right) \\ \gamma &= \frac{3}{8\pi} \left(\frac{m_t^2}{v_1^2} \right)^2 \left[2 \ln \frac{m_{\tilde{t}}^2}{m_t^2} - \frac{2 A_t A_T}{m_{\tilde{t}}^2} - \frac{A_t^2 A_T^2}{6 m_{\tilde{t}}^4} \right] \end{aligned} \qquad (7)$$

In this result only top and stop contributions were taken into account. We numerical calculated $m_{S_1^{max}}$ in the region $175\text{GeV} \leq m_t \leq 190\text{GeV}$, $250\text{GeV} \leq x, A_\lambda, A_t, m_{\tilde{t}} \leq 1000\text{GeV}$ and $2 \leq \tan\beta \leq 20$ and obtained [8]

$$120 \leq m_{S_1^{max}} \leq 156\text{GeV} \qquad (8)$$

4. Production of scalar Higgs bosons at e^+e^- Colliders

The upper bound $m_{S_1} \leq 120 - 156\text{GeV}$ suggests that the accessible area of the parameter space at LEP1 with $\sqrt{s} = m_Z$ might be very small. Actually we showed that the existing LEP1 data do not exclude the existence of S_1 with $m_{S_1} = 0\text{GeV}$ [12].

For colliders with $\sqrt{s} = 500, 1000$ or 2000GeV the situation is different. In this case the production cross section of one S_i via the Higgsstrahlung $e^+e^- \to ZS_i$ with real Z and S_i is always possible as the collider energy is larger than $E_T = 212 - 248\text{GeV}$. E_T is a kind of threshold energy and is an important quantity of a model.

In this case it is possible to derive a lower bound for the production cross section σ_i of S_i as a function of the collision energy only. This lower bound would give information about how far the model could be tested.

In order to derive the lower bound of σ_i we consider the production cross sections of S_1, S_2, S_3 via the Higgsstrahlungs process, denoted by $\sigma_1, \sigma_2, \sigma_3$, which can be expressed in terms of the standard model Higgs production cross section σ_{SM} and R_1 and R_2 defined in section 2:

$$\begin{aligned} \sigma_1(m_{S_1}) &= R_1^2 \sigma_{SM}(m_{S_1}) \\ \sigma_2(m_{S_2}) &= R_2^2 \sigma_{SM}(m_{S_2}) \\ \sigma_3(m_{S_3}) &= (1 - R_1^2 - R_2^2) \sigma_{SM}(m_{S_3}) \end{aligned} \qquad (9)$$

A useful observation is that $\sigma_i(m_{S_i}^{max}) \leq \sigma_i(m_{S_i})$ which allows one to derive parameter independent lower limits on σ_i as we will see in the following.

First we determine at a fixed set of m_{S_i}, R_1, R_2 the cross sections $\sigma_1(R_1, R_2, m_{S_1})$, $\sigma_2(R_1, R_2, m_{S_2^{max}})$ and $\sigma_3(R_1, R_2, m_{S_3^{max}})$. Then we keep R_1 and R_2 fixed, but vary m_{S_i} from its minimum to its maximum value and determine the quantity $\sigma(R_1, R_2)$ defined by

$$\sigma(R_1, R_2) = \min_{0 \leq m_{S_i} \leq m_{S_i^{max}}} [\max(\sigma_1, \sigma_2, \sigma_3)] \qquad (10)$$

where $\sigma_1 = \sigma_1(R_1, R_2, m_{S_1})$, $\sigma_2 = \sigma_2(R_1, R_2, m_{S_2^{max}})$ and $\sigma_3 = \sigma_3(R_1, R_2, m_{S_3^{max}})$. As a last step we vary R_1^2 and R_2^2 from 0 to 1 with $R_1^2 + R_2^2 \leq 1$ and plot $\sigma(R_1, R_2)$ in the R_1-R_2-plane. It is plausible that $\sigma(R_1, R_2) = 0$ for $\sqrt{s} < E_T = m_z + m_{S_1^{max}} = 212 - 248\text{GeV}$ in the entire R_1-R_2-plane. This is the case for LEP2 with $\sqrt{s} \leq 205$ GeV. Therefore this method does not give any results for LEP2. For $\sqrt{s} > E_T$ $\sigma(R_1, R_2)$ never vanishes and the minimum of $\sigma(R_1, R_2)$ is a parameter independent lower limit of one of the σ_i. This minimum is thus a characteristic quantity of the model.

In Fig. 3 we plotted $\sigma(R_1, R_2)$ for $\sqrt{s} = 500$ GeV and $m_{S_1^{max}} = 145$ GeV. The minimum is about 16 fb. When the discovery limit is about 30 events, one would need a luminosity of about 25 fb, which is a realistic one. Fig. 4 (Fig. 5) shows $\sigma(R_1, R_2)$ for $\sqrt{s} = 1000(2000)$ GeV with minimum cross section of 4 fb (1 fb). Fig. 6 shows the minimum of $\sigma(R_1, R_2)$ as a function of $\sqrt{s}$ and $m_{S_1^{max}}$ as a parameter. We see that the effect of $m_{S_1^{max}}$ on σ_{min} is very big around $\sqrt{s} = 300$ GeV, but rather small for $\sqrt{s} \geq 500$ GeV.

Fig. 7 shows the tree level cross sections σ_1, σ_2 and σ_3 for an exemplary set of parameters with the contributions from (i) the Higgsstrahlungsprocess $e^+e^- \to ZS_i \to b\bar{b}S_i$, (ii) the process where S_i is radiated off from b or $\bar{b}$ and (iii) $e^+e^- \to Z \to P_jS_i \to b\bar{b}S_i$, where $P_j (j = 1, 2)$ is a pseudoscalar Higgs boson.

Fig. 8 shows the same as Fig. 7, but with one loop contributions via the effective potential. The higher order contribution is rather important for the energy region around 150 GeV and decreases with $\sqrt{s}$. In this parameter region the dominant production is that of S_2 at $\sqrt{s} = 500$ GeV and is about 13 fb.

We conclude that the Higgs sector of the NMSSM can most probably be tested conclusively at the future linear e^+e^--colliders with 500, 1000 or 2000 GeV c.m. energies.

References

[1] J. P. Deredinger and C. A. Sarvoy, Nucl. Phys. **B237** (1984) 307

[2] J. Ellis, J. E. Ellis, J. E. Gunion, H. E. Haber, L. Roszkowski and F. Zwirner, Phys. Rev. **D39** (1989) 844

[3] M. Drees, Int. J. Mod. Phys. **A4** (1989) 3635

[4] H. P. Nilles, Phys. Rep. **110** (1984)
H. E. Haber and G. L. Kane, Phys. Rep. 117 (1985) 75

[5] J. R. Espinosa and M. Quiros, Phys. Lett. **B279** (1992) 92

[6] P. Binetury and C. A. Savoy, Phys. Lett. **B277** (1992) 453

[7] U. Ellwanger and M. Lindner, Phys. Lett. **B301** (1993) 365

[8] B. R. Kim and S. K. Oh, PITHA 94/46, 1994

[9] P. N. Pandita, Z. Phys. C59 (1993) 575

[10] U. Ellwanger, Phys. Lett. **B303** (1993) 271

[11] T. Elliot, S. F. King and P. L. White, Phys. Rev. **D49** (1994) 2435

[12] B. R. Kim, S. K. Oh and A. Stephan, in *Proceedings of the Workshop on Physics and Experiments with Linear e^+e^--Colliders*, eds. F. A. Harris et. al., World Scientific (Singapure 1993) p. 860

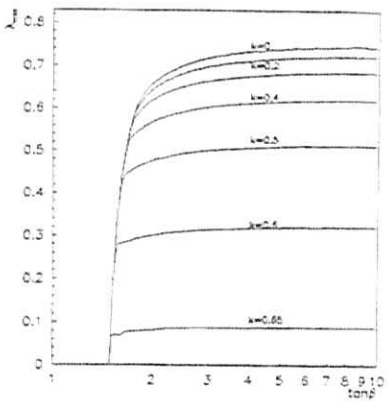

Figure 1: Upper bound for λ as a funtion of $\tan\beta$ for $m_{top} = 175$ GeV.

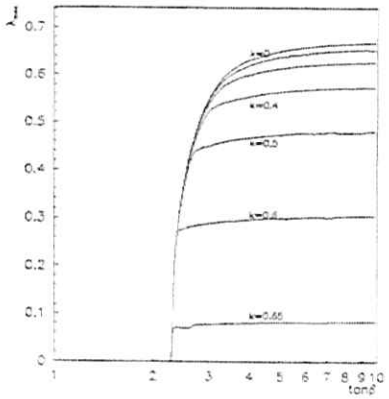

Figure 2: Upper bound for λ as a funtion of $\tan\beta$ for $m_{top} = 190$ GeV.

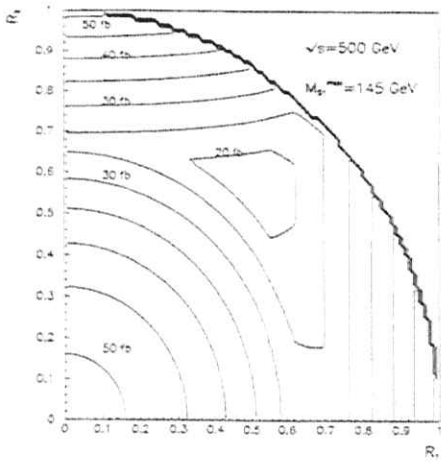

Figure 3: $\sigma(R_1, R_2)$ as definded in the text for $\sqrt{s} = 500$ GeV.

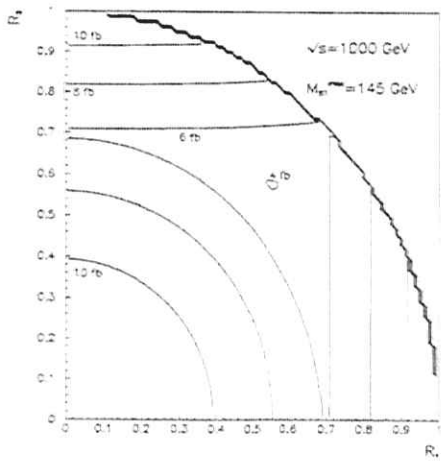

Figure 4: $\sigma(R_1, R_2)$ for $\sqrt{s} = 1000$ GeV.

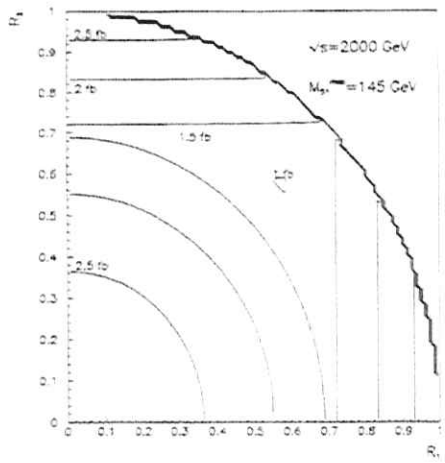

Figure 5: $\sigma(R_1, R_2)$ for $\sqrt{s} = 2000$ GeV.

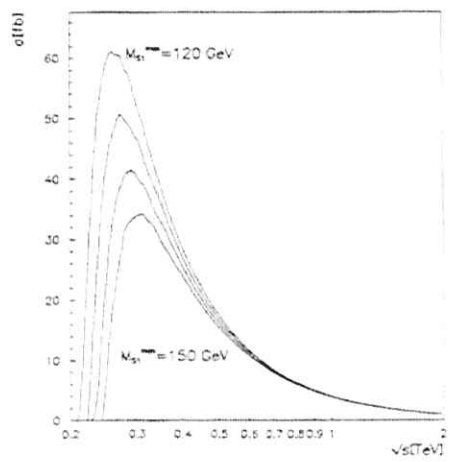

Figure 6: Minimal value of $\sigma(R_1, R_2)$ as a function of $\sqrt{s}$ for various values of $m_{\tilde{S}_1^{max}}$

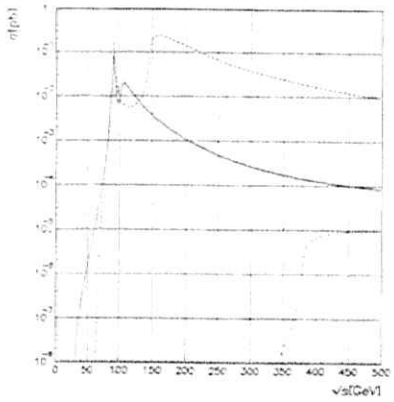

Figure 7: Cross section for $e^+e^- \rightarrow Z\tilde{b}\bar{\tilde{b}}$ for $A_\lambda = 220$ GeV, $A_k = 160$ GeV, $x = 1000$ GeV, $\tan\beta = 2, k = 0.04, \lambda = 0.12$. Masses and mixing angles have calculated from the tree level protential.

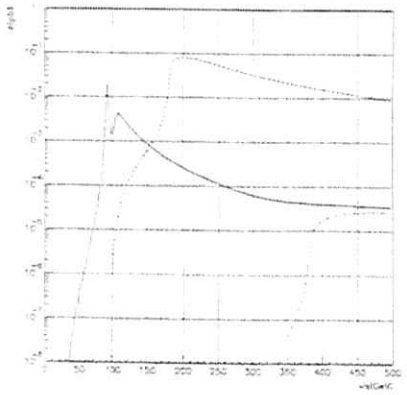

Figure 8: The same as above, but with masses and mixing angles obtained from the one loop effective potential. The top mass is 175 GeV, $m_{\tilde{t}_L} = m_{\tilde{t}_R} = 1$ TeV and $A_t = 0$ GeV.

Electroweak Gauge Bosons

P. Boudjema[1], G. Gounaris[2], J. D. Hansen[3] and K. Mönig[4]

[1] *ENSLAPP-Annecy, France*
[2] *University of Thessaloniki, Greece*
[3] *Niels Bohr Inst. , Denmark*
[4] *CERN, Switzerland*

The electroweak gauge bosons will be produced in abundance in all modes of the linear collider: e^-e^- , e^-e^- , $\gamma\gamma$ and $e\gamma$. Indeed cross sections for the production of Z and W's will be much larger than the usual pair production of fermions and therefore could constitute some large backgrounds in the search for New Physics. An exhaustive list of cross sections for up to four vector boson production is now available[1]. Moreover the full radiative corrections to the main two body processes ($e^+e^- \to W^-W^-$, $\gamma\gamma \to W^+W^-$ and $e\gamma \to W\nu$) have been performed[2].

At the same time, the detailed study of the properties of the electroweak gauge bosons that the clean environment of the e^-e^- collider allows, could hold the clue to the mechanism of symmetry breaking, $\mathcal{SB}$. This is because the Goldstone Bosons that are essentially a reflection of the longitudinal degree of freedom of the gauge bosons originate from this sector, as does the Higgs.

In this respect Higgs production can be exploited to probe $\mathcal{SB}$. To this aim, a detail study of the collisions $\gamma\gamma \to W^+W^-$, ZZ , $Z\gamma$, $\gamma\gamma$, H , HH and $e^-e^- \to HZ$, $H\gamma$, has been performed and the observable effects of all possible $dim = 6$, $SU(2) \times U(1)$ gauge invariant operators were analysed, in the framework of a linear representation of $\mathcal{SB}$. The sensitivities to the strength of the New Physics (NP) interactions described by the aforementioned operators for an e^-e^- collider at energies between 500 and 2000GeV have been investigated. Unitarity considerations for each operator have been used to translate these sensitivities into magnitudes of NP scales which can possibly be felt in the e^-e^- colliders. The Montpellier Thessaloniki group[3] finds that one could attain scales of a few tens of TeV in boson pair processes and up to 65TeV in single Higgs production.

On the other hand, especially if the Higgs is too heavy or not present, the W's are our best window on $\mathcal{SB}$. In this case one needs to perform precision measurements involving a variety of observables provided by different W production mechanisms. In this respect W production both in the e^-e^- and $\gamma\gamma$ mode offers probably the best prospect, through tests of the so-called anomalous couplings of the W. The already detailed investigations that have been performed in the previous Workshops have been improved and carried over to the higher energy regime, above the TeV scale. On the theoretical side there is now a general consensus to express these anomalies through an explicit gauge invariant formulation which leads to a hierarchy of couplings. It is important to stress that the LEP data do now require the genuine non-Abelian contributions[4] and indirectly suggest a natural order for the expected magnitude on the parameters of the effective Lagrangian. For instance one expects $\Delta\kappa$ of order $O(10^{-3})$. The studies on W pair production do show that this order of magnitude can well be experimentally resolved already with a 500GeV collider[5, 6, 7] with yet about an order of magnitude improvement at $1.5-2$TeV[8, 9]. As an example, the contribution of the supersymmetric spectrum to these tri-linear couplings has been found[10] to be of the above order. Therefore one could hope to indirectly probe some supersymmetric particles before one reaches their threshold. Note however, that in this case, one should rely on the full supersymmetric contribution to $e^-e^- \to W^-W^-$. For instance, box effects that can not be parameterised through tri-linear couplings are non-negligible.

Considerable improvement in the extraction of the self-couplings of the W, especially in $e^+e^- \to W^-W^-$, has been achieved with more realistic simulations of the experimental situation[9, 6] as well as more powerful fitting procedures [5, 6, 7]. Most analyses now exploit the full information contained in all the available kinematical variables provided by the four-fermion final states, rather than the restricted angular distribution at the level of the W. At the same time since binning in the full 5-dimensional variables requires high statistics, a χ^2 fit (as had been done previously when using few variables) is not the optimum way of extracting these couplings. Most analyses now rely on the maximum likelihood method. Another alternative has been suggested based on using *optimal observables*[11]. Initial state polarisation is easily implemeted and is of some help in improving the limits[8]. Although most studies restrict their analysis to the semi-leptonic decay mode of the W pair, it has been found that one should also exploit the other modes, notably the all-jets events[6]. The impact of the 4-fermion final states background not mediated by the W has also been investigated with the conclusion that it can be brought under control and does not degrade the results based on the resonant WW contribution[7]. Another important aspect that has also been addressed[6, 9] and which is particularly crucial as the energy of the collider increases is due beamstrahlung. The latter induces a large energy loss that can lead to a biais which is larger than the expected precision on the couplings one wishes to extract. Luckily, it has been shown that this can be easily taken care of, at the expense of some little loss in the precision on the measurement of the couplings. However, since the large energy loss due to beamstrahlung prohibits the use of constrained fitting techniques proposed for lower energies, a good detector resolution becomes more important.

Compared to the results that one would obtain from the LHC concerning the limits on the tri-linear couplings, the NLC fares better, even with $\sqrt{s} = 500GeV$[7]. Unfortunately, it is not as constraining as regards the quartic couplings if the e^-e^- energy is below 1TeV. Going higher in energy, the effective W luminosity becomes substantial enough to allow for the study of WW scattering. Most interesting is W_LW_L that may reveal new resonances and a new regime for the electroweak interaction. In fact, even in this eventuality the $e^-e^- \to W^-W^-$ cross section is very useful since it could be exploited to extract the strong rescattering effect, $WW \to VV$. For instance, Barklow[8]finds that with a luminosity of $80fb^{-1}$ one could exclude a techni-rho vector boson up to a mass of about 2.5TeV. At 1.5TeV a 2TeV techni-rho would produce a 37σ signal while that with a 6TeV mass to 4.8σ. Of course with these energies scalar dominated models can be probed through the effective W contained in the electron in $e^-e^- \to l\!\!l V_1V_2$. For these models, and with 1.5-2TeV the NLC is very competitive with the LHC. The combination of these two machines will thus be invaluable and will probe all the currently discussed scenarios of $S\!B$.

The $\gamma\gamma \to W^-W^-$ channel, especially when combined with the conventional $e^-e^- \to W^-W^-$ mode can be most welcome[7]. Because of the importance of this channel and the very large statistics that it offers, the full radiative corrections have been calculated[12]. There is perfect agreement between two independent calculations[2]. One of the characteristics of the effect of these corrections is that they do not involve those usually large corrections, like those associated to the running of α (because the photons are real) as well as the usual collinear logs. Moreover a heavy Higgs decouples. On the other hand, especially at very high energies, purely bosonic loops from boxes and triangles (WW rescattering) can be large. The extraction of the anomalous couplings in this channel has also been improved by taking into account the full 4-fermion final state and relying on the maximum likelihood method[7]. In conjuction with $e^-e^- \to W^-W^-$ one can reach much better precision on these couplings.

The $e\gamma$ mode has also been re-investigated[13], not only in probing the anomalous couplings but also as a means for producing a right-handed W and heavy neutrino as predicted in left-right models. This channel does not seem to compete with the $\gamma\gamma \to W^-W^-$ and $e^-e^- \to W^-W^-$ mode as concerns the self-couplings.

W^- pair production in e^-e^- has also been investigated afresh[14]. Observation of this process would be a sign for lepton number violation and thus a good test on new physics, like for instance the presence of Majorana neutrinos. It is found that although present constraints on neutrino masses and mixings, as well as unitarity considerations, could allow for a signal at a linear collider in 0.5-2TeV, the constraints from neutrinoless

double beta decay are so strong that only extremely contrived and unnatural scenarios could possibly lead to a signal.

References

[1] M. Baillargeon et al., *Cross sections for electroweak boson production.*

[2] For a nice review on the radiative corrections to $e^-e^- \to W^-W^-$ and related issues, see W. Beenakker and A. Denner, *Int. J. Mod. Phys.* **A9** (1994) 4837. The effect of radiative corrections on $e\gamma \to e\gamma, eZ$ and W_L is summarised by A. Denner and S. Dittmaier in Part C of the DESY e^-e^- Proceedings, DESY-93-123C, p. 171, edited by P. Zerwas. Radiative to $\gamma\gamma \to W^-W^-$ are discussed in this volume, see the contributions of G. Jikia and A. Denner, S. Dittmaier and R. Schuster.

[3] G. J. Gounaris et al., *Residual new physics effects in e^-e^- and $\gamma\gamma$ collisions at NLC.*

[4] S. Dittmaier, D. Schildknecht and G. Weiglein, BI-TP 95/31, hep-ph/9510386; S. Dittmaier, D. Schildknecht and M. Kuroda Nucl. Phys. **B426** (1994); P. Gambino and A. Sirlin, Phys. Rev. Lett. **73** (1994) 621.

[5] R.L. Sekulin, *Aspects of the determination of triple gauge coupling from $e^-e^- \to W^-W^-$ at 500GeV.*

[6] J. B. Hansen and J. D. Hansen, *Measuring trilinear gauge couplings at 500 GeV.*

[7] M. Baillargeon et al., *Anomalous couplings and chiral Lagrangians; an update.*

[8] T.Barklow, SLAC-PUB-6618, Aug. 1994.

[9] K. Moenig, *Measurements of the three boson couplings at 2TeV.*

[10] A. Ahrib, J.L. Kneur and G. Moultaka, CERN-TH-/95-344, hep-ph/9512437.

[11] M. Diehl and O. Nachtman, *Optimal observables for measuring three-gauge-boson couplings in $e^-e^- \to W^-W^-$.*

[12] A. Denner, S. Dittmaier and R. Schuster, *Electroweak radiative corrections to $\gamma\gamma \to W^-W^-$.*

[13] K. Huitu, J. Maalampi and M. Raidal, *Single-W boson production in $e^-\gamma$ colliders.*

[14] G. Bélanger, F. Boudjema, D. London and H. Nadeau, *Majorana neutrinos in $e^-e^- \to W^-W^-$ and neutrinoless double beta decay.*

Cross Sections for Electroweak Boson Production at the Linear Collider

M. Baillargeon[1], G. Bélanger[2], F. Boudjema[2], K. Cheung[3], F. Cuypers[4] G. Jikia[5], K. Kolodziej[6] and Y. Kurihara[7]

[1] *GTAE, Lisbon, Portugal*
[2] *ENSLAPP-Annecy, France*
[3] *University of Texas, Austin, USA*
[4] *PSI, Switzerland*
[5] *IHEP, Protvino, Russia*
[6] *Inst. of Physics, Katowice, Poland*
[7] *Minami-Tateya, KEK, Japan*

Once the thresholds for W and Z production open up, the cross sections for the production of the electroweak gauge bosons quickly pick up to the point that the linear collider can be considered as a W factory. This occurs in all modes of the collider: e^-e^-, e^-e^+, $e\gamma$ and $\gamma\gamma$, even if it is more pronounced in the photon mode (see Figs 1, 2). For the linear collider energies these cross sections are much larger than the usual pair production of fermions and therefore they have to be known quite precisely since they could be potential backgrounds to searches for new physics. Note, however, that for the largest cross sections, the W's are rather forward. Nonetheless, even after imposing moderate cuts these processes correspond to large W and Z yields. For many W processes, contrary to typical s-channel annihilation reactions one will be doing "pb physics".
It is also worth observing, that within the SM , all the W and Z processes in e^-e^- have an equivalent process in the e^-e^- mode with roughly the same total cross section, Fig. 1. Radiative corrections to all the two-body production mechanisms have now been performed[1]. Higher order corrections to single W production in e^-e^- and e^-e^-, which are dominated by a t-channel photon exchange, can be implemented by correcting the process $e\gamma \to W\nu$ and convoluting with the photon flux.

A remaining challenge is to take into account the finite width of the massive bosons. This will lead to multi-fermion final states which have to be combined with non-resonating contributions (not proceeding through a W or a Z). In the case of 4-fermion final states in e^-e^-, many programs exist and agree very well at LEP2 energies[2]. However they have to be optimised when going to high energies. A similar analysis for the 4-fermion final state in $\gamma\gamma$ is in progress[3]. One may, at high energy, need to consider processes with more than 4-final states.

References

[1] For a nice review on the radiative corrections to $e^-e^- \to W^-W^-$ and related issues, see W. Beenakker and A. Denner, *Int. J. Mod. Phys.* **A9** (1994) 4837. The effect of radiative

Figure 1: *Typical sizes of cross sections for weak boson production in e^-e^- and e^-e^+. No polarisation is assumed.*

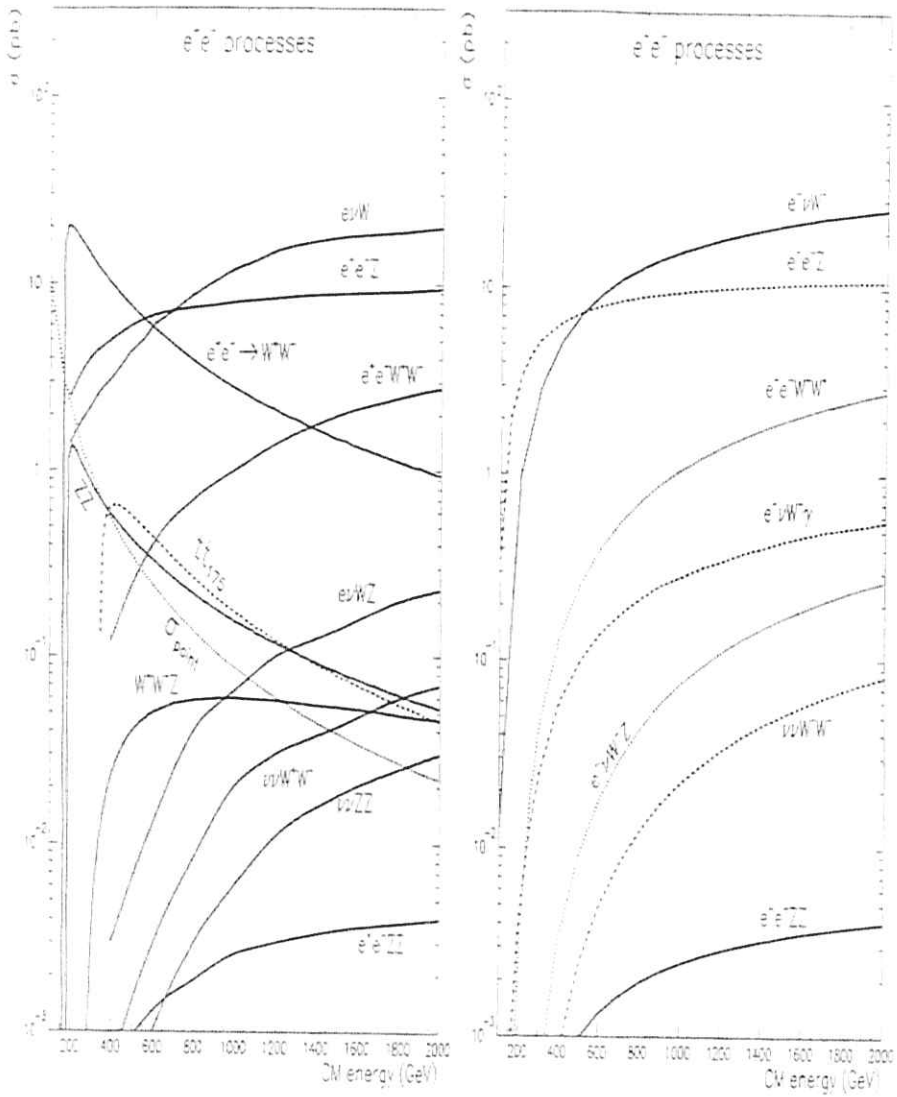

Figure 2: *Typical sizes of cross sections for weak boson production in $\gamma\gamma$ and $e\gamma$. No polarisation is assumed. If not indicated the dotted curves correspond to the $e\gamma$ mode. For Higgs production, $M_H = 100GeV$. The one-loop induced $\gamma\gamma \to ZZ$ is shown for both $M_H = 300GeV$ and $M_H = 800GeV$. For the latter the resonance does not stand out.*

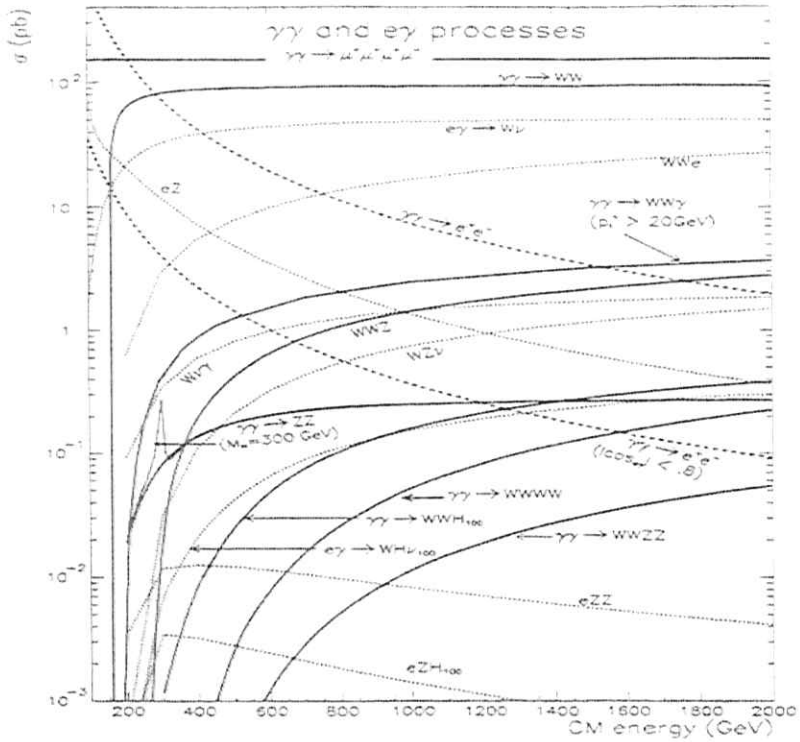

corrections on $e\gamma \to e\gamma$, eZ and $W\nu$ is summarised by A. Denner and S. Dittmaier in Part C of the DESY e^+e^- Proceedings, DESY-93-123C, p. 171, edited by P. Zerwas. Radiative to $\gamma\gamma \to W^+W^-$ are discussed in this volume, see the contributions of G. Jikia and A. Denner, S. Dittmaier and R. Schuster.

[2] 4-fermion processes are discussed at length in the LEP2 Yellow Book, CERN 1996 in Press, edited by G. Altarelli, T. Sjöstrand and F. Zwirner. See in particular the *Standard Model Processes* and *Event Generators for WW Physics* contributions.

[3] M. Baillargeon, G. Bélanger and F. Boudjema, in Progress.

Electroweak Radiative Corrections to $\gamma\gamma \to W^+W^-$

A. Denner[1], S. Dittmaier[2] and R. Schuster[1,*]

[1] *Institut für Theoretische Physik, Universität Würzburg, Germany*

[2] *Theoretische Physik, Universität Bielefeld, Germany*

1 Introduction

A particularly interesting process at $\gamma\gamma$ colliders is W-pair production. Its total cross-section approaches a constant of about 80 pb at high energies corresponding to 8×10^5 W pairs for $10\,\mathrm{fb}^{-1}$. Although this large cross-section is drastically reduced by angular cuts, even for $|\cos\theta| < 0.8$ it is still 15 and 4 pb at a center-of-mass energy of 500 and 1000 GeV, respectively, and thus much larger as e.g. the one for $e^+e^- \to W^+W^-$. Hence $\gamma\gamma \to W^+W^-$ is very well-suited for precision investigations of the SM.

Most of the existing works on $\gamma\gamma \to W^+W^-$ concentrated on tree-level predictions and on the influence of anomalous non-Abelian gauge couplings [1–3]. At tree level, the process $\gamma\gamma \to W^+W^-$ depends both on the triple γWW and the quartic $\gamma\gamma$WW coupling, and no other vertices are involved in the unitary gauge. The sensitivity to the γWW coupling is comparable and complementary to the reactions $e^+e^- \to W^+W^-$ and $e^-\gamma \to W^-\nu$ [2]. Because the sensitivity to the $\gamma\gamma$WW coupling is much larger than the one in e^+e^- processes, $\gamma\gamma \to W^+W^-$ is the ideal process to study this coupling [3].

The one-loop diagrams involving a resonant Higgs boson have been calculated in order to study the possible investigation of the Higgs boson via $\gamma\gamma \to H^* \to W^+W^-$ [4–7]. Based on our complete one-loop calculation [8], we have supplemented these investigations by a discussion of the heavy-Higgs effects in Ref. [9]. As a matter of fact, only the (suppressed) channels of longitudinal W-boson production are sensitive to the Higgs mechanism, but the (dominant) channels of purely transverse W-boson production are extremely insensitive. This insensitivity to the Higgs sector renders $\gamma\gamma \to W^+W^-$ even more suitable for the investigation of the non-Abelian self couplings.

In this paper we summarize our results for the *complete* virtual and soft-photonic $\mathcal{O}(\alpha)$ corrections. We give a survey of the leading corrections and restrict the numerical discussion to unpolarized W bosons. More detailed results and a discussion of their evaluation can be found in Refs. [8,9].

*Supported by the Deutsche Forschungsgemeinschaft.

2 Lowest-order cross-section

The Born cross-section of $\gamma\gamma \to W^+W^-$ is given by the formulae

$$\left(\frac{\mathrm{d}\sigma}{\mathrm{d}\Omega}\right)^{\mathrm{Born}}_{\mathrm{unpol}} = \frac{3\alpha^2\beta}{2s}\left\{1 - \frac{2s(2s-3M_W^2)}{3(M_W^2-t)(M_W^2-u)} + \frac{2s^2(s^2+3M_W^4)}{3(M_W^2-t)^2(M_W^2-u)^2}\right\} \tag{1}$$

for the unpolarized differential cross-section and

$$\sigma^{\mathrm{Born}}_{\mathrm{unpol}} = \frac{6\pi\alpha^2}{s}\beta\cos\theta_{\mathrm{cut}}\left\{1 - \frac{4M_W^2(s-2M_W^2)}{s^2\beta\cos\theta_{\mathrm{cut}}}\log\left(\frac{1-\beta\cos\theta_{\mathrm{cut}}}{1+\beta\cos\theta_{\mathrm{cut}}}\right) + \frac{16(s^2+3M_W^4)}{3s^2(1-\beta^2\cos^2\theta_{\mathrm{cut}})}\right\} \tag{2}$$

for the unpolarized cross-section integrated over $\theta_{\mathrm{cut}} < \theta < 180^\circ - \theta_{\mathrm{cut}}$. Here $\beta = \sqrt{1-4M_W^2/s}$ denotes the velocity of the W bosons and s, t, and u are the usual Mandelstam variables. Concerning kinematics, polarizations, input parameters, etc., we follow the conventions of Ref. [8] throughout.

As can be seen from Table 1, the lowest-order cross-sections are dominated by transverse (T) W bosons. The massive t-channel exchange gives rise to a constant cross-section at high energies, $s \gg M_W^2$, for $\theta_{\mathrm{cut}} = 0$

$$\sigma^{\mathrm{Born}}_{\pm\pm\mathrm{LL}}, \sigma^{\mathrm{Born}}_{\pm\mp\mathrm{LL}} \xrightarrow{s\to\infty} \sigma^{\mathrm{Born}}_{\pm\pm\mathrm{TT}}, \sigma^{\mathrm{Born}}_{\pm\mp\mathrm{TT}} \xrightarrow{s\to\infty} \frac{8\pi\alpha^2}{M_W^2} = 80.8\,\mathrm{pb}. \tag{3}$$

For a finite cut, $\sigma^{\mathrm{Born}}_{\pm\pm\mathrm{LU}}$ and $\sigma^{\mathrm{Born}}_{\pm\mp\mathrm{LU}}$ behave as $1/s$ for large s. This is illustrated in Fig. 1 for two different angular cuts $\theta_{\mathrm{cut}} = 10^\circ, 20^\circ$. Close to threshold the differential and integrated cross-sections for all polarization configurations vanish like β.

3 Leading corrections

Electroweak radiative corrections contain leading contributions of universal origin. In the on-shell renormalization scheme with input parameters α, M_W, M_Z these affect the corrections to $\gamma\gamma \to W^+W^-$ as follows:

- Since the *two* external photons are on mass shell, the relevant effective coupling is the one at zero-momentum transfer and the running of α is not relevant.

$\sqrt{s}$/GeV	θ	unpol.	$\pm\pm$TT	$\pm\pm$LL	$\pm\mp$TT	$\pm\mp$LL	$\pm\mp$(LT + TL)
500	$0° < \theta < 180°$	71.6	32.2	6.10×10^{-2}	70.2	9.99×10^{-1}	1.66
	$20° < \theta < 160°$	36.7	42.7	3.17×10^{-2}	25.2	9.89×10^{-1}	1.46
1000	$0° < \theta < 180°$	80.1	52.8	3.54×10^{-3}	76.9	2.52×10^{-1}	1.70×10^{-1}
	$20° < \theta < 160°$	14.2	16.8	7.18×10^{-4}	11.2	2.44×10^{-1}	1.21×10^{-1}
2000	$0° < \theta < 180°$	80.6	81.6	2.14×10^{-4}	73.5	6.41×10^{-2}	1.30×10^{-2}
	$20° < \theta < 160°$	4.07	4.84	1.27×10^{-5}	3.23	6.11×10^{-2}	8.26×10^{-3}

Table 1: *Lowest-order integrated cross-sections in pb for several polarizations, the lowest-order cross-section for* $\pm\mp$(LT + TL) *vanishes.*

- In order to handle the Higgs-boson resonance at $s = M_H^2$, in the literature [5–7] the Higgs-boson width has been introduced naïvely by the replacement

$$\frac{F^H(s)}{s - M_H^2} \longrightarrow \frac{F^H(s)}{s - M_H^2 + \mathrm{i}M_H\Gamma_H} \tag{4}$$

  in the resonant contribution. However, this treatment destroys gauge invariance at the level of non-resonant $O(\alpha)$ corrections. In order to preserve gauge invariance, we decompose the Higgs-resonance contribution into a gauge-invariant resonant part and a gauge-dependent non-resonant part and introduce Γ_H only in the former:

$$\frac{F^H(s)}{s - M_H^2} \longrightarrow \frac{F^H(M_H^2)}{s - M_H^2 + \mathrm{i}M_H\Gamma_H} + \frac{F^H(s) - F^H(M_H^2)}{s - M_H^2}. \tag{5}$$

- Outside the region of Higgs resonance the Higgs-mass dependence is small for unpolarized W bosons. For all polarizations no corrections involving $\log(M_H/M_W)$ or M_H^2/M_W^2 arise in the heavy-Higgs limit [9]. However, for $\sqrt{s} \gg M_H \gg M_W$ corrections proportional to M_H^2/M_W^2 appear for the cross-sections involving longitudinal (L) gauge bosons as a remnant of the unitarity cancellations. These terms give rise to large effects in particular for cross-sections with longitudinal W bosons.

- The top-mass-dependent corrections are also small and behave similar to the Higgs-mass-dependent corrections for $\sqrt{s} \gg m_t \gg M_W$: more precisely neither corrections proportional to m_t^2 nor proportional to $\log m_t$ occur in this limit for fixed M_W.

- As $\gamma\gamma \to W^+W^-$ involves no light charged external particles, no large logarithmic corrections associated with collinear photons show up (apart from the region of very high energies, $s \gg M_W^2$). As a consequence, the photonic corrections are not enhanced with respect to the weak corrections.

- Close to threshold, i.e. for $\beta \ll 1$, the Coulomb singularity gives rise to the large universal correction

$$\delta\sigma^{\mathrm{Coul}} = \frac{\alpha\pi}{2\beta}\sigma^{\mathrm{Born}}. \tag{6}$$

  The factor β^{-1} is typical for the pair production of stable (on-shell) particles. For the generalization to unstable (off-shell) particles see Ref. [10].

At high energies, $s \gg M_W^2$, the radiative corrections are dominated by terms like $(\alpha/\pi)\log^2(s/M_W^2)$, which arise from vertex and box diagrams. At 1 TeV these are about 10%, setting the scale for the (weak) radiative corrections at this energy.

4 Numerical results

Electromagnetic and genuine weak corrections cannot be separated in a gauge-invariant way on the basis of Feynman diagrams. As no leading collinear logarithms occur in $\gamma\gamma \to W^+W^-$, the only source of enhanced photonic corrections are the soft-photon-cut-off-dependent terms which yield the relative correction

$$\delta_{\mathrm{cut}} = -\frac{2\alpha}{\pi}\log\left(\frac{\Delta E}{E}\right)\left(1 - \frac{s - 2M_W^2}{s\beta}\log\frac{1+\beta}{1-\beta}\right). \tag{7}$$

Since we are mainly interested in the weak corrections, we discard the (gauge-invariant) cut-off-dependent terms (7) by setting the soft-photon cut-off energy ΔE equal to the beam energy E and consider the rest as a suitable measure of the weak corrections. If not stated otherwise, the correction δ stands in the following for the complete relative soft-photonic and virtual electroweak corrections with $\Delta E = E$.

Figure 1 shows the "weak" corrections to the total cross-sections integrated over $10° \le \theta \le 170°$ and $20° \le \theta \le 160°$ for unpolarized W bosons. The corrections for different photon polarizations almost coincide with each other and reach roughly -20% for $\theta_{\mathrm{cut}} = 10°$ and -35% for $\theta_{\mathrm{cut}} = 20°$ at $\sqrt{s} = 2\,\mathrm{TeV}$. At low energies the cross-sections with equal photon and W boson helicities are dominated by the Higgs resonance. Note that owing to helicity conservation the other cross-sections are not affected by the Higgs resonance.

In Table 2 we list the unpolarized cross-sections and the corresponding corrections for several energies and scattering angles. We include the corrections for a soft-photon-energy cut-off $\Delta E = 0.1E$, i.e. the cut-off-dependent corrections δ_{cut} from (7), and the individual (gauge-invariant) fermionic δ_{ferm} and bosonic corrections δ_{bos}. The fermionic corrections consist of all loop diagrams and counterterm contributions involving fermion loops, all

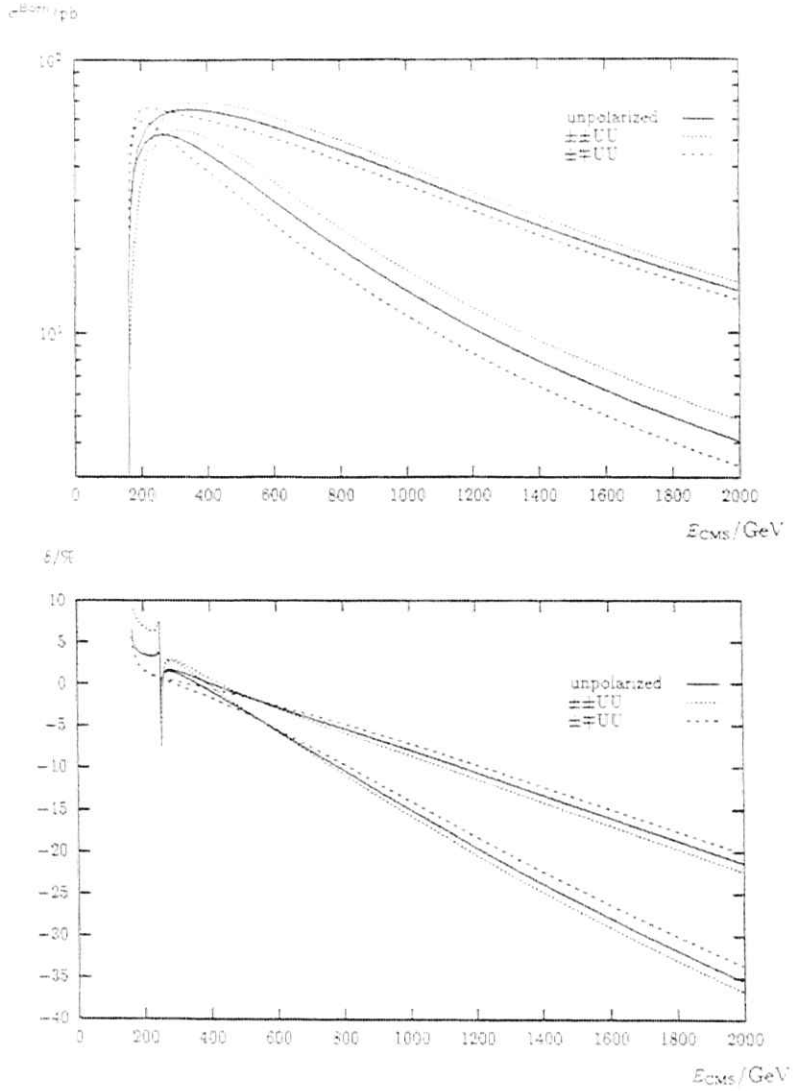

Figure 1: *Integrated lowest-order cross-sections and corresponding relative corrections for an angular cut $10^\circ \leq \theta \leq 170^\circ$ (upper set of curves in each plot) and $20^\circ \leq \theta \leq 160^\circ$ (lower set).*

$\sqrt{s}$/GeV	θ	$\sigma^{\rm Born}$/pb	$\delta_{\Delta E=1\,\mathrm{GeV}}$/%	$\delta_{\rm rad}$/%	$\delta_{\Delta E=E}$/%	$\delta_{\rm bos}$/%	$\delta_{\rm ferm}$/%
500	5°	98.13	0.02	−2.79	2.81	1.49	1.32
	20°	26.04	−2.68	−2.79	0.11	−0.08	0.19
	90°	0.724	−10.79	−2.79	−8.00	−5.62	−2.38
	$0^\circ < \theta < 180^\circ$	77.55	−3.38	−2.79	−0.59	−0.65	0.06
	$10^\circ < \theta < 170^\circ$	60.74	−4.27	−2.79	−1.48	−1.21	−0.27
	$20^\circ < \theta < 160^\circ$	36.67	−6.06	−2.79	−3.27	−2.39	−0.89
1000	5°	291.9	−2.06	−4.31	2.25	1.04	1.21
	20°	15.61	−11.90	−4.31	−7.59	−6.37	−1.22
	90°	0.193	−31.64	−4.31	−27.33	−21.93	−5.40
	$0^\circ < \theta < 180^\circ$	80.05	−7.05	−4.31	−2.77	−2.71	−0.06
	$10^\circ < \theta < 170^\circ$	37.06	−12.26	−4.31	−7.95	−6.65	−1.30
	$20^\circ < \theta < 160^\circ$	14.16	−19.29	−4.31	−14.98	−12.20	−2.78
2000	5°	418.8	−7.14	−5.80	−1.33	−1.59	0.25
	20°	5.163	−30.31	−5.80	−24.51	−20.96	−3.55
	90°	0.049	−59.59	−5.80	−53.78	−45.47	−8.32
	$0^\circ < \theta < 180^\circ$	80.59	−9.85	−5.80	−4.04	−3.95	−0.09
	$10^\circ < \theta < 170^\circ$	14.14	−27.15	−5.80	−21.35	−18.34	−3.01
	$20^\circ < \theta < 160^\circ$	4.068	−41.22	−5.80	−35.41	−30.12	−5.29

Table 2: *Lowest-order cross-sections and relative corrections for unpolarized particles*

other contributions form the bosonic corrections. The fermionic corrections stay below 5–10% even for high energies. The bosonic contributions are responsible for the large corrections at high energies, in particular in the central angular region.

In Ref. [2] the total cross-section and the ratios

$$R_{\rm TO} = \frac{\sigma(|\cos\theta| < 0.4)}{\sigma(|\cos\theta| < 0.8)}, \qquad R_{\rm LT} = \frac{\sigma_{\rm LL}}{\sigma_{\rm TT}}, \qquad R_{02} = \frac{\sigma_{++}}{\sigma_{--}}, \tag{8}$$

have been investigated in view of their sensitivity to anomalous couplings.[1] We list the lowest-order predictions together with the $\mathcal{O}(\alpha)$-corrected ones and the relative "weak" corrections for these observables in Table 3 using $|\cos\theta_{\rm cut}| = 0.8$.

In Fig. 2 we plot the integrated cross-section including $\mathcal{O}(\alpha)$ "weak" corrections using $\theta_{\rm cut} = 20^\circ$ for various values of the Higgs-boson mass. While the Higgs resonance is comparably sharp for small Higgs-boson masses, it is washed out by the large width of the Higgs boson for high $M_{\rm H}$. Already for $M_{\rm H} = 400\,\mathrm{GeV}$ the Higgs resonance is hardly visible.

[1] Note that we do not perform a convolution with a realistic photon spectrum but consider the incoming photons as monochromatic.

$\sqrt{s}$/GeV		σ/pb	R_{10}	R_{LT}	R_{02}
500	Born level	15.74	0.265	0.0308	1.934
	corrected	14.82	0.259	0.0325	1.950
	corrections/%	−5.83	−2.02	5.43	0.78
1000	Born level	4.659	0.241	0.0235	2.229
	corrected	3.617	0.227	0.0276	2.184
	corrections/%	−22.36	−5.64	17.08	−2.05
2000	Born level	1.218	0.234	0.0220	2.307
	corrected	0.647	0.207	0.0321	2.168
	corrections/%	−46.86	−11.53	46.11	−6.02

Table 3: *Tree-level and $O(\alpha)$ results for various observables using* $|\cos\theta_{\rm cut}| = 0.8$

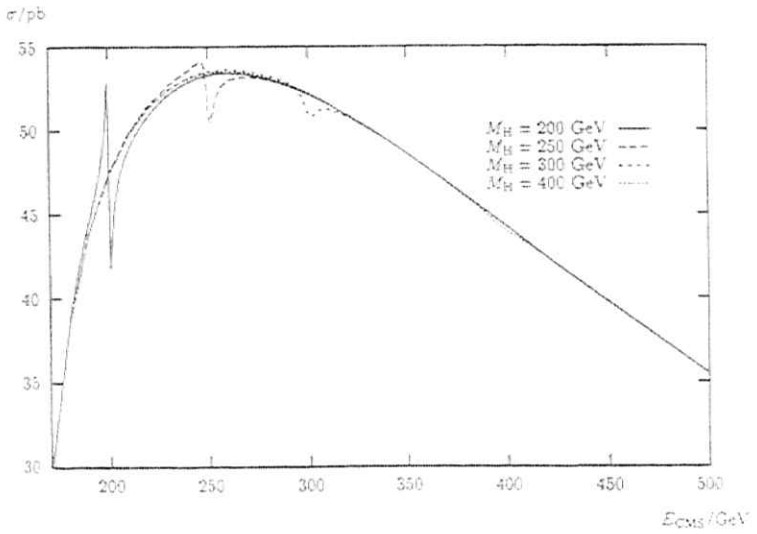

Figure 2: *Integrated unpolarized cross-section including $O(\alpha)$ "weak" corrections for various Higgs-boson masses ($20° < \theta < 160°$)*

5 Summary

The process $\gamma\gamma \to W^+W^-$ will be one of the most interesting reactions at future $\gamma\gamma$ colliders. In particular, it is very useful to study non-Abelian gauge couplings.

We have calculated the one-loop radiative corrections to $\gamma\gamma \to W^+W^-$ within the electroweak Standard Model in the soft-photon approximation for arbitrary polarizations of the photons and W bosons. An interesting peculiarity of $\gamma\gamma \to W^+W^-$ is the absence of most universal leading corrections, such as the running of α and leading logarithms associated with collinear bremsstrahlung. Therefore, theoretical predictions are very clean. The variation of the cross-sections with the top-quark and Higgs-boson masses is small if M_W is kept fixed with the exception of the cross-sections involving longitudinal W bosons at high energies. In the heavy mass limit no leading m_t^2-, $\log m_t$-, and $\log M_H$-terms exist.

The soft-photon-cut-off-independent radiative corrections to the total cross-section are of the order of 10% and can reach up to 50% at 2 TeV. The large corrections are due to bosonic loop diagrams whereas the effects of the fermionic ones are of the order of 5–10%.

References

[1] K.J. Kim and Y.S. Tsai, *Phys. Rev.* **D8** (1973) 3109;
G. Tupper and M.A. Samuel, *Phys. Rev.* **D23** (1981) 1933;
S.Y. Choi and F. Schrempp, *Phys. Lett.* **B272** (1991) 149.

[2] E. Yehudai, *Phys. Rev.* **D44** (1991) 3434.

[3] G. Bélanger and F. Boudjema, *Phys. Lett.* **B288** (1992) 210.

[4] M.A. Shifman et al., *Sov. J. Nucl. Phys.* **30** (1979) 711.

[5] E.E. Boos and G.V. Jikia, *Phys. Lett.* **B275** (1992) 164.

[6] D.A. Morris, T.N. Truong and D. Zappalá, *Phys. Lett.* **B323** (1994) 421.

[7] H. Veltman, *Z. Phys.* **C62** (1994) 235.

[8] A. Denner, S. Dittmaier and R. Schuster, *Nucl. Phys.* **452** (1995) 80.

[9] A. Denner, S. Dittmaier and R. Schuster, *Phys. Rev.* **D51** (1995) 4738.

[10] V.S. Fadin, V.A. Khoze and A.D. Martin, *Phys. Lett.* **B311** (1993) 311; *Phys. Rev.* **D52** (1995) 1377;
D. Bardin, W. Beenakker and A. Denner, *Phys. Lett.* **B317** (1994) 213.

Residual New Physics Effects in e^+e^- and $\gamma\gamma$ Collisions at NLC [*]

G.J. Gounaris[1], J.Layssac[2], J.E. Paschalis[1], F.M. Renard[2] and N.D. Vlachos[1]

[1] *Department of Theoretical Physics, University of Thessaloniki, Greece*

[2] *Physique Mathématique et Théorique, CNRS-URA 768, Université de Montpellier II, France*

1 Introduction

The search for manifestations of New Physics (NP) is an important part of the program of future high energy colliders. If it happens that all new particles are too heavy to be directly produced at these colliders, then the only way NP could manifest itself, is through residual interactions affecting the particles already present in SM. The possibility for such residual NP effects involving the interactions of the gauge bosons with the leptons and to some extent the light quarks, has already been essentially excluded by LEP1. Thus, the self-interactions among the gauge and Higgs bosons and possibly also the heavy quarks constitute the most probable space for some NP. On the other hand the scalar sector is the most mysterious part of the Standard Model (SM) of the electroweak interactions and is the favorite place for generating New Physics (NP) manifestations.

High energy e^+e^- linear colliders will offer many possibilities to test the sector of the gauge boson and Higgs interactions with a high accuracy, firstly in e^-e^- collisions and secondly through $\gamma\gamma$ collisions. The most famous process is $e^-e^- \to W^+W^-$. This has been carefully studied and it has been shown that indeed the 3-gauge boson vertices γW^+W^- and ZW^+W^- can be very accurately constrained through it. If the Higgs boson is not too heavy further processes to consider are $e^-e^- \to ZH, \gamma H$. In SM, the process $e^-e^- \to Z \to ZH$ is allowed at tree level, while $e^-e^- \to \gamma H$ is only possible at 1-loop level and is therefore a dedicated place to look for anomalous Higgs-gauge boson interactions.

A new facility offered by high energy linear e^+e^- colliders is the realization of $\gamma\gamma$ collisions with intense high energy photon beams through the laser backscattering method. This will give access to a new kind of processes namely boson-boson scattering. Five boson pair production processes are thus accessible, $\gamma\gamma \to W^+W^-$, ZZ, $Z\gamma$, $\gamma\gamma$ and HH. Such processes are very interesting, since they are sensitive not only to the 3-gauge boson vertices, but also to 4-gauge boson as well as to Higgs couplings. In addition, provided

[*] Partially supported by the EC contract CHRX-CT94-0579.

the Higgs particle will be accessible at the future colliders, the $\gamma\gamma$ fusion into a single Higgs boson will give direct access to the study of this particle and thus test the scalar sector in a much deeper way, particularly because the standard contribution to $\gamma\gamma \to H$ only occurs at 1-loop. With the high luminosities expected at linear e^-e^- colliders, thousands of Higgs bosons should be produced. The sensitivity to anomalous $H\gamma\gamma$ couplings is therefore very strong.

Below we summarize the studies in [1, 2, 3] and show that they provide very sensitive tests of the various possible forms of NP.

Assuming that the NP scale Λ_{NP} is sufficiently large, the effective NP Lagrangian should be satisfactorily described in terms of $dim = 6$ bosonic operators only. There exist only seven $SU(2) \times U(1)$ gauge invariant such operators called "blind", which are not strongly constrained by existing LEP1 experiments. Three of them

$$\mathcal{O}_W = \frac{1}{3!}\left(\overrightarrow{W}_\mu{}^\nu \times \overrightarrow{W}_\nu{}^\lambda\right) \cdot \overrightarrow{W}_\lambda{}^\mu \quad , \tag{1}$$

$$\mathcal{O}_{W\Phi} = i(D_\mu\Phi)^\dagger \overrightarrow{\tau} \cdot \overrightarrow{W}^{\mu\nu}(D_\nu\Phi) \quad , \quad \mathcal{O}_{B\Phi} = i(D_\mu\Phi)^\dagger B^{\mu\nu}(D_\nu\Phi) \tag{2}$$

induce anomalous triple gauge boson couplings, while the remaining four

$$\mathcal{O}_{UW} = \frac{1}{v^2}(\Phi^\dagger\Phi - \frac{v^2}{2})\,\overrightarrow{W}^{\mu\nu} \cdot \overrightarrow{W}_{\mu\nu} \quad , \quad \mathcal{O}_{UB} = \frac{4}{v^2}(\Phi^\dagger\Phi - \frac{v^2}{2})B^{\mu\nu}\,B_{\mu\nu} \quad , \tag{3}$$

$$\overline{\mathcal{O}}_{UW} = \frac{1}{v^2}(\Phi^\dagger\Phi)\,\overrightarrow{W}^{\mu\nu} \cdot \overrightarrow{\tilde{W}}_{\mu\nu} \quad , \quad \overline{\mathcal{O}}_{UB} = \frac{4}{v^2}(\Phi^\dagger\Phi)B^{\mu\nu}\,\tilde{B}_{\mu\nu} \tag{4}$$

create anomalous CP conserving and CP violating Higgs couplings.

In addition, the "superblind" operator

$$\mathcal{O}_{\Phi 2} = 4\partial_\mu(\Phi^\dagger\Phi)\partial^\mu(\Phi^\dagger\Phi) \quad , \tag{5}$$

which is insensitive to LEP1 physics even at the 1-loop level, induces a wave function renormalization to the Higgs field that may be observable in $e^-e^- \to ZH$.

The effective Lagrangian describing the NP induced by these operators is given by

$$\mathcal{L}_{NP} = \lambda_W \frac{g}{M_W^2}\mathcal{O}_W - \frac{f_{B\Phi'}}{2M_W^2}\mathcal{O}_{B\Phi} + \frac{f_{W\Phi}}{2M_W^2}\mathcal{O}_{W\Phi} - d\,\mathcal{O}_{UW} + \frac{d_B}{4}\,\mathcal{O}_{UB} + \tilde{d}\,\overline{\mathcal{O}}_{UW} + \frac{\tilde{d}_B}{4}\,\overline{\mathcal{O}}_{UB} - \frac{f_{\Phi 2}}{v^2}\mathcal{O}_{\Phi 2} \quad . \tag{6}$$

[1] Because of lack of space, the extensive litterature on the subject is not given explicitely and can be found in [1, 2, 3].

which defines the various couplings. Studying unitarity, we have established relations between these coupling constants and the corresponding NP scales Λ_{NP} (defined as the energy value at which unitarity is saturated). This allows us to express the observability limits directly in terms of Λ_{NP}.

We now study how the aforementioned processes accessible at NLC react to each of these operators and what is the observability limit for the associated NP scale. We also give ways to disentangle the effects of the various operators.

2 Analysis of $e^-e^+ \to Z_{(f\bar{f})}H$ and $e^-e^+ \to \gamma H$.

Using the NP lagrangian given by (6), we have computed in [1] the helicity amplitude for $e^-e^+ \to ZH$. They depend on the SM couplings and on the combinations of NP couplings $d_{\gamma Z} = s_W c_W(d - d_B)$, $d_{ZZ} = dc_W^2 + d_B s_W^2$, $d_{\gamma\gamma} = ds_W^2 + d_B c_W^2$, as well as the corresponding CP-violating ones for $\bar{d}$, $\bar{d}_B$ defined in (6).

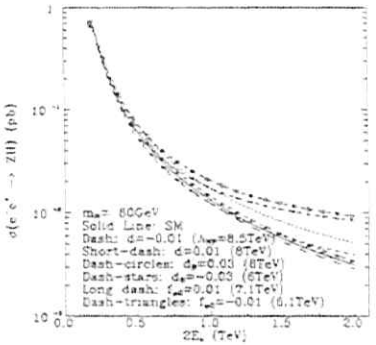

Fig 1

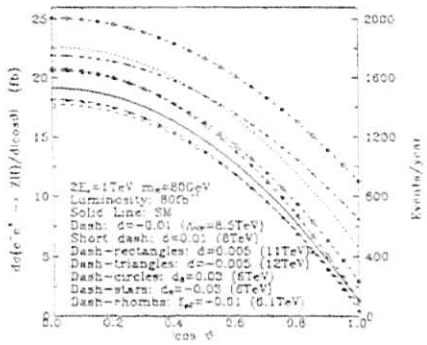

Fig 2

The corresponding total cross section as a function of the e^-e^+ energy is shown in Fig.1 assuming $m_H = 80GeV$. In this figure, we present results for various values of the d and d_B couplings, indicating also the NP scale they correspond to. Identical results are of course also obtained for the same values of the CP-violating couplings $\bar{d}$ and $\bar{d}_B$ respectively. The HZ angular distribution depends on $f_{\phi 2}$ through the Higgs field renormalization factor Z_B, while its dependence on $\mathcal{O}_{UW}$ and $\mathcal{O}_{UB}$ is mainly given by the combination d_{ZZ} (see Fig.2).

Thus at 1 TeV, with 80 fb^{-1} per year, the SM rate gives one thousand events per year. One can then expect a measurement of the cross section with a 3% accuracy. The implied sensitivities to the various couplings are $|f_{\phi 2}| \simeq 0.004$, $|d| \simeq 0.005$ and $|d_B| \simeq 0.015$, corresponding to NP scales of 10, 11 and 9 TeV respectively; compare Fig.1 and Fig.2. Moreover, with such a number of events, informations from the fermionic decay distribution of the Z can be used in order to disentangle the various d-type couplings.

We then compute the Z density matrix in the helicity basis and, assuming that the decay $Z \to f\bar{f}$ is standard, the angular distribution for the $f\bar{f}$ system in the Z rest frame. In [1] it was shown that the ϕ_f azimuthal distribution allows to define four asymmetries A_{13}, A_{12}, A_{14}, A_8, respectively associated to the $\sin 2\phi_f$, $\cos 2\phi_f$, $\sin\phi_f$, $\cos\phi_f$ dependences. The remarkable features are that A_{14}, A_{12} are mainly sensitive on the combination $\bar{d}_{\gamma Z}$ and on its CP-violating partner $\bar{d}_{\gamma Z}$. Thus, the illustrations made for d ,$(\bar{d})$ apply also to $-d_B$, $(-\bar{d}_B)$. They are shown in Figs.3,4.

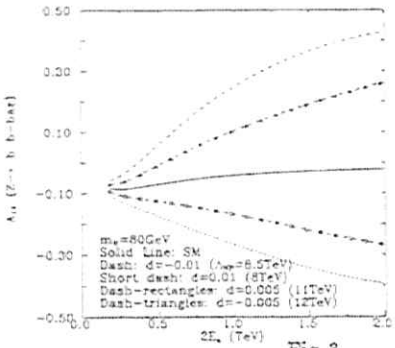

Fig 3

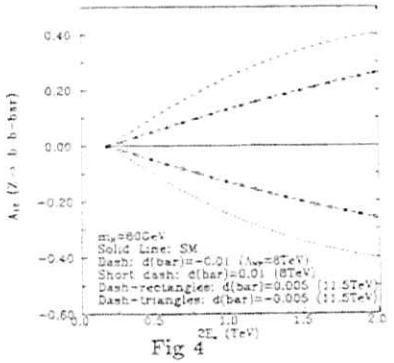

Fig 4

These asymmetries depend on the flavour of the fermion f to which Z decays and are mostly interesting for the $Z \to b\bar{b}$ case. The asymmetry A_{13} shown in Fig.5 does not depend on the type of the fermion f and it is sensitive to the CP-violating combination $\bar{d}_{ZZ}$. Thus, sensitivities to this coupling at the percent level should be possible using this asymmetry. Note that in this case the sensitivities to $\bar{d}_B$ and $\bar{d}$ are related by $\bar{d}_B \simeq \bar{d}c_W^2/s_W^2$. Finally the asymmetry A_8 shown in Fig.6, is also mainly sensitive to $\bar{d}_{ZZ}$ and independent of the flavour of the f fermion. Consequently, the differential cross section for $e^-e^+ \to ZH$, together with the above asymmetries, provide considerable information for disentangling the aforementioned five relevant anomalous couplings at the percent

level. It follows that NP scales of the order of a few TeV could be searched for this way.

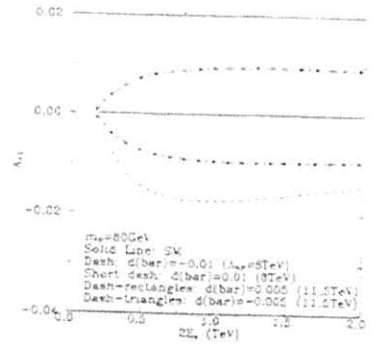

Fig 5

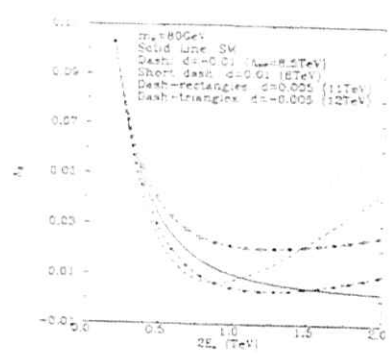

Fig 6

We next turn to the process $e^+e^- \to \gamma H$. In this case [1] the NP contribution is added to the 1-loop SM contribution.

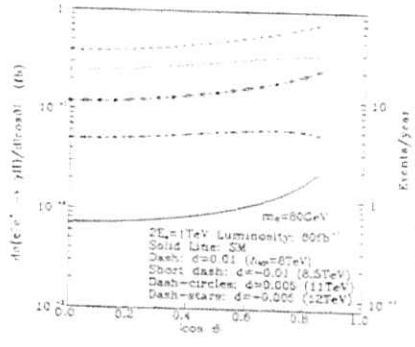

Fig 7a

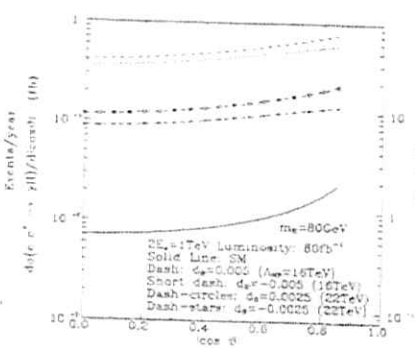

Fig 7b

We have again neglected tree-level contributions quadratic in the anomalous couplings, and also 1-loop contributions linear in the anomalous couplings. This implies that no contribution from $\mathcal{O}_{\Phi 2}$ should be included. At SM the cross section is unobservably small, but it is very sensitive to the four NP interactions and provides informations on combinations of couplings that are different from those appearing in $e^+e^- \to ZH$. The differential cross section could become observable if non negligible anomalous interactions occur . For a $1TeV$ NLC, Fig.7a,b show the sensitivity to $|d| \simeq 0.005$ and $|d_B| \simeq 0.0025$

corresponding to NP scales of 11 TeV and 22 TeV respectively. In these figures we have used for illustration $m_H = 80GeV$, but of course similar results would have been expected for any $m_H \ll 1TeV$.

3 Boson Pair Production Processes in $\gamma\gamma$ Collisions

The boson pair production processes that we consider here [3] are $\gamma\gamma \to W^+W^-$, $\gamma\gamma \to ZZ$, $\gamma\gamma \to HH$ and also $\gamma\gamma \to \gamma Z$, $\gamma\gamma \to \gamma\gamma$.

An efficient way of doing this is by looking at the transverse-momentum distribution of one of the final bosons B_3 and B_4 and cutting-off the small p_T values. It is given by

$$\frac{d\sigma}{dp_T dy} = \frac{y p_T}{8\pi s_{ee} |\Delta|} \int_{\frac{\tau}{z_{max}}}^{z_{max}} dz f_{\gamma/e}^{laser}(z) f_{\gamma/e}^{laser}\left(\frac{\tau}{z}\right) \Sigma |F(\gamma\gamma \to B_3 B_4)|^2 , \qquad (7)$$

where $y \equiv \sqrt{\tau} \equiv \sqrt{\frac{s_{\gamma\gamma}}{s_{ee}}}$, $|\Delta| = \frac{1}{2}\sqrt{s_{\gamma\gamma}(s_{\gamma\gamma} - 4(p_T^2 + m^2))}$, $p_T^2 < \frac{s_{\gamma\gamma}}{4} - m^2$ and $F(\gamma\gamma \to B_3 B_4)$ is the invariant amplitude of the subprocess given in [3]. $f_{\gamma/e}^{laser}(z)$ is the photon flux distribution.

The $\frac{d\sigma}{dp_T}$ distribution provides a very useful way for searching for NP, since it not only takes care of the events lost along the beam pipe, but also because its measurement does not require full reconstruction of both final bosons, at it would be the case for $\frac{d\sigma}{dy}$. For the illustrations below we choose $p_T > p_T^{min} = 0.1TeV/c$. The correspondingly expected number of events per year is obtained by multiplying the above distribution by the integrated e^+e^- annual luminosity $\bar{\mathcal{L}}_{ee}$ taken to be $20, 80, 320 fb^{-1} year^{-1}$ for a 0.5, 1. or 2.TeV collider respectively.

We now summarize the properties of each of the five channels and the way they react to the residual NP lagrangian. SM contributes to $\gamma\gamma \to W^+W^-$ at tree level (through W exchange diagrams in the t, u channels involving the γWW vertex and the $\gamma\gamma WW$ contact term), and at the 1-loop level to the other processes. So the search for NP effects can be done by precision measurements in the W^+W^- channel and by looking for an observable enhancement in the other channels, see Fig.8-11. The results presented below are obtained in ref.[3] using asymptotic expressions for the anomalous parts of the amplitudes in $\gamma\gamma \to W^+W^-$, $\gamma\gamma \to ZZ$, $\gamma\gamma \to \gamma Z$, $\gamma\gamma \to \gamma\gamma$, but exact expressions in the $\gamma\gamma \to HH$ case.

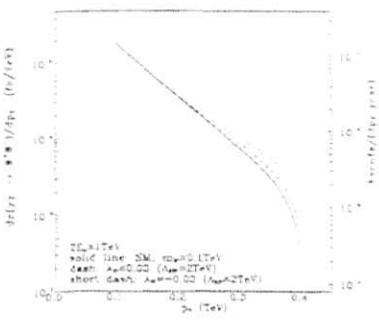

Fig 8

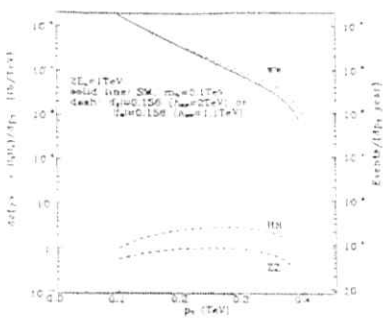

Fig 9

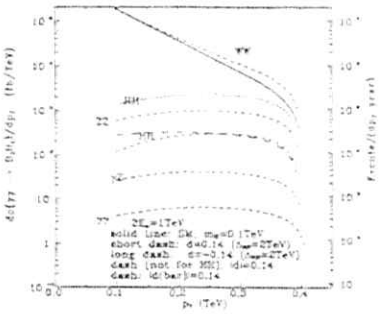

Fig 10

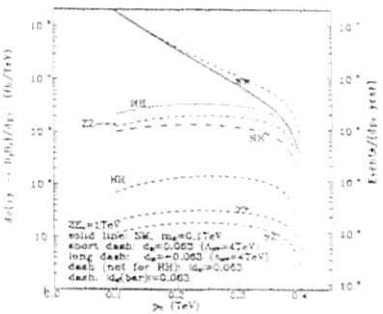

Fig 11

Table 1 shows how each operator contributes to the various channels, and one observes that the disentangling is possible between three groups of operators. In the $\mathcal{O}_W$ case W^+W^- are produced in (TT) states whereas in the $\mathcal{O}_{B\Phi}$ and $\mathcal{O}_{W\Phi}$ cases it is mainly (LL). There is no way to distinguish the contributions of $\mathcal{O}_{B\Phi}$ from that of $\mathcal{O}_{W\Phi}$ in $\gamma\gamma$ collisions. The discrimination between these two operators requires the use of other processes, like $e^+e^- \to W^+W^-$. The disentangling of $\mathcal{O}_{UW}$ from $\mathcal{O}_{UB}$ can then be done by looking at the ratios of the ZZ and WW cross sections. Notice that the linear terms of the WW and ZZ amplitudes for $\mathcal{O}_{UB}$ may be obtained from the corresponding terms for $\mathcal{O}_{UW}$ by multiplying by the factor c_W^2/s_W^2.

There is no way to separate the CP-conserving from the CP-violating terms in these spectra. More detailed spin analyses are required, like *e.g.* the search for imaginary parts

in final W or Z spin density matrices observable through the decay distributions or the measurement of asymmetries associated to linear polarizations of the photon beams.

	SM	$\mathcal{O}_W$	$\mathcal{O}_{W\Phi}$	$\mathcal{O}_{B\Phi}$	$\mathcal{O}_{UW}$	$\mathcal{O}_{UB}$	$\overline{\mathcal{O}}_{UW}$	$\overline{\mathcal{O}}_{UB}$
$\gamma\gamma \to WW$	TT	TT	LL	LL	LL	LL	LL	LL
$\gamma\gamma \to ZZ$			TT	TT	LL	LL	LL	LL
$\gamma\gamma \to HH$			X	X	X	X	X	X
$\gamma\gamma \to \gamma Z$					TT	TT	TT	TT
$\gamma\gamma \to \gamma\gamma$					TT	TT	TT	TT

Table 1: Contributions from the various operators

Table 2 summarizes the observability limits expected for each operator on the basis of W^+W^- production alone. To derive them we assume that a 5% departure of the W^+W^- cross section in the high p_T range from the SM prediction, will be observable. These observability limits on the anomalous couplings give essentially lower bounds for the couplings to be measurable, that correspond to upper limits for observable Λ_{NP}.

	$\mathcal{O}_W$		$\mathcal{O}_{UW}$ or $\overline{\mathcal{O}}_{UW}$		$\mathcal{O}_{UB}$ or $\overline{\mathcal{O}}_{UB}$		$\mathcal{O}_{B\Phi}$ or $\mathcal{O}_{W\Phi}$	
$2E_e$(TeV)	$\lvert\lambda_W\rvert$	Λ_{NP}	$\lvert d\rvert$ or $\lvert\tilde{d}\rvert$	Λ_{NP}	$\lvert d_B\rvert$ or $\lvert\tilde{d}_B\rvert$	Λ_{NP}	$\lvert f_B\rvert$ or $\lvert f_W\rvert$	Λ_{NP}
0.5	0.04	1.7	0.1	2.4	0.04	4.9	0.2	1.8, 1
1	0.01	3.5	0.04	4	0.015	9	0.05	3.5, 2
2	0.003	6.4	0.015	7	0.005	16	0.015	6.5, 3.6

Table 2: Observability limits based on the W^+W^- channel
to the anomalous couplings and the related NP scales Λ_{NP} (TeV).

At 2 TeV, in the case of the operators $\mathcal{O}_{UB}$, $\mathcal{O}_{UW}$, $\overline{\mathcal{O}}_{UB}$, $\overline{\mathcal{O}}_{UW}$ slightly better limits could in principle be obtained by using the $\gamma\gamma \to ZZ$ process. Demanding for example that the NP contribution to this process reaches the level of the SM result for $\gamma\gamma \to ZZ$, we can decrease the limiting value for the couplings $|d|$ (or $|\tilde{d}|$) and $|d_B|$ (or $|\tilde{d}_B|$) down to 0.01 and 0.003 respectively. This means that a 2 TeV collider is sensitive to NP scales up to 20 TeV. A more precise analysis using realistic uncertainties for the detection of the ZZ channel and taking into account the interference between the SM and the NP contributions, could probably improve these limits. This needs more work.

4 The fusion $\gamma\gamma \to H$

The cross section for $\gamma\gamma \to H$ is given by [2]

$$\sigma = \mathcal{L}_{\gamma\gamma}(\tau_H) \left(\frac{8\pi^2}{m_H}\right) \frac{\Gamma(H \to \gamma\gamma)}{s_{ee}} \quad , \tag{8}$$

where the luminosity function $\mathcal{L}_{\gamma\gamma}(\tau_H)$ for $\tau_H = m_H^2/s_{ee}$ is explicitly given in terms of the $f_{\gamma/e}^{laser}$ distribution in [2, 3]. Essentially $\mathcal{L}_{\gamma\gamma}$ is close to the e^+e^- linear collider luminosity $\mathcal{L}_{ee}$ up to $\tau_{max} = (0.82)^2$.

The $H \to \gamma\gamma$ decay width is computed in terms of the one-loop SM contribution and tree level NP ones [2] obtained from the Lagrangian given in eqs. (8):

$$\Gamma(H \to \gamma\gamma) = \frac{\sqrt{2}G_F}{16\pi} m_H^3 \left(\left| \frac{\alpha}{4\pi}\left(\frac{4}{3}F_t + F_W\right) - 2d_B s_W^2 - 2d_B c_W^2 \right|^2 + 4|\tilde{d}s_W^2 + \tilde{d}_B c_W^2|^2 \right) , \tag{9}$$

where the standard top (F_t) and W (F_W)contributions are explicitey given in [2].

The resulting rate is shown in Fig.12-13 for a 1 TeV collider. The number of events indicated in these figures corresponds to an e^+e^- luminosity of 80 fb^{-1}.

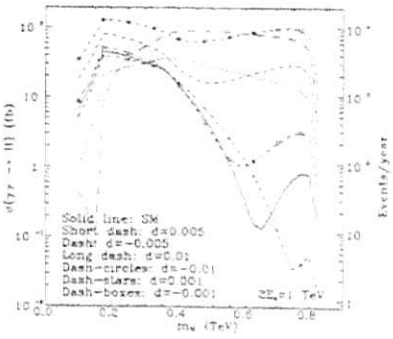

Fig 12

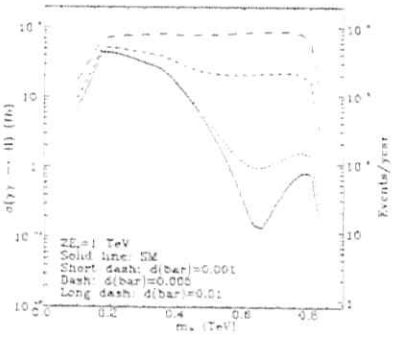

Fig 13

Strong interference effects may appear (depending on the Higgs mass) between the SM and the CP-conserving NP contributions; (compare Fig.12). But in the case of CP-violating contributions (Fig.13) there are never such interferences. In the figures we have only illustrated the cases of $\mathcal{O}_{UW}$ and $\overline{\mathcal{O}}_{UW}$. The corresponding results for $\mathcal{O}_{UB}$ and $\overline{\mathcal{O}}_{UB}$ can be deduced according to eq(9) from Fig.12-13, by the replacement

$d\,[\tilde{d}] \to c_W^2/s_W^2\, d_B\,[\tilde{d}_B]$. So the sensitivity to these last two operators is enhanced by more than a factor 3 in the cross section.

With the aforementioned designed luminosities, one gets a few thousands of Higgs bosons produced in the light or intermediate mass range. Assuming conservatively an experimental detection accuracy of about 10% on the production rate, one still gets an observability limit of the order of 10^{-3}, 4.10^{-3}, 3.10^{-4}, 10^{-3} for d, $\tilde{d}$, d_B and $\tilde{d}_B$ respectively. The corresponding constraints on the NP scale are 26, 13, 65, 36 TeV respectively.

5 NP searches through ratios of Higgs decay widths

In this Section we show that independently of the Higgs production mechanism, the study of the Higgs branching ratios can be very fruitful for NP searches and for disentangling contributions from the various operators.

The expression of the $H \to \gamma\gamma$ width has been given in (9). Correspondingly, the $H \to \gamma Z$ width is also expressed in terms of a 1-loop SM contribution and of the NP contributions from the four operators. The $H \to W^+W^-, ZZ$ widths are explicitely given in [2]. They receive a tree level SM contribution which interferes with the ones from the CP-conserving operators $\mathcal{O}_{UB}, \mathcal{O}_{UW}$. Finally we note that the $H \to b\bar{b}$ decay width is purely standard and particularly important if $m_H < 140GeV$. In Figs. 14a,b the ratios $\Gamma(H \to \gamma\gamma)/\Gamma(H \to b\bar{b})$ and $\Gamma(H \to \gamma Z)/\Gamma(H \to b\bar{b})$ are plotted versus m_H for a given value of d or $\tilde{d}$. The case of d_B or $\tilde{d}_B$ can be obtained by the respective replacements $d \to d_B c_W^2/s_W^2$ for the $\gamma\gamma$ amplitude and of $d \to d_B$ for the γZ one. The m_H and d dependences of the $\gamma\gamma/b\bar{b}$ ratio are obviously similar to the ones of the production cross section $\sigma(\gamma\gamma \to H)$. The ratios $\gamma Z/b\bar{b}$ and $\gamma\gamma/\gamma Z$ have independent features that may help disentangling the various couplings. They can also be seen from the ratio shown in Fig.14c.

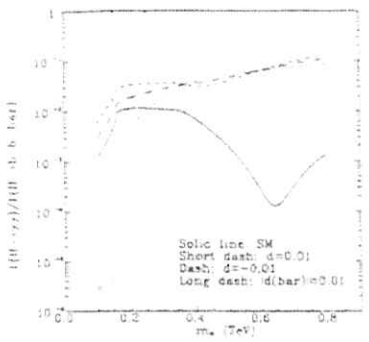

Fig 14a

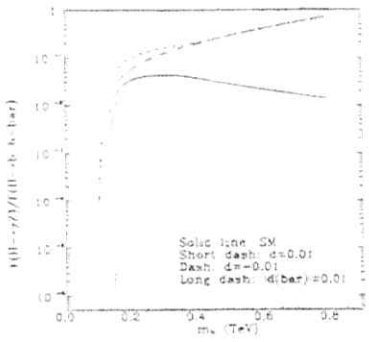

Fig 14b

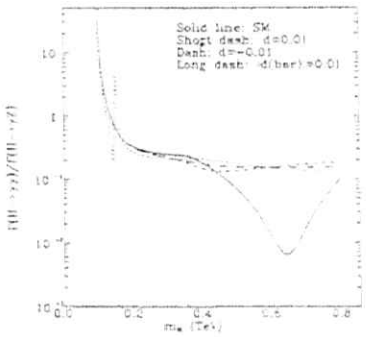

Fig 14c

The sensitivity of the $WW/b\bar{b}$ and $ZZ/b\bar{b}$ ratios is much weaker as expected from the occurrence of tree level SM contributions. Because of this these ratios are only useful for $|d| \gtrsim 0.1$. The ratios $\gamma\gamma/WW$ and $\gamma\gamma/ZZ$ are shown in Figs.14d,e and present the same features as the ratio $\gamma\gamma/b\bar{b}$. They can however be useful in the range of m_H where the WW, ZZ modes are dominant.

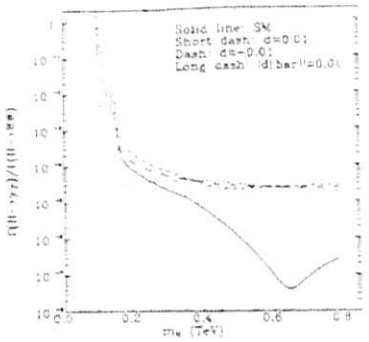

Fig 14d

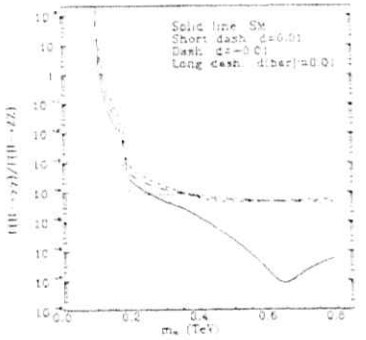

Fig 14e

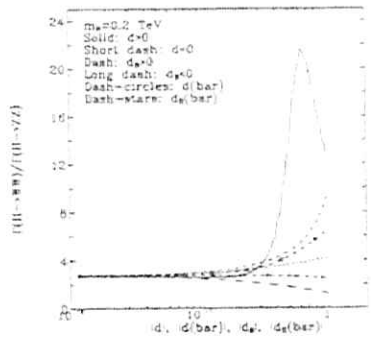

Fig 15a

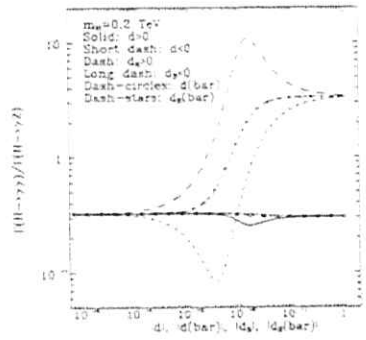

Fig 15b

Finally we discuss the ratios WW/ZZ and $\gamma\gamma/\gamma Z$ for a given value of m_H (chosen as $0.2TeV$ in the illustrations made in Fig.15a,b), versus the coupling constant values of the four operators. This shows very explicitly how these ratios can be used for disentangling the various operators. They have to be taken in a complementary way to the $\sigma(\gamma\gamma \to H)$ measurement. As in the $WW/b\bar{b}$ case, the WW/ZZ ratio is only useful for $|d| \gtrsim 0.1$, while $\gamma\gamma/\gamma Z$ ratio allows for disentangling d values down to 10^{-2} or even less. The corresponding sensitivity limit for $d_B, \tilde{d}_B$ should then be lying at the level of a few times 10^{-4}.

6 Final discussion

We have concentrated our analysis on the residual NP effects described by seven blind and one superblind $dim = 6$ $SU(2) \times U(1)$ gauge invariant operators $\mathcal{O}_W$, $\mathcal{O}_{B\Phi}$, $\mathcal{O}_{W\Phi}$, $\mathcal{O}_{UB}$, $\mathcal{O}_{UW}$, $\overline{\mathcal{O}}_{UB}$, $\overline{\mathcal{O}}_{UW}$, $\mathcal{O}_{\Phi 2}$. The first three ones should be essentially studied in the process $e^+e^- \to W^+W^-$ but they also contribute to $\gamma\gamma \to WW$. The five other ones only affect the Higgs couplings to themselves and to gauge bosons, and their effects have been considered in all processes in which a Higgs can be exchanged or produced.

We started with the Higgs production process $e^+e^- \to ZH$. We have analyzed the angular distributions for HZ as well as the four azimuthal asymmetries in $Z \to f\bar{f}$ decays associated to the $\cos\phi_f$, $\sin\phi_f$, $\sin 2\phi_f$ and $\cos 2\phi_f$ distributions controlled by the Z spin density matrix elements. The disentangling of the five relevant operators should be achievable down to the percent level for the NP couplings, implying sensitivities to NP scales of the order of 10, 8 and 12 TeV for $\mathcal{O}_{\Phi 2}$, $\mathcal{O}_{UB}$ and $\mathcal{O}_{UW}$ respectively. This study is further augmented by looking at the angular distribution of $e^+e^- \to \gamma\gamma$, which is sensitive to a different combination of the $\mathcal{O}_{UB}$ and $\mathcal{O}_{UW}$ couplings, implying also sensitivities to NP scales of 20 and 12 TeV.

We have then considered $\gamma\gamma$ collision processes. In boson pair production one can feel NP effects associated to scales up to $\Lambda_{NP} \simeq 20 TeV$ for collider energies up to $2TeV$. This can be achieved by simply measuring final gauge boson p_T distributions. A comparison of the effects in the various final states WW, ZZ, HH, γZ and $\gamma\gamma$ including an analysis of final spin states, (i.e. separating $W_T(Z_T)$ from $W_L(Z_L)$ states), should allow a selection among the seven candidate operators.

At a linear e^+e^- collider the cross section of the process $\gamma\gamma \to H$ is the best way to study the Higgs boson, if its mass allows its production. We showed that the sensitivity limits on the NP couplings are at the 10^{-3} level, implying new physics scales up to 65 TeV, depending on the nature of the NP operator.

We have then shown that independently of the production mechanism, having at our disposal a few thousands of Higgs produced (either in $e^+e^- \to HZ$ or in $\gamma\gamma \to H$), enables the disentangling of the $\mathcal{O}_{UB}$ and $\mathcal{O}_{UW}$ operators by looking at the Higgs branching ratios into WW, ZZ, $\gamma\gamma$, γZ. Because these branching ratios react differently to the presence of each of these operators. This is illustrated with the ratios of these channels to the $b\bar{b}$ one which is unaffected by this kind of NP. Most spectacular for the disentangling of the various operators seem to be the ratios WW/ZZ and $\gamma\gamma/\gamma Z$. The first one, which

is applicable in the intermediate and high Higgs mass range, allows to disentangle $\mathcal{O}_{UB}$ from $\mathcal{O}_{UW}$ down to values of the order of 10^{-1}, whereas the second one, applicable in the light Higgs case, is sensitive to couplings down to the 10^{-3} level or less.

A direct identification of CP violation requires either an analysis of the W or Z spin density matrix through their fermionic decay distributions [1], or the observation of a suitable asymmetry with linearly polarized photon beams.

Finally we emphasize that the occurrence of anomalous terms in gauge or Higgs boson couplings would be of great interest for tracing the origin of NP and its basic properties.

Acknowledgements

This work has been partially supported by the EC contract CHRX-CT94-0579.

References

[1] G.J. Gounaris, F.M. Renard and N.D. Vlachos, Montpellier and Thessaloniki preprint PM/95-30, THES-TP 95-08, to appear in Nucl.Phys.B..

[2] G.J. Gounaris and F.M. Renard, hep-ph/9505429 Montpellier and Thessaloniki preprint PM/95-20, THES-TP 95/07, to appear in Zeit. f. Physik.

[3] G.J. Gounaris, J. Layssac and F.M. Renard, hep-ph/9505430 Montpellier and Thessaloniki preprint PM/95-11, THES-TP 95/06, to appear in Zeit. f. Physik.

Anomalous couplings and chiral lagrangians: an update

M. Baillargeon[1], U. Baur[2], G. Bélanger[3], F. Boudjema[3], G. Couture[4], M. Gintner[5] and S. Godfrey[5]

[1] *GTAE, Lisbon, Portugal*
[2] *SUNY Buffalo, Buffalo, USA*
[3] *ENSLAPP-Annecy, France*
[4] *UQAM, Montreal, Canada*
[5] *Carleton University, Ottawa, Canada*

1 Introduction

In case a Higgs boson is not found by the time the linear collider is running, one will have to rely on studying the dynamics of the Goldstone Bosons, i.e. how the W and Z interact, in order to probe the mechanism of symmetry breaking. In this scenario one expects the weak interactions to enter a new regime where the weak bosons become strongly interacting at effective energies of the order of a few TeV. At this scale new resonances might appear. However, the new dynamics could already be felt at lower energies through more subtle and indirect effects on the properties of the weak bosons. These effects may be revealed by precision measurements with the most prominent effects appearing in the self-couplings of the W and Z bosons. Detailed investigations of these self-couplings therefore would provide a window to the mechanism of symmetry breaking. Present precision data leave no doubt about the local gauge symmetry [1, 2] while the proximity of the ρ parameter to one can be considered as strong evidence for a residual global (custodial) $SU(2)$ symmetry. Whatever the new dynamics may be, it should respect these "low energy" constraints. In turn, this makes it possible to easily parameterize possible effects of new physics in the W sector by the introduction of a restricted set of higher order operators. Such constructions have been discussed at length [3, 4] and therefore, in this short note, we we will only recall the minimal set of operators that describe the residual effect of the new dynamics in the absence of Higgs boson field:

$$\mathcal{L}_{9R} = -ig'\frac{L_{9R}}{16\pi^2}Tr(B^{\mu\nu}D_\mu\Sigma^\dagger D_\nu\Sigma) \qquad \mathcal{L}_{9L} = -ig\frac{L_{9L}}{16\pi^2}Tr(W^{\mu\nu}D_\mu\Sigma D_\nu\Sigma^\dagger)$$
$$\mathcal{L}_1 = \frac{L_1}{16\pi^2}\left(Tr(D^\mu\Sigma^\dagger D_\mu\Sigma)\right)^2 \qquad \mathcal{L}_2 = \frac{L_2}{16\pi^2}\left(Tr(D^\mu\Sigma^\dagger D_\nu\Sigma)\right)^2 \tag{1}$$

The first two operators contribute to the tri-linear couplings $\Delta\kappa_\gamma$ and $\Delta\kappa_Z$. Only L_{9L} affects Δg_1^Z . $L_{1,2}$ contributes solely to the quartic couplings (see for instance [3]). There is, in fact, yet another operator in conformity with the above symmetries:

$$\mathcal{L}_{10} = gg'\frac{L_{10}}{16\pi^2}Tr(B^{\mu\nu}\Sigma^\dagger W^{\mu\nu}\Sigma) \tag{2}$$

However, because it contributes to the two-point function, it is strongly constrained through the S parameter [5] by LEP data: $L_{10} = -\pi S$. Current limits [2] lead to

$$-0.7 < L_{10} < 2.4 \tag{3}$$

It will be very difficult to improve this limit in experiments at future colliders. This poses a naturalness problem, since one would expect the other operators to be of the same order [6]. If this were the case the improvement that might result from high energy colliders would, at best, be marginal. For instance, such a situation is encountered with a naive scaled-up-QCD technicolour. One way out is to associate the smallness of L_{10} to a symmetry that forbids its appearance, in the same way that the custodial $SU(2)$ symmetry prevents large deviations of the ρ parameter from one. L_{10} represents the breaking of the axial global $SU(2)$ symmetry [7]. Models that naturally incorporate the L_{10} constraint include dynamical vector models that deviate from the usual scaled up versions of QCD by having (heavy) degenerate vectors and axial-vectors like the extended BESS model [8]. The latter implements an $(SU(2)_L \times SU(2)_R)^3$ symmetry. In the following we will follow a model independent approach, assuming that the couplings of Eq. (1) are independent parameters. Taking $L_{10} \sim 0$ we investigate whether future machines could do as well as LEP1 in constraining the remaining operators.

2 Tri-linear couplings: L_{9L}, L_{9R}

In the past, extensive studies on the extraction on the anomalous tri-linear couplings have been performed. Our aim here is to update some of those results for the particular case of the chiral lagrangian approach (Eq. (1)).

2.1 Strategy and analysis at the NLC

At the NLC, the best channels to look for $L_{9L,R}$ are $e^-e^- \to W^-W^-$ and $\gamma\gamma \to W^-W^-$. In the e^-e^- mode one could also use $e^-e^- \to \nu_e\bar{\nu}_e\gamma$ [9] (which singles out the photonic part) or $e^-e^- \to \nu\bar{\nu}Z$ [10] (which isolates the WWZ part). Beside the fact that within the chiral Lagrangian approach both non-standard $WW\gamma$ and WWZ couplings appear, the latter channels are found not to be competitive with W pair production. One reason is that W pair production has a much richer helicity structure that can directly access the longitudinal modes of the W. $WW\gamma$ and WWZ [11] production in e^-e^- collisions are quite interesting but, as far as tri-linear couplings are concerned, they can compete with the WW channel only for TeV energies since they suffer from much lower rates [11]. However they are well suited to study possible quartic couplings. In this respect WWZ production can probe the all important $\mathcal{L}_{1,2}$ operator.
In the e^-e^- mode one can investigate the tri-linear couplings through $e^-e^- \to e^-W^-\nu$ [12], which unfortunately exhibits the same shortcomings as $e^-e^- \to \bar{\nu}_e\nu_e Z$. Cuypers has studied the potential of this reaction in probing the tri-linear couplings by taking into account the possibility of polarized beams, fits have only been done to the scattering angle of the final electron. The limits do not compare well with those obtained from $e^-e^- \to W^-W^-$. The $\gamma\gamma$ mode is ideal in probing the photonic couplings due to the very large cross section for WW production [13]. In the chiral approach this reaction will only constrain the combination $L_{9L} + L_{9R}$ but, as we shall see, in conjunction with the e^-e^- mode this is

very helpful.

W pair production, both in $\gamma\gamma$ and e^+e^- collisions, provides a large data sample and involves different helicity states. To fully exploit these reactions it is then important to reconstruct all the elements of the density matrix for these reactions (both in the $\gamma\gamma$ and e^+e^- mode). This can be achieved by analysing all the information provided by the complete set of the kinematical variables related to the decay products of the W's, rather than restricting the analysis to the angular distribution at the level of the W. Since binning in the 5 variables characterizing a $WW \to 4$ fermion event requires high statistics, a χ^2 fit is not very efficient and a maximum likelihood technique is used. Initial state polarization can also be easily implemented. The results presented here are based on using the semi-leptonic final states only. The impact of the the non-resonant diagrams (which could introduce a bias) is also quantified. The issue of luminosity and the improvement in the limits by going to higher energy will be discussed, and we shall compare our results with those of Barklow [14] which include initial state radiation effects.

2.2 Analysis at the LHC

Before discussing the limits on the parameters of the chiral Lagrangian that one hopes to achieve at the different modes of the linear colliders it is essential to compare with the situation at the LHC. For this we assume the high luminosity option with 100 fb^{-1}. The LHC limits are based on a very careful study [15] that includes the very important effects of the QCD NLO corrections as well as implementing the full spin correlations for the most interesting channel $pp \to WZ$. WW production with $W \to jets$ production is fraught with a huge QCD background, while the leptonic mode is extremely difficult to reconstruct due to the 2 missing neutrinos. Even so, a thorough investigation (including NLO QCD corrections) for this channel has been done [16], which confirms the superiority of the WZ channel. The NLO corrections for WZ and WW production at the LHC are huge, especially at large W and Z boson transverse momenta where effects of the anomalous couplings are expected to show up. In the inclusive cross section this is mainly due to, first, the importance of the subprocess $q_1 g \to Z/W q_1$ (large gluon density at the LHC) followed by the "splitting" of the quark q_1 into W/Z. The probability for this splitting increases with the p_T of the quark (or Z/W): $\mathrm{Prob}(q_1 \to q_2 W) \sim \alpha_w/4\pi \ln^2(p_T^2/M_W^2)$. To reduce this effect one has to define an exclusive cross section that should be as close to the LO WZ cross section as possible by cutting on the extra high p_T quark, rejecting any jet with $p_T^{jet} > 50\ GeV, |\eta_{jet}| < 3$). This defines a NLO WZ – "0 jet" cross section which is stable against variations in the choice of the Q^2 but which nonetheless can be off by as much as 20% from the prediction of the Born $S\mathcal{M}$ result.

2.3 Comparison and Discussion

Fig. 1 compares the limits one expects from the NLC and LHC while quantifying the various approximations that can affect the $e^+e^- \to W^+W^-$ analysis. First, the issue of the non-resonant contributions can be quantified. Gintner, Godfrey and Couture [17]

Figure 1: *Limits on (L_{9L}, L_{9R}) from e^+e^- collisions including ISR and beam polarization effects with only the resonant diagrams. The effect of keeping all resonant diagrams for the semi-leptonic final state is also shown. Limits from $\gamma\gamma \to W^+W^-$, and WZ and WW production at the LHC, are also shown for comparison.*

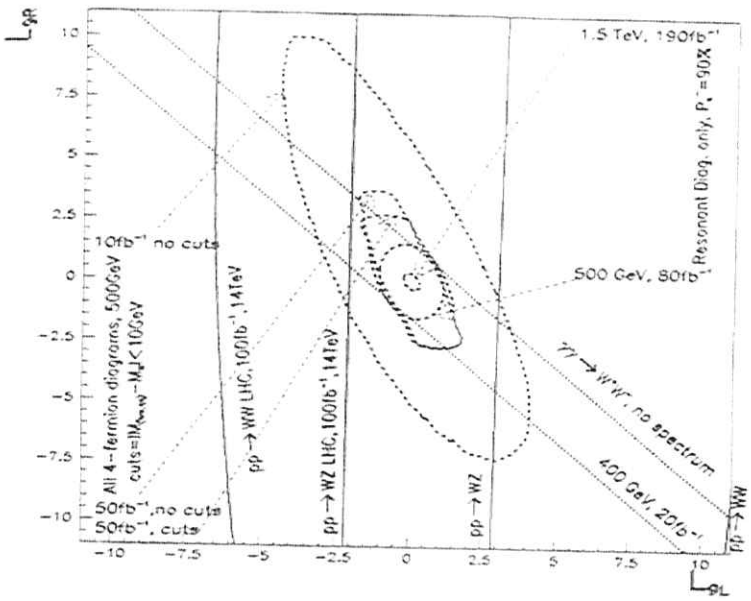

considered all diagrams that contribute to to the semi-leptonic WW final state. Requiring that the jj and $l\nu$ invariant masses are both within 10 GeV of M_W, one essentially selects the doubly-resonant, WW mediated, process. Taking into account all contributions including the background to WW production only marginally degrades the limits. Changing the luminosity can to a very good approximation be accounted for by a scaling factor, $\sim \sqrt{\mathcal{L}}$ (compare the analysis done with a luminosity of 10 fb^{-1} and 50 fb^{-1}). This result is confirmed also by the analysis conducted by Barklow [14] which assumes higher luminosities but incorporates ISR effects as well as beam polarization. When polarization is assumed, the total luminosity shown on the plot is shared equally between a left-handed and a right-handed electron (assuming 90% longitudinal electron polarization).

The important conclusion drawn from Fig. 1 is that through $e^+e^- \to W^+W^-$ alone one indeed reaches the domain of precision measurements with an integrated luminosity of

$50 - 80$ fb^{-1}, matching the accuracy of LEP1 for L_{10}. It is quite fascinating that we can achieve this level of precision already with $\sqrt{s} = 500$ GeV. Moving to the TeV range, the limits improve by an additional order of magnitude (see Fig. 1).

$\gamma\gamma \to W^+W^-$ is quite important. The results [18] shown in Fig. 1 consider a luminosity of 20 fb^{-1} with a peaked fixed spectrum corresponding to a center of mass $\gamma\gamma$ energy of 400 GeV (80% of $\sqrt{s_{ee}} = 500$ GeV). Convolution with a photon spectrum has not been done, since recent studies show that there is still much uncertainty concerning the form of the spectrum due to multiple rescattering effects [19]. Clearly the $\gamma\gamma$ mode helps to improve the limits extracted for e^+e^- collisions at $\sqrt{s} = 500$ GeV and integrated luminosities of 50 fb^{-1} or less.

Fig. 1 also compares the situation with the LHC. One observes that the limits obtained from $W^\pm Z$ production are considerably better than those derived from the WW channel. This is mostly due to the absence of serious background contributions in the WZ case. In the WW case, $t\bar{t}$ production is the main background which is difficult to suppress [16]. However, since $pp \to WZ$ effectively only constrains L_{9L} (through Δg_1^Z), the LHC is not very sensitive to L_{9R}. As a result, with 50 fb^{-1} and 500 GeV, the NLC constrains the two-parameter space much better than the LHC.

Finally, we briefly comment on the genuine quartic couplings, which are parameterized through $L_{1,2}$. These are extremely important as they are the only couplings which involve the longitudinal modes and hence are of crucial relevance when probing the Goldstone interaction. They are best probed through $V_LV_L \to V_LV_L$ scattering. However, for $\sqrt{s} = 500$ GeV the V_L luminosity inside an electron is unfortunately rather small, and one has to revert to $e^+e^- \to W^+W^-Z$ production, as suggested in [11]. This channel has been re-investigated by A. Miyamoto [20] who conducted a detailed simulation including b-tagging to reduce the very large background from top pair production. With a luminosity of 50 fb^{-1} at 500 GeV, the limits are not very promising and do not pass the benchmark criterium $L_i < 10$. It is found that $-95 < L_1 < 71$, $-103 < L_2 < 100$ (one parameter fits). These limits agree very well with the results of a previous analysis [11]. To seriously probe these special operators one needs energies in excess of 1 TeV. At 1 TeV the bounds improve to $L_{1,2} \sim 6$ [3]. However, it is difficult to beat the LHC here, where limits of $\mathcal{O}(1)$ are possible [4] through $pp \to W_L^\pm W_L^\pm$.

In conclusion, it is clear that already with a 500 GeV e^-e^- collider and an integrated luminosity of about $50 - 80$ fb^{-1} one can reach a precision on the parameters that probe SB in the genuine tri-linear WWV couplings which is similar to that which can be achieved with LEP1 from oblique corrections to the Z boson parameters. The sensitivity of the NLC is further enhanced if $\gamma\gamma \to W^+W^-$ can be studied.
Results from this channel would provide invaluable information on the mechanisms of symmetry breaking, if no new particle is observed at the LHC or NLC (Light Higgs and SUSY). The NLC is particularly unique in probing the vector models that contribute to L_9 (with $L_{1,2} \sim 0$) and hence is complementary to the LHC. The latter is extremely efficient at constraining the "scalar" models. To probe deeper into the structure of symmetry breaking, a linear collider with an energy range $\sqrt{s} \geq 1.5$ TeV would be most welcome.

References

[1] S. Dittmaier, D. Schildknecht and G. Weiglein, BI-TP 95/31, hep-ph/9510386; S. Dittmaier, D. Schildknecht and M. Kuroda Nucl. Phys. **B426** (1994); P. Gambino and A. Sirlin, Phys. Rev. Lett. **73** (1994) 621.

[2] P. Langacker, NSF-ITP-95-140, UPR-0683T, Oct. 1995.

[3] F. Boudjema, Proceedings of the *Workshop on Physics and Experiments with Linear e^+e^- Colliders*, eds. F.A. Harris *et al.*, World Scientific, 1994, p. 712.

[4] J. Bagger, S. Dawson and G. Valencia, Nucl. Phys. **B399** (1993) 364.

[5] M. Peskin and T. Takeuchi, Phys. Rev. Lett. **65** (1990) 964.

[6] A. de Rújula, M.B. Gavela, P. Hernandez and E. Massó, Nucl. Phys. **B384** (1992) 3.

[7] T. Inami, C. S. Lim and A. Yamada, Mod. Phys. Lett. **A7** (1992) 2789. See also, T. Inami, C. S. Lim in Proceedings of INS Workshop "*Physics of e^-e^- , $e^-\gamma$ and $\gamma\gamma$ Collisions at Linear Accelerators*, edts Z. Hioki, T. Ishii and R. Najima, p.229, INS-J-181, May 1995.

[8] R. Casalbuoni, S. De Curtis, D. Dominici and R. Gâtto, Phys. Lett. **B155**, 95 (1985); Nucl. Phys. **B282** (1987) 235. R. Casalbuoni et al., UGVA-DPT 1995/10-96, hep-ph/9510431.

[9] G. Couture, S. Godfrey, Phys. Rev. **D50** (1994) 5607.
K. J. Abraham, J. Kalinowski and P. Ściepko, Phys. Lett. **B339** (1994) 136.
A. Miyamoto, in Proceedings of the *Workshop on Physics and Experiments with Linear e^+e^- Colliders*, p. 141, op. cit.

[10] S. Ambrosanio and B. Mele, Nucl. Phys. **B374** (1992) 3; G. Couture, S. Godfrey and R. Lewis, Phys. Rev. **D45** (1992) 777; G. Couture, S. Godfrey, Phys. Rev. **D49** (1994) 5709.

[11] G. Bélanger and F. Boudjema, Phys. Lett. **B288** (1992) 201.

[12] D. Choudhury and F. Cuypers, Phys. Lett. **B325** (1994) 500.

[13] For a list of references on this process, see G. Bélanger and F. Boudjema, Phys. Lett. **B288** (1992) 210.

[14] T. Barklow, SLAC-PUB-6618, Aug. 1994.

[15] U. Baur, T. Han and J. Ohnemus, Phys. Rev. **D51** (1995) 3381, hep-ph/9410226.

[16] U. Baur, T. Han and J. Ohnemus, Phys. Rev. **D53** (1996) 1098, hep-ph/9507336.

[17] M. Gintner, S. Godfrey and G. Couture, Phys. Rev. **D52** (1995) 6249.

[18] M. Baillargeon,G. Bélanger and F. Boudjema, in progress. See also Proceedings of *Two-photon Physics from DAΦNE to LEP200 and Beyond*, Paris, eds. F. Kapusta and J. Parisi, World Scientific, 1995 p. 267.

[19] For an update, see D. J. Schulte, these proceedings.

[20] A. Miyamoto, in the proceedings of the LCW95, Morioka, Japan, Sep. 1995, to appear.

Strongly Interacting Higgs Sectors

Timothy L. Barklow

1 Introduction

With the discovery of the top quark and the measurement of its mass, the Higgs boson mass has become the only parameter of the Standard Model about which we know very little. The Higgs boson mass is a free parameter of the Standard Model and can only be determined by experiment: indeed it is only through experiment that the question of the existence of a Higgs boson resonance can be resolved. From an experimental standpoint alone it is therefore appropriate to consider Higgs bosons of arbitrary mass, including very large masses, as well as to consider the possibility that the Higgs boson resonance doesn't exist.

When the Higgs boson mass gets very large (greater than about 800 GeV), or the Higgs boson resonance disappears altogether, the interactions between the heavier particles of the Standard Model — the $W^{\pm}$, Z bosons and the top quark — become strong at an energy scale of 1 TeV. The Higgs sector is then said to be strongly interacting. In this paper we examine how well an e^+e^- linear collider with a center of mass energy of 500-1500 GeV (the NLC) can study a strongly interacting Higgs sector. We also compare the estimated sensitivity of such a collider with that of the LHC.

2 The Reaction $e^+e^- \to W^+W^-$

Strong electroweak symmetry breaking affects the reaction $e^+e^- \to W^+W^-$ through anomalous couplings at the $W^+W^-\gamma$ and W^+W^-Z vertices and through enhancements in the production of $W_L^+W_L^-$ from $I = J = 1$ resonances. This dual effect on $e^+e^- \to W^+W^-$ is displayed schematically in Fig. 1. Form factors at the three-boson vertex describe multipole moments of the W boson such as the magnetic dipole and electric quadrupole moments. These multipole moments are related to the chiral Lagrangian parameters L_{9L} and L_{0R}. [1] The technipion form factor F_T parameterizes the strong $W_L^+W_L^-$ interaction in the $I = J = 1$ state; it is analogous to the rho-dominated pion form factor in $e^+e^- \to \pi^+\pi^-$.

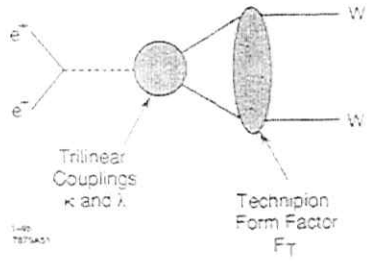

Figure 1: Generalized form of W^+W^- pair-production in e^+e^- annihilation.

Whether one is measuring trilinear vector boson couplings or searching for an enhancement in $W_L^+W_L^-$ production, the experimental goal is the same: disentangle the W^+W^- polarization states, and in particular isolate the polarization state $W_L^+W_L^-$. We shall use the final-state helicity analysis described in the paper by Barklow [2] for this purpose.

2.1 Experimental Cuts

Experimental cuts are used to suppress background to $e^+e^- \to W^+W^-$ and to eliminate genuine W^+W^- events with initial state radiation (beamstrahlung and/or bremsstrahlung) or off-shell W bosons. We impose two cuts. First, we require that $|\cos\Theta| < 0.9$ in order to ensure that the event is well within the detector (assumed hermetic for $|\cos\theta| < 0.98$). For the second cut we form a χ^2 variable which tests the consistency of the event with the production of a pair of on-shell W^+W^- bosons with W^+W^- center of mass energy equal to the nominal e^+e^- center of mass energy. In order to construct this χ^2 variable we reconstruct the mass of the leptonically decaying W (M_{W_l}) and the mass of the hadronically decaying W (M_{W_h}).

The masses M_{W_l} and M_{W_h} are reconstructed by performing a kinematic fit of the momentum of the lepton, $\vec{P}_l$, and the momentum four-vector of the hadronically decaying W, $(E_H, \vec{P}_H)$, subject to the constraint

$$E_H + E_l - \sqrt{\vec{P}_l^2} = \sqrt{s} \tag{1}$$

where

$$\vec{P}_\nu = -(\vec{P}_l + \vec{P}_H) \tag{2}$$

and E_l is the lepton energy.

We define

$$\chi^2 \equiv \frac{(M_{W_1} - M_W)^2}{\Gamma_W^2} + \frac{(M_{W_2} - M_W)^2}{\Gamma_W^2} \quad (3)$$

where M_W is the W boson pole mass. Our second cut is then

$$\chi^2 < 30 \quad (4)$$

2.2 Results for $e^-e^- \to W^-W^-$

The maximum likelihood method is used to fit for chiral Lagrangian parameters or for the real and imaginary parts of the technipion form factor. Our maximum likelihood function L is given by

$$L = \prod_1^N f(\vec{x}_i, \vec{a}) \quad (5)$$

where N is the number of events, f is the probability density function, $\vec{x}_i$ are the measured variables $\vec{x}$ for event i, and $\vec{a}$ are the fit parameters. The probability density function is normalized to unity. The measured variables $\vec{x}$ are $\vec{x} = (\cos\Theta, \cos\theta^*, \phi^*, \cos\bar{\theta}^*, \bar{\phi}^*)$. The fit parameters are $\vec{a} = (L_{9L}, L_{9R})$ or $\vec{a} = (Re(F_T), Im(F_T))$. The covariance matrix V for the $\vec{a}$ which maximizes L is given by

$$(V^{-1})_{ij} = N \int d\vec{x}\, \frac{1}{f} \left(\frac{\partial f}{\partial a_i}\right)\left(\frac{\partial f}{\partial a_j}\right) \quad (6)$$

It is usually more convenient to work with an unnormalized probability density function $\mu(\vec{x}, \vec{a})$ in which case we have

$$f = \frac{\mu}{\Xi}, \quad \Xi(\vec{a}) = \int d\vec{x}\, \mu(\vec{x}, \vec{a}) \quad . \quad (7)$$

Our unnormalized probability density function is given by

$$\mu(\vec{x}, \vec{a}) = R_T \eta_\chi \epsilon(\vec{x}, \vec{a}) \quad (8)$$

where $\epsilon(\vec{x}, \vec{a})$ is the narrow width multi-differential cross section at the nominal $\sqrt{s}$. The factor $R_T = 1.4$ is the ratio of the total W^-W^- cross section calculated with beamstrahlung, bremsstrahlung, and finite W width effects included to the total W^-W^- cross section calculated in the narrow width approximation at the nominal $\sqrt{s}$. The factor $\eta_\chi = 0.45$ is the detection efficiency of the χ^2 cut, Eq. (4), applied to a Monte Carlo event sample generated with beamstrahlung, bremsstrahlung, and finite W width effects included.

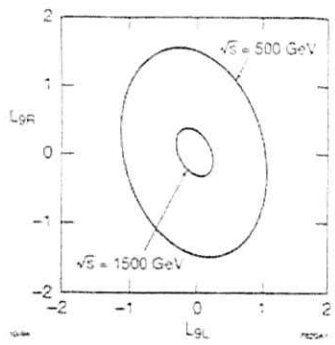

Figure 2: The 95% confidence level contours for L_{9L} and L_{9R} at $\sqrt{s} = 500$ GeV with 80 fb^{-1}, and at $\sqrt{s} = 1500$ GeV with 190 fb^{-1}. The outer contour is for $\sqrt{s} = 500$ GeV. In each case the initial state electron polarization is 90%.

Fig. 2 shows the 95% confidence level contours for the chiral Lagrangian parameters L_{9L} and L_{9R} at $\sqrt{s} = 500$ GeV with 80 fb^{-1}, and at $\sqrt{s} = 1500$ GeV with 190 fb^{-1}. The outer contour is for $\sqrt{s} = 500$ GeV. Technirho resonances with masses of 1.5 and 2.0 TeV would induce values of $L_{9L} = L_{9R} = 2.6$ and 1.6, respectively. [1] Hence, an e^+e^- collider with $\sqrt{s} = 500$ GeV would be sensitive to technirho's with masses of a little over 2 TeV through a measurement of L_{9L} and L_{9R}. An e^+e^- collider would probe much higher mass scales by measuring L_{9L} and L_{9R} at $\sqrt{s} = 1500$ GeV.

As the e^-e^- center of mass energy approaches a technirho resonance the production of longitudinally polarized W's is enhanced. The effects of a $I = J = 1$ resonanace are incorporated [3] by multiplying the standard model amplitude for $e^+e^- \to W_L W_L$ by the complex technipion form factor F_T where

$$F_T = \exp\left[\frac{1}{\pi}\int_0^\infty ds' \delta(s', M_\rho, \Gamma_\rho)\left(\frac{1}{s' - s - i\epsilon} - \frac{1}{s'}\right)\right], \quad (9)$$

$$\delta(s) = \frac{1}{96\pi}\frac{s}{v^2} + \frac{3\pi}{8}\left[\tanh\left(\frac{s - M_\rho^2}{M_\rho \Gamma_\rho}\right) + 1\right]. \quad (10)$$

$v = 240$ GeV, M_ρ is the technirho mass and Γ_ρ is the technirho width. Note that for an infinite technirho mass $\delta(s)$ becomes

$$\delta(s) = \frac{1}{96\pi}\frac{s}{v^2}. \quad (11)$$

reflecting the low energy theorem (LET) amplitude for longitudinal gauge boson scattering.

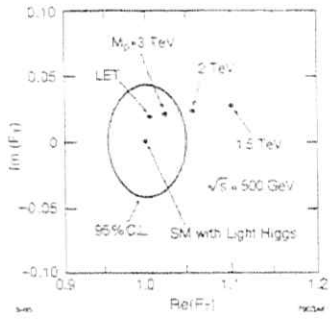

Figure 3: 95% confidence level contours for the real and imaginary parts of F_T at $\sqrt{s} = 500$ GeV with 80 fb^{-1}. The values of F_T for various technirho masses are indicated.

The maximum likelihood formalism is used to fit for the real and imaginary parts of F_T. Fig.3 shows the 95% confidence level contour for the real and imaginary parts of F_T at $\sqrt{s} = 500$ GeV with 80 fb^{-1}. Initial state electron polarization does not play a role in these fits since the form factor F_T is common to both the $W^+W^-\gamma$ and W^+W^-Z amplitudes.

We see that the NLC at $\sqrt{s} = 500$ GeV can exclude technirho masses up to about 2.5 TeV and can discover technirho resonances with masses of more than 1.5 TeV. The significance of the 1.5 TeV technirho signal would be 6.7σ. A 1.0 TeV technirho would produce an 17.7σ signal. Note that the technirho mass reach using the technipion form factor formalism is roughly equal to the mass reach using the chiral Lagrangian formalism.

Fig. 4 contains confidence level contours for the real and imaginary parts of F_T at $\sqrt{s} = 1500$ GeV with 190 fb^{-1}. Shown is the 95% confidence level contour about the light Higgs value of F_T, as well as the 68% confidence level (i.e., 1σ probability) contour about the value of F_T for a 4 TeV technirho. Even the non-resonant LET point is well outside the light Higgs 95% confidence level region and corresponds to a 4.5σ signal. The 6 TeV, 4 TeV and and 3 TeV technirho points correspond to 4.8σ, 6.5σ, and 11σ signals, respectively. A 2 TeV technirho would produce a 37σ signal.

It might appear that the value of F_T, and hence the significance of technirho signals,

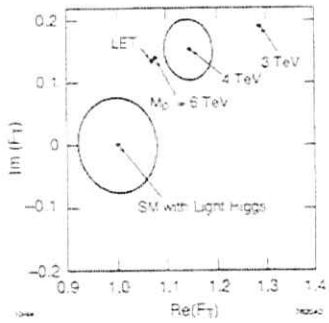

Figure 4: Confidence level contours for the real and imaginary parts of F_T at $\sqrt{s} = 1500$ GeV with 190 fb^{-1}. The contour about the light Higgs value of $F_T = (1.0)$ is 95% confidence level and the contour about the $M_\rho = 4$ TeV point is 68% confidence level.

would be very sensitive to the technirho width when $\sqrt{s}$ is much less than the technirho mass. This is not true, however. The results presented above were obtained assuming that $\Gamma_\rho/M_\rho = 0.22$. If, for example, the technirho width is reduced to $\Gamma_\rho/M_\rho = 0.03$ then the 1 TeV signal at $\sqrt{s} = 500$ GeV is reduced from 17.7σ to 16.3σ, the 1.5 TeV signal at $\sqrt{s} = 500$ GeV is reduced from 6.7σ to 6.4σ, and the 4 TeV signal at $\sqrt{s} = 1500$ GeV is reduced from 6.5σ to 6.3σ.

3 The Reaction $e^+e^- \to \nu\bar{\nu}W^+W^-$ and $\nu\bar{\nu}ZZ$

The important gauge boson scattering processes $W_L^+W_L^- \to W_L^+W_L^-$ and $W_L^+W_L^- \to Z_LZ_L$ are studied at the NLC with the reactions $e^+e^- \to \nu\bar{\nu}W^+W^-$ and $e^+e^- \to \nu\bar{\nu}ZZ$. In this section we describe the analysis that Barger *et al.* [4] have performed to estimate the size of strong symmetry breaking signals at the NLC from these processes.

Barger *et al.* use several models to test the effectiveness of their analysis of $e^+e^- \to \nu\bar{\nu}W^+W^-$ and $\nu\bar{\nu}ZZ$:

1. Standard Model Higgs Boson with Mass $m_H = 1$ TeV.
2. Chirally-Coupled Scalar (CCS) Model (Techni-σ). A scalar mass and width of 1 TeV and 0.35 GeV, respectively, are used.

3. Chirally-Coupled Vector (CCV) Model (Techni-ρ). A technirho mass and width of 1 TeV and 0.03 TeV, respectively, are used.

4. Low-Energy Theorem (LET) Model. When the W^+W^- center of mass energy is much less than the mass of the lightest resonance, then $W_L^+W_L^-$ scattering is expected to be described by the same low energy theorems that govern low energy $\pi^+\pi^-$ scattering. In the LET model, the amplitude for $W_L^+W_L^- \to Z_LZ_L$ is given by s/v^2, which is the LET amplitude for $\pi^+\pi^- \to \pi^0\pi^0$ with the pion decay constant replaced by the Higgs vacuum expectation value v.

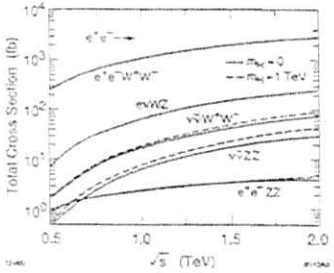

Figure 5: Total cross section versus e^-e^- center of mass energy for processes of the form $e^-e^- \to l_1l_2V_1V_2$ where l_i denotes an electron or electron-neutrino and V_i denotes a $W^\pm$ or Z gauge boson.

The total cross section for processes of the form $e^-e^- \to l_1l_2V_1V_2$, where l_i denotes an electron or electron-neutrino and V_i denotes a $W^\pm$ or Z gauge boson, is shown in Fig. 5 as a function of e^-e^- center of mass energy. The cross sections for the Standard Model Higgs with $m_H = 1$ TeV are given by the dashed curves and are representative of the cross sections for the strongly interacting models we have been discussing. The signal is the difference between the dashed and solid curves.

Barger *et al.* utilize a series of cuts to produce an event sample that is rich in the final states $\nu\bar{\nu}W_L^+W_L^-$ and $\nu\bar{\nu}Z_LZ_L$. Fig. 6 shows the M_{WW} and M_{ZZ} distributions after all cuts. The 1 TeV Higgs scalar resonance stands out in both the $\nu\bar{\nu}WW$ and $\nu\bar{\nu}ZZ$ final states. The 1 TeV vector resonance is prominent in the M_{WW} distribution (of course such a resonance would have been seen much earlier as a 16σ signal at $\sqrt{s} = 0.5$ TeV, in $e^-e^- \to W^-W^-$). The LET signal is larger for the final state $\nu\bar{\nu}ZZ$ than it is for $\nu\bar{\nu}WW$.

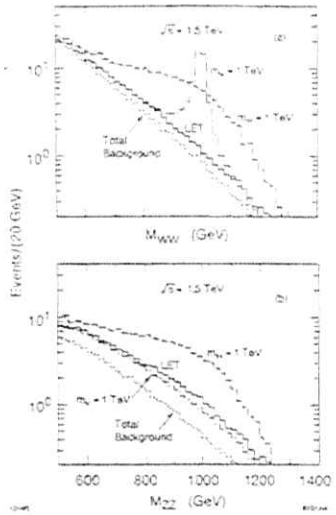

Figure 6: Expected numbers of W^+W^-, $ZZ \to (jj)(jj)$ signal and background events after all cuts for 200 fb^{-1} luminosity at $\sqrt{s} = 1.5$ TeV: (a) $e^-e^- \to \nu\bar{\nu}W^+W^-$, (b) $e^-e^- \to \nu\bar{\nu}ZZ$. Dijet branching fractions and $W^\pm/Z$ identification/misidentification factors are included. The dotted histogram shows total SM background including misidentifications. The solid, dashed and dot-dashed histograms show signal plus background for the LET, SM, and CCV models, respectively; CCS model results are close to the SM case.

Signal (S) or Background (B)	SM $M_H = 1$ TeV	Scalar $M_S = 1$ TeV	Vector $M_V = 1$ TeV	LET
$S(e^-e^- \to \nu\bar{\nu}W^-W^-)$	160	160	46	31
B(backgrounds)	170	170	45	170
$S/\sqrt{B}$	12	12	22	2.4
$S(e^-e^- \to \nu\bar{\nu}ZZ)$	120	130	36	45
B(backgrounds)	63	63	63	63
$S/\sqrt{B}$	15	17	4.5	5.7

Table 1: Signal and background for $e^-e^- \to \nu\bar{\nu}W^-W^-$ and $e^-e^-\nu\bar{\nu}ZZ$ with 0% inital state electron polarization.

Signal (S) or Background (B)	SM $M_H = 1$ TeV	Scalar $M_S = 1$ TeV	Vector $M_V = 1$ TeV	LET
$S(e^+e^- \to \nu\bar{\nu}W^+W^-)$	330	320	92	62
B(backgrounds)	280	280	7.1	280
$S/\sqrt{B}$	20	20	35	3.7
$S(e^+e^- \to \nu\bar{\nu}ZZ)$	240	260	72	90
B(backgrounds)	110	110	110	110
$S/\sqrt{B}$	23	25	6.8	8.5

Table 2: Signal and background for $e^+e^- \to \nu\bar{\nu}W^+W^-$ and $e^+e^-\nu\bar{\nu}ZZ$ with 100% inital state electron polarization.

The statistical significance of the signals for the different models is given in Table 1 assuming 0% e^- polarization at $\sqrt{s} = 1.5$ TeV and $200 fb^{-1}$ luminosity. It is advantageous to give the electron beam a left-handed polarization, as illustrated in Table 2. With 100% initial state electron polarization the number of signal events is doubled while the background to $\nu\bar{\nu}W^+W^-$ is increased by only 65%. Note that the statistical significance of the LET signal is 8.5σ in the $\nu\bar{\nu}ZZ$ channel.

4 The Reaction $e^+e^- \to \nu\bar{\nu}t\bar{t}$

If there is no light Higgs boson then the process $t\bar{t} \to W^+W^-$ violates unitarity at the 1 TeV energy scale. It is natural then to ask if strong symmetry breaking can be detected through the process $W^+W^- \to t\bar{t}$. This process would be studied at the NLC by observing the reaction $e^+e^- \to \nu\bar{\nu}t\bar{t}$.

The total cross sections [5] for $e^+e^- \to e^-e^-t\bar{t}$ and $e^+e^- \to \nu\bar{\nu}t\bar{t}$, as well as the gauge boson helicity components of these cross sections are displayed in Fig. 7. The cross sections are shown as a function of top quark mass assuming that the e^+e^- center of mass energy is 2 TeV. The cross sections for $\sqrt{s} = 1.5$ TeV should be similar.

For $\sqrt{s} = 2$ TeV and $200 fb^{-1}$ luminosity we would have 1200 events from $e^+e^- \to e^+e^-t\bar{t}$ and 60 (400) events from $e^+e^- \to \nu\bar{\nu}t\bar{t}$ for $m_H = 0.1$ (1.0) TeV. A 1 TeV Higgs boson therefore produces a 30% increase in the sum of the cross sections for $e^+e^- \to e^+e^-t\bar{t}$ and $e^+e^- \to \nu\bar{\nu}t\bar{t}$ before any cuts are applied. The same 1 TeV Higgs boson produces

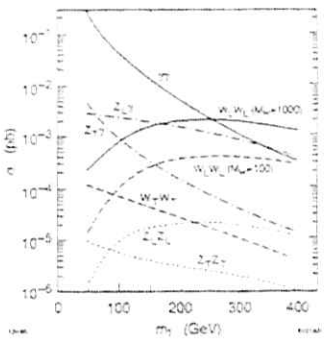

Figure 7: Contributions from various subprocesses to the total cross sections for $e^-e^- \to e^-e^-t\bar{t}$ and $e^+e^- \to \nu\bar{\nu}t\bar{t}$. The contributions are plotted as a function of the top quark mass m_t. The e^+e^- center of mass energy is 2 TeV.

only a 0.3% increase in the sum of the cross sections for $e^-e^- \to e^+e^-W^-W^-$ and $e^+e^- \to \nu\bar{\nu}W^+W^-$.

The strong symmetry breaking signal can perhaps be further enhanced by performing a helicity analysis on the $t\bar{t}$ final state to isolate the helicity combinations $t_L\bar{t}_L$ and $t_R\bar{t}_R$. Projecting out these helicity combinations would be the analog of projecting out the $W_L^+W_L^-$ and Z_LZ_L final states in gauge boson scattering.

5 Statistical significances at LHC versus NLC

The statistical significances of strong symmetry breaking signals at the NLC and LHC are summarized in Table 3. The LHC results come from the ATLAS collaboration. [6] If an entry is blank it may mean that the process is insensitive to the corresponding model or that the analysis has not been done; no distinction is made between the two possibilities. The entries for the direct gauge boson scattering processes at the NLC ($W^-W^- \to ZZ$ and $W^-W^- \to W^-W^-$) assume that the electron beam always has 90% left-handed polarization. For both the NLC and LHC results it was assumed that the 1.5 TeV technirho had a width of 0.33 TeV.

Some points about Table 3 are worth noting:

Collider	Process	$\sqrt{s}$ (TeV)	$\mathcal{L}$ (fb^{-1})	M_ρ = 1.5 TeV	M_H = 1 TeV	LET
NLC	$e^-e^- \to W^-W^-$	.5	80	7σ	-	-
NLC	$e^-e^- \to W^-W^-$	1.0	200	35σ	-	-
NLC	$e^-e^- \to W^-W^-$	1.5	190	366σ	-	5σ
NLC	$W^-W^- \to ZZ$	1.5	190	-	22σ	8σ
NLC	$W^-W^- \to W^-W^-$	1.5	190	-	4σ	6σ
LHC	$W^-W^- \to W^-W^-$	14	100	-	14σ	-
LHC	$W^-W^- \to W^-W^-$	14	100	-	3σ	6σ
LHC	$W^-Z \to W^-Z$	14	100	7σ	-	-

Table 3: Statistical significances of strong symmetry breaking signals at the NLC and LHC.

1. Although the LHC can access larger W^-W^- center of mass energies, the statistical significance of the NLC signal is always larger: 366σ versus 7σ for the 1.5 TeV technirho, 22σ versus 14σ for the 1 TeV Higgs boson, and 8σ versus 6σ for the LET model. Electron beam polarization, smaller backgrounds, and the utilization of the full e^-e^- center of mass energy for vector resonances has allowed the NLC to more than make up for its lower range of W^-W^- center of mass energies.

2. The NLC has a special ability to detect vector resonances. At $\sqrt{s} = 500$ GeV the technirho mass reach of the NLC is equal to that of the LHC. At $\sqrt{s} = 1500$ GeV the technirho mass reach of the NLC extends up to arbitrarily large values, and technirho's with masses up to 4 TeV can be distinguished from non-resonant strong $W_L^-W_L^-$ scattering.

3. Signal significances for $W^-W^- \to t\bar{t}$ were not included in Table 3 because detector simulations have not yet been performed. From the discussion in Sec. 4, however, it appears that this is a promising reaction for the study of strong symmetry breaking at the NLC. It is probably very difficult to study $W^-W^- \to t\bar{t}$ at LHC due to the large background from $gg \to t\bar{t}$.

Finally it is important to remember that the significances shown in Table 3 include statistical errors only. Systematic errors have largely been ignored in analyses so far, both for the LHC and for the NLC.

6 Conclusion

An e^-e^- linear collider with $\sqrt{s} = 500 - 1500$ GeV would be an effective partner to the LHC in the study of strong symmetry breaking. It provides important complementary capabilities for the discovery of vector resonances and the extraction of chiral Lagrangian parameters. The NLC and LHC are expected to have similar statistical errors for scalar resonance and non-resonant signals in gauge boson scattering; however, the physics environments at the two machines are very different, and the systematic errors for the NLC analyses are probably smaller. The NLC is the only machine that can study $W^-W^- \to t\bar{t}$, a process that looks very promising for the study of a strongly interacting Higgs sector.

Acknowledgments

This work was supported in part by U.S. Department of Energy contract DE-AC03-76SF00515.

References

[1] J. Bagger, S. Dawson, and G. Valencia, *Nucl. Phys.* **B399**, 364 (1993).

[2] T. Barklow, in *Workshop on Physics and Experiments with Linear Colliders*, Morioka-Appi, Iwate, Japan, 1995, and in SLAC-PUB-7087.

[3] M. Peskin, in *Physics in Collisions IV*, Santa Cruz, CA, 1984, ed. A. Seiden (Éditions Frontières, Gif-Sur-Yvette, France, 1984).

[4] V. Barger, K. Cheung, T. Han, and R.J.N. Phillips, *Phys. Rev.* **D52**, 3815 (1995).

[5] R.P. Kauffman, *Phys. Rev.* **D41**, 3343 (1990).

[6] ATLAS Collaboration, *ATLAS Technical Proposal for a General Purpose pp Experiment at the Large Hadron Collider at CERN*, CERN/LHCC/94-43, LHCC/P2 (December, 1994).

Aspects of the Determination of Triple Gauge Coupling Parameters from the reaction $e^+e^- \to W^+W^-$ at 500 GeV

R L Sekulin

Rutherford Appleton Laboratory, Chilton, GB-Didcot OX11 0QX, UK

1 Introduction

In this report I consider two aspects of the determination of the trilinear gauge coupling (TGC) parameters from data anticipated at a possible e^+e^- collider at 500 GeV from the reaction $e^+e^- \to W^+W^- \to f_1\bar{f}_2f_3\bar{f}_4$. First, the precision attainable in measurements of particular couplings is estimated using a sample of simulated $e^+e^- \to W^+W^-$ events corresponding to statistics of $10 fb^{-1}$ in the $jj\ell\nu$ channel, in which one W decays into hadron jets and the other leptonically into e or μ. Results are given for fits to one and two TGC parameters. Second, the ambiguities encountered in certain 2-parameter fits are investigated.

The study follows closely a similar one performed for anticipated LEP2 data [1], and a comparison is made with some of the results obtained in [1]. These studies were performed using events generated in the narrow W-width approximation and without inclusion of initial state radiation or of the possible effects of the experimental reconstruction procedure. Subsequent studies [2] have shown that the degradation in precision due to neglect of these factors is not too serious ($\sim 20-30\%$) at LEP2 energies. On the other hand, the ambiguities in 2-parameter fits are shown to arise from properties of the production helicity amplitudes, and the discussion of such effects is best conducted in the present idealized framework.

The TGC parameters considered here are those derived from the C- and P-conserving effective Lagrangian describing the interaction of three vector particles,

$$\begin{aligned}\mathcal{L} &= -ie(A_\mu + g_{ZWW}Z_\mu)(W^{-\mu\nu}W^+_\nu - W^{+\mu\nu}W^-_\nu) \\ &\quad -ie(\kappa_\gamma F_{\mu\nu} + \kappa_Z g_{ZWW}Z_{\mu\nu})W^{+\mu}W^{-\nu} \\ &\quad +\frac{ie}{M_W^2}(\lambda_\gamma F^{\nu\lambda} + \lambda_Z \cot\theta_W Z^{\nu\lambda})W^-_{\lambda\mu}W^{+\mu}_\nu , \qquad (1)\end{aligned}$$

(where the notation is as defined in [1]), but including only contributions from $SU(2) \times U(1)$-conserving operators of dimension ≤ 6 whose effects have not been excluded by analysis of LEP1 and other low energy data. This leads [2] to inclusion of the Standard Model terms, with the WWZ coupling strength given by $g_{ZWW} = \cot\theta_W$, the γ and Z dipole couplings $\kappa_\gamma = \kappa_Z = 1$ and the quadrupole couplings $\lambda_\gamma = \lambda_Z = 0$, and to possible contributions from three further operators. $\mathcal{L}_{W\Phi} \equiv \frac{f_W}{\Lambda^2}(D_\nu\Phi)^\dagger \hat{W}^{\mu\nu} D_\mu\Phi$, $\mathcal{L}_{B\Phi} \equiv \frac{f_{B\Phi}}{\Lambda^2}(D_\nu\Phi)^\dagger B^{\mu\nu} D_\mu\Phi$, and $\mathcal{L}_W \equiv \frac{f_W}{\Lambda^2} tr\hat{W}^\nu_\mu \hat{W}^\lambda_\nu \hat{W}^\mu_\lambda$. Their respective contributions α_{W_Φ}, α_{B_Φ} and α_W are related to the couplings in (1) by

$$\begin{aligned}\alpha_{W_\Phi} &= \delta g_Z s_w c_w , \\ \alpha_{B_\Phi} &= \delta\kappa_\gamma - \delta g_Z s_w c_w , \\ \alpha_W &= \lambda_\gamma , \\ \delta_{\kappa_Z} &= -\frac{s_w^2}{c_w^2}\delta\kappa_\gamma + \delta g_Z , \\ \lambda_Z &= \lambda_\gamma , \qquad (2)\end{aligned}$$

where s_w and c_w are the sine and cosine of the Weinberg angle and $\delta\kappa_\gamma$ and δg_Z represent deviations from SM values. The motivation for this model for the parametrization of anomalous TGCs and alternative formulations have been discussed in detail in the literature (see, for instance, [2]); it should be noted that they include both theoretical considerations and the practical concern that data likely to be accumulated at any presently conceived e^+e^- collider is unlikely to be sufficient to permit a simultaneous determination of all the parameters in the Lagrangian (1).

2 Generator level studies of attainable precision

In this section estimates of the precision attainable in 1- and 2-parameter fits to α_{W_Φ}, α_{B_Φ} and α_W are given using a sample of 13000 events simulated at 500 GeV. The method follows that in [1], in which an extended maximum likelihood fit was made to angular data. Three sets of such data are considered: fits to the production angle, $\cos\theta$, alone; fits to the production angle and to the decay angles of the two Ws , but with the decay angles $(\cos\theta_j, \phi_j)$ of the hadronically decaying W folded according to the ambiguity $(\cos\theta_j \leftrightarrow -\cos\theta_j, \phi_j \leftrightarrow \phi_j + \pi)$; and fits to the production and decay angles without any folding. The second of these configurations corresponds to the situation which will be encountered in practice in analysis of the $jj\ell\nu$ channel due to the inability to distinguish quark from antiquark jets, while the third configuration represents the ideal case, not realizable in practice. The production angle θ is that between the directions of the incoming e^- and the outgoing W^-; the decay angles $(\cos\theta_1, \phi_1)$ and $(\cos\theta_2, \phi_2)$ are defined by the directions of the

lepton (or antilepton) in the W^- and W^+ frames with respect to the W directions in the e^+e^- frame. Precise definitions of these coordinate systems and of the likelihood function used in the maximization fit have been given in [1] and are not repeated here. In terms of these variables the differential cross-section can be expressed as a sum of products of production and decay helicity amplitudes [3, 4]:

$$\frac{d\sigma}{d\cos\theta d\cos\theta_1 d\phi_1 d\cos\theta_2 d\phi_2} = \frac{9\beta}{1024\pi I}\sum_{\lambda\tau_1\tau_2\tau_1'\tau_2'} F_{\lambda\tau_1\tau_2}(\cos\theta)F^*_{\lambda\tau_1'\tau_2'}(\cos\theta)A^{(1)}_{\tau_1\tau_1'}(\cos\theta_1,\phi_1)A^{(2)}_{\tau_2\tau_2'}(\cos\theta_2,\phi_2), \quad (3)$$

where λ, τ_1 and τ_2 represent the helicities of the incoming e^- and the outgoing W^- and W^+ respectively.

Results of 1-parameter fits to α_{W_Φ}, α_{B_Φ} and α_W are shown in table 1 and of 2-parameter fits in the planes of $(\alpha_{W_\Phi}, \alpha_{B_\Phi})$ and $(\alpha_{W_\Phi}, \alpha_W)$ in fig. 1. For comparison, the table includes results taken from ref. [2] of a study of anticipated LEP2 data using the same analysis procedure. It can be seen (in agreement with the results of other NLC studies [5]) that the assumed statistics of $10fb^{-1}$ at 500 GeV provide a ~ 1 order of magnitude improvement in precision in the TGC parameters over that anticipated at LEP2. Also, in common with the conclusions of LEP2 studies [1, 4], it is seen that substantial gains in precision are made by using all the available angular information: the use of the maximum likelihood method, applied to production and available decay angles, ensures that this is the case. In the case of 2-parameter fits, we conclude that, if the production angular distribution only is used, substantial areas of the parameter planes considered remain acceptable at the defined (95%) significance level, and that certain ambiguities remain even if, in addition, decay angular information is used.

3 Ambiguities in 2-parameter fits

The curious shape of the region accepted with 95% confidence in the 2-parameter fit of $(\alpha_{W_\Phi}, \alpha_{B_\Phi})$ to the $\cos\theta$ distribution shown in fig. 1 (and the similar shape observed if the $(\alpha_{W_\Phi}, \alpha_W)$ results, shown in the same figure, are plotted on a smaller scale) is clearly of some interest. I now discuss this phenomenon and show that it is to be expected from the properties of the helicity amplitudes contributing to the cross-section. The discussion follows that in ref. [1], where the possible occurrence of ambiguities in similar fits at 190 GeV was explained. It was shown there that such ambiguities arise for the following reasons:

Parameter	Angular data used	190 GeV	500 GeV
α_{W_Φ}	$\cos\theta$	0.027	0.0026
	$\cos\theta$, $(\cos\theta_\ell, \phi_\ell)$, $(\cos\theta_j, \phi_j)_{\text{folded}}$	0.022	0.0020
	$\cos\theta$, $(\cos\theta_1, \phi_1)$, $(\cos\theta_2, \phi_2)$	0.018	0.0017
α_{B_Φ}	$\cos\theta$	0.109	0.0050
	$\cos\theta$, $(\cos\theta_\ell, \phi_\ell)$, $(\cos\theta_j, \phi_j)_{\text{folded}}$	0.080	0.0038
	$\cos\theta$, $(\cos\theta_1, \phi_1)$, $(\cos\theta_2, \phi_2)$	0.061	0.0034
α_W	$\cos\theta$	0.046	0.0045
	$\cos\theta$, $(\cos\theta_\ell, \phi_\ell)$, $(\cos\theta_j, \phi_j)_{\text{folded}}$	0.032	0.0025
	$\cos\theta$, $(\cos\theta_1, \phi_1)$, $(\cos\theta_2, \phi_2)$	0.022	0.0014

Table 1: 1 standard deviation errors on the fitted values of TGC parameters α_{W_Φ}, α_{B_Φ} and α_W (defined in the text) for simulated data in the $jj\ell\bar{\nu}$ ($\ell \equiv e, \mu$) channel from integrated luminosities of $500pb^{-1}$ at 190 GeV and $10fb^{-1}$ at 500 GeV. Results are shown for fits to various combinations of the angular data.

- Since the helicity amplitudes $F_{\lambda\tau_1\tau_2}(\cos\theta)$ in (3) are linear in the TGC parameters,

$$F_{\lambda\tau_1\tau_2}(\cos\theta) = f_{0,\lambda\tau_1\tau_2} + p_1 f_{1,\lambda\tau_1\tau_2} + p_2 f_{2,\lambda\tau_1\tau_2}, \quad (4)$$

  where p_1 and p_2 represent the deviations of any two TGC parameters from their Standard Model values $(0,0)$, the solution of the equation $\sum_\lambda |F_{\lambda\tau_1\tau_2}(p_1, p_2, \cos\theta)|^2 = \sum_\lambda |F_{\lambda\tau_1\tau_2}(0,0,\cos\theta)|^2$, corresponding to the contribution to the differential cross-section from given W^- and W^+ helicities, summed over electron helicities, will imply a continuous set of ambiguous solutions in the (p_1, p_2) plane described by a conic section (which we take to be an ellipse). In general, the ambiguity ellipse will be different for each value of $\cos\theta$ and for each helicity pair $(\tau_1\tau_2)$.

- Three tree-level diagrams contribute to the reaction $e^+e^- \to W^-W^+$: t-channel ν exchange and s-channel γ and Z exchange. The contributions to any helicity amplitude from the s-channel diagrams all have the same partial wave composition, reflecting the vector nature of the exchange, and thus share a common $\cos\theta$ dependence. This may be factored out from the equation of the ambiguity ellipse, which then takes the form [1]

$$p_1^2(\tilde{f}^2_{1,-1/2} + \tilde{f}^2_{1,1/2}) + p_2^2(\tilde{f}^2_{2,-1/2} + \tilde{f}^2_{2,1/2}) + 2p_1p_2(\tilde{f}_{1,-1/2}\tilde{f}_{2,-1/2} + \tilde{f}_{1,1/2}\tilde{f}_{2,1/2}) + 2p_1(\tilde{f}_{0,-1/2}(\cos\theta)\tilde{f}_{1,-1/2} + \tilde{f}_{0,1/2}\tilde{f}_{1,1/2}) + 2p_2(\tilde{f}_{0,-1/2}(\cos\theta)\tilde{f}_{2,-1/2} + \tilde{f}_{0,1/2}\tilde{f}_{2,1/2}) = 0 \quad (5)$$

[1] Eq. (5) assumes equal phases for the contributing amplitudes, which is the case for the CP-conserving interactions considered here. If p_1 and p_2 represent contributions from operators of opposite CP, no ambiguities of the type considered here occur.

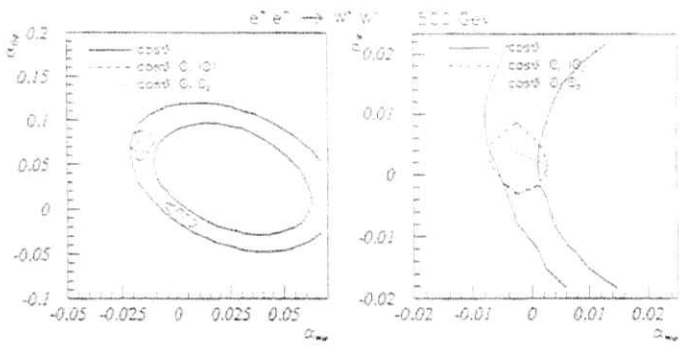

Figure 1: Contours enclosing the 95% confidence limit in the planes of TGC parameters $(\alpha_{W\Phi}, \alpha_{B\Phi})$ and $(\alpha_{W2}, \alpha_{W})$ (defined in the text) for simulated data in the $jj\ell\nu$ $(\ell \equiv e, \mu)$ channel from an integrated luminosity of $10 fb^{-1}$ at 500 GeV. Results are shown for fits to the production angle alone, to the production and decay angles with the decay angles of the hadronically decaying W folded to reflect the ambiguity in distinguishing quark from antiquark jets, and to the production and decay angles with no folding.

where the $\tilde{f}_{i\lambda}$ are the $f_{i\lambda\tau_1\tau_2}$ of (4) above divided by the common factor in $\cos\theta$ and with the common indices $(\tau_1\tau_2)$ suppressed. Only the explicitly shown $\cos\theta$ dependence remains. This comes from the ν exchange contribution to $F_{\lambda\tau_1\tau_2}$, which is zero for $\lambda = -1/2$, does not involve TGCs, and hence contributes only to $f_{0,-1/2\tau_1\tau_2}$.

The points made above (taken from [1]) may now be invoked to explain the ambiguity structure observed in fig. 1. The ambiguity ellipses for various WW helicity pairs $(\tau_1\tau_2)$ are shown in figs 2a and 2b for several values of $\cos\theta$ in the $(\alpha_{W\Phi}, \alpha_{B\Phi})$ plane. In general, these are all different, due to the remaining $\cos\theta$ dependence in (5) and to the fact that the f_i represent different kinematic factors for each helicity pair. However, explicit evaluation of the factor $\tilde{f}_{0,-1/2}$ for $(\tau_1\tau_2) = (00)$ for large $\sqrt{s}$ shows that the $\cos\theta$ dependence occurs in the ratio $\left\{s(1-\cos\theta) + 2M_W^2\right\} / \left\{s(1-\cos\theta) - 2M_W^2\right\}$, which, for $s = 500^2$ GeV^2, is ~ 1 for $\cos\theta \lesssim 0.3$. Thus the ambiguity ellipses for this helicity pair in the range $-1 \leq \cos\theta \lesssim 0.3$ will be more or less coincident, as can be seen from fig. 2a. Moreover, in this region of $\cos\theta$ the (00) amplitude is the dominant TGC-sensitive amplitude at $\sqrt{s} = 500$ GeV, as is evident from fig. 2c, where the $\cos\theta$ dependence of

all helicity amplitude pairs is depicted. (The $(1\ -1) + (-1\ 1)$ amplitudes provide the numerically greatest contribution, but, with $J = 2$ in the s-channel, they are populated only by the ν exchange diagram). Thus, in this $\cos\theta$ region, the extension of eq. (5) to a sum over all helicity amplitudes will show an ambiguity structure dominated by that of the (00) helicity pair on its own. This is demonstrated by the solutions to the equation $\sum_{\lambda\tau_1\tau_2} |F_{\lambda\tau_1\tau_2}(p_1, p_2, \cos\theta)|^2 = \sum_{\lambda\tau_1\tau_2} |F_{\lambda\tau_1\tau_2}(0, 0, \cos\theta)|^2$ shown in fig. 2d. As $\cos\theta$ increases from ~ 0.3 to 1, the (00) ambiguity ellipse shrinks towards the origin (fig. 2a), but the influence of the kinematic factors occurring in the (01) and $(-1\ 0)$ amplitudes, which now join the (00) amplitude in numerical importance, conspires to retain the overall ambiguity ellipse approximately in its previous position. In this situation it is not surprising that, for fixed experimental statistics and for a defined statistical significance level, the ambiguity of fig. 1 is encountered when the production angular distribution is analyzed. However, since more than one WW amplitude pair $(\tau_1\tau_2)$ is involved in the argument given above, it is also understandable that the ambiguity is resolved when the W decay angular distributions are used, as these act as analyzers of the helicity composition of the produced W's.

The preceding discussion gives rise to several more points:

- As can be seen from the plots in fig. 2, an ambiguity persisting over much of the $\cos\theta$ range occurs only in the (00) amplitude pair. These amplitudes contain contributions from the dipole TGC parameters and from δg_Z, but not from the quadrupole parameters λ_γ and λ_Z.

- The s-dependence of the helicity amplitudes (given explicitly, for example, in [4]) is such that, with increasing s, the dominant TGC-sensitive amplitude becomes that from $(\tau_1\tau_2) = (00)$. Also, the $\cos\theta$-dependence of the factor $\tilde{f}_{0,-1/2}$ for this helicity pair, given above, is such that it will remain constant over an increasingly large part of the $\cos\theta$ range as s increases. Thus the ambiguity encountered here may be expected to become worse at still higher energies.

- It is instructive to compare the ambiguities encountered in the analysis at 500 GeV presented here with those at 190 GeV, discussed in ref. [1]. It was shown there that the form (5) for the ambiguity ellipses implied that, for given $(\tau_1\tau_2)$, the ellipses for all values of $\cos\theta$ intersect at two common points (one, clearly, being the origin of the (p_1, p_2) plane). The ambiguity encountered in fits on the $(\delta g_Z, \kappa_\gamma)$ plane studied there was ascribed to the proximity of the (00) and $((01) + (0\ -1))$ intersection points, shown to be at relative location $(1, \frac{1}{2}(1 + 2M_W^2/s))$. Although this ambiguity

(which translates trivially through (2) to a similar relation on the $(\alpha_{W_\Phi}, \alpha_{B_\Phi})$ plane) is expected to improve with increasing s, it is evident that it still affects the 500 GeV results shown in fig. 1, as a secondary solution for $(\alpha_{W_\Phi}, \alpha_{B_\Phi})$ is seen to be acceptable even when decay angular information is used in the analysis [2].

4 Conclusions

Two principal conclusions can be drawn from the study described above. First, data corresponding to an integrated luminosity of $10 fb^{-1}$ at 500 GeV will permit determination of TGC parameters from the reaction $e^+e^- \to W^+W^-$ with a precision about one order of magnitude better than that anticipated from LEP2 data of $500 pb^{-1}$ at 190 GeV. A significant increase in precision is gained by using all the available angular data rather than that from the production angular distribution alone. Use of the maximum likelihood method achieves this aim. Second, in 2-parameter fits to the data, ambiguous solutions are encountered, as previously observed in studies at LEP2 energies. These ambiguities are particularly severe in fits to parameters affecting the longitudinal WW helicity state if only the production angular distribution is used, but is partially resolved by use of the W decay correlations.

References

[1] R. L. Sekulin, Phys. Letts. B 338 (1994) 369.

[2] G. Gounaris *et al.* "Triple Gauge Boson Couplings", HEP-PH/9601233 (1996), to appear in *Physics at LEP2*, G. Altarelli and F. Zwirner eds., CERN Report 1996.

[3] K. Hagiwara, R. D. Peccei, D. Zeppenfeld and K. Hikasa, Nucl. Phys. B 282 (1987) 253.

[4] M. Bilenky, J. L. Kneur, F. M. Renard and D. Schildknecht, Nucl. Phys. B 409 (1993) 22.

[5] M. Bilenky, J. L. Kneur, F. M. Renard and D. Schildknecht, Nucl. Phys. B 419 (1994) 240.

[2] It is of interest to note that this ambiguity should be most severe when the relative intersection defined above is at (1,1) i.e. for $\sqrt{s} = 113$ GeV, just above the planned LEP2 range.

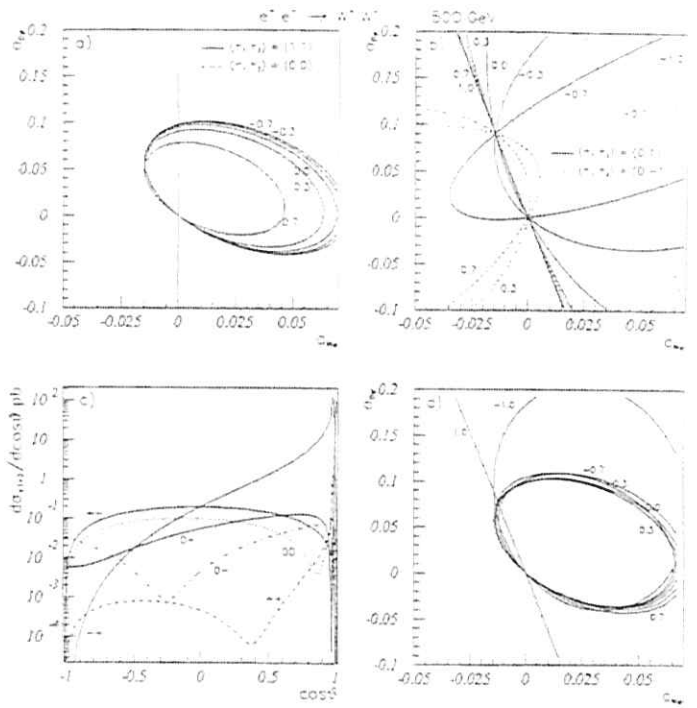

Figure 2: a), b): Loci in the plane of parameters $(\alpha_{W_\Phi}, \alpha_{B_\Phi})$ for which the contributions from various combinations of the helicity amplitudes for $e^+e^- \to W^+W^-$ at 500 GeV are equal to those for Standard Model values of the parameters. For each helicity amplitude combination, solutions are shown for various values of production angle $\cos\theta$, indicated adjacent to the corresponding curve.
a): Solutions for helicity amplitudes $(\tau_1\tau_2) = (11)$ and (00), summed over electron helicities;
b): Solutions for $(\tau_1\tau_2) = (01) + (-10)$ and $(0-1) + (10)$, summed over electron helicities.
c): Contributions from W^+W^- helicity states $(\tau_1\tau_2)$ to the differential cross-section $d\sigma/d\cos\theta$. Each contribution is shown summed over electron helicities. The curves designated as $(0-)$, $(0-)$ and $(+-)$ show the contributions from these states plus their charge conjugates.
d): As a) and b), for solutions summed over all helicities.

MEASURING TRILINEAR GAUGE COUPLINGS AT 500 GEV

Jorgen Beck Hansen
E-mail: Beck@nbi.dk
and
Jorn Dines Hansen
E-mail: Dines@nbi.dk
Niels Bohr Institute, Blegdamsvej 17, DK-2100 Copenhagen, Denmark.

1 Introduction

The production of W pairs at linear colliders allows a detailed study of the gauge structure of the electroweak standard model in the clean environment of e^+e^- collisions. The first measurements of the trilinear gauge couplings via the process $e^+e^- \rightarrow W^+W^-$ will happen with the advent of LEP2 in the near future. The results from LEP2 will improve the bounds on non-standard trilinear gauge couplings substantially. However, with an accuracy of the order of 0.1, only large deviations from the standard model couplings can be observed at LEP2. To reach a sensitivity better than the level of radiative corrections, i.e. of order 10^{-2}–10^{-3}, sufficient to detect new physics far beyond the mass scales of by then existing colliders, it is advantageous to have high energy, clean conditions, and high statistics—all in favour of a linear collider. The potential sensitivity with which the trilinear gauge couplings (TGC) can be determined at a linear collider has been investigated earlier by several authors[1, 2, 3]. Here we study the possible precision obtained under situations closer to reality by using the maximum likelihood method adapted to ISR at linear collider energies of 500 GeV.

2 Gauge Boson Production

The most general parameterisation of the trilinear gauge boson sector involves 14 independent couplings, 7 for each W^+W^-V vertex. Gauge boson pair production in e^+e^- collisions has been studied in great detail, and several groups[4, 5, 6] have calculated the helicity amplitudes for the process $e^+e^- \rightarrow W^+W^-$ for the full set of TGCs[1]. Various naming conventions exist for the TGCs; here we have adopted the notation in [4], where the couplings are parameterised as deviations from their standard model values.

[1] Narrow width approximation and for massless fermions

A complete model independent analysis of the trilinear gauge sector would require a fit with all 14 TGCs as free parameters. However, theoretical assumptions based on general symmetry requirements, dynamical behaviour and expected nature of new physics, restricts the possible non-standard TGCs and introduce constraints among the TGCs. In the following reference will be made to 2 of such models [4] and their respective couplings denoted α_{W_ϕ} and α_{B_ϕ}. The models and the notation are defined in [7].

3 Determination of Trilinear Gauge Couplings

Several methods can be applied to fit the TGCs, differing in the amount of information available and the use of the information. In previous studies at most 3 angular variables where used in a χ^2 fit. As binning in the full five dimensional angular space requires very high statistics, a χ^2 fit is not the optimum way of extracting the TGCs. Instead the TGCs can be determined using a generalised maximum likelihood fit [8] (GML), in which an additional constraint is exploited by assuming that the measured number of events is Poisson distributed around the expected number of events, N_e, i.e.

$$\mathcal{L} = \frac{N_e^N(\overline{\alpha})e^{-N_e(\overline{\alpha})}}{N!}\prod_{i=1}^{N} P(\Omega_i,\overline{\alpha}). \qquad (1)$$

$P(\Omega_i,\overline{\alpha})$ is the probability density for an event with angular configuration Ω_i as function of the TGCs $\overline{\alpha}$, constructed from the differential cross-section and normalised to unity. N_e is a function of the TGCs (via the total cross-section), the integrated luminosity and acceptance.

Studies of the potential accuracies for the different W^+W^- event topologies using the GML in idealised Monte Carlo studies can be found in [7] or in [9].

3.1 Extending the Method to include ISR and Acceptance

As a first step towards a more realistic experimental situation we have studied the impact from ISR and finite width of the W's on the fitted TGCs. Systematic biases originating from these two effects may come from different parts of the analysis and a thorough discussion would involve both the reconstruction of a W^+W^- event as well as the subsequent fit to the measured angular distributions. In many aspects the comments made on ISR also apply to beamstrahlung since, from a experimental point of view, the signatures are identical; missing energy and missing longitudinal momentum.

Detailed studies at energies reachable at LEP2 [10] indicate that neglect of ISR and finite width introduce systematic biases which is slightly less than the envisaged precision at LEP2 for one parameter fits. At linear collider energies the average energy loss induced

by ISR is considerably larger and the effects on the reconstructed angular information is foreseen to be worse. Additional biases may appear when the TGCs are extracted via a generalised maximum likelihood fit not including ISR and finite width. Fortunately the corrections to the total cross-section arising from ISR and finite width, are smaller at linear collider energies than in the threshold region[11], but at the same time the sensitivity increases.

The energy loss from ISR and beamstrahlung will increase at higher energies in comparison with the expected energy resolution ($\delta E/\sqrt{E} \sim 0.5\%$) of the detectors at future linear colliders[3] allowing a reconstruction of the ISR. The question is then what to do with events affected by ISR. One option is to remove such events but at the cost of lower statistics, while still leaving the bulk of events with small ISR effects in the sample. Another possibility is to include ISR in the reconstruction and the subsequent fit of the TGCs. The advantage of this procedure is the increased statistics, but on the other hand the sensitivity in events with ISR is slightly reduced due to their lower centre-of-mass energy. Nevertheless both methods could give rise to biases which have to be corrected afterwards, but it is highly desirable to minimise these biases.

Here we will follow the last method and take into account ISR in the determination of the TGCs by extending the generalised maximum likelihood method to include ISR and acceptance.

In the structure or flux function approximation (good up 3% on the total cross-section), where ISR factorises, the GML may be written (up to terms independent of the TGCs)

$$\ell = \sum_i^N \ln \frac{d\sigma}{d\Omega}(\Omega_i, \overline{\alpha}, s_i') - L \times \int A(\Omega)\, P_{\rm ISR}(s, s')\, \frac{d\sigma}{d\Omega}(\Omega, \overline{\alpha}, s')\, d\Omega\, ds', \qquad (2)$$

for total integrated luminosity L and acceptance function $A(\Omega)$, which in general is not a simple function in the five angular variables. This analysis uses instead

$$\ell = \sum_i^N \ln \frac{d\sigma}{d\Omega}(\Omega_i, \overline{\alpha}, s_i') - L \times < A(\Omega) > \times \int P_{\rm ISR}(s, s')\, \frac{d\sigma}{d\Omega}(\Omega, \overline{\alpha}, s')\, d\Omega\, ds', \qquad (3)$$

where $< A(\Omega) >$ is calculated using the standard model and the cuts discussed in section 4. P_{ISR} is the spectrum of centre-of-mass energy and $d\sigma/d\Omega$ is the differential cross-section for W^-W^- production. The use of Eq. (2) or (3) requires that events can be reconstructed including ISR, such that $s_i' = M^2_{W^-W^-}$, and that Ω_i is determined in the W^-W^- reference frame on an event by event basis.

The systematic biases induced by neglecting ISR and finite width of the W's are summarised in table 1 for fits to α_{W_e} using the full angular information together with fits to the angular information which is available for the different W^-W^- event topologies:

Source of bias	$\cos\vartheta,\ \Theta_1,\ \Theta_2$	$\overline{\cos\vartheta},\ \overline{\Theta}_1,\ \overline{\Theta}_2$	$\cos\vartheta,\ \Theta_1,\ \overline{\Theta}_2$	$\overline{\cos\vartheta,\ \Theta_{l1},\ \Theta_{l2}}$
Finite width (F)	< 1 s.d	0.002	0.001	-0.094
F+ISR (rescaled)	-0.175	-0.108	-0.154	-0.180
F+ISR (CMS angles)	-0.012	-0.012	-0.015	-0.020
F+ISR (ext. GML)	< 1 s.d.	< 1 s.d.	≤ 1 s.d	0.008

Table 1. The systematic shifts induced by neglecting finite width of the W's and using different methods to account for ISR for one parameter fits to α_{W_e} using different set of angular information ($\sigma^{expected}_{\alpha_{W_e}} \sim \mathcal{O}(0.001)$). A set of decay angles $(\cos\theta,\ \phi)$ is denoted by Θ, and $\overline{\Theta}$ means that folding has been applied. In the last column the folding is done for the two-fold lepton ambiguity.

- For purely leptonic W^-W^- decays, $\ell\nu\ell\nu$, the momenta of the 2 neutrinos are undetermined. Constraining the mass of the two lepton-neutrino systems to the W mass in addition to the usual four-momentum conservation the momenta of the two neutrinos can be determined up to a two-fold ambiguity [5].

- In the semi-leptonic decays, $\ell\nu jj$, the W charge is known and the leptonic W decay is completely determined. The missing information about the original flavour of either jets implies the ambiguity $(\cos\theta_j \leftrightarrow -\cos\theta_j,\ \phi_j \leftrightarrow \phi_j + \pi)$, i.e. swapping particle and anti-particle for the quarks.

- In the case of hadronic decays, $jjjj$, neither the W charge nor the quark flavours are known resulting in an eight-fold ambiguity.

In the first row in table 1 the shifts in the fitted TGCs with respect to the ideal case is given for events generated with finite width but analysed in the narrow width approximation. The second row in table 1 lists the shifts in the TGCs obtained by fitting events generated with ISR and finite width assuming no ISR and narrow width, where energy and momentum conservation is assured by simple rescaling. The third row gives the shifts found when reconstructing the angles in the W^-W^- centre-of-mass frame but ignoring the energy loss due to ISR. The last row contain the shifts obtained by fitting the events using the GML method defined in Eq. 3. From the table we see that the shifts from ISR is larger than those from finite width. Furthermore table 1 shows that the biases can be considerably larger than the expected precision at a 500 GeV linear collider depending on the reconstruction of the angles. Clearly, accurate knowledge of the energy loss due to ISR (Beamstrahlung) is vital in the reconstruction of the angular information and for the fit to the TGCs in order to avoid large biases, as can be seen from the last row.

4 Precision in TGC Measurements at 500 GeV

In this section we will present and discuss the accuracy that can be expected at a linear collider at 500 GeV for the different W^+W^- event types in a setup closer to the realistic experimental situation, focusing on event reconstruction, detector resolution and backgrounds. Similar studies has been done by others [2, 3]. We will expand on some of these studies and include progress made in understanding the fit of the TGCs.

4.1 Experimental simulation

A complete understanding of the many experimental aspects that play a role for the attainable precision in the TGCs will require the full simulation of a detector for a linear collider. However, these studies has been done using $e^+e^- \to W^+W^-$ events generated with PYTHIA [12] at 500 GeV with ISR and finite width and subsequent smeared according to a conceptual linear collider detector:

Tracking In the central region the momentum resolution is taken to be

$$\frac{\delta p}{p_t^2} = 10^{-3}\mathrm{GeV}^{-1}.$$

In the forward region ($\tan\theta < 0.71$) the resolution is degraded

$$\frac{\delta p}{p_t^2} = (\frac{0.71}{\tan\theta})^2 \times 10^{-3}\mathrm{GeV}^{-1}.$$

Energy resolution Combining calorimeters and tracking give an energy flow measurement with resolution

$$\frac{\delta E}{\sqrt{E}} = 0.5\sqrt{\mathrm{GeV}}.$$

For charged particles the better of tracking or energy flow is applied.

Hermetic coverage The very forward peaked W^+W^- production requires a very good coverage in the forward direction and we consider region of acceptance

$$|\cos\theta| < 0.98.$$

The generated data sample has an integrated luminosity of 10 fb^{-1}, corresponding to one year of running. Finally, two background samples with ZZ and $Z\gamma$ respectively, have been generated and passed through the same smearing.

4.2 W^+W^- → Hadron-Hadron

With a W hadronic branching ratio of $\frac{2}{3}$, the purely hadronic W^+W^- decay channel is statistical superior ($\sim 48\%$ with QCD corrections) when compared to the semi-leptonic and purely leptonic channels. The disadvantages of this decay channel is that a priori knowledge of the primary particle flavour knowledge is lost or hard to retrieve in addition to the missing information on the W-charge. Furthermore the background contributions from ZZ and $Z\gamma$ are difficult to remove.

The main characteristics of $jjjj$ events are high multiplicity and large visible energy and this is reflected in the selection criteria:

- Large multiplicity, $N_{charged} > 15$;
- Significant visible energy, $E_{total} > 400$ GeV;
- No high-energetic leptons, $E_{lepton}^{max} < 50$ GeV;
- The event is forced into 4 jets with at least 4 particles in each jet to ensure well reconstructed jets.

In addition to the above selection criteria cuts on sphericity/thrust and angles between jets give high discrimination against the background but their efficiency diminish with energy and any cut on angular distributions is a potential source for biases.

For events satisfying the cuts a kinematic fit is applied to improve the resolution of the jets by imposing external constraints. In contrast to simple rescaling[2] of the jets to fulfill energy and momentum conservation, the kinematic fit allows inclusion of additional information using the characteristics of W^+W^- events. Many different kinematic fits exist [10]; for this study a fit taking into account the ISR spectrum in the LL approximation and Breit Wigners for the two W's has been used.

The advantage is that we get an estimate of the ISR from the correlations among the jets in the event. Instead one could just take the ISR as the missing momenta along the beam, but then missing particles would also contribute as well and the ISR spectrum well be overestimated. The ISR spectra for the two different methods are plotted in figure 1. From the plot it is evident that the kinematic fit does a better job in obtaining the ISR spectrum. The bend-over observed in the spectrum from the kinematic fit originate from the ability to separate ISR and detector resolution effects, and it can be seen that the fit can reconstruct ISR down to about 3 GeV.

[2] At 500 GeV the difference in improvement in resolution of kinematic fitting versus rescaling is small.

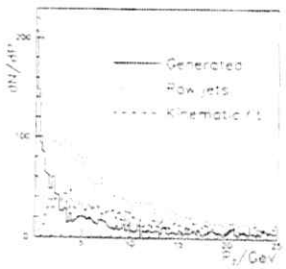

Figure 1: The ISR spectra from simple rescaling and kinematic fitting: plotted together with the generated spectrum.

The inclusion of Breit Wigners in the kinematic fit can be combined with a cut on the χ^2 from the fit to choose the best pairing of the 4 jets into two W's and further constrain the background while at the same time improve the energy resolution of the jets. The obtained efficiencies for W^-W^- and background events can be found in table 2.

4.3 $W^-W^- \rightarrow$ Lepton-Hadron

The semi-leptonic W^+W^- decay channel is in general considered to be the optimal for measurements of the TGCs because almost complete information can be obtained on the W-pair production. In contrast to the purely hadronic W^+W^- events only the flavour composition of the hadonic decay is unknown, but the drawback is the missing neutrino affecting the kinematic reconstruction. The branching fraction is sizable ($\sim 42\%$), but $\frac{1}{3}$ of the events contain a τ which give additional complications and have been excluded in this analysis, reducing the useful branching ratio to about 28%.

The dominant backgrounds are expected to come from semi-leptonic W^+W^- events with a leptonic τ decay ($B^{\tau}_{e\mu} \sim 35\%$), $Z\gamma$ events with leptons from heavy flavour decays and ZZ events. The typical selection criteria used for $\ell\nu jj$ aim at reducing these backgrounds by requiring

- Significant multiplicity, $7 < N_{charged} < 30$;
- Identified electron or muon with large momentum, P> 100 GeV;
- The missing transverse momentum should be larger than 10 GeV. Eliminates $Z\gamma$ events with a photon down the beam-pipe.
- The hadronic part of the event is split into 2 jets with at least 4 particles in each jet to ensure well reconstructed jets.

As for the hadronic W^-W^- events a kinematic fit with ISR and Breit Wigners is applied but the effect on the energy resolution is limited due to the missing neutrino momentum lowering the number of constraints. A cut is imposed on the χ^2 from the kinematic fit. The resulting efficiencies for W^-W^- and background events can be found in table 2.

4.4 $W^+W^- \rightarrow$ Lepton-Lepton

With a W leptonic branching ratio of $\frac{1}{3}$, the purely leptonic W^+W^- decay channel is the least statistically significant ($\sim 10\%$) when compared to the semi-leptonic and hadronic channels. The extra neutrino in $W \rightarrow \tau\bar{\nu}_\tau \rightarrow X\nu_\tau\bar{\nu}_\tau$ decays makes it impossible to reconstruct such events, reducing the effective branching ratio to around 5%. Furthermore, the missing neutrino momenta imply that the W-direction cannot be determined unambiguously, a priori making this channel difficult to exploit.

The selection criteria used in this study to select $\ell\nu\ell\nu$ events are

- The event contains exactly 2 reconstructed leptons, electrons or muons.
- The missing transverse momentum should be larger than 10 GeV. The purpose of this cut is to remove $Z \rightarrow l\bar{l}$ with a possible photon down the beam-pipe.
- In case of equal flavours the lepton-lepton system should not have a mass close to M_Z.

$$M_{ll} < M_Z - 4\Gamma_Z \text{ and } M_Z + 4\Gamma_Z < M_{ll}.$$

The background from $Z\gamma$ and ZZ can be easily discarded by requiring different flavours of the 2 leptons, but this would remove half of the signal events.

For $\ell\nu\ell\nu$ events the momenta of the 2 neutrinos are unknown, but in the case of no ISR and under the assumption that the event consists of two decaying W's, we have six constraints allowing us to reconstruct the momenta of the neutrinos up to a two-fold ambiguity [5]. Finite width effects and ISR influence the existence of solutions[3], and for background events the required existence of solutions gives a very strong suppression.

It should be stressed that the reconstruction of purely leptonic W^+W^- events requires the use of all kinematical information available in the event, leaving no further possibilities of removing background events or account for ISR and finite width.

[3]About 20% of the events at generator level have no solutions due to ISR and finite width effects.

Event type	$jjjj$	$\ell\nu jj$	$\ell\nu\ell\nu$
Signal (%)	38.2	33.2	34.9
Background (%)		0.0	
$Z\gamma$	0.16	(50K events)	0.24
ZZ	2.53	0.08	0.13

Table 2: Final efficiencies for the different W^+W^- event types and the dominant background processes for smeared Monte Carlo events ($\sigma_{WW} \sim 0.1 \times \sigma_{Z\gamma} \sim 10 \times \sigma_{ZZ}$).

	$\overline{\cos\vartheta}$, $\overline{\Theta}_1$, $\overline{\Theta}_2$	$\cos\vartheta$, Θ_1, $\overline{\Theta}_2$	$\overline{\cos\vartheta}$, Θ_{11}, Θ_{12}
Bias	-0.073	-0.015	-0.060
Precision	0.002	0.003	0.006
Bias (ISR)	-0.072	-0.013	-
Precision (ISR)	0.002	0.003	-

Table 3: The total systematic shifts and precisions obtained for one parameter fits to α_{W_e} for different set of angular information. The fits have been made using the GML method the assumption of no ISR and with ISR, respectively.

4.5 Results

The resulting efficiencies for the different W^+W^- event topologies after selection and reconstruction can be found in table 2. The table also lists the rejection efficiencies for the various backgrounds. From the results in table 2 it is seen that the overall efficiencies for the various W^+W^- event types are similar, with $\ell\nu jj$ being lowest. The background rejection efficiencies show that the $Z\gamma$ background is the most dominant ($\sigma_{WW} \sim 0.1\sigma_{Z\gamma}$); especially for the $\ell\nu\ell\nu$ events, whereas ZZ contribute to $jjjj$However, it is possible to further improve the efficiencies by more sophisticated cuts. The main reason for the low efficiencies is that a substantial part of the events are lost because the decay particles from the very forward W's are boosted outside the angular acceptance region. For the $jjjj$ and $\ell\nu jj$ channels there is furthermore an implicit cut on very larger ISR via the cut on the χ^2 from the kinematic fit. To study the effects of detector resolution and events reconstruction one parameter fits for α_{W_e} and two parameter fits for $(\alpha_{W_e}, \alpha_{B_e})$ have been performed for the 3 basic decay modes with events passing the different sets of cuts. For a definition of the fitted TGCs and the related theoretical assumptions the reader may refer to [7] in these proceedings or [10]. In the one parameter case the fits were performed using the generalised maximum log-likelihood method adapted to ISR described in section 3.1 and, for comparison, with no ISR. The obtained precisions and biases from the one parameter fits are summarised in table 3. In figure 2 the corresponding 95% confidence plots from the two parameter fits are shown for fits to detector smeared

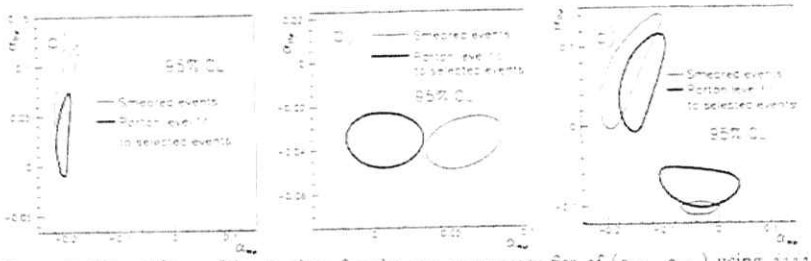

Figure 2: The 95% confidence plots for the two parameter fits of $(\alpha_{W_e}, \alpha_{B_e})$ using $jjjj$ (a), $\ell\nu jj$ (b) and $\ell\nu\ell\nu$ (c) events. For a discussion of the complex structure seen in c) the reader may refer to [9] or [7].

events and fits using parton level information for events passing all cuts. From the results in table 3 and the 95% confidence plots in figure 2 several conclusions may be drawn.

In the pure hadronic channel the 8-fold ambiguity result in loss of sensitivity but given that this is the dominant decay channel in W^+W^- events the higher statistics partly compensates for that, and besides, the use of this channel clearly can be improved by jet-charge and quark tagging techniques — after all, half of the hadronic W decays contain a c-quark with very little background from b-quarks. The purely leptonic channel is seen to have a very high sensitivity to the TGCs — as good as (or better) than the semi-leptonic case considering the limited number of events used in the fit for this channel. The reason for this is that the five-fold differential cross-section used in the fit is largely unaffected under the transformation of one solution of the neutrino momenta to the other and preserves a clear one to one correlation in contrast to the semi-leptonic case, where no correlation is observed. The strong correlation remains unaffected varying α_{W_e} from -1 to 1. Furthermore, from the different plots it is clear that the acceptance for the $jjjj$ and $\ell\nu\ell\nu$ decay channels gives large biases compared to the precisions.

Table 3 shows that the inclusion of ISR in the fit results in very small changes however, the dominant effect comes the reconstruction of the angles, which is common for the $jjjj$ and $\ell\nu jj$ fits in table 3.

As can be seen the $\ell\nu\ell\nu$ and $jjjj$ channels suffer large biases due to reconstruction. For $\ell\nu\ell\nu$ this is because the reconstruction cannot take into account the ISR, while for the $jjjj$ channel the reason is due bad jet reconstruction affecting the resolution and the jet-jet pairing. Naively one would expect that the jets at linear collider energies would be narrow and easy to separate but the W's tend to decay along the direction of flight and the "backward" jet is boosted on top of the forward jet, mimicking a single jet, or one could loose part of a jet in the forward dead area.

5 Conclusion

The purpose of this study was to investigate the experimental aspects of trilinear gauge coupling determination at 500 GeV. We have employed a method that have recently been used in the preparations for LEP2. With LEP2 the quantitative content of the many Monte Carlo studies with this method can be cross-checked to consolidate and improve the statements for the linear collider. We have studied the usefulness of the different W^+W^- event types in more realistic experimental environments. Of particular interest is the observation that ISR and Beamstrahlung can be controlled and accounted for in the fits. Finally, it is observed that acceptance and reconstruction can give rise to substantial biases.

References

[1] M. Bilenky, D. Schildknecht, J.L. Kneur and F.M. Renard, in Proceedings of the Workshop on e^+e^- *collisions at 500 Gev: The physics potential*, **DESY 93-123C** (1993) 187.

[2] M. Frank, P. Mättig, R. Settles and W. Zeuner, in Proceedings of the Workshop on e^+e^- *collisions at 500 Gev: The physics potential*, **DESY 92-123A** (1992) 223.

[3] R. W. Forty, J. B. Hansen, J. D. Hansen and R. Settles, in Proceedings of the Workshop on e^+e^- *collisions at 500 Gev: The physics potential*, **DESY 93-123C** (1993) 235.

[4] M. Bilenky, J.L. Kneur, F.M. Renard and D. Schildknecht, *Nucl. Phys.* **B409** (1993) 22.

[5] K. Hagiwara, R. Peccei, D. Zeppenfeld and K. Hikasa, *Nucl. Phys.* **B282** (1987) 253.

[6] G. Gounaris, J. Layssac, G. Moultaka and F.M. Renard, *Int. J. Mod. Phys.* **A8** (1993) 3285.

[7] R.L. Sekulin, these proceedings.

[8] A.G. Frodesen, O. Skjeggestad and H. Tofte, *Probability and Statistics in Particle Physics* (Universitetsforlaget, Bergen, 1978).

[9] J.B. Hansen and J.D. Hansen, to appear in Proceedings of LC2000 Workshop on *Physics and Experiments with Linear* e^+e^- *colliders*, Morioka, Japan (1995).

[10] Internal note from LEP2 work groups, to appear as CERN yellow report.

[11] D. Bardin, M. Bilenky, A. Olchevski and T. Riemann, in Proceedings of the Workshop on e^+e^- *collisions at 500 Gev: The physics potential*, **DESY 93-123C** (1993) 159.

[12] T. Sjostrand, *Computer Physics Commun.* **82** (1994) 74.

[13] R.L. Sekulin, *Phys. Lett.* **B338** (1994) 369.

Measurement of the Three Boson Couplings at 2 TeV

Klaus Mönig, CERN

1 Introduction

If no light Higgs boson can be found at LEP or LHC the precise understanding of the three boson couplings is a good possibility to get some inside in the mechanism, masses are generated in nature. It is generally known since some time that the precision, these couplings can be measured, gets better with increasing centre of mass energy. On the other hand at very high beam energies analyses are seriously disturbed by a large energy spread due to beamstrahlung.

The aim of this study is to get a quantitative estimate how well the three boson couplings can be measured at a centre of mass energy of 2 TeV. Events have been generated and smeared according to a given detector. These events have been fitted taking into account all smearing and acceptance effects.

2 Event Generation

For this study events have been generated with the PYTHIA Monte Carlo [1] and tracks have been smeared according to the "TeV detector" described in [2]. Only events of the type $e^+e^- \rightarrow W^+W^-$ where one W decays leptonically and the other one hadronically have been considered. The main features of the simulated detector are:

- Charged track resolution: $\delta\frac{p_t}{p_t} = 2 \cdot 10^{-4} GeV^{-1}$,
- Electromagnetic calorimeter resolution: $\frac{\delta E}{\sqrt{E}} = 0.1\sqrt{GeV}$,
- Hadron calorimeter resolution: $\frac{\delta E}{\sqrt{E}} = 0.65\sqrt{GeV}$,
- Hermeticity: $|\cos\theta| < 0.985$.

For the beamstrahlung an energy spectrum with a mean energy loss of 18% and an energy spread of 16% has been assumed.

3 Event Reconstruction and Selection

The event selection has been designed not only to reject background but also to reject events that have been badly reconstructed or where too much energy was lost due to radiation. The following cuts have been used:

- Exactly one lepton is seen outside hadronic jets.
- The polar angle of the lepton is larger than 20°.
- The number of charged particles is larger than 6.
- The hadronic energy is larger than 700 GeV.
- The hadronic mass is between 70 GeV and 100 GeV.
- The square of the missing mass is less than $4.5 \cdot 10^5 GeV^2$.

Fig. 1 a) shows the centre of mass energy after radiation for all events with $|\cos\theta_W| < 0.9$ and for those passing all cuts.

Since at 2 TeV the detector resolution is smaller than the average energy loss due to radiation the constrained fitting techniques proposed for lower energies are no longer useful. Instead the neutrino momentum was reconstructed assuming that the lepton neutrino pair has the W mass and that all photons were radiated along the beampipe. In general this leads to two possible solutions of which, if both solutions were physical, the one with the smaller acolinearity between the W's has been chosen. From the information of this reconstruction the effective centre of mass energy, the W production angle and the decay angles of the leptonically decaying W have been reconstructed. The decay angles of the hadron side have been reconstructed by forcing the hadrons into two jets and using the jets as approximation of the quarks. No attempt has been made to distinguish the quark and the antiquark. Fig. 1 b) shows the resolution of the polar decay angle for the lepton and the hadron side.

Several sources of background to the selected process have been studied. The only one that turns out to be relevant is the W pair production where one W decays hadronically and the other one into $\tau\bar{\nu}_\tau$ and the τ decays leptonically. Due to the large energy loss from radiation these events cannot be rejected by missing mass criteria. Thus the size of the background is about equal to the leptonic branching ratio of the τ (17%). Due to the additional energy carried away by neutrinos the events are dominantly reconstructed

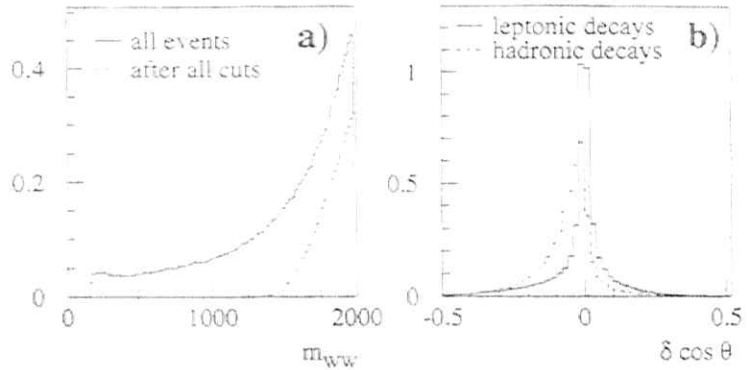

Figure 1: *a) invariant mass of the W pair for all events with $|cos\theta_W| < 0.9$ and for events that passed all cuts. b) Polar decay angle resolution for all leptonically (solid line) and hadronically (dashed line) decaying W's.*

at a cosine of the polar decay angle close to -1 and an azimuthal decay angle close to 0 or π. A large fraction of these events can, however, be removed by the use of a silicon microvertex detector.

4 Fit procedure and results

To fit the data, including all smearing and acceptance corrections, a binned maximum likelihood fit has been used. Since for multidimensional distributions the number of bins becomes rapidly very large, only the W production angle ($\cos\theta_W$) and the polar decay angle for the lepton ($\cos\theta_l^*$) and the quark side ($|\cos\theta_q^*|$) were considered.

To calculate the likelihood for a given anomalous coupling a large number of Monte Carlo events with standard couplings have been generated. These events have been weighted according to the ratio of differential cross sections assuming the given anomalous couplings to the one assuming standard couplings. To calculate the weights the generated angles have been used, where the cross section was evaluated at the true centre of mass energy after radiation. The weights have been summed up in bins of the measured quantities and then been compared with the "data" assuming Poisson statistics. This procedure takes into account all corrections due to smearing and beamstrahlung effects exactly. Since no analytical formulae for W production with anomalous coupling including a finite W width and QED corrections exist, Born level formulae in the zero width approximation according to [3] have been used. To account partially for QED corrections the events have been boosted into the W^+W^- rest frame before calculating the "true" decay angles. Per construction this procedure introduces no bias if the true couplings are equal to the standard ones, even if the formulae used are not exactly correct. Fits have been performed with one to three anomalous couplings left free and constraints amongst the other ones as suggested in [3]. To examine the effect of beamstrahlung another dataset has been generated without this effect. Table 1 summarizes the fit results with and without beamstrahlung assuming a total integrated luminosity of 320 fb^{-1}. Fig. 2 shows the 95% confidence limit contours from a fit to (x_γ, y_γ) assuming the same luminosity. In all cases the total cross section has not been used in the fit. However the improvement using it is only about 10%. In this case, however, the luminosity and acceptance must be known to about 0.1%.

Free parameters	Constraints	Error with Bs.	Error without Bs.
δ_Z		$\pm 1.4 \cdot 10^{-4}$	$\pm 1.6 \cdot 10^{-4}$
x_γ	$\delta_Z = \frac{s_W}{c_W} x_\gamma$, $x_Z = -\frac{s_W}{c_W} x_\gamma$	$\pm 4.8 \cdot 10^{-5}$	$\pm 3.2 \cdot 10^{-5}$
y_γ	$y_Z = \frac{c_W}{s_W} y_\gamma$	$\pm 2.1 \cdot 10^{-4}$	$\pm 1.5 \cdot 10^{-4}$
x_γ	$\delta_Z = \frac{s_W}{c_W} x_\gamma$, $x_Z = -\frac{s_W}{c_W} x_\gamma$	$\pm 5.2 \cdot 10^{-5}$	$\pm 3.3 \cdot 10^{-5}$
y_γ	$y_Z = \frac{c_W}{s_W} y_\gamma$	$\pm 2.2 \cdot 10^{-4}$	$\pm 1.6 \cdot 10^{-4}$
δ_Z		$^{+4.2}_{-3.6} \cdot 10^{-3}$	$^{+3.0}_{-1.3} \cdot 10^{-3}$
z_γ	$z_Z = -\frac{s_W}{c_W} z_\gamma$	$^{+3.4}_{-0.8} \cdot 10^{-3}$	$^{+4.1}_{-0.4} \cdot 10^{-3}$
δ_Z		$^{+4.2}_{-3.6} \cdot 10^{-3}$	$^{+3.0}_{-1.3} \cdot 10^{-3}$
z_γ	$x_Z = -\frac{s_W}{c_W} x_\gamma$	$^{+3.5}_{-0.8} \cdot 10^{-3}$	$^{+4.2}_{-0.4} \cdot 10^{-3}$
y_γ	$y_Z = \frac{c_W}{s_W} y_\gamma$	$\pm 2.3 \cdot 10^{-4}$	$\pm 1.6 \cdot 10^{-4}$

Table 1: *Results of different fits to anomalous coublings with and without beamstrahlung. The notation of [3] is used. Non fitted parameters not mentioned under "Contraints" are fixed to their SM value.*

5 Conclusions

The possibility to measure the anomalous couplings of gauge bosons at a 2 TeV collider has been studied. With an integrated luminosity of 320 fb^{-1} precisions of about 10^{-4} can be obtained. The degradation of the results due to the presence of beamstrahlung is about 30% not justifying any strong attmept to reduce the beamstrahlung parameter, especially if this would result in a significantly lower luminosity.

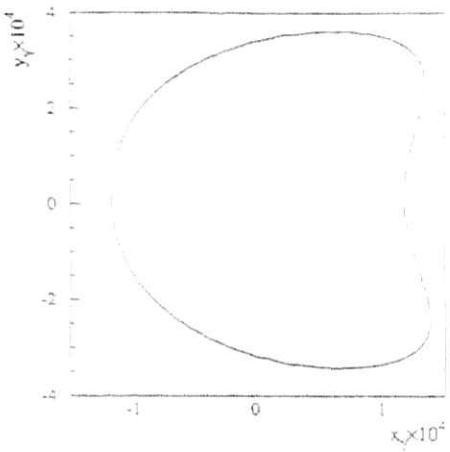

Figure 2: *95% confidence level contours with (solid line) and without (dashed line) for the (z_γ, y_γ) fit. The constraints amongst the other couplings are as described in table 1.*

References

[1] T. Sjostrand, Comp. Phys. Com. **82** (1994) 74.

[2] R. Settles, *Machine Physics and Detector Interplay at the Next e^-e^- Linear Collider* in *e^-e^- Collisions at 500 GeV: The Physics Potential, Part C*, DESY 93–123C.

[3] M. Bilenkii et al., Nucl. Phys. **B409** (1993) 22.

Optimal Observables for measuring three-gauge-boson couplings in $e^+e^- \to W^+W^-$

M. Diehl and O. Nachtmann

1 Introduction

In this contribution we propose a method to measure the trilinear gauge couplings in the reaction $e^+e^- \to W^+W^-$. For the WWZ and $WW\gamma$ vertices we use the most general parametrisation consistent with Lorentz invariance of Hagiwara et al. [1]. It describes each vertex by seven form factors f_i, three of which correspond to CP violating couplings.

We shall consider the decay channels $WW \to \ell\nu_\ell$ + jet jet, where ℓ is a light lepton e or μ and the jets originate from a quark-antiquark pair. For these channels a complete kinematical reconstruction of the four-fermion final state is possible, apart from the ambiguity to associate the jets with the quark and the antiquark in case the jet charge cannot be measured.

In the following section we present a method to measure the form factors f_i with maximal statistical sensitivity, and in sec. 3 we describe some numerical results for the accuracy to be attained at a 500 GeV collider. Details can be found in [2].

2 The method of optimal observables

Let us denote by ϕ the full set of reconstructed kinematical variables, e.g. the scattering angle of the W^- in the c.m. frame and the decay angles of the W in their respective rest frames. Furthermore let g_i be the difference between f_i and its value in the SM at tree level. Since the trilinear gauge couplings enter linearly in the amplitude of our process the differential cross section can be written as

$$\frac{d\sigma}{d\phi} = S_0(\phi) + \sum_i S_{1,i}(\phi)\, g_i + \sum_{i,j} S_{2,ij}(\phi)\, g_i g_j \,, \tag{1}$$

where it is understood that one has symmetrised over any kinematical ambiguities. The idea of optimal observables is to measure the distribution of the functions[1]

[1] The functions $O_i(\phi)$ defined here are available as a FORTRAN routine from the authors.

$$O_i(\phi) = \frac{S_{1,i}(\phi)}{S_0(\phi)} \tag{2}$$

and to determine the couplings from their mean values $\langle O_i \rangle$. To first order[2] in the g_i one has

$$\langle O_i \rangle = \langle O_i \rangle_0 - \sum_j c_{ij}\, g_j \,, \tag{3}$$

from which the g_i can be extracted since $\langle O_i \rangle_0$ and c_{ij} are calculable given (2) and (1). From the distribution of the O_i one also obtains the statistical errors on their mean values, and the observables O_i have been constructed to minimise the induced statistical errors on the extracted couplings g_i [3]. More precisely, it can be shown [2] that in the limit of small g_i they cannot be smaller in *any* other method, including a fit to the full distribution of the variables ϕ.

To have tractable expressions for the observables, some approximations such as taking the cross section (1) at tree level will be necessary in practice. They need however not be made in the extraction of the couplings: various theoretical and experimental effects such as radiative corrections or detector resolution might be taken into account when calculating the coefficients $\langle O_i \rangle_0$ and c_{ij} in eq. (3).

This method is particularly well suited for testing discrete symmetries, because for an observable which corresponds to a CP violating coupling g_i, a nonzero mean $\langle O_i \rangle$ is an unambiguous sign for CP violation in the reaction, provided detector and data selection are CP blind.[3] A similar statement holds for the study of absorptive parts in the scattering amplitude.

3 Numerical estimates for a 500 GeV collider

To estimate the statistical precision of our method we have calculated the errors in measuring real and imaginary parts of the form factors f_i^Z and f_i^γ of [1]. For an integrated luminosity of 10 fb^{-1} at $\sqrt{s} = 500$ GeV and unpolarised beams we find 1-σ errors between $2 \cdot 10^{-4}$ and $2 \cdot 10^{-2}$. With the additional information of the jet charge in each event they decrease by a factor between 1.2 and 2.7.

[2] A leading order expansion in g_i is used here, assuming that deviations from the SM at tree level are small, but this is not essential for the method to work.

[3] Optimal observables have already been used to search for CP violation in τ-pair production at LEP1, with a clear gain of sensitivity over non optimised observables [4].

For some of the form factors the errors are strongly correlated. This holds in particular for pairs of f_i^Z and f_i^γ, because due to the interference of the $WW\gamma$ and $WW Z$ vertices they appear as linear combinations in the amplitude. For left and right handed incident electrons these are, respectively,

$$\begin{aligned} f_i^L &= 4\sin^2\theta_W f_i^\gamma - (2 - 4\sin^2\theta_W)\frac{s}{s - M_Z^2} f_i^Z \\ f_i^R &= 4\sin^2\theta_W f_i^\gamma - 4\sin^2\theta_W \frac{s}{s - M_Z^2} f_i^Z \,, \end{aligned} \tag{4}$$

where θ_W is the weak mixing angle. The correlations for pairs f_i^L and f_i^R turn out to be much weaker. With the above parameters the errors are between $2 \cdot 10^{-4}$ and $2 \cdot 10^{-2}$ for the f_i^L, and between $5 \cdot 10^{-4}$ and $7 \cdot 10^{-2}$ for the f_i^R. With beams of left handed e^- or right handed e^- one would exclusively measure the f_i^L. We find that given the same number of events the statistical errors on the f_i^L are almost the same with or without polarisation.

References

[1] K. Hagiwara, K. Hikasa, R. D. Peccei and D. Zeppenfeld, Nucl. Phys. B282 (1987) 253

[2] M. Diehl and O. Nachtmann, Z. Phys. C62 (1994) 397

[3] D. Atwood and A. Soni, Phys. Rev. D45 (1992) 2405

[4] OPAL Collaboration, Z. Phys. C66 (1995) 31

A Monte Carlo algorithm for Multiphoton Beamstrahlung in Monte Carlo event generators*

Harald Anlauf

TH Darmstadt, Darmstadt, Germany, and Universität Siegen, Siegen, Germany

Abstract

We describe a simple algorithm that calculates the distributions of electrons and positrons under multiphoton beamstrahlung at a future linear collider. The evolution equation as given by Chen is solved by a Monte Carlo algorithm. Explicit multiple beamstrahlung photons are generated. We present first results from an implementation of beamstrahlung into the Monte Carlo event generator `WOPPER`, that calculates the QED radiative corrections to the process $e^+e^- \to 4$ fermions through resonating W pairs.

1 Introduction

At future linear e^+e^- colliders with center of mass energies of 0.5 TeV and above, beamstrahlung [1, 2], the synchrotron radiation from the colliding e^+e^- beams, will become of significant physical interest. On one hand, beamstrahlung may carry away a substantial fraction of primary beam energy and lead to a degradation of the effective center of mass energy for e^+e^- collisions, on the other hand, the lower energy e^+e^- and γ's contribute to background processes.

In general, the full treatment of beam-beam interactions and beamstrahlung is a complicated many-body problem, and dedicated codes for the calculation of beam-beam effects exist [3] or are being developed [4]. However, from the high energy physics perspective the availability of a simplified analytical or numerical treatment is desired for the study of interesting processes, (e.g., $e^+e^- \to W^+W^-$), at the level of Monte Carlo event generators.

As long as the average number of beamstrahlung photons per beam particle is much less than unity, the radiation spectrum is given by the Sokolov-Ternov spectrum [5]. In the case of the proposed linear colliders, the average number of radiated photons per beam particle at design luminosity is typically $\mathcal{O}(1)$. Therefore, the effects of multiple radiation of beamstrahlung photons have to be taken into account.

Multiphoton beamstrahlung has already been discussed in [6, 7] (and references quoted therein). In this note we will follow the approach by Chen et al., however, without using any approximation to the radiation spectrum. We shall derive a recursive solution of the evolution equation, which is well suited for a numerical implementation.

The Monte Carlo algorithm for beamstrahlung presented below is considered complementary to a full treatment of all beam-beam effects as performed in [3]. The main purpose of this Monte Carlo approach is to provide a simple package that can be incorporated into or interfaced with Monte Carlo event generators for physics at future e^+e^- colliders. In section 2 we will review the electron energy spectrum under multiphoton beamstrahlung. Section 3 outlines our Monte Carlo approach, while in section 4 we present preliminary results. Further details of the calculation will be presented elsewhere [8].

*Supported by Bundesministerium für Bildung, Wissenschaft, Forschung und Technologie, Germany

2 Electron Energy Spectrum

In this section we recapitulate the derivation of the electron energy spectrum due to multiphoton beamstrahlung in the spirit of Chen et al. [6, 7]. We use $\hbar = c = 1$.

Let $v(x,t)$ be the distribution function of the electron with energy fraction $x = E/E_0$ at time t, normalized such that

$$\int_0^1 dx\, v(x,t) = 1\,. \tag{1}$$

We shall assume that the emission of the photons takes place in an infinitesimally short time interval. Therefore the interference between successive emissions may be neglected, and one can describe the time evolution of the electron distribution by the rate equation

$$\frac{\partial v}{\partial t} = -\nu(x)v(x,t) + \int_x^1 dx'\, F(x,x')v(x',t)\,, \tag{2}$$

where the first and second term on the r.h.s. correspond to the sink and source for the evolution of v, respectively. F is the spectral function of radiation, and

$$\nu(x) = \int_0^x dx''\, F(x'',x) \tag{3}$$

represents the average number of photons radiated per unit time by an electron with energy fraction x. Electrons and positrons from pair production in photon-photon processes are not taken into account.

The spectral function of radiation is conventionally characterized by the beamstrahlung parameter Υ, which is defined as

$$\Upsilon = \frac{E_0}{m_e}\frac{B}{B_c}\,, \tag{4}$$

where B is the effective field strength in the beam, and $B_c = m_e^2/e$ is the Schwinger critical field. The e^-e^- beams generally have Gaussian charge distributions, and thus the local field strength varies inside the beam volume. However, it has been shown [2] through integration over the impact parameter and the longitudinal variations, that the overall beamstrahlung effect can be simply described as if all particles experience a uniform mean field B_{mean} during an effective collision time $\tau = l_{eff}/2 = \sqrt{3}\sigma_z$. In what follows, we will assume the obtained mean beamstrahlung parameter Υ_{mean} and effective beam length l_{eff} but drop the subscripts.

The spectral function of synchrotron radiation was derived by Sokolov and Ternov [5] and reads

$$F(x,x') = \frac{\nu_{cl}}{\Upsilon}\frac{2}{3\pi}\frac{1}{x^2}\left\{\int_\eta^\infty du\, K_{5/3}(u) - \frac{(\xi\eta)^2}{1+\xi\eta}K_{2/3}(u)\right\}\theta(x'-x)\,, \tag{5}$$

where $\xi = (3\Upsilon/2)x'$, $\eta = (2/3\Upsilon)(1/x - 1/x')$, and K_ν denotes the modified Bessel function of order ν.

We define

$$\nu(x) = \int_0^x dx'\, F(x',x) \equiv \nu_{cl}\cdot U_0(x\Upsilon)\,, \tag{6}$$

where ν_{cl} is the number of photons per unit time in the classical limit,

$$\nu_{cl} = \frac{5}{2\sqrt{3}}\frac{\alpha m_e^2}{E_0}\Upsilon\,, \tag{7}$$

which is independent of the particle energy for a given field strength due to (4).

The function $U_0(y)$ behaves as

$$U_0(y) = \begin{cases} 1 & y \to 0 \\ const.\times y^{-1/3} & y \to \infty \end{cases}\,, \tag{8}$$

exhibiting the asymptotic approach to the classical limit and the suppression of radiation in the deep quantum regime, respectively.

Finally, the differential e^-e^- luminosity can be expressed as the convolution of the effective electron energy distributions of the colliding beams [7],

$$\frac{d\mathcal{L}(s)}{ds} = \mathcal{L}_0\int dx_1 dx_2\,\delta(s - x_1x_2s_0)v(x_1)v(x_2)\,. \tag{9}$$

where $\mathcal{L}_0$ is the nominal luminosity of the collider, including the enhancement factor due to beam disruption, and the effective energy distribution $v(x)$ is obtained by averaging over the longitudinal position within the beam,

$$v(x) = \frac{2}{l}\int_0^{l/2} v(x,z)\,. \tag{10}$$

3 Multiphoton Beamstrahlung by Monte Carlo

The evolution equation (2) may be solved by a Monte Carlo algorithm. Here we will outline only the basic idea, deferring the full presentation and discussion to a forthcoming publication [8].

To determine the electron distribution $v(x,t)$, let us decompose it into a suitable set of time independent functions $\phi_n(x)$ using the ansatz

$$v(x,t) = \sum_{n=0}^{\infty}\phi_n(x)\cdot\frac{(\nu t)^n}{n!}e^{-\nu t}\,, \tag{11}$$

where ν is a parameter that will be determined below. The normalization condition (1) translates into

$$\int_0^1 dx\,\phi_n(x) = 1\,. \tag{12}$$

Plugging the ansatz (11) into the evolution equation (2) we obtain a recursion relation for the ϕ_n,

$$\phi_n(x) = \int_0^1 dx'\left[\left(1 - \frac{\nu(x)}{\nu}\right)\delta(x-x') + \frac{F(x,x')}{\nu}\right]\phi_{n-1}(x') \quad \text{for } n \geq 1\,, \tag{13}$$

with initial condition

$$\phi_0(x) = v(x,0)\,. \tag{14}$$

If we neglect the intrinsic (Gaussian) energy spread of the accelerator, the initial condition of the electron distribution is simply given by

$$v(x,0) = \delta(1-x)\,, \tag{15}$$

and thus

$$\phi_0(x) = \delta(1-x)\,. \tag{16}$$

The functions $\phi_n(x), n > 0$, can be determined, e.g., by numerical integration. Here we suggest a different way to exploit the recursion relations. First note that the kernel given by the square brackets in (13) is positive for $x' > x$. Furthermore, since $\nu(0) \geq \nu(x) \geq \nu(1)$, the kernel is positive if we choose $\nu = \nu(0) = \nu_{cl}$. The functions ϕ_n will then be positive, and together with the normalization condition (12) they will allow for a probabilistic interpretation.

Using our ansatz (11), the effective electron energy distribution (10) reads

$$v(x) = \sum_n\left[1 - \frac{\gamma(1+n;N_{cl})}{n!}\right]\phi_n(x)\,. \tag{17}$$

Parameter	SBLC	TESLA	NLC	JLC-S	JLC-X	CLIC	VLEPP
Luminosity $[10^{33}\mathrm{cm}^{-2}\mathrm{s}^{-1}]$	5.3	6.1	6.9	4.6	5.1	?	9.7
Particles/bunch $[10^{10}]$	1.1	3.63	0.65	1.44	0.63	0.8	20
σ_x [nm]	335	845	320	260	260	250	2000
σ_y [nm]	15.1	18.9	3.2	3.04	3.04	7.5	3.9
σ_z [μm]	300	700	100	120	90	200	750
Υ_{mean}	0.049	0.029	0.090	0.213	0.120	0.072	0.064
$N_\mathrm{cl} = \nu_\mathrm{cl} \cdot l/2$	1.42	1.93	0.87	2.47	1.04	1.4	4.6
$\mathcal{L}(s > 0.99\, s_0)/\mathcal{L}_0$	0.58	0.55	0.68	0.32	0.62	0.56	0.18

Table 1: *Selected parameters of some proposed linear collider designs.*

where $\gamma(1+n; N_\mathrm{cl})$ is the incomplete gamma function, and $N_\mathrm{cl} = \nu_\mathrm{cl} \cdot l/2$ is the average number of photons per beam particle radiated during the entire collision, in the classical limit. Due to the positivity of the term in square brackets in (17) and the functions ϕ_n, the electron energy distribution can be determined straightforwardly by a multichannel Monte Carlo method [8].

4 Results

Of the abundance of available parameter sets for future linear e^-e^- colliders, we have taken a hopefully representative selection from [9] that comprises many of the proposed linear collider designs. Table 1 lists some of the parameters that are relevant for our numerical results. Υ_{mean} was determined similarly to [7].

We have calculated the differential luminosity of the e^-e^- beams under beamstrahlung, eq. (9), using our Monte Carlo algorithm based on (13). The result of the simulation for the normalized luminosity is shown in figure 1. For the sake of brevity we have selected only a subset of four designs which essentially cover the interesting parameter range: the TESLA design with rather large bunch length but small effective beamstrahlung parameter and a correspondingly rather soft beamstrahlung spectrum, the JLC-S design with shorter bunches but large Υ and large mean energy loss due to a hard beamstrahlung spectrum, NLC with short bunches and moderate Υ, having a small number of radiated photons N_cl, and VLEPP with a large multiplicity of beamstrahlung photons. We have also calculated the relative luminosity for collisions with $s > 0.99\, s_0$, the result being displayed in the last line of table 1.

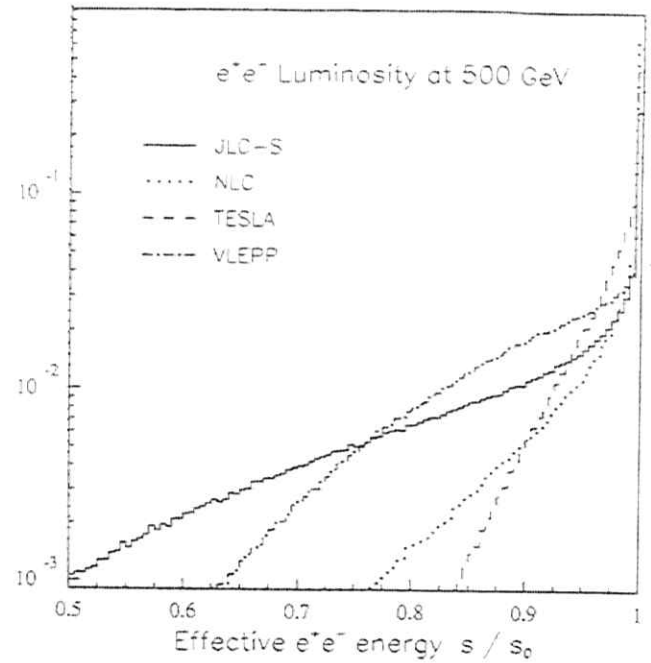

Figure 1: *Differential e^-e^- luminosity.*

In high energy e^-e^- processes, besides beamstrahlung one also has to take into account the radiative corrections to the process under consideration. The single most important universal contribution of the radiative corrections are the leading logarithms $\alpha^n \log^n(s/m_e^2)$, which are due to QED initial state radiation (ISR). These large logarithms can be resummed to all orders in the structure function approach, with the electron structure function [10]:

$$D(z;\mu^2) = \frac{\beta}{2}(1-z)^{\frac{\beta}{2}-1}\left(1-\frac{\beta}{8}\beta\right) - \frac{1}{4}\beta(1+z) - \mathcal{O}(\beta^2)\,, \tag{18}$$

where

$$\beta = \frac{2\alpha}{\pi}\left(\log\frac{\mu^2}{m_e^2} - 1\right)\,. \tag{19}$$

μ^2 is the factorization scale of order s, and z is the electron energy fraction after initial state radiation.

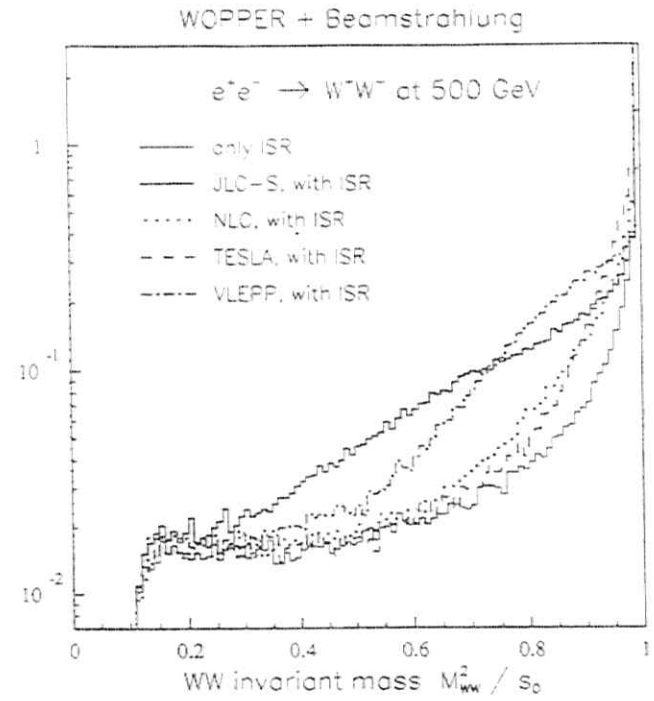

Figure 2: *Final state invariant mass distribution with and without beamstrahlung.*

As an application, we have interfaced our Monte Carlo routines for beamstrahlung with the Monte Carlo event generator WOPPER [11]. WOPPER simulates the process $e^+e^- \to (W^+W^-) \to 4f$ including QED radiative corrections in the abovementioned leading logarithmic approximation with explicit photons. In figure 2 we show the normalized invariant mass distribution M^2_{WW} of the final state (assuming a 100% reconstruction efficiency for simplicity),

$$\frac{1}{\sigma_0}\frac{d\sigma}{dM^2_{WW}} = \int dx_1 dx_2 dz_1 dz_2\; \mathcal{C}(x_1)\mathcal{C}(x_2)\cdot D(z_1;\mu^2)D(z_2;\mu^2)\cdot\frac{1}{\sigma_0}\sigma_0(x_1z_1x_2z_2s)\,. \qquad (20)$$

using the same collider designs as in figure 1. The thin continuous line represents the corresponding distribution from ISR alone. For events with a significantly reduced invariant mass the corrections due to beamstrahlung are numerically much larger than due to pure ISR, and the shape of the distribution is essentially dominated by the beamstrahlung spectrum. This result clearly shows the importance of beamstrahlung and the need to include beamstrahlung into Monte Carlo event generators for physics at future e^+e^- colliders.

References

[1] For an overview see e.g. D.V. Schroeder, Ph.D. thesis, SLAC-371, UC-414, (unpublished), and references quoted therein.

[2] P. Chen, in *Frontiers of Particle Beams*, Lectures Notes in Physics 296, Springer Verlag, Berlin 1988.

[3] K. Yokoya, *Nucl. Instr. Meth.* **A251** (1986) 1; SLAC-AAS-27, 1987 (unpublished).

[4] P. Chen, G. Horton-Smith, T. Ohgaki, A.W. Weidemann, and K. Yokoya, *Nucl. Instr. Meth.* **A355** (1995) 107.

[5] A.A. Sokolov and I.M. Ternov, in *Radiation from Relativistic Electrons*, AIP Translation Series, AIP, New York, 1986.

[6] T. Barklow, P. Chen, and W. Kozanecki, in *Proceedings of the Workshop e^+e^- Collisions at 500 GeV: The Physics Potential – Munich, Annecy, Hamburg, February 4 to September 3, 1991*, DESY 92-123.

[7] P. Chen, *Phys. Rev.* **D46** (1992) 1186.

[8] H. Anlauf, in preparation.

[9] H. Weise, private communication.

[10] E.A. Kuraev and V.S. Fadin, *Yad. Fiz.* **41** (1985) 733;
G. Altarelli and G. Martinelli, in *Physics at LEP*, CERN 86-02, Geneva 1986;
W. Beenakker, F.A. Berends and W.L. van Neerven, *Proceedings of the Ringberg workshop on Electroweak Radiative Corrections*, April 1989.

[11] H. Anlauf, J. Biebel, H.D. Dahmen, A. Himmler, P. Manakos, T. Mannel, and W. Schönau, *Comp. Phys. Comm.* **79** (1994) 487;
H. Anlauf, H.D. Dahmen, P. Manakos, and T. Ohl, WOPPER *Version 1.5*, work in progress.

Single W-boson production in $e^-\gamma$ colliders

K. Huitu[a], J. Maalampi[b] and M. Raidal[c]

[a]Research Institute for High Energy Physics, University of Helsinki
[b]Department of Theoretical Physics,University of Helsinki
[c]Department of Theoretical Physics, University of Valencia

Single W-boson production in $e^-\gamma$ collisions with polarized beams is investigated. In the framework of the Standard Model the updated estimates for the measurement precision of photon anomalous coupling parameters κ_γ, λ_γ at the Next Linear Collider with $\sqrt{s_{ee}} = 420$GeV are obtained. The production of right-handed gauge bosons W_2^- in this collision mode is also analysed. If the associated neutrino is light, the channel would give the best discovery reach for W_2^- in the Next Linear Collider.

1 Introduction

In addition to the electron-positron option, the electron-electron and electron-photon collision modes of the Next Linear Collider (NLC) are also technically realizable [1]. During the recent years the physics potential of the latter options has been under intense study. While e^-e^- collisions have been found to be particularly suitable for the study of possible lepton number violating phenomena [2], the $e^-\gamma$ operation mode will also be well motivated from the point of view of new physics.

So far, the $e^-\gamma$ collisions have been studied using the photon spectrum of classical Bremsstrahlung. In the linear collider it will be possible to obtain high luminosity photon beams by backscattering intensive laser pulses off the electron beam [3] without considerable losses in the beam energy and with very high polarizability and monochromaticity [4]. This possibility makes the $e^-\gamma$ collisions ideal for studying heavy gauge boson production processes [5, 6, 7], since the initial state photon provides us with a possibility to probe directly the gauge boson self-interactions.

We will consider a single massive vector boson production in $e^-\gamma$ collision,

$$e^-\gamma \to W^-N, \tag{1}$$

for any combination of beam polarization. Here W^- may stand for the ordinary SM charged vector boson W_1^- and N for the massless Dirac electron neutrino ν_e. However,

we do not restrict ourselves only to this case, since a wide class of models beyond the SM predicts a existence of new heavy vector bosons and massive neutrinos. For example, in the left-right symmetric model (LRM) [8] the vector boson may also be a heavy right-handed weak boson W_2. The present lower limit for the mass of W_2 coming from high energy experiment is $M_{W_2} \geq 652$ GeV [9], so that the right-handed boson production will be kinematically forbidden at least in the initial phase of the NLC. At the final phase of the NLC, however, the reaction (1) may be kinematically allowed and even favoured compared with, *e.g.* , the W_2 pair production in e^-e^- collisions, since the mass of the associated neutrino could be smaller than the mass of W_2. In the case of a sizeable mixing between the light, predominantly left-handed and the heavy, predominantly right-handed neutrinos the study of the process (1) may extend the kinematical discovery range of W_2 almost up to the energy $\sqrt{s_{ee}}$.

2 Anomalous triple boson coupling in the Standard Model

There are two Feynman diagrams contributing at the tree level to the reaction (1) (see Fig. 1). One of them, the t-channel diagram, involves a triple gauge boson coupling making the process suitable for testing the non-Abelian gauge structure of the theory. A particularly interesting feature of the process (1) is that it is sensitive only to the possible anomalous coupling of the photon, allowing one to discriminate between the photon anomalous coupling and the anomalous coupling of massive neutral gauge boson Z^0. Since the deviation from the SM coupling is expected to be small, one can use of polarization of the initial state particles to enhance these effects.

The most general CP-conserving γWW interaction allowed by the electromagnetic gauge invariance is of the form [10]

$$\begin{aligned}\mathcal{L}_{WW\gamma} &= -ie(W^+_\mu W^-_\nu A^\nu - W^+_\mu A_\nu W^{\mu\nu} + \kappa_\gamma W^+_\mu W_\nu F^{\mu\nu} + \\ &\quad \frac{\lambda_\gamma}{M_W^2} W^+_\nu W^\nu_\rho F^{\rho\mu}),\end{aligned} \tag{2}$$

where $W_{\mu\nu} = (\partial_\mu - ieA_\mu)W_\nu - (\partial_\nu - ieA_\nu)W_\mu$ and $F_{\mu\nu} = \partial_\mu A_\nu - \partial_\nu A_\mu$. The coefficients κ_γ and λ_γ are related to the magnetic moment μ_W and the electric quadrupole moment Q_W of W according to

$$\mu_W = \frac{e}{2M_W}(1 + \kappa_\gamma + \lambda_\gamma), \qquad Q_W = -\frac{e}{M_W^2}(\kappa_\gamma - \lambda_\gamma).$$

In a gauge theory at tree level the coefficients have the values $\kappa_\gamma = 1$ and $\lambda_\gamma = 0$.

In the context of the SM, the process (1) has already been investigated previously [5, 6, 11, 12], and its sensitivity to the photon anomalous coupling has been found to be comparable with the estimated sensitivity of the W pair production processes [6]. We have updated these analysis for a 500 GeV e^-e^- collider, taking into account the effects of beam polarization and final state polarization as well as the recent developments in the linear collider design. The expressions for the general helicity amplitudes of the process are given in ref.[13]. For determination the cross sections from the helicity amplitudes we have assumed 100% longitudinally polarized electron and linearly polarized photon beams. This is an often used approximation since in practice the polarizations will be more than 90%.

The scattering of linearly polarized laser light off the electron beam produces a polarized photon beam with very hard spectrum strongly peaked at the maximum energy, which is about 84% of the electron beam energy [3]. There are two different collision schemes of the photon colliders possible [4]. In the first case the photon conversion region is very close to the interaction point and the entire photon spectrum interacts with the electron beam. From the physics point of view this realization of the $e^-\gamma$ collisions is undesired because of the high rate of the background processes initiated by the electrons which have been used for creating the photon beam and also because of the low monochromaticity of the photon beam.

In the case of the second collision scheme the distance between the conversion and interaction points is longer. The electrons used for producing the photon beam are removed by applying strong magnetic field and therefore the $e^-\gamma$ collisions are clean. Since the electron beam probes only the hardest photons of the γ beam the collisions are highly monochromatic. The achievable luminosities in this case are found to vary from 30 fb^{-1} at VLEPP to 200 fb^{-1} at TESLA per year [4]. Therefore, we have carried out our analysis for the center of mass energy $\sqrt{s_{ee}} = 420$ GeV corresponding to the peak value of the photon spectrum, assuming that the relatively small nonmonochromaticity effects of the photon beam as well as the nonmonochromaticity effects of the electron beam due to the energy losses in beamstrahlung (both at the level of a few percent) will be taken into account in the analysis of experimental data. The other relevant NLC parameters which we have used are the following: integrated luminosity $L_{int} = 50$ fb^{-1}, the covering region of a detector $|\cos\theta| \leq 0.95$ and W^- reconstruction efficiency of 0.1.

We have used five observables for testing the parameters κ_γ and λ_γ. Obviously, the

differential cross section $d\sigma_{\tau_1=\pm1}/d\cos\theta$ and the total cross section $\sigma^{tot}_{\tau_1=\pm1}$ for different photon beam polarization $\tau_1 = \pm1$ can be analysed. Since the differential cross sections are strongly peaked in the backward direction one would expect that also the forward backward asymmetries

$$A_{\pm}^{FB} = \frac{\sigma_{\tau_1=\pm1}(\cos\theta \geq 0) - \sigma_{\tau_1=\pm1}(\cos\theta \leq 0)}{\sigma_{\tau_1=\pm1}(\cos\theta \geq 0) + \sigma_{\tau_1=\pm1}(\cos\theta \leq 0)} \tag{3}$$

could be sensitive to the anomalous coupling. The quantity, which reflects the effects of the beam polarization, is the polarization asymmetry A_{pol} defined as

$$A_{pol}(\cos\theta) = \frac{d\sigma_{\tau_1=-1} - d\sigma_{\tau_1=+1}}{d\sigma_{\tau_1=-1} + d\sigma_{\tau_1=+1}}. \tag{4}$$

We have also studied whether the measurement of the final state W-boson polarization could offer sensitive tests for κ_γ and λ_γ. The information about the polarization of W-boson can be obtained by measuring the angular distribution of its decay products. A suitable quantity would be the forward-backward asymmetry of the leptons produced in W^- decay, which is related to the cross sections corresponding to the different W^- polarization states $\tau_2 = \pm1$ as follows (see *e.g.* ref.[11]):

$$\chi_{\pm}^{FB} = \frac{3}{4}\frac{\sigma^{\tau_2=-1}_{\tau_1=\pm1} - \sigma^{\tau_2=+1}_{\tau_1=\pm1}}{\sigma^{tot}_{\tau_1=\pm1}}. \tag{5}$$

We have carried out a χ^2 analysis by comparing the SM prediction of the observables with those corresponding ones to the anomalous κ_γ and λ_γ. The limits are calculated at 90% confidence level, which corresponds to $\Delta\chi^2 = 4.61$. The statistical errors are computed assuming the NLC parameters given above. The systematic errors are estimated by assuming the uncertainty of the cross section measurement to be at the level of $\sim 2\%$ [14], coming mainly from the errors in the luminosity measurement, the acceptance, the background subtraction and the knowledge of branching ratios.

Both forward-backward asymmetries, $A_{\tau_1}^{FB}$ and $\chi_{\tau_1}^{FB}$, turned out to be several times less sensitive to the anomalous coupling than the other three observables. Polarization asymmetry A_{pol} and the total cross sections $\sigma^{tot}_{\tau_1=\pm1}$ are more sensitive to the deviations from the SM but still do not allow to constrain couplings sufficiently. The most sensitive observable to the photon anomalous coupling is the differential cross section. The contours of allowed regions in $(\kappa_\gamma, \lambda_\gamma)$ space obtained from its analysis are plotted in Fig. 2. The curves for the different photon polarization states $\tau_1 = \pm1$ are indicated in the figure. The contour resulting from the combined analysis is denoted by a. As can be seen from Fig. 2 the most stringent constraints for the anomalous coupling are obtained in the case

of left-handedly polarized electron and right-handedly polarized photon beams. This is an expected result, since the s-channel diagram in Fig. 1 does not contribute in this case and the entire cross section comes from the t-channel diagram, which probes the triple boson coupling.

As a result, by studying the reaction (1) in the NLC with the assumed set of parameters, one could constrain the anomalous triple boson coupling parameters κ_γ and λ_γ to the following regions:

$$-0.01 \leq 1 - \kappa_\gamma \leq 0.01, \qquad -0.012 \leq \lambda_\gamma \leq 0.007.$$

At this level of precision the radiative corrections are expected to start to play a role [15]. Since the size of the SM radiative corrections depends crucially on the beam polarization, the use of polarized beams allows one to discriminate between the the radiative corrections and corrections from the new physics.

We have repeated the analysis with the integrated luminosity of $10 fb^{-1}$ which gives ~ 1.4 times weaker bounds for parameter κ_γ and ~ 1.6 times weaker bounds for parameter λ_γ. This shows that the measurement uncertainties are largely dominated by the systematic errors. In order to see the relevance of the beam polarization and to compare our results with the earlier works with unpolarized beams we also repeated the analysis using the NLC parameters of ref.[6] i.e. $|\cos\theta| \leq 0.7$ and the integrated luminosity of $10 fb^{-1}$. It turned out that the beam polarization (together with the monochromaticity of the photon beam) gives an improvement of a factor of 3 in the measurement precision of the anomalous coupling parameters κ_γ and λ_γ.

3 Single heavy vector boson production in left-right model

The LRM [8] is an extension of the SM, in which the gauge interactions of left-handed and right-handed fundamental fermions are treated on equal basis. The LRM is based on the gauge symmetry $SU(2)_R \times SU(2)_L \times U(1)_{B-L}$, and there are hence two new weak bosons, W_2 and Z_2, in addition to the ones known in the SM. The left-right symmetry, not present in the low energy world, is broken by a $SU(2)_R$ triplet Higgs field $\Delta = (\Delta^{++}, \Delta^{+}, \Delta^{0})$. The only new fermions the model predicts are the right-handed neutrinos.

The energy scale $v_R =< \Delta^0 >$ of the breaking of the LRM symmetry to the SM symmetry, which also sets, up to coupling constants, the mass scale of the new weak

bosons and right-handed neutrinos, is not given by the theory itself. In the Tevatron one has made a direct search of W_2 in the channel $p\bar{p} \to W_2 \to eN$. The bound they give is $M_{W_2} \geq 652$ GeV [9]. The result is based on several assumptions on the LRM: the quark-W_2 coupling has the SM strength, the CKM matrices for the left-handed quarks and the right-handed quarks are similar and the right-handed neutrino does not decay in the detector but appears as missing E_T. If one relaxes the first two assumptions, the mass bound will be weakened considerably, as was pointed out in ref.[16]. The third assumption is also crucial: if the right-handed neutrino is heavy, with a mass of say 100 GeV or more, it will decay in the detector into charged particles with no missing energy. For this case, which is natural in the LRM, Tevatron search would be ineffective. Therefore, it was argued in ref.[16], that the lower limit for M_{W_2} could be as low as 300 GeV.

The mass dependence of the total cross section of the process $e_R^-\gamma \to W_2^- N$ can be seen in Fig. 3, where we plot the cross section as a function of W_2^- mass for the center of mass energy $\sqrt{s_{ee}} = 1.5$ TeV, expected to be possible to achieve in the final stage of NLC, assuming the left- (Fig. 3 (I)) and right-handedly (Fig. 3 (II)) polarized photon beams. The curves denoted by a and b correspond to the neutrino masses $M_N = 300$ GeV and $M_N = 600$ GeV, respectively. The cross sections are found to be reasonably large for almost the entire kinematically allowed mass region, decreasing faster with M_{W_2} for the $r_1 = 1$ photons. At low W_2 masses the difference between a and b curve is small but for heavy W_2 masses the cross section depends strongly on the neutrino mass. If $M_N \leq M_{W_2}$, the reaction (1) enables us to study heavier vector bosons than what is possible in the W_2^- pair production in e^-e^+ or e^-e^- collisions.

The reaction would be even more useful in this respect if the mixing between the heavy and the light neutrino is large enough to give observable effects. In Fig. 4 we plot the cross section of the reaction $e_R^-\gamma \to W_2^-\nu$ for different photon polarizations assuming a vanishing mass of ν and the neutrino mixing angle of $\sin\theta_N = 0.05$. For this set of parameters the process should be observable up to W-boson mass $M_W = 1.2$ TeV.

4 Summary

We have studied usefulness of the reaction $e^-\gamma \to W_2 N$ in the NLC for finding signals of the physics beyond the SM. The NLC with $\sqrt{s} = 420$ GeV $e^-\gamma$ option will be able to probe γWW interaction at the level of the SM quantum corrections. We have also pointed out the possibility to test the left-right symmetry of electroweak interactions at

the energies of the final phase of the NLC through the same reaction. If the right-handed neutrino is light, this reaction offers a much better discovery reach for W_2 than the pair production in e^+e^- or e^-e^- collisions.

Acknowledgements. We are indebted to Aarre Pietilä, Turku, for useful discussions. This work has been supported by the Academy of Finland.

References

[1] See *e.g.* , *Proc. of the Workshop on Physics and Experiments with Linear Colliders* (Saariselkä, Finland, September 1991), eds. R. Orava, P. Eerola and M. Nordberg (World Scientific, 1992);
Proc. of the Workshop on Physics and Experiments with Linear Colliders (Waikoloa, Hawaii, April 1993), eds. F.A. Harris, S.L. Olsen, S. Pakvasa and X. Tata (World Scientific, 1993).

[2] See *e.g.* , P. Helde, K. Huitu, J. Maalampi and M. Raidal, Nucl. Phys. **B 437** (1995) 305, and references therein.

[3] I. Ginzburg, G. Kotkin, V. Serbo and V. Telnov, Nucl. Instrum. Methods **205** (1983) 47.

[4] V. Telnov, *Proc. of the First Arctic Workshop on Future Physics and Accelerators* (Saariselkä, Finland, 1994), eds. M. Chaichian, K. Huitu and R. Orava (World Scientific, 1995).

[5] A. Grau and J.A. Grifols, Nucl. Phys. **B 233**(1984) 375.

[6] S.Y. Choi and F. Schrempp, Phys. Lett. **B 272** (1991) 149.

[7] K. Cheung, Nucl. Phys. **B 403** (1993) 572.

[8] J.C. Pati and A. Salam, Phys. Rev. **D 10** (1974) 275;
R.N. Mohapatra and J.C. Pati, Phys. Rev **D 11** (1975) 566, 2558;
G. Senjanovic and R.N. Mohapatra, Phys. Rev. **D 12** (1975) 1502.

[9] F. Abe *et al.*, Phys. Rev. Lett. **74** (1995) 2900.

[10] K.J.F. Gaemers and G.J. Gounaris, Z. Phys. **C 1** (1979) 159;
K. Hagiwara, R.D. Peccei, D.Zeppenfeld and K.Hikasa, Nucl. Phys. **B 282** (1987) 253.

[11] E. Yehudai, Phys. Rev. **D 44** (1991) 3434.

[12] O. Phillipsen, Z. Phys. **C 54** (1992) 643.

[13] M. Raidal, Nucl. Phys. **B 441** (1995) 49.

[14] M. Frank, P.Mätting, R. Settles and Z. Zeuner, in *Proc. of the Workshop "e^+e^- Collisions at 500 GeV: The Physics Potential,"* ed. P.M. Zerwas (1991), DESY 92-123B.

[15] J. Kodaira, H. Tochimura, Y. Yasui and I. Watanabe, preprints HUPD-9509, OCHA-PP-57;
A. Arhrib, J.L. Kneur and G. Moultaka, preprint CERN-TH/95-344.

[16] T. Rizzo, Phys. Rev. **D 50** (1994) 325, and *ibid.* 5602.

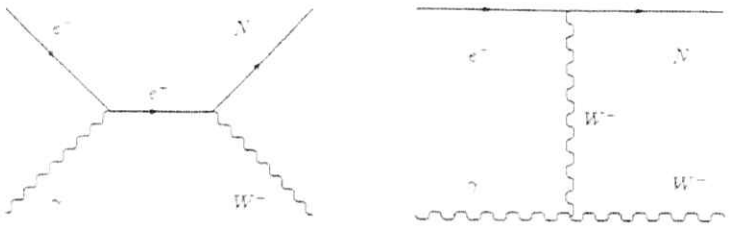

Figure 1: Feynman diagrams for the process $e^-\gamma \to W^-N$.

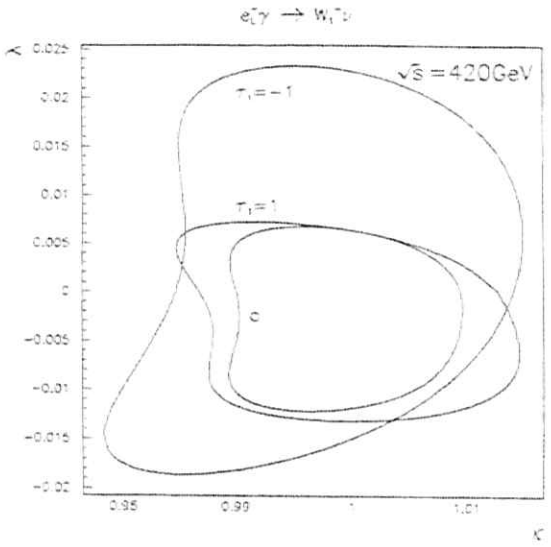

Figure 2: The allowed domains of the photon anomalous coupling parameters $\kappa_\gamma, \lambda_\gamma$ obtained by analysing the SM differential cross sections of different photon polarization states (as indicated on figure). The curve of combined analysis of the differential cross sections is denoted by a.

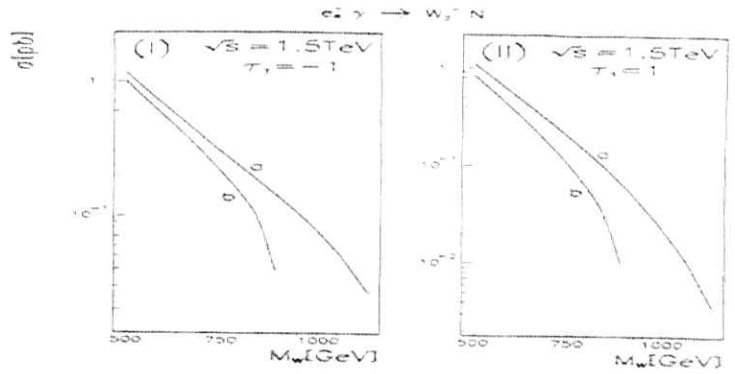

Figure 3: The total cross section of the process $e_R^-\gamma \to W_2^-N$ as a function of heavy gauge boson mass for the left- (figure (I)) and right-handedly (figure (II)) polarized photon beams. The masses of heavy neutrino are taken to be $M_N = 300$ GeV and $M_N = 600$ GeV for curves a and b, respectively.

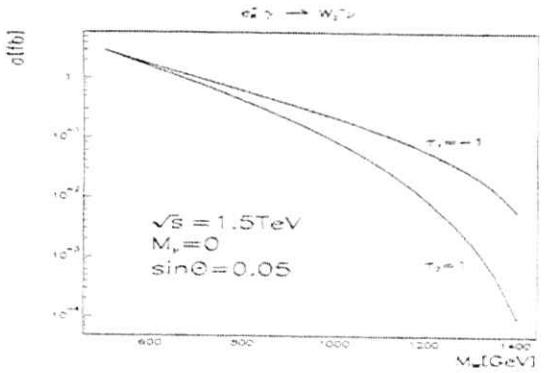

Figure 4: The total cross section of the process $e_R^-\gamma \to W_2^-\nu$ as a function of heavy gauge boson mass for the left- and right-handedly polarized photon beams. The neutrino mixing angle is taken to be $\sin\theta = 0.05$.

Majorana neutrinos in $e^-e^- \to W^-W^-$ and neutrinoless double beta decay

G. Bélanger[1], F. Boudjema[1], D. London[2,3], H. Nadeau[3]

[1] *ENSLAPP-Annecy, France* [2] *Université de Montréal, Canada*
[3] *McGill University, Canada*

1. Introduction

The e^-e^- mode of a linear collider (LC) offers the possibility of probing the existence of a Majorana mass for neutrinos through W^-W^- production[1]. This process is strictly forbidden in the standard model with Dirac neutrinos. After taking into account phenomenological constraints on neutrino masses and mixings, as well as unitarity considerations, a signal in W^- pair production could potentially be observed at an LC of .5-1 TeV [2]. However, a neutrino with a Majorana mass will also contribute to $\Delta L = 2$ lepton-number-violating processes such as neutrinoless double beta decay, $\beta\beta_{0\nu}$, through the subprocess $W^-W^- \to e^-e^-$. Limits from $\beta\beta_{0\nu}$ have often been ignored but will clearly affect the "inverse" reaction, $e^-e^- \to W^-W^-$. In fact, once the constraints from $\beta\beta_{0\nu}$ are taken into account, we find that, except for extremely contrived scenarios, the cross section for $e^-e^- \to W^-W^-$ is simply too small for it to be seen at a 500 GeV or 1 TeV LC [3]. An LC of at least $\sqrt{s} = 2$ TeV will be necessary in order to have a hope of observing this process.

2. $e^-e^- \to W^-W^-$ and unitarity

The process $e^-e^- \to W^-W^-$ occurs through t- and u-channel exchange of Majorana neutrinos, N_i, of mass M_i.[1] In the high energy limit $s \gg M_W^2$, the cross section is well-approximated by that for the production of a pair of longitudinal W's:

$$\frac{d\sigma}{d\cos\theta} = \frac{g^4}{1024\pi M_W^4}\left(\sum_i M_i (U_{ei})^2\left[\frac{t}{(t-M_i^2)} + \frac{u}{(u-M_i^2)}\right]\right)^2 . \qquad (1)$$

Here U is a unitary matrix which describes the mixing of ν_e with other neutrinos,

$$\nu_e = \sum_i U_{ei} N_i . \qquad (2)$$

Phenomenological limits imply a small mixing with other neutrinos [5]:

$$\sum_{i=1} |U_{ei}|^2 < 6.6 \times 10^{-3} \quad (90\%\ c.l.) . \qquad (3)$$

This limit, which is conservative in that it allows for the possibility that the other charged fermions also mix with new, exotic charged particles [6], is essentially independent of the $SU(2)_L$ transformation properties of the neutrino(s) with which the ν_e mixes.

[1] Right-handed W's can also be produced, either singly or in pairs, through similar diagrams. Here we consider only ordinary W's in the final state - the production of W_R's is discussed in Refs. [4].

As $s \to \infty$, the cross section tends towards a constant. In this particular case this indicates a violation of unitarity, since the amplitude (which is a pure s-wave) grows as $\sqrt{s}$. There are basically two ways in which this unitarity violation can be cured. The first is through the inclusion of a diagram in which a doubly charged Higgs, belonging to a triplet, is exchanged in the s-channel. However, this type of solution has been virtually eliminated by the precision LEP data. The v.e.v. of the Higgs triplet, which induces the Majorana mass term for the neutrino, breaks lepton number spontaneously, producing a Majoron. The failure to observe Majorons in Z decays renders such models untenable. Although there are ways to evade the LEP bounds [7], they are rather unnatural.

The second solution to cure the unitarity problem is to require that the neutrinos' masses and mixing angles satisfy

$$\sum_i (U_{ei})^2 M_i = 0 . \qquad (4)$$

Although this relation may appear arbitrary at first sight, it is in fact automatically satisfied. It is straightforward to show that $\sum_i (U_{ei})^2 M_i = M_{\nu_e}$, where M_{ν_e} is the Majorana mass of the ν_e. However, because there are no Higgs triplets, this mass is equal to zero, so that Eq. 4 holds. If the ν_e mixes with only one neutrino, as in the seesaw mechanism in which one adds a right-handed neutrino N_R to the spectrum, the mixing of the ν_e with the N is tiny: $\sin\theta \sim 10^{-6}$ for $M_i \sim 1$ TeV. As $\sigma(e^-e^- \to W^-W^-) \propto \sin^4\theta$, no events can be expected in this case. However, if the ν_e mixes with more neutrinos, it is, in principle, possible to satisfy Eq. 4 without having such small values of U_{ei}. This is perhaps a bit artificial, and probably requires some fine-tuning, but it remains a possibility.

Although it is interesting to understand how unitarity is restored in different models, the above discussion demonstrates that the cross section for $e^-e^- \to W^-W^-$ is essentially unconstrained by such considerations - the U_{ei} and M_i can take any values consistent with the phenomenological limits in Eq. 3. This is not the case when the experimental limits on neutrinoless double beta decay are taken into account, as will be demonstrated in the next section.

3. Limits from $\beta\beta_{0\nu}$ and $e^-e^- \to W^-W^-$

As $e^-e^- \to W^-W^-$ is essentially the inverse of neutrinoless double beta decay, one might expect that the limits on the latter process could constrain the former. The analysis of $\beta\beta_{0\nu}$ depends on whether the neutrinos are light, $M_i \ll 1$ GeV, or heavy relative to the energy scale of double beta decay.

For light neutrinos, the quantity which contributes to $\beta\beta_{0\nu}$ is $\langle m_\nu \rangle = \sum_i (U_{ei})^2 M_i$, where the sum is over the light neutrinos. With the experimental limit, $\langle m_\nu \rangle \lesssim 1$ eV [8], the cross section $\sigma(e^-e^- \to W^-W^-) \leq 1.3 \times 10^{-17}\ fb$, independently of $\sqrt{s}$. This is clearly unobservable at any future collider.

Heavy neutrinos, $M_i \gg 1$ GeV, can potentially lead to much larger cross sections, but

one must fold in the constraint from $\beta\beta_{0\nu}$. The relevant quantity is

$$\langle m_\nu^{-1} \rangle_M = \sum_i{}'' (U_{ei})^2 \frac{1}{M_i} , \tag{5}$$

where the sum is over the heavy neutrinos. The experimental limit on $\beta\beta_{0\nu}$ implies the following [9]:

$$\langle q^2 \rangle \sum_i{}'' (U_{ei})^2 \frac{1}{M_i} \lesssim 1 \text{ eV} , \tag{6}$$

where q is an average nuclear momentum transfer. A careful calculation of all the nuclear effects gives

$$\sum_i{}'' (U_{ei})^2 \frac{1}{M_i} < 7 \times 10^{-5} \text{ TeV}^{-1} . \tag{7}$$

This limit combines the results of the nuclear matrix element calculation of Ref. [10] with the latest lower bound of 5.1×10^{24} yr on the half-life for $^{76}Ge \to {}^{76}Se + 2e^-$ [11]. A new independent analysis [12] also confirms this bound which can also be arrived at by taking q to be roughly of order 100 MeV.

Assuming no cancellations, $\beta\beta_{0\nu}$ then constrains the neutrinos to be very massive:

$$M_i > 1.4 \times 10^4 (U_{ei})^2 \text{ TeV} . \tag{8}$$

which for $(U_{ei})^2 \sim 5 \times 10^{-3}$ corresponds to $M_i > 75$ TeV!

The cross section for $e^-e^- \to W^-W^-$ can be computed assuming it is dominated by a single massive neutrino. Of course, additional heavier neutrinos are present to satisfy the bound from unitarity. Note however that the cross section would not change significantly with the addition of heavier neutrinos since the mixing angles of all the neutrinos must be correspondingly reduced in order to satisfy the constraint in Eq. 7.

In Fig. 1 we present the discovery limit for $e^-e^- \to W^-W^-$ at the LC for several centre-of-mass energies as a function of M_i and $(U_{ei})^2$. We demand 10 events for discovery, and assume a luminosity of $80(\sqrt{s}/(1 \text{ TeV}))^2$ fb^{-1}. We also superimpose the phenomenological limit on $(U_{ei})^2$, as well as the constraint from $\beta\beta_{0\nu}$. Note that we have not included efficiencies for the detection of the W's, nor have we included any backgrounds. Our discovery limits are therefore as optimistic as they possibly could be.

As is clear from this figure, for $\sqrt{s} = 500$ GeV and 1 TeV, the values of M_i and $(U_{ei})^2$ which produce an observable $e^-e^- \to W^-W^-$ cross section are already ruled out by neutrinoless double beta decay. For $\sqrt{s} = 2$ TeV, the discovery limit and the limit from $\beta\beta_{0\nu}$ are roughly equal. Note, however, that if polarized e^- beams are used, the 2 TeV LC opens a very small region of parameter space, and hence does slightly better than $\beta\beta_{0\nu}$. On the other hand, by the time such a collider is built the $\beta\beta_{0\nu}$ limits will probably have become more stringent, so the prospects for a 2 TeV LC to improve upon neutrinoless double beta decay are marginal at best. Finally, for 4 TeV and 10 TeV LC's, there exists a sizeable region of M_i–$(U_{ei})^2$ parameter space, not ruled out by $\beta\beta_{0\nu}$, which produces an observable signal for $e^-e^- \to W^-W^-$.

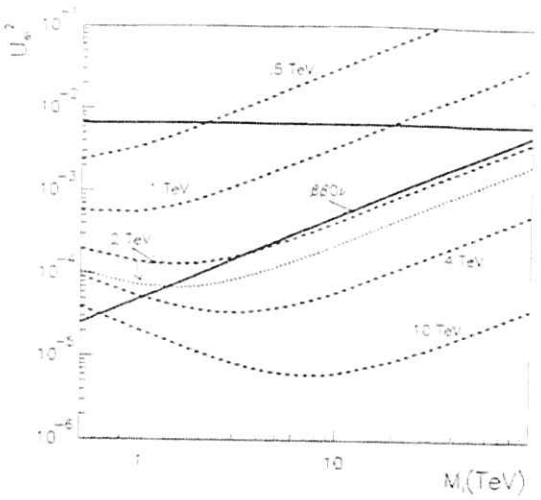

Figure 1: *Discovery limit for $e^-e^- \to W^-W^-$ at the LC as a function of M_i and $(U_{ei})^2$ for $\sqrt{s} = 500$ GeV, 1 TeV, 2 TeV, 4 TeV and 10 TeV (dashed lines). We assume unpolarized e^- beams and a luminosity of $80(\sqrt{s}/(1 \text{ TeV}))^2$ fb^{-1}. For $\sqrt{s} = 2$ TeV, the limit assuming polarized e^- beams is also shown (dotted line). In all cases, the parameter space above the line corresponds to observable events. We also superimpose the experimental limit from $\beta\beta_{0\nu}$ (diagonal solid line), as well as the limit on $(U_{ei})^2$ (horizontal solid line). Here, the parameter space above the line is ruled out.*

4. Can one evade the $\beta\beta_{0\nu}$ constraint?

One might ask if it could be possible to evade the constraint from $\beta\beta_{0\nu}$ and still have an observable cross section in $e^-e^- \to W^-W^-$. Clearly the order-of-magnitude bound from $\beta\beta_{0\nu}$ can be evaded if one allows cancellations among the various terms. We consider two different scenarios for this cancellation: either (i) all the heavy neutrino masses are roughly equal, or (ii) they are different.

For roughly equal masses, there is an upper limit on the mixing as a function of the neutrino mass. From Eq. 7 we have $\sum_i{}'' (U_{ei})^2 < 7 \times 10^{-5} (M/1 \text{ TeV})$. It is therefore possible to have neutrino masses lighter than 100 TeV, but only at the expense of smaller mixing angles. For M in the range 500 GeV to 10 TeV the small mixing angles render the cross section for $e^-e^- \to W^-W^-$ unobservable, $O(10^{-4}$–$10^{-3})$ fb.

In the second scenario the cancellations occur between terms involving neutrinos of quite different masses. This in itself is quite contrived – it requires a fair amount of fine tuning, since the masses and mixing angles have to be carefully adjusted to have such a

cancellation. This requires either that the heavier neutrinos have larger mixings with the ν_e than the lighter ones, or that there be a large number of heavy neutrinos. However, one has to go even further to obtain an observable cross section for $e^-e^- \to W^-W^-$.

Consider for example the case of a heavy neutrino of $M \sim 1$ TeV, with a mixing $U^2 = 5 \times 10^{-3}$ which would be easily observable at an LC. To circumvent the constraint from $\beta\beta_{0\nu}$ one possibility is to add a lighter neutrino N_l, say with mass $M = 100$ GeV and a mixing $U^2 = -5 \times 10^{-4}$. However, such a light neutrino would be first observed directly in the process $e^-e^- \to \nu_e N_l$ [13] and the decay products of the N_l would indicate that it is a Majorana neutrino. Another possibility is to add ten neutrinos of mass $M = 10$ TeV and mixing $U^2 = -5 \times 10^{-3}$. This possibility is clearly exceedingly baroque.

Consider next the case of a heavy neutrino $M \sim 1$ TeV, with a mixing $U^2 = 5 \times 10^{-4}$. The constraint from $\beta\beta_{0\nu}$ could be satisfied with the addition of a single heavier neutrino of $M = 10$ TeV and mixing $U^2 = -5 \times 10^{-3}$. In this case, the cross section for $e^-e^- \to W^-W^-$ is $\sigma \simeq 0.04\ fb$, which might be just observable. Still, in addition to requiring the fine-tuned cancellation of two terms, this scenario requires the heavier neutrino to have a *larger* mixing angle than the lighter neutrino. This is rather unnatural, and is not what happens in the quark sector.

Of course, there are many other ways of arranging the neutrino masses and mixings in order to evade the low-energy constraint from $\beta\beta_{0\nu}$, and to produce an observable cross section from $e^-e^- \to W^-W^-$. However, the above examples give a flavour of what is necessary – one must construct extremely contrived models in order to do this.

Finally we remark that since the constraint from $\beta\beta_{0\nu}$ clearly applies only to ν_e, if the ν_ℓ ($\ell = \mu, \tau$) is Majorana, it will mediate processes such as $\ell^-\ell^- \to W^-W^-$. In a $\mu^-\mu^-$ collider, the region that can be probed corresponds to the one shown in Fig. 1, once the constraint from $\beta\beta_{0\nu}$ has been removed. If such a collider is not available, the only possibility is to look at the contribution $\ell^-\ell^- \to W^-W^-$ or its inverse to a number of $2 \to 4$ processes involving the various modes of the LC. Specifically, if the ν_ℓ is Majorana, it will mediate $\gamma\gamma \to \ell^-\ell^-W^-W^-$, $e^-\gamma \to \nu_e\ell^-\ell^-W^+$ and $e^-e^- \to \nu_e\nu_e\ell^-\ell^-$. However, as was shown in [3] the cross sections involved are simply too small. Colliders of at least 4 TeV would be required to observe a handful of events.

5. Other Models with Lepton-Number Violation

Although our analysis and conclusions are made explicitly for the case of a Majorana neutrino, it is worth commenting on whether the e^-e^- option would be a more helpful tool in other models with lepton number violation.

Consider the case of a doubly-charged Higgs boson which could be exchanged in the s-channel of e^-e^-. If this Higgs emerges from a triplet we have already argued that the LEP bounds are such that this scenario is untenable. Doubly-charged scalars can also emerge from quite exotic Higgs representations [14]. Again, limits from the ρ parameter are so stringent that the allowed models do not permit the doubly-charged Higgses to

couple to W^-W^-. The authors of Ref. [14] conclude that the advantage of the e^-e^- collider (at 500 GeV) would depend on the detailed analysis of the properties of these scalars, if one can sit on the resonance. However, this assumes that these scalars will already have been produced at the LHC [14].

In left-right symmetric models it is possible to fine-tune parameters to evade low-energy limits (including double beta decay) in order to look for lepton-number violation in e^-e^-. However, as in the previous case, this presupposes the *direct* production of a new particle, here a right-handed W [15].

Other scenarios for lepton-number violation include those classes of supersymmetric models with R-parity violation [16]. These models have been shown to be very much constrained by double beta decay [12, 16]. In fact, in the context of our analysis the question is whether these new contributions could interfere destructively with those from a Majorana neutrino (that could also be present) with the result of evading those limits on the Majorana neutrino that we have used. Though such fine tuning seems unnatural, in this eventuality $e^-e^- \to W^-W^-$ could be used to single out the $\Delta L = 2$ lepton-number violation due to the Majorana neutrino. However, it is found from the analysis on double beta decay in Ref. [12] that these contributions add up coherently and that the limits on the Majorana neutrinos we have used remain valid. In this case clearly our conclusions hold.

Although this is not an exhaustive survey of all models which involve lepton-number violation, it does demonstrate the robustness of our conclusions.

6. Conclusions

We have critically reexamined the prospects for the observation of $e^-e^- \to W^-W^-$, mediated by a Majorana neutrino, at a high-energy e^-e^- collider . This process is essentially the inverse of neutrinoless double beta decay ($\beta\beta_{0\nu}$). Once the constraints from $\beta\beta_{0\nu}$ are taken into account, we have found that $e^-e^- \to W^-W^-$ is unobservable at an LC of $\sqrt{s} < 2$ TeV. It is possible to evade the constraints, but this requires models which are extremely contrived and fine-tuned. A $\sqrt{s} = 2$ TeV LC essentially reproduces the limits from $\beta\beta_{0\nu}$, and for $\sqrt{s} > 2$ TeV, there is a sizeable region of parameter space, not ruled out by $\beta\beta_{0\nu}$, which produces an observable signal for $e^-e^- \to W^-W^-$.

This conclusion relies on the calculation of nuclear matrix elements in double beta decay which are subject to uncertainties. However, one would need to relax the constraint from $\beta\beta_{0\nu}$ by almost two orders of magnitude to alter our conclusion that a 1 TeV collider cannot observe inverse neutrinoless double beta decay, while different calculations of this matrix element all obtain roughly the same result [10, 12].

ACKNOWLEDGMENTS

We thank J. Cline for enlightening conversations and B. Kayser for helpful communications. D. London and H. Nadeau are grateful for the hospitality of ENSLAPP, where most of this work was done. This work was supported in part by the NSERC of Canada

and les Fonds FCAR du Québec.

References

[1] T.G. Rizzo, *Phys. Lett.* **116B** (1982) 23; D. London, G. Bélanger and J.N. Ng, *Phys. Lett.* **188B** (1987) 155.

[2] C.A. Heusch and P. Minkowski, *Nucl. Phys.* **B416** (1994) 3; J. Gluza and M. Zrałek, University of Silesia report TP-USl/95/04, hep-ph/9507269.

[3] G. Bélanger, F. Boudjema, D. London and H. Nadeau, hep-ph/9508317, to be published in Phys. Rev. **D** (1996).

[4] J. Maalampi, A. Pietilä and J. Vuori, *Phys. Lett.* **297B** (1992) 327;. T.G. Rizzo, *Phys. Rev.* **D50** (1994) 5602.

[5] E. Nardi, E. Roulet and D. Tommasini, *Phys. Lett.* **344B** (1995) 225.

[6] P. Langacker and D. London, *Phys. Rev.* **D38** (1988) 886.

[7] K. Choi and A. Santamaria, *Phys. Lett.* **267B** (1991) 504.

[8] For a review, see, M. Moe and P. Vogel, *Ann. Rev. Nucl. Part. Sci.* 44, (1994) 247.

[9] For discussions of the contribution of heavy Majorana neutrinos to $\beta\beta_{0\nu}$, see, for example, J.D. Vergados, *Phys. Rep.* **C133** (1986) 1; R.N. Mohapatra and P.B Pal, *Massive Neutrinos in Physics and Astrophysics*, World Scientific Lecture Notes in Physics – Vol 41, Singapore, 1991, p. 204;

[10] G. Pantis, A. Faessler, W.A. Kaminski and J.D. Vergados, *J. Phys. G: Nucl. Part. Phys.* **18** (1992) 605.

[11] A. Balysh et al., in *Proceedings of the XXVII International Conference on High Energy Physics*, 20-27 July 1994, Glasgow UK, eds. P. J. Bussey and I. G. Knowles, IOP Publishing, London, 1995, p. 939.

[12] M. Hirsch, H. V. Klapdor-Kleingrothaus and S. G. Kovalenko, *Phys. Lett.* **352B** (1995) 1.

[13] W. Buchmuller and C. Greub, *Nucl. Phys.* **B363** (1991) 345.

[14] J. F. Gunion, University of California Davis Preprint, UCD-95-36, hep-ph/9510350, Oct. 95.

[15] T. G. Rizzo, hep-ph/9510349, Oct. 95.

[16] See, for example, R. N. Mohapatra, University of Maryland Preprint, UMD-PP-95-147, hep-ph/9507234, July 95.

Radiative Contributions to TGC in the MSSM

A. Arhrib [a], J.-L. Kneur [a,1] and G. Moultaka [a]

[a] LPM, U.R.A. du CNRS N° 040768, Univ. Montpellier II, France

[*] Theory Division, CERN, Geneva, Switzerland

1 Radiative Contributions to TGC

With an expected accuracy of $O(10^{-3})$ or better [1], the measurement of Triple Gauge Couplings (TGC) at a 0.5–2 TeV e^+e^- collider will truly constitute a *precision* experiment. Therefore, apart from testing possible departures from the SM $WW\gamma$, WWZ vertices at tree-level, with an accuracy improved by more than an order of magnitude with respect to LEP2 [2], it is legitimate to expect detectable loop-level TGC contributions from different models of New Physics. Actually, one-loop TGC contributions are certainly present in any renormalizable model, but such virtual effects are suppressed by a factor of $(g^2/16\pi^2) \simeq 2.7\ 10^{-3}$. Moreover, further suppression is expected from the decoupling properties of heavy particles in most renormalizable models. For instance, SM one-loop TGC predictions are known [3, 4] and give, at $\sqrt{s} = 190$ GeV [2] ($\sqrt{s} = 500$ GeV): $\Delta\kappa_\gamma \simeq 4.1$–$5.7 \times 10^{-3}$ (5.5–$(-5.4) \times 10^{-4}$), for $M_{Higgs} = 0.065$–1 TeV and $m_{top} = 175$ GeV (with $\Delta\kappa_Z$ of the same order and even smaller contributions to $\lambda_{\gamma,Z}$). The smallness of those SM contributions at 500 GeV is due to their fast decreasing at high energies, $q^2 >> M_{W,Z}^2, m_{top}^2$, in accordance with the good unitarity behaviour, while even for a heavy Higgs its effects in $\Delta\kappa_{\gamma,Z}$ are screened, giving non-decoupling but small (constant) contributions for $M_{Higgs} \to \infty$.

A more interesting situation is thus expected if, for example, some particles in the loops have a stronger non-decoupling behavior (e.g due to Yukawa type couplings) and/or are close to their production threshold. The latter is likely to be the case in the Minimal Supersymmetric Standard Model (MSSM) [5] since, as is well known, the resolution of the hierarchy problem requires the spectrum of supersymmetric partners to appear at $O(1$ TeV) or below. A study of MSSM one-loop contributions to TGC [6, 7] can therefore provide a complementary information on a range of MSSM parameter values which may not be available from direct particle production.

[1] On leave from U.R.A. 768 du C.N.R.S., 34095 Montpellier France

2 Extracting TGC from Loops

In momentum space the vertex issued from the C-, P-conserving part of the general TGC effective Lagrangian [8] reads ($V \equiv \lambda, Z$)

$$\Gamma^V_{\alpha\beta\delta} = i g_{WWV}\{f_V[2g_{\alpha\beta}\Delta_\alpha - 4(g_{\alpha\alpha}Q_\beta - g_{\beta\alpha}Q_\alpha)] \qquad (1)$$
$$+2\Delta\kappa'_V(g_{\beta\alpha}Q_\beta - g_{\beta\alpha}Q_\alpha) + 4\frac{\Delta Q_V}{M_W^2}\Delta_\alpha(Q_\alpha Q_\beta - g_{\alpha\beta}\frac{Q^2}{2})\},$$

where $2Q_\alpha$, $(\Delta - Q)_\beta$, and $-(\Delta - Q)_\delta$ designate the four-momenta and Lorentz indices of the *incoming* γ (or Z), W^+_α and W^-_β respectively, and the (q^2-dependent) coefficients in (1) are related to the more conventional TGC parameters [8, 2] as $\Delta\kappa'_V \equiv \kappa_V - 1 + \lambda_V = \Delta\kappa_V + \lambda_V$; $\Delta Q_V \equiv -2\lambda_V$.

Naively, TGC are obtained by summing all MSSM contributions to the appropriate parts in eq. (1) from vertex loops with entering γ (or Z) and outgoing W^+, W^-. But, as is well known, the vertex graphs with virtual gauge bosons need to be combined with parts of box graphs for the full process, $e^+e^- \to W^+W^-$, to form a gauge-invariant contribution. This is most conveniently done by the pinch technique [4], i.e 'pinching' in an appropriate manner the irrelevant propagator lines from boxes, which preserves all the well-behaved features and properties expected from radiative corrections (Ward identities, good unitarity behaviour, infra-red finiteness, etc). The resulting combinations define purely s-dependent -and in that sense universal- TGC since, by definition, t and u-dependent box contributions are left over in this procedure. In what follows we have evaluated the complete set of s-dependent TGC, using the pinch technique for the relevant graphs. The sfermions, gauginos, and Higgses contribute separately to vertex graphs at the one-loop level, and we illustrate in fig. 1 those three contributions to $\Delta\kappa_\gamma$ for a representative choice of MSSM parameters [3] (contributions to $\Delta\kappa_Z$ are of the same order [7]). As a general remark, we note that the total contributions from the three sectors are comfortably of the order of the expected accuracy, but most particles give their maximal contributions when their masses are slightly above their direct production thresholds, showing a decoupling behavior for larger masses, as expected. An exception occurs for the sfermions, whose largest (and indeed dominant) contributions are obtained for a large mass splitting among up and down components (a situation where one does not expect any decoupling behavior, and in fact $\Delta\kappa_V$ tend to a constant in that case).

Now it is not clear whether the remnant (u,s)- and (t,s)-dependent boxes -which also form a gauge-invariant set by themselves- do not contribute a substantial part of

[3] For illustration we choose values which give somewhat maximal effects

the full radiative corrections to TGC, especially at such high energies. Even if the above concept of a gauge-invariant, universal quantity defined from the pinch technique could be theoretically useful, one practical problem (as far as TGC measurements are concerned) is that there are no planned experimental procedure to distinguish among "universal" and "remnant" TGCs: clearly *anything* contributing at the loop-level to the coefficients in eq.(1) will be extracted from the data (provided, of course, that it gives large enough contribution to be detected). We thus illustrate as well in fig. 2 some partial (but gauge-invariant) box contributions, with internal sleptons and gauginos. Although partial, this indicates what relative amount of universal versus "remnant box" contributions may be expected at those energies.

References

[1] G. Gounaris et al. *e^+e^- Collisions at 500 GeV: the Physics potential*, ed. P. Zerwas, DESY 92-123B, p.735; T. Barklow, in *Proceedings of the Workshop on Physics with Linear Colliders*, Saariselka, Finland (1992) p.423; M. Bilenky et al. Nucl. Phys. B 419 (1994) 240; M. Gintner, S. Godfrey, G. Couture, Phys.Rev. D52 (1995) 6249; V. Andreev, A. Pankov, N. Paver, IC/95/293 (September 95).

[2] G. Gounaris et al., Triple Gauge Boson Couplings, in *Physics at LEP2*, CERN report 1996, G. Altarelli and F. Zwirner eds. (hep-ph/9601233), and references therein.

[3] W. Beenakker et al. Nucl. Phys. B304(1988) 463; J. Fleischer, F. Jegerlehner and M. Zralek, Z. Phys. C42 (1989) 409; J. Fleischer et al. Nucl. Phys. B378 (1992) 443; E. Argyres et al. Nucl. Phys. B391 (1993) 23; and earlier references therein.

[4] J. Papavassiliou and K. Philippides, Phys. Rev. D48 (1993) 4255.

[5] for a review see e.g. H.P. Nilles, Phys. Rep. 110 (1984) 1; H. E. Haber and G. L. Kane, Phys. Rep. 117 (1985) 75.

[6] A. Lahanas and V. Spanos, Phys. Lett. B334 (1994)378; E. Argyres et al. UA/NPPS-18B (October 95).

[7] A. Arhrib, J.-L. Kneur, G. Moultaka, CERN-TH/95-344 (hep-ph/9512437), to appear in *Phys. Lett. B*.

[8] K. Gaemers and G. Gounaris, Z. Phys. C1 (1979) 259; K. Hagiwara et al. Nucl. Phys. B 282 (1987) 253.

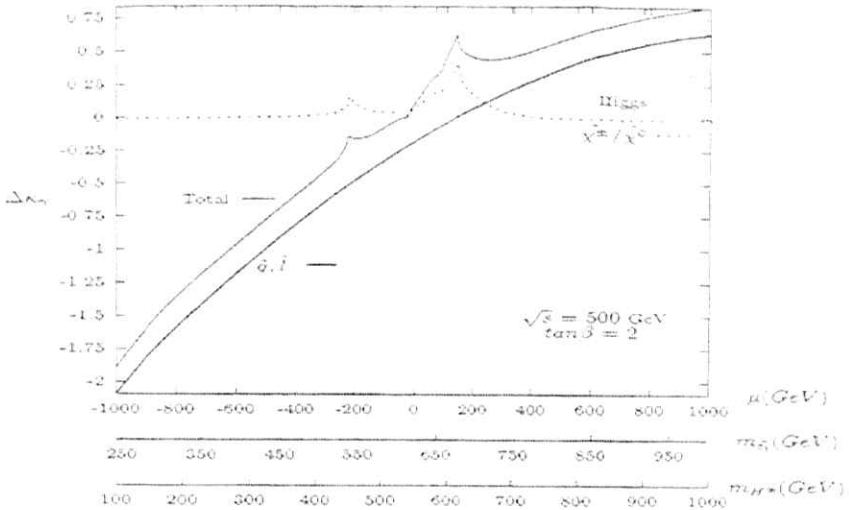

Figure 1: s-dependent $\Delta\kappa_\gamma$ contributions (in units of $g^2/16\pi^2$) from Higgses, sfermions and gauginos. Other parameters fixed to $m_{\tilde{l}_1} = m_{\tilde{l}_2} = m_{\tilde{l}_3} = m_{\tilde{e}_R} = m_{\tilde{l}_4} = m_{\tilde{l}_5} = m_{\tilde{e}_L}$, $m_{\tilde{l}_1} = m_{\tilde{e}_L} = 1.245$ TeV and $m_{\tilde{l}_4} = m_{\tilde{e}_{L,R}} = 1.47$ TeV; $M = 190$ GeV, $M' = 70$ GeV.

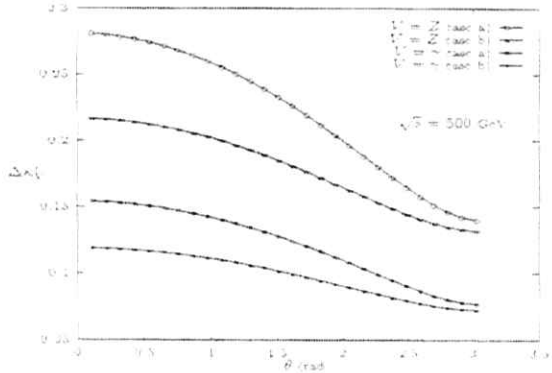

Figure 2: t-dependent non-pinch box contributions (in units of $g^2/16\pi^2$) with one chargino (resp. neutralino), two sneutrinos (resp. selectrons) and one selectron (resp. sneutrino) versus the W^- production angle θ. $m_{\tilde{e}_L} = m_{\tilde{\nu}_L} = 260$ GeV, zero left-right mixing angle; case a: $M = \mu = 150$ GeV, $M' = 100$ GeV, $\tan\beta = 15$; case b: $M = M' = \mu = 250$ GeV, $\tan\beta = 2$.

Z' Reservation at LC2000

J. Layssac[c], G. Montagna[a], O. Nicrosini[b], F. Piccinini[b]
F.M. Renard[c] and C. Verzegnassi[d]

[a]Dipartimento di Fisica Nucleare e Teorica, Università di Pavia
and INFN, Sezione di Pavia, Via A.Bassi 6, 27100, Pavia, Italy.

[b] INFN, Sezione di Pavia, Via A.Bassi 6, 27100, Pavia, Italy.

[c]Physique Mathématique et Théorique, CNRS-URA 768,
Université de Montpellier II, F-34095 Montpellier Cedex 5.

[d] Dipartimento di Fisica, Università di Lecce
CP193 Via Arnesano, I-73100 Lecce,
and INFN, Sezione di Lecce, Italy.

Abstract

We consider the possibility that one extra $Z \equiv Z'$ exists with a mass of more then two TeV and fermion couplings that do not violate (charged) lepton universality. We show that, in such a situation, a functional relationship is generated between the deviations from the SM values of three leptonic observables of two-fermion production at LC 2000 that is completely independent of the values of the Z' mass and couplings. This selects a certain region in the 3-d space of the deviations (Z' "reservation") that is characteristic of the model and that would have no observable intersection with analogous regions corresponding to other interesting models of new physics.

Models with one extra $Z \equiv Z'$ have been extensively discussed in recent years [1], and their experimental implications have been analyzed in a number of reports [2]. As a result of these investigations, it appears nowadays that future searches at CDF, LEP2 and LHC will be able to identify a particle of this type provided that its mass does not exceed a value of the order (depending on the specific model) of a few TeV. If no evidence of a Z' were reported at the end of the LHC running, future searches could only be pursued by looking for virtual effects at e^+e^- colliders whose c.m. energy were sufficient to feel the effect of a Z' of such a large mass. At $LC2000$ this would be possible, as it has been shown in a different contribution to this working group report [3], for $M_{Z'}$ values larger than 10 TeV, which could be considered as a realistic experimental final limit for Z' searches in the first part of the next century.

The aim of this short paper is that of showing that, from the combined analysis of leptonic processes at $LC2000$, it would be possible to identify the virtual signals of a Z' of the most general type i.e. with general (but universal) couplings with charged leptons (no universality assumption on the contrary on the couplings with the remaining fermions).

Considering a most general Z' of the type just illustrated can be explained, or justified, by two main simple reasons. The first one is the fact that some of the strong theoretical motivations that supported "canonical" schemes like e.g. the special group E_6 have become undeniably weak in the last few years. The second one is that a number of different models with one extra U(1) have meanwhile been proposed, or have resurrected [4]. These facts lead us to the conclusion that a totally general analysis might be more relevant than a few specific ones. Obviously, one will be able to recover the "canonical" results as special cases of our investigation.

In this spirit, we have started by considering the theoretical expression of the scattering amplitude of the process $e^+e^- \to l^+l^-$ ($l = e, \mu, \tau$) at squared c.m. energy q^2 in the presence of one Z'. At tree level, this can be written as :

$$A_{ll}^{(0)}(q^2) = A_{ll}^{(0)\gamma,Z}(q^2) + A_{ll}^{(0)Z'}(q^2) \tag{1}$$

where

$$A_{ll}^{(0)\gamma}(q^2) = \frac{ie_0^2}{q^2}\bar{v}\gamma_\mu u_l \bar{u}\gamma^\mu v_l \tag{2}$$

$$A_{ll}^{(0)Z}(q^2) = \frac{i}{q^2 - M_{0Z}^2}\left(\frac{g_0^2}{4c_0^2}\right)\bar{v}\gamma_\mu\left(g_{Vl}^{(0)} - \gamma^5 g_{Al}^{(0)}\right)u_l \bar{u}\gamma^\mu\left(g_{Vl}^{(0)} - \gamma^5 g_{Al}^{(0)}\right)v_l \tag{3}$$

and (note the particular normalization)

$$A_{ll}^{(0)Z'}(q^2) = \frac{i}{q^2 - M_{0Z'}^2}\left(\frac{g_0^2}{4c_0^2}\right)\bar{v}\gamma_\mu\left(g_{Vl}^{\prime(0)} - \gamma^5 g_{Al}^{\prime(0)}\right)u_l \bar{u}\gamma^\mu\left(g_{Vl}^{\prime(0)} - \gamma^5 g_{Al}^{\prime(0)}\right)v_l \tag{4}$$

($e_0 \equiv g_0 s_0$, $c_0^2 \equiv 1 - s_0^2$).

Following the usual approach, we shall treat the Z' effect at one loop in the SM sector and at "effective" tree level for the Z' exchange diagram, whose interference with the analogous photon and Z graphs will give the relevant virtual contributions. The Z' width will be considered "sufficiently" small with respect to $M_{Z'}$ to be safely neglected in the

Z' propagator, and from what previously said the $Z-Z'$ mixing angle will be ignored. If we stick ourselves to final charged leptonic states, we must therefore deal with only two "effective" parameters, more precisely the ratios of the quantities $g'_{Vl}/\sqrt{M^2_{Z'}-q^2}$ and $g'_{Al}/\sqrt{M^2_{Z'}-q^2}$, that contain the (conventionally defined) "physical" Z' mass and two "physical" $Z'll$ couplings, whose meaningful definition would be related to a Z' discovery and to measurements of its various decays, that are obviously missing. This will not represent a problem in our case since in our approach these parameters, as well as any intrinsic overall (scale) ambiguity related to their actual definition, will disappear in practice, being replaced by model independent functional relationships between different leptonic observables.

For what concerns the treatment of the SM sector, a prescription has been very recently given [5] that corresponds to a "Z-peak subtracted" representation of two-fermion production, in which a modified Born approximation and "subtracted" one-loop corrections are used. These corrections, that are "generalized" self-energies, i.e. gauge-invariant combinations of self-energies, vertices and boxes, have been called in refs.[5], to whose notations and conventions we shall stick, $\hat{\Delta}\alpha(q^2)$, $R(q^2)$ and $V(q^2)$ respectively. As it has been shown in ref.[5], they turn out to be particularly useful whenever effects of new physics must be calculated. In particular, the effect of a general Z' can be treated in this approach as a particular modification of purely "box" type to the SM values of $\hat{\Delta}\alpha(q^2)$, $R(q^2)$ and $V(q^2)$ given by the following prescriptions:

$$\hat{\Delta}^{(Z')}\alpha(q^2) = -\frac{q^2}{M^2_{Z'}-q^2}\frac{1}{4s_1^2c_1^2}[g'^2_{Vl}(\xi_{Vl}-\xi_{Al})^2 \tag{5}$$

$$R^{(Z')}(q^2) = (\frac{q^2-M^2_Z}{M^2_{Z'}-q^2})\xi^2_{Al} \tag{6}$$

$$V^{(Z')}(q^2) = -(\frac{q^2-M^2_Z}{M^2_{Z'}-q^2})(\frac{g_{Vl}}{2s_1c_1})\xi_{Al}(\xi_{Vl}-\xi_{Al}) \tag{7}$$

where we have used the definitions :

$$\xi_{Vl} \equiv \frac{g'_{Vl}}{g_{Vl}} \tag{8}$$

$$\xi_{Al} \equiv \frac{g'_{Al}}{g_{Al}} \tag{9}$$

with $g_{Vl}=-\frac{1}{2}(1-4s_1^2)$; $g_{Al}=-\frac{1}{2}$ and $s_1^2 \equiv 1-c_1^2$; $s_1^2c_1^2=\pi\alpha(0)/\sqrt{2}G_\mu M_Z^2$.

To understand the philosophy of our approach it is convenient to write the expressions at one-loop of the three independent leptonic observables that could be measured at $LC2000$, i.e. the muon cross section and forward-backward asymmetry and the lepton longitudinal polarization asymmetry (we assume that longitudinal polarized e^-e^- beams will be available). Leaving aside specific QED corrections, these expressions read:

$$\sigma_{-}(q^2) = \sigma_{-}^{Born}(q^2)\{1+\frac{2}{\kappa^2(q^2-M_Z^2)^2+q^4}[\kappa^2(q^2-M_Z^2)^2\hat{\Delta}\alpha(q^2)$$

$$-q^4(R(q^2)+\frac{1}{2}V(q^2))]\} \tag{10}$$

$$A_{FB,-}(q^2) = A_{FB,-}^{Born}(q^2)\{1-\frac{q^4-\kappa^2(q^2-M_Z^2)^2}{\kappa^2(q^2-M_Z^2)^2+q^4}\hat{\Delta}\alpha(q^2)+R(q^2)]$$
$$-\frac{q^4}{\kappa^2(q^2-M_Z^2)^2+q^4}V(q^2)]\} \tag{11}$$

$$A^l_{LR}(q^2) = A^{l,Born}_{LR}(q^2)\{1+[\frac{\kappa(q^2-M_Z^2)}{\kappa(q^2-M_Z^2)-q^2}-\frac{2\kappa^2(q^2-M_Z^2)^2}{\kappa^2(q^2-M_Z^2)^2+q^4}]\hat{\Delta}\alpha(q^2)$$
$$+R(q^2)]-\frac{4c_1s_1}{v_l}V(q^2)\} \tag{12}$$

where κ^2 is a numerical constant ($\kappa^2 \equiv (\frac{\pi}{3\sqrt{3}\alpha(M_Z)})^2 \simeq 7$) and we defer to ref.[5] for a more detailed derivation of the previous formulae.

A comparison of eqs.(10)-(12) with eqs.(5)-(7) shows that, in the three leptonic observables, only two effective parameters, that could be taken for instance as $\xi_{Vl}M_Z/\sqrt{M^2_{Z'}-q^2}$, $(\xi_{Vl}-\xi_{Al})M_Z/\sqrt{M^2_{Z'}-q^2}$ (to have dimensionless quantities, other similar definitions would do equally well), enter. This leads to the conclusion that it must be possible to find a relationship between the relative Z' shifts $\frac{\delta\sigma_-^{(Z')}}{\sigma_-}$, $\frac{\delta A^{(Z')}_{FB,-}}{A_{FB,-}}$ and $\frac{\delta A^{l,(Z')}_{LR}}{A^l_{LR}}$ (defining the shift, for each observable $\equiv \mathcal{O}$, through $\mathcal{O} \equiv \mathcal{O}^{SM}-\delta\mathcal{O}^{(Z')}$) that is completely independent of the values of these effective parameters. This will correspond to a region in the 3-d space of the previous shifts that will be fully characteristic of a model with the most general type of Z' that we have considered. We shall call this region "Z' reservation"[1].

To draw this reservation would be rather easy if one relied on a calculation in which the Z' effects are treated in first approximation, i.e. only retaining the leading effects, and not taking into account the QED (initial-state) radiation. After a rather straightforward calculation one would then be led to the following approximate expressions that we only give for indicative purposes:

$$[\frac{\delta A^{l,(Z')}_{LR}}{A^l_{LR}}]^2 \simeq f_1f_3(\frac{8c_1^2s_1^2}{v_l^2})[\frac{\delta\sigma_-^{(Z')}}{\sigma_-}][\frac{\delta A^{(Z')}_{FB,-}}{A_{FB,-}}-\frac{1}{2}f_2\frac{\delta\sigma_-^{(Z')}}{\sigma_-}] \tag{13}$$

where

$$f_1 = \frac{\kappa^2(q^2-M_Z^2)^2+q^4}{\kappa^2(q^2-M_Z^2)^2} \tag{14}$$

$$f_3 = \frac{\kappa^2(q^2-M_Z^2)^2-q^4}{\kappa^2(q^2-M_Z^2)^2} \tag{15}$$

[1] Reservation : "Tract of land reserved for exclusive occupation by native tribe" Oxford Dictionary 1950

$$f_3 = \frac{\kappa^2(q^2 - M_Z^2)^2 - q^4}{\kappa^2(q^2 - M_Z^2)^2 - q^4} \tag{16}$$

Eq.(13) is only an approximate one. A more realistic description can only be obtained if the potentially dangerous QED effects are fully accounted for. In order to accomplish this task, the QED structure function formalism [6] has been employed as a reliable tool for the treatment of large undetected initial-state photonic radiation. Using the structure function method amounts to writing, in analogy with QCD factorization, the QED corrected cross section [7] as a convolution of the form [2]

$$\sigma(q^2) = \int dx_1\, dx_2\, D(x_1, q^2) D(x_2, q^2) \sigma_0\left((1 - x_1 x_2) q^2\right) \{1 + \delta_{fs}\}\, \Theta(\text{cuts}), \tag{17}$$

where σ_0 is the lowest-order kernel cross section, taken at the energy scale reduced by photon emission, and $D(x, q^2)$ is the electron (positron) structure function. Its expression, as obtained by solving the Lipatov–Altarelli–Parisi evolution equation in the non-singlet approximation, is given by [6]:

$$\begin{aligned} D(x, q^2) &= \Delta' \frac{\beta}{2}(1 - x)^{\frac{\beta}{2} - 1} - \frac{\beta}{4}(1 + x) \\ &+ \frac{1}{32}\beta^2 \left[-4(1 + x)\ln(1 - x) + 3(1 + x)\ln x - 4\frac{\ln x}{1 - x} - 5 - x\right], \end{aligned} \tag{18}$$

with

$$\beta = 2\frac{\alpha}{\pi}(L - 1) \tag{19}$$

where $L = \ln(q^2/m^2)$ is the collinear logarithm. The first exponentiated term is associated to soft multiphoton emission, the second and third ones describe single and double hard bremsstrahlung in the collinear approximation. The K-factor Δ' is of the form

$$\Delta' = 1 + \left(\frac{\alpha}{\pi}\right)\Delta_1 + \left(\frac{\alpha}{\pi}\right)^2 \Delta_2 \tag{20}$$

where Δ_1 and Δ_2 contain respectively $\mathcal{O}(\alpha)$ and $\mathcal{O}(\alpha^2)$ non-leading QED corrections known from explicit perturbative calculations. The actual expression used for these non-leading corrections is the one valid in the soft-photon approximation, which is justified by the fact that, in order to avoid the Z radiative return, a cut on the hard-photon tail is imposed. In eq. (17) $\Theta(\text{cuts})$ represents the rejection algorithm to implement possible experimental cuts, δ_{fs} is the correction factor to account for QED final-state radiation. Since only a cut on the invariant mass $s' = x_1 x_2 q^2$ of the event after initial-state radiation is imposed in our numerical analysis (see below), the simple formula $\delta_{fs} = 3\pi/4\alpha$ holds. In order to proceed with the numerical simulation of the Z' effects under realistic experimental conditions, the master formula (17) has been implemented in a Monte Carlo event generator which has been first checked against currently used LEP1 software [8], found to be in very good agreement and then used to produce our numerical results. The Z' contribution has been included in the kernel cross section σ_0 computing the $s-$channel Feynman diagrams associated to the production of a ll pair in a e^+e^- annihilation mediated by the exchange of a photon, a standard model Z and an additional Z' boson. In the calculation, which has been carried out within the helicity amplitude formalism for massless fermions and with the help of the program for the algebraic manipulations SCHOONSCHIP [9], the coupling of the Z' boson to the leptons has been parametrized, as already pointed out, as:

$$\gamma^\mu \left(g_{Vl}^{(0)} - g_{Al}^{(0)}\gamma_5\right) \tag{21}$$

and the Z' propagator has been included in the zero-width approximation (see above). Moreover, the bulk of non-QED corrections has been included in the form of Improved Born Approximation, choosing $\bar{\alpha}(q^2)$, M_Z, G_F, together with Γ_Z, as input parameters. The values used for the numerical simulation are [10]: $M_Z = 91.1887$ GeV, $\Gamma_Z = 2.4979$ GeV; the center of mass energy has been fixed at $\sqrt{q^2} = 2000$ GeV and the cut $s'/q^2 > 0.003$ has been imposed in order to remove the events due to Z radiative return and hence disentangle the interesting virtual Z' effects. These have been investigated allowing the previously defined ratios ξ_V and ξ_A to vary within the ranges $-2 \leq \xi_A \leq 2$ and $-10 \leq \xi_V \leq 10$. Higher values might be also taken into account; the reason why we chose the previous ranges was that, to our knowledge, they already include all the most popular existing models.

The results of our calculation are shown in Fig. 1. The central box corresponds to the "dead" area where a signal would not be distinguishable corresponds to an assumed (relative) experimental error of 1% for σ_t and A_{FB}^t and to 10% for A_{LR}^t. The region that remains outside the dead area represents the Z' reservation at $LC2000$, to which the effect of the most general Z' must belong.

[2] The actual implementation of QED corrections is performed, in the Monte Carlo code, at the level of the differential cross section, taking into account all the relevant kinematical effects according to [7]; in the present paper only a simplified formula is described, for the sake of simplicity.

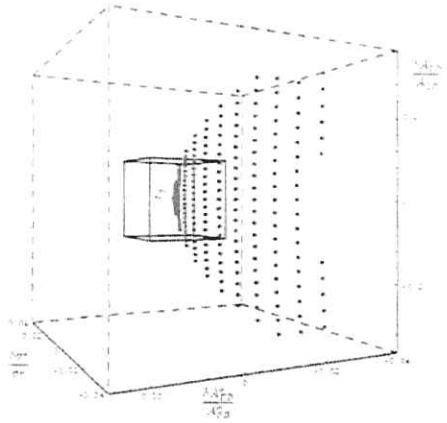

Fig 1

One might be interested in knowing how different the realistic Fig. 1 is from the approximate "Born" one, corresponding in particular to the simplest version given by eq. (13). This can be seen in Fig. 2, where we showed the two surfaces (the points correspond to the realistic situation, Fig. 1). One sees that the simplest Born calculation is a very good approximation to a realistic estimate, which could be very useful if one first wanted to look for sizeable effects.

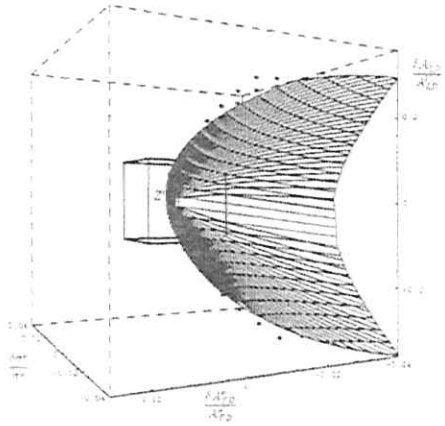

Fig 2

The next relevant question that should be now answered is whether the correspondence between Z' and reservation is of the one to one type, which would lead to a unique identification of the effect. We have tried to answer this question for two specific and relevant cases, that of virtual effects produced by anomalous gauge couplings (AGC) and that of effects produced by general technicolour-type (TC) models. In particular, we have considered the case of the most general, dimension six, $SU(2) \otimes U(1)$ invariant effective Lagrangian recently proposed [11]. For technicolour models we have examined a rather general situation in which a pair of strongly coupled vector and axial resonances exist. The details have been fully discussed in a separate paper [12], where the previously mentioned "Z-peak subtracted" approach has been used. The resulting AGC and TC reservations in the $(\sigma_h, A_{FB,h}, A_{LR})$ plane are certain regions, drawn, for simplicity, in Born approximation as suggested by the previous remarks. In Fig. 3 we have plotted these regions and they can be compared to the general Z' one plotted in Fig.2.

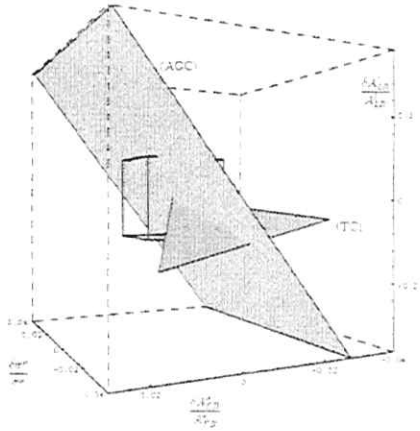

Fig 3

As one sees, the three reservations do not overlap in the meaningful region. Although we cannot prove this property in general, we can at least conclude that, should a clear virtual effect show up at $LC2000$, it would be possible to decide unambiguously to which among three very popular proposed models it does belong.

References

[1] For a review see, e.g., L. Hewett and T.G. Rizzo, Phys. Rep. **C183** (1989) 193.

[2] Proc. LHC Workshop, CERN 90-10, ECFA 90-133, vol.II, (1990), p.685; Proc. e^+e^- Collisions at 500 GeV: The Physics Potential, DESY 92-123B (1992), p.479; Z' Physics at LEP2, working group report, P. Chiappetta et al. to appear.

[3] A. Leike and S. Riemann, contribution to this working group.

[4] D. Kosower, Phys. Rev. **D48** (1993) 1288.

[5] F.M. Renard and C. Verzegnassi, Phys. Rev. **D52** (1995) 1369; F.M. Renard and C. Verzegnassi, preprint PM/95-35 (1995), to appear in Phys.Rev.D.

[6] E. A. Kuraev and V. S. Fadin, Sov. J. Nucl. Phys. 41 (1985) 466;
G. Altarelli and G. Martinelli, *Physics at LEP*, CERN Report 86-02, J. Ellis and R. Peccei, eds. (Geneva, 1986); see also:
O. Nicrosini and L. Trentadue, Phys. Lett. *B196* (1987) 551; Z. Phys. *C39* (1988) 479.
For a review see also:
O. Nicrosini and L. Trentadue, in *Radiative Corrections for e^+e^- Collisions*, J. H. Kühn, ed. (Springer, Berlin, 1989), p. 25; in *QED Structure Functions*, G. Bonvicini, ed., AIP Conf. Proc. No. 201 (AIP, New York, 1990), p. 12; O. Nicrosini, ibid., p. 73.

[7] G. Montagna, O. Nicrosini and F. Piccinini, Phys. Rev. *D48* (1993) 1021, and references therein.

[8] G. Montagna, O. Nicrosini, G. Passarino and F. Piccinini, "`TOPAZO 2.0` - A program for computing deconvoluted and realistic observables around the Z^0 peak", Comput. Phys. Commun. 93 (1996) 120; G. Montagna, O. Nicrosini, G. Passarino, F. Piccinini and R. Pittau, Comput. Phys. Commun. 76 (1993) 328.

[9] `SCHOONSCHIP`, a program for symbolic handling by M. Veltman, see H. Strubbe, Comput. Phys. Commun. 8 (1974) 1.

[10] Review of Particle Properties, Phys. Rev. *D50* (1994) 1173.

[11] K. Hagiwara, S. Ishihara, R. Szalapski and D. Zeppenfeld, Phys. Lett. **B283** (1992) 353 and Phys. Rev. **D48** (1993) 2182.

[12] F.M. Renard and C. Verzegnassi, preprint PM/95-35 (1995), to appear in Phys.Rev.D.

Z' Constraints from $e^+e^- \to f\bar{f}$ at NLC

A. Leike[a], S. Riemann[b]

[a] *Ludwigs-Maximilians-Universität, Sektion Physik, Theresienstr. 37, D-80333 München, Germany*

E-mail: leike@graviton.hep.physik.uni-muenchen.de

[b] *Deutsches Elektronenh-Synchrotron DESY, Institut für Hochenergiephysik IfH, Zeuthen, Platanenallee 6, D-15735 Zeuthen, Germany*

E-mail: riemanns@ifh.de

Abstract

Constraints on extra neutral gauge bosons are obtained from $e^+e^- \to f\bar{f}$ at NLC energies. Model independent limits on the $Z'f\bar{f}$ couplings are discussed as well as lower limits on the Z' mass $M_{Z'}^{lim}$. Typical GUT's with $M_{Z'} = 3$ to $6\sqrt{s}$ can be excluded, while distinction between different GUT scenarios demands $M_{Z'} \leq 3\sqrt{s}$. Radiative corrections give only small changes to the Z' exclusion limits providing that appropriate cuts are applied. The inclusion of systematic errors leads to slightly worse results for $M_{Z'}^{lim}$.

1 Introduction

The search for extra neutral gauge bosons is an important task of the physics programme of all present and future colliders. Up to now, no Z' signals are found. These negative experimental results are usually reported as lower limits on excluded Z' masses $M_{Z'}^{lim}$ or as upper limits on the ZZ' mixing angle for selected Z' models. Future colliders can put much stronger constraints on this particle, see [1, 2, 3].

In this paper and in a more extensive analysis [4], we examine the Z' constraints which can be obtained from $e^-e^- \to f\bar{f}$ at c.m. energies $\sqrt{s} = 500\,GeV$ with $L_{int} = 20 fb^{-1}$ (NLC500) and $\sqrt{s} = 2\,TeV$ with $L_{int} = 320 fb^{-1}$ (NLC2000) and $P = 80\%$ beam polarization in both scenarios. In comparison to [1, 2, 3], we take into account all available QED, electroweak and QCD corrections and apply kinematical cuts to approach a more realistic description of future detectors. We go beyond [1, 2] including more observables in our analysis. In contrast to [3], we include the expected systematic errors.

We set the ZZ' mixing angle to zero because of present experimental constraints [5, 6, 7]. CDF data indicates that NLC500 will operate below a Z' peak [8]. Similarly, LHC will be able to exclude a Z' which could be produced at NLC2000 on resonance. We assume that NLC2000 will operate below the Z' peak too. Throughout we presume universality of generations. Theories including extra neutral gauge bosons usually predict new fermions [9, 10]. Their effects are neglected here.

We consider Z' models which are described by the following effective Lagrangian at low energies.

$$\mathcal{L} = eA_\mu J_\gamma^\mu + g_1 Z_\mu J_Z^\mu - g_2 Z'_\mu J_{Z'}^\mu. \tag{1}$$

The term proportional to g_2 contains the new interactions of the Z' with SM fermions.

Although we mainly focus on model independent Z' limits, we will also refer to some special models predicted in an E_6 GUT [10, 11] and in a Left-Right Model [11, 12].

$$J_{Z'}^\mu = J_\chi^\mu \cos\beta + J_\psi^\mu \sin\beta, \quad J_{Z'}^\mu = \alpha_{LR} J_{3R}^\mu - \frac{1}{2\alpha_{LR}} J_{B-L}^\mu. \tag{2}$$

Some completely specified cases are $Z' = \chi$, ψ and η $\left(\beta = -\arctan\sqrt{5/3}\right)$ in the E_6 GUT. Special cases in the Left-Right Model are obtained for α_{LR} equal to $\sqrt{2/3}$ and $\sqrt{\cot^2\theta_W - 1}$. The first value of α_{LR} gives again the χ model, while the second number gives the Left-Right Symmetric Model (LR). The Sequential Standard Model (SSM) is also considered. It contains a heavy Z' which has exactly the same couplings to fermions as the Standard Z boson.

The presence of an extra neutral gauge boson leads to an additional amplitude of fermion pair production at the Born level.

$$\begin{aligned}\mathcal{M}(Z') &= \frac{g_2^2}{s - m_{Z'}^2} \bar{u}_e \gamma_\beta (\gamma_5 a'_e + v'_e) u_e \, \bar{u}_f \gamma^\beta (\gamma_5 a'_f + v'_f) u_f \\ &= -\frac{4\pi}{s} \left[\bar{u}_e \gamma_\beta (\gamma_5 a_e^N + v_e^N) u_e \, \bar{u}_f \gamma^\beta (\gamma_5 a_f^N + v_f^N) u_f\right]\end{aligned} \tag{3}$$

$$\text{with } a_f^N = a'_f \sqrt{\frac{g_2^2}{4\pi} \frac{s}{m_{Z'}^2 - s}}, \; v_f^N = v'_f \sqrt{\frac{g_2^2}{4\pi} \frac{s}{m_{Z'}^2 - s}}, \text{ and } m_{Z'}^2 = M_{Z'}^2 - i\Gamma_{Z'} M_{Z'}. \tag{4}$$

Equations (3) and (4) show that far below the resonance the effect of a Z' is described by the two parameters a_f^N and v_f^N and not by a'_f, v'_f and $m_{Z'}$ separately. The fermionic couplings of a fixed Z' define a point in the (a_f^N, v_f^N) planes ($f = \nu, l, u, d$). Various observables can detect a Z' in different regions of the (a_f^N, v_f^N) planes.

e^+e^- colliders provide several observables depending on couplings to leptons only as

$$\sigma_{tot}^l, \; A_{FB}^l, \; A_{LR}^l, \; A_{pol}^l, \; A_{pol,FB}^l \text{ and } A_{LR,FB}^l. \tag{5}$$

Therefore, the Z' couplings to leptons (a_l^N, v_l^N) can be constrained independently of the quarkonic Z' couplings. The index l stands for electrons and muons and in the final state. Only the s channel is considered for electrons in the final state. Neglecting fermion masses, the last four leptonic observables are related at the Born level.

$$A_{LR}^l = A_{pol}^l = \frac{4}{3} A_{pol,FB}^l = \frac{4}{3} A_{LR,FB}^l. \tag{6}$$

Therefore, they are equivalent for a Z' search. Without loss of generality, we will consider only A_{LR} as a representative. It is expected to have the smallest error compared to the other three observables.

The hadronic observables can be divided into three groups: Observables containing in addition to the obligatory $Z'l\bar{l}$ couplings the $Z'b\bar{b}$ couplings only, as

$$R_b = \sigma_b^f/\sigma_l^f,\ A_{FB}^b,\ A_{LR}^b, \tag{7}$$

the $Z'c\bar{c}$ couplings only, and all couplings of the Z' to quarks. The analysis of the first two groups is very similar. However, we will not consider the second group because c-quark flavour identification leads to systematic errors which are considerably larger than those from b-quark identification. The third group has the smallest errors because it doesn't require flavour identification. We consider

$$R^{had} = \sigma_l^{had}/\sigma_l^\mu = \sigma_l^{e^-e^+s\bar{s}c\bar{c}}/\sigma_l^\mu \text{ and } A_{LR}^{had} = A_{LR}^{e^+e^-s\bar{s}c\bar{c}}. \tag{8}$$

The statistical errors of all observables for N detected events are

$$\frac{\Delta\sigma_l}{\sigma_l} = \frac{1}{\sqrt{N}},\quad \Delta A_{FB} = \sqrt{\frac{1-A^2}{N}},\quad \Delta A_{LR} = \sqrt{\frac{1-(PA_{LR})^2}{NP^2}}. \tag{9}$$

We assume a systematic error of the luminosity measurement of 0.5% . Further, we include a systematic error of 0.5% for the measurement of each observable. We assume 1% systematic error due to b-quark identification and take into account the efficiency of quark tagging. Statistical and systematic errors are added in quadrature. The resulting combined errors are equal for NLC500 and NLC2000:

$$\Delta\sigma_l^l/\sigma_l^l = 1\%,\ \Delta A_{FB}^l = 1\%,\ \Delta A_{LR}^l = 1.2\%,$$
$$\Delta R_b = 2.2\%,\ \Delta A_{FB}^b = 2.2\%,\ \Delta A_{LR}^b = 1.5\%,\ \Delta R^{had} = 0.9\%, \Delta A_{LR}^{had} = 0.7\%. \tag{10}$$

To obtain confidence levels for different sets of parameters, we calculate the prediction for all observables in the Standard Model $O_i(\mathrm{SM})$ and in a theory including a Z' $O_i(\mathrm{SM}, v_l^N, a_l^N)$ and consider the deviation of

$$\chi^2 = \sum_{O_i} \left[\frac{O_i(\mathrm{SM}) - O_i(\mathrm{SM}, v_l^N, a_l^N)}{\Delta O_i}\right]^2 \tag{11}$$

from the minimum.

With our assumptions, the Z' can be detected only through small deviations of observables from their Standard Model predictions. It is known that radiative corrections have to be included to meet the expected experimental precision. For all energies considered here, the QED corrections are numerically most important. The energy spectrum of the radiated photons has a huge peak for energies $E_\gamma/E_{beam} \approx 1 - M_Z^2/s$. This is due to the radiative return to the Z resonance. Such events do not contain information about new heavy particles. They have to be eliminated by a cut on hard photons. This can be realized by a cut on the photon energy, $E_\gamma/E_{beam} = \Delta < 1 - M_Z^2/s$, or by a cut on the acollinearity angle of the two outgoing fermions. Satisfying these conditions, the analysis is much less sensitive to further cuts.

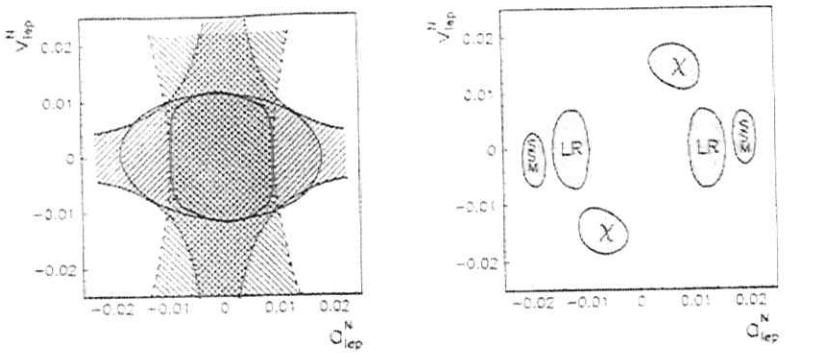

Fig. 1: *Areas in the $(a_l^N,\ v_l^N)$ plane indistinguishable from the SM at NLC500 (95% confidence). σ_l^l cannot detect models inside the shaded ellipse. A_{FB}^l (A_{LR}^l) are blind to models inside the hatched areas with falling (rising) lines. The region from all observables combined is also shown (thick line).*

Fig. 2: *Resolution power of NLC500 (95% confidence) by all leptonic observables combined for different models and $M_{Z'} = 3\sqrt{s} = 1.5\,TeV$.*

2 Model independent Z' limits

Our analysis is performed by the code `ZEFIT` [7] which works together with `ZFITTER` [13]. Hence, we have all SM corrections and all possibilities to apply kinematical cuts available in `ZFITTER`. The code `ZEFIT` contains the additional Z' contributions. It was already applied to LEP 1 data to set bounds to the ZZ' mixing angle [6] and is now adapted to a model independent Z' analysis. QED corrections to the new Z' interferences are applied to the same order as to the SM cross section.

In our fits, we used the full one-loop electroweak corrections, the 1-loop QCD corrections and soft photon exponentiation for photons in the initial and final states. The initial state radiation was taken at two-loops. We forbid hard photons taking $\Delta = 0.9$ for NLC500 and $\Delta = 0.98$ for NLC2000. As a simple simulation of the detector acceptance, we demand that the angle between the outgoing leptons and the beam axis is larger than 20°. We apply no angular restrictions to outgoing quarks. Possible correlations between the errors of different observables are neglected.

Figure 1 shows our model independent discovery limits on the couplings of the Z' to leptons from different observables. The corresponding figures for NLC500 and NLC2000 are almost identical because we expect the same number of events for both colider scenarios and a_l^N and v_l^N are normalized. We see that σ_l^l constrains both, the vector and the axial vector couplings, while A_{FB}^l constrains mainly the axial vector couplings. A_{LR}^l gives only a minor improvement to the discovery limits. The region obtained by all leptonic observables combined is also shown. The changes of figure 1 for experimental errors

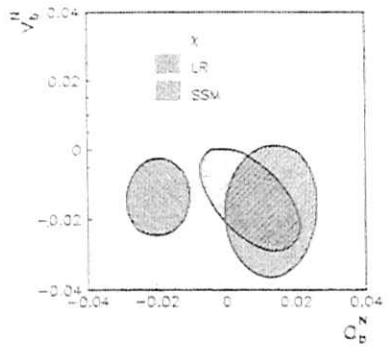

Fig. 3: *Resolution power of NLC500 in the (a_i^N, v_i^N) plane (95% confidence) by all b-quark observables combined. Different Z' models with $M_{Z'} = 1.5\,TeV$ are assumed.*

different from our assumption are described by the Born formulae given in ref. [2].

Assuming the existence of a Z' one can distinguish between different models at NLC500. This is shown in figure 2 for $M_{Z'} = 3\sqrt{s}$. The corresponding figure for NLC2000 does not differ from figure 2. In contrast to figure 1, A_{LR}^l is a really important input because it is sensitive to the sign of the Z' couplings. Note that a simultaneous change of the sign of both leptonic Z' couplings can never be detected by the reaction $e^+e^- \to ff$.

The constraints on a_i^N and v_i^N by the three leptonic observables could in principle lead to contradicting results. This could happen, if an area allowed by two observables, e.g. σ_t^l and A_{FB}^l is excluded by a third observable (e.g. A_{LR}^l). Such a case would be an indication for new physics beyond a Z'.

Non-zero Z' to lepton couplings are necessary for a Z' signal in the hadronic observables. To be definite, we assume that the Z' is described by one of the models χ, LR or SSM considered in figure 2. As in the leptonic case, different b-quark observables are blind in different directions. Polarized beams give a large improvement to the measurement of $Z'b\bar{b}$ couplings. Combined, all b-quark observables define a closed region in the (a_i^N, v_i^N) plane. Figure 3 shows that for all three models one can detect a non-zero Z' signal also in the $Z'b\bar{b}$ couplings. However, one cannot discriminate between χ and LR as it was possible in the leptonic sector. We refer to [4] for more details.

3 Model dependent Z' limits

We now discuss the result of several one parameter fits with and without systematic errors.

The lower limits to the Z' mass $M_{Z'}^{lim}$ for different Z' models are given in table 1. To these fits, R^{had} and A_{LR}^{had} give an important input. Table 1 shows three rows for every collider. The first row contains the limits from leptonic observables only. The second

		χ	ψ	η	LR	SSM
NLC500	leptonic observables only	2670	1900	1570	2700	3720
	all observables	2850	2000	1730	3470	4450
	all observables no systematic errors	3230	2160	2000	4040	5500
NLC2000	leptonic observables only	9500	6950	5780	9820	13560
	all observables	9590	6980	6020	10300	14000
	all observables no systematic errors	11200	7850	6840	12700	17800

Tab. 1: Maximal Z' masses $M_{Z'}^{lim}$ (in GeV) which can be excluded by leptonic observables only and by all observables combined for NLC500 and NLC2000.

row includes leptonic and hadronic observables. The third row includes all observables as the second row but without systematic errors. Comparing the first two rows of a certain collider, we see that the hadronic observables improve the mass limits between 5% and 10%. Therefore, both the leptonic and hadronic observables are important for measurements of $M_{Z'}^{lim}$. The difference between the numbers of the second and third row is about 10%. Hence, the mass limits obtained for a definite Z' model are rather insensitive to the assumptions about systematic errors.

The errors of hadronic observables are dominated by systematic uncertainties. Following, the relatively large vector and axialvector couplings of the Z' in the SSM cause a larger sensitivity of $M_{Z'}^{lim}$ to systematic errors.

As a result, e^+e^- colliders can exclude a Z' with a mass lighter than $M_{Z'}^{lim} \sim 3$ to $6\sqrt{s}$ for polpular GUT's and $M_{Z'}^{lim} \sim 8\sqrt{s}$ for the SSM.

To summarize, we investigated the limits on extra neutral gauge bosons which can be achieved at future linear e^+e^- colliders. We included radiative corrections, kinematical cuts and systematic errors in our analysis. The influence of radiative corrections on the Z' mass limits is small after applying appropriate cuts. Systematic errors have a moderate influence on the Z' mass limits.

References

[1] A. Djouadi, A. Leike, T. Riemann, D. Schaile, C. Verzegnassi, Proc. of the "Workshop on Physics and Experiments with Linear Colliders", Sept. 1991, Saariselkä, Finland, ed. R. Orava, Vol. II, p. 515;
A. Djouadi, A. Leike, T. Riemann, D. Schaile, C. Verzegnassi, Z. Phys. **C56** (1992) 289.

[2] A. Leike, Z. Phys. **C62** (1994) 265.

[3] F.del Aguila, M. Cvetič, P. Langacker, Phys. Rev. **D48** (1993) R969;
F.del Aguila, M. Cvetič, Phys. Rev. **D50** (1994) 3158;
F.del Aguila, M. Cvetič, P. Langacker, Phys. Rev. **D52** (1995) 37

[4] A. Leike, S. Riemann, in preparation.

[5] P. Langacker, M. Luo, Phys. Rev. **D45** (1992) 278;
G. Altarelli, et al., Phys. Lett. **B318** (1993) 139.

[6] L3 collaboration, Phys. Lett. **B306** (1993) 187.

[7] A. Leike, S. Riemann, T. Riemann, Phys. Lett. **B291** (1992) 187.

[8] D. Bardin et al., ZFITTER Version 4.3 FORTRAN package;
D. Bardin et al., Preprint CERN-TH/6443/92;
D. Bardin et al., Z. Phys. **C44** (1989) 493;
D. Bardin et al., Nucl. Phys. **B351** (1991) 1;
D. Bardin et al., Phys. Lett. **B255** (1991) 290.

[9] J. Maalampi, M. Roos, Phys. Rep. **186** (1990) 53.

[10] For a review see e.g. J.L. Hewett, T.G. Rizzo, Phys. Rep. **183** (1989) 193.

[11] L.S. Durkin, P. Langacker, Phys. Lett. **B166** (1986) 436.

[12] For a review see e.g. R.N. Mohapatra, *Unifications and Supersymmetries*, Springer, New York 1989.

[13] D. Bardin et al., CERN-TH.6443/92, hep-ph/9412201.

[14] A. Leike, T. Riemann, M. Sachwitz, Phys. Lett. **B241** (1990) 267; A. Leike, T. Riemann, Z. Phys. **C51** (1991) 321.

Anomalous Z' effects in the WW channel at $LC2000$

P. Chiappetta[a], F.M. Renard[b] and C. Verzegnassi[c]

[a]Centre de Physique Théorique, UPR 7061,
CNRS Luminy, Case 907, F-13288 Marseille Cedex 9.

[b]Physique Mathématique et Théorique, CNRS-URA 768,
Université de Montpellier II, F-34095 Montpellier Cedex 5.

[c] Dipartimento di Fisica, Università di Lecce
CP193 Via Arnesano, I-73100 Lecce,
and INFN, Sezione di Lecce, Italy.

Abstract

We consider the virtual signals of a Z' of very general type in the process $e^+e^- \to W^+W^-$ at a future linear e^+e^- collider of 2000 GeV c.m. energy ($LC2000$). We show that possible deviations from the SM predictions in this channel are related to similar deviations in the purely leptonic one in a way that is only characteristic of this Z' model, and not in general of possible competitor models with anomalous gauge couplings.

1 Introduction

Virtual effects in the final two fermion channel at $LC2000$, due to a Z' whose mass is larger then a few TeV, have been examined in this working group report [1], in a quite general and model independent way. The aim of this short report is that of presenting a generalization of this analysis to a final WW state. As we shall show, the combination of the WW channel with the purely leptonic ones would evidentiate special correlations between the different effects that would be an intrinsic characteristics of any model with such a general Z'.

The virtual effects of a Z' in the process of e^+e^- annihilation into leptons or W pairs at c.m. squared energy $\equiv q^2 = 2TeV$ can be described, at tree level, by adding to the Standard Model γ, Z and ν exchanges the diagram with Z' exchange (the $Z - Z'$ mixing can safely be neglected). The overall effect in the relevant scattering amplitudes will be summarized by the following expressions:

$$A_{ll}^{(0)}(q^2) = A_{ll}^{(0)(\gamma,Z)}(q^2) + A_{ll}^{(0)(Z')}(q^2) \tag{1}$$

$$A_{lW}^{(0)}(q^2) = A_{lW}^{(0)(\gamma,Z,\nu)}(q^2) + A_{lW}^{(0)(Z')}(q^2) \tag{2}$$

where $l = e, \mu, \tau$ and we assume universal $Z'll$ couplings. In eq.(1) one should read:

$$A_{ll}^{(0)(\gamma)}(q^2) = \frac{s_0^2}{q^2}\bar{v}_l\gamma_\mu u_l\bar{u}_l\gamma^\mu v_l \tag{3}$$

$$A_{ll}^{(0)(Z)}(q^2) = \frac{i}{q^2 - M_{0Z}^2}(\frac{g_0^2}{4c_0^2})\bar{v}_l\gamma_\mu(g_{Vl}^{(0)} - \gamma_5 g_{Al}^{(0)})u_l\bar{u}_l\gamma^\mu(g_{Vl}^{(0)} - \gamma_5 g_{Al}^{(0)})v_l \tag{4}$$

$$A_{ll}^{(0)(Z')}(q^2) = \frac{i}{q^2 - M_{0Z'}^2}(\frac{g_0^2}{4c_0^2})\bar{v}_l\gamma_\mu(g_{Vl}^{\prime(0)} - \gamma_5 g_{Al}^{\prime(0)})u_l\bar{u}_l\gamma^\mu(g_{Vl}^{\prime(0)} - \gamma_5 g_{Al}^{\prime(0)})v_l \tag{5}$$

($e_0^2 = g_0^2 s_0^2$, $s_0^2 = 1 - c_0^2$). Note the choice of normalization in eq.(4): $g_{Al}^{(0)} = -\frac{1}{2}$ and $g_{Vl}^{(0)} = g_{Al}^{(0)} - 2Q_l s_0^2$.

Analogous expressions can be easily derived for eq.(2). We shall only give here the relevant Z' contribution, which reads:

$$A_W^{(0)(Z')}(q^2) = \frac{i}{q^2 - M_{0Z'}^2}(\frac{g_0}{2c_0})\bar{v}_l\gamma^\mu(g_{Vl}^{\prime(0)} - \gamma_5 g_{Al}^{\prime(0)})u_\nu c_0 g_{Z'WW}P_{\beta\alpha\mu}\epsilon_0^\beta(p_1)\epsilon_0^\alpha(p_2) \tag{6}$$

where

$$P_{\beta\alpha\mu} = g_{\mu\beta}(2p_2 - p_1)_\alpha + g_{\beta\alpha}(p_1 - p_2)_\mu - g_{\mu\alpha}(2p_1 + p_2)_\beta \tag{7}$$

and $p_{1,2}$ are the four-momenta of the outgoing W^-, W^+. In this expression we have assumed that the $Z'W^+W^-$ vertex has the usual Yang-Mills form. We do not consider the possibility of anomalous magnetic or quadrupole type of couplings. In fact in most of the popular

examples based on extended gauge models [2], even with a strong coupling regime [3], or in compositeness inspired schemes [4], only the Yang-Mills form appears or at least dominates over anomalous forms in the large $M_{Z'}/M_Z$ limit (there are however exceptions, see for example [5]). An analysis with anomalous ZWW and $Z'WW$ coupling forms is possible along the lines of ref.[6] but is beyond the scope of this paper. Our analysis will be nevertheless rather general as the trilinear $Z'WW$ coupling $g_{Z'WW}$ will be treated as a free parameter, not necessarily proportional to the $Z - Z'$ mixing angle as for example it would happen in a "conventional" E_6 picture.

For the purposes of this paper, it will be particularly convenient to describe the virtual Z' effect as an "effective" modification of the Z and γ couplings to fermions and W pairs. As one can easily derive, this corresponds to the use of the following "modified" leptonic γ, Z couplings (denoted in the following with a star) to describe the $e^+e^- \to l^+l^-$ process:

$$e_0^* = e_0[1 - \frac{q^2}{M_{Z'}^2 - q^2}(\frac{g_{Vl}^{(0)2}}{4s_0^2c_0^2})(\xi_{Vl} - \xi_{Al})^2]^{1/2} \tag{8}$$

$$g_{Al}^{*(0)} = g_{Al}^{(0)}[1 - \frac{q^2 - M_Z^2}{M_{Z'}^2 - q^2}\xi_{Al}^2]^{1/2} \tag{9}$$

$$g_{Vl}^{*(0)} = g_{Vl}^{(0)}[1 - \frac{q^2 - M_Z^2}{M_{Z'}^2 - q^2}\xi_{Al}(\xi_{Vl} - \xi_{Al})].[1 - \frac{q^2 - M_Z^2}{M_{Z'}^2 - q^2}\xi_{Al}^2]^{1/2} \tag{10}$$

and to the use of the following modified trilinear couplings that fully describe the effect in the final $e^-e^- \to WW$ process (without modifying the initial γ, Z leptonic couplings):

$$g_{\gamma WW}^{*(0)} = g_{\gamma WW}^{(0)} - g_{Z'WW}^{(0)}\frac{q^2}{M_{Z'}^2 - q^2}g_{Vl}^{(0)}(\xi_{Vl} - \xi_{Al}) \tag{11}$$

$$g_{ZWW}^{*(0)} = g_{ZWW}^{(0)} - g_{Z'WW}^{(0)}\frac{q^2 - M_Z^2}{M_{Z'}^2 - q^2}\xi_{Al} \tag{12}$$

In the previous equations, the following definitions have been used:

$$\xi_{Vl} = g_{Vl}^{*(0)}/g_{Vl}^{(0)} \tag{13}$$

$$\xi_{Al} = g_{Al}^{*(0)}/g_{Al}^{(0)} \tag{14}$$

Our normalization is such that:

$$g_{\gamma WW}^{(0)} = 1 \tag{15}$$

$$g_{ZWW}^{(0)} = c_0/s_0 \tag{16}$$

Note that, strictly speaking, only bare quantities should appear in the previous equations. In practice, however, we shall treat the Z' effect on the various observables at one loop in the (γ, Z) Standard Model sector, and in an "effective" tree level for what concerns the Z'

parameters. As a result of this (standard) approach, whose validity is obviously related to the (implicit) assumption that $M_{Z'}^2$ is "large" at the energy scale of the experiment, only the physical γ, Z parameters, the "physical" Z' mass and the "physical" Z' couplings will remain in the various theoretical expressions. Note that the definition of "physical" Z' couplings is plagued with an intrinsic ambiguity that would only be solved once this particle were discovered and its decays measured. This will not represent a problem in our approach, as we shall see, since our philosophy will rather be that of calculating functional relationships between different (experimentally measurable) Z' shifts. In this spirit, we shall use from now on only notations without "bare" indices on the various parameters.

The basic idea of our approach is provided by the observation that the modified trilinear gauge couplings eqs.(11),(12) contain the same combinations of modified fermionic γ, Z couplings eqs.(8-10) that would appear in the leptonic final state, with only one extra free parameter i.e. the $Z'WW$ coupling $g_{Z'WW}$. This implies that it must be possible to find a precise relationship between the two modified trilinear gauge couplings eqs.(11),(12) and some set of leptonic observables by simply eliminating the free parameter $g_{Z'WW}$ in these expressions. To fully understand what type of relationships will emerge, it is oportune to write down at this point the expression of the Z' effects in the two leptonic observables that will certainly be measured to a very good accuracy at $LC2000$, i.e. the muon ($\equiv$ lepton) cross section $\sigma_\mu(q^2)$ and the muon forward-backward asymmetry $A_{FB,\mu}(q^2)$. To calculate these expressions is straightforward and the rigorous derivation has been already performed in previous papers, to which we refer for a detailed discusssion [7]. Here we shall only show for sake of self-completeness an approximate procedure where only the numerically relevant terms are retained. For this aim it will be sufficient to start from the following expressions of σ_μ, $A_{FB,\mu}$ at Born level without the Z' contribution:

$$\sigma_\mu^{(0)}(q^2) = \frac{q^2}{12\pi}[(\frac{e_0^2}{q^2})^2 + \frac{1}{(q^2 - M_{0Z}^2)^2}(\frac{g_0^2}{4c_0^2})^2(g_{Vl}^{(0)2} + g_{Al}^{(0)2})^2] \tag{17}$$

(we have omitted the $\gamma - Z$ interference that is numerically negligible [7]).

$$A_{FB,\mu}^{(0)}(q^2) = \frac{\pi q^2}{\sigma_\mu(q^2)}[\frac{1}{(q^2 - M_{0Z}^2)^2}(\frac{1}{4\pi^2})(\frac{g_0^2}{4c_0^2})^2 g_{Vl}^{(0)2} g_{Al}^{(0)2} + \frac{1}{q^2(q^2 - M_{0Z}^2)}(\frac{1}{8\pi^2})(\frac{g_0^2}{4c_0^2})e_0^2 g_{Al}^{(0)2}] \tag{18}$$

The prescription for deriving the Z' effect is now the following. One replaces the quantities e_0, $g_{Al}^{(0)}$, $g_{Vl}^{(0)}$ that appear in eqs.(17),(18) by the starred ones given in eqs.(8)-(10). All the remaining bare (γ, Z) parameters will then be replaced by the known Standard Model expressions valid at one loop, that will contain certain "physical" quantities and certain one-loop "corrections". For the purposes of this paper, where only the (small) Z' effects are considered, the latter corrections can be ignored and one can write the relevant shifts in terms of Z' parameters and of γ, Z "physical" quantities (more precisely, as one can guess, $\alpha(0)$ and $s_{Eff}^2(M_Z^2)$), and for a more detailed discussion we refer to ref. [7].

Defining the relative Z' shifts as :

$$\frac{\delta\sigma_{\mu}^{(Z')}}{\sigma_{\mu}} = \frac{\sigma_{\mu}^{(\gamma,Z,Z')} - \sigma_{\mu}^{(\gamma,Z)}}{\sigma_{\mu}^{(\gamma,Z)}} \tag{19}$$

(and an analogous definition for the asymmetry), it is now relatively simple to derive the expressions:

$$\frac{\delta\sigma_{\mu}}{\sigma_{\mu}} = \frac{2}{\kappa^2(q^2 - M_Z^2)^2 + q^4}[\kappa^2(q^2 - M_Z^2)^2\hat{\Delta}^{(Z')}\alpha(q^2) - q^4(R^{(Z')}(q^2) + \frac{1}{2}V^{(Z')}(q^2))] \tag{20}$$

$$\frac{\delta A_{FB,\mu}}{A_{FB,\mu}} = \frac{q^4 - \kappa^2(q^2 - M_Z^2)^2}{\kappa^2(q^2 - M_Z^2)^2 + q^4}[\hat{\Delta}^{(Z')}\alpha(q^2) - R^{(Z')}(q^2)] + \frac{q^4}{\kappa^2(q^2 - M_Z^2)^2 - q^4}V^{(Z')}(q^2)] \tag{21}$$

with (using the same notations as in ref.[7]):

$$\hat{\Delta}^{(Z')}\alpha(q^2) = \frac{q^2}{q^2 - M_{Z'}^2}(\frac{v_1^2}{16s_1^2c_1^2})(\xi_{V1} - \xi_{A1})^2 \tag{22}$$

$$R^{(Z')}(q^2) = (\frac{q^2 - M_Z^2}{M_{Z'}^2 - q^2})\xi_{A1}^2 \tag{23}$$

$$V^{(Z')}(q^2) = (\frac{q^2 - M_Z^2}{M_{Z'}^2 - q^2})(\frac{v_1}{4s_1c_1})\xi_{A1}(\xi_{V1} - \xi_{A1}) \tag{24}$$

where

$$\kappa = \frac{\alpha M_Z}{3\Gamma_l} \tag{25}$$

and $v_l = -2g_{Vl} = 1 - 4s_l^2$; $s_1^2c_1^2 = \frac{\pi\alpha}{\sqrt{2}G_\mu M_Z^2}$.

As one sees from the previous equations, the Z' effects can be expressed by certain quadratic expressions of the parameters ξ_{Al}, $(\xi_{Vl} - \xi_{Al})$. A much simpler dependence is exhibited by the modified trilinear couplings, as one sees from eqs.(11),(12). Adopting the notations that are found in recent literature [8], [6], we find for the Z' effect in this case

$$\delta_z^{(Z')} \equiv g_{ZWW}^z - 1 = g_{Z'WW}(\frac{q^2}{M_{Z'}^2 - q^2})g_{Vl}(\xi_{Vl} - \xi_{Al}) \tag{26}$$

$$\delta_x^{(Z')} \equiv g_{ZWW}^z - cot\theta_W = -g_{Z'WW}(\frac{q^2 - M_Z^2}{M_{Z'}^2 - q^2})\xi_{Al} \tag{27}$$

From eqs. (26), (27) one can derive the following constraint:

$$\delta_z^{(Z')} = tg\theta_A\delta_x^{(Z')} \tag{28}$$

where

$$tg\theta_A = \frac{-q^2}{q^2 - M_Z^2}(\frac{\xi_{Vl} - \xi_{Al}}{\xi_{Al}})g_{Vl} \tag{29}$$

A few comments are appropriate at this point. In this description both $g_{\gamma WW}$ and g_{ZWW} couplings are modified by form factor effects whose scale is $M_{Z'}$. They identically vanish for $q^2 = 0$ and $q^2 = M_Z^2$ respectively. The vanishing of δ_γ at $q^2 = 0$ is absolutely required by conservation of electric charge. We then notice that the virtual effect of a general Z' in the WW channel is, at first sight, quite similar to that of a possible model with anomalous gauge couplings, that would also produce shifts δ_γ, δ_Z both in the γWW and in the ZWW couplings (in the conventional description of anomalous gauge boson couplings the appearence of both δ_γ and δ_Z is rather unusual[6], but can be obtained using effective lagrangians with $dim = 6$ and $dim = 8$ operators [8]). For this reason, we have called such effects "anomalous" Z' effects. But the Z' shifts satisfy in fact the constraint given by eq.(28), that corresponds to a certain line in the $(\delta_\gamma, \delta_Z)$ plane whose angular coefficient is fixed by the model i.e. by the values of ξ_A, $(\xi_V - \xi_A)$. For example:

$$tg\theta_A = \frac{-q^2}{q^2 - M_Z^2}[\frac{v_l}{2} + \frac{cos\beta}{\sqrt{\frac{2}{3}}sin\beta - cos\beta}] \tag{30}$$

in E_6 models $(-1 < cos\beta < +1)$,

$$tg\theta_A = \frac{-q^2}{q^2 - M_Z^2}[\frac{v_l}{2} - \frac{2}{\alpha_{RL}}(\frac{1}{2\alpha_{RL}} - \frac{\alpha_{RL}}{4})] \tag{31}$$

in Right-Left symmetric models $(\sqrt{\frac{2}{3}} < \alpha_{RL} < \sqrt{2})$,

$$tg\theta_A = \frac{-q^2}{q^2 - M_Z^2}cot\theta_W \tag{32}$$

in Y models,

$$tg\theta_A = \frac{q^2}{q^2 - M_Z^2}cot\theta_W(\frac{s_l^2 - \lambda_Y^2}{1 - s_l^2 - \lambda_Y^2}) \tag{33}$$

in Y_L models $(0 < \lambda_Y^2 < 1 - s_l^2)$.

The values of ξ_A, $(\xi_V - \xi_A)$ are, in turn, directly responsible for deviations in the leptonic channel that would affect σ_μ and $A_{FB,\mu}$. This means that a precise functional relationship will exist between the value of $tg\theta_A$ defined by eq.(29) and those of the shifts $\delta\sigma_\mu$, $\delta A_{FB,\mu}$ defined by eqs.(20),(21) that would correspond to a certain surface in the 3-dim $(tg\theta_A, \delta^{(Z')}\sigma_\mu/\sigma_\mu, \delta^{(Z')}A_{FB,\mu}/A_{FB,\mu})$ space. To draw this surface requires a dedicated numerical analysis that carefully takes into account the QED initial radiation and the precise experimental set up, which is beyond the purposes of this short paper. Here we shall only illustrate, with a couple of particularly simple examples, what would be typical signatures of this type of Z' effects.

We begin with the case [9] of a Z' whose couplings to the fermions are "essentially" the same as those of the Standard Model Z (this is usually called the "standard Z' model"), leaving the $Z'WW$ coupling free. In this case $\delta_V^{(Z')} = 0$ and $\delta_Z^{(Z')}$ is given by eq.(27) with ξ_{Ai} of order one. Eqs.(20),(21) become now at 2000 GeV:

$$\frac{\delta\sigma_\mu^{(Z')}}{\sigma_\mu}(\xi_{Vi} = \xi_{Ai}) \simeq -0.25\frac{q^2 - M_Z^2}{M_{Z'}^2 - q^2}\xi_{Ai}^2 \tag{34}$$

$$\frac{\delta^{(Z')}A_{FB,\mu}}{A_{FB,\mu}}(\xi_{Vi} = \xi_{Ai}) \simeq -0.84\frac{q^2 - M_Z^2}{M_{Z'}^2 - q^2}\xi_{Ai}^2 \tag{35}$$

showing that, for this situation, the asymmetry is more sensitive to the effect. In terms of the asymmetry we have now:

$$\delta_Z^{(Z')}(\xi_{Vi} = \xi_{Ai}) \simeq (\frac{g_{Z'WW}}{0.84\xi_{Ai}})\frac{\delta^{(Z')}A_{FB,\mu}}{A_{FB,\mu}} = -g_{Z'WW}\frac{q^2 - M_Z^2}{M_{Z'}^2 - q^2}\xi_{Ai} \tag{36}$$

We shall now introduce the following ansatz concerning the theoretical expressions of $g_{Z'WW}$, that we shall write as:

$$g_{Z'WW} = [c\frac{M_Z^2}{M_{Z'}^2}]cot g\theta_W \tag{37}$$

The constant c would be of order one for the "conventional" models [2] where the Z' couples to W only via the $Z - Z'$ mixing (essentially contained in the bracket). But for a general model, c could be larger, as one can see for some special cases of composite models, for example with excited Z^* states [5] or when the Z' participates in a strong coupling regime [3].

In fact, a stringent bound on c comes from the request that the Z' width into WW is "small" compared to the Z' mass. Imposing the (reasonable) limit

$$\Gamma_{Z'WW} \lesssim \frac{1}{10}M_{Z'} \tag{38}$$

leads to the condition

$$c \lesssim 10 \tag{39}$$

and this will be our very general working assumption.

Using eq.(37) we can rewrite the Z' effect as

$$\delta_Z^{(Z')}(\xi_{Vi} = \xi_{Ai}) = -\xi_{Ai}\frac{q^2 - M_Z^2}{M_{Z'}^2 - q^2}c[\frac{M_Z^2}{M_Z^2}]cot\theta_W \tag{40}$$

For $\xi_{Ai} \simeq 1$, at the $LC2000$ energy with a luminosity of $320 fb^{-1}$, the detectability request [6], $|\delta_Z| \gtrsim 2 \times 10^{-3}$ corresponds to the condition:

$$c \gtrsim 2.4 \times 10^{-6}[\frac{M_Z^2}{M_Z^2}\frac{M_{Z'}^2 - (2TeV)^2}{M_Z^2}] \tag{41}$$

which obeys the constraint eq.(39) for all values of $M_{Z'}$ such that

$$M_{Z'} \lesssim 4.4TeV \tag{42}$$

and, for the limiting value $M_{Z'} = 4.4TeV$, a relative shift of approximately twenty percent in the asymmetry $A_{FB,\mu}$ would be produced, that would not be missed. A relative effect of about 6.5 percent should also appear in the muonic cross section.

As a second example, we consider the orthogonal case $\xi_{Ai} = 0$ for "large" values of ξ_{Vi} (say, $\xi_{Vi} \simeq 10$). Such an order of magnitude corresponds to several "conventional" models. For example in E_6

$$\xi_{Vi} = -\frac{4s_1 cos\beta}{v_1\sqrt{6}} \tag{43}$$

reaches $\xi_{Vi} \simeq 5$ for the χ model ($cos\beta = 1$),
and for a Y model

$$\xi_{Vi} = \frac{3s_1 c_1}{v_1\lambda_Y}(1 - \frac{\lambda_Y^2}{1 - s_1^2})^{1/2} \tag{44}$$

reaches $\xi_{Vi} \simeq 13$ for $\lambda_Y^2 = s_1^2$. In this situation, $\delta_Z^{(Z')} = 0$, and

$$\frac{\delta\sigma_\mu^{(Z')}}{\sigma_\mu}(\xi_{Ai} = 0) \simeq -1.5 \times 10^{-2}\frac{q^2}{M_{Z'}^2 - q^2}\xi_{Vi}^2 \tag{45}$$

$$\frac{\delta^{(Z')}A_{FB,\mu}}{A_{FB,\mu}} \simeq 7.3 \times 10^{-3}\frac{q^2}{M_{Z'}^2 - q^2}\xi_{Vi}^2 \tag{46}$$

and one sees that now the sensible quantity is σ_μ. For $M_{Z'} = 4.4TeV$ the relative shift is

$$\frac{\delta\sigma_\mu^{(Z')}}{\sigma_\mu} \simeq -4 \times 10^{-3}\xi_{Vi}^2 \tag{47}$$

For the trilinear shift $\delta_\zeta^{(Z')}$ we have:

$$\delta_\zeta^{(Z')}(\xi_{Ai} = 0) \simeq g_{Vi}\xi_{Vi}\frac{q^2}{M_{Z'}^2 - q^2}c[\frac{M_Z^2}{M_Z^2}]cot\theta_W \tag{48}$$

In correspondence to the limiting value $c = 10$ and for $M_{Z'} = 4.4TeV$, we get

$$\delta_\zeta^{(Z')}(\xi_{Ai} = 0) \simeq -1.5 \times 10^{-4}\xi_{Vi} \tag{49}$$

For $\xi_{Vi} = O(10)$ one obtains a value $\delta_\zeta^{(Z')} = O(10^{-3})$ i.e. the same size as $\delta_Z^{(Z')}$ in the first example (the relative shift in σ_μ would now be of approximately forty percent).

In conclusion, we can summarize the main points of our (preliminary) analysis as follows. A Z' belonging to a quite general model, with "reasonable" couplings to W (and to fermions), would produce effects in the WW and in the leptonic channel that would be related in a quite special way and, at least in some simple cases, visible in both channels at a 2000 GeV e^+e^- collider. If, at the time of a possible LC2000 run, models with anomalous gauge couplings will not be ruled out, this fact would certainly be a powerful

tool for discrimination. In fact, in the anomalous gauge coupling case, the parameters that affect the WW channel are totally independent of those that affect the leptonic one so that no kind of relationships will in general exist. If, on the contrary, anomalous gauge couplings were out of interest, the constraints that we derived would certainly help to achieve a proper Z' identification, in case this particle were actually produced e.g. at the CERN LHC.

Acknowledgements

This work has been partially supported by the EC contract CHRX-CT94-0579.

References

[1] A. Leike and S. Riemann, contribution to this working group; G. Montagna et al, contribution to this working group.

[2] F. Del Aguila, M. Quiros and F. Zwirner, Nucl. Phys. **B287** (1987) 419.

[3] J.L. Kneur and D. Schildknecht, Nucl. Phys. **B357** (357) 1991;

J.L. Kneur, M. Kuroda and D. Schildknecht, Phys. Lett. **B262** (93) 1991 ;

M. Bilenky *et.al.* , Phys. Lett. **B316** (1993) 345 ;

R. Casalbuoni, S. de Curtis, D. Dominici and R. Gatto, Phys. Lett. **B155** (1985) 95 ; Nucl. Phys. **B282** (1987) 235.

[4] M.Kuroda, D.Schildknecht and K.H.Schwarzer, Nucl. Phys. **B261** (432) 1985.

[5] U.Baur, D.Schildknecht and K.H.Schwarzer, Phys. Rev. **D37** (297) 1987.

[6] M. Bilenky, J.L. Kneur, F.M. Renard and D. Schildknecht, Nucl. Phys. **B409** (1993) 22 and **B419** (1994) 240.

[7] F.M. Renard and C. Verzegnassi, preprint PM/95-35 (1995).

[8] G.J. Gounaris and F.M. Renard, Z. Phys. **C59** (1993) 133.

[9] G. Altarelli, B. Mele and M. Ruiz Altaba, Z. Phys. **C45** (1989) 109; erratum Z. Phys. **C47** (1990) 676.

A STRONG ELECTROWEAK SECTOR AT FUTURE LINEAR COLLIDERS *)

R. Casalbuoni [a,b], S. De Curtis [b], D. Dominici [a,b],
A. Deandrea [c], R. Gatto [c] and M. Grazzini [d,e]

a) Dipartimento di Fisica, Univ. di Firenze, I-50125 Firenze, Italy.
b) I.N.F.N., Sezione di Firenze, I-50125 Firenze, Italy.
c) Dépt. de Phys. Théor., Univ. de Genève, CH-1211 Genève 4.
d) Dipartimento di Fisica, Univ. di Parma, I-43100 Parma, Italy.
e) I.N.F.N., Gruppo Collegato Parma, I-43100 Parma, Italy.

*) Partially supported by the Swiss National Foundation. This work is part of the EEC project "Tests of electroweak symmetry breaking and future european colliders", CHRXCT94/0579 (OFES 95.0200).

ABSTRACT

An effective lagrangian describing a strong interacting electroweak sector is considered. It contains new vector and axial-vector resonances all degenerate in mass and mixed with W and Z. The model, for large mass of these degenerate gauge bosons, becomes identical to the standard model in the classical limit of infinite Higgs mass. The limits on the parameter space of this model from future e^+e^- colliders are presented.

1 The Model

In view of future projects of e^+e^- linear colliders it is important to study the possible phenomenology at such colliders from a strong electroweak sector [1]. We shall study the effects of the strong electroweak sector at future linear colliders, assuming a low energy effective theory. The effective lagrangian contains vector and axial-vector resonances as the most visible manifestations at low energy of the strong interacting sector [2]. This model is an extension of the BESS model where only new vector resonances are present [3]. It leads to an interesting and appealing phenomenology.

Let us call G the symmetry group of the theory, spontaneously broken. Among the Goldstone bosons, three are absorbed to give mass to W and Z. The vector and axial-vector mesons will transform under the unbroken subgroup H of G. Following the *hidden gauge symmetry* approach [4][5], theories with non linearly realized symmetry $G \to H$ can be linearly realized by enlarging the gauge symmetry G to $G \otimes H' \to H_D = diag(H \otimes H')$. H' is a local gauge group and the vector and axial-vector are the gauge fields associated to H'.

Let us consider such an effective lagrangian parameterization for the electroweak symmetry breaking, using $G = SU(2)_L \otimes SU(2)_R$, $H' = SU(2)_L \otimes SU(2)_R$. The nine Goldstone bosons resulting from the spontaneous breaking of $G' = G \otimes H'$ to H_D, can be described by three independent $SU(2)$ elements: L, R and M, with the following transformations properties

$$L' = g_L L h_L^\dagger, \quad R' = g_R R h_R^\dagger, \quad M' = h_R^\dagger M h_L \tag{1.1}$$

with $g_{L,R} \in SU(2)_{L,R} \subset G$ and $h_{L,R} \in H'$. Moreover we shall require the invariance under the discrete left-right transformation P: $L \leftrightarrow R$, $M \to M^\dagger$ which combined with the usual space inversion allows to build the parity transformation on the fields. If we ignore the transformations of eq. (1.1), the largest possible global symmetry of the low-energy theory is given by the requirement of maintaining for the transformed variables L', R' and M' the character of $SU(2)$ elements, or $G_{max} = [SU(2) \otimes SU(2)]^3$, consisting of three independent $SU(2) \otimes SU(2)$ factors, acting on each of the three variables separately. As we shall see, it happens that, for specific choices of the parameters of the theory, the symmetry G' gets enlarged to G_{max} [6].

The most general $G' \otimes P$ invariant lagrangian is given by [7]

$$L_G = -\frac{v^2}{4}[a_1 I_1 + a_2 I_2 + a_3 I_3 + a_4 I_4] \tag{1.2}$$

plus the kinetic terms L_{kin}. The four invariant terms I_i ($i = 1,\dots,4$) are given by:

$$I_1 = tr[(V_0 - V_1 - V_2)^2] \quad I_2 = tr[(V_0 + V_2)^2] \quad I_3 = tr[(V_0 - V_2)^2] \quad I_4 = tr[V_1^2] \tag{1.3}$$

where

$$V_0^\mu = L^\dagger D^\mu L \quad V_1^\mu = M^\dagger D^\mu M \quad V_2^\mu = M^\dagger (R^\dagger D^\mu R) M \tag{1.4}$$

and the covariant derivatives are

$$D_\mu L = \partial_\mu L - L\mathbf{L}_\mu \quad D_\mu R = \partial_\mu R - R\mathbf{R}_\mu \tag{1.5}$$

$$D_\mu M = \partial_\mu M - M\mathbf{L}_\mu + \mathbf{R}_\mu M \tag{1.6}$$

where $\mathbf{L}_\mu(\mathbf{R}_\mu)$ are gauge fields of $SU(2)_{L(R)} \subset H'$ (instead of working with vector and axial-vector we work with these left and right combinations).

The kinetic terms are given by

$$L_{kin} = \frac{1}{g''^2} tr[F_{\mu\nu}(\mathbf{L})]^2 + \frac{1}{g''^2} tr[F_{\mu\nu}(\mathbf{R})]^2 \tag{1.7}$$

where g'' is the gauge coupling constant for the gauge fields $\mathbf{L}_\mu$ and $\mathbf{R}_\mu$, and $F_{\mu\nu}(\mathbf{L})$, $F_{\mu\nu}(\mathbf{R})$ are the usual field tensors.

The model we will consider is characterized by the following choice of parameters $a_4 = 0$, $a_2 = a_3$ [2, 6]. In order to discuss the symmetry properties that make such a choice natural it is useful to observe that the invariant I_1 could be re-written as $I_1 = -tr(\partial_\mu U^\dagger \partial^\mu U)$ with $U = LM^\dagger R^\dagger$ and the lagrangian as

$$L_G = \frac{v^2}{4}\{a_1\, tr(\partial_\mu U^\dagger \partial^\mu U) + 2\, a_2\, [tr(D_\mu L^\dagger D^\mu L) + tr(D_\mu R^\dagger D^\mu R)]\} \tag{1.8}$$

Each of the three terms in the above expression is invariant under an independent $SU(2)\otimes SU(2)$ group

$$U' = g_L U g_R^\dagger, \quad L' = g_L L h_L^\dagger, \quad R' = g_R R h_R^\dagger \tag{1.9}$$

The overall symmetry is $G_{inv} = [SU(2)\otimes SU(2)]^2$, with a part H' realized as a gauge symmetry. With the particular choice $a_4 = 0$, $a_5 = a_2$, as we see from eq. (1.8), the mixing between $\mathbf{L}_\mu$ and $\mathbf{R}_\mu$ is vanishing, and the new states are degenerate in mass. Moreover, as it follows from eq. (1.8), the longitudinal modes of the fields are entirely provided by the would-be Goldstone bosons in L and R. This means that the pseudoscalar particles remaining as physical states in the low-energy spectrum are those associated to U. They in turn can provide the longitudinal components to the W and Z particles, in an effective description of the electroweak breaking sector.

The peculiar feature of the model is that the new bosons are not coupled to those Goldstone bosons which are absorbed to give mass to W and Z. As a consequence the channels $W_L Z_L$ and $W_L W_L$ are not strongly enhanced as it usually happens in models with a strongly interacting symmetry breaking sector [3]. This also implies larger branching ratios of the new resonances into fermion pairs.

The coupling of the model to the electroweak $SU(2)_W \otimes U(1)_Y$ gauge fields is obtained via the minimal substitution

$$D_\mu L \to D_\mu L + \mathbf{W}_\mu L \quad D_\mu R \to D_\mu R + \mathbf{Y}_\mu R \quad D_\mu M \to D_\mu M \tag{1.10}$$

where

$$\begin{aligned} \mathbf{W}_\mu &= ig\tilde{W}^a_\mu \frac{\tau^a}{2} \quad \mathbf{Y}_\mu = ig'\tilde{Y}_\mu \frac{\tau^3}{2} \\ \mathbf{L}_\mu &= i\frac{g''}{\sqrt{2}}\tilde{L}^a_\mu \frac{\tau^a}{2} \quad \mathbf{R}_\mu = i\frac{g''}{\sqrt{2}}\tilde{R}^a_\mu \frac{\tau^a}{2} \end{aligned} \tag{1.11}$$

with g, g' the $SU(2)_W \otimes U(1)_Y$ gauge coupling constant and τ^a the Pauli matrices. We have used tilded quantities to reserve untilded variables for mass eigenstates.

By introducing the canonical kinetic terms for $\tilde{W}^a_\mu$ and $\tilde{Y}_\mu$ and going into the unitary gauge we get

$$\begin{aligned} \mathcal{L} &= -\frac{v^2}{4}\left[a_1 tr(\tilde{W}_\mu - \tilde{Y}_\mu)^2 + 2a_2 tr(\tilde{W}_\mu - \tilde{L}_\mu)^2 - 2a_2 tr(\tilde{Y}_\mu - \tilde{R}_\mu)^2\right] \\ &+ \mathcal{L}^{kin}(\tilde{W}, \tilde{Y}, \tilde{L}, \tilde{R}) \end{aligned} \tag{1.12}$$

The standard model (SM) relations are obtained in the limit $g'' \gg g, g'$. Actually, for very large g'', the kinetic terms for the fields $\tilde{L}_\mu$ and $\tilde{R}_\mu$ drop out, and $\mathcal{L}$ reduces to the first term in eq. (1.12). This term reproduces precisely the mass term for the ordinary gauge vector bosons in the SM, provided we assume $a_1 = 1$. Finally let us consider the couplings to the fermions:

$$\begin{aligned} \mathcal{L}_{fermion} &= \bar{\psi}_L i\gamma^\mu \left(\partial_\mu - ig\tilde{W}^a_\mu \frac{\tau^a}{2} + \frac{i}{2}g'(B-L)\tilde{Y}_\mu\right)\psi_L \\ &+ \bar{\psi}_R i\gamma^\mu \left(\partial_\mu - ig'\tilde{Y}_\mu \frac{\tau^3}{2} - \frac{i}{2}g'(B-L)\tilde{Y}_\mu\right)\psi_R \end{aligned} \tag{1.13}$$

where $B\,(L)$ is the baryon (lepton) number, and $\psi = (\psi_u, \psi_d)$. We have not introduced direct couplings to $\tilde{L}$ and $\tilde{R}$, so the new gauge bosons will couple to fermions only via mixing.

By separating the charged and the neutral gauge bosons, the quadratic lagrangian is given by:

$$\begin{aligned} \mathcal{L}^{(2)} &= \frac{v^2}{4}[(1+2a_2)g^2\tilde{W}^+_\mu\tilde{W}^{\mu-} + a_2 g''^2(\tilde{L}^+_\mu\tilde{L}^{\mu-} + \tilde{R}^+_\mu\tilde{R}^{\mu-}) \\ &- \sqrt{2}a_2 g g''(\tilde{W}^+_\mu\tilde{L}^{\mu-} + \tilde{W}^+_\mu\tilde{L}^{\mu-})] \\ &- \frac{v^2}{8}[(1+2a_2)(g^2\tilde{W}^2_3 + g'^2\tilde{Y}^2) + a_2 g''^2(\tilde{L}^2_3 + \tilde{R}^2_3) \\ &- 2gg'\tilde{W}_{3\mu}\tilde{Y}^\mu - 2\sqrt{2}a_2 g''(g\tilde{W}_3\tilde{L}^3 - g'\tilde{Y}_\mu\tilde{R}^3_3)] \end{aligned} \tag{1.14}$$

Therefore the R^3 fields are unmixed and their mass can be easily read: $M_{R^3} \equiv M = vg''\sqrt{a_2}/2$. All the other heavy fields have degenerate mass M in the large g'' limit (for this reason we call this model Degenerate BESS), and W and Z masses get corrections of order $(g/g'')^2$ [2]. We will parameterize the model by using, in addition to the SM parameters, M and g/g''.

By using eq. (1.14) one can show that, at the leading order in q^2/M^2, the contribution of the model to all ϵ parameters [8] is equal to zero [2]. This is due to the fact that in the $M \to \infty$ limit, this model decouples. We can perform the low-energy limit at the next-to-leading order and study the virtual effects of the heavy particles. Working at the first order in $1/g''^2$ we get $\epsilon_1 = -(c_\theta^4 + s_\theta^4)/(c_\theta^2)\, X$, $\epsilon_2 = -c_\theta^2 X$, $\epsilon_3 = -X$ with $X = 2(M_W^2/M^2)(g/g'')^2$. All these deviations are of order X which contains a double suppression factor M_W^2/M^2 and $(g/g'')^2$. The sum of the SM contributions, functions of the top and Higgs masses, and of these deviations has to be compared with the experimental values for the ϵ parameters, determined from the all available LEP data and the M_W measurement at Tevatron [9]: $\epsilon_1 = (3.8 \pm 1.5)\cdot 10^{-3}$, $\epsilon_2 = (-6.4 \pm 4.2)\cdot 10^{-3}$, $\epsilon_3 = (4.6 \pm 1.5)\cdot 10^{-3}$. Taking into account the SM values $(\epsilon_1)_{SM} = 4.4\cdot 10^{-3}$, $(\epsilon_2)_{SM} = -7.1\cdot 10^{-3}$, $(\epsilon_3)_{SM} = 6.5\cdot 10^{-3}$ for $m_{top} = 180$ GeV and $m_H = 1000$ GeV, we find, from the combinations of the previous experimental results, the 90% C.L. limit on g/g'' versus the mass M given in Fig. 1. The allowed region is the one below the solid line.

2 e^+e^- future colliders

In this section we will discuss the sensitivity of the model at LEP2 and future e^+e^- linear colliders, for different options of total centre of mass energies and luminosities.

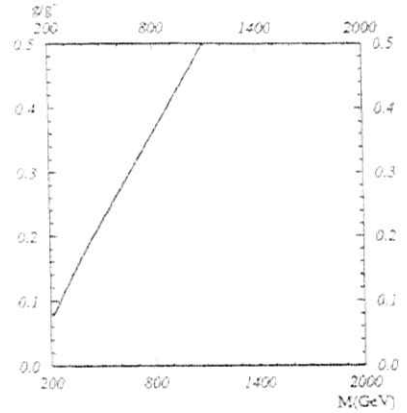

Fig. 1 - *90% C.L. contour on the plane $(M,\ g/g')$ obtained by comparing the values of the ϵ parameters from the model to the experimental data from LEP. The allowed region is below the curve.*

Cross-sections and asymmetries for the channel $e^-e^- \to f^-f^-$ and $e^-e^- \to W^-W^-$ in the SM and in the degenerate BESS model at tree level have been studied [2]. The BESS states relevant for the analysis at e^-e^- colliders are L_3 and R_3. Their coupling to fermions can be found in [2]. We will not consider the direct production of R_3 and L_3 from e^-e^-, but rather their indirect effects in the $e^-e^- \to f^-f^-$ and $e^-e^- \to W^-W^-$ cross-sections. In the fermion channel the study is based on the following observables: the total hadronic ($\mu^-\mu^-$) cross-sections σ^h ($\sigma^{\mu\mu}$), the forward-backward and left-right asymmetries $A^{e^-e^-\to u^+u^-}_{FB}$, $A^{e^-e^-\to b\bar{b}}_{FB}$, $A^{e^-e^-\to e^+e^-}_{LR}$, $A^{e^-e^-\to h}_{LR}$ and $A^{e^-e^-\to \mu\mu}_{LR}$. At LEP2 we can add to the previous observables the W mass measurement. The result of this analysis shows that LEP2 will not improve considerably the existing limits [10].

In Fig. 2 we present the 90% C.L. contour on the plane $(M,\ g/g')$ from e^-e^- at $\sqrt{s} = 1000\ GeV$ with an integrated luminosity of $80 fb^{-1}$ for various observables. The dashed-dotted line represents the limit from σ^h with an assumed relative error of 2%; the dashed line near to the preceeding one is σ^μ (relative error 1.3%), the dotted line is A^u_{FB} (error 0.5%) and the uppermost dashed line is A^b_{FB} (error 0.9%).

As it is evident more stringent bounds come from the cross-section measurements. Asymmetries give less restrictive bounds due to a compensation between the L_3 and R_3 exchange. By combining all the deviations in the previously considered observables we get the limit shown by the continuous line.

Polarized electron beams allow to get further limit in the parameter space as shown in Fig. 3. We neglect the error on the measurement of the polarization and use a polarization value equal to 0.5. The dashed-dotted line represents the limit from A^u_{LR} (error 0.6%), the dashed line from A^b_{LR} (error 0.4%), the dotted line from A^h_{LR} (error

SUPERSYMMETRY

Conveners:

R. Barbieri [1], *A. Bartl* [2], *J.-F. Grivaz* [3], *S. Katsanevas* [4], *A. Masiero* [5]

Working Group:

W. de Boer [6], *G. Burkart* [6], *A. Culatti* [7], *G. Degrassi* [7], *H. Dreiner* [8], *H. Eberl* [9], *R. Ehret* [6], *F. Feruglio* [7], *H. Fraas* [10], *F. Franke* [10], *H. Genten* [11], *K. Huitu* [12], *B.R. Kim* [4], *S. Kraml* [9], *S. Lola* [13], *J. Maalampi* [14], *W. Majerotto* [9], *W. Oberschulte-Beckmann* [6], *W. Porod* [2], *M. Raidal* [12], *S. Rigolin* [7], *U. Schwickerath* [6], *L. Silvestrini* [7], *A. Sopczak* [15], *A. Vicini* [7]

[1] *Dipartimento di Fisica, Universitá di Pisa e INFN Pisa, Pisa, Italy*

[2] *Institut für Theoretische Physik, Universität Wien, Wien, Austria*

[3] *Laboratoire de l'Accélérateur Linéaire, IN2P3-CNRS et Université de Paris-Sud, Orsay, France*

[4] *Physics Laboratory, University of Athens, Athens, Greece*

[5] *Dipartimento di Fisica, Universitá di Perugia e INFN Perugia, Perugia, Italy*

[6] *Institut für Experimentelle Kernphysik, Universität Karlsruhe, Karlsruhe, Germany*

[7] *Dipartimento di Fisica, Universitá di Padova e INFN Padova, Padova, Italy*

[8] *Rutherford Appleton Laboratory, Chilton, United Kingdom*

[9] *Institut für Hochenergiephysik der Österreichischen Akademie der Wissenschaften, Wien, Austria*

[10] *Institut für Theoretische Physik, Universität Würzburg, Würzburg, Germany*

[11] *III. Physikalisches Institut A, RWTH, Aachen, Germany*

[12] *Research Institute for High Energy Physics, University of Helsinki, Helsinki, Finland*

[13] *Theory Division, CERN, Geneva, Switzerland*

[14] *Department of Physics, University of Helsinki, Helsinki, Finland*

[15] *DESY-Zeuthen, c/o PPE Division, CERN, Geneva, Switzerland*

CONTENTS:

Introduction and Summary

A. Bartl [1] *and W. Majerotto* [2]

[1] *Institut für Theoretische Physik, Universität Wien, Wien, Austria*

[2] *Institut für Hochenergiephysik der Österreichischen Akademie der Wissenschaften, Wien, Austria*

Supersymmetry (SUSY) is one of the most attractive extensions of the Standard Model (SM) [1]. There is evidence that the unification of all three gauge couplings at the scale $M_{GUT} \approx 10^{16}$ GeV can be achieved in the SUSY extension of the SM, but not in the SM itself. Further attractive features of the SUSY extension of the SM are the radiative symmetry breaking mechanism of the electroweak symmetry group $SU(2) \times U(1)$, and the stabilization of the Higgs mass against radiative corrections.

The Minimal Supersymmetric Standard Model (MSSM) [1] is a well defined model, which can be confronted with experimental data. Modifications of the MSSM, as the Next-to-Minimal Supersymmetric Standard Model (NMSSM), or models with R-parity violation, also allow clear predictions which can be compared with experimental data. Searches for SUSY particles are already performed at the present colliders LEP, HERA, TEVATRON, and TRISTAN. The discovery potential of an e^+e^- Linear Collider with $\sqrt{s} = 500$ GeV for the detection of SUSY particles was clearly demonstrated in the previous workshops [2]. It may happen that some SUSY particles will already be detected at one of the present colliders or at LHC even before the e^+e^- Linear Collider will be operating. In this case it is expected that the detection of the other SUSY particles and the complete determination of the specific SUSY model will only be possible at the e^+e^- Linear Collider.

In the previous workshops the studies concentrated on the physics at $\sqrt{s} = 500$ GeV. Experimental and theoretical studies on the production of selectrons, smuons, charginos, and neutralinos within the MSSM were perfomed [2,3]. In addition, production of neutralinos and Higgs particles in the NMSSM, R-parity violating models, as well as CP-violating effects were studied [4]. In this workshop these studies have been continued, specifically emphasizing those aspects not treated so far. The energy range $\sqrt{s} = 0.5 - 2$ TeV has been considered. The following topics concerning SUSY at the e^+e^- Linear Collider collider have been treated:

Constrained Minimal Supersymmetry and Discovery Potential at a Linear Collider [5]

In this study predictions for the SUSY and Higgs particle mass spectrum have been given. The authors have performed a fit within the MSSM, taking into account all relevant experimental data, and assuming gauge coupling unification. Both the low $\tan\beta$ and the high $\tan\beta$ scenarios have been studied, corresponding to $SU(5)$ and $SO(10)$ unification, respectively. Production cross sections for charginos, neutralinos, and the lightest Higgs particle have been given.

Search of Stop, Sbottom, and Stau at an e^+e^- Linear Collider with $\sqrt{s} = 0.5 - 2$ TeV [6]

Pair production of stops, sbottoms, and staus, $e^+e^- \to \tilde{t}_i\bar{\tilde{t}}_j$, $e^+e^- \to \tilde{b}_i\bar{\tilde{b}}_j$, $e^+e^- \to \tilde{\tau}_i\bar{\tilde{\tau}}_j$, $i,j = 1,2$, and the decays of these particles are studied in the energy range $\sqrt{s} = 500$ GeV to 2 TeV. Particular attention is paid to the influence of left-right mixing. Numerical predictions within the MSSM for cross sections and decay rates are presented. SUSY QCD corrections and corrections due to initial state radiation are included. A Monte Carlo study of $e^+e^- \to \tilde{t}_1\bar{\tilde{t}}_1$ at $\sqrt{s} = 500$ GeV with the decays $\tilde{t}_1 \to c\tilde{\chi}_1^0$ and $\tilde{t}_1 \to b\tilde{\chi}_1^+$ is performed for two representative sets of particle masses. Kinematical cuts are applied to reduce the known background reactions.

Fermion Virtual Effects in $e^+e^- \to W^+W^-$ Cross Section [7]

The contributions of new heavy virtual fermions to the cross section of $e^+e^- \to W^+W^-$ are analyzed at one-loop level. The constraints coming from the LEP1 results are taken into account. There is an interplay between the vector boson self-energies and the vertex corrections. The deviation from the SM prediction strongly depends on the nature of the heavy fermion. Two examples of heavy fermions are considered: (i) An extra doublet of heavy sequential quarks, and (ii) the charginos and neutralinos of the MSSM. In the first case a substantial deviation from the SM prediction is obtained which may be detectable at the e^+e^- Linear Collider with $\sqrt{s} = 500$ GeV or 1000 GeV. The largest effect is predicted in the channel where both vector bosons are longitudinally polarized. In the second case the final effect turns out to be negligible due to cancellations between the vertex corrections and the vector boson self-energy contributions.

QCD Corrections to the Decays $H^+ \to t\bar{b}$ and $H^+ \to \tilde{t}_i\bar{\tilde{b}}_j$ in the MSSM [8]

The $\mathcal{O}(\alpha_s)$ QCD corrections to the widths of the decays $H^+ \to t\bar{b}$ and $H^+ \to \tilde{t}_i\bar{\tilde{b}}_j$, $i,j = 1,2$ are calculated in the MSSM. It is found that these corrections are important, and that the gluino-exchange contributions can be comparable or even larger than the standard QCD corrections in the energy range of the Linear Collider.

Supersymmetry and CP-Violating Correlations in Top-Quark Production and Decay [9]

Analytic formulae for the cross section of the sequential processes $e^+e^- \to t\bar{t}$ and $t \to bl^+\nu/\bar{t} \to \bar{b}l^-\bar{\nu}$ in the laboratory frame are presented. These formulae contain explicitely the dependence on the triple product correlations induced by CP violation both in the production and the decay. Different observables sensitive to CP violation are defined. They are of the order of $10^{-4} - 10^{-3}$ in the MSSM.

Production of Nonminimal SUSY Neutralinos at an e^+e^- Linear Collider [10]

In this contribution neutralino production in the Next-to-Minimal Supersymmetric Standard Model (NMSSM) is analyzed. Numerical predictions for the production cross sections at $\sqrt{s} = 500$ GeV are given. Two scenarios are studied, in the first one the

lightest neutralino is almost a pure isosinglet, in the second one also the other neutralinos have significant isosinglet components. The differences between the NMSSM and the MSSM are discussed.

Test of Nonlinear Supersymmetric Standard Model at an e^+e^- Collider [11]

In their contribution the authors study the Higgs sector of the nonlinear SUSY model. The Higgs sector of the nonlinear SUSY extension of the SM, recently proposed by B. R. Kim, contains two isodoublets and one isosinglet, like the NMSSM. The authors work out the differences between the nonlinear SUSY model and the NMSSM. They show that for $\sqrt{s}$ larger than a "critical" energy the cross sections for the processes $e^+e^- \to Z^0 S_i$, $i = 1,2,3$, where $S_{1,2,3}$ are the scalar Higgs bosons, have characteristic lower bounds. This is a specific feature of the nonlinear SUSY model which can be tested at the e^+e^- Linear Collider.

Resonant Single Superparticle Productions via Supersymmetric R-parity Violation [12]

The authors study single chargino and neutralino production in the R-parity violating processes $e^+e^- \to \bar{\chi}_1^{\pm} \bar{f}^{\mp}$ and $e^+e^- \to \bar{\chi}_1^0 \bar{\nu}$. They present analytic formulae for these reactions which proceed via sneutrino exchange. They work out the case of resonant sneutrino production. They present numerical results for the cross sections for chargino and neutralino masses of 200 GeV, 400 GeV, and 490 GeV, assuming an R-parity violating coupling $\lambda_{LLE} = 0.01$. The authors also calculate the rates for the chargino decays into R_P even states. For $m_{\tilde{\chi}_1^{\pm}} = 400$ GeV they find that at $\sqrt{s} = 500$ GeV sneutrinos in the mass range $m_{\tilde{\nu}} \approx 300 - 580$ GeV will be observable.

Supersymmetric Left–Right Model at NLC [13]

In this contribution the supersymmetric left–right model with spontaneously broken R-parity is discussed. The production of the doubly charged higgsino in e^-e^-, e^-e^-, γe^-, and $\gamma\gamma$ reactions is studied. Slepton pair production which is mediated by the exchange of the doubly charged higgsino, is also considered. Numerical predictions for the cross sections at $\sqrt{s} = 1$ TeV are given. The possibilities of detecting the doubly charged higgsino at the e^+e^- Linear Collider are discussed.

In conclusion, at the present workshop a substantial extension of the previous studies on the analysis of SUSY particle production at the e^+e^- Linear Collider with $\sqrt{s} = 0.5 - 2$ TeV has been achieved.

References

[1] H.P. Nilles, Phys. Rep. 110 (1984) 1;
H.E. Haber and G.L. Kane, Phys. Rep. 117 (1985) 75;
R. Barbieri, Riv. Nuovo Cimento 11 (1988) 1.

[2] J.-F. Grivaz, Proc. of the Workshop "e^+e^- collisions at 500 GeV: The Physics Potential", Munich-Annecy-Hamburg, DESY 92-123B, p. 663, ed. P.M. Zerwas; R. Becker and R. Starosta, ibidem, p. 691; C. Vander Velde, ibidem, p. 681; R. Becker and C. Vander Velde, ibidem, DESY 93-123C, p. 457.

[3] A. Brignole et al., Proc. of the Workshop "e^+e^- collisions at 500 GeV: The Physics Potential", DESY 92-123B, p. 613; A. Bartl, W. Majerotto and B. Mösslacher, ibidem, p. 641; A. Bartl and W. Majerotto, ibidem, DESY 93-123C; F. Cuypers, G. J. van Oldenborgh and R. Rückl, ibidem, p. 475.

[4] B. R. Kim, S. K. Oh and A. Stephan, Proc. of the Workshop "e^+e^- collisions at 500 GeV: The Physics Potential", DESY 92-123B, p. 697; DESY 93-123C, p. 491; U. Ellwanger and M. Rausch de Traubenberg, ibidem, DESY 92-123B, p. 703; H. Dreiner and S. Lola, ibidem, p. 707; Y. Kizukuri and N. Oshimo, ibidem, p. 713; DESY 93-123C, p. 507.

[5] W. de Boer, G. Burkart, R. Ehret, W. Oberschulte-Beckmann, U. Schwickerath, V. Bednyakov, A. V. Gladyshev, D. Kazakov, S. G. Kovalenko, these Proceedings.

[6] A. Bartl, H. Eberl, S. Kraml, W. Majerotto, W. Porod, A. Sopczak, these Proceedings.

[7] A. Culatti, G. Degrassi, F. Feruglio, A. Masiero, S. Rigolin, L. Silvestrini, A. Vicini, these Proceedings.

[8] A. Bartl, H. Eberl, K. Hidaka, T. Kon, W. Majerotto, Y. Yamada, these Proceedings.

[9] A. Bartl, E. Christova, T. Gajdosik, W. Majerotto, these Proceedings.

[10] F. Franke, H. Fraas, these Procedings.

[11] H. Genten, S. W. Ham, B.R. Kim, S.K. Oh, these Proceedings

[12] H. Dreiner, S. Lola, these Proceedings.

[13] K. Huitu, J. Maalampi, M. Raidal, these Proceedings.

Constrained Minimal Supersymmetry and Discovery Potential at a Linear Collider

W. de Boer[1], G. Burkart[2], R. Ehret[3],
W. Oberschulte-Beckmann[4] U. Schwickerath[5]
Inst. für Experimentelle Kernphysik, Univ. of Karlsruhe
Postfach 6980, D-76128 Karlsruhe 1, FRG

V. Bednyakov, A.V.Gladyshev, D. Kazakov, S.G. Kovalenko
Bogoliubov Lab. of Theor. Physics, Joint Inst. for Nucl. Research,
141 980 Dubna, Moscow Region, RUSSIA

Abstract

We perform a combined fit of the Minimal Supersymmetric Standard Model (MSSM) taking into account various theoretical and experimental constraints from gauge coupling unification, the quark- and lepton masses of the third generation, the lower limit on the as yet unobserved supersymmetric particles, the Z^0-boson mass, the radiative decay $b \to s\gamma$ observed by the CLEO collaboration and the lower limit on the lifetime of the universe. No restriction is made on $\tan\beta$, the ratio of vacuum expectation values of the neutral components of the Higgs fields. Therefore we analyze both the low $\tan\beta$ and the high $\tan\beta$ solutions expected in the SU(5) and in SO(10) unification schemes, respectively.

1 Introduction

The Minimal Supersymmetric Standard Model (MSSM) [1] has become the leading candidate for a low energy theory consistent with the GUT idea. The precisely measured coupling constants at LEP exclude unification in the Standard Model, while in the MSSM unification is possible[2, 3, 4].
Within the Constrained Minimal Supersymmetric Model (CMSSM) it is possible to predict the low energy gauge couplings and masses of the 3 generation particles from a few parameters at the GUT scale. Moreover, the CMSSM predicts electroweak symmetry breaking due to large radiative corrections from the Yukawa couplings, thus relating the Z^0 boson mass to the top quark mass via the renormalization group equations (RGE). As a result, low energy data on masses and couplings provide strong constraints on the CMSSM parameter space, as discussed recently by many groups. [5, 6, 7, 8, 9, 10, 11, 12, 13, 14, 15, 16, 17, 18, 19].

2 The Constrained MSSM parameter space

In this section the various low energy GUT predictions are compared with data. The most restrictive constraints are the coupling constant unification and the requirement that the unification scale has to be above 10^{15} GeV from the proton lifetime limits, assuming decay via s-channel exchange of heavy gauge bosons. They exclude the SM [2, 3, 4] as well as many other models [3, 20, 21]. The only model known to be able to fulfill all constraints simultaneously is the MSSM.
The input and fitted output variables have been summarized in table 1. The requirement of bottom-tau Yukawa coupling unification strongly restricts the possible solutions in the m_t versus $\tan\beta$ plane. With the top mass measured by the CDF and D0-Collaborations [22, 23] only two regions of $\tan\beta$ give an acceptable χ^2 fit, as shown in the bottom part of fig. 1 for two values of the SUSY scales $m_0, m_{1/2}$.

[1]Email: deboer@ekpux3.physik.uni-karlsruhe.de
[2]E-mail: gerd@ekpux3.physik.uni-karlsruhe.de
[3]E-mail: ralf.ehret@cern.ch
[4]E-mail: wulf@afsmail.cern.ch
[5]E-mail: ulrich@ekpux3.physik.uni-karlsruhe.de

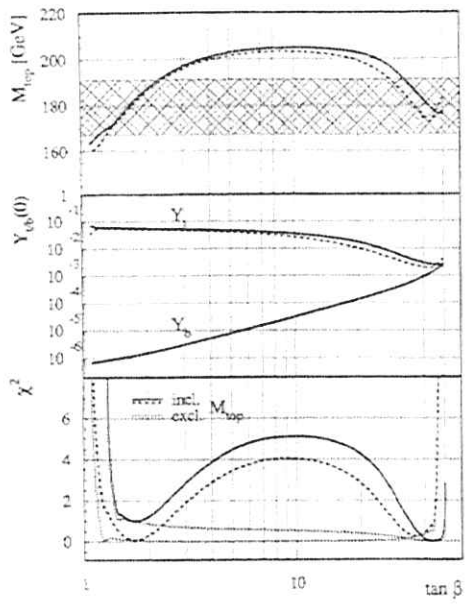

Figure 1: The top quark mass as function of $\tan\beta$ (top) for values of $m_0, m_{1/2}$ optimized for low and high $\tan\beta$, as indicated by the dashed and solid lines, respectively. The middle part shows the corresponding values of the Yukawa coupling at the GUT scale and the lower part the obtained χ^2 values. If the top constraint ($m_t = 179 \pm 12$, horizontal band) is not applied, all values of $\tan\beta$ between 1.2 and 50 are allowed (thin dotted lines at the bottom), but if the top mass is constrained to the experimental value, only the regions $1 < \tan\beta < 3$ and $15 < \tan\beta < 50$ are allowed.

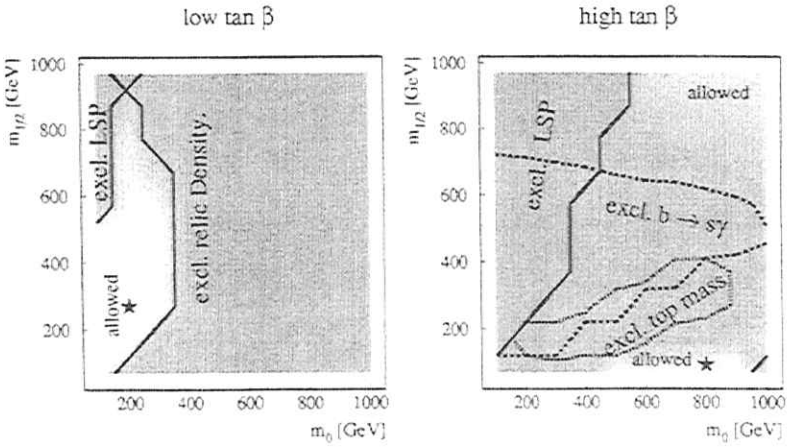

Figure 2: The total χ^2-distribution for low and high $\tan\beta$ solutions (top) as well as the projections (bottom). The different shades indicate steps of $\Delta\chi^2 = 2$, so basically only the light shaded region is allowed.

exp. input data	$\Rightarrow$	Fit parameters	
		low $\tan\beta$	high $\tan\beta$
$\alpha_1, \alpha_2, \alpha_3$	minimize χ^2	M_{GUT} , α_{GUT}	M_{GUT} , α_{GUT}
m_t		$Y_t^0, Y_b^0 = Y_\tau^0$	$Y_t^0 = Y_b^0 = Y_\tau^0$
m_b		m_0 ,$m_{1/2}$	m_0 ,$m_{1/2}$
m_τ		$\tan\beta$	$\tan\beta$
M_Z		μ	μ
$b \to s\gamma$		(A_0)	A_0
$\tau_{universe}$			

Table 1: Summary of fit input and output variables. For the low $\tan\beta$ scenario the parameter A_0 is not very relevant as indicated by the brackets. For large $\tan\beta$ $\tau_{universe}$ does not yield any constraints (see text).

which are optimized for the low and high $\tan\beta$ range, respectively, as will be discussed below. The curves at the top show the solution for m_t as function of $\tan\beta$ in comparison with the experimental value of $m_t = 179 \pm 12$ GeV. The m_t predictions were obtained by imposing gauge coupling unification and electroweak symmetry breaking for each value of $\tan\beta$, which allows a determination of μ, α_{GUT}, and M_{GUT} from the fit for the given choice of $m_0, m_{1/2}$. Note that the results do not depend very much on this choice.

The best χ^2 is obtained for $\tan\beta = 1.7$ and $\tan\beta = 41$, respectively. They correspond to solutions where $Y_t \gg Y_b$ and $Y_t \approx Y_b$, as shown in the middle part of fig. 1. The latter solution is the one typically expected for the SO(10) symmetry, in which the up and down type quarks as well as leptons belong to the same multiplet, while the first solution corresponds to b-tau unification only, as expected for the minimal SU(5) symmetry. In SO(10) exact top-bottom Yukawa unification is difficult, mainly because of the requirement of radiative electroweak symmetry breaking. In that case both, the mass parameters in the Higgs potential (m_1 and m_2) as well as the Yukawa couplings, stay similar at all energies. Since the large $\tan\beta$ solutions require a judicious fine tuning in case of exact unification at the GUT scale, a small non-unification is assumed, which could result from threshold effects or running of the parameters between the Planck scale and the GUT scale. E.g. if the SO(10) symmetry would be broken into SU(5) below the Planck scale, but well above the GUT scale, the top Yukawa coupling could be larger than the bottom Yukawa coupling, as estimated from the SU(5) RGE. Therefore, in the following analysis Y_t is taken to be 25% larger than Y_b at the GUT scale and a similar splitting was introduced between m_1^2 and m_2^2, i.e. $m_1^2 = 1.25\, m_0^2 - \mu^2$ and $m_2^2 = 1.0\, m_0^2 - \mu^2$ at the GUT scale. It is interesting to note that the SU(5) RGE predicts $Y_t > Y_b$ at the GUT scale. With the above mentioned deviations from exact unification, the fits converge easily with an acceptable χ^2. For $Y_t < Y_b$ at the GUT scale the fits do not yield acceptable χ^2 values.

In fig. 2 the total χ^2 distribution is shown as funtion of m_0 and $m_{1/2}$ for the two values of $\tan\beta$ determined above. One observes clear minima at $m_0, m_{1/2}$ around (200,270) and (900,70), as indicated by the stars in the projections. The different shades correspond to $\Delta\chi^2$ steps of 2. Note the sharp increase in χ^2, so basically only the light shaded regions are allowed independent of the exact χ^2 cut. Contours show the regions excluded by different constraints used in the analysis: the requirement for the LSP to be the lightest neutralino, constraints from the relic density, $b \to s\gamma$ and the top quark mass. The main contributions to χ^2 are different for the two $\tan\beta$ regimes: for large $\tan\beta$ only small values of $m_{1/2}$ yield good fits, because of the simultaneous constraints of $BR(b \to s\gamma)$ and the large corrections to the b-quark mass, while at low $\tan\beta$ most of the $m_0, m_{1/2}$ region is eliminated by the requirement $\Omega h_0^2 < 1$. The small effect of the relic density constraint in the case of the large $\tan\beta$ solution can be explained on the account of the larger Higgsino admixture in the neutralino mass eigenstate. This leads to an enhancement of $\tilde{\chi} - \tilde{\chi}$ annihilation via the s-channel Z boson exchange pushing the relic density Ωh_0^2 to lower values. As a result, in the large $\tan\beta$ case the constraint $\Omega h_0^2 < 1$ is almost always satisfied unlike in the case of the low $\tan\beta$.

Fitted SUSY parameters and masses		
Symbol	low $\tan\beta$	high $\tan\beta$
m_0	200	800
$m_{1/2}$	270	90
$\mu(M_Z)$	-550	-220
$\tan\beta$	1.7	41
$Y_t(m_t)$	0.008	0.005
M_t^{pole}	177	165
$1/\alpha_{GUT}$	24.8	24.3
M_{GUT}	$1.6\ 10^{16}$	$2.5\ 10^{16}$
$\tilde{\chi}_1^0(\tilde{B})$	116	35
$\tilde{\chi}_2^0(\tilde{W}^3)$	230	65
$\tilde{\chi}_1^\pm(\tilde{W}^\pm)$	230	65
$\tilde{g}$	660	240
$\tilde{l}$	260	800
$\tilde{q}$	620	820
$\tilde{t}$	230	630
$\tilde{b}$	580	510
$\tilde{t}$	530	500
$\tilde{\chi}_3^0(\tilde{H}_1)$	560	(-)240
$\tilde{\chi}_4^0(\tilde{H}_2)$	(-) 570	250
$\tilde{\chi}_2^\pm(\tilde{H}^\pm)$	570	250
h	81	110
H	740	270
A	730	270
$H^\pm$	740	290

Table 2: Values of the fitted SUSY parameters (upper part) and corresponding susy masses (lower part) for low and high $\tan\beta$ solutions. The scale is either M_Z, m_t, or GUT, as indicated in the first column by (M_Z), (m_t) or (0), respectively. The (-) in front of the neutralinos indicates that it is a CP-odd state.

The gluino contribution to $BR(b \to s\gamma)$ a'priori might be important for the high $\tan\beta$ solution. However, as we verified numerically, this contribution does not noticable change the fit results for either low or large tb solutions. Therefore, one can safely neglect the gluino contribution to $BR(b \to s\gamma)$ as non essential.

The mass of the lightest chargino is about $0.7 - 0.8\, m_{1/2}$. The low value of $m_{1/2}$ for the best fit at large $\tan\beta$ implies a chargino mass of about 65 GeV, which is just above the LEP 1.5 limit and might be detectable at LEP II or alternatively, the large $\tan\beta$ scenario can be excluded at LEP II, at least the minimal version. Of course, this conclusion depends sensitively on the $BR(b \to s\gamma)$ value. For large $m_{1/2}$ values, the prediction for this branching ratio is only 2 or 3 standard deviations above its experimental value In non-minimal models, e.g. ones with large splittings between m_1 and m_2 at the GUT scale, as studied by Borzumati et al. [24], the prediction for this branching ratio can be brought into agreement with experiment in the large $m_{1/2}$ region.

Without the contraints from $b \to s\gamma$ and dark matter, large values of the SUSY scale cannot be excluded, since the χ^2 from gauge and Yukawa coupling unification and electroweak symmetry breaking alone does not exclude these regions although there is a clear preference for the lighter SUSY scales.

At large $\tan\beta$ the b-mass has large, but finite corrections in the MSSM. Both, $BR(b \to s\gamma)$ and Δm_b are sensitive functions of the mixing in the quark sector, given by the off-diagonal terms in the mass matrices. Fitting both values simultaneously requires the trilinear coupling A_0 at the GUT scale to be non-zero: the χ^2 for large $\tan\beta$ and $A_0 = 0$ is much worse than for fits, in which A_0 is left free.

The fitted values of the trilinear couplings and the Higgs mixing parameter μ are strongly correlated with $m_{1/2}$, so the ratio of these parameters at the electroweak scale and the gluino mass ($M_{\tilde{g}} \approx 2.7\, m_{1/2}$)

is relatively constant and largely independent of m_0. Note that although the trilinear couplings A_t, A_b and A_τ have equal values at the GUT scale, they are quite different at the electroweak scale due to the different RGE's.
The large values of μ at low $\tan\beta$ imply little mixing in the neutralino sector and leads to eigenvalues of approximately M_1, M_2 and μ in the mass matrix. Since M_1 is the smallest value, the LSP will be almost purely a bino, which leads to strong constraints on the parameters from the lifetime of the universe.
For high $\tan\beta$ only negative μ- values are allowed, since positive μ-values yield a too high b-mass due to the large positive corrections in that case.
The upper limits for particles other than the lightest Higgs are considerable higher, unless restricted by some fine tuning argument: if the masses of the superpartners and the normal particles are different, the famous cancellation of quadratic divergencies in supersymmetry does not work anymore and the corrections to the Higgs masses quickly increase. These corrections lead to large corrections in the electroweak scale as well. It is a question of taste, if one considers the corrections large or small and if one should exclude some region of parameter space. In our opinion the fine tuning argument is difficult to use for a mass scale below 1 TeV, and the whole region up to 1 TeV should be considered, leading to quite large upper limits in case of the low $\tan\beta$ scenario[13].

3 Discovery Potential at the Next Linear Colliders

The programs SUSYGEN [25] and special SUSY routines [26] in ISAJET [27] have been used to calculate the production cross-sections for charginos, neutralinos and the lightest Higgses as function of the SUSY mass scales m_0 and $m_{1/2}$.
The absolute value of the Higgs mass parameter μ was determined from the electroweak symmetry breaking condition; its sign was chosen positive. For negative μ values the cross sections are about 50% higher due to the lighter Higgs mass in that case. For large values of $\tan\beta$ only negative values of μ give acceptable fits, mainly because of the large corrections to the bottom mass, which prohibit tau-bottom unification for positive μ. For low $\tan\beta$ the Higgs masses are below 105 GeV, for high $\tan\beta$ below 125 GeV [29], so the low $\tan\beta$ scenario can be covered by LEP II, while the high $\tan\beta$ scenario requires a linear collider. For these results the large radiative corrections to A_t and A_b were taken into account, so they have nonzero values at the electroweak scale, typically $A_t = -0.7M_{\tilde{g}}$ and $A_b = -1.5M_{\tilde{g}}$.
The neutralino and chargino cross sections have both s- and t-channel contributions, the latter by the exchange of a sfermion and sneutrino, respectively. The t-channel exchanges interfere with the s-channel exchange, so the cross sections depend sensitively on the masses of the scalar sparticles, which are characterized by a common mass scale m_0 at the GUT scale in the MSSM. The masses of the neutralinos and charginos are obtained from the diagonalization of the mass matrices, whose main elements are given by the common gaugino mass $m_{1/2}$ at the GUT scale and the Higgs mixing parameter μ. In the typical case $\mu \gg m_{1/2}$, as required by electroweak symmetry breaking, the cross sections only depend on m_0 and $m_{1/2}$. This dependence is shown in fig. 3 for different values of $\tan\beta$. The cross section for neutralino production is only appreciable for small values of m_0, as shown by the contour plots for $\sigma = 0.1$ pb in fig. 3.

4 Acknowledgment

The research described in this publication was made possible in part by support from the Human Capital and Mobility Fund (Contract ERBCHRXCT 930345) from the European Community, by support from the German Bundesministerium für Bildung und Forschung (BMBF) (Contract 05-6KA16P) and by support from the DFG for the Graduiertenkolleg in Karlsruhe.

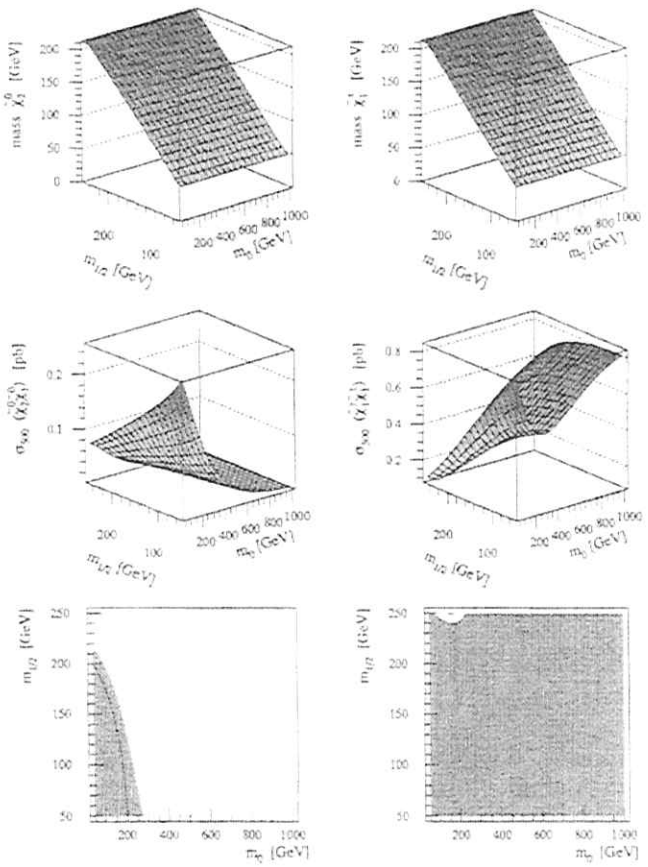

Figure 3: The neutralino and chargino masses (upper row), cross sections for $E_{CM} = 500$ GeV (middle row), and contours for $\sigma = 0.1$ pb (lower row) as function of the common gaugino mass $m_{1/2}$ and the common scalar mass m_0. the Higgs mixing parameter μ was choosen to be much larger than $m_{1/2}$, namely 1 TeV. In this limiting case, which is the preferred one in the MSSM requiring electroweak symmetry breaking, the visible neutralino and chargino cross section depend practically only on m_0 and $m_{1/2}$. The small dependence on the $\tan\beta$ is shown by the solid lines ($\tan\beta = 45$) and grey contours ($\tan\beta = 1.5$) in the bottom row.

References

[1] For references see the review papers:
H.-P. Nilles, Phys. Rep. **110** (1984) 1;
H.E. Haber, G.L. Kane, Phys. Rep. **117** (1985) 75;
A.B. Lahanas and D.V. Nanopoulos, Phys. Rep. **145** (1987) 1;
R. Barbieri, Riv. Nuo. Cim. **11** (1988) 1.

[2] J. Ellis, S. Kelley, and D. V. Nanopoulos. *Nucl. Phys.* **B373** *(1992) 55.*

[3] U. Amaldi, W. de Boer, and H. Fürstenau. *Phys. Lett.* **B260** *(1991) 447.*

[4] P. Langacker and M. Luo. *Phys. Rev.* **D44** *(1991) 817.*

[5] G. G. Ross and R. G. Roberts. *Nucl. Phys.* **B377** *(1992) 571.*

[6] M. Carena, S. Pokorski, and C. E. M. Wagner. *Nucl. Phys.* **B406** *(1993) 59.*

[7] V. Barger, M. S. Berger, and P. Ohmann.
Phys. Rev. **D47** *(1993) 1093., Phys. Rev. Lett.* **49***(1994) 4908.*

[8] M. Olechowsi and S. Pokorski. *Nucl. Phys.* **B404** *(1993) 590.*

[9] P.E. Chankowski et al. *IFT-95-9, MPI-PTE-95-58 and ref. therein.*

[10] P. Langacker and N. Polonsky. *Phys. Rev.* **D49** *(1994) 1454; UPR-0642-T and ref. therein.*

[11] J. L. Lopez, D.V. Nanopoulos, and A. Zichichi. *Progr. in Nucl. and Particle Phys.*, **33** *(1994) 503 and ref. therein.*

[12] W. de Boer. *Progr. in Nucl. and Particle Phys.*, **33** *(1994) 201 and ref. therein.* .

[13] W. de Boer, R. Ehret, and D. Kazakov. *Phys. Lett.* **B334** *(1994) 220, W. de Boer et al., IEKP-KA/95-07 (to be published in Zeit. f. Physik).*

[14] *J. L. Lopez, D.V. Nanopoulos, A. Zichichi, CTP-TAMU-40-93 (1993); CTP-TAMU-55-93 (1993); CERN-TH-6954-93(1993);CERN-TH-6926-93-REV (1993); CERN-TH-6903-93 (1993);*
J. L. Lopez, et al., Phys. Lett. **B306** *(1993) 73.*

[15] S.P. Martin and P. Ramond, *Phys. Rev.* **D48** *(1993) 5365*
D.J. Castano, E.J. Piard, and P. Ramond, *Phys. Rev.* **D49** *(1994) 4882.*

[16] G. L. Kane, C. Kolda, L. Roszkowski, and J. D. Wells. *Phys. Rev.* **D49** *(1994) 6173.*

[17] C. Kolda, L. Roszkowski, and J. D. Wells and G. L. Kane. *Phys. Rev.* **D50** *(1994) 5498.*

[18] M. Carena and C. E. M. Wagner. *CERN-TH-7393-94 and ref. therein.*

[19] M. Carena, M. Olechowski, S. Pokorski, and C. E. M. Wagner. *Nucl. Phys.* **419** *(1994) 213.*

[20] U. Amaldi, W. de Boer, P. H. Frampton, H. Fürstenau, and J.T. Liu.
Phys. Lett. **B281** *(1992) 374.*

[21] H. Murayama and T. Yanagida, *Mod. Phys. Lett.* **A7** *(1992) 147;*
T. G. Rizzo, *Phys. Rev.* **D45** *(1992) 3903;*
T. Moroi, H. Murayama and T. Yanagida, *Phys. Rev.* **D48** *(1993) 2995.*

[22] CDF Collab., F. Abe, et al. *Phys. Rev. Lett.* **74** *(1995) 2626.*

[23] D0 Collab., S. Abachi, et al. *Phys. Rev. Lett.* **74** *(1995) 2632.*

[24] F.M. Borzumati, M. Olechowski and S. Pokorski, *Phys. Lett.* **B349** *(1995) 311.*

[25] S. Katsanevas. *SUSYGEN,private communication.*

[26] H. Baer et. al. *Int. Journ. of mod. phys.Vol.4,16(1989)4111.*

[27] F.E Paige and S.D. Protopopescu. *ISAJET7.11,Fermilab.*

[28] R. Ammar et al. CLEO-Collaboration. *Phys. Rev. Lett.* **74** *(1995) 2885.*

[29] A.V.Gladyshev et al., MSSM Predictions of the Neutral Higgs Boson Massses and LEP II production cross sections, University of Karlsruhe Preprint, IEKP-KA/96-01
M. Carena et al., hep-ph 9602250, Higgs Physics at LEP II, and references therein.

Search of Stop, Sbottom, and Stau at an e^+e^- Linear Collider with $\sqrt{s} = 0.5 - 2$ TeV

A. Bartl[1], H. Eberl[2], S. Kraml[2],
W. Majerotto[2], W. Porod[1], A. Sopczak[3]*

(1) Institut für Theoretische Physik, Universität Wien, A-1090 Vienna, Austria
(2) Institut für Hochenergiephysik, Österreichische Akademie der Wissenschaften, A-1050 Vienna, Austria
(3) DESY-Zeuthen, D-15738, Zeuthen, Germany

Abstract

We discuss pair production and decays of stops, sbottoms, and staus in e^+e^- annihilation in the energy range $\sqrt{s} = 500$ GeV to 2 TeV. We present numerical predictions within the Minimal Supersymmetric Standard Model for cross sections and decay rates. We study the stop discovery potential for $\sqrt{s} = 500$ GeV and 10 fb^{-1} integrated luminosity with full statistics background simulation.

1 Introduction

In the experimental search for supersymmetry (SUSY) particular attention is paid to those particles which are expected to be relatively light. The scalar top quark, the SUSY partner of the top quark, may be the lightest squark, and may even be the lightest visible SUSY particle (LVSP) [1, 2]. The stop can be light for two reasons: (i) Due to the large top Yukawa terms in the renormalization group equations, the scalar mass parameters of the stop can be much smaller than the corresponding parameters of the first and second generation squarks [3, 4]. (ii) The off-diagonal elements of the mass mixing matrix of the stop can be large, and this leads to strong $\tilde{t}_L - \tilde{t}_R$ mixing. If the parameter $\tan\beta$ is large enough ($\tan\beta \gtrsim 10$) the scalar bottom quark [5] or the scalar tau lepton could also be relatively light and even be the LVSP. The existence of a relatively light stop would have many interesting phenomenological implications.

*c/o PPE Division, CERN

A light stop would significantly influence the branching ratios of the decays $Z^0 \to b\bar{b}$, $t \to bW$, $b \to s\gamma$ and some other physical observables (see, e.g. [6]).

In this contribution we shall present results for the production of stops, sbottoms, and staus in e^+e^- annihilation at energies between $\sqrt{s} = 500$ GeV and 2 TeV and details on signal selection and background rejection for stop production at $\sqrt{s} = 500$ GeV and $\mathcal{L} = 10$ fb^{-1}. The production cross sections and the decay rates, and thus the discovery reach of these sfermions show a distinct dependence on the L–R mixing angles. The most important decay modes of these sfermions are those into fermions and neutralinos or charginos.

Our framework is the Minimal Supersymmetric Standard Model (MSSM) [7] which contains the Standard Model (SM) particles, sleptons, $\tilde{l}^{\pm}$, $\tilde{\nu}_l$, squarks, $\tilde{q}$, gluinos $\tilde{g}$, two pairs of charginos, $\tilde{\chi}_i^{\pm}$, $i = 1, 2$, four neutralinos, $\tilde{\chi}_i^0$, $i = 1, \ldots, 4$, and five Higgs particles, h^0, H^0, A^0, $H^{\pm}$ [8]. The phenomenology of stops, sbottoms, staus, and their decay products is determined by the following parameters: M and M', the (soft breaking) $SU(2)$ and $U(1)$ gaugino masses, μ, the higgsino mass parameter, $\tan\beta = v_2/v_1$ (where v_1 and v_2 are the vacuum expectation values of the neutral members of the two Higgs doublets), and $M_{\tilde{L}}$, $M_{\tilde{E}}$, $M_{\tilde{Q}}$, $M_{\tilde{U}}$, $M_{\tilde{D}}$, A_τ, A_t, A_b, which are soft–breaking parameters entering the mass mixing matrices of the stau, stop, and sbottom systems. We assume the GUT relations $M'/M = \frac{5}{3}\tan^2\Theta_W \approx 0.5$, and $m_{\tilde{g}}/M = \alpha_s/\alpha_2 \approx 3$, where $m_{\tilde{g}}$ is the gluino mass. Furthermore, we assume that the $\tilde{\chi}_1^0$ is the lightest SUSY particle (LSP).

The lower model independent mass bound for stops obtained at LEP is 45 GeV [9, 10]. Stronger limits up to 55 GeV are reported from the data taking at LEP at 130–140 GeV [11]. The D0 experiment at the TEVATRON excludes the mass range 40 GeV $\lesssim M_{\tilde{t}} \lesssim$ 100 GeV for the stop, if the mass difference $M_{\tilde{t}} - m_{\tilde{\chi}_1^0} \gtrsim 30$ GeV [12].

In Section 2 we shortly review the basic facts about L–R mixing of stops, sbottoms, and staus, and present our numerical results for the production cross sections for unpolarized beams as well as for polarized e^- beams. In Section 3 we describe the decays of stops, sbottoms, and staus and present numerical results for the important branching ratios. We also list the signatures which are expected to be relevant at $\sqrt{s} = 500$ GeV. In Section 4 we describe an event generator for $\tilde{t}_1\bar{\tilde{t}}_1$ production and decay. In Section 5 experimental sensitivities are determined based on Monte Carlo simulations. Section 6 contains a summery.

2 Cross Sections for Pair Production of Stops, Sbottoms, and Staus

The SUSY partners of the SM fermions with left and right helicity are the left and right sfermions. In the case of the stop, sbottom and stau the left and right states are

in general mixed. In the $(\tilde{f}_L, \tilde{f}_R)$ basis the mass matrix is [1, 8]

$$M_{\tilde{f}}^2 = \begin{pmatrix} M_{\tilde{f}_L}^2 & a_f m_f \\ a_f m_f & M_{\tilde{f}_R}^2 \end{pmatrix} \tag{1}$$

with

$$M_{\tilde{f}_L}^2 = M_{\tilde{F}}^2 + m_Z^2 \cos 2\beta (T_f^3 - e_f \sin^2 \Theta_W) + m_f^2, \tag{2}$$

$$M_{\tilde{f}_R}^2 = M_{\tilde{F}'}^2 + e_f m_Z^2 \cos 2\beta \sin^2 \Theta_W + m_f^2, \tag{3}$$

$$m_t a_t \equiv m_t (A_t - \mu \cot \beta), \;\; m_b a_b \equiv m_b (A_b - \mu \tan \beta), \;\; m_\tau a_\tau \equiv m_\tau (A_\tau - \mu \tan \beta), \tag{4}$$

where e_f and T_f^3 are the charge and the third component of weak isospin of the sfermion $\tilde{f}$, $M_{\tilde{F}} = M_{\tilde{Q}}$ for $\tilde{f}_L = \tilde{t}_L, \tilde{b}_L$, $M_{\tilde{F}} = M_{\tilde{L}}$ for $\tilde{f}_L = \tilde{\tau}_L$, $M_{\tilde{F}'} = M_{\tilde{U}}, M_{\tilde{D}}, M_{\tilde{E}}$ for $\tilde{f}_R = \tilde{t}_R, \tilde{b}_R, \tilde{\tau}_R$, respectively, and m_f is the mass of the corresponding fermion. Evidently, there can be strong $\tilde{t}_L$-$\tilde{t}_R$ mixing due to the large top quark mass. Similarly, for sbottoms and staus L–R mixing is non-negligible if $\tan\beta \gtrsim 10$. The mass eigenvalues for the sfermion $\tilde{f} = \tilde{t}, \tilde{b}, \tilde{\tau}$ are

$$M_{\tilde{f}_{1,2}}^2 = \frac{1}{2} \left(M_{\tilde{f}_L}^2 + M_{\tilde{f}_R}^2 \mp \sqrt{(M_{\tilde{f}_L}^2 - M_{\tilde{f}_R}^2)^2 + 4 m_f^2 a_f^2} \right) \tag{5}$$

where $\tilde{t}_1$, $\tilde{b}_1$ and $\tilde{\tau}_1$ denote the lighter eigenstates.

It is well known that the cross section for $e^+e^- \to \tilde{t}_1\bar{\tilde{t}}_1$ depends on the stop–mixing parameters. In particular the $Z^0\tilde{t}_1\bar{\tilde{t}}_1$ coupling vanishes for the mixing angle $\Theta_{\tilde{t}} = 0.98$ [13]. The cross sections for $e^+e^- \to \tilde{b}_1\bar{\tilde{b}}_1$ and $e^+e^- \to \tilde{\tau}_1\bar{\tilde{\tau}}_1$ also show a characteristic dependence on their mixing angles. The $Z^0\tilde{b}_1\bar{\tilde{b}}_1$ coupling vanishes at $\Theta_{\tilde{b}} = 1.17$, and the $Z^0\tilde{\tau}_1\bar{\tilde{\tau}}_1$ coupling vanishes at $\Theta_{\tilde{\tau}} = 0.82$. The interference between the γ and Z^0 exchange contributions leads to characteristic minima of the cross sections for $e^+e^- \to \tilde{f}_1\bar{\tilde{f}}_1$ which occur at specific values of the mixing angles $\theta_{\tilde{f}}$. They are given by

$$\cos^2 \Theta_{\tilde{f}|min} = \frac{e_f}{T_f^3} \sin^2 \Theta_W [1 + (1 - s/m_Z^2) F(\sin^2 \Theta_W)] \,. \tag{6}$$

The function $F(\sin^2\Theta_W)$ depends on the polarization of the e^- beam and is given by $F(\sin^2\Theta_W) = \cos^2\Theta_W (L_e + R_e)/(L_e^2 + R_e^2) \approx -0.22$, $F(\sin^2\Theta_W) = \cos^2\Theta_W / L_e \approx -2.9$, and $F(\sin^2\Theta_W) = \cos^2\Theta_W / R_e \approx 3.3$, for unpolarized, left and right polarized e^- beams, respectively, where $L_e = -\frac{1}{2} + \sin^2\Theta_W$ and $R_e = \sin^2\Theta_W$. For polarized e^- beams the dependence on the mixing angles is much more pronounced than for unpolarized beams. The corresponding minima of the cross sections of $e^+e^- \to \tilde{f}_2\bar{\tilde{f}}_2$ occur at $1 - \cos^2\Theta_{\tilde{f}|min}$.

In the calculations of the cross sections we have used the tree level formulae of [13, 15, 16]. We have also included SUSY QCD corrections taking the formulae of [17] (see also [13] and [18]) and corrections due to initial state radiation [19].

In Fig. 1a we show contour lines of the total cross section $e^+e^- \to \tilde{t}_1\bar{\tilde{t}}_1$ in the $M_{\tilde{t}_1} - \cos^2\Theta_{\tilde{t}}$ plane for $\sqrt{s} = 500$ GeV and unpolarized beams. For $M_{\tilde{t}_1} \simeq 100$ GeV this cross section can reach 220 fb. A substantial dependence on $\cos^2\Theta_{\tilde{t}}$ can be seen for $M_{\tilde{t}_1} \lesssim 150$ GeV. In Fig. 1b we show the $\cos^2\Theta_{\tilde{t}}$ dependence of the cross section $e^+e^- \to \tilde{t}_1\bar{\tilde{t}}_1$ for left and right polarized and unpolarized e^- beams for $\sqrt{s} = 500$ GeV and $M_{\tilde{t}_1} = 200$ GeV. The polarization asymmetry depends quite strongly on the mixing angle. Therefore, experiments with polarized e^- beams would be necessary for a precise determination of the mixing angle $\Theta_{\tilde{t}}$. The determination of the stop masses and mixing angle gives information on the basic SUSY parameters $M_{\tilde{Q}}$, $M_{\tilde{U}}$ and A_t. This is discussed in [14].

Similarly, Fig. 2 is a contour plot of the total cross section of $e^+e^- \to \tilde{t}_2\bar{\tilde{t}}_2$ in the $M_{\tilde{t}_2} - \cos^2\Theta_{\tilde{t}}$ plane at $\sqrt{s} = 2$ TeV, for left and right polarized e^- beams. Here we observe a strong dependence on the stop mixing angle. For $M_{\tilde{t}_2} \simeq 900$ GeV the cross section at this energy is about 1 fb.

In Fig. 3 we show the cross section for $e^+e^- \to \tilde{t}_1\bar{\tilde{t}}_2 + \bar{\tilde{t}}_1\tilde{t}_2$ at $\sqrt{s} = 1$ TeV as a function of $M_{\tilde{t}_1}$, for various values of $M_{\tilde{t}_2}$. Here we have fixed the mixing angle $\cos^2\Theta_{\tilde{t}} = 0.5$ where the cross section has its maximum. For other values of the mixing angle this cross section scales as $\sin^2\Theta_{\tilde{t}} \cos^2\Theta_{\tilde{t}}$. For $M_{\tilde{t}_1} \simeq 100$ GeV and $M_{\tilde{t}_2} \simeq 200$ GeV this cross section can reach 20 fb. Note that $e^+e^- \to \tilde{b}_1\bar{\tilde{b}}_2$ has the same cross section as $e^+e^- \to \tilde{t}_1\bar{\tilde{t}}_2$, if the masses and the mixing angles are the same (neglecting corrections due to gluino exchange). The cross section for $e^+e^- \to \tilde{\tau}_1\bar{\tilde{\tau}}_2$ is a factor of approximately 1/3 smaller because of the colour factor and the QCD radiative corrections which have to be included for squark production. Due to the factor $\sin^2\Theta_{\tilde{f}} \cos^2\Theta_{\tilde{f}}$, the cross section depends strongly on the mixing angle.

In Fig. 4a we show the contour plot of the total cross section of $e^+e^- \to \tilde{b}_1\bar{\tilde{b}}_1$ in the $M_{\tilde{b}_1} - \cos^2\Theta_{\tilde{b}}$ plane at $\sqrt{s} = 1$ TeV, for unpolarized beams. For $M_{\tilde{b}_1} \simeq 100$ GeV (450 GeV) this cross section can reach a value of about 50 fb (1 fb). For $M_{\tilde{b}_1} \lesssim 300$ GeV the cross section depends appreciably on $\cos^2\Theta_{\tilde{b}}$. For polarized e^- beams we have again a much stronger $\cos^2\Theta_{\tilde{b}}$ dependence of the cross sections, as shown in Fig. 4b for $M_{\tilde{b}_1} = 300$ GeV and $\sqrt{s} = 1$ TeV.

The influence of the SUSY QCD corrections as a function of $\sqrt{s}$ is demonstrated in Fig. 5, where we have taken $\cos\Theta_{\tilde{t}} = 0.7$, $M_{\tilde{t}_1} = 150$ GeV, $M_{\tilde{t}_2} = 300$ GeV and $m_{\tilde{g}} = 300$ GeV. $\delta\sigma^s$ is the conventional QCD correction and $\delta\sigma^{\tilde{g}}$ is the correction due to gluino exchange. Note that at high energies $\delta\sigma^{\tilde{g}}$ has the opposite sign of $\delta\sigma^s$, and its absolute value is increasing with $\sqrt{s}$. For a more detailed discussion of SUSY QCD corrections see [17]. They increase the cross section values up to 40 %. The corrections due to initial state radiation turn out to be of the order of 10 %.

The cross sections for $e^+e^- \to \tilde{\tau}_1\bar{\tilde{\tau}}_1$ at $\sqrt{s} = 500$ GeV for left and right polarized

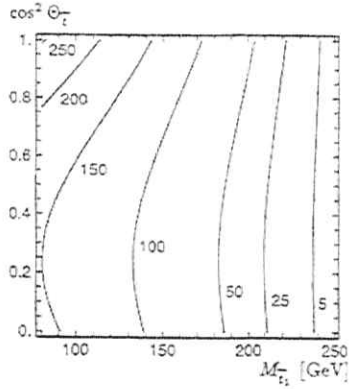

Fig. 1a: Contour lines for the total cross section of $e^+e^- \to \tilde{t}_1\bar{\tilde{t}}_1$ in fb at $\sqrt{s}$ = 500 GeV as a function of $\cos^2\Theta_{\tilde{t}}$ and $M_{\tilde{t}_1}$.

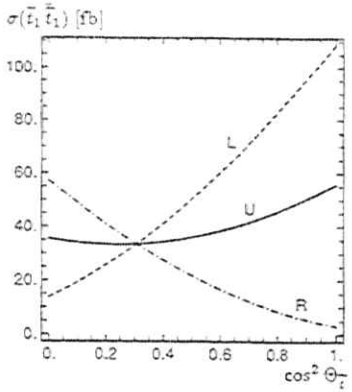

Fig. 1b: Total cross section of $e^+e^- \to \tilde{t}_1\bar{\tilde{t}}_1$ in fb at $\sqrt{s}$ = 500 GeV as a function of $\cos^2\Theta_{\tilde{t}}$, for unpolarized (U) as well as left (L) and right (R) polarized e^- beams and $M_{\tilde{t}_1}$ = 200 GeV.

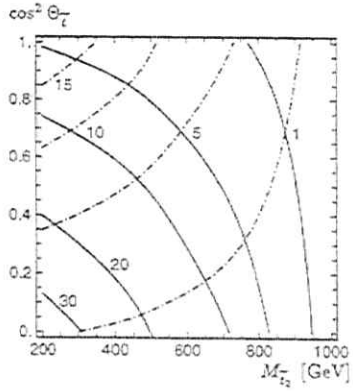

Fig. 2: Contour lines for the total cross section of $e^+e^- \to \tilde{t}_2\bar{\tilde{t}}_2$ in fb at $\sqrt{s}$ = 2 TeV as a function of $\cos^2\Theta_{\tilde{t}}$ and $M_{\tilde{t}_2}$ for left (solid lines) and right (dashdotted lines) polarized e^- beams.

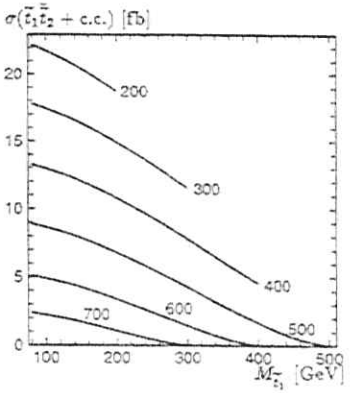

Fig. 3: Total cross section of $e^+e^- \to \tilde{t}_1\bar{\tilde{t}}_2$ + c.c. in fb at $\sqrt{s}$ = 1 TeV as a function of $M_{\tilde{t}_1}$ for $\cos^2\Theta_{\tilde{t}}$ = 0.5 and various masses of $\tilde{t}_2$.

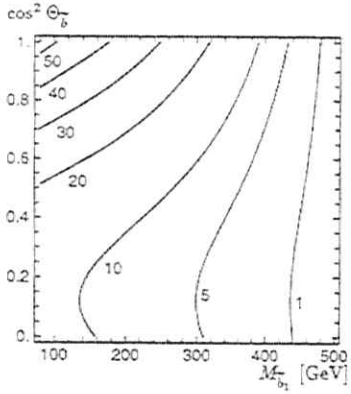

Fig. 4a: Contour lines for the total cross section of $e^+e^- \to \tilde{b}_1\bar{\tilde{b}}_1$ in fb at $\sqrt{s}$ = 1 TeV as a function of $\cos^2\Theta_{\tilde{b}}$ and $M_{\tilde{b}_1}$.

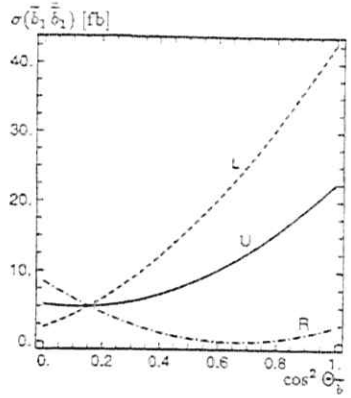

Fig. 4b: Total cross section of $e^+e^- \to \tilde{b}_1\bar{\tilde{b}}_1$ in fb at $\sqrt{s}$ = 1 TeV as a function of $\cos^2\Theta_{\tilde{b}}$, for unpolarized (U), and left (L), and right (R) polarized e^- beams for $M_{\tilde{b}_1}$ = 300 GeV.

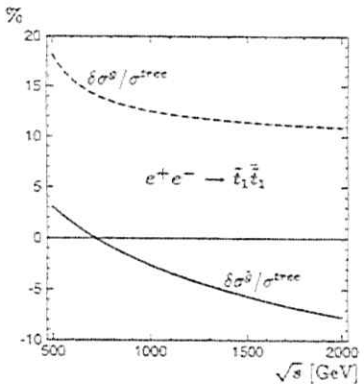

Fig. 5: SUSY-QCD corrections $\delta\sigma^a/\sigma^{tree}$ and $\delta\sigma^b/\sigma^{tree}$ for $e^+e^- \to \tilde{t}_1\bar{\tilde{t}}_1$ as a function of $\sqrt{s}$ for $\cos\Theta_{\tilde{t}}$ = 0.7, $M_{\tilde{t}_1}$ = 150 GeV, $M_{\tilde{t}_2}$ = 300 GeV and $M_{\tilde{g}}$ = 300 GeV.

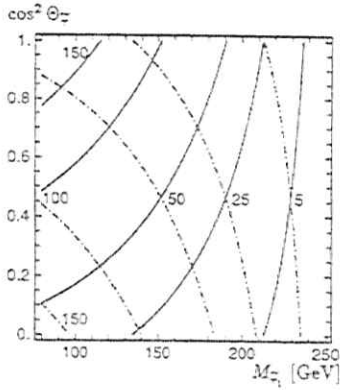

Fig. 6: Contour lines for the total cross section of $e^+e^- \to \tilde{\tau}_1\bar{\tilde{\tau}}_1$ in fb at $\sqrt{s}$ = 500 GeV as a function of $\cos^2\Theta_{\tilde{\tau}}$ and $M_{\tilde{\tau}_1}$ for left (solid lines) and right (dashdotted lines) polarized e^- beams.

e^- beams, as a function of $M_{\tilde{\tau}_1}$ and $\cos^2\Theta_{\tilde{\tau}}$ are shown in Fig. 6. For both beam polarizations these cross sections can reach values of approximately 150 fb, again exhibiting a strong dependence on the mixing angle.

3 Stop, Sbottom, and Stau Decays

The sfermions of the third generation can decay according to

$$\tilde{t}_i \to t\tilde{\chi}^0_k, \qquad b\tilde{\chi}^+_k \tag{7}$$

$$\tilde{b}_i \to b\tilde{\chi}^0_k, \qquad t\tilde{\chi}^-_k \tag{8}$$

$$\tilde{\tau}_i \to \tau\tilde{\chi}^0_k, \qquad \nu_\tau\tilde{\chi}^+_k \tag{9}$$

Due to the Yukawa terms and because of L–R mixing the decay patterns of stops, sbottoms, and staus will be different from those of the sfermions of the first two generations [20]. Stops and sbottoms may also decay into gluinos,

$$\tilde{t}_i \to t\tilde{g}, \qquad \tilde{b}_i \to b\tilde{g}, \tag{10}$$

and if these decays are kinematically allowed, then they are dominant. Otherwise, the decays (7), (8) are the most important ones. Moreover, in case of strong L–R mixing the splitting between the two mass eigenstates may be so large that the following additional decay modes are present [5]: $\tilde{t}_2 \to \tilde{t}_1 Z^0(h^0, H^0, A^0)$, $\tilde{b}_2 W^+(H^+)$, $\tilde{b}_2 \to \tilde{b}_1 Z^0(h^0, H^0, A^0)$, $\tilde{t}_1 W^-(H^-)$. The transitions $\tilde{t}_1 \to \tilde{b}_1 W^+(H^+)$ or $\tilde{b}_1 \to \tilde{t}_1 W^-(H^-)$ can occur if the mass difference is large enough.

If the $\tilde{t}_1$ is the LVSP and $m_{\tilde{\chi}^0_1} + m_b + m_W < M_{\tilde{t}_1} < m_{\tilde{\chi}^0_1} + m_t$, then the decay $\tilde{t}_1 \to b\,W^+\,\tilde{\chi}^0_1$ is important. If $M_{\tilde{t}_1} < m_{\tilde{\chi}^0_1} + m_b + m_W$ the higher-order decay $\tilde{t}_1 \to c\,\tilde{\chi}^0_1$ dominates [15]. In the parameter domain where $\tilde{t}_1 \to b\,W^+\,\tilde{\chi}^0_1$ is possible it is usually more important than $\tilde{t}_1 \to c\,\tilde{\chi}^0_1$. If $\tilde{b}_1$ or $\tilde{\tau}_1$ is the LVSP, then it decays according to $\tilde{b}_1 \to b\,\tilde{\chi}^0_1$ or $\tilde{\tau}_1 \to \tau\,\tilde{\chi}^0_1$. In the case that $M_{\tilde{\tau}_1} < M_{\tilde{t}_1}$ also $\tilde{t}_1 \to b\,\nu_\tau\,\tilde{\tau}_1$ may play a role.

In Fig. 7 a and b we show the parameter domains in the $M-\mu$ plane for the decays of $\tilde{t}_1$ and $\tilde{b}_1$, eqs. (7), (8), (10), taking $M_{\tilde{t}_1} = 400$ GeV, $\tan\beta = 2$, and $M_{\tilde{b}_1} = 400$ GeV, $\tan\beta = 30$, respectively. The parameter domains for the $\tilde{\tau}_1$ decays into neutralinos are almost identical to those of the corresponding $\tilde{b}_1$ decays, if the masses of $\tilde{\tau}_1$ and $\tilde{b}_1$ are the same.

The branching ratios for the $\tilde{t}_1$ decays as a function of the mixing angle $\cos\Theta_{\tilde{t}}$ are shown in Fig. 8a for $M_{\tilde{t}_1} = 400$ GeV, $\tan\beta = 2$, and taking $M = 150$ GeV and $\mu = 500$ GeV. The decay into $b\tilde{\chi}^+_1$ dominates near $\cos\Theta_{\tilde{t}} = \pm 1$, $\tilde{t}_1 \approx \tilde{t}_L$, whereas the decay into $t\tilde{\chi}^0_1$ dominates near $\cos\Theta_{\tilde{t}} = 0$, $\tilde{t}_1 \approx \tilde{t}_R$. $\mathrm{BR}(\tilde{t}_1 \to b\tilde{\chi}^+_1)$ vanishes for $\cos\Theta_{\tilde{t}} \approx -0.3$ because gauge coupling and Yukawa coupling terms cancel each other. On the other hand, $\mathrm{BR}(\tilde{t}_1 \to t\tilde{\chi}^0_1)$ has a maximum for $\cos\Theta_{\tilde{t}} \approx -0.3$ because the two contributions add up. Similarly, Fig. 8b exhibits the branching ratios for the $\tilde{b}_1$ decays

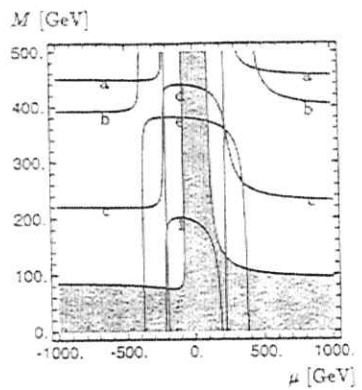

Fig. 7a: Kinematically allowed parameter domains in the (M, μ) plane for $M_{\tilde{t}_1} = 400$ GeV and $\tan\beta = 2$ for the decays: a) $\tilde{t}_1 \to t\,\tilde{\chi}^0_1$, b) $\tilde{t}_1 \to b\,\tilde{\chi}^+_1$, c) $\tilde{t}_1 \to t\,\tilde{\chi}^0_2$, d) $\tilde{t}_1 \to t\,\tilde{\chi}^0_3$, e) $\tilde{t}_1 \to b\,\tilde{\chi}^+_2$, f) $\tilde{t}_1 \to t\,\tilde{\chi}^0_4$. $\tilde{t}_1 \to c\,\tilde{\chi}^0_1$ and $\tilde{t}_1 \to b\,W^-\,\tilde{\chi}^0_1$ are allowed in the whole parameter range shown. The grey area is covered by LEP2 for $\sqrt{s} = 192$ GeV.

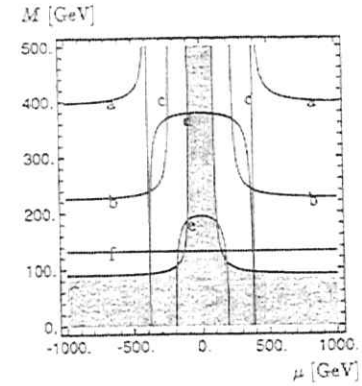

Fig. 7b: Kinematically allowed parameter domains in the (M, μ) plane for $M_{\tilde{b}_1} = 400$ GeV and $\tan\beta = 30$ for the decays: a) $\tilde{b}_1 \to b\,\tilde{\chi}^0_1$, b) $\tilde{b}_1 \to t\,\tilde{\chi}^-_1$, c) $\tilde{b}_1 \to b\,\tilde{\chi}^0_3$, d) $\tilde{b}_1 \to b\,\tilde{\chi}^0_4$, e) $\tilde{b}_1 \to t\,\tilde{\chi}^-_2$, f) $\tilde{b}_1 \to b\,\tilde{g}$. $\tilde{b}_1 \to b\,\tilde{\chi}^0_2$ is allowed in the whole parameter range shown. The grey area is covered by LEP2 for $\sqrt{s} = 192$ GeV.

as a function of $\cos\Theta_{\tilde{b}}$ for $M_{\tilde{b}_1} = 400$ GeV, $\tan\beta = 30$, $M = 150$ GeV and $\mu = 500$ GeV. Here the branching ratio for the decay into $t\tilde{\chi}^-_1$ is smaller than that of $\tilde{t}_1 \to b\tilde{\chi}^+_1$, because it has less phase space. For $\tan\beta \gtrsim 10$ the branching ratios are almost symmetric under the simultaneous interchange $\mu \to -\mu$ and $\cos\Theta_{\tilde{t}} \to -\cos\Theta_{\tilde{t}}$. Note that in supergravity models [4], for large $\tan\beta$ and large $|\mu|$, $\cos\Theta_{\tilde{b}}$ has the same sign as μ, because otherwise the parameter A_b would be too large (see eq.(3)).

In Table 1 we list the most important signatures for $\tilde{t}_1$, $\tilde{b}_1$ and $\tilde{\tau}_1$ for $\sqrt{s} = 500$ GeV. If the decays $\tilde{t}_1 \to b\,\tilde{\chi}^+_1$ or $\tilde{\tau}_1 \to \nu_\tau\,\tilde{\chi}^-_1$ occur, the $\tilde{\chi}^\pm_1$ would be discovered first and its properties would be known. This would help identify these events. The decay $\tilde{t}_1 \to b\,W^+\,\tilde{\chi}^0_1$ leads to the same final states as $\tilde{t}_1 \to b\,\tilde{\chi}^+_1$ (provided $\tilde{\chi}^+_1 \to H^+\,\tilde{\chi}^0_1$ is not allowed). From the decay $\tilde{\tau}_1 \to \tau\,\tilde{\chi}^0_1$ information about the neutralino parameters can be obtained by measuring the τ polarization, as discussed in [21].

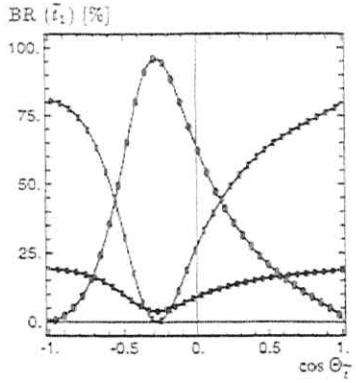

Fig. 8a: Branching ratios for the $\tilde{t}_1$ decays as a function of the mixing angle $\cos\Theta_{\tilde{t}}$ for $M_{\tilde{t}_1} = 400$ GeV, $\tan\beta = 2$, $M = 150$ GeV, and $\mu = 500$ GeV. The curves correspond to the following transitions: $\circ\ \tilde{t}_1 \to t\,\tilde{\chi}_1^0$, $\square\ \tilde{t}_1 \to t\,\tilde{\chi}_2^0$, $\blacksquare\ \tilde{t}_1 \to b\,\tilde{\chi}_1^+$.

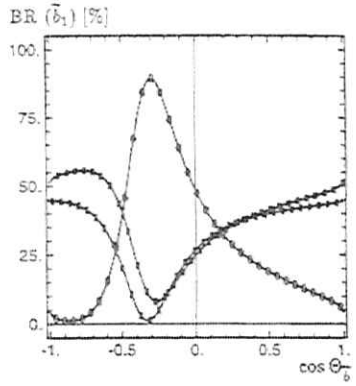

Fig. 8b: Branching ratios for the $\tilde{b}_1$ decays as a function of $\cos\Theta_{\tilde{b}}$ for $M_{\tilde{b}_1} = 400$ GeV, $\tan\beta = 30$, $M = 150$ GeV, and $\mu = 500$ GeV. The curves correspond to the following transitions: $\circ\ \tilde{b}_1 \to b\,\tilde{\chi}_1^0$, $\square\ \tilde{b}_1 \to b\,\tilde{\chi}_2^0$, $\blacksquare\ \tilde{b}_1 \to t\,\tilde{\chi}_1^-$.

	Signatures
$\tilde{t}_1 \to b\,\tilde{\chi}_1^+$	1 b-jet + 1 l^+ + $\not{p}_T$, 1 b-jet + 2 jets + $\not{p}_T$
$\tilde{t}_1 \to c\,\tilde{\chi}_1^0$	1 jet + $\not{p}_T$
$\tilde{b}_1 \to b\,\tilde{\chi}_1^0$	1 b-jet + $\not{p}_T$
$\tilde{b}_1 \to b\,\tilde{\chi}_2^0$	1 b-jet + l^+l^- + $\not{p}_T$, 1 b-jet + 2 jets + $\not{p}_T$
$\tilde{\tau}_1 \to \tau\,\tilde{\chi}_1^0$	τ + $\not{p}_T$
$\tilde{\tau}_1 \to \tau\,\tilde{\chi}_2^0$	$\tau + l^+l^-$ + $\not{p}_T$, τ + 2 jets + $\not{p}_T$
$\tilde{\tau}_1 \to \nu_\tau\,\tilde{\chi}_1^-$	l^- + $\not{p}_T$, 2 jets + $\not{p}_T$

Table 1: Expected signatures for $\tilde{t}_1$, $\tilde{b}_1$, and $\tilde{\tau}_1$ production for $\sqrt{s} = 500$ GeV. Due to pair production all combinations of the corresponding signatures may occur.

4 Stop Event Generation

In this section we describe the event generator for $e^+e^- \to \tilde{t}_1\bar{\tilde{t}}_1$ with the stop decay modes $\tilde{t}_1 \to c\tilde{\chi}_1^0$ and $\tilde{t}_1 \to b\tilde{\chi}_1^+$. The chargino decays via $\tilde{\chi}_1^+ \to W^+\tilde{\chi}_1^0$, where W^+ can be either virtual or real. The event generator is based on the calculation of the 4-momenta distributions of the stop and antistop decay products $\tilde{\chi}_1^0 c\ \tilde{\chi}_1^0\bar{c}$ and $\tilde{\chi}_1^+ b\ \tilde{\chi}_1^-\bar{b}$. The large effects of QCD corrections are included in the cross section calculation. Stop production and decay have been defined as new processes in the PYTHIA program package [22]. The event generation process includes the modelling of hadronic final states.

In the first step of the event generation, initial state photons are emitted using the program package REMT [22] which takes into account the expected stop cross section from zero to the nominal center-of-mass energy. Beamstrahlung photons are emitted using the beam parameters of the NLC 1992 design. The effective center-of-mass energy is calculated for the initial production of the 4-momenta of the final-state particles. These 4-momenta are then boosted to the lab-frame according to the momentum of the emitted photons. For the hadronization process of the $c\bar{c}$ in the $\tilde{\chi}_1^0 c\ \tilde{\chi}_1^0\bar{c}$ and of the $b\bar{b}$ in the $\tilde{\chi}_1^+ b\ \tilde{\chi}_1^-\bar{b}$ decay mode, a color string with invariant mass of the quark-antiquark-system is defined. The possible gluon emission and hadronization are performed using the Lund model of string fragmentation with the PYTHIA program package [22]. The Peterson *et al.* [23] fragmentation parameters for the c- and b-quarks are used: $\epsilon_c = 0.03$ and $\epsilon_b = 0.0035$. Finally, short-lived particles decay into their observable final state. Details of the event generator and of a stop analysis at LEP2 energies are given in [24].

5 Simulation and Selection

The investigated background reactions and their cross sections are shown in Fig. 11. They are simulated for $\mathcal{L} = 10$ fb^{-1}, and 1000 signal events are simulated in the $\tilde{\chi}_1^0 c\tilde{\chi}_1^0\bar{c}$ and $\tilde{\chi}_1^+ b\tilde{\chi}_1^-\bar{b}$ decay channels. The L3 detector at CERN including the upgrades for LEP2 served as an example for an e^+e^- 500 GeV detector. Details of the parametric detector simulation are given in [25]. An important feature is the overall hadronic energy resolution of about 7%.

In both channels, the $\tilde{\chi}_1^0$'s escape the detector and cause large missing energy. In the case $\tilde{\chi}_1^0 c\tilde{\chi}_1^0\bar{c}$, the c-quarks form mostly two acoplanar jets. A mass combination of $M_{\tilde{t}_1} = 180$ GeV and $m_{\tilde{\chi}_1^0} = 100$ GeV is investigated in detail. For $\tilde{\chi}_1^+ b\tilde{\chi}_1^-\bar{b}$ on average the visible energy is larger. In this channel, the mass combination $M_{\tilde{t}_1} = 180$ GeV, $m_{\tilde{\chi}_1^+} = 150$ GeV, and $m_{\tilde{\chi}_1^0} = 60$ GeV has been studied. Typically four jets are formed, two from the b-quarks, and two from the boosted W's.

In the first step of the event selection, unbalanced hadronic events are selected using the following selection requirements:

$$25 < \text{hadronic clusters} < 110, \qquad 0.2 < E_{\text{vis}}/\sqrt{s} < 0.7,$$

$$E_{\parallel}^{\text{imb}}/E_{\text{vis}} < 0.5, \qquad \text{Thrust} < 0.95, \qquad |\cos\theta_{\text{Thrust}}| < 0.7\ .$$

A large part of the background of back-to-back events without missing energy is rejected. Table 2 shows the number of initially produced events per $\mathcal{L} = 10$ fb^{-1} at $\sqrt{s} = 500$ GeV, and the number of events which pass this preselection. The requirement of a large number of hadronic clusters removes e^+e^-, $\mu^+\mu^-$, and most $\tau^+\tau^-$ events. The minimum energy cut reduces most of the $\gamma\gamma$ events and ensures almost

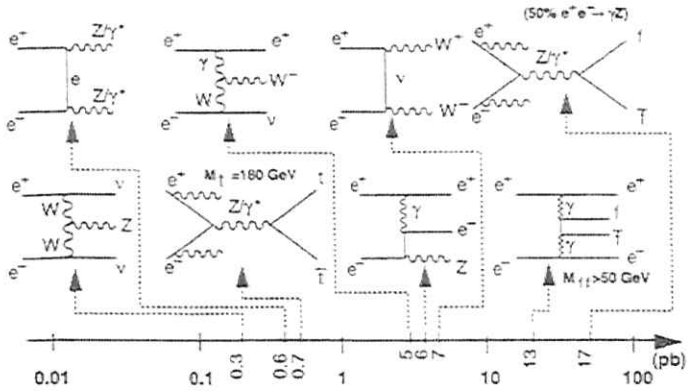

Figure 11: Background reactions and their cross sections for $\sqrt{s} = 500$ GeV.

Channel	$\tilde{\chi}_1^0 c \tilde{\chi}_1^0 \bar{c}$	$\tilde{\chi}_1^- b \tilde{\chi}_1^+ \bar{b}$	qq	WW	eWν	tt	ZZ	eeZ
Total (in 1000)	1	1	125	70	50	7	6	60
After preselection (in 1000)	0.4	0.7	1.7	2.2	3.2	1.3	0.2	0.3

Table 2: Expected events per 10 fb^{-1} at $\sqrt{s} = 500$ GeV, and number of events after the preselection as defined in the text.

100% trigger efficiency. The background from $\gamma\gamma$ events can, in addition, be strongly reduced by rejecting events where a scattered initial electron is detected at low angles. The upper energy cut reduces all standard background reactions. Beam gas events and events where much energy goes undetected along the beam axis are removed by rejection of events with very large parallel imbalance. The thrust cut removes remaining $\tau^+\tau^-$ events and reduces largely $q\bar{q}$ and Z^0Z^0 background. The $\cos\theta_{\mathrm{Thrust}}$ cut removes events where most probably much energy escaped undetected along the beam axis.

The final $\tilde{\chi}_1^0 c \tilde{\chi}_1^0 \bar{c}$ event selection is summarized in Table 3. The following cuts are applied:

- A hard upper energy cut reduces all standard background except $eW\nu$ (Fig. 12).
- Jets are clustered using the JADE algorithm. The y-cut value is optimized to obtain two jets for the signal.
- Semileptonic decays of the top quark can induce missing energy. These events are partly removed by requiring no isolated electron or muon.
- Events with large longitudinal energy imbalance are removed where probably much energy escaped undetected along the beam axis.

- The invariant mass of the two jets is required to be larger than 120 GeV to remove almost entirely $eW\nu$ events (Fig. 13).
- The acoplanarity angle is defined as the angle between the jets in the plane perpendicular to the beam axis. A maximum value of 2.9 rad is important to reduce the remaining background.

The result of this study is 4.3% detection efficiency and 9 background events. A detection confidence level of 3σ (99.73%) is expected for a cross section of 23 fb. Expected signal and background are shown in Fig. 16.

Channel	$\tilde{\chi}_1^0 c \tilde{\chi}_1^0 \bar{c}$	qq	WW	eWν	tt	ZZ	eeZ
Total (in 1000)	1	125	70	50	7	6	60
After Preselection	391	1652	2163	3185	1259	182	318
$E_{\mathrm{vis}}/\sqrt{s} < 0.4$	332	**202**	**285**	3032	**70**	4	**98**
Njet = 2	293	172	182	2892	**17**	3	72
No isolated e or μ	218	152	**98**	2757	**5**	3	**9**
$E_{\parallel}^{\mathrm{imb}}/E_{\mathrm{vis}} < 0.3$	185	**101**	70	2049	5	2	4
Invariant mass of jets>120GeV	52	**25**	**12**	**7**	1	0	0
Acoplanarity < 2.9rad	43	0	5	3	1	0	0

Table 3: Final event selection cuts, expected signal efficiencies, and the number of expected background events. Bold face numbers indicate major background reductions.

The final $\tilde{\chi}_1^- b \tilde{\chi}_1^+ \bar{b}$ event selection is summarized in Table 4. Here the cuts are:

- A hard lower energy cut reduces most of the $eW\nu$ background.
- Topologies with back-to-back jets are reduced by an upper cut on the event thrust (Fig. 14).
- A lower cut on the number of hadronic clusters reduces efficiently low-multiplicity background final states (Fig. 15).
- Jets are clustered using the JADE algorithm. The y-cut value is optimized to obtain four jets for the signal.
- Events with an isolated electron or muon are rejected.
- An upper cut on the visible energy reduces $q\bar{q}$, W^+W^-, and $t\bar{t}$ background.
- Finally, the remaining $t\bar{t}$ background events are reduced by requiring less than 30% perpendicular energy imbalance.

Concerning the number of b-quarks per event, the decay $\tilde{\chi}_1^- b \tilde{\chi}_1^+ \bar{b} \to W^+ \tilde{\chi}_1^0 b W^- \tilde{\chi}_1^0 \bar{b}$ leads to the same final states as expected for $t\bar{t}$ background. Therefore, the tagging of b-quarks has not proved to be efficient to reduce this background.

The result of this study is 4.5% detection efficiency and 8 background events. A detection confidence level of 3σ (99.73%) is expected for a cross section of 19 fb. Expected signal and background are shown in Fig. 16.

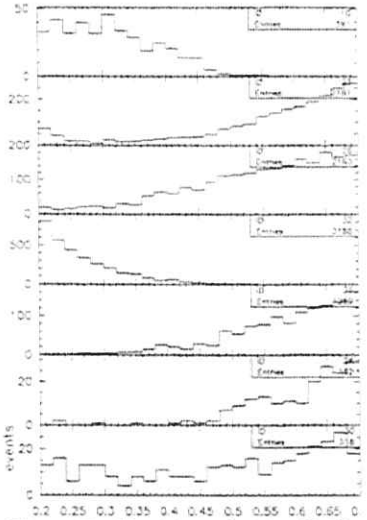

Figure 12: $E_{vis}/\sqrt{s} < 0.4$ for $\tilde{\chi}_1^0 c\tilde{\chi}_1^0\bar{c}$, qq, WW, eW$\nu$, tt, ZZ, eeZ.

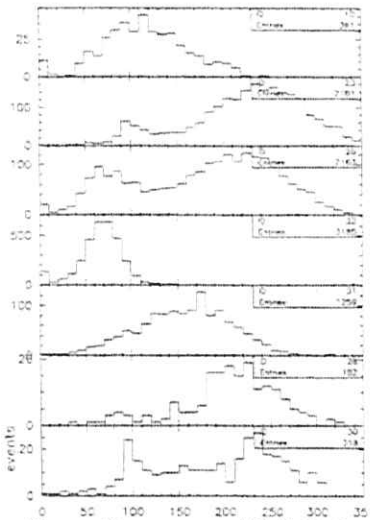

Figure 13: $m_{inv} > 120$ GeV for $\tilde{\chi}_1^0 c\tilde{\chi}_1^0\bar{c}$, qq, WW, eW$\nu$, tt, ZZ, eeZ.

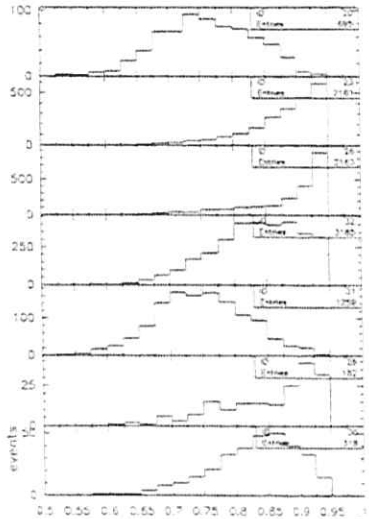

Figure 14: Thrust < 0.85 for $\tilde{\chi}_1^+ b\tilde{\chi}_1^-\bar{b}$, qq, WW, eW$\nu$, tt, ZZ, eeZ.

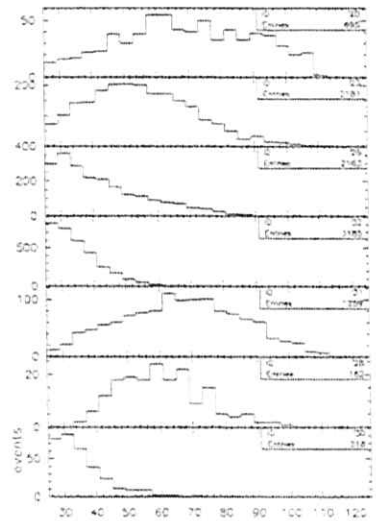

Figure 15: Ncluster ≥ 60 for $\tilde{\chi}_1^+ b\tilde{\chi}_1^-\bar{b}$, qq, WW, eW$\nu$, tt, ZZ, eeZ.

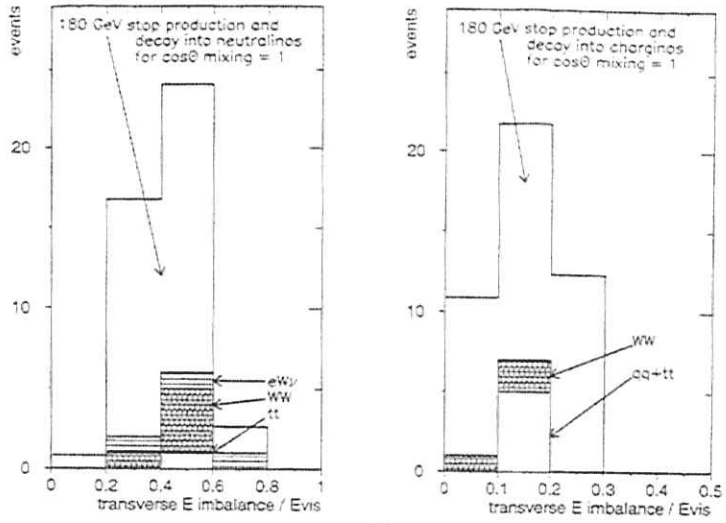

Figure 16: Left: Sensitivity for an $e^+e^- \to \tilde{t}_1\bar{\tilde{t}}_1 \to \tilde{\chi}_1^0 c\tilde{\chi}_1^0\bar{c}$ signal. Open histograms show the simulated signal, solid and hatched histograms show the remaining background after all selection cuts are applied. Right: Sensitivity for an $e^+e^- \to \tilde{t}_1\bar{\tilde{t}}_1 \to \tilde{\chi}_1^+ b\tilde{\chi}_1^-\bar{b}$ signal.

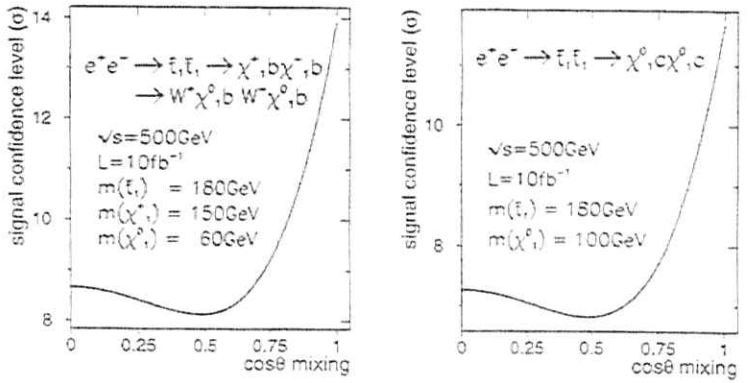

Figure 17: Detection confidence levels. Left: $\tilde{\chi}_1^+ b\tilde{\chi}_1^-\bar{b}$ channel. Right: $\tilde{\chi}_1^0 c\tilde{\chi}_1^0\bar{c}$ channel.

Channel	$\tilde{\chi}_1^+ b \tilde{\chi}_1^- \bar{b}$	qq	WW	eWν	tt	ZZ	eeZ
Total (in 1000)	1	125	70	50	7	6	60
After Preselection	695	1652	2163	3185	1259	182	318
$E_{vis}/\sqrt{s} > 0.35$	610	1494	2011	**337**	1234	178	239
Thrust < 0.85	536	**326**	**420**	**24**	1141	**69**	137
Ncluster ≥ 60	399	195	134	**0**	769	41	3
Njet $= 4$	211	53	72	0	432	22	0
No isolated e or μ	99	41	49	0	**105**	16	0
$E_{vis}/\sqrt{s} < 0.55$	57	3	8	0	**23**	0	0
$E_\perp^{miss}/E_{vis} < 0.3$	45	1	3	0	4	0	0

Table 4: Final event selection cuts, expected signal efficiencies, and the number of expected background events. Bold face numbers indicate major background reductions.

At a future e^+e^- collider with $\sqrt{s} = 500$ GeV, a large discovery potential for scalar top quarks is already expected within one year of data-taking ($\mathcal{L} = 10$ fb^{-1}). Detector performances known from LEP detectors result in good background reduction. Full hermeticity of the detector is essential.

The confidence level for discovering a signal is shown in Fig. 17, where the confidence level is given in $\sigma = N_{\text{expected}}/\sqrt{N_{\text{background}}}$. The sensitivity is sufficient to discover a 200 GeV stop independently of the values of the mixing angle with 3σ in both $\tilde{\chi}_1^0 c$ and $\tilde{\chi}_1^+ b$ decay modes for the investigated neutralino and chargino mass combinations. A complete set of mass combinations remains to be studied. Beam polarization could be crucial for determining the stop mass after a discovery.

6 Summary

In this contribution we have discussed the production of stop, sbottom, and stau pairs in e^+e^- annihilation in the energy range $\sqrt{s} = 500$ GeV to 2 TeV. We have presented numerical predictions within the Minimal Supersymmetric Standard Model for the production cross sections and the decay rates and analyzed their SUSY parameter dependence. If $\tan\beta \gtrsim 10$, not only the t Yukawa terms, but also the b and τ Yukawa terms have important effects. The production cross sections as well as the decay rates of stops, sbottoms and staus depend in a characteristic way on the mixing angles.

A Monte Carlo study of $e^+e^- \to \tilde{t}_1 \bar{\tilde{t}}_1$ at $\sqrt{s} = 500$ GeV with the decays $\tilde{t}_1 \to c\tilde{\chi}_1^0$ and $\tilde{t}_1 \to b\tilde{\chi}_1^+$ has been performed for $M_{\tilde{t}_1} = 180$ GeV, $M_{\tilde{\chi}_1^0} = 100$ GeV, and $M_{\tilde{t}_1} = 180$ GeV, $M_{\tilde{\chi}_1^\pm} = 150$ GeV, $M_{\tilde{\chi}_1^0} = 60$ GeV, respectively. A suitable set of kinematical cuts has been applied to reduce the known background reactions. Detection confidence levels as a funtion of $\cos\Theta_{\tilde{t}}$ have been given. In summary, an e^+e^- collider is an ideal machine for detecting and studying scalar top and bottom quarks and scalar tau leptons.

Acknowledgements

We thank our colleagues at this Workshop for many useful discussions. This work was supported by the "Fonds zur Förderung der wissenschaftlichen Forschung" of Austria, project no. P10843-PHY.

References

[1] J. Ellis, S. Rudaz, Phys. Lett. B128 (1983) 248

[2] G. Altarelli, R. Rückl, Phys. Lett. B144 (1984) 126
I. Bigi, S. Rudaz, Phys. Lett. B153 (1985) 335

[3] W. de Boer, R. Ehret, D. I. Kazakov, Phys. Lett. B334 (1994) 220
W. de Boer et al., these proceedings

[4] See for a review e.g., M. Drees and S.P. Martin, Wisconsin preprint, MADPH-95-879

[5] A. Bartl, W. Majerotto, W. Porod, Z. Phys. C64 (1994) 499

[6] M. Fukugita, H. Murayama, M. Yamaguchi, T. Yanagida, Phys. Rev. Lett. 72 (1994) 3009
T. Kon, T. Nonaka, preprint ITP-SU-94/02, RUP-94-06
J. D. Wells, G. L. Kane, Phys. Rev. Lett. 76 (1996) 869
A. Brignole, F. Feruglio, F. Zwirner, CERN-TH/95-340

[7] H.E. Haber, G.L. Kane, Phys. Rep. 117 (1985) 75

[8] J. F. Gunion, H. E. Haber, Nucl. Phys. B272 (1986) 1

[9] J.-F. Grivaz, Rapporteur Talk, International Europhysics Conference on High Energy Physics, Brussels, 1995

[10] OPAL Collaboration, R. Akers et al., Phys. Lett. B337 (1994) 207
ALEPH Collaboration, Contribution #0416 to the International Europhysics Conference on High Energy Physics, Brussels, 1995

[11] ALEPH Collaboration, CERN-PPE/96-10, Jan. 1996
H. Nowak and A. Sopczak, L3 Note 1887, Jan. 1996
S. Asai and S. Komamiya, OPAL Physics Note PN-205, Feb. 1996

[12] D0 Collaboration, FERMILAB-Conf-95/393-E, Proc. of the 10th Topcial Workshop on "Proton–Antiproton Collider Physics", FNAL (1995)

[13] M. Drees, K. I. Hikasa, Phys. Lett. B252 (1990) 127

[14] A. Bartl, H. Eberl, W. Majerotto, W. Porod, Proc. of the US-Polish Workshop "Physics from Planck Scale to Electroweak Scale", Warshsaw 1994, p. 370, World Scientific (P. Nath, T. Taylor, S. Pokorski eds.)

[15] K. I. Hikasa, M. Kobayashi, Phys. Rev. D36 (1987) 724

[16] A. Bartl, H. Eberl, S. Kraml, W. Majerotto, W. Porod, preprint UWThPh-1996-18, HEPHY-PUB 642/96

[17] H. Eberl, A. Bartl, W. Majerotto, preprint UWThPh-1996-6, HEPHY-PUB 640/96

[18] W. Beenakker, R. Höpker, P. M. Zerwas, Phys. Lett. B349 (1995) 463

[19] See e.g. M. Peskin, 17th SLAC Summer Institute, SLAC-PUB-5210 (1990)

[20] A. Bartl, W. Majerotto, B. Mösslacher, N. Oshimo, S. Stippel, Phys. Rev. D43 (1991) 2214

[21] M. Nojiri, Phys. Rev. D51 (1995) 6281

[22] T. Sjöstrand, Comp. Phys. Comm. 82 (1994) 74

[23] C. Peterson *et al.*, Phys. Rev. D27 (1983) 105

[24] A. Sopczak, L3 note #1860 (1995), to be published in the LEP2 CERN Workshop report

[25] A. Sopczak, Proc. Workshop on physics and experiments with linear e^+e^- colliders, Waikoloa, Hawaii, USA, 26–30 April 1993 (World Scientific) p. 666; Z. Phys. C65 (1995) 449

FERMION VIRTUAL EFFECTS IN $e^+e^- \to W^+W^-$ CROSS SECTION

A. CULATTI[1], G. DEGRASSI†, F. FERUGLIO†, A. MASIERO‡,
S. RIGOLIN†, L. SILVESTRINI*, A. VICINI†

† *Dipartimento di Fisica - Università di Padova e INFN Padova, Italy*
‡ *Dipartimento di Fisica - Università di Perugia e INFN Perugia, Italy*
* *Dipartimento di Fisica - Università di Roma II "Tor Vergata" e INFN Roma II, Italy*

ABSTRACT

We analyze the contribution of new heavy virtual fermions to the $e^+e^- \to W^+W^-$ cross section. We find that there exists a relevant interplay between trilinear and oblique corrections. The result strongly depends on the chiral or vector-like nature of the new fermions. As for the chiral case we consider sequential fermions: one obtains substantial deviation from the Standard model prediction, making the effect possibly detectable at $\sqrt{s} = 500$ or 1000 GeV linear colliders. As an example for the vector-like case we take a SUSY extension with heavy charginos and neutralinos: due to cancellations, the final effect turns out to be negligible.

We present here a study of virtual effects from new physics in the cross-section for $e^+e^- \to W^+W^-$. This analysis has been motivated by the following questions. What room is left for deviations with respect to the SM predictions, once the constraints coming from the LEP1 results have been properly accounted for? Are these deviations entirely due to the appearance of anomalous trilinear vector-boson couplings, as generally assumed? Is there any role played by the so-called oblique corrections?

To deal with these questions we have focused on two simple SM extensions:

- Model 1: **the SM plus heavy chiral fermions.** In particular we consider an extra doublet of heavy quarks, exact replica of the SM counterparts, as far as their electroweak and strong quantum numbers are concerned;
- Model 2: **the SM plus heavy vector-like fermions.** As an example we take the Minimal Supersymmetric Standard Model (MSSM) with heavy (above the production threshold) electroweak gauginos and higgsinos, and very heavy (decoupled) squarks, sleptons and additional higgses.

In both models the 1-loop corrections to the process in question are concentrated in vector-bosons self-energies and three-point functions, which makes it possible to analyze the interplay between the two contributions. Box corrections are obviously absent in the first model, while they are negligibly small in the second case, provided that the scalar masses are sufficiently large. Then the only relevant contributions remain those of gauginos and higgsinos.

[1] Present address: Dep. de Fisica Teorica y del Cosmos, Universidad de Granada, Spain.

The constraints coming from LEP1 results are quite different in the two models. A mass splitting between the two new quarks, whose left-handed components are partners of a common $SU(2)_L$ doublet, results in a potentially large contribution to the ϵ_1 parameter. To avoid disagreement with the experimental result [1], we will consider the case of degenerate quarks (a detailed discussion concerning this point is provided in [2]). A more stringent limitation comes from the ϵ_3 variable, which depends mildly on the quark masses. Each new degenerate quark doublet contributes to ϵ_3 with the positive amount

$$\delta\epsilon_3 = \frac{G_F m_W^2}{4\pi^2\sqrt{2}} \simeq 1.3 \cdot 10^{-3} \qquad (1)$$

For $m_t = 175\ GeV$ and $m_H = 100\ GeV$, a single new coloured doublet (with the possible addition of a lepton doublet) saturates the present 2σ upper bound on ϵ_3, and additional chiral doublets beyond the multiplet considered here are experimentally ruled out.

On the contrary, the version of the MSSM here analyzed easily respects the constraints from LEP1. Indeed contributions to the ϵ's variables come in inverse power of the gaugino's and higgsino's masses and they turn out to be numerically quite small, within the experimental bound. For practical purposes we have considered the case of degenerate electroweak gauginos of mass M and degenerate higgsinos of mass μ. This is the case when the mixing terms among gauginos and higgsinos are much smaller compared to the SUSY breaking gaugino mass term M and the supersymmetric μ contribution coming from the $H_1 H_2$ term in the superpotential.

After the inclusion of the 1-loop corrections due to the new particles and of the appropriate counterterms, the reduced amplitude for the process at hand reads, following the conventions of ref. [4]:

- $\Delta\lambda = \pm 2$

$$\tilde{\mathcal{M}} = -\frac{\sqrt{2}}{\sin^2\theta}\delta_{\Delta\sigma,-1}\left[1 - \frac{\sin^2\bar{\theta}}{\cos 2\bar{\theta}}\Delta r_W - \epsilon_6\right]\frac{1}{1+\beta^2-2\beta\cos\Theta} \qquad (2)$$

- $\Delta\lambda = \leq 1$

$$\begin{aligned}
\tilde{\mathcal{M}}^\gamma &= -\beta\delta_{|\Delta\sigma|,1}\left[1+\Delta\alpha(s)\right]\left[A^\gamma_{\lambda\bar{\lambda}} + \delta A^\gamma_{\lambda\bar{\lambda}}(s)\right] \\
\tilde{\mathcal{M}}^Z &= \beta\frac{s}{s-m_Z^2}\left[\delta_{\Delta\sigma,1} - \frac{\delta_{\Delta\sigma,-1}}{2\sin^2\theta(1-\Delta k(s))}\right] \\
&\quad \left[1+\Delta\rho(s) + \frac{\cos 2\bar{\theta}}{\cos^2\bar{\theta}}\Delta k(s)\right]\left[A^Z_{\lambda\bar{\lambda}} + \delta A^Z_{\lambda\bar{\lambda}}(s)\right]
\end{aligned}$$

$\lambda\bar{\lambda}$	$A^{\gamma}_{\lambda\bar{\lambda}} = A^{Z}_{\lambda\bar{\lambda}}$	$B_{\lambda\bar{\lambda}}$	$C_{\lambda\bar{\lambda}}$
$++\,,\ --$	1	1	$1/\gamma^2$
$-0\,,\ 0-$	2γ	2γ	$2(1-\beta)/\gamma$
$0-\,,\ -0$	2γ	2γ	$2(1-\beta)/\gamma$
00	$2\gamma^2+1$	$2\gamma^2$	$2/\gamma^2$

Table 1: Standard Model coefficients expressed in terms of $\gamma^2 = s/4m_W^2$.

$$\bar{\mathcal{M}}^{\nu} = \frac{\delta_{\Delta\sigma,-1}}{2\sin^2\bar{\theta}\,\beta}\left[1-\frac{\sin^2\bar{\theta}}{\cos 2\bar{\theta}}\Delta r_W - e_6\right]\left[B_{\lambda\bar{\lambda}} - \frac{1}{1+\beta^2-2\beta\cos\Theta}C_{\lambda\bar{\lambda}}\right] \quad (3)$$

In eq. (3) the contribution from photon, Z and ν exchange are shown separately, $\beta = (1-4m_W^2/s)^{1/2}$, Θ is the scattering angle of W^- with respect to e^- in the e^+e^- c.m. frame: σ, $\bar{\sigma}$, λ, $\bar{\lambda}$ are the helicities for e^-, e^+, W^- and W^+, respectively; $\Delta\sigma = \sigma - \bar{\sigma}$; $A^{\gamma}_{\lambda\bar{\lambda}}$, $A^{Z}_{\lambda\bar{\lambda}}$, $B_{\lambda\bar{\lambda}}$ and $C_{\lambda\bar{\lambda}}$ are tree-level SM coefficients listed in Table 1; $\Delta\alpha(s)$, $\Delta\bar{k}(s)$, $\Delta\rho(s)$, Δr_W and e_6 are finite self-energy corrections [3, 5], given in the Appendix where also the effective weak angle $\bar{\theta}$ is defined. Finally, $\delta A^{\gamma}_{\lambda\bar{\lambda}}$ and $\delta A^{Z}_{\lambda\bar{\lambda}}$ represent the corrections to the trilinear gauge boson vertices. For the models considered, they can be expressed in terms of the P-invariant form factors $\delta f_i^{\gamma,Z}$ $(i=1,2,3,4)$ according to the relations:

$$\begin{aligned}
\delta A^{V}_{+-} &= \delta A^{V}_{--} = \delta f_1^V \\
\delta A^{V}_{+0} &= \delta A^{V}_{0-} = \gamma(\delta f_3^V - i\delta f_4^V) \\
\delta A^{V}_{0-} &= \delta A^{V}_{+0} = \gamma(\delta f_3^V + i\delta f_4^V) \\
\delta A^{V}_{00} &= \gamma^2\left[-(1+\beta^2)\delta f_1^V + 4\gamma^2\beta^2\delta f_2^V + 2\delta f_3^V\right]
\end{aligned} \quad (4)$$

Here δf_i^V $(i=1,2,3,4)$ $(V=\gamma,Z)$ includes both the contribution coming from the 1-loop correction to the vertex VWW and the wave-function renormalization of the external W legs, taken on the mass-shell. This makes the terms δf_i^V finite.

Some comments are in order. The tree-level SM amplitudes are recovered from the above formulae by taking $\Delta\alpha(s) = \Delta\bar{k}(s) = \Delta\rho(s) = \Delta r_W = e_6 = \delta A^{\gamma}_{\lambda\bar{\lambda}} = \delta A^{Z}_{\lambda\bar{\lambda}} = 0$. In the high-energy limit, the individual SM amplitudes from photon, Z and ν exchange are proportional to γ^2 when both the W are longitudinally polarized (LL) and proportional to γ when one W is longitudinal and the other is trasverse (TL). The cancellation of the γ^2 and γ terms in the overall amplitude is guaranteed by the tree-level, asymptotic relation $A^{\gamma}_{\lambda\bar{\lambda}} = A^{Z}_{\lambda\bar{\lambda}} = B_{\lambda\bar{\lambda}}$. When one-loop contributions are included, one has new terms proportional to γ^2 and γ (see $\delta A^{\gamma}_{\lambda\bar{\lambda}}$ and $\delta A^{Z}_{\lambda\bar{\lambda}}$ in eq. (4)) and the cancellation of those terms in the high-energy limit entails relations among oblique and vertex corrections. We have explicitly checked that in all cases considered, this cancellation does take place. We stress that omitting, for instance, the gauge boson self-energies such

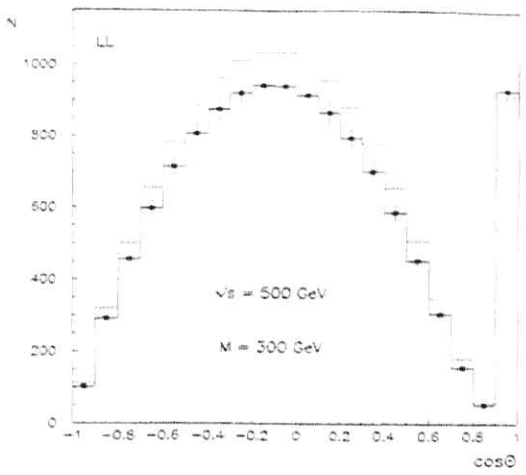

Figure 1: Number of W^+W^- events per bin versus $\cos\Theta$ at $s = (500\ \mathrm{GeV})^2$ in the logitudinal-longitudinal channel, taking $M = 300$ GeV and assuming a luminosity of 20 fb^{-1}.

cancellation does not occur any longer and the resulting amplitudes violate the requirement of perturbative unitarity.

On the other hand, one of the possibilities one can think of to have appreciable deviations in the cross-section is to delay the behaviour required by unitarity. This may happen if in the energy window $m_W << \sqrt{s} \leq 2M$ (M denoting the mass of the new particles) the above cancellation is less efficient and terms proportional to positive power of γ survive in the total amplitude. If γ is sufficiently large, then a sizeable deviation from the SM prediction is not unconceivable.

We now come to the quantitative discussion.

• Model 1: **Chiral fermions.**

In fig. 1 we plot N, the number of W^+W^- events per bin, versus Θ at $\sqrt{s} = 500$ GeV in the channel LL, taking $M = 300$ GeV and assuming a luminosity of 20 fb^{-1}.

The error bars refer to the statistical error, the full line denotes the SM expectation at tree level[2], while the dashed line gives the prediction for model 1.

We notice a clear indication of a significant signal, fully consistent with

[2]SM corrections shift both curves in fig. 1 by the same amount. Hence, although they change the number N, they do not affect our result concerning the size of the deviation due to the presence of new physics.

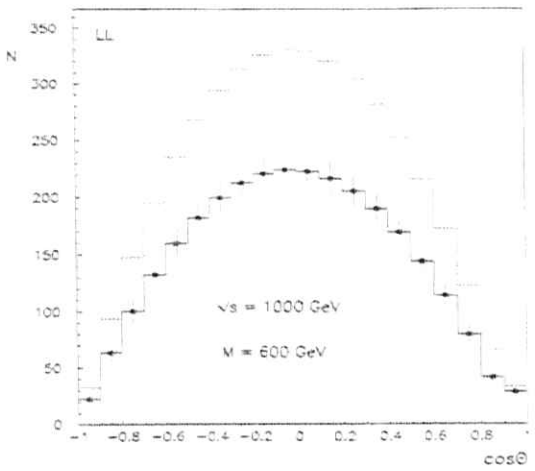

Figure 2: Number of W^+W^- events per bin versus $\cos\Theta$ at $s = (1000\,\mathrm{GeV})^2$ in the logitudinal-longitudinal channel, taking $M = 600$ GeV and assuming a luminosity of 100 fb^{-1}.

present experimental bounds. The departure from the SM prediction [6] becomes even more conspicuous for larger $\sqrt{s}$. In fig.2 we report the result for $\sqrt{s} = 1000$ GeV, $M = 600$ GeV and a luminosity of 100 fb^{-1}.

For $\cos\Theta$ not close to 1, and in the limit $m_W << M, \sqrt{s}$ we have derived the following analytical expression for the relative deviation ΔR_{LL}:

$$\Delta R_{LL} = |1 + 2K|^2 - 1 \tag{5}$$

$$K = \frac{g^2}{16\pi^2} N_c \left(\frac{M^2}{s}\right) \cdot F\left(\frac{M^2}{s}\right) \cdot \frac{s}{m_W^2} \tag{6}$$

$$F(z) = 1 - \sqrt{4z-1}\; ArcTan \frac{1}{\sqrt{4z-1}}, \tag{7}$$

where ΔR is defined as

$$\Delta R = \frac{\left(\frac{d\sigma}{d\cos\Theta}\right) - \left(\frac{d\sigma}{d\cos\Theta}\right)_{SM}}{\left(\frac{d\sigma}{d\cos\Theta}\right)_{SM}} \tag{8}$$

For $s >> M^2$, F grows only logarithmically and unitarity is respected. When $M^2 >> s$, $F \simeq s/12M^2$ and the decoupling property is violated, as one

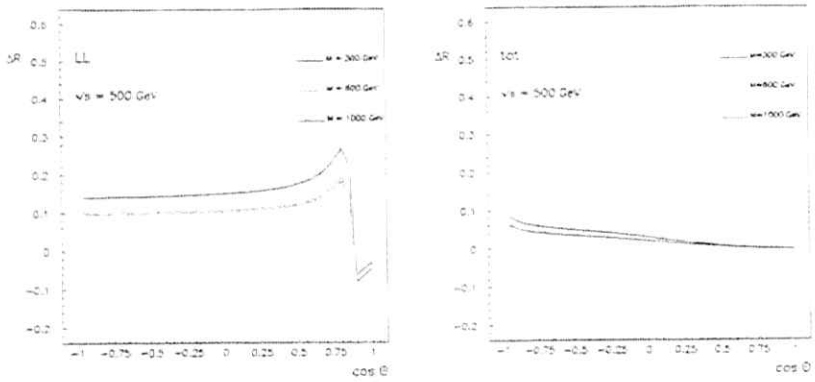

Figure 3: Relative deviation ΔR versus $\cos\Theta$ in the LL polarization channel and for the unpolarized cross section (tot) at $s = (500\,\mathrm{GeV})^2$ and $M = 300, 600, 1000$ GeV for model 1.

expects in the case of heavy chiral fermions. In the range of energies we are interested in, $m_W << \sqrt{s} \leq 2M$, K is of order $G_F M^2$, which explains the magnitude of the effect exhibited in fig. 1 and 2. A similar behaviour is also exhibited by the TL channel. Indeed, the absolute deviation in the TL channel is of $O(\gamma)$, but an additional γ factor comes from the SM cross section in the denominator of ΔR. In fig. 3 we depict the quantity ΔR as a function of $cos\Theta$ for LL channel and for the unpolarized cross section at $\sqrt{s} = 500$ GeV. Notice that the effect which is so large in the LL channel for all the angles essentially disappears in the unpolarized cross section for $cos\Theta \simeq 1$ where bigger is the number of events expected. This makes it clear that for the observation of the effect under discussion good identification of the W polarization and large luminosity are essential.

• Model 2: **Vector-like fermions.**

In this case the deviations at $\sqrt{s} = 500$ GeV or even higher energies reach at most a few per mille making it questionable to have a chance at all to observe the effect [7]. The analytic espressions for ΔR both in the LL and in the TL channel, in the limit $m_W << M, \sqrt{s}$, are vanishing, showing that in the case of gauginos or higgsinos, which have vector-like coupling, no unitarity delay takes place. This is in agreement with the decoupling theorem [8].

To exemplify the danger of including in the cross-section only the contribution of trilinear anomalous gauge couplings, we have computed the ΔR_{LL} ratio at $\sqrt{s} = 500$ GeV, for model 2, $M = 300$ GeV and $\mu >> M$, by leaving out the contribution from the vector boson self-energies. Due to the improvident omission

of an essential part of the 1-loop correction, one gets an irrealistic $\Delta R_{LL} \simeq -0.2$, with failure of unitarity when higher energies are considered.

Appendix

The quantities $\Delta\alpha(s)$, $\Delta k(s)$, $\Delta\rho(s)$, Δr_W and e_6 appearing in eqs. (2) and (3) are defined by the following relations in terms of the unrenormalized vector-boson vacuum polarizations:

$$\begin{aligned}
e_1 &= \frac{\Pi_{ZZ}(0)}{m_Z^2} - \frac{\Pi_{WW}(0)}{m_W^2} \\
e_2 &= \Pi'_{WW}(0) - \cos^2\bar\theta\ \Pi'_{ZZ}(0) - 2\cos\bar\theta\sin\bar\theta\ \frac{\Pi_{\gamma Z}(m_Z^2)}{m_Z^2} \\
&\quad - \sin^2\bar\theta\ \Pi'_{\gamma\gamma}(m_Z^2) \\
e_3(s) &= \frac{\cos\bar\theta}{\sin\bar\theta}\left\{\sin\bar\theta\cos\bar\theta\left[\Pi'_{\gamma\gamma}(m_Z^2) - \Pi'_{ZZ}(0)\right] + \cos 2\bar\theta\ \frac{\Pi_{\gamma Z}(s)}{s}\right\} \\
e_4 &= \Pi'_{\gamma\gamma}(0) - \Pi'_{\gamma\gamma}(m_Z^2) \\
e_5(s) &= \Pi'_{ZZ}(s) - \Pi'_{ZZ}(0) \\
e_6 &= \Pi'_{WW}(m_W^2) - \Pi'_{WW}(0) \qquad (9) \\
\Delta\alpha(s) &= \Pi'_{\gamma\gamma}(0) - \Pi'_{\gamma\gamma}(s) \\
\Delta k(s) &= -\frac{\cos^2\bar\theta}{\cos 2\bar\theta}\,(e_1 - e_4) + \frac{1}{\cos 2\bar\theta}\,e_5(s) \\
\Delta\rho(s) &= e_1 - e_5(s) \\
\Delta r_W &= -\frac{\cos^2\bar\theta}{\sin^2\bar\theta}\,e_1 + \frac{\cos 2\bar\theta}{\sin^2\bar\theta}\,e_2 - 2\,e_3(m_Z^2) - e_4 \qquad (10) \\
\epsilon_1 &= e_1 - e_5(m_Z^2) \\
\epsilon_2 &= e_2 - \sin^2\bar\theta\,e_4 - \cos^2\bar\theta\,e_5(m_Z^2) \\
\epsilon_3 &= e_3(m_Z^2) - \cos^2\bar\theta\,e_4 - \cos^2\bar\theta\,e_5(m_Z^2) \qquad (11)
\end{aligned}$$

with

$$\Pi'_{VV}(s) = \frac{\Pi_{VV}(s) - \Pi_{VV}(m_V^2)}{(s - m_V^2)} \qquad \text{with} \quad (V = \gamma, Z, W) \qquad (12)$$

If $s = m_Z^2$ then $\Delta\alpha(s)$, $\Delta k(s)$, $\Delta\rho(s)$ coincides with the corrections $\Delta\alpha$, Δk, $\Delta\rho$ which characterize the electroweak observables at the Z resonance. Finally, the effective weak angle $\bar\theta$ is defined by:

$$\sin^2\bar\theta = \frac{1}{2} - \sqrt{\frac{1}{4} - \frac{\pi\alpha(m_Z^2)}{\sqrt{2}G_F m_Z^2}} \qquad (13)$$

References

[1] G. Altarelli, talk given at the meeting on LEP physics "GELEP 1995", Genova, April 10-12, 1995.

[2] F. Feruglio, A. Masiero, S. Rigolin, R. Strocchi, *Phys Lett.* **B355** (1995) 329.

[3] R. Barbieri, F. Caravaglios and M. Frigeni, *Phys. Lett.* **B279** (1992) 169.

[4] K.J.F. Gaemers, G.J. Gounaris, *Z. Phys.* **C1** (1979) 259.
K. Hagiwara, K. Hikasa, R. Peccei and D. Zeppenfeld, *Nucl. Phys.* **B282** (1987) 253.

[5] G. Altarelli and R. Barbieri, *Phys. Lett.* **B253** (1991) 161.
G. Altarelli, R. Barbieri and S. Jadach, *Nucl. Phys.* **B369** (1992) 3.
G. Altarelli, R. Barbieri and F. Caravaglios, *Nucl. Phys.* **B405** (1993) 3 and preprint CERN-TH.6859/93.

[6] E.N. Argyres, C.G. Papadopoulos, *Phys. Lett.* **B263** (1991) 298.
E.N. Argyres, G. Katsilieris, A.B. Lahanas, C.G. Papadopoulos, V.C. Spanos, *Nucl. Phys.* **B391** (1993) 23.
J. Fleischer, J.L. Kneur, K. Kolodziej, M. Kuroda, D. Schildknecht, *Nucl. Phys.* **B378** (1992) 443. *Nucl. Phys.* **B426** (1994) 246.

[7] A.B. Lahanas, V.C. Spanos, *Phys. Lett.* **B334** (1994) 378.
A.B. Lahanas, V.C. Spanos, hep-ph 9504340.
A. Culatti, *Z. Phys.* **C65** (1995) 537

[8] T. Appelquist and J. Carazzone, *Phys. Rev.* **D11** (1975) 2856.

QCD Corrections to the Decays $H^+ \to t\bar{b}$ and $H^+ \to \tilde{t}\bar{\tilde{b}}$ in the MSSM

A. Bartl,[1] H. Eberl,[2] K. Hidaka,[3] T. Kon,[4]
W. Majerotto[2], and Y. Yamada[5*]

[1] *Institut für Theoretische Physik, Universität Wien, A-1090 Vienna, Austria*
[2] *Institut für Hochenergiephysik der Österreichische Akademie der Wissenschaften, A-1050 Vienna, Austria*
[3] *Department of Physics, Tokyo Gakugei University, Koganei, Tokyo 184, Japan*
[4] *Faculty of Engineering, Seikei University, Musashino, Tokyo 180, Japan*
[5] *Theory Group, National Laboratory for High Energy Physics (KEK), Tsukuba, Ibaraki 305, Japan*

Abstract

We calculate the $O(\alpha_s)$ QCD corrections to the widths of the decays $H^+ \to t\bar{b}$ and $H^+ \to \tilde{t}\bar{\tilde{b}}$ within the Minimal Supersymmetric Standard Model. We find that the QCD corrections are important, and that the supersymmetric QCD corrections can be comparable to the standard QCD corrections, due to effects of large left-right mixings of stop ($\tilde{t}$) and sbottom ($\tilde{b}$).

The Minimal Supersymmetric Standard Model (MSSM) [1] predicts the existence of five physical Higgs bosons h^0, H^0, A^0, and $H^\pm$ [2, 3]. The e^+e^- Linear Collider will be the most promising machine to search for the charged Higgs particle $H^\pm$ [4]. If all supersymmetric (SUSY) particles are heavy enough, H^+ decays dominantly into $t\bar{b}$ above the $t\bar{b}$ threshold [2, 5]. In the case that SUSY-particles are relatively light, the $\tilde{t}\bar{\tilde{b}}$ mode can be dominant [6]. Thus it is important to calculate the QCD corrections to the decay modes $H^+ \to t\bar{b}$ and $H^+ \to \tilde{t}\bar{\tilde{b}}$ as they could significantly affect the phenomenology of the $H^\pm$ searches. The standard QCD corrections to both

*Present address: Physics Department, University of Wisconsin, Madison, WI 53706, USA

decay modes can vary in the range +10% to -50% [7]. The SUSY QCD corrections to $H^+ \to t\bar{b}$ were also calculated in [8].

In this contribution we present a complete calculation of the $O(\alpha_s)$ QCD corrections to the widths of $H^+ \to t\bar{b}$ and $H^+ \to \tilde{t}\bar{\tilde{b}}$ within the MSSM. We include the left-right mixings of both the $\tilde{t}_{L,R}$ squarks and the $\tilde{b}_{L,R}$ squarks. We shall adopt the on-shell renormalization scheme for $H^+ \to t\bar{b}$ and the $\overline{\rm DR}$ scheme for $H^+ \to \tilde{t}\bar{\tilde{b}}$.

We begin with the decay $H^+(p) \to t(k_t)\bar{b}(k_{\bar{b}})$ ($p = k_t + k_{\bar{b}}$). The one-loop corrected amplitude can be written as

$$\mathcal{M} = i\bar{t}(Y_1 P_R + Y_2 P_L)b \tag{1}$$

with $P_{R,L} = \frac{1}{2}(1 \pm \gamma_5)$ and the one-loop corrected couplings:

$$Y_i = y_i + \delta Y_i^{(v)} + \delta Y_i^{(w)} + \delta Y_i^{(0)} \ (i = 1, 2), \tag{2}$$

where y_i are the tree-level couplings $y_1 = h_b \sin\beta = g/(\sqrt{2}m_W)m_b \tan\beta$, $y_2 = h_t \cos\beta = g/(\sqrt{2}m_W)m_t \cot\beta$, with g being the SU(2) coupling. $\delta Y_i^{(v)}$, $\delta Y_i^{(w)}$, and $\delta Y_i^{(0)}$ are the contributions from vertex corrections, wave function renormalization, and quark mass renormalization, respectively (see Fig. 1). $\delta Y_i^{(0),(v),(w)}$ receive contributions from gluon and gluino exchanges, i. e. $\delta Y_i^{(v)} = \delta Y_i^{(v,g)} + \delta Y_i^{(v,\tilde{g})}$ etc.

The vertex corrections due to gluon and gluino exchanges are given by:

$$\begin{aligned}
\delta(Y_1 P_R + Y_2 P_L)^{(v,g)} &= \frac{\alpha_s}{3\pi}\Big\{2[B_0(m_t^2, 0, m_t^2) - B_0(m_{\tilde{b}}^2, 0, m_{\tilde{b}}^2) - r \\
&\quad -(m_{H^+}^2 - m_t^2 - m_b^2)C_0(\lambda^2, m_t^2, m_b^2)](y_1 P_R + y_2 P_L) \\
&\quad -2m_t C_1(\lambda^2, m_t^2, m_{\tilde{g}}^2)[(m_t y_1 + m_b y_2)P_R + (m_t y_2 + m_b y_1)P_L] \\
&\quad -2m_b C_2(\lambda^2, m_t^2, m_{\tilde{b}}^2)[(m_t y_2 + m_b y_1)P_R + (m_t y_1 + m_b y_2)P_L]\Big\}, \\
\delta(Y_1 P_R - Y_2 P_L)^{(v,\tilde{g})} &= \frac{\alpha_s}{3\pi}\Big\{2G_{ij}\Big[m_{\tilde{g}} C_0(m_{\tilde{g}}^2, m_{\tilde{t}_i}^2, m_{\tilde{b}_j}^2)\{R_{iL}^{\tilde{t}} R_{jR}^{\tilde{b}} P_R + R_{iR}^{\tilde{t}} R_{jL}^{\tilde{b}} P_L\} \\
&\quad -m_t C_1(m_{\tilde{g}}^2, m_{\tilde{t}_i}^2, m_{\tilde{b}_j}^2)\{R_{iL}^{\tilde{t}} R_{jL}^{\tilde{b}} P_L + R_{iR}^{\tilde{t}} R_{jR}^{\tilde{b}} P_R\} \\
&\quad +m_b C_2(m_{\tilde{g}}^2, m_{\tilde{t}_i}^2, m_{\tilde{b}_j}^2)\{R_{iL}^{\tilde{t}} R_{jL}^{\tilde{b}} P_R + R_{iR}^{\tilde{t}} R_{jR}^{\tilde{b}} P_L\}\Big]\Big\}.
\end{aligned} \tag{3}$$

G_{ij} are the tree-level couplings of H^+ to $\tilde{t}_i\bar{\tilde{b}}_j$ $(i, j = 1, 2)$ reading:

$$G_{ij} = \frac{g}{\sqrt{2}m_W} R^{\tilde{t}} \begin{pmatrix} m_b^2 \tan\beta + m_t^2 \cot\beta - m_W^2 \sin 2\beta & m_b(A_b \tan\beta + \mu) \\ m_t(A_t \cot\beta + \mu) & 2m_t m_b / \sin 2\beta \end{pmatrix} (R^{\tilde{b}})^\dagger, \tag{4}$$

where $R^{\tilde{q}}$ ($\tilde{q} = \tilde{t}$ or $\tilde{b}$) is the $\tilde{q}$–mixing matrix which diagonalizes the squark mass matrix, $\tilde{q}_i = R^{\tilde{q}}_{i\alpha}\tilde{q}_\alpha$, ($i = 1,2$; $\alpha = L, R$). We introduce a gluon mass λ for the regularization of the infrared divergence. The functions B and C are defined as in [9]. The parameter τ in eq. (3) and following equations is $\tau = 1$ for dimensional regularization and $\tau = 0$ for the dimensional reduction (DR) [10]. The dependence on τ, however, disappears in our final result.

The correction to the amplitude from the quark wave–function renormalization has the form:

$$\delta(Y_1 P_R + Y_2 P_L)^{(w)} = -\tfrac{1}{2}(\hat{\Pi}^t_L(m_t^2) + \Pi^b_R(m_b^2))y_1 P_R - \tfrac{1}{2}(\Pi^t_R(m_t^2) + \Pi^b_L(m_b^2))y_2 P_L + (m_t\dot{\Sigma}^t(m_t^2) - m_t^2\dot{\Pi}^t(m_t^2) - m_b\dot{\Sigma}^b(m_b^2) - m_b^2\dot{\Pi}^b(m_b^2))(y_1 P_R + y_2 P_L)\,. \tag{5}$$

with $\dot{\Pi}^q \equiv \frac{1}{2}(\dot{\Pi}^q_L + \dot{\Pi}^q_R)$ and $\dot{X} \equiv \frac{dX}{dk^2}$. The quark two-point functions $\Pi^q_L(k^2)$, $\Pi^q_R(k^2)$, and $\Sigma^q(k^2)$ can be expressed in terms of the standard B functions. Their explicit forms are given in [11].

The corrections $\delta Y_i^{(0)}$ due to the renormalization of the quark masses is

$$\delta Y_1^{(0)} = \delta y_1 = \frac{g}{\sqrt{2}m_W}\delta m_b \tan\beta\,, \quad \delta Y_2^{(0)} = \delta y_2 = \frac{g}{\sqrt{2}m_W}\delta m_t \cot\beta\,, \tag{6}$$

with

$$\delta m_q = \delta m_q^{(g)} + \delta m_q^{(\tilde{g})} = \mathrm{Re}\left[\frac{m_q}{2}(\Pi^q_L(m_q^2) + \Pi^q_R(m_q^2)) - \Sigma^q(m_q^2)\right]. \tag{7}$$

The one–loop corrected decay width to $\mathcal{O}(\alpha_s)$ is then given by

$$\Gamma(H^+ \to t\bar{b}) = \frac{N_C\kappa}{16\pi m_{H^+}^3}\left[(m_{H^+}^2 - m_t^2 - m_b^2)\left(y_1^2 + y_2^2 + 2y_1\mathrm{Re}(\delta Y_1) + 2y_2\mathrm{Re}(\delta Y_2)\right) - 4m_t m_b(y_1 y_2 + y_1\mathrm{Re}(\delta Y_2) + y_2\mathrm{Re}(\delta Y_1))\right]. \tag{8}$$

where $\kappa = \kappa(m_{H^+}^2, m_t^2, m_b^2)$, $\kappa(x,y,z) \equiv ((x-y-z)^2 - 4yz)^{1/2}$, and $N_C = 3$. $\Gamma^{tree}(H^+ \to t\bar{b})$ is obtained by putting $\delta Y_{1,2} = 0$.

For the cancellation of the infrared divergencies ($\lambda \to 0$) it is necessary to include the $\mathcal{O}(\alpha_s)$ contribution from real gluon emission, $H^+ \to t + \bar{b} + g$:

$$\Gamma(H^+ \to t\bar{b}g) = \frac{\alpha_s}{\pi^2 m_{H^+}}\left[(y_1^2 + y_2^2)\{(m_{H^+}^2 - m_t^2 - m_b^2)^2 I_{12} - \frac{1}{2}I_1^2 + \frac{1}{2}I_2^2 + I - (m_{H^+}^2 - m_t^2 - m_b^2)(m_t^2 I_{11} + m_b^2 I_{22} - I_1 - I_2)\} - 4m_t m_b y_1 y_2\{m_t^2 I_{11} - m_b^2 I_{22} - I_1 + I_2 - (m_{H^+}^2 - m_t^2 - m_b^2)I_{12}\}\right], \tag{9}$$

where the functions I are standard integrals with the explicit form given in [9].

The one–loop corrected decay width to $\mathcal{O}(\alpha_s)$ including the real gluon emission can be written as:

$$\Gamma^{corr}(H^+ \to t\bar{b} + t\bar{b}g) \equiv \Gamma(H^+ \to t\bar{b}) + \Gamma(H^+ \to t\bar{b}g) = \Gamma^{tree} + \delta\Gamma(gluon) + \delta\Gamma(gluino)$$

In Fig. 2 we show the m_{H^+} dependence of Γ^{tree}, $\Gamma^{tree} - \delta\Gamma(\mathrm{gluon})$, and $\Gamma^{corr} = \Gamma^{tree} - \delta\Gamma(\mathrm{gluon}) + \delta\Gamma(\mathrm{gluino})$ for $\tan\beta = 2$ and 12, and $(m_{\tilde{g}}, \mu, M_{\tilde{Q}}, A) = (400, -300, 200, 200)$ (GeV). For simplicity we assume $M_{\tilde{Q}} = M_{\tilde{U}} = M_{\tilde{D}}$ and $A_t = A_b \equiv A$. We take $m_t = 180$ GeV, $m_b = 5$ GeV, $m_W = 80$ GeV, $m_Z = 91.2$ GeV, $\sin^2\theta_W = 0.23$, $g^2/(4\pi) = \alpha_2 = \alpha/\sin^2\theta_W = 0.0337$ and $\alpha_s = \alpha_s(m_{H^+})$. We use $\alpha_s(Q) = 12\pi/\{(33 - 2n_f)\ln(Q^2/\Lambda^2_{n_f})\}$ with $\alpha_s(m_Z) = 0.12$ and the number of quark flavors $n_f = 5(6)$ for $m_b < Q \le m_t$ (for $Q > m_t$). The parameter values correspond to fixed stop and sbottom masses: $m_{\tilde{t}_1} = 90$ GeV, $m_{\tilde{t}_2} = 366$ GeV, $m_{\tilde{b}_1} = 193$ GeV, and $m_{\tilde{b}_2} = 213$ GeV (for $\tan\beta = 2$) and $m_{\tilde{t}_1} = 173$ GeV, $m_{\tilde{t}_2} = 333$ GeV, $m_{\tilde{b}_1} = 152$ GeV, and $m_{\tilde{b}_2} = 247$ GeV (for $\tan\beta = 12$). We see that the correction $\delta\Gamma(\mathrm{gluino})$ can be quite large and that it is comparable to or even larger than $\delta\Gamma(\mathrm{gluon})$. Quite generally, the corrections $\delta\Gamma(\mathrm{gluon})$ and $\delta\Gamma(\mathrm{gluino})$ are bigger for larger $\tan\beta$. The correction $\delta\Gamma(\mathrm{gluon})$ has already been calculated in [7]. We agree agree numerically within 10%. Our results for $\delta\Gamma(\mathrm{gluon}) - \delta\Gamma(\mathrm{gluino})$ agree with those of [8].

In the calculation of the SUSY QCD corrections to $H^+ \to \tilde{t}_i\bar{\tilde{b}}_j$ we proceed in an analogous way. As an example we show in Fig. 3 the widths $\Gamma^{tree}(\tilde{t}\bar{\tilde{b}}) \equiv \sum_{i,j}\Gamma^{tree}(H^+ \to \tilde{t}_i\bar{\tilde{b}}_j)$, $\Gamma^{corr}(\tilde{t}\bar{\tilde{b}}) \equiv \sum_{i,j}\Gamma^{corr}(H^+ \to \tilde{t}_i\bar{\tilde{b}}_j)$, and $\Gamma^{corr}(H^+ \to \tilde{t}_i\bar{\tilde{b}}_j)$ for $(i,j) = (1,1)$ and $(1,2)$, as well as the tree level branching ratio $B^{tree}(\tilde{t}\bar{\tilde{b}}) \equiv \sum_{i,j}B^{tree}(H^+ \to \tilde{t}_i\bar{\tilde{b}}_j)$, as a function of m_{H^+}. Here we have chosen $m_t(pole) = 180$ GeV, $M = 120$ GeV, $\mu = 300$ GeV, $\tan\beta = 2$, $M_{\tilde{Q}} = 250$ GeV, $A = 650$ GeV. As one can see, the $\tilde{t}\bar{\tilde{b}}$ mode is dominant in a wide range of m_{H^+}. The QCD corrections are significant, but they do not invalidate the dominance of the $\tilde{t}\bar{\tilde{b}}$ mode. More details can be found in [12].

Summarizing, we have performed a complete calculation of the $\mathcal{O}(\alpha_s)$ QCD corrections to the width of $H^+ \to t\bar{b}$ and $H^+ \to \tilde{t}_i\bar{\tilde{b}}_j$ within the MSSM. We have found that the QCD corrections are important, and that the SUSY–QCD corrections can be comparable to or even larger than the standard QCD corrections. Here the

mixings of $\tilde{t}_L - \tilde{t}_R$ and $\tilde{b}_L - \tilde{b}_R$ play a crucial role.

Acknowledgements

The work of Y.Y. was supported in part by the Fellowships of the Japan Society for the Promotion of Science and the Grant-in-Aid for Scientific Research from the Ministry of Education, Science and Culture of Japan, No. 06-1923 and 07-1923. The work of A.B., H.E., and W.M. was supported by the "Fonds zur Förderung der wissenschaftlichen Forschung" of Austria, project no. P10843-PHY.

References

[1] H. E. Haber and G. L. Kane, Phys. Rep. 117 (1985) 75.

[2] J. F. Gunion, H. E. Haber, G. L. Kane, and S. Dawson, The Higgs Hunter's Guide, Addison-Wesley (1990).

[3] J. F. Gunion and H. E. Haber, Nucl. Phys. B272 (1986) 1; B402 (1993) 567 (E).

[4] P. Eerola and J. Sirkka, Proc. of the Workshop "e^+e^- Collisions at 500 GeV: The Physics Potential", DESY 92-123A, p. 133, ed. P. M. Zerwas; A. Sopczak, ibidem, DESY 93-123C, p. 121.

[5] Z. Kunszt and F. Zwirner, Nucl. Phys. B385 (1992) 3.

[6] A. Bartl, K. Hidaka, Y. Kizukuri, T. Kon and W. Majerotto, Phys. Lett. B315 (1993) 357.

[7] A. Méndez and A. Pomarol, Phys. Lett. B252 (1990) 461; A. Djouadi, M. Spira, P. M. Zerwas, DESY 95-210.

[8] R. A. Jiménez and J. Solà, Preprint hep-ph/9511292.

[9] A. Denner, Fortschr. Phys. 41 (1993) 307.

[10] W. Siegel, Phys. Lett. B84 (1979) 193;
D. M. Capper, D. R. T. Jones, and P. van Nieuwenhuizen, Nucl. Phys. B167 (1980) 479.

[11] A. Bartl, H. Eberl, K. Hidaka, T. Kon, W. Majerotto, and Y. Yamada, Preprint hep-ph/9511385.

[12] A. Bartl, H. Eberl, K. Hidaka, T. Kon, W. Majerotto, and Y. Yamada, Preprint hep-ph/9508283.

Figure Captions

Fig. 1 All diagrams relevant for the calculation of the $\mathcal{O}(\alpha_s)$ QCD corrections to the width of $H^- \to t\bar{b}$ in the MSSM.

Fig. 2 m_{H^-} dependence of $\Gamma^{\rm tree}$ (dashed line), $\Gamma^{\rm tree} + \delta\Gamma(\text{gluon})$ (dot-dashed line), and $\Gamma^{\rm corr} = \Gamma^{\rm tree} + \delta\Gamma(\text{gluon}) + \delta\Gamma(\text{gluino})$ (solid line) for $\tan\beta = 2$ (a) and 12 (b), and $(m_{\tilde{g}}, \mu, M_{\tilde{Q}}, A) = (400, -300, 200, 200)$ (GeV).

Fig. 3 The m_{H^-} dependence of $\Gamma^{\rm tree}(\sum \tilde{t}_i \bar{\tilde{b}}_j) \equiv \Gamma^{\rm tree}(\tilde{t}\bar{\tilde{b}})$ (dashed line), $\Gamma^{\rm corr}(\sum \tilde{t}_i \bar{\tilde{b}}_j) \equiv \Gamma^{\rm corr}(\tilde{t}\bar{\tilde{b}})$ (solid line), and $B^{\rm tree}(\tilde{t}\bar{\tilde{b}})$ (short-dashed line) for (m_t(pole)(GeV), M(GeV), μ(GeV), $\tan\beta$, $M_{\tilde{Q}}$(GeV), A(GeV))=(180, 120, 300, 2, 250, 650). $\Gamma^{\rm tree}(\tilde{t}_i \bar{\tilde{b}}_j) \equiv \Gamma^{\rm tree}_{ij}$ (dashed lines) and $\Gamma^{\rm corr}(\tilde{t}_i \bar{\tilde{b}}_j) \equiv \Gamma^{\rm corr}_{ij}$ (solid lines) are separately shown for (i,j) =(1,1) and (1,2).

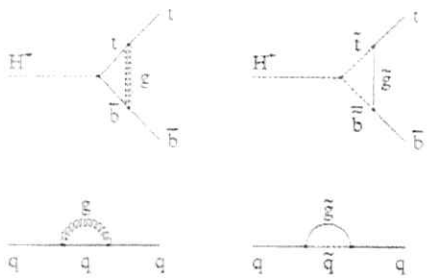

Fig. 1

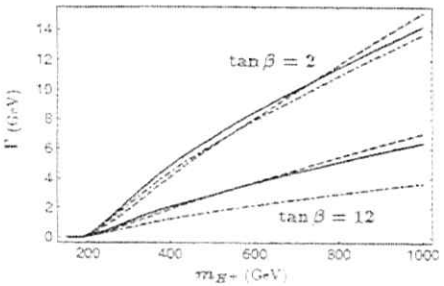

Fig. 2

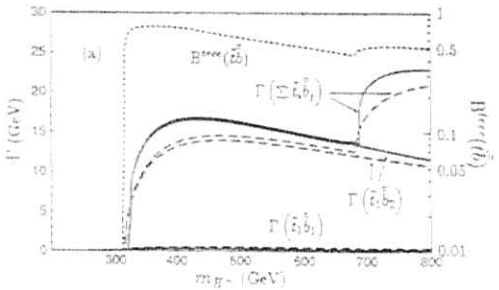

Fig. 3

Supersymmetry and CP–Violating Correlations in Top–Quark Production and Decay

A. Bartl[1], E. Christova[2], T. Gajdosik[3], W. Majerotto[3]

ABSTRACT

We present analytic formulae for the cross section of the sequential processes of $e^+e^- \to t\bar{t}$ and $t \to bl^+\nu$ / $\bar{t} \to \bar{b}l^-\bar{\nu}$ in the laboratory frame, showing explicitly the dependence on triple product correlations induced by CP violation both in the production and the decay processes. Different observables sensitive to CP–violation are defined and calculated in the MSSM. They are of the order of 10^{-3}.

1. Precision measurements of various production and decay modes of the top quark will also provide new information about CP violation. In the Standard Model (SM) these effects are expected to be small. Observation of CP non–invariance in top–quark physics would therefore definitely be a signal for physics beyond the SM [1, 2, 3, 4]. As possible evidence of CP noninvariance we consider T–odd triple product correlations of the type $(\mathbf{q}_1\mathbf{q}_2\mathbf{q}_3) \equiv (\mathbf{q}_1 \times \mathbf{q}_2 \cdot \mathbf{q}_3)$, where $\mathbf{q}_{1,2,3}$ can be any one of the 3–momenta in $e^+e^- \to t\bar{t}$ and of the t ($\bar{t}$)–decay products $t \to bl^+\nu$ ($\bar{t} \to \bar{b}l^-\bar{\nu}$), previously proposed in [1,2]. In collider experiments top–antitop quark pairs will be copiously produced and the decay modes $t \to bl^+\nu$ and $\bar{t} \to \bar{b}l^-\bar{\nu}$ will occur simultaneously. Therefore, it will be possible to form the difference between the two conjugate processes in the same experiment.

In this contribution we shall consider triple product correlations among the 3–momenta of the particles in the sequential processes:

$$e^+ + e^- \to t + \bar{t} \to \bar{t}bl^+\nu \ , \qquad e^+ + e^- \to t + \bar{t} \to t\bar{b}l^-\bar{\nu}. \tag{1}$$

We shall obtain a general analytic expression for the cross section of (1), in which the dependence on the triple product correlations sensitive to CP violation in the production and in the decay is in evidence. Previously the problem of CP violation in $t\bar{t}$ production and t decay was considered in [4]. Here we shall work in the Minimal Supersymmetric Standard Model (MSSM) where there are more possibilities to introduce complex couplings than in the SM. However, our method is completely general and can also be applied to study any other sources of CP violation.

[1] Institut für Theoretische Physik, Universität Wien, A–1090 Vienna, Austria

[2] Institute of Nuclear Research and Nuclear Energy, Boul. Tzarigradsko Chaussee 72, Sofia 1784, Bulgaria.

[3] Institut für Hochenergiephysik, Österreichische Akademie der Wissenschaften, A – 1050 Vienna, Austria

2. After some calculations, outlined in [5], we obtain the cross section in the c.m.system for reactions (1) as

$$\begin{aligned} d\sigma^{t,\bar{t}} &= \sigma^{t,\bar{t}}_{SM}\{\,1 + \frac{1}{1-\beta(\hat{\mathbf{p}}_t\hat{\mathbf{p}}_{l^-})}\,[\,(\hat{\mathbf{q}}_1\hat{\mathbf{p}}_t\hat{\mathbf{p}}_{l^-})\,A_1^{t,\bar{t}} - (\hat{\mathbf{q}}_1\hat{\mathbf{p}}_t\hat{\mathbf{p}}_b)\,A_2^{t,\bar{t}} \\ &\quad - (\hat{\mathbf{p}}_t\hat{\mathbf{p}}_{l^-}\hat{\mathbf{p}}_b)\,A_3^{t,\bar{t}} + (\hat{\mathbf{q}}_1\hat{\mathbf{p}}_{l^-}\hat{\mathbf{p}}_b)\,A_4^{t,\bar{t}}\,]\,\}\,d\Omega_t d\Omega_b d\Omega_l \ , \end{aligned} \tag{2}$$

where $\hat{\mathbf{q}}_1$, $\hat{\mathbf{p}}_t$, $\hat{\mathbf{p}}_b$ and $\hat{\mathbf{p}}_{l^-}$ denote the unit 3–vectors in the direction of the e^-–beam, t, b and l^-, respectively.

$$\sigma^{t,\bar{t}}_{SM} = \frac{\alpha^2}{4\pi^4}\left(\frac{g}{2\sqrt{2}}\right)^4 \frac{\beta\,[m_t^2 - 2(p_t p_{l^-})]}{s\ m_t\Gamma_t\, m_W\Gamma_W}\,\frac{E_b^2}{m_t^2 - m_W^2}\,\frac{E_l^2}{m_W^2}\,N\,A^{t,\bar{t}}_{SM} \tag{3}$$

is the expression for the SM cross sections of (1). $A^{t,\bar{t}}_{SM} = (p_t p_{l^-}) = m_t(\xi^{t,\bar{t}}_{SM} p_{l^-})$ where $\xi^{t,\bar{t}}_{SM}$ are the polarization 4–vectors [5] of $t,\bar{t}$ determined by the $t\bar{t}$–production process. In the c.m.system $E_b = (m_t^2 - m_W^2)/[2E(1-\beta(\hat{\mathbf{p}}_t\hat{\mathbf{p}}_b))]$ is the energy of the b–quark, $E_l = m_W^2/[2E(1-\beta(\hat{\mathbf{p}}_t\hat{\mathbf{p}}_{l^-})) - 2E_b(1-(\hat{\mathbf{p}}_b\hat{\mathbf{p}}_{l^-}))]$ is the energy of the final lepton and $E = \sqrt{s}/2$. The asymmetries A_i are

$$\begin{aligned} A_1^{t,\bar{t}} &= \mp\beta\left(\tfrac{D}{2} - \tfrac{m_t}{\sqrt{s}}E_b P_- \tfrac{\Im m g_R}{m_W}\right) , & A_2^{t,\bar{t}} &= \mp\beta\tfrac{m_t}{\sqrt{s}}E_b P_- \tfrac{\Im m g_R}{m_W} , \\ A_3^{t,\bar{t}} &= -\beta\tfrac{m_t}{\sqrt{s}}E_b P_- \tfrac{\Im m g_R}{m_W} , & A_4^{t,\bar{t}} &= \mp\tfrac{m_t}{\sqrt{s}}E_b P_- \tfrac{\Im m g_R}{m_W} , \end{aligned} \tag{4}$$

where

$$\begin{aligned} P_- &= \frac{8h_Z}{N}\left[2h_Z\, c_V c_A g_V^2 - \frac{4}{3}c_A g_V + \beta\cos\theta\,(h_Z\,(c_V^2 + c_A^2)\,g_V g_A - \frac{2}{3}c_V g_A)\right] \\ P_+ &= -\frac{8h_Z}{N}\left[h_Z\,(c_V^2 - c_A^2)\,g_V g_A - \frac{2}{3}c_V g_A + 2\beta\cos\theta\, h_Z\, c_V c_A g_V^2\right] \\ D &= \frac{8h_Z}{N}[\,2h_Z\, c_V c_A g_V\,\Im m\, d^Z - c_A\left(g_V\,\Im m\, d^\gamma - \frac{2}{3}\Im m\, d^Z\right) \\ &\quad + \beta\cos\theta\,(h_Z\,(c_V^2 + c_A^2)g_A\,\Im m\, d^Z - c_V g_A\,\Im m\, d^\gamma)\,] \\ N &= \beta^2(1+\cos^2\theta)(c_V^2 + c_A^2)g_A^2 - 8\beta\cos\theta\, h_Z c_A g_A\left(h_Z c_V g_V - \frac{1}{3}\right) \\ &\quad + (2 - \beta^2\sin^2\theta)\left(\frac{4}{9} - \frac{4}{3}h_Z c_V g_V + h_Z^2(c_V^2 + c_A^2)g_V^2\right) \end{aligned}$$

Here $\beta = \sqrt{1-4m_t^2/s}$ is the velocity of the t in the c.m.system, θ is the angle between the momenta of the initial e^- and the t, and $h_Z = s/[(s-m_Z^2)\sin^2 2\theta_W]$, $c_V = -1/2 - 2\sin^2\theta_W$, $c_A = 1/2$, $g_V = 1/2 - 4/3\sin^2\theta_W$, $g_A = -1/2$.

The correlations $(\hat{\mathbf{q}}_l\hat{\mathbf{p}}_t\hat{\mathbf{p}}_l)$ and $(\hat{\mathbf{q}}_l\hat{\mathbf{p}}_{\bar{t}}\hat{\mathbf{p}}_{\bar{b}})$ contain both the production and t–decay planes. Thus CP violation from both $d^{\gamma,Z}$ and g_R may contribute. The correlations $(\hat{\mathbf{p}}_{\bar{t}}\hat{\mathbf{p}}_l\hat{\mathbf{p}}_b)$ and $(\hat{\mathbf{q}}_l\hat{\mathbf{p}}_l\hat{\mathbf{p}}_b)$ contain only the decay plane, and it is only the t–decay vertex that can contribute. One expects that the triple–product correlations discussed above are less sensitive to CP violation in top–decay then in $t\bar{t}$ production, because $\Im m g_R$ is multiplied by the SM–polarization P_z and by $E_b/\sqrt{s}$.

With the set of triple products $\mathcal{T}_1 = (\hat{\mathbf{q}}_l\hat{\mathbf{p}}_t\hat{\mathbf{p}}_l)$, $\mathcal{T}_2 = (\hat{\mathbf{q}}_l\hat{\mathbf{p}}_{\bar{t}}\hat{\mathbf{p}}_{\bar{b}})$, $\mathcal{T}_3 = (\hat{\mathbf{p}}_{\bar{t}}\hat{\mathbf{p}}_l\hat{\mathbf{p}}_{\bar{b}})$ and $\mathcal{T}_4 = (\hat{\mathbf{q}}_l\hat{\mathbf{p}}_l\hat{\mathbf{p}}_{\bar{b}})$ we define the observables

$$O_i = \frac{N[\mathcal{T}_i > 0] - N[\mathcal{T}_i < 0]}{N[\mathcal{T}_i > 0] + N[\mathcal{T}_i < 0]} \tag{5}$$

where $N[\mathcal{T}_i > 0 (< 0)]$ is the number of events in which $\mathcal{T}_i > 0 (< 0)$.

The truly CP–violating effect would be a nonzero value of $\mathcal{O}_i = O_i - \bar{O}_i$, $i = 1,2,4$ and $\mathcal{O}_3 = O_3 + \bar{O}_3$, where $\bar{O}_i$ refer to the second equation of reactions (1).

3. Now we shall give numerical predictions in the MSSM [6] for the observables defined above. In the MSSM d^γ, d^Z and $\Im m g_R$ are generated at one–loop order, irrespectively of generation mixing. The main contribution comes from diagrams with gluino and scalar quarks in the loop. The CP–violating phases ϕ_A and $\phi_{\tilde{g}}$ appear in the stop–squark mixing matrix and in the Majorana mass term of the gluinos respectively. They enter in the combination $\phi_A - \phi_{\tilde{g}}$. In our numerical analysis we have assumed maximal CP violation, $\sin(\phi_A - \phi_{\tilde{g}}) = 1$, and maximal stop mixing, $\sin 2\tilde{\theta} = 1$, where $\tilde{\theta}$ is the stop–mixing angle.

We choose the following set of reference values: $\sqrt{s} = 500$ GeV, $m_t = 175$ GeV, $m_{\tilde{g}} = 200$ GeV, $m_{\tilde{t}_1} = 150$ GeV, $m_{\tilde{t}_2} = 400$ GeV, and $m_{\tilde{b}_L} = 200$ GeV. In the Figure we show the dependence of O_i on one of the parameters: $m_{\tilde{g}}$(a), $m_{\tilde{t}_1}$(b) and $\sqrt{s}$(c) with the other parameters fixed at their reference values. O_2 and O_4 are the largest observables and have values of the order of 10^{-3}. Above the threshold region and up to $\sqrt{s} \approx 1$ TeV the observables are almost independent of s.

We thank Helmut Eberl for his constructive assistance in the evaluation of the loop integrals. E.C.'s work has been partially supported by the Bulgarian National Science Foundation. Grant Ph-510.

References

[1] B.Grzadkowski and J.Gunion, *Phys.Lett.* **B287** (1992) 237
C.Schmidt, *Phys.Lett.* **B293** (1992) 111
B.Grzadkowski, *Phys.Lett.***B305** (1993) 384 and *Phys.Lett.***B316** (1993) 137
B.Grzadkowski and W.Keung, *Phys.Lett.* **B319** (1993) 526
E.Christova and M.Fabbrichesi, *Phys.Lett.* **320**(1994) 299

[2] D.Atwood and A.Soni, *Phys.Rev.* D45 (1992) 2405
E.Christova and M.Fabbrichesi, *Phys.Lett.* **B315** (1993) 113

[3] E.Christova and M.Fabbrichesi, *Phys.Lett.* **B315** (1993) 338

[4] W.Bernreuther, O.Nachtmann, P.Overmann, T.Schröder, *Nucl.Phys.* **388** (1992) 53
W.Bernreuter, P.Overmann, *Z.Phys.* **C61** (1994) 599

[5] A.Bartl, E.Christova, W.Majerotto, *Nucl.Phys.* **460** (1996) 235

[6] H.E.Haber and G.Kane, *Phys.Rep.* **117** (1985) 75
J.Gunion and H.E.Haber, *Nucl.Phys.* **B272** (1986) 1

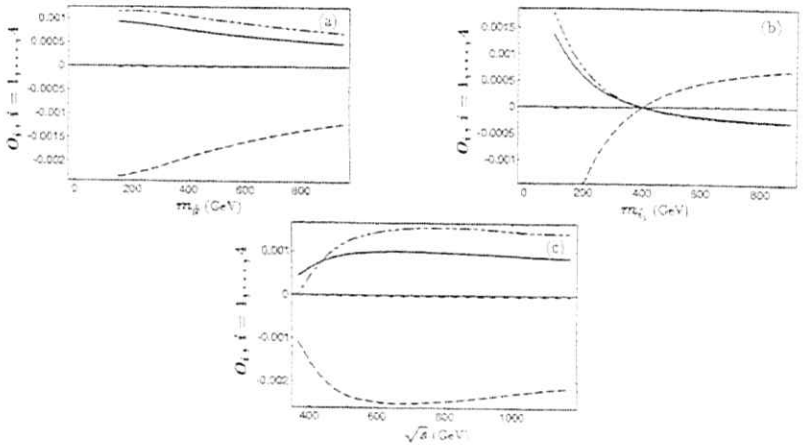

Figure: Observables O_i, $i = 1,\ldots 4$, as a function of (a) $m_{\tilde{g}}$, (b) $m_{\tilde{t}_1}$ and (c) $\sqrt{s}$ for $m_t = 175$ GeV, $m_b = 0$, $m_{\tilde{t}_2} = 400$ GeV and $m_{\tilde{b}_L} = 400$ GeV.

Production of nonminimal SUSY neutralinos at an e^+e^- linear collider

F. Franke, H. Fraas*
Institut für Theoretische Physik, Universität Würzburg

1 Introduction

The search for neutralinos is one of the most exciting challenges at a future e^+e^- linear collider. First, a clear supersymmetric signature could be expected. Second, the opportunity to distinguish between the Minimal Supersymmetric Standard Model (MSSM) and extended supersymmetric models may be offered. The minimal extension of the MSSM by a singlet superfield, the Next-To-Minimal Supersymmetric Standard Model (NMSSM) [1, 2], is characterized by the trilinear Higgs terms in the superpotential $W \ni \lambda H_1 H_2 N - 1/3 k N^3$, where H_1 and H_2 are the Higgs doublets with hypercharge $-1/2$ and $1/2$ and vacuum expectation value (vev) v_1 and v_2 ($\tan\beta = v_2/v_1$), respectively. N is the Higgs singlet with hypercharge 0 and vev x, and λ and k are dimensionless coupling parameters. The NMSSM contains five neutralinos $\tilde{\chi}_i^0$ being mixtures of photino, zino, the doublet higgsinos and the singlet higgsino. The 5×5 neutralino mass matrix [3, 4] depends on six parameters: the gaugino mass parameters M and M', $\tan\beta$, x, λ, and k. We assume in the following the usual gaugino mass relation $M' \approx 0.5M$.

The search for NMSSM neutralinos and Higgs bosons at linear e^+e^- colliders has been the topic of some previous studies [5], where cross sections for special NMSSM scenarios are given. In the present contribution we analyze neutralino production for the whole parameter range -500 GeV $< M <$ 500 GeV, $x <$ 1000 GeV and discuss explicitly the possible differences between NMSSM and MSSM. The lightest neutralino is assumed to be the LSP and hence invisible. For a detailed discussion of the subsequent neutralino decays we refer to ref. [6].

2 Scenarios

All cross sections are calculated in the (M, x)-plane for two values of the coupling k with fixed parameters $\lambda = 0.8$ and $\tan\beta = 2$. In the case of the small coupling $k = 0.001$, the LSP is mainly a pure singlet in the whole plane with a mass between about 10 GeV at large x values and 70 GeV for a small singlet vev. The second lightest neutralino in this scenario is light enough to be pair produced at $\sqrt{s} = 500$ GeV, while $\tilde{\chi}_2^0\tilde{\chi}_3^0$ ($\tilde{\chi}_3^0\tilde{\chi}_3^0$) production is kinematically possible only in a limited range if either $x \lesssim 400\,(200)$ GeV or $|M| \lesssim 300\,(200)$ GeV.

Contrary to this scenario where the mixings of all other neutralinos except the LSP are similar to the MSSM with $\mu = \lambda x$ almost in the whole (M, x)-plane, we also consider a larger coupling $k = 0.5$ where now all neutralinos may contain large singlet components in some parameter domains. In this scenario, the three light neutralinos have significant singlet components for $x \lesssim 400$ GeV, while for larger x values only the mixings of the heavy neutralinos contain non-neglectable singlet contributions. Furthermore, the second lightest neutralino is rather heavy for a large singlet vev x, so that at $\sqrt{s} = 500$ GeV $\tilde{\chi}_2^0$ pair production is kinematically possible only for $x \lesssim 400$ GeV or $|M| \lesssim 200$ GeV, $\tilde{\chi}_3^0$ can be produced only in the small x-region $x \lesssim 400$ GeV.

*Supported by Deutsche Forschungsgemeinschaft under contract FR 1064/2-1

3 Cross sections

In both scenarios we compute the cross sections for the neutralino production at a center-of-mass energy $\sqrt{s} = 500$ GeV and for selectron masses $m_{\tilde{e}_L} = m_{\tilde{e}_R} = 300$ GeV. For $k = 0.001$ (Fig. 1) the production of the LSP together with a visible neutralino is suppressed for large x values where $\tilde{\chi}_1^0$ is mainly singlet-like. Only for $M \approx 100$ GeV small cross sections up to 50 fb for $\tilde{\chi}_1^0\tilde{\chi}_2^0$-production are reached. The largest cross sections of about 200 fb in this scenario are obtained for pair production of $\tilde{\chi}_2^0$, but also $\tilde{\chi}_3^0$ is produced with considerable rates.

Fig. 2 shows the cross sections for $k = 0.5$. Since the singlet component of the lightest neutralino now is considerably smaller, $\tilde{\chi}_1^0\tilde{\chi}_2^0$-production is enhanced in most of the parameter domain with cross sections up to 120 fb also in the large x region. The other production channels with the second and third neutralino, however, are reduced either due to their singlet components or due to the phase space factor because of the larger neutralino masses.

4 Discovery regions in NMSSM and MSSM

In Fig. 3 we compare the cross sections of NMSSM and MSSM with $\mu = \lambda x$ in the (M, x)-plane for our scenarios. Shown are the contour lines for the sum of the cross sections in the channels with visible neutralinos. Our scenarios illustrate that according to the choice of the couplings λ and k in the superpotential either a larger or a smaller part of the (M, x) parameter space is covered by a linear collider, if the NMSSM is realized in the nature instead of the MSSM.

Assuming a discovery limit of 10 fb, the whole plane could be explored in the NMSSM for $k = 0.001$, but not in the corresponding MSSM scenario. The reason is, that in this scenario the second lightest NMSSM neutralino has a similar mass as the LSP in the MSSM, but can be identified by its decays. Generally, a light neutralino can be detected or excluded at a linear collider if the gaugino mass parameter is bounded by about $|M| \lesssim \sqrt{s}$.

For $k = 0.5$ and $x \lesssim 400$ GeV, however, the identification of a NMSSM scenario may not be possible even if a MSSM neutralinos with similar masses are detectable, since in this parameter domain all light neutralinos have significant singlet components. The difference between the covered parameter space in NMSSM and MSSM is the larger the higher the discovery limit is, it almost vanishes in the large x region where only the heavy neutralinos beyond the range of a 500-GeV linear collider have large singlet components.

5 Conclusions

The linear collider considerably extends the explorable parameter space of the NMSSM. If no neutralino is found

- small k values can be excluded;
- the mass bounds for the lightest neutralino are significantly raised, especially a light singlet-like neutralino which can survive LEP2 can be excluded.

On the other hand there are good chances of detecting a neutralino at the linear collider. In this case, distinction between the NMSSM and the MSSM may be possible

- by the decays of the next-to-lightest neutralinos, if the LSP has a large singlet component. Especially, the decay of the second lightest neutralino into a Higgs boson plus the LSP and the loop decay into a photon and the LSP may be enhanced (for details see [6]).
- by detecting a deviation of the production cross sections. This should be possible if several of the produced neutralinos have significant singlet components which affect the cross sections without suppressing them so strongly that they fall below the discovery limit.

In the NMSSM, not only the neutralino but also the Higgs sector is extended. The linear colliders offers the unique possibility to search for neutralinos and supersymmetric Higgs bosons in order to verify or to exclude minimal or nonminimal supersymmetry.

References

[1] M. Drees, Int. J. of Mod. Phys. **A4** (1989) 3635

[2] J. Ellis, J.F. Gunion, H.E. Haber, L. Roszkowski and F. Zwirner, Phys. Rev. **D 39** (1989) 844a

[3] B.R. Kim, S.K. Oh and A. Stephan, Phys. Lett. **B 336** (1994) 200

[4] F. Franke, H. Fraas and A. Bartl, Phys. Lett. **B 336** (1994) 415

[5] B.R. Kim, S.K. Oh and A. Stephan, Proceedings of the Workshop e^+e^- Collisions at 500 GeV: The Physics Potential, Munich, Annecy, Hamburg, Ed. P. Zerwas, DESY 92-123B (1992) 697; DESY 93-123C (1993) 491

[6] F. Franke and H. Fraas, WUE-ITP-95-021, hep-ph/9511275, to appear in Z. Phys. C

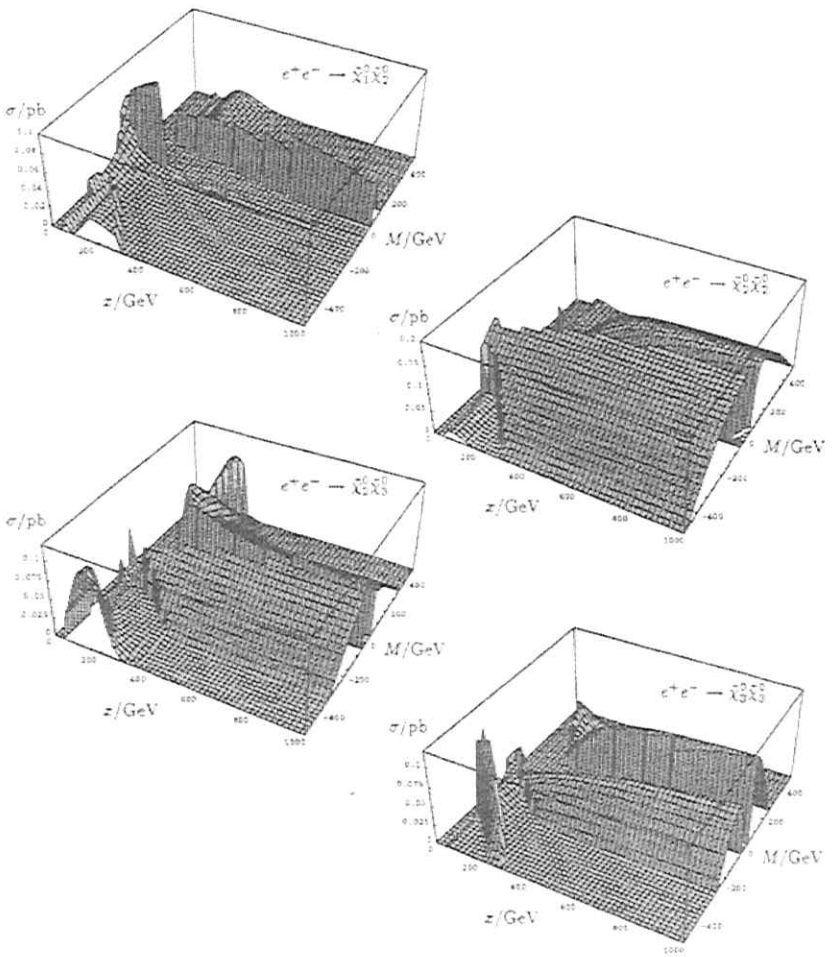

Figure 1: Cross section at a center-of-mass energy $\sqrt{s} = 500$ GeV for $\lambda = 0.8$, $k = 0.001$, $\tan\beta = 2$, $m_{\tilde{e}_L} = m_{\tilde{e}_R} = 300$ GeV.

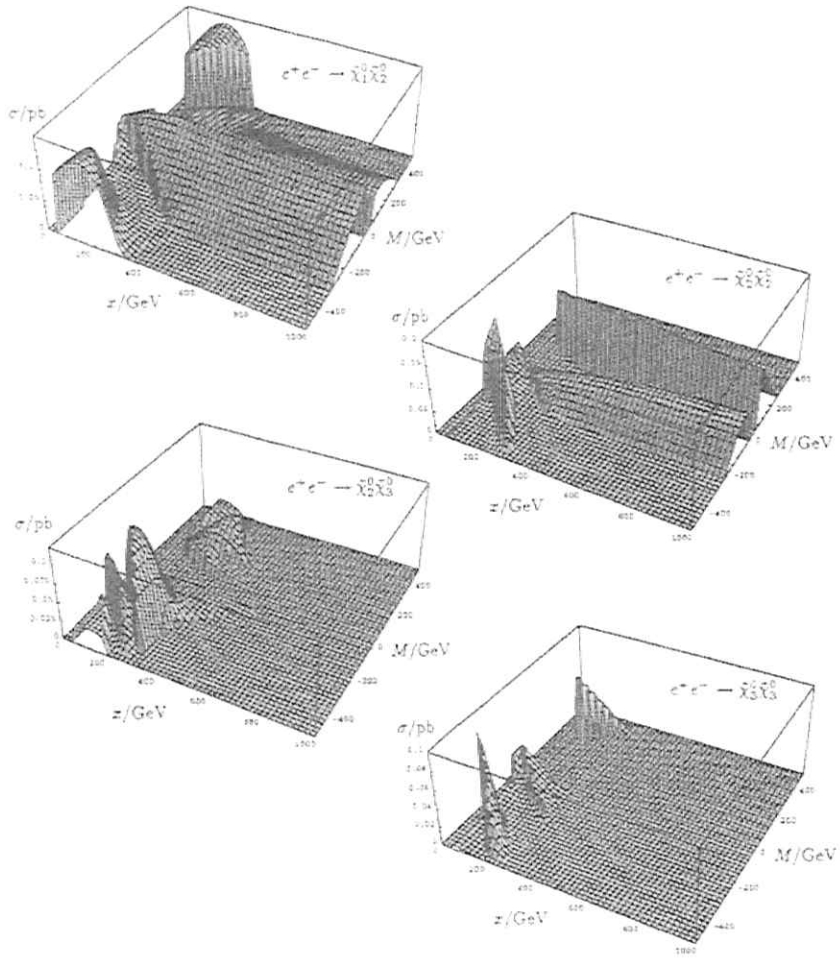

Figure 2: Cross section at a center-of-mass energy $\sqrt{s} = 500$ GeV for $\lambda = 0.8$, $k = 0.5$, $\tan\beta = 2$, $m_{\tilde{\epsilon}_L} = m_{\tilde{\epsilon}_R} = 300$ GeV.

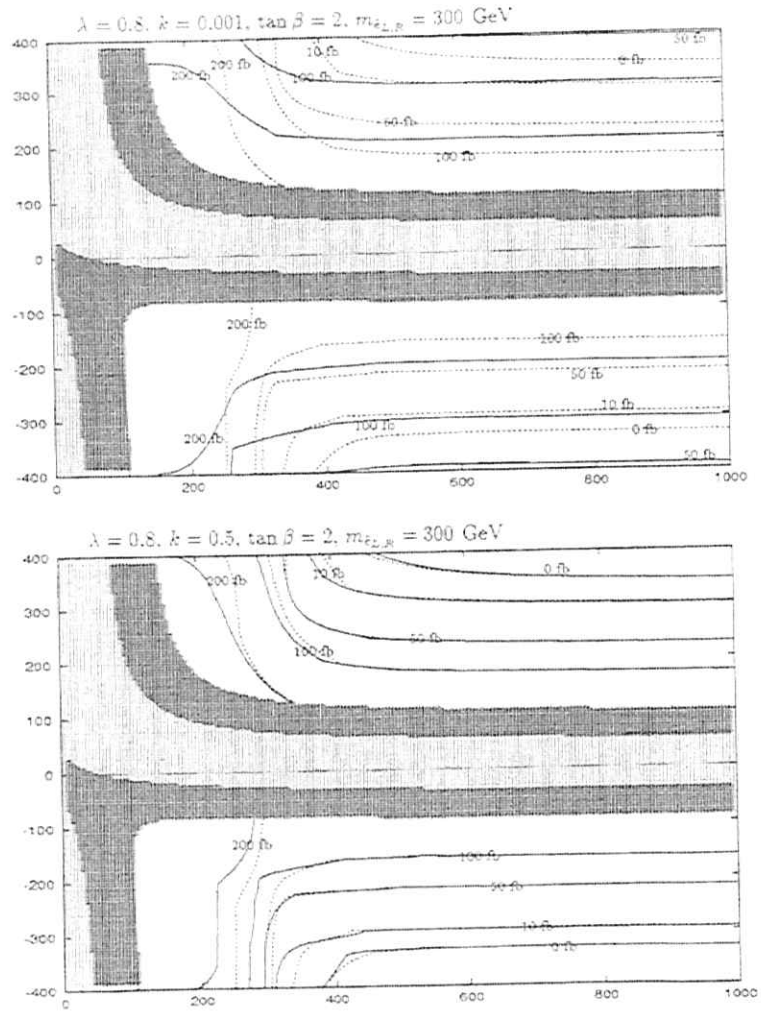

Figure 3: Contour lines of the sum of the cross sections in the production channels with at least one visible neutralino in the NMSSM (solid lines) and the MSSM with $\mu = \lambda x$ (dashed lines).

Test of Nonlinear Supersymmetric Standard Model at an e^+e^- Collider *

H. Genten[1], S. W. Ham[2], B. R. Kim[1], and S. K. Oh[2]

[1] III. Phys. Inst. A, RWTH Aachen, Aachen, Germany
[2] Dept. of Physics, Kon-Kuk University, Seoul, Korea

1 Introduction

Supersymmetry [1] is one of the most attractive candidates for the extention of the standard model of electroweak interactions. For more than a decade, the phenomenology of the supersymmetric models has been studied, and the search for supersymmetric particles is one of the main goals of the existing and future accelerators.

Most of those supersymmetric models investigated so far are linear models, i.e., the SUSY is realized linearly. However, it is still an open question whether the supersymmetry may be realized linearly or nonlinearly, and the nonlinear models are on the verge of drawing attentions recently. Some years ago, Samuel and Wess [2] have developed the formalism for extending the standard model supersymmetrically in a nonlinear way. Recently, one of us has constructed the most general form of the nonlinear supersymmetric standard model in the curved space and derived the Higgs potential in the flat limit [3].

The nonlinear supersymmetric models are economical in the sense that they need not the supersymmetric partners for the conventional particles in the standard model while the linear models require those partners. In global nonlinear supersymmetric models, one needs to introduce at most only one new particle, the Akulov-Volkov field [4], which is a Goldstone fermion. Experimentally, no Goldstone fermion has been observed. The goldstino can be removed by moving into the curved space, i.e., into supergravity, where it can be gauged away.

In the flat limit, the supergravity multiplet decouples from the ordinary matter such that the only reminiscence of the SUSY manifests itself in the Higgs sector. The Higgs sector of the nonlinear models is larger than that of the standard model because it requires at least two Higgs doublets. This requirement is also shared by linear models. However, whereas two Higgs doublets suffice for linear models, the nonlinear models require an additional Higgs singlet. The Higgs singlet may be introduced either as an auxiliary field or as a dynamical field or as both. In case the Higgs singlet is both auxiliary and dynamical, the Higgs boson spectra of the nonlinear models are similar to those of the

*This work is supported in part by Ministry of Education, Korea, BSRI-95-2442

next-to-minimal supersymmetric standard model (NMSSM), a linearly realized model with two Higgs doublets and a Higgs singlet [5]. Thus, the nonlinear models where the Higgs singlet is both auxiliary and dynamical, as well as the NMSSM, have three scalar, two pseudoscalar and a charged Higgs bosons. However, the structure of the Higgs potential is different between the nonlinear models and the NMSSM, as can be seen shortly.

In this note we investigate the phenomenology of a nonlinear supersymmetric model where the additional Higgs singlet is both both auxiliary and dynamical. In particular, we are interested in how far the Higgs sector of this model can be tested at future e^+e^- colliders.

2 The Model

The complete Higgs potential of the nonlinear supersymmetric model where the Higgs singlet is both auxiliary and dynamical reads in the flat limit as [3]

$$\begin{aligned} V &= \frac{1}{8}(g_1^2+g_2^2)(|H^1|^2-|H^2|^2)^2+\frac{1}{2}g_2^2|H^{1\dagger}H^2|^2 \\ &\quad +\mu_1^2|H^1|^2+\mu_2^2|H^2|^2+\mu_0^2|N|^2 \\ &\quad +\lambda_0^2|H^{1T}\epsilon H^2|^2+k^2|N^\dagger N|^2+|N|^2(\lambda_1^2|H^1|^2+\lambda_2^2|H^2|^2) \\ &\quad -k\lambda_0[(H^{1T}\epsilon H^2)^\dagger N^2+\text{h.c.}] \\ &\quad +[\lambda_1\mu_1|H^1|^2N+\lambda_2\mu_2|H^2|^2N+\lambda_0\mu_0(H^{1T}\epsilon H^2)^\dagger N+\text{h.c.}] \\ &\quad +[k\mu_0 N^\dagger N^2+\text{h.c.}] \end{aligned} \tag{1}$$

Note that the first three terms come from the D-part of the Lagrangian and the rest from the F-part. The two Higgs doublets H^1 and H^2 as well as the Higgs singlet N develop the vacuum expectation values v_1, v_2, and x, respectively. The three scalar Higgs bosons appear as the eigenstates of the relevant mass term for the real components of three neutral Higgs fields, when it is diagonalized by a 3×3 orthogonal matrix U.

The upper bound on the mass of the lightest scalar Higgs boson S_1 at the tree level is obtained in a similar way as in the NMSSM by

$$m_{S_1}^2 \le m_{S_1,max}^2 = m_Z^2(\cos^2 2\beta + 2\lambda_g^2\sin^2 2\beta) \tag{2}$$

where $\tan\beta = v_2/v_1$ and $\lambda_g = \lambda_0^2/(g_1^2+g_2^2)$. This tree-level relation predicts that $m_{S_1} \le m_Z$ for $\lambda_0 \le \sqrt{(g_1^2+g_2^2)/2} \approx 0.52$ and $m_{S_1} \le 1.92\lambda_0 m_Z$ for $\lambda_0 > 0.52$. In the latter case, the maximum value of λ_0 determines the upper bound of m_{S_1}. For $m_t = 175$ GeV and with the GUT scale as the cut-off scale, one obtains $m_{S_1} \le 130$ GeV.

It is very instructive to notice that the upper bounds on m_{S_2} and m_{S_3} can be derived from the upper bound on m_{S_1} and m_{S_3}. Let us introduce two parameters R_1 and R_2 such that

$$\begin{aligned} R_1 &= U_{11}\cos\beta + U_{12}\sin\beta \\ R_2 &= U_{21}\cos\beta + U_{22}\sin\beta \end{aligned} \tag{3}$$

Clearly, R_1 and R_2 are complicated functions of the relevant parameters. Note that $0 \leq R_1^2 + R_2^2 \leq 1$. Then, the upper bounds on m_{S_2} and m_{S_3} are given as

$$m_{S_2}^2 \leq m_{S_2,max}^2 = \frac{m_{S_1,max}^2 - R_1^2 m_{S_1}^2}{1 - R_1^2}$$
$$m_{S_3}^2 \leq m_{S_3,max}^2 = \frac{m_{S_1,max}^2 - (R_1^2 + R_2^2) m_{S_1}^2}{1 - (R_1^2 + R_2^2)} \qquad (4)$$

where $m_{S_1,max}$ is the maximum value of the S_1 mass.

3 Higgs Production

The upper bound $m_{S_1} \leq 130$ GeV suggest that there are parameter regions where none of the three Higgs scalars can be produced at LEP I for $\sqrt{s} = m_Z$. Fig. 1 shows the contour lines of m_{S_1} and those of the production cross section of S_1 from the Higgs-strahlung process, bremsstrahlung off fermions and associated pair production $P_j S_1$, where $P_j (j = 1, 2)$ is a pseudoscalar Higgs boson. The discovery limit is about 1 pb at LEP I. Thus the region, where the cross section is greater than 1 pb is excluded. The production

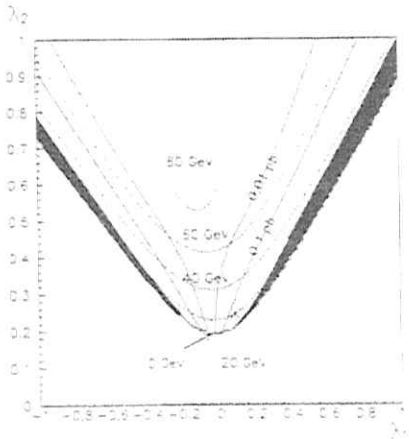

Figure 1: Contour lines of the lightest Higgs boson mass m_{S_1} (dotted) and of the production cross section σ (solid) at $\sqrt{s} = m_Z$, as functions of λ_1 and λ_2 for $\tan\beta = 3$, $\lambda_0 = 0.4$, $k = 0.02$ and $m_C = 200$ GeV. The shaded area marks the parameter region excluded by LEP I, defined as the region where the production cross section is greater than 1 pb.

cross section of S_2 is smaller than 12.3 fb in the entire plane and that of S_3 vanishes. Thus Fig. 1 shows that LEP I data allow the existence of massless S_1. We obtained similar results for LEP II energies of 175, 192, and 205 GeV [6].

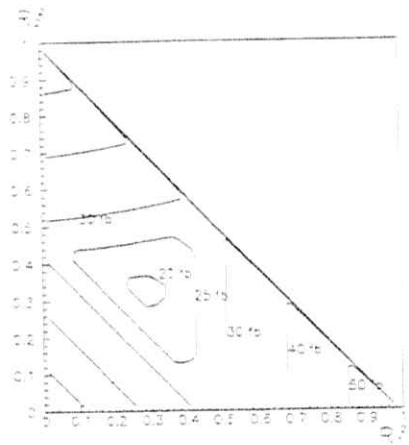

Figure 2: Contour lines of $\sigma(R_1, R_2)$ defined by eq(6) for $\sqrt{s} = 500$ GeV. The minimum value is about 19 fb.

For $\sqrt{s} \geq 500$ GeV the situation is different. In this case the production via the Higgs-strahlung process is possible for at least one of S_i. Thus one should consider the production of S_1, S_2, and S_3 simultaneously. In order to be systematic, we consider the production cross section of S_1, S_2, and S_3 via the Higgs-strahlung process, denoted by σ_1, σ_2, σ_3 and given by

$$\begin{aligned} \sigma_1(m_{S_1}) &= \sigma_{SM}(m_{S_1}) R_1^2 \\ \sigma_2(m_{S_2}) &= \sigma_{SM}(m_{S_2}) R_2^2 \\ \sigma_3(m_{S_3}) &= \sigma_{SM}(m_{S_3})(1 - R_1^2 - R_2^2) \,, \end{aligned} \qquad (5)$$

where $\sigma_{SM}(m)$ is the cross section in the standard model for the production of the Higgs boson of mass m via the Higgs-strahlung process. An useful observation is that $\sigma_i(m_{S_i,max}) \leq \sigma_i(m_{S_i})$ which allows to derive parameter independent lower limits of σ_i as we will show in the following. First we determine at a fixed set of m_{S_i}, R_1, R_2 the cross sections $\sigma_1(R_1, R_2, m_{S_1})$, $\sigma_2(R_1, R_2, m_{S_2,max})$ and $\sigma_3(R_1, R_2, m_{S_3,max})$. Second we keep R_1, R_2 fixed, but vary m_{S_i} from the minimum to the maximum and determine the quantity $\sigma(R_1, R_2)$

$$\sigma(R_1, R_2) = \min[\max(\sigma_1, \sigma_2, \sigma_3)] \,. \qquad (6)$$

where $\sigma_i = \sigma_i(R_1, R_2, m_{S_i})$. As last step we vary R_1^2 and R_2^2 from 0 to 1: $0 \leq R_1^2 \leq 1$, $0 \leq R_2^2 \leq 1$ and plot $\sigma(R_1, R_2)$ in R_1^2-R_2^2 plane. In order for this plot to be useful there is a critical energy, a kind of threshold, namely $E_C = m_Z + m_{S_i,max}$. For $\sqrt{s} < E_C = m_Z + m_{S_i,max}$ $\sigma(R_1, R_2) = 0$ and this plot is useless. In the present model we obtained $m_{S_i,max} = 130$ GeV, thus $E_C = m_Z + 130$ GeV $= 222$ GeV. Now the anticipated energies of LEP II are 175, 195 and 205 GeV. Thus our method does not yield any useful results for LEP II [5]. The situation is different when the collider energy is greater than E_C. In this case $\sigma(R_1, R_2) > 0$ in the entire region of R_1^2-R_2^2 and the minimum of $\sigma(R_1, R_2)$ in the R_1^2-R_2^2 plane is a parameter independent lower limit of one of σ_1, σ_2 and σ_3. This minimum is thus a characteristic quantity of the model. In fig 2 we plotted $\sigma(R_1, R_2)$ for $\sqrt{s} = 500$ GeV. The minimum is about 19 fb. When the discovery limit is about 10 events, one would needs a luminosity of about 0.5 fb^{-1} in order to test the model. A luminosity of this order is more than a realistic one. For 1000 GeV (2000 GeV) the minimum cross section is about 5 fb (1.2 fb). Thus this model may most probably tested conclusively at the planned e^+e^- colliders.

References

[1] H. E. Haber and G. L. Kane, **Phys. Rep. 117** (1985) 75; H. P. Nilles, **Phys. Rep. 110** (1984) 1.

[2] S. Samuel and J. Wess, Nucl. Phys. **B233** (1984) 488; **B226** (1983) 289.

[3] B. R. Kim, Z. Phys. **C67** (1995) 337.

[4] D. V. Volkov and V. P. Akulov, JETP Lett. 16 (1972) 438.

[5] J.-P. Derendinger and C. A. Savoy, Nucl. Phys. **B 237** (1984) 307;
J. Ellis, J. F. Gunion, H. E. Haber, L. Roszkowski, F. Zwirner, Phys. Rev. **D 39** (1989) 844;
M. Drees, **Int. J. Mod. Phys. A 4** (1989) 3635.

[6] H. Genten, S. W. Ham, B. R. Kim, and S. K. Oh, in the proceedings of the LEP 200 workshop 1995.

Resonant Single Superparticle Productions via Supersymmetric R-parity Violation

Herbi Dreiner[1] and Smaragda Lola[2]

[1] Rutherford Appleton Laboratory, Oxfordshire, OX11 0QX, UK
[2] Theory Division, CERN, CH-1211 Geneva, Switzerland

Abstract

We study single supersymmetric particle productions via the processes $e^+e^- \to \{(\tilde{\chi}_1^\mp, l^\pm), (\tilde{\chi}_1^0, \nu)\}$. We present analytical formulas for the cross sections and study the resonant s-neutrino production that is involved in the process. We compute the decay rate of the chargino to an R-parity even final state and discuss the branching fraction. We then determine the event rate and scalar neutrino mass reach.

1 Introduction

To date, the main working tool for experimental searches of supersymmetry has been the Minimal Supersymmetric Standard Model (MSSM) [1], which has the minimal particle content and couplings consistent with the known theory at low energies. However, we do not believe that the phenomenology of supersymmetry should be restricted to the MSSM, since it does not include several important features of possible supersymmetric extensions of the theory. The most general $SU(3)_c \times SU(2)_L \times U(1)_Y$ invariant superpotential with the minimal field content of the supersymmetric standard model also contains the terms [2]

$$W = \lambda_{ijk} L_i L_j \bar{E}_k + \lambda'_{ijk} L_i Q_j \bar{D}_k + \lambda''_{ijk} \bar{U}_i \bar{D}_j \bar{D}_k \tag{1}$$

where L, (Q) are the left-handed lepton (quark) superfields while $\bar{E}, \bar{D}$, and $\bar{U}$ are the corresponding right-handed fields. The first two operators violate lepton number, while the third violates baryon number. If both lepton and baryon number violating operators were present at the same time in the low energy Lagrangian, they would lead to unacceptably fast proton decay. However it has been shown [3] that there exist symmetries which allow the violation of only a subset of these operators, leading to very rich phenomenology [4, 5, 6, 7], while being consistent with the limits on proton decay. Since the baryon number violating operators result in processes with a strong QCD background, we consider the phenomenology of the lepton number violating interactions as the most promising. For $\lambda, \lambda' \gtrsim 10^{-6}$ the lightest supersymmetric particle decays inside the detector, thus altering drastically the supersymmetry search strategies. Instead of dominantly missing energy signals the final state will contain several charged leptons.

$SU(2)$ and $SU(3)$ invariance indicate that there exist 45 R-parity violating operators, 36 associated with lepton number violation and 9 with baryon number violation. It is possible to study all these operators in a single processes. For example Z^0 couples to all fermions and may lead to single superparticle productions through any one of the operators. Although the signals are very exotic [8, 9], this process (which is suppressed due to its three-body phase space) was found to be more relevant for hadron colliders [9], where the expected luminosity and available energy is larger compared to LEP and NLC. Similarly superparticle pair production [10] and subsequent decay via R-parity violating operators [1] could give us information about various

[1] Such processes arise via gauge couplings and are favoured for very small R-parity violating couplings.

operator flavours, however the existence of two massive particles in the final state limits the mass range that we can probe [11].

For these reasons, we will here concentrate on single superparticle productions, arising from the terms $\lambda_i L_e L_i \bar{E}_e$, $i = \mu, \tau$. In particular we shall work with the resonant scalar-neutrino production and the decay to an R-parity *odd* final state

$$e^+e^- \to (\tilde{\nu}_i)^* \to \bar{l}_i^\mp \tilde{\chi}^\pm \tag{2}$$
$$e^+e^- \to (\tilde{\nu}_i)^* \to \nu_i \tilde{\chi}^0 \tag{3}$$

which will lead to multilepton events. The above processes only involve a single R_p-odd particle in the final state and thus the mass reach can be considerably larger than for MSSM processes at the same machine. We do not consider the related final states involving a $W^\pm$ or Z^0 boson [11] since again the production of two massive states limits the mass range that we can probe. The chargino and neutralino will decay to an R-parity even final state involving several charged leptons

$$\tilde{\chi}_1^\mp \to \{(\tilde{\chi}_1^0, l^m, \nu), (e^-, l_i^-, e^+), (e^-, \nu_e, \nu_i)\} \tag{4}$$
$$\tilde{\chi}_1^0 \to \{(e^\mp, l_i^\pm, \nu_e), (e^\mp, e^\pm, \nu_i)\} \tag{5}$$

These signals should be clearly visible at an e^+e^--collider provided the cross-section is sufficiently large. The cross section depends on how large the unknown coupling λ will be. All the information that we have about that coupling is the inequality [5]

$$\lambda_{i=\mu,\tau} < (0.04, 0.1) \frac{\tilde{m}_{\tilde{\nu}_i}}{100\,GeV}, \tag{6}$$

In our analysis we shall assume that $\tilde{\chi}_1^0$ is the LSP and that only one operator $LL_i\bar{E}$ is dominant. We first determine the production cross sections. Then we discuss the chargino decays and their branching fractions[2]. We finish by determining the event rates.

2 Production Cross Sections

In this section we calculate the square amplitude, as well as the differential and total cross section for single chargino and neutralino productions at electron-positron colliders.

• chargino production :

Ignoring contributions to the vertices of the MSSM from mass terms, we have two channels present (s and t) for chargino production. For the s-channel diagram we need to take into account the contribution due to the partial width for the decay of the scalar neutrino, $\Gamma_{\tilde{\nu}}$. There are two contributions to this width, $\Gamma_1 \equiv \tilde{\nu} \to e^i e^j$ and $\Gamma_2 \equiv \tilde{\nu}^j \to \chi_1^0 \nu_k, \chi_1^\mp \ell_k^\pm$. These are given in [5] to be

$$\Gamma_1 = \frac{\lambda_{ijk}^2}{16\pi} m_{\tilde{\nu}^j}, \quad \Gamma_2 = C' \frac{g^2}{16\pi} m_{\tilde{\nu}^j} \left(1 - \frac{M_{\tilde{\chi}_1^0}^2}{m_{\tilde{\nu}^j}^2}\right)^2 \tag{7}$$

In the above formulas, λ_{ijk} is the R-parity violating Yukawa coupling. $C' = |V_{i1}|^2$ for chargino-plus-charged-lepton modes and $C' = |N_{i2}|^2/2\cos^2\theta_W$ for neutralino-plus-neutrino modes. V_{i1} and N_{i2} are the relevant matrix elements in the mixing matrix for charginos and neutralinos respectively.

[2] The neutralino decays have been discussed elsewhere [7].

For this process the square amplitude for the production of the lighter chargino is given by

$$\overline{M_{fi}^2} = \frac{1}{4}\left(\frac{U_{11}\lambda e}{\sin\theta_W}\right)^2 \left\{ \frac{C_s}{(s-m^2_{\tilde{\nu}_{\mu,\tau}})^2+\Gamma^2_{\tilde{\nu}} m^2_{\tilde{\nu}_{\mu,\tau}}} + \frac{C_t}{(t-m^2_{\tilde{e}_L})^2} + \frac{C_{st}(s-m^2_{\tilde{\nu}_{\mu,\tau}})}{[(s-m^2_{\tilde{\nu}_{\mu,\tau}})^2+\Gamma^2_{\tilde{\nu}} m^2_{\tilde{\nu}_{\mu,\tau}}](t-m^2_{\tilde{e}_L})} \right\} \quad (8)$$

where

$$\begin{aligned} C_s &= s(s-m^2_{\tilde{\chi}^\pm}) \quad C_t = t(t-m^2_{\tilde{\chi}^\pm}) \\ C_{st} &= s(s-m^2_{\tilde{\chi}^\pm}) + t(t-m^2_{\tilde{\chi}^\pm}) - u(u-m^2_{\tilde{\chi}^\pm}) \end{aligned} \quad (9)$$

Here s, t and u are the Mandelstam variables and a factor 1/4 has been included due to averaging over the spins of the incoming particles. Near the sneutrino resonance, the s-channel contribution is the dominant one, however, in the general case away from the resonance the contributions from the other channel is significant.

The analytic expression for this cross section is:

$$\sigma_{\tilde{\chi}^\pm} = \frac{\alpha_{em}\lambda^2 U_{11}^2}{16\sin^2\theta_W s}(X_1 + X_2 + 2X_3) \quad (10)$$

where

$$\begin{aligned} X_1 &= (1-\mu^2_{\tilde{\chi}^\pm})^2/f \\ X_2 &= (\mu^2_{\tilde{\chi}^\pm} - 2\mu^2_{\tilde{e}_L})v - 1 - \mu^2_{\tilde{\chi}^\pm} + \frac{(\mu^2_{\tilde{\chi}^\pm}-1)(\mu^2_{\tilde{e}_L}-\mu^2_{\tilde{\chi}^\pm})}{(\mu^2_{\tilde{\chi}^\pm}-\mu^2_{\tilde{e}_L}-1)} \\ X_3 &= (\mu^2_{\tilde{e}_L}v + \mu^2_{\tilde{\chi}^\pm} - 1)(\mu^2_{\tilde{\nu}_{\mu,\tau}}-1)/f \\ f &= (1-\mu^2_{\tilde{\nu}_{\mu,\tau}})^2 + \Gamma^2_{\tilde{\nu}}\mu^2_{\tilde{\nu}_{\mu,\tau}} \\ v &= \ln\left(\frac{1+\mu^2_{\tilde{\nu}_{\mu,\tau}}-\mu^2_{\tilde{\chi}^\pm}}{\mu^2_{\tilde{\nu}_{\mu,\tau}}}\right). \end{aligned} \quad (11)$$

We note that in the final expression for the cross section, we have used the normalised masses (i.e $\mu_{\tilde{x}} = \frac{m_{\tilde{x}}}{\sqrt{s}}$, where s is the total center of mass energy squared).

• neutralino production :

Neutralino production has the same phase space as the chargino production, but now both the t and u channels are present, together with the resonant sneutrino production of the s-channel. For the matrix element square we find:

$$\begin{aligned} \overline{M_{fi}^2} = \frac{2}{4}\lambda^2 \Bigg\{ & V_1^2\frac{C_s}{(s-m^2_{\tilde{\nu}_{\mu,\tau}})^2+\Gamma^2_{\tilde{\nu}}m^2_{\tilde{\nu}_{\mu,\tau}}} + V_2^2\frac{C_t}{(t-m^2_{\tilde{e}_L})^2} + V_3^2\frac{C_u}{(u-m^2_{\tilde{e}_L})^2} \\ & -V_1V_2^*\frac{C_{st}(s-m^2_{\tilde{\nu}_{\mu,\tau}})}{[(s-m^2_{\tilde{\nu}_{\mu,\tau}})^2+\Gamma^2_{\tilde{\nu}}m^2_{\tilde{\nu}_{\mu,\tau}}](t-m^2_{\tilde{e}_L})} - V_1V_3^*\frac{C_{su}(s-m^2_{\tilde{\nu}_{\mu,\tau}})}{[(s-m^2_{\tilde{\nu}_{\mu,\tau}})^2+\Gamma^2_{\tilde{\nu}}m^2_{\tilde{\nu}_{\mu,\tau}}](u-m^2_{\tilde{e}_L})} \\ & -V_2V_3^*\frac{C_{tu}}{(t-m^2_{\tilde{e}_L})(u-m^2_{\tilde{e}_L})} \Bigg\} \end{aligned} \quad (12)$$

where

$$V_1 = -\frac{1}{2}\frac{g}{\cos\theta_W}N'^*_{j2}$$

$$\begin{aligned} V_2 &= \left(-eN'^*_{j1} - \frac{g}{\cos\theta_W}\frac{1}{2} - \sin\theta_W{}^2\right)N'^*_{j2} \\ V_3 &= -eN'^*_{j1} + \frac{g\sin\theta_W{}^2}{\cos\theta_W}N'^*_{j2} \end{aligned} \quad (13)$$

Here the additional functions C_u, C_{su} and C_{tu} with respect to the previous process are given by

$$\begin{aligned} C_u &= u(u-m^2_{\tilde{\chi}^\pm}) \\ C_{su} &= s(s-m^2_{\tilde{\chi}^\pm}) - t(t-m^2_{\tilde{\chi}^\pm}) + u(u-m^2_{\tilde{\chi}^\pm}) \\ C_{tu} &= -s(s-m^2_{\tilde{\chi}^\pm}) + t(t-m^2_{\tilde{\chi}^\pm}) + u(u-m^2_{\tilde{\chi}^\pm}) \end{aligned} \quad (14)$$

The analytic expression for the neutralino production cross section is:

$$\sigma_{\tilde{\chi}^0} = \frac{\lambda^2}{32s}[V_1^2X_1 + (V_2^2+V_3^2)X_2 + 2(V_1V_2^* + V_1V_3^*)X_3 - V_2V_3^*X_4] \quad (15)$$

where the only unknown contribution comparable to the chargino production is X_4 which comes from the interference term between the t and u channels. This is given by

$$X_4 = \frac{2\mu^2_{\tilde{e}}(\mu^2_{\tilde{\chi}^0}-\mu^2_{\tilde{e}}-1)v - (\mu^2_{\tilde{\chi}^0}-\mu^2_{\tilde{e}}-1)^2 - \mu^2_{\tilde{e}}}{\mu^2_{\tilde{\chi}^0}-2\mu^2_{\tilde{e}}-1}. \quad (16)$$

Here, we again use normalised masses in this final expression.

3 Decay Rates and Branching Fractions

To determine the event rates for the multilepton signals, we also need to know the branching fractions for the chargino and neutralino decays. Concerning the chargino decays, we would like to stress that there exist two possible decay modes. The first is the known cascade decay via the lightest neutralino

$$\tilde{\chi}_1^- \to \tilde{\chi}_1^0 + (W^-)^* \to \tilde{\chi}_1^0 + f\bar{f}' \quad (17)$$

where $f\bar{f}'$ are the decay fermions of the (virtual) W-boson. However, there exists an alternative possibility: The chargino can decay directly via the operator $L_eL_iE_e$

$$\tilde{\chi}_1^- \to (e^-e^+l_i^-, \nu_e\nu_i e^-) \quad (18)$$

In this latter case the signal is even more distinct since it involves 4 leptons at the final state (from which 3 are in the same semi-plane) without any missing energy, unlike the cascade decay which always involves neutrinos at the final state. Which of the two processes will appear, depends on (i) The strength of the R-parity violating operator: the strongest the operator the larger the decay rate for a direct decay of the chargino (ii) The relative mass of chargino-neutralino: If the mass gap between the two states is very small, then the cascade decay is suppressed by phase space. An analytic discussion of this aspect is given in [12]. The neutralino decay is straightforward.

Using this information, we calculated the event rates for neutralino and chargino productions, which appear in Figs. 1 and 2. From these figures we see that it is possible to observe single sparticle production significantly off the sneutrino resonance. For example for single chargino production and a chargino mass of 400 GeV we should be able to observe a sneutrino mass in the range of 300 - 580 GeV.

References

[1] For a review of the MSSM see H. E. Haber and G. L. Kane, Phys. Rept. 117 (1985) 75 and references therein.

[2] See for example L. J. Hall and M. Suzuki, Nucl. Phys. B 231, 419 (1984).

[3] L. E. Ibanez and G. G. Ross, Phys. Lett. B 260 (1991) 291; Nucl. Phys. B 368 (1992) 3; H. Dreiner and A. Chamseddine, Nucl. Phys. B 458 (1996) 65.

[4] S. Dimopoulos, R. Esmaizadeh, L. Hall and G. Starkman, Phys. Rev. D 41, 2099 (1990);

[5] V. Barger, G. F. Giudice and T. Han, Phys. Rev. D 40 (1989) 2987.

[6] P. Binetruy *et al*, Proceedings of the Large Hadron Collider Workshop, Vol II (1990) 666; H. Dreiner and G. G. Ross, Nucl. Phys. B 365 (1991) 597; H. Dreiner and J. Butterworth, Nucl. Phys. B 397 (1993) 3;

[7] H. Dreiner and P. Morawitz, Nucl. Phys. B 428 (1994) 31.

[8] D. E. Brahm and L. J. Hall, Phys. Rev. D 40 (1989) 2449.

[9] S. Lola and J. McCurry, Nucl. Phys. B 381 (1992) 559.

[10] M. Chen, C. Dionisi, M. Martinez and X. Tata, Phys. Rep. 159, 201 (1988).

[11] H. Dreiner and S. Lola, in Munich/Annecy/Hamburg 1991 proceedings, e^+e^- collisions at 500 GeV.

[12] H. Dreiner and S. Lola in preparation.

Figure 1: Cross section for $e^+e^- \to \nu\chi^0$ for three different neutralino masses. $\sqrt{s} = 500\,GeV$. We have fixed the R-parity violating coupling of the $L_1 L \bar{E}_1$ operator to $\lambda_{LLE} = 0.01$. The cross section scales with λ^2_{LLE}. We have included a line which corresponds to 10 events at 20 fb^{-1}/yr.

Figure 2: The same as in Figure 1 for the process $e^+e^- \to \nu\chi^0$. Now we have varied the chargino mass.

RESONANT SNEUTRINO PRODUCTION

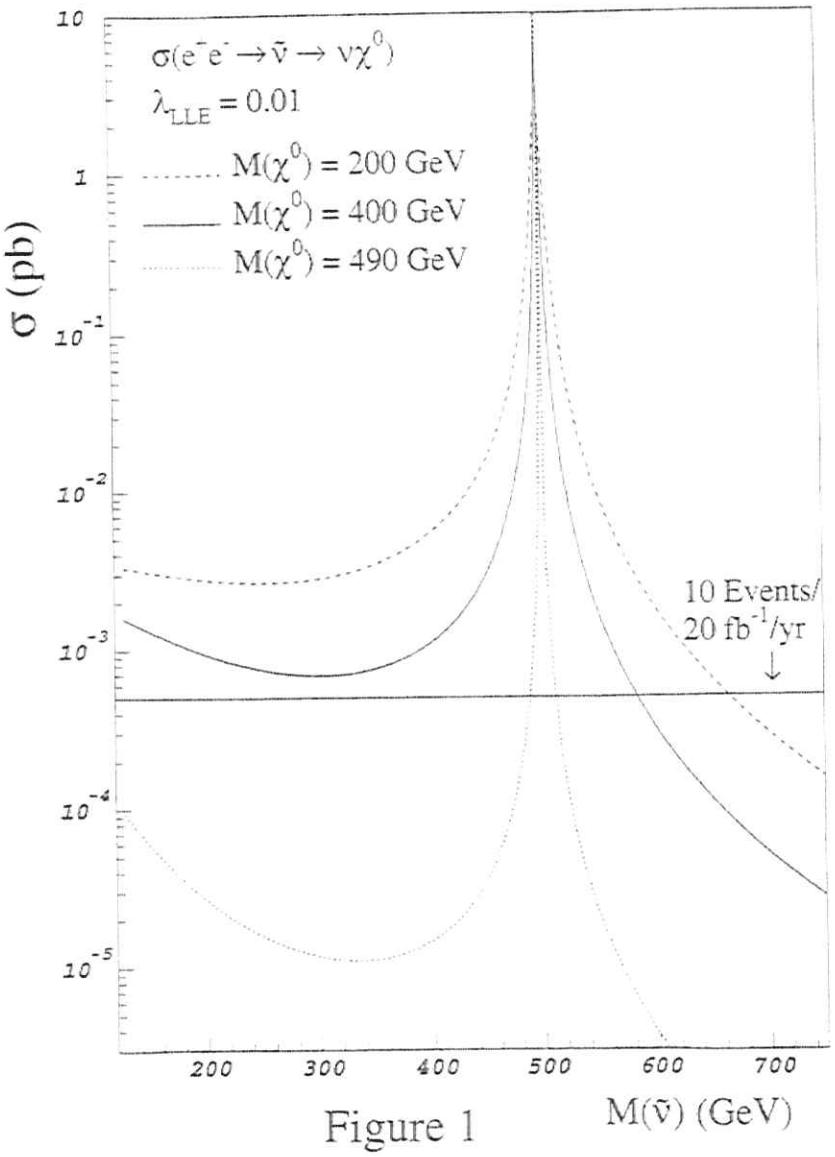

Figure 1

RESONANT SNEUTRINO PRODUCTION

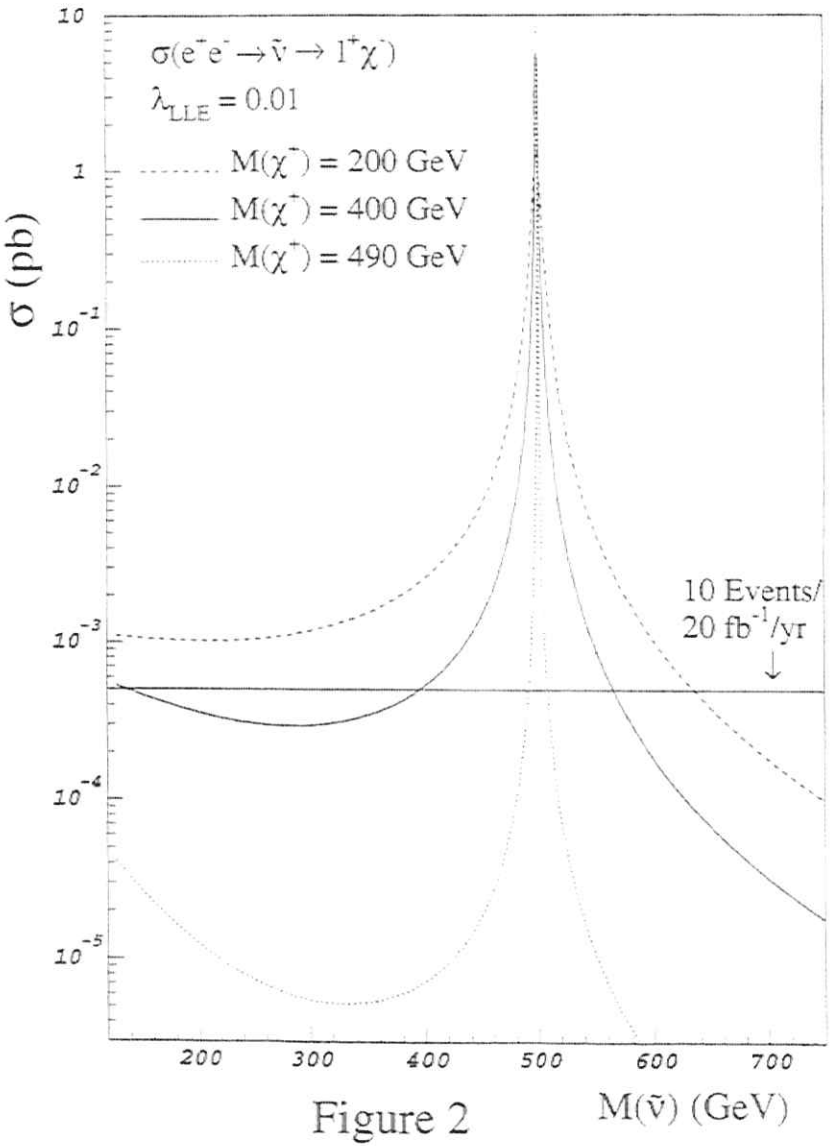

Figure 2

SUPERSYMMETRIC LEFT-RIGHT MODEL AT NLC

KATRI HUITU[a], JUKKA MAALAMPI[b] and MARTTI RAIDAL[a,b,c]
[a] *Research Institute for High Energy Physics, University of Helsinki, Finland*
[b] *Department of Physics, Theory Division, University of Helsinki, Finland*
[c] *Department of Theoretical Physics, University of Valencia, Spain*

ABSTRACT

We review here our study of a supersymmetric left-right model (SLRM). In the model the R-parity is spontaneously broken. Phenomenologically novel feature of the model is the occurrance of the doubly charged particles in the Higgs sector, which are possibly light enough to be seen in the next linear collider. Detection of the doubly charged higgsinos in the next linear collider is discussed.

1. Introduction

The left-right symmetric electroweak model based on the $SU(2)_L \times SU(2)_R \times U(1)_{B-L}$ symmetry has many attractive features. In particular, in the see-saw [1] mechanism it offers a beautiful and very natural explanation for the lightness of the ordinary neutrinos. On the other hand, like in the Standard Model it has a hierarchy problem in the scalar sector, which can be solved by making the theory supersymmetric.

The left-right models are especially interesting, if the experiments on solar [2] and atmospheric [3] neutrinos continue to show deviation from the standard model, as well as the existence of the hot dark matter component [4] explaining some features of the power spectrum of density fluctuations of the Universe persists. All these results seem to indicate that neutrinos indeed have a small mass.

To achieve the see-saw mechanism, the $SU(2)_L \times SU(2)_R \times U(1)_{B-L}$ symmetry has to be broken by scalar triplets of $SU(2)_R$. A novel feature of the model is that the triplet superfields contain among others also doubly charged particles.

2. The supersymmetric left-right model (SLRM)

The model is described by the superpotential

$$\begin{aligned} W &= h_{sQ}\hat{Q}_L^T i\tau_2 \hat{\phi} \hat{Q}_R^c + h_{\chi Q}\hat{Q}_L^T i\tau_2 \hat{\chi} \hat{Q}_R^c \\ &+ h_{sL}\hat{L}_L^T i\tau_2 \hat{\phi} \hat{L}_R^c + h_{\chi L}\hat{L}_L^T i\tau_2 \hat{\chi} \hat{L}_R^c + h_\Delta \hat{L}_R^{cT} i\tau_2 \hat{\Delta} \hat{L}_R^c \\ &+ \mu_1 \mathrm{Tr}(i\tau_2 \hat{\phi}^T i\tau_2 \hat{\chi}) + \mu_2 \mathrm{Tr}(\hat{\Delta}\hat{\delta}), \end{aligned} \tag{1}$$

where $\hat{Q}_{L(R)}$ denote the left (right) handed quark superfield doublets and similarly for the leptons $\hat{L}_{L(R)}$. The triplet and the bidoublet Higgs superfields of $SU(2)_L \times SU(2)_R \times U(1)_{B-L}$ are given by

$$\hat{\Delta} = \begin{pmatrix} \hat{\Delta}^-/\sqrt{2} & \hat{\Delta}^0 \\ \hat{\Delta}^{--} & -\hat{\Delta}^-/\sqrt{2} \end{pmatrix}, \quad \hat{\delta} = \begin{pmatrix} \hat{\delta}^-/\sqrt{2} & \hat{\delta}^{--} \\ \hat{\delta}^0 & -\hat{\delta}^-/\sqrt{2} \end{pmatrix}$$
$$\hat{\phi} = \begin{pmatrix} \hat{\phi}_1^0 & \hat{\phi}_1^+ \\ \hat{\phi}_2^- & \hat{\phi}_2^0 \end{pmatrix}, \quad \hat{\chi} = \begin{pmatrix} \hat{\chi}_1^0 & \hat{\chi}_1^- \\ \hat{\chi}_2^+ & \hat{\chi}_2^0 \end{pmatrix}. \tag{2}$$

where the different fields transform as $\hat{\Delta} \sim (1,3,-2)$, $\hat{\delta} \sim (1,3,2)$, $\hat{\phi} \sim (2,2,0)$, and $\hat{\chi} \sim (2,2,0)$. Corresponding to each scalar multiplet with non-zero $U(1)$ quantum number, one has to include another multiplet with an opposite $U(1)$ quantum number in order to avoid chiral anomalies for the fermionic superpartners. Also another bidoublet Higgs superfield is added to get a nontrivial Kobayashi-Maskawa matrix.

We find a region in the parameter space for which the scalar fields in the minimum have the following vacuum expectation values [5]:

$$\langle \Delta^0 \rangle = v_\Delta, \quad \langle \delta^0 \rangle = v_\delta, \quad \langle \phi_1^0 \rangle = \kappa_1, \quad \langle \chi_2^0 \rangle = \kappa_2, \quad \langle \tilde{\nu} \rangle = \sigma_R. \tag{3}$$

Applying the minimization conditions $\partial V/\partial\kappa_1 = \partial V/\partial\kappa_2 = \partial V/\partial v_\Delta = \partial V/\partial v_\delta = \partial V/\partial\sigma_R = 0$ one can find the scalar masses. In the minimum the $mass^2$ of all the scalars in the Higgs sector must be positive. This requirement has fundamental consequences for the R-parity, $R = (-1)^{3(B-L)+2S}$. The R-parity is automatically conserved in Lagrangian in this type of models [6], but necessarily at least one of the $\langle \tilde{\nu} \rangle \neq 0$ [7,8].

However, if a right-sneutrino has vev, it is found that ranges of parameters exist, where all the squares of the Higgs masses are positive. Furthermore, one of the doubly charged Higgses turns out to be lighter than 500 GeV for $h_\Delta \leq 0.8$ [5]. The majority of the scalars are heavier than 1 TeV.

3. Testing SLRM at NLC

Another particle of interest in the Higgs sector is the supersymmetric counterpart of the doubly charged Higgs. This particle is very suitable for experimental search for many reasons. It is doubly charged, which means that it does not mix with other particles. Consequently its mass is given by a single parameter, the susy Higgs mixing parameter μ_2.

The next generation linear electron colliders will, besides the usual e^-e^- reactions, be able to work also in e^-e^-, $e^-\gamma$ and $\gamma\gamma$ modes. The high energy photon beams can be obtained by back-scattering an intensive laser beam on high energy electrons. The doubly charged higgsinos can be produced in any of these operation modes [8]:

$$e^-e^- \to \tilde{\Delta}^{++}\tilde{\Delta}^{--}, \tag{4}$$

$$e^-e^- \to \tilde{\Delta}^{--}\tilde{\chi}^0, \tag{5}$$

$$\gamma e^- \to \tilde{l}^+\tilde{\Delta}^{--}, \tag{6}$$

$$\gamma\gamma \to \tilde{\Delta}^{--}\tilde{\Delta}^{++}. \tag{7}$$

We have chosen these reactions for investigation because they all have a clean experimental signature: a few hard leptons and missing energy. Furthermore, they all have very small background from other processes.

In large regions of the parameter space, the kinematically favoured decay mode of the triplet higgsino is $\tilde{\Delta}^{++} \to \tilde{l}^+l^+$. Which of the slepton decay modes is dominant, depends on kinematics, but one possibility is the decay to a lepton and the lightest neutralino: $\tilde{l} \to l\tilde{\chi}^0$. The experimental signature of the doubly charged higgsino could be then

$$\tilde{\Delta}^{--} \to \tilde{l}^-l^- \to l^-l^-\tilde{\chi}^0. \tag{8}$$

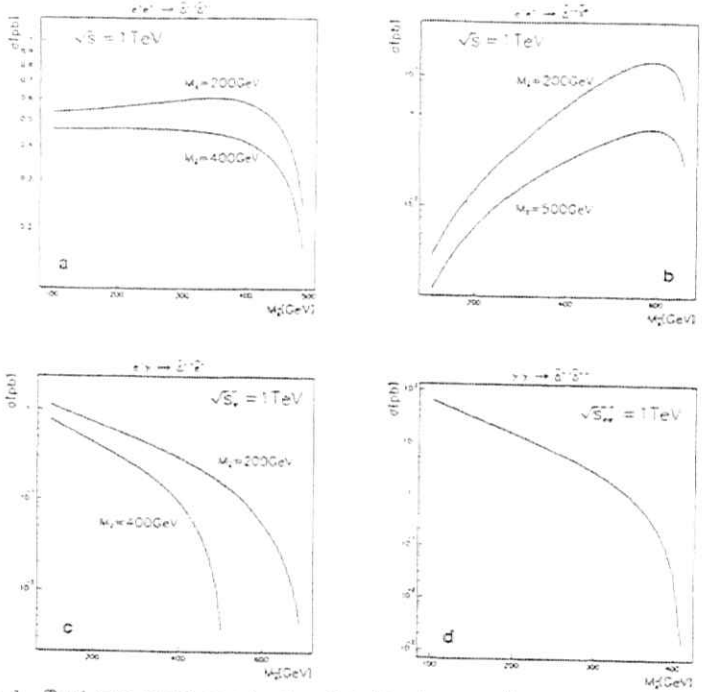

Fig. 1. Total cross section as a function of the higgsino mass $M_{\tilde{\Delta}}$ for reactions a) $e^+e^- \to \tilde{\Delta}^{++}\tilde{\Delta}^{--}$, b) $e^-e^- \to \tilde{\chi}^0\tilde{\Delta}^{--}$, c) $\gamma e^- \to \tilde{l}^-\tilde{\Delta}^{--}$, all for two values of selectron mass $m_{\tilde{l}}$, and d) $\gamma\gamma \to \tilde{\Delta}^{++}\tilde{\Delta}^{--}$. In a)-d) the electron-positron or electron-electron collision energy is 1 TeV

where l can be any of the e, μ, and τ with practically equal probabilities. We have here ignored the effect of selectron mixing with charged Higgses due to the R-parity breaking. The mixing would lengthen the lifetime of the doubly charged higgsino and on the other hand offer new decay channels for slepton, though suppressed by the mixing angle. In Fig. 1 the total cross section for the process (4) is shown to be for the given parameters about 0.5 pb and quite constant up to the threshold. The process (5) occurs via a selectron exchange in t-channel. The signal for (5) is two same-sign leptons with missing energy. It may be distuinguished from the leading background process, $e^-e^- \to \tilde{e}^-\tilde{e}^- \to e^-e^-+$ missing energy by using the fact that $|\Delta L| = 2$ Yukawa couplings need not be diagonal and consequently the signature leptons may be of different flavour. In process (6), the background of $e^-\gamma \to e^-Z^*$ may also be cut down by a suitable choice of final state leptons. The reaction (7) is a model independent way to produce doubly charged higgsinos, since it depends only on the parameter μ_2. For $\mu_2 \lesssim 300$ GeV its cross section is larger than 1 pb (Fig. 1). The experimental signature is same than in (4), i.e. four charged leptons with missing energy.

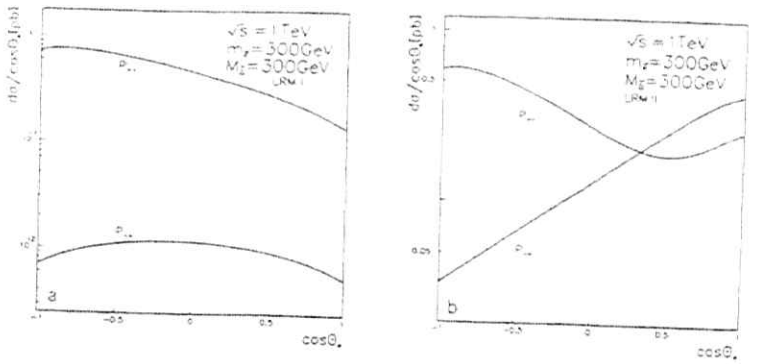

Fig. 2. The angular distribution of the final state electron in the cascade process $e^-e^- \to \tilde{e}^-\tilde{e}^- \to e^-e^-\tilde{\chi}_1^0\tilde{\chi}_1^0$ for $\sqrt{s} = 1$ TeV, $M_{\tilde{\Delta}} = m_{\tilde{e}} = 300$ GeV in the model, in which neutralinos are mainly a) higgsinos and b) gauginos. P_{+-} corresponds to the case where the incoming electron has positive and the incoming positron has negative longitudinal polarization, and P_{-+} corresponds to the opposite case.

The slepton pair production

$$e^-e^- \to \tilde{l}^-\tilde{l}^- \tag{9}$$

tests also the Higgs sector of the theory since the process is mediated among others by the doubly charged higgsino [9].

The selectron pair production in supersymmetric LR-model has a larger cross section than the corresponding process in the MSSM by about an order of magnitude [9]. This is due to two factors, firstly the number of gauginos in t-channel is larger and secondly the triplet higgsino contribution in u-channel is large, though dependent on the unknown triplet higgsino coupling to the electron and selectron.

The u-channel exchange of the doubly charged higgsino occurs only for a right-handed electron and a left-handed positron (P_{--} polarization), whereas in s- and t-channel processes also other chirality combinations may enter. Use of polarized beams could therefore give us more information of the triplet higgsino contribution. For P_{--} polarization there is a peak in the backward direction in the angular distribution of the final state electron, Fig. 2. Whether there is a forward peak, depends on the neutralino content. For gaugino dominated neutralinos, the peak exists, but for higgsino dominated neutralinos it is suppressed by the lepton Yukawa couplings.

The cross section of the pair production of smuons and staus are in general expected to be smaller than that of selectron pair production, since the neutralinos do not contribute. On the other hand the cross sections are in general larger than in the case of the MSSM because of the nondiagonal couplings of the triplet higgsinos.

The work has been supported by the Academy of Finland.

1. M. Gell-Mann, P. Ramond and R. Slansky, in *Supergravity*, eds. P. van Nieuwenhuizen and D.Z. Freedman (North Holland 1979); T. Yanagida, in Proceedings of

Workshop on Unified Theory and Baryon Number in the Universe, eds. O. Sawada and A. Sugamoto (KEK 1979).
2. K. Lande et al., in Proc. XXVth Int. Conf. on High Energy Physics, eds. K.K. Phua and Y. Yamaguchi (World Scientific, Singapore, 1991); K.S. Hirata et al., Phys. Rev. Lett. **66** (1990) 1301. K. Nakamura, Nucl. Phys. **B 31** (Proc. Suppl.) (1993); A.I. Abazov et al., Phys. Rev. Lett. **67** (1991) 3332; V.N. Gavrin, in Proc. XXVIth Int. Conf. in High Energy Physics (Dallas 1992), to appear.
3. K.S. Hirata et al., Phys. Lett. **B 280** (1992) 146; D. Casper et al., Phys. Rev. Lett. **66** (1993) 2561.
4. M. Davis, F.J. Summers, D. Schlegel, Nature 359 (1992) 393; A. N. Taylor, M. Rowan-Robinson, ibid. 396.
5. K. Huitu, J. Maalampi, Phys. Lett. **B 344** (1995) 217.
6. R.N. Mohapatra, Phys. Rev. **D34** (1986) 3457; A. Font, L.E. Ibanez, F. Quevedo, Phys. Lett. **B 228** (1989) 79; S.P. Martin, Phys. Rev. **D46** (1992) 2769.
7. R. Kuchimanchi, R. N. Mohapatra, Phys. Rev. **D48** (1993) 4352.
8. K. Huitu, J. Maalampi, M. Raidal, Nucl. Phys. **B 420** (1994) 449.
9. K. Huitu, J. Maalampi, M. Raidal, Phys. Lett. **B 328** (1994) 60.

$\gamma\gamma$ Physics at Linear Colliders

Conveners: P. Aurenche, A. Finch, M. Greco, D.J. Miller

Working group: M. Baillargeon, G. Bélanger, J. Blümlein, F. Boudjema, M. Cacciari, D. Choudhury, A. Corsetti, V. Del Duca, R. Engel, M. Fontannaz, I.F. Ginzburg, R.M. Godbole, J.-Ph. Guillet, G. Jikia, M. Krämer, M. Krawczyk, E. Laenen, G. Pancheri, J. Ranft, S. Riemersma, D.J. Schulte, T. Sjöstrand, A. Vogt

1 Introduction

As it is well known, there are several ways to generate photon-photon collisions at linear e^+e^- colliders. Bremsstrahlung and/or beamstrahlung photons radiated by the incoming electrons will interact with a center of mass energy which is only a small fraction of the available e^+e^- energy. These collisions are a nuisance for studies in electroweak interactions as they reduce the available e^+e^- luminosity at a given energy and generate an important hadronic background. Much work is going on to reduce this component. However it will be seen that this mechanism can be used to understand the deep structure of the photon. On the other hand, dedicated photon linear colliders can be constructed using backward Compton scattering of a beam electron on a laser photon, which will yield a photon-photon energy similar to the e^+e^- energy with a high luminosity: such colliders are invaluable for the study of multiple gauge boson couplings and will also allow studies of the hadronic structure of the photon at short distances never reached before. In this chapter we deal, partially, with all these aspects. Bremsstrahlung and/or beamstrahlung collisions will be discussed from the point of view of its relevance for QCD studies while for the photon linear colliders we discuss both its implications for QCD and electroweak theories.

Compared to previous reports [1] it will be seen that considerable progress has been achieved concerning both soft and hard (hadronic) physics studies: this is the result of the recent LEP2 [2, 3] workshop as well as the recent experimental studies at HERA [4]-[6]. More progress is obviously expected in the near future so that one should have a quantitative description of hadronic phenomena and therefore a good control of the "background" to "interesting" or new physics. Roughly speaking, making use of proton-antiproton studies at the FERMILAB collider and photon-proton studies at HERA one should be able, based on a loose concept of factorization, to predict reliably photon-photon physics at high energies. LEP2 results will provide a stringent test of these ideas. Concerning electroweak studies, during this workshop, radiative corrections to W pair production have been calculated as required for future precision studies and detailed signature of anomalous gauge boson couplings are being proposed, which are more stringent than those in the e^+e^- channel.

The report opens with Ginzburg overall perspective of the physics possibilities of photon linear colliders: in QCD the extended kinematical range available will make it possible to probe the so-called BFKL or Lipatov Pomeron which is now under discussion in connection with recent Hera data. The relevance of a linear collider for Higgs discovery in the range 80 GeV to $2M_Z$ is stressed as well as its importance as a W boson factory and corresponding precision tests. A fundamantal theoretical problem still to be solved is that of gauge theories with unstable particles.

As a prerequisite to more detailed physics studies, Schulte gives a status report of the beamstrahlung spectrum and its associated bakground at TESLA before discussing the possible configuration and features of a linear $\gamma\gamma$ collider.

The study of the deep-inelastic structure of the photon is discussed next: the basic

process is $\gamma^*\gamma$ scattering, the virtual photon being necessarily emitted by bremsstrahlung. The main limitations arise from the detector configuration: if no $e^{\pm}$ detector is installed inside the shielding mask the available kinematical range is drastically reduced: $Q^2 > 10^3$ GeV^2 and $x > 10^{-2}$ leaving no overlap with the LEP2 results. To explore the full range of $x > 3.10^{-4}$ and Q^2 values up to 10^5 GeV^2 it will be necessary to use $e\gamma$ colliders . At such small x values the behavior of the photon structure function may not be controlled by the Dokshitser-Gribov-Lipatov-Altarelli-Parisi evolution equations and it may be necessary to resum the large $\ln x$ factors: the case of the gluon distribution is analysed below.

Turning to quasi real photon collisions new tools have been developped and event generators now exist (PYTHIA [7], PHOJET [8]) which take into account both soft and hard physics and which should be adequate up to the highest possible energies available for linear colliders. Detailed studies are going on to fine-tune these generators to all available photon initiated collisions (TRISTAN, LEP2, HERA) and compare their predictions. Particularly interesting are the possibilities to elucidate the nature of the perturbative Pomeron (semi-hard regime) in relation to rapidity gap events: $\gamma\gamma$ collisions have two avantages over hadron induced collisions: a) the variable $\gamma\gamma$ initial energy makes it possible to factorize the parton dynamics from the effect of parton-parton luminosities; b) choosing one initial photon to be virtual reduces the "underlying" event contribution which tends to fill the rapidity gaps in hadronic reactions. In the hard perturbative regime jet production can be used to probe the gluon content of the photon and thus complement the structure function studies which are essentially constraining the quark content.

Several aspects of heavy flavor production are examined both in $\gamma\gamma$ and $\gamma^*\gamma$ collisions in the next-to-leading order approximation of QCD. Inclusive rates as well as correlations are discussed. The production rate of charm is very large. Heavy flavor production offers the unique feature of separating a direct "component" unambiguously predicted in perturbative QCD from a "resolved" component sensitive to the gluon content of the photon: both component can be compared separatly to experimental data.

Of course, a e^+e^- collider is not going to be built only to further probe QCD at very short distances! The main aim is to discover the mechanism of symmetry breaking and understand the dynamics of electro-weak gauge boson interactions. Considerable progress has been made with the complete one-loop calculation (both real and virtual diagrams included) of the process $\gamma\gamma \to W^+W^-$ in the Standard Model. This is discussed below.

The study of anomalous $WW\gamma$ couplings has witnessed important developments: taking into account the $W \to f\bar{f}$ decay, interference between the anomalous W_LW_L channel and the standard W_TW_T channel is possible and found to be large so that an enhanced sensitivity to anomalous $WW\gamma$ couplings is obtained. Using, furthermore, a multivariable maximum likelihood fit a considerable improvement on the determination of the anomalous couplings is possible. This requires however $\gamma\gamma$ energies of the order of 800 GeV. The study of the process $\gamma\gamma \to W^+W^-Z$ shows that WWZ couplings can also be probed at $\gamma\gamma$ energies above 1 TeV. These results call for more detailed studies.

Finally, a case is made for a low energy (10 GeV) linear $\gamma\gamma$ collider in order to probe the light Higgs sector, not presently excluded by LEP data, in the Two Higgs Doublet

Model.

References

[1] e^+e^- Collisions at 500 GeV: The Physics Potential, P.M. Zerwas ed., DESY 93-123C; Proceedings of the Workshop on Physics and Experiments with Linear e^+e^- Colliders, Waikaloa, Hawaii, April 1993, eds. F.A. Harris et al.

[2] $\gamma\gamma$ generators, L. Lönnblad and M. Seymour convenors, in *Physics at LEP2*, CERN Yellow report, CERN 96-01, G. Altarelli, T. Sjöstrand, F. Zwirner eds.

[3] $\gamma\gamma$ physics, P. Aurenche and G.A. Schuler convenors, in *Physics at LEP2*, CERN Yellow report, CERN 96-01, G. Altarelli, T. Sjöstrand, F. Zwirner eds.

[4] Proceedings of the Workshop on Two-Photon Physics at LEP and HERA, Lund, May 1994, G. Jarlskog and L. Jönsson *eds.* (Lund Univ., 1994).

[5] 10th Workshop on Photon-Photon Collisions (PHOTON'95), Sheffield, U.K, April 1995, B. Cartwright, D.J. Miller and V.A. Khoze *eds.*

[6] Workshop on Deep Inelastic Scattering and QCD, Paris, April 1995, J.F. Laporte and Y. Sirois *eds.*

[7] G. A. Schuler and T. Sjöstrand, Nucl. Phys. B407 (1993) 539; $\gamma\gamma$ and γp events at high energies, CERN-TH.7193/94, presented at the Workshop on Two-Photon Physics, Paris, 1994

[8] R. Engel, Z. Phys. C66 (1995) 203; R. Engel and J. Ranft, Hadronic photon-photon collisions at high energies, ENSLAPP-A-540/95 (hep-ph/9509373)

2 Key points of a physics program at photon colliders

Ilya F. Ginzburg

Institute of Mathematics, Novosibirsk. Russia

2.1 Basic points

Most of future e^+e^- linear colliders (LC) will be simultaneously photon colliders (PLC), *i.e.* $e\gamma$ or $\gamma\gamma$ colliders [1]. Modern studies show that one can expect the following features for PLC[1] (below we use the notation: E – initial electron energy, E_γ – photon energy, $E_{\gamma\gamma}$ or $E_{e\gamma}$ – c.m. energy of the photon–photon or electron–photon system):

- characteristic photon energy[2]: $E_\gamma \approx 0.8E$;
- mean energy spread: $< \Delta E_{\gamma\gamma}/E_{\gamma\gamma} > \approx 0.1$ (*monochromatic variant*);
- polarized photons with mean helicity $\lambda \approx 0.95$;
- measurements at small angles limited by difficulties of design only. Therefore, it is useful to add to the wide angle detector (which will be common for all modes of LC) a small angle detector for the PLC modes;
- expected annual luminosity: $\mathcal{L} \approx 10 \div 20$ fb^{-1} in the *monochromatic variant*. (It is $\sim 10\%$ of the geometrical luminosity $\mathcal{L}_g$. One can make $\mathcal{L}_g$ higher than the luminosisty for the basic e^+e^- LC. In particular for the TESLA project, one can obtain $\mathcal{L}_g \approx 10\ \mathcal{L}_{basic}$ [6].);
- in each case, possible *non-monochromatic variant* with $\gamma\gamma$ luminosity$\sim$ 5times higher with wide energy spectrum (and with almost the same high energy part of spectrum as in the monochromatic variant). The additional, softer photons are almost unpolarized in this case;
- in principle, possible *super-monochromatic variant* with $E_\gamma \approx 0.95E$; $< \Delta E_{\gamma\gamma}/E_{\gamma\gamma} > \approx 0.015 \div 0.02$ but with $\mathcal{L}$ about $10 \div 20$ times less;
- the monitoring of differential luminosity is necessary.

When the PLC is based on the e^-e^- collisions, the deflection of electrons after conversion is unnecessary[3]. Indeed, we do not expect any specific processes in the e^-e^- collisions (if such exotic processes exist, they should be studied without conversion). Most of the "parasitic" processes (from e^-e^-) with the production of some final state F are $\gamma^*\gamma^* \to F$ and $\gamma^*\gamma \to F$. The effect of these (almost real) virtual photons shows up entirely in the *measured* photon luminosity spectrum. These virtual photons give a small deviation in the soft part of this spectrum. The highly virtual photons are accompanied by the (observable) electrons, scattered at large enough angle. Their flux is small. The specific $e\gamma$ processes like $e\gamma \to W\nu$, $e\gamma \to eWW, \cdots$ are known in advance. They can be studied simultaneously with the $\gamma\gamma$ processes owing to the specific signature.

[1] *The conversion region is an $e\gamma$ and a $\gamma\gamma$ collider with a small c.m. energy about 1 MeV, but with a huge luminosity $10^6 \div 10^8$ fb^{-1} per year.* It gives the possiblity to search for very light particles [4, 5].

[2] The free electron laser with the variable frequency seems to be useful to fix this relation at the initial electron energy variation.

[3] For the very dense electron beams this fact was established by Balakin (in this case these electrons are bent by strong electromagnetic field of opposite bunch).

Below I present only the key points of a physics program. I shall try not to repeat the problems, considered in other reports here. My list of references is very incomplete.

I will call the photon collider with the c.m. energy in the range 80–180 GeV PLC1. It can be the first stage of an entire linear collider project.

2.2 Hadron Physics and QCD

Hadron physics and QCD are the traditional fields for the $\gamma\gamma$ collisions. The $\gamma\gamma$ experiments provide new type of collisions and with the simplest quark structure of the pointlike initial state. The PLC will extend these studies to new regions. The results from PLC together with those from the Tevatron and HERA, will produce the entire set of data related to a factorized (in the old Regge sense) set of processes. In this respect, HERA gets a new importance of a bridge between PLC and Tevatron/LHC.

1) **Total cross section $\sigma(\gamma\gamma \to hadrons)$ and diffraction like processes in soft region.** The expected values are: $\sigma^{tot} \equiv \sigma_{\gamma\gamma\to hadrons} \sim 0.3\ \mu b$ in the SLC energy region, and $\sigma^{tot} \sim 0.5 \div 1\ \mu b$ at $E_{\gamma\gamma} \sim 2$ TeV [8]. Besides, $\sigma(\gamma\gamma \to \rho^0\rho^0) \sim 0.1\sigma^{tot}$ (see [9]). It is important to study the energy dependence of this cross section (together with the Q^2 dependence — in γe collisions). Its comparison with $\sigma_{pp}(\sigma_{p\bar{p}})$ and $\sigma_{\gamma p}$ will allow us to understand the nature of the hadron cross sections growth with energy. The crucial problem is to test the possible factorization of these cross sections (this factorization is assumed in ref. [8]). How can we measure this cross section?

2) **The semihard processes** are those, for which the characteristic value of transverse momentum is small in comparison with total energy but large in comparison with the strong interaction scale $\mu \sim 300$ MeV : $s \gg p_\perp^2 \gg \mu^2$. We consider here the diffraction like processes, including small angle jet production with rapidity gap. These phenomena give us information about the perturbative Pomeron and Odderon, mechanisms of shadowing in pQCD, etc. In this region, a new parameter appears in the pQCD series, $\alpha_s(p_\perp^2)ln(s/p_\perp^2) \approx \alpha_s(p_\perp^2)\eta$ or $\alpha_s(Q^2)ln(1/x)$, that becomes large while s increases. Therefore, the entire pQCD series should be taken into account, and studies here provide opportunity to test the inner structure of pQCD in all orders. Due to the simple pointlike nature of photons, the nontrivial results in pQCD could be obtained almost without model assumptions. Unfortunately, the influence of the hadronlike component of the photon is expected to be relatively small at large enough $p_\perp$ only. For example, for the diffraction like processes it is expected to be at $p_\perp > 7$ GeV [10].

The processes $\gamma\gamma \to \rho^0 X$, $\gamma\gamma \to \gamma X$, $\gamma\gamma \to \rho^0\phi$ with rapidity gap are described

by pure Pomeron exchange. They present the best opportunity to study the Pomeron. The processes $\gamma\gamma \to \pi^0 X$, $\gamma\gamma \to \pi^0 a_2$ with rapidity gap are described only by Odderon exchange. They present a unique opportunity for Odderon studies. This is in contrast with the fact that the Pomeron and the Odderon have identical status in pQCD. The cross sections of some processes, integrated over the range of $p_\perp > 7$ GeV[4] and with large enough rapidity gap, are estimated from below as [11, 12]:

$$\sigma_{\gamma\gamma\to\rho^0 X} \gtrsim 1\,pb, \quad \sigma_{\gamma\gamma\to\gamma X} \gtrsim 0.2\,pb, \quad \sigma_{\gamma\gamma\to\pi^0 X} \gtrsim 0.4\,pb$$

The first two quantities should be multiplied by the growing BFKL factor (see[13, 14]). Where is the corresponding boundary for the jet production with a rapidity gap? Where are the real bounds for the description of $s/p_\perp^2$ dependence with perturbative Pomeron or Odderon (both from below in $p_\perp$ and from above in $s/p_\perp^2$)?

2.3 Higgs Boson (Higgs) Physics

1) **The discovery of the Higgs.** The PLC1 seems to be the best machine for the discovery of Higgs with mass in the 80–180 GeV interval [15]. The process $\gamma\gamma \to H \to b\bar{b}$ with QED background $\gamma\gamma \to b\bar{b}$ was considered in [16, 17, 18]. In the monochromatic variant of PLC with zero total initial photon pair helicity, one can observe Higgs with mass $80 < M_H < 140$ GeV, based on a total luminosity about 3 fb^{-1}. The mass interval 140 GeV $< M_H < 2M_Z$ is difficult for the Higgs discovery. The decay $H \to WW$ dominates here, but the WW production cross section via Higgs is less than that without this intermediate state. It was noted in ref. [19], that the total width of such a Higgs will be high enough to resolve details of WW spectrum within this width interval. Besides, the amplitude of the $\gamma\gamma \to H \to WW$ process is complex with a phase which varies rapidly: $\mathcal{M} \propto \Gamma(\gamma\gamma \to H)(s - M_H^2 + i\Gamma_H M_H)^{-1}\Gamma(H \to WW)$. Therefore, the interference of this amplitude with that for the QED process $\gamma\gamma \to W^+W^-$ is high. Ref. [19] shows the spectacular curves for 180 GeV $< M_H <$ 400 GeV[5]. Special simulation work is necessary to understand, what requirements are imposed on either PLC (monochromatization degree) or detector (accuracy of W decay products momenta measurements), to see the Higgs in the widest mass interval.

2) **At the PLC only, one can measure the Higgs two photon width.** This width is the counter for SM particles heavier than Higgs.

3) **The investigation of the Higgs coupling with the matter** is necessary to obtain whether the observed particle is actually a Higgs of the Standard Model (SM) or something else.

If $M_H < 150$ GeV, one could try to study the Higgs decay into $\tau\bar{\tau}$ or $c\bar{c}$ with SM branching ratios ~ 0.06 or 0.04 (cf.[18]). These opportunities need for new work on simulation.

[4] It corresponds to the production angle above 70-100 mrad at PLC1.

[5] The amplitude of this interference is higher at lower s, since W's from Higgs decay are mainly longitudinal and the fraction of longitudinal W's from $\gamma\gamma \to W^+W^-$ process decreases with s.

If $M_H > 2M_Z$, one can compare Higgs coupling with Z and W (by comparison of Higgs production via reaction $\gamma\gamma \to H \to ZZ$ and via interference in $\gamma\gamma \to W^+W^-$ reaction).

If $M_H \sim 2M_t$, the interference between the QED process $\gamma\gamma \to t\bar{t}$ and resonant one $\gamma\gamma \to H \to t\bar{t}$ can be used to see the value of the Higgs coupling with the t-quark [20].

3) **The anomalous interactions of Higgs.** The SM Higgs with $M > 500$ GeV will be invisible in $\gamma\gamma$ collision. Therefore, any Higgs signal at a PLC in this region manifests the existence of either some heavier SM particles or nonstandard interactions of Higgs, having the scale about a few TeV [21, 36].

2.4 Gauge boson physics

The sketch of the main processes with W and Z production at PLC within the SM is given in refs. [22, 23]. The scale of these phenomena at PLC is the cross section of the $\gamma\gamma \to W^+W^-$ process at high enough energies $\sigma_W = 8\pi\alpha^2/M_W^2 \approx 81$ pb. Besides, in this limit we have $\sigma_{e\gamma\to W\nu} = \sigma_W/8\sin^2\Theta_W \approx 43$ pb. These very processes determines PLC as **W factory** with $10^6 \div 10^7$ W's per year.

The processes $e\gamma \to W\nu$ and $\gamma\gamma \to W^+W^-$ with their dependence on helicities of photon λ_γ and electron λ_e were considered in ref. [24]. The angular distribution of produced W's for both processes is more favorable for W recording than that in process $e^+e^- \to W^+W^-$. The $e\gamma$ cross sections at $E_{e\gamma} < 200$ GeV and the $\gamma\gamma$ cross sections at $E_{e\gamma} < 300$ GeV vary strongly with a variation of photon helicities. This polarization dependence disappears at higher energies.

Besides, the process $e\gamma \to W\nu$ is switched on or off entirely with variation of electron helicity ($\sigma_{e\gamma\to W\nu} = (1 - 2\lambda_e)(\sigma + \lambda_\gamma\tau)$). This means, that this process is very sensitive to an admixture of right–handed currents in W coupling with matter. On the other hand, this process can be used for testing initial electrons polarizations.

When the energy increases, the cross sections of a number of higher–order processes become large enough. The catalogue of such processes of third order in the SM is given in ref. [25]. Among the processes of highest interest is the process $e\gamma \to eW^+W^-$ with high cross section (25 pb at $\sqrt{s} \sim 2$ TeV). The difference of cross sections with opposite electron helicities (~ 5 pb) is proportional to the amplitude of the $\gamma Z \to WW$ subprocess (axial current contribution). Besides, a large enough fraction of cross section with unpolarized electrons occurs in the region of electron transverse momenta 50–150 GeV, which is very sensitive to the γZWW interaction [26].

In the processes with four gauge bosons in the final state (4-th order processes) we can see subprocesses with heavy gauge boson scattering. The SM cross sections for the processes $\gamma\gamma \to WWWW$ and $\gamma\gamma \to WWZZ$ are $\sim 0.3 \div 0.1$ pb [27]. The cross section of the process $e\gamma \to eWWZ$ is of the same order of value: $(\alpha/\pi)^2 \ln(s/m_e^2) \cdot \ln^2(s/4M_W^2)\sigma_{\gamma\gamma W^+W^-}$.

Some process of fifth and sixth order will be observable at high enough energies, for

example, $e\gamma \to e^+e^- eWW$, $e\gamma \to e^+e^- \nu WZ$, $\gamma\gamma \to e^+e^- \mu\bar{\mu}WW$, etc.

Problems in the gauge boson physics

1) **The incorporation of the W width and the problem of quantization.** To describe gauge boson production with real final states of the W decay, one should use the W propagator near its physical pole. To avoid divergence, it is necessary to insert in this propagator the W width Γ_W, for example, $(k^2 - M_W^2 - i\varepsilon)^{-1} \Rightarrow (k^2 - M_W^2 - iM\Gamma_W)^{-1}$. This simple change violates gauge invariance [28] and unitarity. It results in inaccuracy $\sim (1 \div 3)\Gamma/M$. The more likely recipes should eliminate the above violations. However, this requirement gives no unambiguous recipe. One can expect that the ambiguity of the result when using the different recipes, both unitary and gauge invariant, without genuine theory will be $\sim \alpha\Gamma/M$ ($\sim 10^{-3}$ or larger), i.e. the accuracy of such recipes seems to be deficient for the description of the data. Therefore, the well-known fundamental problem of quantum field theory becomes of practical importance here (see e.g. [29]):

It is necessary to construct a genuine theory of unstable gauge bosons.

2) The underlying interactions could manifest itself as the deviations from the SM in some **anomalous interactions of gauge bosons.** These anomalies are described by effective Lagrangians. The standard approach is to consider here operators of lower dimension – 4 and 6 (e.g. an anomalous magnetic moment, quadruple moment, etc.). These effects increase with energy, the larger energy is the better for their detection. Some results have been obtained for the e^+e^-500 LC (including PLC) [31, 32].

Usually the joined effect of all these anomalies is studied for some small set of processes ($e^+e^- \to WW$,...). The different processes (and different kinematical regions for one process) are sensitive in different manner to various possible anomalous gauge boson interactions. The PLC with their large set of observable processes provide opportunity to study various anomalies almost separately in the different processes. Special work is necessary to present detail program in this field.

3) One can measure the **elements of the Cabibbo–Kobayashi–Maskawa mixing matrix** on the mass shell of W. Their comparison with those obtained in the past and present experiments (far from W mass shell) can give an idea about their dependence on W boson virtuality.

4) The possibility of **strong interactions in the Higgs sector** seems to be a very probable one at $\sqrt{s} \gtrsim 1$ TeV. It could manifest itself at PLC as some resonances in the gauge boson systems, unusual energy dependence, multiple W production, etc. Its first signals could be obtained in the production of longitudinal W's and Z's. (For more details, see a number of papers, e.g., [33]). The SM cross section $\gamma\gamma \to Z_L Z_L$ is small [34]. However, experience in pion physics permits us to expect here large effects due to some heavy states (like ω in the t-channel for $\gamma\gamma \to \pi\pi$).

At large enough energies, one can expect to see the strong interaction of transverse W's driven by the strong Higgs self-interaction. Where does this energy region begin?

2.5 New Physics

Two opportunities are considered, when we speak about New Physics effects — the discovery of **new particles** and **new nonstandard interactions** of known particles.

PLC provide the best place to discover many new particles — in comparison with other colliders, having similar energy. The reasons for this statement are (see in more detail ref. [35]):

1) The signal to background ratio at PLC is often much better than that at hadron colliders.

2) The photons are "democratic" respective to all charged particles. Therefore, the analyses of new particles production have no additional ambiguities due to production mechanism at PLC (which exists in collisions with hadrons).

3) The (electrodynamic) cross sections of charged particles production at $\gamma\gamma$ PLC are larger than those at e^+e^- LC. Even if PLC luminosity is 5 times less than that for basic e^+e^- LC (standard monochromatic variant), the number of produced pairs at e^+e^- collider is no more than that at $\gamma\gamma$ collider. Besides, this production in $\gamma\gamma$ collision decreases with energy slower than that in e^+e^- collision. Therefore, one can study new particles relatively far from threshold with a good enough rate. In this region, the decay products of these particles overlapp weakly, and their detailed study becomes more feasible.

4) The $\gamma\gamma$ collisions often produce pairs of identical particles with identical decays (e.g., $\gamma\gamma \to \tilde{\mu}\bar{\tilde{\mu}}$). This makes easier the analysis of events with missing $p_\perp$.

5) In contrast with hadrons, a photon is pointlike, its quark content is well known. The entire photon energy is used to see the small distance phenomena of interest.

6) In some cases $e\gamma$ collisions are preferable (for example, reactions $e\gamma \to e^*$, $e\gamma \to W\nu_e^*$, $e\gamma \to \tilde{e}\tilde{\gamma}$.)

On the contrary, gauge invariance strongly constrains interactions of matter with photons. Therefore, the effects of some new interactions are suppressed here. On the other hand, it means that the originof observed effects would be separated easily.

Acknowledgement

This work is supported by grants of INTAS – 93 – 1180 and of Russian Fund of Fundamental Investigations RFFI.

References

[1] I.F. Ginzburg, G.L. Kotkin, V.G. Serbo, V.I. Telnov, Preprint 81 – 50 Inst. Nucl. Phys. Novosibirsk, 25.02.1981; Sov. ZhETF Pis'ma. 34 (1981) 514; Nucl. Instr. and Methods in Research (NIMR) 205 (1983) 47; I.F. Ginzburg, G.L. Kotkin, S.L. Panfil, V.G. Serbo, V.I. Telnov, NIMR 219 (1983) 5; V.I. Telnov, NIMR A294(1990) 72, see also [2,3].

[2] Proc. LBL Workshop, March 1994, NIMR 355 (1995) 1-194.

[3] Proc. Workshop on Physics and Experiments with Linear e^+e^- Colliders. Hawaii (1993) World Sc. Singapore.
[4] S.I. Polityko, Sov. Yad. Fiz. 43 (1986) 146; 56 (1993) 144.
[5] I.F. Ginzburg, G.L. Kotkin, S.I. Polityko, Sov. Yad. Fiz. 37 (1983) 368; 40 (1984) 1495; Phys. At. Nucl.56 (1993) 1487.
[6] V. Shiltsev. Private communication.
[7] Proc. 9th International Workshop on Photon-Photon Collisions, San Diego (1992) World Sc. Singapore.
[8] P. Chen, T. Barklow, M. Peskin, Phys. Rev. D49 (1994) 3209; R. Engel et al., see below.
[9] Budnev V.M., I.F.Ginzburg, G.V.Meledin & V.G.Serbo, Phys.Rep. 15C (1975) 181.
[10] I.F. Ginzburg, D.Yu. Ivanov. Submitted to Phys. Rev. D
[11] I.F. Ginzburg, et al., Nucl.Phys. B284 (1987) 685; B296 (1988) 569.
[12] I.F. Ginzburg and D.Yu. Ivanov, Nucl. Phys. B (Proc. Suppl.) 25B (1992) 224; Nucl.Phys. B388 (1992) 376.
[13] A.D.Mueller Nucl. Phys. B415 (1994) 373.
[14] D.Yu. Ivanov. Phys. Rev. D, in print.
[15] V.E. Balakin, I.F. Ginzburg, in ref. [3].
[16] D.L. Borden, D.A. Bauer, D.O. Caldwell, Phys. Rev. D48 (1993) 4018.
[17] V. Khoze, in Proc. Sheffield Workshop on Photon–Photon Collisions, April 1995.
[18] G. Jikia, A. Tkabaladze, NIMR A355 (1995) 81.
[19] D.A. Morris, T.N. Truong, D. Zappala, Phys. Lett. B323 (1994) 421.
[20] E.E. Boos, et al., Zeit. Phys. C56 (1992) 487.
[21] I.F. Ginzburg, Preprint TP 28 (182) Inst. of Mathem. Novosibirsk (1990).
[22] I.F. Ginzburg, Sov.Yad.Fiz. (Phys. At. Nucl.) 58 (1995) 326.
[23] G. Belanger, F. Boudjema, I.F. Ginzburg, in preparation.
[24] I.F. Ginzburg, G.L. Kotkin, S.L. Panfil, V.G. Serbo, Nucl. Phys. B228 (1983) 285, E.: B243 (1984) 550.
[25] I.F. Ginzburg, et al., Sov.Yad.Fiz. 56 (1993) 39.
[26] I.F. Ginzburg, V.A. Ilyin, A.E. Pukhov, V.G. Serbo, In preparation.
[27] G. Jikia, NIMR A355 (1995) 84.
[28] A. Aeppli, F. Cuypers, G.J. van Oldenborgh, Phys.Lett. B314 (1993) 413
[29] M. Veltman, Physica 29 (1963) 186; R.G. Stuart, Phys.Lett. B262 (1991) 113; preprint UM-TH-95-13; A. Sirlin, Phys. Rev. Lett. 67 (1991) 2127; H. Veltman, DESY 92-076 (1992).
[30] "Tests of alternative models at a 500 GeV NLC", eds. F.Boudjema and F.M.Renard, ENSLAPP-A-365/92 (1992).
[31] S.Y.Choi, F.Shrempp, Phys. Lett. B272 149; E.Yehudai, SLAC-Report-383 (1991).
[32] F.Boudjema et al., Phys. Rev. D43 (1991) 3683.
[33] K.Hikasa in Proc. 2-nd Workshop on JLC, KEK 91-10 (1991).
[34] G. Jikia, Phys.Lett. B298 (1993) 224; Nucl.Phys. B405 (1993) 24; G. Jikia, A. Tkabaladze, Phys. Lett. B323 (1994) 453.
[35] I.F. Ginzburg. NIMR A355 (1995) 63.
[36] I.F. Ginzburg, in ref. [7].

3 γ spectra and backgrounds in Tesla

D. J. Schulte

DESY, Hamburg, Germany

Photon-photon physics can be studied in a linear electron-positron collider by the use of the virtual photons accompanying the beam particles as is done in storage rings. In the linear collider case the beam will be lost after the interaction anyway, so one can think of producing real photons from the beam particles and thus achieve a harder photon-photon spectrum. In addition, some of the major background sources in the electron-positron collider are due to two photon processes. These effects are increased by the production of real photons during the crossing of the bunches. While the above processes have been studied in some detail, for TESLA the investigation of the possibility of achieving high centre of mass energy photon-photon collisions has just started. In the following some preliminary estimates will be presented about the luminosity and backgrounds. For a detailed review of many relevant processes I refer to [1].

3.1 Beamstrahlung

At the interaction point of an electron-positron linear collider two sources of photons exist. The electrons and positrons are accompanied by virtual photons. In the leading logarithmic approximation, this bremsstrahlung spectrum (of quasi real photons) is given by

$$n_\gamma(x,Q^2) = \frac{\alpha}{2\pi}\frac{1-(1-x)^2}{x}\ln\frac{Q^2(1-x)}{x^2m^2}$$

with the fine structure constant α, the electron mass m and the Q^2 scale defined by the process. The photon has a fraction x of the electrons energy.

Due to their high charge and small dimensions the bunches will produce strong electromagnetic fields. A particle traveling through the oncoming bunch of oppositely charged particles will therefore be accelerated towards the beam axis. If the fields are strong enough, the transverse bunch size will thus decrease which leads to an effective luminosity L that is larger than the geometric L_0 by the luminosity enhancement factor H_D.

$$L = H_D L_0 = H_D \frac{N^2}{4\pi\sigma_x^*\sigma_y^*} N_b f_r. \tag{1}$$

Here $\sigma_{x,y}^*$ are the transverse bunch dimension, N is the number of particles per bunch, N_b the number of bunches per train and f_r the repetition frequency with which trains are accelerated.

The bending of the trajectories will also cause the beam particles to emit photons, the beamstrahlung. This is comparable to the synchrotron radiation well known in circular

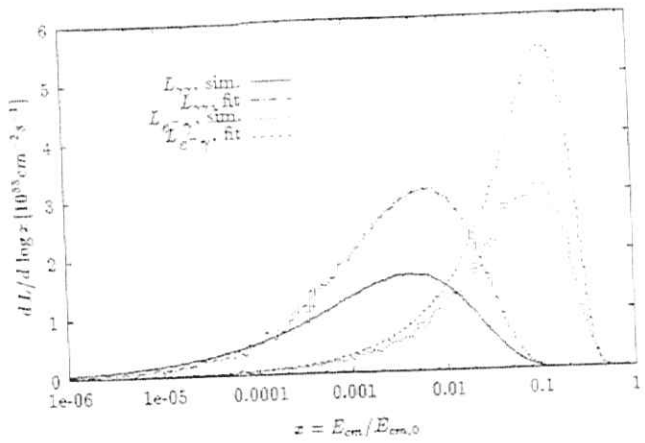

Figure 1: Comparison of half the beamstrahlung spectrum and the $L_{e\gamma}$ spectrum from the simulation and the fit.

accelerators. The average photon energy of the beamstrahlung will be of the order of a few GeV depending on the design. The beamstrahlung will cause a tail in the e^+e^--luminosity spectrum towards low energies that can be compared to the effect of initial state radiation. To suppress beamstrahlung flat beams are used. The average relative loss of energy δ is roughly proportional to $\Upsilon^2\sigma_z$ with $\Upsilon = 5Nr_e^2\gamma/(6\alpha(\sigma_x^* + \sigma_y^*)\sigma_z)$, the beamstrahlung parameter; r_e is the classical electron radius. The minimal bunch height and the bunch length σ_z are related via $\sigma_y^* \approx \sqrt{\sigma_z\epsilon_y}$, with the vertical emittance ϵ_y. This leads to

$$L \propto H_D\sqrt{\frac{\delta}{\epsilon_y}}\eta P_{AC} \tag{2}$$

where P_{AC} is the total power consumption of the accelerator and η the efficiency of turning this power into beam power. The pinch enhancement factor varies only slowly with the parameters so it can be taken as constant. The beamstrahlung will thus limit the achievable luminosity. It will in addition increase the background due to photon-photon interactions.

Since analytic calculation of the pinch effect is very difficult if not impossible, one has to simulate it. A program that also simulates the background processes is GUINEA-PIG [2]. It was used for all following calculations.

The current TESLA parameters are $\sigma_x^* = 850\,nm$, $\sigma_y^* = 19\,nm$, $\sigma_z = 700\,\mu m$, $\gamma\epsilon_x = 14\cdot10^{-6}\,m$, $\gamma\epsilon_y = 0.25\cdot10^{-6}\,m$, $N = 3.63\cdot10^{10}$, $N_b = 1135$ and $f_r = 5\,Hz$. This leads to $\delta \approx 2.5\%$, $H_D \approx 1.6$ and $L \approx 6\cdot10^{33}\,cm^{-2}s^{-1}$.

The beamstrahlung contributes mainly to the medium energy photon spectrum around

a few GeV. Since for small energies it shows a $x^{(-2/3)}$ behaviour, it is small compared to the virtual photon spectrum while at high energies it is exponentially suppressed. In [3] an approximate formula for the beamstrahlung spectrum based on simulation results was derived. Figure 1 shows the agreement between this formula and the simulation in the case of TESLA.

3.2 Background

3.2.1 Pair Production

Two sources of pair production exist. In the coherent process a photon turns into an electron-positron pair in a strong external field. This source is exponentially suppressed for small beamstrahlung parameters. Its contribution to the total number and energy of the pairs can be neglected in the case of TESLA.

In the incoherent process the pair is produced in a two photon collision: $\gamma\gamma \to e^+e^-$. To this process the real photons from beamstrahlung contribute as well as the virtual photons from the beam particles. Averaging over the polarizations in the initial state and summing over the polarizations in the final state the cross section is given by

$$\frac{d\sigma}{dt} = \frac{2\pi r_e^2 m^2}{s^2}\left[\left(\frac{t-m^2}{u-m^2}-\frac{u-m^2}{t-m^2}\right)-4\left(\frac{m^2}{t-m^2}-\frac{m^2}{u-m^2}\right)-4\left(\frac{m^2}{t-m^2}-\frac{m^2}{u-m^2}\right)^2\right], \quad (3)$$

where s, t and u are the Mandelstam variables.

The produced particles are deflected by the fields of the beams. After the interaction most of them have either a small angle with respect to the beam axis or a small transverse momentum. With the help of an external solenoidal field they can thus be trapped in conical masks with small opening angles. A small number will have a large transverse momentum and a relatively large angle from the production. These can hit the detectors, especially the vertex detector.

3.2.2 Hadrons and Minijets

The two photon collisions will lead to the production of hadrons. The dependence of the hadronic cross section on the centre of mass energy of the photons is not known. A reasonable assumption may be to scale the two hadron total cross sections down. The two photon cross section can then be expressed as $\sigma_{\gamma\gamma} \approx \sigma_{\gamma p}\cdot\sigma_{\gamma p}/\sigma_{pp}$. This assumption leads to [4]

$$\sigma_{\gamma\gamma} = 200\,nb\left[1-6.3\cdot10^{-2}\ln^2\frac{s}{GeV^2}+1.96\left(\frac{s}{GeV^2}\right)^{-0.37}\right].$$

The dynamics of photon-photon collisions both in the soft and hard regime (e.g. jet production) is discussed in more details below [5]. Here, our results are based on calculations in the leading logarithmic approximation using the Drees and Grassie (DG) parametrization of the photon structure function.

3.2.3 Results

The total number of background electrons and positrons produced per bunch crossing is $N_{e^+e^-} \approx 1.0\cdot10^5$ with a total energy of $E_{e^+e^-} \approx 1.5\cdot10^5\,GeV$. The number of hadronic events with a centre of mass energy of more than $5\,GeV$ expected is $N_H = 0.15$. The number of minijets with a transverse momentum $p_\perp > 3.2\,GeV/c$ is $N_{MJ} = 0.4\cdot10^{-2}$ using the DG-parametrization. During the time of about $700\,ns$ between two bunch crossings within a train, most of the detectors could be read out.

3.3 Photon-Photon Collider: Basic Idea

The virtual photon spectra provide high centre of mass energy photon-photon collisions with only a limited luminosity. If one is for example interested only in two photon events with 60% of the nominal centre of mass energy one will have $\mathcal{L}_{\gamma\gamma} \approx 5\cdot10^{-4}\mathcal{L}$. The beamstrahlung does not improve this. In the case of TESLA the additional photon-photon luminosity is smaller by additional six order of magnitude. A method to achieve harder photon spectra is the use of backward Compton scattering. In this method two electron beams are focussed as for electron-positron collision. At some distance d from the interaction point in the conversion region one lets the electrons collide with a very dense laser beam. The backscattered hard photons will move in direction of the incident electron and thus provide the required photon-photon luminosity in the interaction point.

To prevent the electron beams, after conversion, from contributing to the luminosity in the interaction point, one could use a small dipole magnet that gives them an angular kick. It could also be possible to use a plasma lens after the conversion that will over focus the beam. It will then be very dilute at the interaction point. Another method is simply to let the beams collide. Since both bunches consist of electrons they will deflect each other thus naturally decreasing the luminosity.

3.4 Compton Scattering

The differential cross section for Compton scattering is given by

$$\frac{d\sigma}{dx} = \frac{2\pi r_e^2}{z}\left[\frac{1}{1-y}-1-y-4r(1-r)-2\lambda P_r r z(1-2r)(2-y)\right] \quad (4)$$

where $z(mc^2)^2$, related to the square of the centre of mass energy ($z(mc^2)^2 = s - m^2$), is $z(mc^2)^2 = 4\hbar\omega_L E_0\cos^2(\theta_0/2)$ with $\hbar\omega_L$ the energy of the laser photon and E_0 that of the electron. The crossing angle between electron and laser beam is θ_0. $yE_0 = \hbar\omega$ the energy of the backscattered photon and $r = y/(z(1-y))$ is introduced for convenience.

The helicity of the electron is λ and the polarization of the photon P. For $\lambda P = 0$ the spectrum is slightly peaked at the maximal photon energy. For $\lambda P = -1, 2$ the peak will become more enhanced while the high energy part of the spectrum will be suppressed for $\lambda P = 1/2$. Polarization of the electron as well as the laser photon beam will thus be advantageous and result in a luminosity spectrum with a higher peak at the maximal centre of mass energy. The polarization of the hard part of the backscattered photon spectrum will also improve.

The maximal energy of the backscattered photons $\hat{E}_\gamma$ depends on the electron E_0 and laser photon energy as $\hat{E}_\gamma = y_m E_0$ with $y_m = x/(x+1)$. To achieve the largest centre of mass energy the photon energy should thus be maximal. If on the other hand $\hbar\omega\hbar\omega_L > 4(mc^2)^2$ the hard Compton photons and the laser photons can produce pairs via the incoherent process. The cross section is comparable to the Compton cross section. To suppress the pair production one can require $y_m x < 4$. This leads to $x < 2\left(1+\sqrt{2}\right) \approx 4.8$ and in turn to $y_m \approx 0.83$. For $E_0 = 250\,GeV$ the required laser photon energy would thus be $\hbar\omega_L \approx 1.25\,eV$.

3.5 Conversion

The required soft photons can be produced with a laser. The details of the conversion and the choice of parameters for the laser beam will depend on the technology used.

3.5.1 Thickness of the Laser Target

For an unlimited laser power one can assume the laser beam to be longitudinally and transversely uniform. The conversion can be described with the help of k_L, the laser target thickness in number of interaction lengths. The probability that an electron will at least scatter once, the conversion efficiency, is given by $k = 1 - \exp(-k_L)$. The scattered electrons can scatter again producing softer Compton photons. Since the cross section is increasing for smaller centre of mass energies the produced soft tail of the photon spectrum will increase faster than the high energy peak. The thickness chosen for the laser target has thus to be a compromise between required efficiency and the sharpness of the spectrum

In a more precise model the collision between the laser beam and the electron beam can be described as any beam-beam collision without pinch effect. The laser beam emittance in this case is $\varepsilon_\gamma = \lambda/(4\pi)$. A reasonable approach is to choose the laser bunch length and its beta function β_γ to be of the same order as the electron bunch length. The resulting spot size will in the present case be much larger than the transverse dimension of the electron beam, so that in the case of head on collision the target is indeed transverly almost uniform. Longitudinally, there is some difference but the effect on photon-photon luminosity spectrum is not very strong.

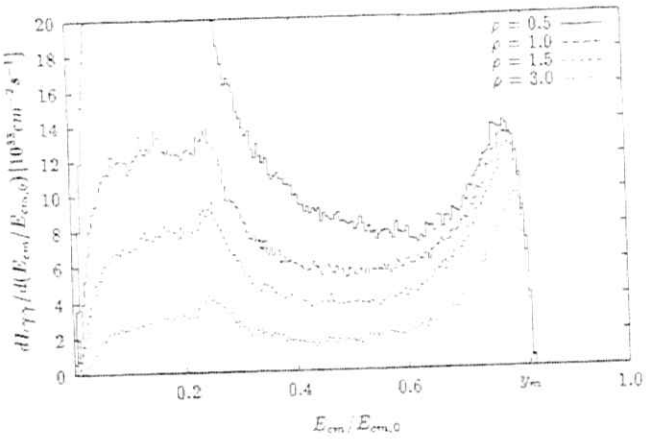

Figure 2: The photon-photon centre of mass spectrum for different distances ρ between the conversion region and the interaction point.

3.5.2 Monochromatization of the Spectrum

The backscattered photons will have small angles θ_γ with respect to the direction of motion of the initial electron. These angles are of the order of mc^2/E_0 and depend on the energy of the backscattered photon:

$$\theta_\gamma(y) = \frac{mc^2}{E_0}\sqrt{\frac{x-(x+1)y}{y}}.$$

Without this angle the photon-photon luminosity would be simply $L_{\gamma\gamma} \approx L_0 n_\gamma^2$, where n_γ is the average number of backscattered photons per incoming beam particle. The luminosity would differ slightly from the geometric because the transverse dimensions of the bunch change over its length.

The scattering angle leads to a dependence of the luminosity on the distance between the interaction point and the conversion region. Since the low energy photons have larger angles than the hard ones the luminosity for the former will decrease faster with the distance than for the latter. A convenient dimensionless parameter to describe the distance is $\rho = dmc^2/(E_0\sigma_y)$. Figure 2 shows the dependence of the absolute luminosity spectrum for a target thickness of one conversion length and several distances. The parameters of the collider in this case are the ones for TESLA discussed below. A perfect beam polarization and no contribution of the electron bunches to the luminosity was assumed.

3.6 Luminosity and Choice of Parameters

To find a reasonable parameter set for the photon-photon version of TESLA it is sensible to start from the e^-e^--parameters. The $\gamma\gamma$ luminosity will be approximately proportional to the geometric luminosity which should therefore be maximized. In equation 1 the factor $NN_b f_r$ is proportional to the beam energy which in turn is proportional to the total power consumption of the linac. Assuming that this value is the same as for the e^-e^--option and thus fixed, the geometrical luminosity is proportional to the charge per bunch and inversely proportional to the transverse dimensions. Since these dimensions are given by $\sigma = \sqrt{\epsilon\beta}$, with ϵ the emittance and β the beta function at the interaction point, one can in principle lower either the emittance or the beta-function. Since an e^-e^--machine profits from a small vertical emittance the same way a photon-photon collider does one should assume this value the same for both options. A reduction of the vertical beta function will lead to a slightly increased luminosity but one will be limited by the hourglass effect and the Oide limit. The first is simply due to the fact that in order to achieve the small spot size the angular spread of the beam particles has to be large so that the bunch transverse dimensions will change significantly over its length. During the collision the bunches will therefore look like a hourglass. The Oide effect is due to the energy loss of the particles in the final magnets that will lead to focusing different from the nominal. With the help of an additional magnet which reduces the Oide effect and shorter bunches which reduce the hourglass effect it is possible to achieve a vertical bunch size of $\sigma_y \approx 10\,nm$ [7]. In the following the vertical bunch size is the same as in the electron-positron collider. For the

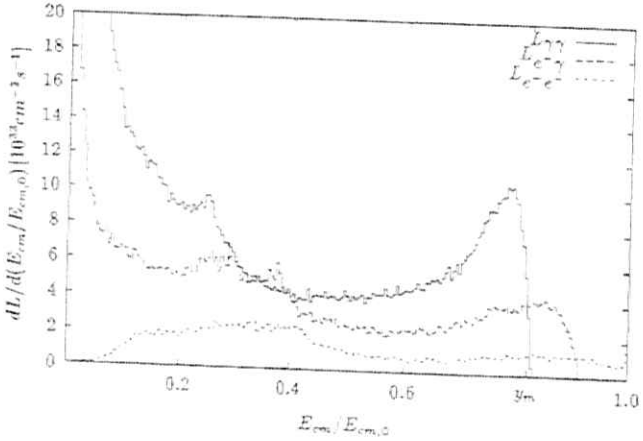

Figure 3: The photon-photon, electron-photon and electron-electron centre of mass spectrum for the TESLA parameters as described in the text.

horizontal dimension the case is completely different. The lower limit for σ_x is not given by the emittance at the e^-e^--machine but by the beamstrahlung. If one needs not care about

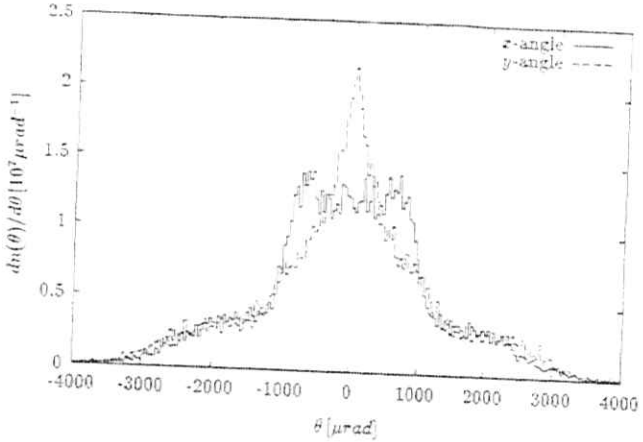

Figure 4: The angular electron distribution after the interaction point for the same case as in the previous figure.

this effect, σ_x can be reduced by a factor of two simply by reducing the beta function. In addition one can think of decreasing the horizontal emittance, which does not help for the e^-e^--machine and is thus not advocated strongly there. A reduction of the emittance by a factor two seems feasible, leading to a horizontal spot size of $\sigma_x \approx 200\,nm$ [8]. The third option is to increase the bunch charge. This has the disadvantage that the blow up of the vertical emittance $\Delta\epsilon_y$ in the linac due to single bunch wake fields will increase since $\Delta\epsilon_y \propto N^2$. While $\Delta\epsilon_y$ is small in TESLA one can nevertheless think of using this option but careful studies have to be done.

3.7 Results

The Compton scattering was simulated for the above mentioned approximations for a beam polarization of 80%. The resulting photons and electrons were transported to the interaction point and used as an input for the beam-beam simulation programme GUINEA-PIG. As a first idea the following parameters were used: $\rho = 1.5$, $k_\xi = 1$, $\sigma_y^* = 200\,nm$, $\sigma_y^* = 19\,nm$, $\sigma_z = 700\,\mu m$, $\gamma\epsilon_x = 7 \cdot 10^{-6}\,m$, $\gamma\epsilon_y = 0.25 \cdot 10^{-6}\,m$, $N = 3.63 \cdot 10^{10}$, $N_b = 1135$ and $f_r = 5\,Hz$. No separation of the beams was assumed. Figure 3 shows the resulting luminosity spectra for photon-photon, photon-electron and electron-electron scattering. The resulting photon-photon luminosity with a centre of mass energy of more than $300\,GeV$ is about $L_{\gamma\gamma} \approx 1.6 \cdot 10^{33}\,cm^{-2}s^{-1}$. The total photon-photon luminosity is roughly $9.1 \cdot 10^{33}\,cm^{-2}s^{-1}$, $L_{e^-\gamma} = L_{\gamma e^-} = 4.7 \cdot 10^{33}\,cm^{-2}s^{-1}$ and $L_{e^-e^-} = 1.3 \cdot 10^{33}\,cm^{-2}s^{-1}$. The first source of backgrounds will be the conversion region. Since the dependence of most of these backgrounds on the actual layout and the laser used is

significant it will not be considered here. Another very important source of background may come from the so called spent beam that is the beam behind the interaction point. The angular distribution may become rather large, see figure 4. This also depends very much on the layout of the detector. Both backgrounds mentioned will need detailed study. In the following only the backgrounds produced in the interaction point will be considered. They can be calculated using the same way as for the electron-positron machine.

The values found are $N_{e^-e^-} \approx 87 \cdot 10^3$, $E_{e^-e^-} \approx 3.2 \cdot 10^5\, GeV$, $N_H \approx 0.62$, $N_{MJ}(p_\perp > 3.2\, GeV/c) \approx 0.27$ and $N_{MJ}(p_\perp > 10.0\, GeV/c \approx 5.4 \cdot 10^{-3}$.

References

[1] V. Telnov, NIM **A 355** (1995) 3.
[2] D. Schulte, thesis, in preparation.
[3] P. Chen, Phys. Rev. **D 46** (1992) 1186.
[4] P. Chen, T. L. Barklow and M. E. Peskin, SLAC-PUB-5873.
[5] R. Engel et al., see next section.
[6] M. Drees and K. Grassie, Z. Phys. **C 28** (1985).
[7] R. Brinkmann, private communication
[8] O. Napoly, private communication.

4 Kinematical coverage for determining the photon structure function F_2^γ

D.J. Miller[1], A. Vogt[2]

[1] *University College London, Great Britain* [2] *DESY, Hamburg, Germany*

In this section we briefly address the potential of a high–energy linear collider for measuring the photon structure function. See ref. [1] for a discussion at the previous linear collider workshop. We will restrict ourselves to an e^+e^- center-of-mass energy of $\sqrt{s}$ = 500 GeV. With respect to the electroweak part of the process, we will consider only the electromagnetic one-photon-exchange process, i.e. we assume that radiative corrections and contributions due to the exchange of weak bosons have been subtracted.

It is convenient for the following discussion to recall the basic kinematics of deep-inelastic lepton–photon scattering in e^+e^- collisions in this approximation. In Fig. 5a the so-called 'single-tag' situation is shown, where the electron or the positron is detected at some $\theta_{tag} > \theta_0$, with a veto against a second tag anywhere in the detector covering $\theta_0 < \theta < \pi - \theta_0$. The generalization to 'double-tag' events is obvious, such events will however play no role at the linear collider. θ_0 is an essential apparatus parameter for the kinematical coverage and event rates for structure function measurements.

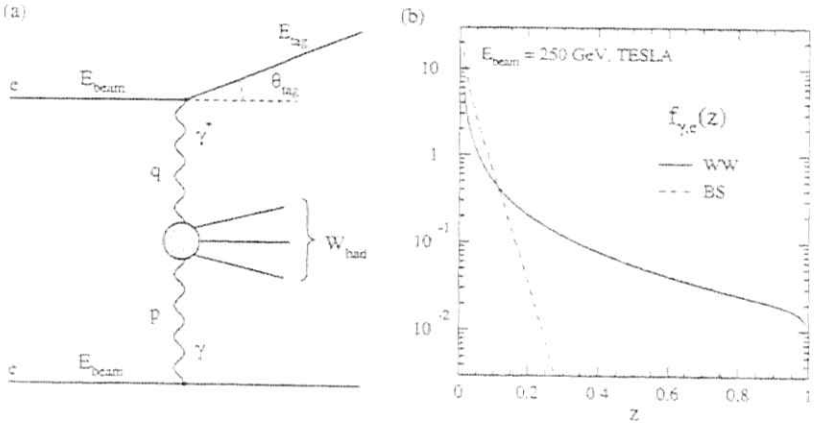

Figure 5: (a) The kinematics of a single–tag inclusive $\gamma\gamma$ event. (b) The flux functions for Weizsäcker-Williams (WW) bremsstrahlung and beamstrahlung (BS) photons at a 500 GeV linear collider. In the WW case the emitting electron is assumed to be anti-tagged with θ_0 = 40 mr; the BS parameters are Υ = 0.039 and σ_z = 500 μm.

The cross section for (unpolarized) inclusive lepton–photon scattering reads to lowest order in the electromagnetic coupling α:

$$\frac{d\sigma(e\gamma \to eX)}{dE_{tag}\, d\cos\theta_{tag}} = \frac{4\pi\alpha^2 E_{tag}}{Q^4 y}\left[\{1-(1-y)^2\}F_2^\gamma(x,Q^2) - y^2 F_L^\gamma(x,Q^2)\right]. \qquad (5)$$

Here $F_{2,L}^\gamma(x,Q^2)$ denote the structure functions of the real photon. The virtuality of the probing photon and the invariant mass of the (hadronic) final state are given by

$$Q^2 \equiv -q^2 = 2E_{beam}E_{tag}(1-\cos\theta_{tag}), \qquad W_{had}^2 = (q+p)^2, \qquad (6)$$

and we have introduced the usual dimensionless variables

$$x = \frac{Q^2}{Q^2 + W_{had}^2}, \qquad y = 1 - \frac{E_{tag}}{E_{beam}}\cos^2\left(\frac{\theta_{tag}}{2}\right). \qquad (7)$$

Experimentally E_{tag} is restricted by background suppression cuts, typically at least to $E_{tag} > 0.5\,E_{beam}$. Hence Q^2 is limited by eq. (6) to $Q^2 \gtrsim 0.5\,E_{beam}^2\,\theta_0^2$, which in turn restricts the reach towards small x via eq. (7). Moreover, the left hand side of eq. (5) is then entirely dominated by F_2^γ. We will confine ourselves to the prospects for measuring this quantity in what follows.

In order to yield the experimentally observable cross section, eq. (5) has to be convoluted with the flux $f_{\gamma/e}(z = E_\gamma/E_{beam})$ of the incoming photons. Firstly, we will study the case of the standard Weizsäcker-Williams (WW) spectrum [2] for the quasi-real photons emitted by the anti-tagged electron, see eq. (22) in Section 6.1.1. This leads to a high-P^2 tail up to $P_{max}^2 \simeq (1-z)\,E_{beam}^2\,\theta_0^2$ for the target photon virtuality $P^2 \equiv -p^2$, which has to be corrected for in determinations of $F_2^\gamma(x,Q^2)$. Secondly, we will consider the case of real-photon beamstrahlung (BS) [3] for the TESLA design of the linear collider. In this case we take the approximate expression and parameters for the BS spectrum as given in Section 6.1.2, eqs. (24)–(26). The two spectra are compared in Fig. 5b. Note the very soft energy distribution of the BS photons for this design.

A possible option at a linear collider which is especially well suited for photon structure function measurements is the conversion of one of the electron beams to a photon beam by backscattering of laser photons (BL) [4]. Under suitable polarization conditions a rather monochromatic photon beam, $\Delta E_\gamma \approx 0.1\,E_\gamma$, with $E_\gamma \simeq 0.8E_{beam}$, can be obtained in this way. For our purpose a rough approximation of the actual momentum spectrum is sufficient, we have taken $f(z) = 375(z-0.63)^2$ for $0.63 \le z \le 0.83$, and $f(z) = 0$ else, for our simulations discussed below.

The fact that the momentum p of the (quasi-)real photon is unknown in the WW and BS cases leads to a key systematic problem in the measurement of the photon structure functions: W_{had} in eq. (6) and hence x in eq. (7) cannot by determined from the outgoing electron alone, in contrast to the situation in the BL $e\gamma$ mode and usual (electromagnetic) lepton–nucleon deep–inelastic scattering. Thus the measurement has to rely on the hadronic final state, of which however in general only a part W_{vis} of the invariant mass is seen in the calorimeters. The resulting problem of reconstructing W_{had} from W_{vis} is especially severe at high W_{had}, i.e. at small-x [5].

It is useful to recall what can be maximally done on F_2^γ before the linear collider becomes operational, i.e. at LEP2 [6]. Here the minimum angle of the main detector coverage is about $\theta_0 \simeq 30$ mr due to synchrotron radiation shielding masks. Therefore Q^2 is limited to the region $Q^2 \gtrsim 3.5$ GeV^2, kinematically allowing for measurements down to about $x \approx 5 \cdot 10^{-4}$. Since here the photon remnant can be expected to be measureable to some extend in the forward calorimeters, a sufficient correlation between $W_{\rm vis}$ and $W_{\rm had}$ may be possible, allowing an unfolding of $F_2^\gamma(x, Q^2)$ at small x. Current studies at LEP show that there may be large systematic errors at low x (not taken into account in Fig. 6) due to uncertainties in the final state fragmentation. At high Q^2, the structure function measurement at LEP2 will run out of statistics at a few hundred GeV^2. The resulting maximal potential of LEP2 is illustrated in Fig. 6.

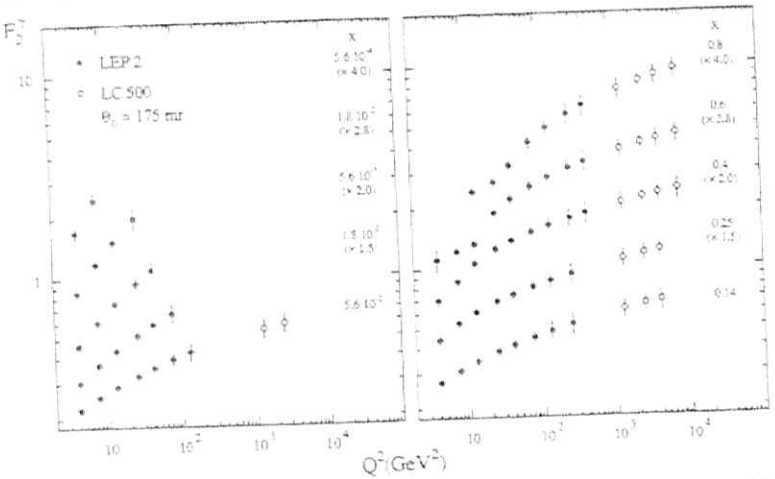

Figure 6: The kinematical coverage and maximal accuracy of the measurement of F_2^γ at LEP2 and at a 500 GeV linear collider, in the latter case assuming that electron tagging is only possible outside the shielding masks at about 10 degrees. See the text below the next figure for a discussion of the error estimates. Note that uncertainties in fragmentation may lead to much larger systematic errors at small x.

At the linear collider, the radiation shielding masks are expected to be located at about 10 degrees. A minimal scenario is to assume that electron tagging will be possible only outside this shielding, i.e. $\theta_0 = 175$ mr. The maximally possible F_2^γ measurements using the WW spectrum for this case are compared to the corresponding LEP2 expectation in Fig. 6. Under these circumstances, all one obtains are some 5000 events at 'high' x in the previously unaccessible range $Q^2 > 1000$ GeV^2. Hence no overlap with the LEP2 results can be achieved, which would allow for adjusting the relative normalizations of the measurements. It should be noted that, at least for the TESLA design considered here, beamstrahlung cannot very much improve the situation with respect to statistics, due to

the softness of its energy spectrum shown in Fig. 5b.

Consequently for an F_2^γ determination with wide kinematical coverage and high precision, electron tagging inside the shielding is mandatory. Expected event numbers for the measurement of $F_2^\gamma(x, Q^2)$, are given in Fig. 7 in bins in x and Q^2 for $\theta_0 = 40$ mrad, resulting in $Q^2_{\rm min} = 50$ GeV^2, for both the WW and BS cases. If this can be achieved practically, a precise measurement overlapping with LEP2 results is possible, taking over with high statistics at $Q^2 \simeq 100$ GeV^2 where the accuracy at LEP2 begins to degrade. Also in this case beamstrahlung does not appreciably modify the kinematical coverage and expected accuracies, as it increases the number of events significantly only where enough statistics is already expected.

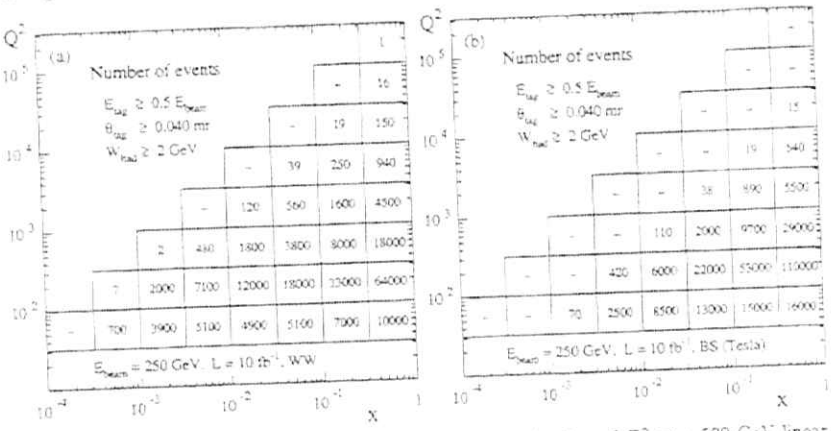

Figure 7: The expected number of events for the determination of F_2^γ at a 500 GeV linear collider in case that electron tagging well inside the shielding is possible. In (a) the standard anti-tag WW photon spectrum has been used $\theta < 40$ mr, and (b) is the same for the TESLA BS case. Q^2 is given in GeV^2.

The event numbers in Fig. 7 have been calculated using the leading order (LO) GRV parametrization of the photon's parton densities [7], together with the LO $\gamma^*\gamma \to c\bar{c}$ and $\gamma^* g \to c\bar{c}$ Bethe-Heitler charm contributions. See Section 8.2 for a detailed discussion of the latter processes. Only simple cuts have been applied: on $E_{\rm tag}$, $\theta_{\rm tag}$ and $W_{\rm had}$. In order to account crudely for the additional suppression due to further experimental final state cuts – $W_{\rm vis}$ instead of $W_{\rm had}$, number of tracks etc. – the nominal luminosity has been scaled down by a factor of two. The suppression of $F_2^\gamma(x, Q^2, P^2)$ with respect to $F_2^\gamma(x, Q^2)$ for the high-P^2 tail of the WW spectrum has also not been taken into account, and F_L has been neglected in eq. (5).

The corresponding maximal accuracy and kinematical coverage of the F_2^γ measurement is displayed in Fig. 8 for the WW case. Here we have simply assumed that the systematic error is equal to the statistical one inferred from Fig. 7a, but amounts to at least 5%.

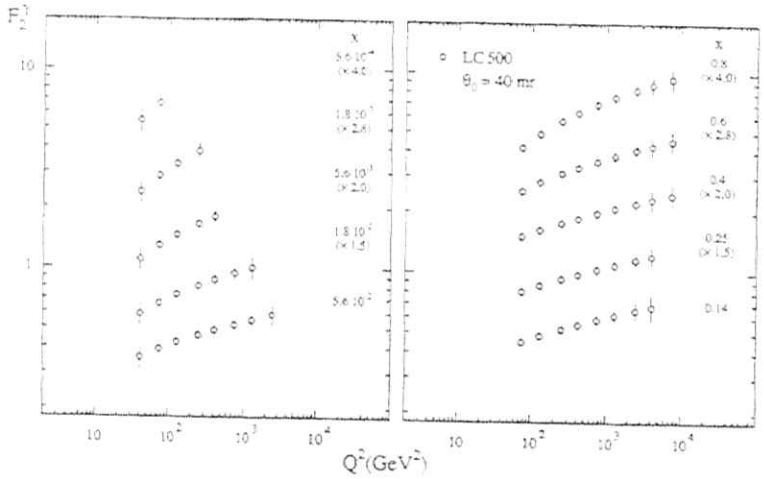

Figure 8: The kinematical coverage and maximal accuracy of the F_2^γ measurement using WW photons measurement a 500 GeV linear collider. Note that presumably no unfolding of $F_2^\gamma(x, Q^2)$ will be possible at $x < 0.1$. The values of F_2 have been multiplied be the x-dependent number indicated in brackets.

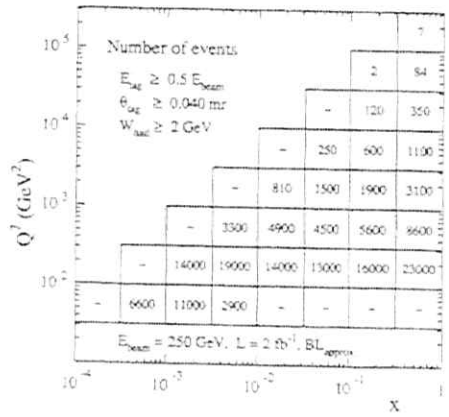

Figure 9: The expected number of events for the determination of F_2^γ in the backscattered-laser $e\gamma$ mode of a 500 GeV linear collider, assuming that 20% of the e^-e^- luminosity can be reached in this mode for a rather monochromatic photon beam.

Shown is the quadratic sum of these two contributions. The errors shown in Fig. 6 have been obtained in the same way from corresponding event number estimates not given here. See ref. [6] for the LEP2 case. With respect to the small-x region in Figs. 7 and 8 it must be noted that, unlike at LEP2, due to the higher minimum angle of the calorimetric detector coverage and the higher beam energy the bulk of the photon remnants will be lost at the linear collider. This will presumably prohibit any unfolding of F_2^γ significantly below $x \approx 0.1$.

Thus for reaching small x the $e\gamma$ mode is most probably needed. Moreover, it can be expected to allow for significantly reduced systematic errors in the regime which can be covered also in e^-e^- collisions. With respect to statistics Fig. 9 indicates that reaching about 20% of the e^-e^- luminosity in this mode is sufficient for a high-statistics measurement over almost the full range of Fig. 8. Due to the hard BL photon spectrum, there is a slight shift towards higher Q^2 and smaller x.

Let us summarize: if electron tagging inside the shielding masks at about 10 degrees is not feasible, then roughly 5000 events for F_2 in the previously unexplored high-Q^2 range can be expected. Neither overlap with LEP2 results, nor sensitivity to small-x will be obtained. To achieve these goals, an electron tagging device inside the shielding, down to about 40 mrad would be needed. This would however still not be sufficient to get measurements at small x, due to the problem of unfolding the data at very high W. In order to circumvent this problem, and also to reduce the main systematic errors at high x, the conversion to an $e\gamma$ collider by laser backscattering is the ideal mode.

Acknowledgement

This work was supported in part by the German Federal Ministry for Research and Technology under contract No. 05 6MU93P.

References

[1] D.J. Miller et al., Proceedings of the Workshop on Physics and Experiments with Linear e^+e^- Colliders, Waikaloa, Hawaii, April 1993, eds. F.A. Harris et al. (World Scientific 1993), p. 577
[2] V.M. Budnev et al., Phys. Rep. **15C** (1975) 18
[3] P. Chen, Phys. Rev. **D46** (1992) 1186;
P. Chen, T.L. Barklow and M.E. Peskin, Phys. Rev. **D49** (1994) 3209
[4] I.F. Ginzburg et al., Nucl. Inst. Meth. **A205** (1983) 47, **A219** (1984) 5;
V.I. Telnov, Nucl. Inst. Meth. **A94** (1990) 72
[5] L. Lönnblad et al., $\gamma\gamma$ generators, in the Proceedings of the Workshop on *Physics at LEP2*, CERN Yellow report, CERN 96-01, G. Altarelli, T. Sjöstrand, F. Zwirner eds.
[6] P. Aurenche et al., $\gamma\gamma$ physics, in the Proceedings of the Workshop on *Physics at LEP2*, CERN Yellow report, CERN 96-01, G. Altarelli, T. Sjöstrand, F. Zwirner eds.
[7] M. Glück, E. Reya and A. Vogt, Phys. Rev. **D46** (1992) 1973

5 The $k_\perp$ dependent gluon density of the photon

J. Blümlein

DESY, Zeuthen, Germany

In the small x range new dynamical effects are expected to determine the behaviour of structure functions. The evolution of parton densities is effected by terms due to non strong $k_\perp$ ordering. New terms besides those due to mass factorization are expected to contribute. A description of these contributions requires to generalize the factorization of the hadronic matrix elements into coefficient functions and parton densities in which the $k_\perp$ dependence is not integrated out [1]. This factorization covers the case of collinear factorization in the limit that the k^2 dependence of the coefficient function is neglected. The $k_\perp$ dependent gluon density accounts for the resummation of small x effects. Here we will consider contributions due to the Lipatov equation only. Since this equation behaves infrared finite no other singularities will emerge than those appearing in the case of mass factorization. The collinear singularities are delt with in the same way as in the case of $k_\perp$ factorization.

The $k_\perp$ dependent distribution $\Phi(x, k^2, \mu)$ can finally be represented as the convolution of the gluon density in the collinear limit $g(x, \mu)$ and a function $\mathcal{G}(x, k^2, \mu)$ for which an analytic expression will be derived.

5.1 $k_\perp$ Factorization and the $k_\perp$ dependent gluon distribution

The factorization relation for an observable $O_i(x, \mu)$ reads

$$O_i(x, \mu) = \int dk^2 \hat{\sigma}_{O_i}(x, k^2, \mu) \otimes \Phi(x, k^2, \mu) \tag{8}$$

where $\hat{\sigma}_{O_i}(x, k^2, \mu)$ and $\Phi(x, k^2, \mu)$ denote the k^2 dependent coefficient function and parton density[6], respectively. Eq. (8) can be rewritten as [2, 3]

$$O_i(x, \mu) = \hat{\sigma}^0_{O_i}(x, \mu) \otimes G(x, \mu) + \int_0^\infty dk^2 \left[\hat{\sigma}_{O_i}(x, k^2, \mu) - \hat{\sigma}^0_{O_i}(x, \mu)\right] \Phi(x, k^2, \mu) \tag{9}$$

with $\hat{\sigma}^0_{O_i}(x, \mu) = \lim_{k^2 \to 0} \hat{\sigma}_{O_i}(x, k^2, \mu)$. The first term in (9) describes the conventional contribution due to collinear factorization. The second term contains the new contributions. Note that $\Phi(x, k^2, \mu)$ starts with terms $\propto \alpha_s$. It has therefore *not* the interpretation of a probability density and may even become negative.

As shown in [2] the $k_\perp$ dependent gluon distribution associated to eq. (9) reads in moment space

$$\tilde{\Phi}(j, k^2, \mu) = \gamma_e(j, \bar{\alpha}_s) \frac{1}{k^2} \left(\frac{k^2}{\mu^2}\right)^{\gamma_e(j, \bar{\alpha}_s)} \tilde{g}(j, \mu) \tag{10}$$

[6] We will consider the gluon density in the present paper only.

where μ denotes a factorization scale, $\bar{\alpha}_s = N_c \alpha_s(\mu)/\pi$, and $g(x, \mu)$ is the gluon density. Eq. (10) accounts for the small x behaviour due to the Lipatov equation. Here $\gamma_e(j, \bar{\alpha}_s)$ is the eigenvalue of the *homogeneous* equation obeying

$$\rho \equiv \frac{j-1}{\bar{\alpha}_s} = \chi(\gamma_e(j, \bar{\alpha}_s)), \quad \chi(\gamma) = 2\psi(1) - \psi(\gamma) - \psi(1-\gamma). \tag{11}$$

In x space the $k_\perp$ dependent distribution is given by the convolution

$$\Phi(x, k^2, \mu) = \mathcal{G}(x, k^2, \mu) \otimes g(x, \mu). \tag{12}$$

correspondingly, with

$$\int_0^{k^2} dk^2 \Phi(x, k^2, \mu) = g(x, \mu). \tag{13}$$

The function $\mathcal{G}(x, k^2, \mu)$ is universal and can be calculated numerically by a contour integral in the complex plane over the first factor in eq. (10). Since the solution of eq. (11) is multivalued the Mellin inversion to x space requires to select the branch in which for asymptotic values of $j \in \mathcal{C}$ γ_e approaches the perturbative result $\gamma_e(j, \bar{\alpha}_s) \sim \bar{\alpha}_s/(j-1)$ for small values of $\bar{\alpha}_s$.

We solved eq. (11) under this condition numerically using an adaptive Newton algorithm. The solution is characterized by three branch points, see [4] for a detailed discussion and numerical results for the solution of eq. (11) for complex arguments.

5.2 An analytical solution for $\mathcal{G}(x, k^2, \mu)$

The integration contour for the Mellin transformation of $\tilde{\Phi}(j, k^2, \mu)$ to $\Phi(x, k^2, \mu)$ for $j \in \mathcal{C}$ has to be situated outside the range of the singularities of γ_e. One may expand $\gamma_e(j, \bar{\alpha}_s)$ into a Laurent series over ρ

$$\gamma_e(j, \bar{\alpha}_s) = \sum_{l=1}^{\infty} g_l \rho^{-l} \tag{14}$$

in this range.

The coefficients g_l are given in [5] up to $l = 20$ in analytical form extending an earlier result [6].

Using (14) a corresponding expansion may be performed for

$$k^2 \tilde{\mathcal{G}}(j, k^2, \mu) = \gamma_e(j, \bar{\alpha}_s) \exp[\gamma_e(j, \bar{\alpha}_s) L] \tag{15}$$

with $L = \ln(k^2/\mu^2)$. For the single terms of the Laurent series in ρ the Mellin transform can be carried out analytically.

Here it is important to expand the exponential in eq. (15) in such a way that the lowest order term in $\bar{\alpha}_s$ of γ_e is *kept* in exponential form. One obtains

$$k^2 \mathcal{G}(x, k^2, \mu) = \frac{\bar{\alpha}_s}{x} I_0\left(2\sqrt{\bar{\alpha}_s \log(1/x) L}\right) + \frac{\bar{\alpha}_s}{x} \sum_{i=4}^{\infty} d_i(L) \left(\frac{\bar{\alpha}_s \log(1/x)}{L}\right)^{(i-1)/2}$$

$$\cdot\ I_{\nu-1}\left(2\sqrt{\overline{\alpha}_s \log(1/x)L}\right), L > 0. \tag{16}$$

The coefficients $d_\nu(L)$ are given in ref. [5]. Up to $\nu = 20$ they contain at most terms $\propto L^4$. The first term in eq. (16) denotes the Green's function in DLA.

For $L \to 0$ (16) takes the form

$$k^2\mathcal{G}(x,k^2,\mu) = \frac{\overline{\alpha}_s}{x}\sum_{l=1}^{\infty}\frac{l!}{(l-1)!}\left[\overline{\alpha}_s\left(\frac{1}{x}\right)\right]^{l-1}, \tag{17}$$

and for $L < 0$ (i.e. $k^2 < \mu^2$) one has

$$\begin{aligned} k^2\mathcal{G}(x,k^2,\mu) &= \frac{\overline{\alpha}_s}{x}J_0\left(2\sqrt{\overline{\alpha}_s\log(1/x)|L|}\right) + \frac{\overline{\alpha}_s}{x}\sum_{\nu=1}^{\infty}d_\nu(L)\left(\frac{\overline{\alpha}_s\log(1/x)}{|L|}\right)^{(\nu-1)/2} \\ &\cdot\ J_{\nu-1}\left(2\sqrt{\overline{\alpha}_s\log(1/x)|L|}\right). \end{aligned} \tag{18}$$

Thus for $k^2 \to 0$ damped, oscillating modes are obtained which vanish faster than $1/|L|^{3/4}$.

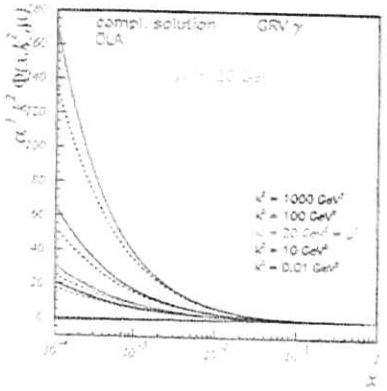

Figure 10: *The $k_\perp$ dependent gluon distribution of the photon scaled by $1/\alpha_{QED}$ as a function of k^2 and x. Full lines: complete solution; dashed lines: solution in DLA. For the input distribution $g(x,\mu)$ the parametrization [7] (LO) was used.*

The $k_\perp$ dependent gluon distribution of the photon $\Phi(x,k^2,\mu)/\alpha_{QED}$ (scaled by k^2) is shown in Fig. 10 as a function of x and k^2 for $\mu^2 = 20\,\mathrm{GeV}^2$ referring to the parametrization of ref. [7] to describe $g(x,\mu)$. The complete solution eq. (12) is larger than the DLA result for $k^2 \gtrsim \mu^2$ at $x \lesssim 10^{-3}$ by 10 to 15% while for $k^2 \to 0$ smaller values are obtained.

At larger values of x the complete solution approaches the DLA result. For $k^2 \to 0$ $\Phi(x,k^2,\mu)$ vanishes. Since the DLA result is proportional to $J_0(2\sqrt{\overline{\alpha}_s\log(1/x)\log(k^2/\mu^2)})$ for $k^2 \to 0$ a damped oscillatory behaviour is obtained in this approximation. The complete solution, on the other hand, behaves monotonous in the whole kinematical range.

Since the shape and size of the complete solution and the DLA solution are rather similar very precise measurements are required to establish the non-DLA contributions at small x although the correction is of importance numerically.

References

[1] M. Ciafaloni, Nucl. Phys. **B296** (1987) 249; S. Catani, M. Ciafaloni, and F. Hautmann, Nucl. Phys. **B366** (1991) 135.

[2] J. Collins and R. Ellis, Nucl. Phys. **B360** (1991) 3.

[3] J. Blümlein, J. Phys. **G19** (1993) 1623.

[4] J. Blümlein, in: Proc. of the XXX Rencontre de Moriond, Les Arcs, March 1995, ed. J. Tran Thanh Van (Ed. Frontières, Paris, 1996).

[5] J. Blümlein, in preparation.

[6] S. Catani, F. Fiorani, and G. Marchesini, Nucl. Phys. **B336** (1990) 18.

[7] M. Glück, E. Reya, and A. Vogt, Phys. Rev. **D46** (1992) 1973.

6 Soft, semihard and hard photon-photon physics

R. Engel[1], P. Aurenche[2], V. Del Duca[3], M. Fontannaz[4], J.Ph. Guillet[2], J. Ranft[5], T. Sjöstrand[6]

[1] *ITP, Leipzig, Germany*
[2] *ENSLAPP-Annecy, France*
[3] *DESY, Hamburg, Germany*
[4] *LPTHE, Orsay, France*
[5] *GAES, Santiago de Compostella, Spain*
[6] *DTP, Lund, Sweden*

6.1 Photon sources at linear colliders

We give here the formulae used to generate the various photon spectra in our studies of photon-photon collisions.

6.1.1 Bremsstrahlung

The flux of weakly virtual photons can be approximated taking into account only transversely polarized photons. Then, the $ee \to eeX$ photoproduction cross section is given by

$$\frac{d^2\sigma_{ep}}{dy_1 dP_1^2 dy_2 dP_2^2} = f_{\gamma/e}^{brems}(y_1, P_1^2)\, f_{\gamma/e}^{brems}(y_2, P_2^2)\, \sigma_{\gamma\gamma}(s, P_1^2, P_2^2). \tag{19}$$

with

$$f_{\gamma/e}^{brems}(y, P^2) = \frac{\alpha}{2\pi P^2}\left[\frac{1+(1-y)^2}{y} - 2m_e^2 y\frac{1}{P^2}\right]. \tag{20}$$

Here, y and $P^2 = -p^2$ denote the energy fraction taken by the photon from the electron and the photon virtuality. m_e is the electron mass. Neglecting the dependence of the $\gamma\gamma$ cross section on P^2 in Eq. (19), the well known equivalent photon approximation [1] is obtained

$$f_{\gamma/e}^{brems}(y, P^2) = \frac{\alpha}{2\pi}\left[\frac{1+(1-y)^2}{y}\ln\frac{P^2_{max}}{P^2_{min}} - 2m_e^2 y\left(\frac{1}{P^2_{min}} - \frac{1}{P^2_{max}}\right)\right]. \tag{21}$$

Taking the kinematic limit $P^2_{min\,kin} = m_e^2 y^2/(1-y)$ as lowest photon virtuality allowed one gets

$$f_{\gamma/e}^{brems}(y) = \frac{\alpha}{2\pi}\left(\frac{1+(1-y)^2}{y}\ln\frac{(1-y)}{m_e^2 y^2}P^2_{max} - \frac{2(1-y)}{y}\right). \tag{22}$$

Given the present configuration of the e^+e^- colliders, the anti-tagging angle on the electrons or positrons will be quite large: $\theta_{max} = 175$ mrad, or may-be $\theta_{max} = 40$ mrad. This leads to large photon virtualities P^2 where the equivalent photon approximation may not be reliable. This point, which has not been studied in detail below, clearly deserves further work.

6.1.2 Beamstrahlung

In case of Gaussian beams, the effective beamstrahlung spectrum has been estimated by Chen et al. [2, 3]. The dependence of this spectrum on the particle-bunch parameters can be expressed by the beamstrahlung parameter Υ:

$$\Upsilon = \frac{5 r_e^2 E N_e}{6\alpha\sigma_z(\sigma_x^* + \sigma_y^*)m_e}. \tag{23}$$

Here, E denotes the beam energy, N_e is the number of electrons or positrons in a bunch, σ_x^* and σ_y^* are the transverse bunch dimensions, and $r_e = 2.818 \cdot 10^{-12}$mm is the classical electron radius. In our calculations we approximate the beamstrahlung spectrum by [3]

$$f_{\gamma/e}^{beam}(y) = \frac{\kappa^{1/3}}{\Gamma(1/3)} y^{-2/3}(1-y))^{-1/3} e^{-\kappa y/(1-y)} \left\{\frac{1-w}{\tilde{g}(y)}\left[1 - \frac{1}{\tilde{g}(y)N_\gamma}\left(1 - e^{-N_\gamma \tilde{g}(y)}\right)\right] + w\left[1 - \frac{1}{N_\gamma}\left(1 - e^{-N_\gamma}\right)\right]\right\}, \tag{24}$$

with

$$\tilde{g}(y) = 1 - \frac{1}{2}(1-y)^{2/3}\left[1 - y - (1-y)\sqrt{1+\Upsilon^{2/3}}\right] \tag{25}$$

and $\kappa = 2/(3\Upsilon)$, $w = 1/(6\sqrt{\kappa})$. The average number of photons N_γ emitted per electron is given by

$$N_\gamma = \frac{5\alpha^2\sigma_z m_e}{2r_e E}\frac{\Upsilon}{\sqrt{1+\Upsilon^{2/3}}}. \tag{26}$$

Here we use $\Upsilon = 3.9\ 10^{-2}$ and $\sigma_z = 500\mu$m, slightly different from the values discussed in [4].

6.1.3 Photon emission by laser-backscattering

Depending on the polarization of the laser light, various photon spectra can be produced [5]-[7]. In the following, only the case of unpolarized electrons and unpolarized laser radiation is considered. If the laser frequency is chosen according to the optimal value $x_c = 2 + \sqrt{8}$ given in [7], the spectrum of the photon flux can be approximated by

$$f_{\gamma/e}^{laser}(y) = \frac{-0.544\ y^3 + 2.17\ y^2 - 2.63\ y + 1.09}{(1-y)^2}\ \Theta(0.828 - y). \tag{27}$$

6.2 Photon-photon cross section predictions

In the following, cross section predictions of a few models are presented. Details about the models used here can be found elsewhere (PYTHIA [8, 9], PHOJET [10, 11], eikonalized minijet model [12]). A discussion of some uncertainties in estimating the inelastic cross

section is given in the next section [12]. All the models are using unitarization schemes to avoid the violation of unitarity at high energies.

Since the total cross section cannot be calculated using only perturbative QCD, several model dependent assumptions are necessary. The models start to determine the free parameters by fits to total, elastic and diffractive cross section of proton-proton /antiproton collisions. The results of the fits depend on the choice of the parton structure functions and cutoffs for the minijet component. Assuming Regge factorization, one proton is substituted by a photon keeping the couplings and parameters belonging to the proton side the same as in proton-proton collisions. This substitution introduces new free parameters corresponding to photon specific properties. These parameters are determined by fitting the total photoproduction cross section and the cross section on quasi-elastic ρ^0 production. Once the model parameters are fixed, photon-photon cross sections can be predicted without introducing new arbitrary parameters. In Fig. 11 the inelastic photon-photon cross section according to PYTHIA, PHOJET and the eikonalized minijet model is shown together with data. Since there is little known about the low-x behaviour of the

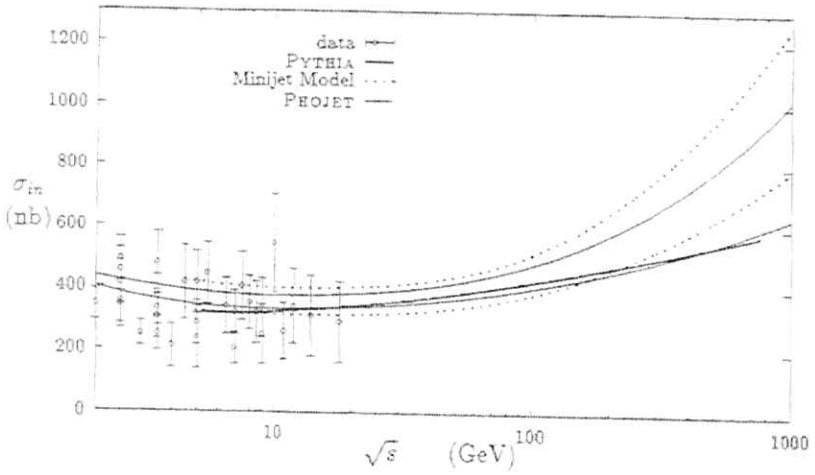

Figure 11: Inelastic photon-photon cross sections calculated with the models PYTHIA [8, 9], PHOJET [10, 11] and an eikonalized minijet model [12] are compared with data. The two curves from PHOJET were calculated using the GRV LO photon structure function [13] (upper curve) and the SaS 2M photon structure function [14] (lower curve). The two curves according to the unitarized minijet model are the highest and the lowest prediction presented in [12].

photon structure function, the predictions of the models at high energies depend strongly on the parton distributions assumed for the photon. A somewhat more optimistic picture is provided by VMD scenarios, where the small-x behaviour of parton distributions and hence the energy dependence of the $\gamma\gamma$ cross section is expected to be qualitatively similar to the observed $p\bar{p}$ ones.

6.3 Photon-photon hadron production

6.3.1 General characteristics

It is expected that photon-photon scattering at high energies behaves similar to hadron-hadron interactions. However, due to the dual nature of the photon and its direct coupling to quarks, some significant differences to purely hadronic reactions are expected. Since the general features of hadronic minimum bias events are well known, it is convenient to characterize photon-photon interactions comparing to proton-proton and photon-proton interactions. In the following some model predictions for inelastic hadron production in proton-proton, photon-proton and photon-photon collisions are compared at fixed center-of-mass (CMS) energies $\sqrt{s}$. In order to compare to $p\bar{p}$ data, elastic/quasi-elastic scattering (i.e. $\gamma + \gamma \rightarrow V + V$, $V = \rho, \omega, \phi$) was excluded in the calculations.

As first discussed by Schuler and Sjöstrand [8, 9], the fraction of hard interactions in minimum bias interactions rises from proton-proton collisions over photon-proton collisions to photon-photon collisions (see Fig. 12.a). The reason for this is the direct photon interaction and the fact, that the photon structure function is considerably harder than the proton structure function. However, these differences in the hard scattering do not

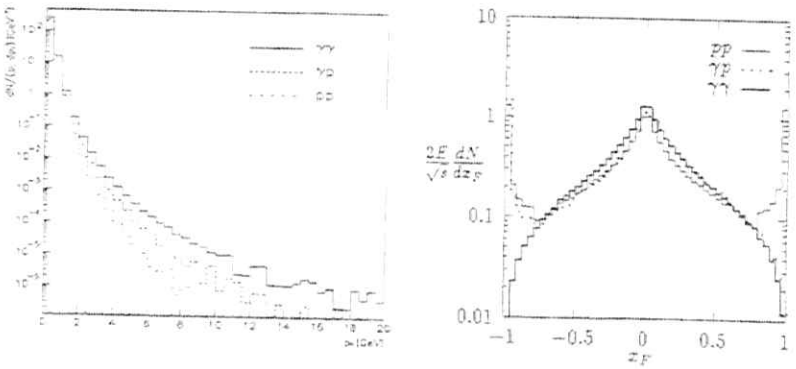

Figure 12: (a) Comparison of the transverse momentum distribution for all charged hadrons produced in proton-proton, photon-proton and photon-photon collisions at $\sqrt{s}$ = 200 GeV. The calculation was done with PYTHIA [9]. (b) Invariant form of the x_F distribution for all charged hadrons produced in proton-proton, photon-proton and photon-photon collisions at $\sqrt{s}$ = 200 GeV. The calculation was done with PHOJET [11] for inelastic collisions.

strongly influence such average properties of the collision as average multiplicities or even average transverse momenta. This can be seen from Table 3, where we collect some average quantities characterizing nondiffractive collisions. The total and charged multiplicities at all energies are rather similar in all channels. The differences in the multiplicities of hadrons like π^- and $\bar{p}$ are more significant, we find them at all energies rising from pp

Table 1: Comparison of average quantities characterizing hadron production in nondiffractive pp, γp and $\gamma\gamma$ collisions at CMS energies at 50 and 200 GeV [11]. The energies are given in GeV and average the transverse momenta are given in GeV/c.

Quantity	pp	γp	$\gamma\gamma$	pp	γp	$\gamma\gamma$
$\sqrt{s}$	50	50	50	200	200	200
n_{tot}	24.8	26.5	26.9	40.1	46.2	47.5
n_{ch}	14.5	15.5	15.6	23.3	26.9	27.6
n_{π^-}	5.49	6.19	6.53	9.16	10.94	11.46
$n_{\bar{p}}$	0.21	0.27	0.34	0.46	0.59	0.67
$\langle p_\perp \rangle_{\pi^-}$	0.33	0.35	0.40	0.35	0.38	0.42
$\langle p_\perp \rangle_{\bar{p}}$	0.44	0.47	0.57	0.47	0.53	0.64

over γp to $\gamma\gamma$ collisions. Also the average transverse momenta rise in the same way.

In Fig. 12.b we compare the longitudinal momentum distributions in the invariant form for the three channels. Significant differences between the three channels are found in the region near $x_F = 1$ or -1. In pp and γp interactions, the single diffractive component is characterized by leading protons which are obviously missing in $\gamma\gamma$ collisions.

6.3.2 Jet production

Data on jet production in collisions of quasi-real photons have been reported by several experiments (a review is given in [15]). Here, we pick out for comparison the fully acceptance corrected, jet data published by the TOPAZ and AMY Collaborations [16, 17]. These data were already compared to leading [18] and to next-to-leading order QCD calculations in [19],[20]. In Figs. 13.a and 13.b we compare PHOJET [11] results calculated using the GRV LO photon structure function [13] with the data on single jet and two jet transverse momentum distributions [16, 17]. The anti-tag conditions and kinematical cuts of the experiments were applied to the PHOJET events. The jets are searched from the Monte Carlo events on hadron level using a cone jet finding algorithm with the cone radius $R = 1$. The cross sections for these jets, which should approximately correspond to the jets identified in the experiment are compared to the data. To illustrate the difference of these hadron jet cross sections to the cross sections treating each hard parton ($p_\perp > 3$GeV/c) as a single jet, we include in the Figs. also the nonfragmented parton cross sections. There is a systematic difference between the model and the TOPAZ data, the model is below the data. It is interesting, that the calculation of Kleinwort and Kramer [20], which uses the same GRV photon structure functions, shows the same disagreement to the single jet data as found using PHOJET in Fig. 13.a.

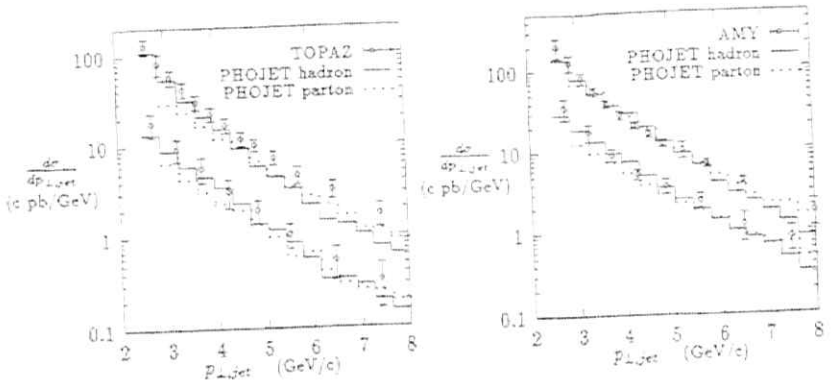

Figure 13: (a) Comparison of single jet $p_\perp$ cross sections (upper curves) and two-jet $p_\perp$ cross sections (lower curves) from [16, 17] with PHOJET [11] results. In addition, the cross section identifying each parton with $p_\perp > 3$ GeV/c with a jet (dottes lines) are shown.

Table 2: Average photon-photon energies and cross sections for the three photon spectra folded with the $\gamma\gamma$ cross section at two linear collider energies. The energies are given in GeV.

$\sqrt{s_{e^+e^-}}$	spectrum	$\sqrt{s_{\gamma\gamma}}$	σ (μb)	$\sqrt{s_{e^+e^-}}$	spectrum	$\sqrt{s_{\gamma\gamma}}$	σ (μb)
500	Bremsst.	50	0.0067	1000	Bremsst.	105	0.0075
500	Beamst.	16.7	0.038	1000	Beamst.	41	0.026
500	B.Laser	252	0.47	1000	B.Laser	509	0.59

6.3.3 Hadron production at Tesla

Two-photon physics at future e^+e^- linear colliders has been discussed by several authors, for example see [21, 3]. These studies are mainly restricted to processes involving large momentum transfers. Here, we consider minimum bias distributions which may be important for background estimatess and detector design. As example, the calculations are done for the TESLA collider design [22].

Using the approximations discussed in Sec. 6.1 we plot in Fig. 14.a the photon spectra according to the equivalent photon approximation, the beamstrahlung spectrum using the bunch parameters [22] as given in the caption of Fig. 14 and a backscattered laser spectrum. The photon virtuality was restricted to $P^2 \leq 2$ GeV^2/c^2. The corresponding photon-photon luminosity functions are shown in in Fig. 14.b. For the calculations, the cut $\sqrt{s_{\gamma\gamma}} > 5$ GeV has been applied. In Table 2 we give the average photon-photon energies and the cross sections for the three processes at two energies. From Fig. 14 and Table 2 we see that the beamstrahlung spectrum of the TESLA project is the softest of the three photon spectra, the backscattered laser spectrum is the hardest. Of course, in

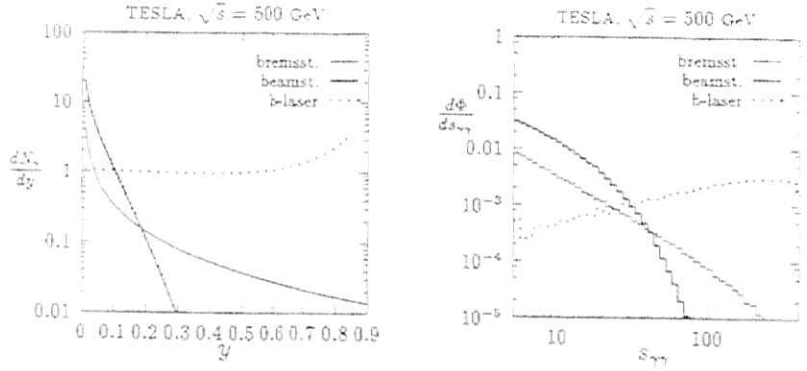

Figure 14: (a) Photon fluxes at a $\sqrt{s} = 500$ GeV linear collider TESLA [22]. Given are the bremsstrahlung spectrum, the beamstrahlung spectrum using the bunch parameters $N_e = 1.8\ 10^{10}$, $\sigma_x = 598$ nm, $\sigma_y = 6.5$ nm and $\sigma_z = 0.5$ mm [22], and a backscattered laser spectrum. (b) photon-photon luminosity function (normalized to the ee luminosity).

the case of a linear collider one has to consider for background problems the superposition of the beamstrahlung spectrum and the bremsstrahlung spectrum.

In Fig. 15.a we plot the cross sections $\sigma dE_\perp/d\eta$ for the transverse energy as function of pseudorapidity for the charged hadron production as function of pseudorapidity. It is clearly visible, that the backscattered laser spectrum is rather hard and has the highest weight. The beamstrahlung spectrum and the bremsstrahlung spectrum are rather comparable, the former has the higher weight, the latter is the harder of these two. The same differences between the three photon spectra are visible in the cross sections $d\sigma/dp_\perp$ for charged hadron production as function of the transverse momentum in Fig. 15.b for the 500 GeV TESLA collider. The $p_\perp$ distributions for the bremsstrahlung spectrum and the beamstrahlung spectrum cross. At low $p_\perp$ the beamstrahlung dominates, at high $p_\perp$ the bremsstrahlung spectrum dominates.

6.3.4 Jet production in semihard processes

We discuss in this section the jet production, inclusive and with rapidity gaps, in the semihard region, $\sqrt{s_{\gamma\gamma}} \gg p_\perp$, with $p_\perp$ the jet transverse energy. In the semihard region a fixed-order perturbative calculation of the jet-production rates may be not sufficient to describe the multiple gluon radiation, and may be necessary to resum the large logarithms, $\ln(s_{\gamma\gamma}/p_\perp^2)$, as is done in the BFKL theory [23]. This predicts that the (enhancement) K-factor of the total parton-parton cross section exhibits a power-like growth in the parton center-of-mass energy $\sqrt{\hat{s}}$. In the case of inclusive two-jet production at large rapidity intervals $\Delta\eta$ between the jets, we obtain $\Delta\eta \simeq \ln(\hat{s}/p_\perp^2)$, and the growth of the K-factor with $\hat{s}$ above mentioned may be read out as the growth of the two-jet K-factor with $\Delta\eta$

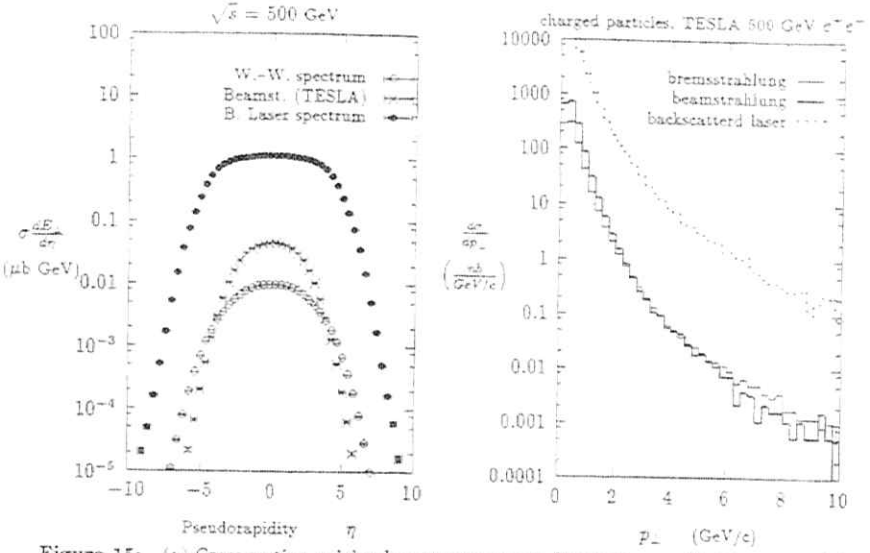

Figure 15: (a) Cross section weighted transverse energy distributions $\sigma dE_\perp/d\eta$ measured in μb GeV at the $\sqrt{s} = 500$ and 1000 GeV TESLA linear colliders [22]. Given are the distributions for the bremsstrahlung photon spectrum, the beamstrahlung spectrum and a backscattered laser spectrum. (b) Transverse momentum cross sections $d\sigma/dp_\perp$ at the $\sqrt{s} = 500$ GeV TESLA linear collider [22]. Given are the distributions for the bremsstrahlung photon spectrum, the beamstrahlung spectrum and a backscattered laser spectrum [11].

[24]. Since $\hat{s} = x_1 x_2 s$, with $x_{1,2}$ the momentum fractions of the incoming partons and $\sqrt{s}$ the hadron center-of-mass energy, $\Delta\eta$ may be increased either by increasing the x's or by increasing s: the former is feasible in a fixed-energy collider, like the Tevatron, but it is not desirable because it introduces a damping in the cross section due to the falling parton luminosity, as $x \to 1$ [25]; the latter is the optimal setting because by fixing the parton densities (up to a residual but mild variation due to $p_\perp$) it looks mainly at the parton dynamics, but it requires a variable-energy collider. An e^-e^- linear collider works like a variable-energy hadron collider if we consider the bremsstrahlung and beamstrahlung spectra for quasi-real photons and ramp the photon-photon center-of-mass energy $\sqrt{\hat{s}} = \sqrt{s_{\gamma\gamma}}$ up, at fixed parton momentum fractions x/y within the photons. For example, for a 1000 GeV TESLA collider let us consider a brems/beamstrahlung spectrum with photon momentum fractions $0.05 \le y_i = y_2 \le 0.5$, and the production of two jets at $x_1/y_1 = x_2/y_2 = 0.2$. This entails that $10 \le \sqrt{\hat{s}} \le 100$ GeV, and for jet transverse momenta $p_\perp \ge 5$ GeV, that $1.4 \le \Delta\eta \le 6$.

Analogously, we can treat two-jet production with a large rapidity gap $\Delta\eta_{gap}$ in hadron production between the jets, with $\Delta\eta_{gap} = \Delta\eta - 2R$ and $\Delta\eta$ the rapidity interval between the jet centers and R the jet-cone size. The absence of gluon radiation between the jets

may be modeled as due to the exchange of a colorless object, with momentum transfer $t \simeq -p_\perp^2$. The probability that this is due to one-gluon exchange falls exponentially with $\Delta\eta$, while the probability of it being due to two-gluon exchange in a colorless combination, i.e. to a perturbative pomeron, is in a first approximation independent of $\Delta\eta$ [26], [27], [28]. However, if the colliding particles are hadrons, or hadron-like, the additional soft interactions between the spectator partons may fill in the gap with soft hadrons [26]. A way of avoiding it is to require that at least one of the colliding particles is point-like, namely in $\gamma\gamma$ collisions that one of the photons is off shell. Thus we consider two-jet production in $\gamma^*\gamma$ DIS events, with one jet in the current fragmentation region, the current jet, and the other close to the γ fragmentation region, the forward jet. To minimize the variation of the parton densities we require as in the inclusive case that the parton momentum fraction x/y within the photon γ is fixed [28]. However we may ramp the off-shell-photon/parton center-of-mass energy $\hat{s}_{\gamma^*p}$ up even at fixed γ-beam energies by decreasing x_{bj}, since $\Delta\eta \simeq \ln(\hat{s}_{\gamma^*p}/Q^2) = \ln(x/yx_{bj})$. In order to maximize the energy we may run the γ beam in the backscattered laser mode, which entails that $s_{ep} \simeq 8 \cdot 10^5\, GeV^2$. Thus for an electron scattered at $\theta \simeq 12.6$ mrad we have $Q^2 \simeq 40\, GeV^2$, and for a realistic electron energy loss $y_e \simeq 0.25$ we find $x_{bj} \simeq 2 \cdot 10^{-4}$. So for $x/y = 0.2$, we obtain $\Delta\eta \simeq 6.9$, which for a jet-cone size $R = 1$ yields gaps of size $\Delta\eta_{gap} \simeq 5$, which is about the size required to make this study relevant [29].

The study of the perturbative Pomeron can also be done using the quasidiffractive channels of type

$$\gamma\gamma \to M\,M', \qquad \gamma\gamma \to M + X \tag{28}$$

in the semihard region

$$s \gg p_\perp^2 = |t| \gg \mu^2, \quad t = (p_{1\gamma} - p_M)^2, \quad \mu = 0.3\,\mathrm{GeV}. \tag{29}$$

Here M is a vector ($V = \rho^0, \omega, \phi, ...\Psi$), or pseudovector ($P = \pi^0, \eta, \eta'$), or tensor ($T = a_2, f_2, f'$) neutral meson and X is a hadron system with not too large invariant mass $M_X^2 \lesssim |t|$. Such processes are discussed in a number of papers [30, 31, 32]. The same enhancement K-factor as discussed above holds also for these processes which may lead to a large production rate already at LEP2 [33]. These processes certainly deserve further investigations at the linear colliders.

6.3.5 Jet production in hard processes

We turn now to inclusive jet production, without rapidity gaps, at large enough transverse momenta so that the usual perturbative QCD framework applies. Precision phenomenology requires next-to-leading order (NLO) calculations [19],[20]. Jet production studies are well known to complement the deep-inelastic structure function studies (see sec. 4) as they are sensitive to the gluon content of the photon which is poorly constrained the structure function data.

In the following we discuss jet production in a e^+e^- collider at 500 GeV and, for the purpose of the discussion, we consider only bremsstrahlung-bremsstrahlung and beamstrahlung-

beamstrahlung collisions. In the former case, the spectrum eq. (22) is used with the constraints $y < .5$ and $\Theta_{max} = 175$ mrad (no detector inside the shielding mask is assumed). As indicated in Fig. 15.b, the bremsstrahlung process dominates at large transverse momentum: we find that it is an order of magnitude larger than the beamstrahlung induced one at $p_T = 30$ GeV/c. Also to be noted is the high rate of jet production: for an integrated luminosity of 20 fb^{-1} we expect about 100 events/GeV/c at $p_T^{jet} = 55$ GeV/c in the pseudo-rapidity interval $-.5 < \eta < .5$. The rapidity distribution of jets with $p_T > 15$ GeV/c is shown in Fig. 16.a: the bremsstrahlung photons being much harder than the beamstrahlung ones (see Fig. 14) the jet rapidity distribution extends over a much wider domain in the former case. The various components of the cross section are displayed in

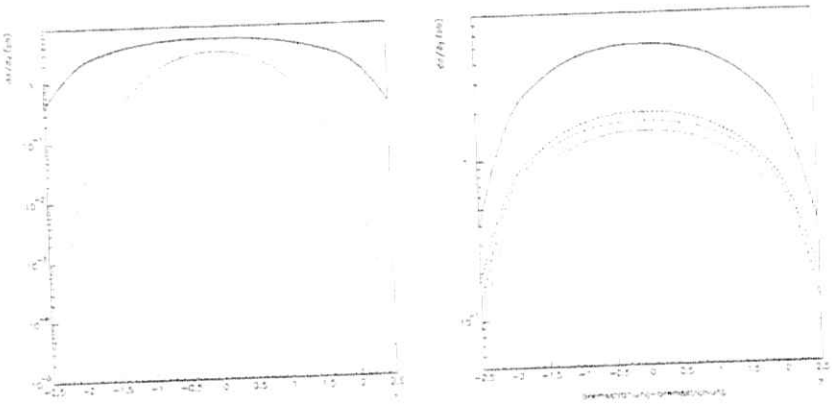

Figure 16: (a) Jet pseudo-rapidity distribution for $p_T > 15$ GeV/c: bremsstrahlung-bremsstrahlung scattering (solid line) and beamstrahlung-beamstrahlung scattering (dashed line). (b) Details of the pseudo-rapidity distribution: full cross section (solid line), direct term (dashed line), one-resolved (dotted line) and two-resolved (dash-dotted line)

Fig. 16.b: all components are rougly similar in size with the "direct" one (both photons couple directly to the hard sub-process) being the largest and the one-resolved one (one photon interacts via its quark or gluon content) being the smallest. Such a hierarchy between the various pieces depend crucially on the shape of the incoming photon spectrum: indeed, in the beamstrahlung process, the double-resolved component becomes considerably suppressed (one order of magnitude smaller) compared to the dominant direct one. This is explained by the rapidly falling parton-parton luminosity for beamstrahlung scattering. In reference to the photon structure let us mention that, even at high energies, the non-perturbative (sometimes called the VDM or hadronic) component plays a non negligible role. For example, for a jet p_T value of 10 GeV/c (corresponding to a hard (scale)$^2 \simeq 100$ GeV^2) one can estimate the VDM component in the photon to still account for about 25% of the cross section: although the non-perturbative component is, a priori, not expected to be so important at large scales, the reason for this is the fact that the

effective x values probed in this process are rather small, and, the smaller the x value is, the larger is the hadronic component (see sec. 4).

All the above is based on leading-order (LO) calculations. The NLO corrections, globally, do not play an important role. For instance studying, at fixed $p_T = 15$ GeV/c and $\eta = 0$, the cross section dependence as a function of the opening "angle" R of the jet we find (all arbitrary scales set equal to p_T), in pb/GeV/c, $d\sigma/dp_T/d\eta = 1.00$, 1.13 and 1.24 for $R = .4$, .7 and 1. respectively to be compared to $d\sigma/dp_T/d\eta = 1.08$ (obviously independent of R) in the LO approximation. From the theoretical point-of-view, the main advantage of the higher-order calculation is a much improved stability of the predictions under changes of the arbitrary scales [19]. On the phenomenological side, it should be known that the smallness of the corrections to the inclusive jet production hides large compensating corrections to the various components as discussed in the LEP2 report [33]. The direct component is decreased (by about 15%) and the double-resolved one is increased by as much as 40% while the one-resolved component remains stable. We conclude that the overall structure of the events is rather affected by the higher-order corrections.

We emphasized above single-jet phenomenology. Using the very recent NLO calculations for di-jet production [20] much precise phenomenology can now be done using this observable. Following HERA studies [34] one could use the di-jet (or the multi-jet) configurations to calculate the fractions x_1, x_2 of parton momenta in the photons from experimental variables and relate directly the shape of the parton distributions to experimental observables [35].

Acknowledgements

This research is supported in part by the EEC program "Human Capital and Mobility", Network "Physics at High Energy Colliders", contract CHRX-CT93-0357 (DG 12 COMA).

References

[1] V. M. Budnev, I. F. Ginzburg, G. V. Meledin and V. G. Serbo: Phys. Rep. 15C (1975) 181
[2] P. Chen: Phys. Rev. D46 (1992) 1186
[3] P. Chen, T. L. Barklow and M. E. Peskin: Phys. Rev. D49 (1994) 3209
[4] D. Schulte, previous section. The parameters used here were the TESLA values in Summer 1995.
[5] I. F. Ginzburg, G. L. Kotkin, V. G. Serbo and V. I. Telnov: Prisma ZHETF 34 (1981) 514; Nucl. Instrum. Methods A205 (1983) 47
[6] I. F. Ginzburg, G. L. Kotkin, S. L. Panfil, V. G. Serbo and V. I. Telnov: Nucl. Instrum. Methods A219 (1984) 5
[7] V. I. Telnov: Nucl. Instrum. Methods A294 (1990) 72

[8] G. A. Schuler and T. Sjöstrand: Nucl. Phys. B407 (1993) 539
[9] G. A. Schuler and T. Sjöstrand: $\gamma\gamma$ and γp events at high energies, CERN-TH.7193/94, presented at the Workshop on Two-Photon Physics, Paris, 1994
[10] R. Engel: Z. Phys. C66 (1995) 203
[11] R. Engel and J. Ranft: Hadronic photon-photon collisions at high energies, ENSLAPP-A-540/95 (hep-ph/9509373)
[12] C. Corsetti, R. M. Godbole and G. Pancheri: see the following section
[13] M. Glück, E. Reya and A. Vogt: Phys. Rev. D46 (1992) 1973
[14] G. A. Schuler and T. Sjöstrand: Low- and high-mass components of the photon distribution functions, CERN-TH/95-62
[15] D. Morgan, M. R. Pennington and M. R. Whalley: J. Phys. G 20 (1994) A1
[16] TOPAZ Collab.: H. Hayashii et al.: Phys. Lett. B314 (1993) 149
[17] AMY Collab.: B. J. Kim et al.: Phys. Lett. B325 (1994) 248
[18] M. Drees and R.M. Godbole, J. Phys. G21 (1995) 1559
[19] P. Aurenche, J. P. Guillet, M. Fontannaz, Y. Shimizu and K. Kato: Prog. Theor. Phys. 92 (1994) 175
[20] T. Kleinwort and G. Kramer: Inclusive one and two-jet cross sections in $\gamma\gamma$-processes at e^+e^- colliders, DESY 96-035
[21] M. Drees and R. M. Godbole: Z. Phys. C59 (1993) 591
[22] R. Brinkmann: SBLC and TESLA general design overview, Presentation at the Linear Collider workshop, Gran Sasso, Italy, 1995
[23] L.N. Lipatov in "*Perturbative QCD*" A.H. Mueller ed., World Scientific 1989, and references therein
[24] A.H. Mueller and H. Navelet: Nucl. Phys. B282 (1987) 727
[25] V. Del Duca and C.R. Schmidt: Phys. Rev. D49 (1994) 4510;
W.J. Stirling: Nucl. Phys. B423 (1994) 56
[26] J.D. Bjorken: Phys. Rev. D47 (1992) 101
[27] A.H. Mueller and W.-K. Tang: Phys. Lett. B284 (1992) 123
[28] V. Del Duca and W.-K. Tang: Phys. Lett. B312 (1993) 225;
Proceedings of the 5th Blois Workshop on Elastic and Diffractive Scattering (1993), ed. H.M. Fried et al., World Scientific 1994
[29] S. Abachi et al. (D0 Collaboration): Phys. Rev. Lett. 72 (1994) 2332;
F. Abe et al. (CDF Collaboration): Phys. Rev. Lett. 74 (1995) 855
[30] V.L. Chernyak and A.R. Zhitnitsky, Nucl. Phys. **B222** (1983) 382; Phys. Rep. **112** (1984) 173; I.F. Ginzburg, D.Yu. Ivanov, V.G. Serbo, Sov.Yad.Fiz. **56** (1993) 45
[31] I.F. Ginzburg, S.L. Panfil, V.G. Serbo, Nucl.Phys. **B284** (1987) 685; I.F. Ginzburg, D.Yu. Ivanov, Nucl. Phys. B (Suppl.) **25B** (1992) 224; Nucl.Phys. **B388** (1992) 376
[32] J.R.Forshaw and M.G.Ryskin, Z.Phys. **C68** (1995) 137
[33] $\gamma\gamma$ physics, P. Aurenche and G.A. Schuler convenors, in CERN Yellow report, CERN 96-01
[34] T. Ahmed, H1 collaboration, Nucl. Phys. **B445** (1995) 195;
M. Derrick, ZEUS collaboration, Phys. Lett. **B348** (1995) 665
[35] $\gamma\gamma$ generators, L. Lönnblad and M. Seymour convenors, in CERN Yellow report, CERN 96-01

7 Eikonalized mini-jet cross-Sections

A. Corsetti[1], R.M. Godbole[2], G. Pancheri[3]

[1] *INFN, Univ. La Sapienza, Roma, Italy* [2] *CTS, IIS, Bangalore, India*
[3] *INFN, Frascati, Italy*

In this note we wish to assess the validity and uncertainties of the eikonalized mini-jet model in predicting σ_{tot}^{incl} and further to ascertain whether measurements at LEP-200 and HERA can constrain various parameters of the model. In its simplest formulation, the eikonalized mini-jet cross-section is given by

$$\sigma_{ab}^{incl} = P_{ab}^{had} \int d^2\vec{b}[1 - e^{-n(b,s)}] \tag{30}$$

where the average number of collisions at a given impact parameter $\vec{b}$ is obtained from

$$n(b,s) = A_{ab}(b)(\sigma_{ab}^{soft} + \frac{1}{P_{ab}^{had}}\sigma_{ab}^{jet}) \tag{31}$$

with $A_{ab}(b)$ the normalized transverse overlap of the partons in the two projectiles and P_{ab}^{had} to give the probability that both colliding particles a, b be in a hadronic state. σ_{ab}^{soft} is the non-perturbative part of the cross-section from which the factor of P_{ab}^{had} has already been factored out and σ_{ab}^{jet} is the hard part of the cross-section. The rise in σ_{ab}^{jet} drives the rise of σ_{ab}^{incl} with energy [1]. We have also assumed the factorization property

$$P_{\gamma p}^{had} = P_{\gamma}^{had}; \quad P_{\gamma\gamma}^{had} = (P_{\gamma}^{had})^2.$$

The predictions of the eikonalised mini-jet model [2] for photon induced processes [3] depend on 1) the assumption of one or more eikonals, 2) the hard jet cross-section $\sigma_{ab}^{jet} = \int_{p_{tmin}} \frac{d^2\sigma}{dp_t^2} dp_t^2$ which in turn depends on the minimum p_t above which one can expect perturbative QCD to hold, viz. p_{tmin}, and the parton densities in the colliding particles a and b, 3) the soft cross-section σ_{ab}^{soft}, 4) the overlap function $A_{ab}(b)$, defined as

$$A_{ab}(b) = \frac{1}{(2\pi)^2} \int d^2\vec{q}\mathcal{F}_a(q)\mathcal{F}_b(q)e^{i\vec{q}\vec{b}} \tag{32}$$

where $\mathcal{F}$ is the Fourier transform of the b-distribution of partons in the colliding particles and 5) last but not the least P_{ab}^{had}.

In this note we shall restrict ourselves to a single eikonal. The hard jet cross-sections have been evaluated in LO perturbative QCD. The dependence of σ_{ab}^{jet} on p_{tmin} is strongly correlated with the parton densities used. Here we show the results using GRV densities [4] (see ref. [5] for the results using the DG densities [6]). For the purposes of this note, we determine $\sigma_{\gamma\gamma}^{soft}$ from $\sigma_{\gamma p}^{soft}$ which is obtained by a fit to the photoproduction data. We use the Quark Parton Model suggestion $\sigma_{\gamma\gamma}^{soft} = \frac{2}{3}\sigma_{\gamma p}^{soft}$.

In the original use of the eikonal model, the overlap function $A_{ab}(b)$ of eq. (32) is obtained using for $\mathcal{F}$ the electromagnetic form factors and thus, for photons, a number of authors [7, 8] have assumed for $\mathcal{F}$ the pole expression used for the pion electromagnetic form factor, on the basis of Vector Meson Dominance (VMD). We shall investigate here another possibility, i.e. that the b-space distribution of partons in the photon is the Fourier transform of their intrinsic transverse momentum distributions. This will correspond to use the functional expression expected for the perturbative part [9]

$$\frac{dN}{dk_t^2} = \frac{1}{k_t^2 + k_o^2} \tag{33}$$

Recently this expression was confirmed by the ZEUS [10] Collaboration, with $k_o = 0.66 \pm 0.22$ GeV. For $\gamma\gamma$ collisions, the overlap function is now simply given by

$$A(b) = \frac{1}{4\pi} k_o^2 b K_1(bk_o) \tag{34}$$

with K_1 the Bessel function of the third kind. It is interesting to notice that for photon-photon collisions the overlap function will have the same analytic expression for both our ansätze: the VMD inspired pion form factor or the intrinsic transverse momentum; the only difference being that the former corresponds to a fixed value of $k_0 = 0.735$ GeV whereas the latter allows us to vary the value of the parameter k_0. Thus both possibilities can be easily studied by simply changing k_0 appropriately. Notice that the region most important to this calculation is for large values of the parameter b, where the overlap function changes trend, and is larger for smaller k_o values.

As for P_{γ}^{had}, this is clearly expected to be $\mathcal{O}(\alpha_{em})$ and from VMD one would expect 1/250. From phenomenological considerations [8]and fits to HERA data, one finds a value 1/200, which indicates at these energies a non-VMD component of $\approx$ 20%. It should be noticed that the eikonalised minijet cross-sections do not depend on $A_{\gamma p}$ and $P_{\gamma\gamma}^{had}$ separately, but depend only on the ratio of the two [11, 12].

Having thus established the range of variability of the quantities involved in the calculation of total photonic cross sections, we now proceed to calculate and compare with existing data the eikonalized minijet cross-section for $\gamma\gamma$ collisions. We use GRV (LO) densities and values of p_{tmin} deduced from a best fit to photoproduction. As discussed in [15], it is possible to include the high energy points in photoproduction using GRV densities and $p_{tmin} = 2$ GeV, but the low energy region would be better described by a smaller p_{tmin}. This is the region where the rise, according to some authors, notably within the framework of the Dual Parton Model, is attributed to the so-called *soft Pomeron*. For our studies here we use $p_{tmin} = 2$. GeV. We also use $P_{\gamma}^{had} = 1/204$ and A(b) from eq.(34) with different values of k_0. One choice for k_0 is the pole parameter value in the photon b-distribution expression, which includes both the intrinsic transverse momentum option 0.66 ± 0.22 GeV as well as the pion form factor value, 0.735 GeV. The other value, 1 GeV, is a possible choice which appears to fit the present data better than everything else. Our predictions are shown in Fig.(17). A comparison with existing $\gamma\gamma$ data shows that all of our choices are compatible with the data within the present experimental errors. At high energies, however, like the ones reachable with the proposed linear photon colliders, these

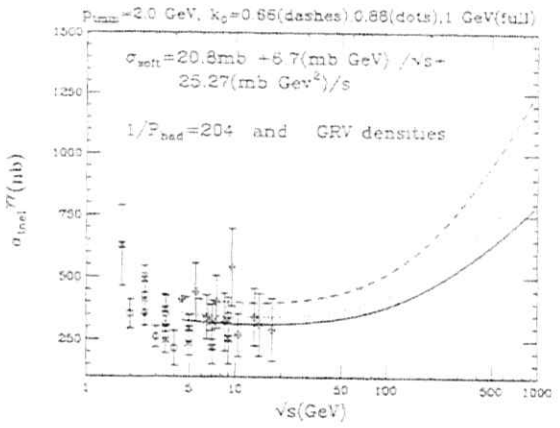

Figure 17: Total inelastic photon-photon cross-section for $p_{t_{min}} = 2.$ GeV and different parton b-distribution in the photon. The solid line corresponds to $k_0 = 1.$ GeV.

predictions vary by about ±25%. Reducing the error in the LEP1 region and adding new data points in the c.m. region attainable at LEP2, can help pinpoint and restrict the choices. Were the LEP1 and LEP2 data to confirm the present values, we believe that the best representation of the present data is obtained with the higher k_0 value.

Acknowledgements

R.M.G. wishes to acknowledge support from C.S.I.R. (India) under grant no. 03(0745)/94/EMR-II. This research is supported in part by the EEC program "Human Capital and Mobility", contract CT92-0026 (DG 12 COMA).

References

[1] D.Cline et al., Phys. Rev. Lett. **31** (1973) 491, T.Gaisser and F.Halzen, Phys. Rev. Lett. **54** (1985) 1754, G.Pancheri and Y.N.Srivastava, Phys. Lett. **B182** (1985).

[2] A. Capella and J. Tran Thanh Van, Z. Phys. **C23** (1984)168, P. l'Heureux, B. Margolis and P. Valin, Phys. Rev. D **32** (1985) 1681, L. Durand and H. Pi, Phys. Rev. Lett. **58** (1987) 58.

[3] J.C. Collins and G.A. Ladinsky, Phys. Rev. D **43** (1991) 2847.

[4] M. Glück, E. Reya and A. Vogt, Phys. Rev. D **46** (1992) 1973.

[5] M. Drees and R.M. Godbole, Z. Phys. **C 59** (1993) 591.

[6] M. Drees and K. Grassie, Z. Phys. **C28** (1985) 451.

[7] K. Honjo et al., Phys. Rev. D 48 (1993) 1048.

[8] R.S. Fletcher, T.K. Gaisser and F.Halzen, Phys. Rev. D 45 (1992) 377; erratum Phys. Rev. **D 45** (1992) 3279.

[9] J. Field, E. Pietarinen and K. Kajantie, Nucl. Phys. B 171 (1980) 377; M. Drees, *In the proceedings of the 23rd International Symposium on Multiparticle Dynamics, Aspen, Colo., Sep. 1993. Eds. M.M. Block and A.R. White.*

[10] M. Derrick et al., ZEUS Collaboration , Phys. Lett. **B 354** (1995) 163.

[11] M. Drees, Univ. Wisconsin report MADPH-95-867, *proceedings of the 4th workshop on TRISTAN physics at High Luminosities*, KEK, Tsukuba, Japan, Nov. 1994.

[12] M. Drees and R.M. Godbole, Journal Phys. G., **G 21** (1995) 1559.

[13] H. Abramowicz, K. Charchula and A. Levy, Phys. Lett. **B 269** (1991) 458.

[14] K. Hagiwara, M. Tanaka, I. Watanabe and T. Izubuchi, Phys. Rev. **D51** (1995) 3197.

[15] C. Corsetti, R.M. Godbole and G. Pancheri, in preparation.

8 Heavy flavor production

M. Cacciari[1], R.M. Godbole[2], M. Greco[3], M. Krämer[1], E. Laenen[4], S. Riemersma[5]

[1] *DESY, Hamburg, Germany*
[2] *CTS, IISc, Bangalore, India*
[3] *Roma III and LNF, Italy*
[4] *CERN, Geneva, Switzerland*
[5] *DESY, Zeuthen, Germany*

The production of heavy flavours in two-photon collisions provides an important tool to study the dynamics of perturbative QCD. The mass of the heavy quark, $m_Q \gg \Lambda_{QCD}$, sets the hard scale for the perturbative analysis and ensures that the separation into direct and resolved processes is unambiguous through next-to-leading order (NLO). Hence production via the direct channel is directly calculable in perturbative QCD (pQCD) and in principle the best way for confronting the pQCD prediction with experiment. Resolved processes, on the other hand, provide a good opportunity to measure the poorly known gluon content of the photon. Experimentally one may separate direct and resolved channels by analyzing deep-inelastic $e\gamma$ scattering, by using non-diffractively produced J/ψ's, or by detecting the photon remnant jet, present in the resolved processes only.

Charm quark production in two-photon collisions has been analysed at the e^+e^- colliders PETRA, PEP, TRISTAN and LEP. The experimental status and prospects for LEP2 have been reviewed in Ref. [1]. The high-statistics data to be expected at the NLC will allow for a detailed comparison of the pQCD predictions with experimental results not only for production rates, but also for various differential distributions. These analyses will yield information on the dynamics of heavy flavour production in a kinematical range very different from that available in $\gamma\gamma$ collisions at present colliders.

In the following we will discuss the theoretical predictions for open heavy flavour production in two-photon collisions and in deep-inelastic $e\gamma$ scattering and briefly mention $\gamma\gamma$ production of quarkonia.

8.1 Heavy flavour production in $\gamma\gamma$ collisions

Three mechanisms contribute to the production of heavy quarks in $\gamma\gamma$ collisions. (i) In the case of direct production, the photons couple directly to the heavy quarks. No spectator particles travel along the γ axes. (ii) If one of the photons first splits into a flux of light quarks and gluons, one of the gluons may fuse with the second photon to form the $Q\overline{Q}$ pair. The remaining light quarks and gluons build up a spectator jet in the split γ direction (single resolved γ contribution). (iii) If both photons split into quarks and gluons, the $Q\overline{Q}$ pair is accompanied by two spectator jets (double resolved γ contribution). It turns out *a posteriori* that the double resolved γ contribution is much smaller than the direct and the single resolved γ contributions.

Total cross sections and various distributions for charm and bottom quark production $e^+e^- \to e^+e^-c/b X$ have been calculated in Ref. [2] including QCD radiative corrections for

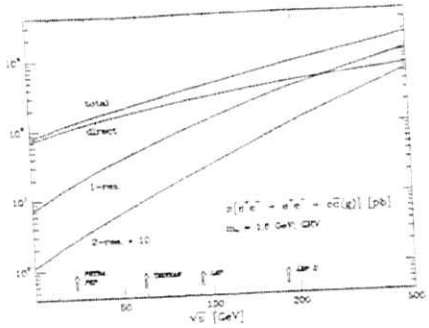

Figure 18: Total cross sections for $e^+e^- \to e^+e^- + c\bar{c}X$ as functions of the e^-e^- collider energy. Parameters as described in Ref. [2].

the leading subprocesses. The energy dependence of the total charm cross section is shown in Fig.18. At low energies in the PETRA/PEP/TRISTAN range, the direct production mechanism is completely dominant, however at LEP2 and higher energies $\gamma\gamma$ production of charm quarks receives contributions in about equal amounts from the direct and single resolved channels. A measurement of the gluon content of the photon, which is currently poorly known, might thus be feasible at LEP2 and the NLC. The agreement between the next-to-leading order predictions [2] and the recent data from PETRA, PEP, TRISTAN and LEP is quite satisfactory [1], even though the experimental errors (statistical and systematic) are large.

At the NLC the higher cms energy and large luminosity will lead to fairly copious production of heavy quark pairs in two-photon collisions [3, 4]. In Table 3 we list the total cross sections $e^-e^- \to e^-e^-c\bar{c}X$ at $\sqrt{s} = 500$ GeV for various input parameters at next-to-leading order accuracy. To compute α_s, we used the two loop expression with $\Lambda^{(5)}_{\overline{\rm MS}} = 0.215$ GeV and $n_{lf} = 3$ active flavours. The open $c\bar{c}$ threshold energy is set to 3.8 GeV, and the GRV parametrization [5] has been adopted for the quark and gluon densities of the photon. We used the Weizsäcker-Williams density of [6] with an anti-tag angle $\theta_{\rm max}$ of 175 mrad. Beamstrahlung is expected to play an important rôle at a future linear collider, so we include its effect here by adopting for its spectrum the expression given in [7], with parameters $\Upsilon_{\rm eff} = 0.039$ and $\sigma_z = 0.5$ mm [8] corresponding to the TESLA design. We will as default coherently superimpose the Weizsäcker-Williams density and the beamstrahlung density, in order to incorporate the case where one photon is of beam- and the other of bremsstrahlung origin.

The cross sections for charmed particle production are very large, giving a total of $\sim 10^8$ events for an integrated luminosity of $\int\mathcal{L} = 20\,{\rm fb}^{-1}$. Beamstrahlung effects are quite important and increase the cross section significantly, by about a factor five. Other beamstrahlung spectra do not change the total rate too much, e.g. by a factor 1.7 for the JCL spectrum. The production of b quarks is suppressed by factor of ~ 200 as compared to charm, a consequence of the smaller bottom electric charge and the phase

space reduction by the large b mass. From the numbers collected in Table 3 we can conclude that the predictions of the cross sections appear to be theoretically firm. A variation of the charm quark mass m_c and the renormalization/factorization scale μ in the range 1.3 GeV $< \mu < 2\,m_c$ and 1.3 GeV $< m_c <$ 1.7 GeV leads to a total theoretical uncertainty of about $\pm$ 30 %. In order to extract the charm signal it might be necessary to impose stringent cuts. Requiring one of the heavy quarks to have rapidity $|y| \leq 1.7$ and transverse momentum $p_\perp \geq 5$ GeV reduces the charm quark cross section by about a factor of 50 and the b cross section by about a factor three. If one demands the event to contain at least one muon with rapidity $|y| \leq 2$ and $p_\perp(\mu) \geq 5$ GeV for charm tagging, the total $c\bar{c}$ cross section is reduced by at least a factor of 2000 [3]. The muon tagging also reduces the contribution from resolved processes to the signal and hence the sensitivity to the gluon content of the photon. For further details we refer to Ref. [1] where the experimental methods for charm tagging in $\gamma\gamma$ collisions have been reviewed.

Given the large statistics at the NLC it will become possible to measure both heavy quarks and analyse their correlations. The study of these correlations has been performed in Ref. [9] and constitutes a more comprehensive test of the theory. To eliminate the uncertainties related to the parton densities in the photon, the authors of Ref. [9] have concentrated on the direct channel, which is in principle the best channel for confronting the pQCD prediction with experiment. A complete analysis including resolved contributions is in preparation [10]. As an example, we show in Fig. 19 the ΔR distribution, defined by $\Delta R = \sqrt{(\Delta\phi)^2 + (\Delta\eta)^2}$, at LO and NLO for both LEP2 and the NLC in the direct channel. Here $\Delta\phi$ is the azimuthal angle between the charm and anticharm in the

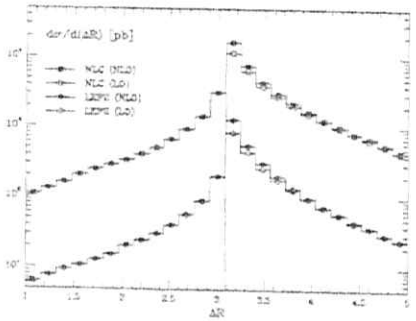

Figure 19: ΔR distribution for charm and anti-charm quark at LEP2 and NLC.

plane transverse to the beam axis and $\Delta\eta$ is the pseudo-rapidity difference of the two heavy quarks. At LO $\Delta R > \pi$, but at NLO ΔR may also assume values below that. It has been demonstrated in Ref. [9] that NLO corrections significantly modify the shapes and normalizations of various distributions and correlations.

In next-to-leading order potentially large terms $\sim \alpha_s \ln(p_\perp/m_Q)$ arise from collinear emission of gluons by a heavy quark at large transverse momentum or from almost collinear branching of gluons or photons into heavy quark pairs. These terms are not

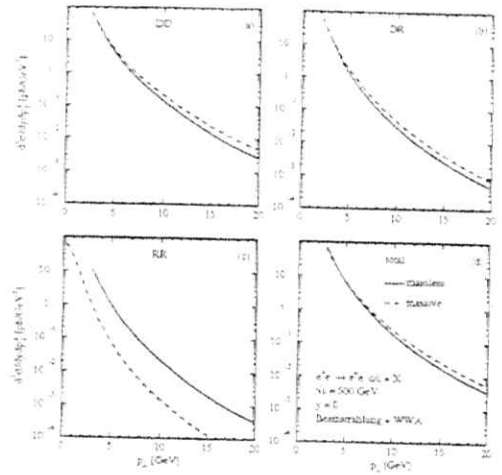

Figure 20: Inclusive cross section $d^2\sigma/dy\,dp_\perp^2$ for $\gamma\gamma$ production of charm quarks as a function of $p_\perp$ for rapidity $y = 0$ in the massless (solid lines) and massive (dashed lines) schemes: (a) direct (DD), (b) single-resolved (DR), (c) double-resolved (RR), and (d) total sum.

expected to affect the total production rates, but they might spoil the convergence of the perturbation series at $p_\perp \gg m_Q$. An alternative way for making predictions at large $p_\perp$ is to treat the heavy quarks as massless partons. The mass singularities of the form $\ln(p_\perp/m_Q)$ are then absorbed into structure and fragmentation functions in the same way as for the light u, d, s quarks. In Ref. [11] the NLO cross section for large $p_\perp$ production of heavy quarks in direct and resolved channels has been calculated in the framework of perturbative fragmentation functions (PFF's) [12]. In Fig. 20 we show the direct (DD), single-resolved (DR) and double resolved (RR) contributions to the differential cross section $d^2\sigma/dy\,dp_\perp^2$ as a function of $p_\perp$ for rapidity $y = 0$ and their sum, respectively, both in fixed-order perturbation theory ("massive") and in the PFF approach ("massless"). The two approaches differ in the definitions and relative contributions of the direct and resolved terms, but essentially agree in their sum. The resummation of the $\alpha_s \ln(p_\perp^2/m^2)$ terms in the PFF approach leads to a softer $p_\perp$ distribution and to a reduced sensitivity to the choice of the renormalization and factorization scales [11]. Similar results have also been obtained in the context of photon-proton collisions in [13].

8.2 Heavy flavour production in deep-inelastic $e\gamma$ scattering

The production of heavy quarks via deep-inelastic $e\gamma$ scattering, i.e. the reaction

$$e^-(p_e) + e^- \to e^-(p_e') + e^- + Q(p_1) + X\,, \tag{35}$$

(here we assume the electron to be tagged) proceeds via the subprocess $\gamma^*(q) + \gamma(k) \to Q(p_1) - X$, where one of the photons is highly virtual and the other one is almost on-mass-shell and transversely polarized. $Q(p_1)$ is a heavy quark with momentum p_1 and X denotes any hadronic state allowed by quantum-number conservation. The cross section of this process can be expressed in terms of structure functions:

$$\frac{d^2\sigma}{dx dQ^2} = \int dz\, f_\gamma^e(z, \frac{S}{m_e^2}) \frac{2\pi\alpha^2}{x Q^4} \left[(1 - (1-y)^2) F_2^\gamma(x, Q^2, m^2) - y^2 F_L^\gamma(x, Q^2, m^2) \right] . \quad (36)$$

Here m is the heavy quark mass, z the momentum fraction of the target photon with respect to its parent lepton, $Q^2 = -q^2 = -(p_e - p_e')^2$, $x = Q^2/2k \cdot q$ and $y = k \cdot q / k \cdot p_e$, α is the fine structure constant and f_γ^e is either the equivalent photon density in the Weizsäcker-Williams (WW) approximation or a beamstrahlung photon density. The $F_k^\gamma(x, Q^2, m^2)$, $k = 2, L$ are the deep-inelastic structure functions for this process. These structure functions receive contributions from both hadronic and pointlike photons, i.e. $F_k^\gamma(m^2) = F_k^{\gamma,PL}(m^2) - F_k^{\gamma,HAD}(m^2)$, $k = 2, L$. Both components were calculated to NLO in QCD in Ref. [14]. Note that the presence of the heavy quark mass ensures that this separation is, through next-to-leading order, unambiguous. It was demonstrated in Ref. [14] (see also [15]) that both components separate naturally in x, as can be seen in Fig. 21: at this high value of Q^2 for $x < 0.01$ the hadronic component dominates, and for $x > 0.1$ the pointlike one. The former is mainly sensitive to the gluon density in the photon, whereas the latter is calculable in perturbative QCD, its only uncertainties stemming from α_s and the charm quark mass.

The high energy and large luminosity of the NLC will lead to a large sample of the single-tag two-photon events containing heavy quarks (mainly charm), making a study of the reaction (35) and its just outlined characteristics very worthwhile.

In Table 4 we give estimates for event rates both for charm and bottom production at the NLC. We show separately the number of events due to beamstrahlung (we again used the TESLA spectrum) and Weizsäcker-Williams bremsstrahlung (we used the expression in Ref. [6] with an "optimistic" anti-tag angle of $\theta_{max} = 40$ mrad) contributions. The numbers are based on the NLO calculation. See Ref. [15] for the parameter choices that went into producing this table and the next. We have summed the contributions due to pointlike and hadronic photons for each entry. For the largest two x bins the contribution of the hadronic component is below 10%, whereas in the two smallest x-bins it is more than 90%. Note that the number of charmed events is truly large, even at large Q^2. The number of events containing bottom quarks is again much smaller due to charge (factor 16) and phase space suppression.

To test the sensitivity to the gluon density, we give in Table 5 the production rate in a small x bin for various choices of parton densities, charm quark mass values and mass factorization scales. Examining the composition of these results, one finds very little contribution due to the hadronic channel from beamstrahlung photons (about 1-2%). Further one finds that the contributions due to pointlike photons both of WW and beamstrahlung origin is similarly small. The numbers therefore indicate that there is a good possibility of measuring the gluon density in the photon using charm quarks at the

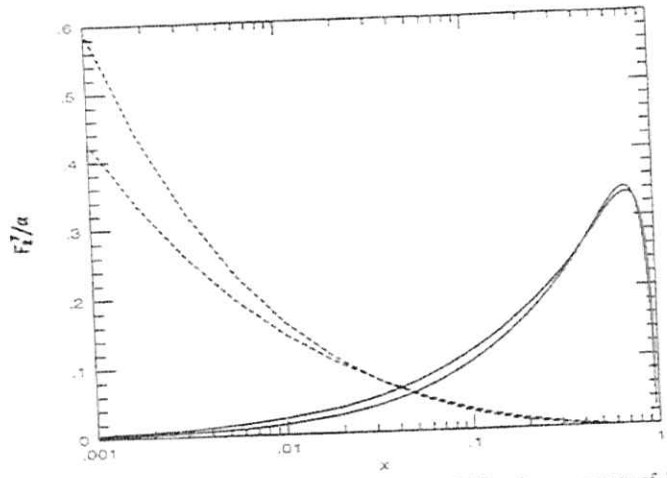

Figure 21: Hadronic (dashed lines) and pointlike (solid lines) components of F_2^γ/α vs. x at $Q^2 = 200\,(GeV/c)^2$. The lower solid line is the leading order (LO), the upper one the next-to-leading order case. The lower dashed line at $x = 0.001$ is the NLO order, the upper one the LO case.

NLC, low charm acceptance notwithstanding. The most significant uncertainty is related to the charm quark mass, however a differentiation of the gluon densities of GRV [5] and ACFGP [16] seems certainly feasible at the NLC.

Bottom quark production is so much more suppressed that a measurement of the photonic gluon density from bottom production in $e\gamma$ scattering at the NLC seems impossible.

For more details and for charm quark kinematic distributions, see Ref. [15].

8.3 Quarkonia production in $\gamma\gamma$ collisions

The radiative decay width of the charmonium states η_c, χ_{c0} and χ_{c2} can directly be measured in two-photon collisions at the NLC. These $\gamma\gamma$ partial widths provide an important test of the non-relativistic quarkonium model (see e.g. Ref. [17] for theoretical details). Accurate analyses of the charmonium states can already be expected at LEP2 [1], while there is little prospect of studying $\gamma\gamma$ production of bottomonium states.

Two-photon production of J/ψ bound states is an attractive tool to determine the gluon distribution in the photon [18]. In contrast to the case of open heavy flavour production, J/ψ mesons are generated predominantly via resolved photons and can be tagged in the leptonic decay modes. The cross section for inelastic J/ψ production in $\gamma\gamma$ collisions at a 500 GeV NLC via the leading colour-singlet channel is predicted to be

~ 50 pb, including NLO corrections [19] and using a coherent superposition of WW and beamstrahlung photons (TESLA design). The cross section appears to be quite sensitive to the parametrization of the gluon density in the photon [20], but clearly more detailed studies including realistic cuts are needed. So-called colour-octet processes, in which the heavy-quark antiquark pair is produced at short distances in a colour-octet state and subsequently evolves non-perturbatively into a physical J/ψ, should contribute to the cross section at some level [21]. The importance of such processes towards a successful description of heavy quarkonia production at the Fermilab Tevatron has recently been investigated in a series of papers [22]. However, their phenomenological significance for J/ψ production has so far not been conclusively established (see Refs. [23] for analyses of colour-octet contributions to J/ψ photoproduction). A measurement of inelastic J/ψ production in $\gamma\gamma$ collisions at the NLC will not only provide information on the gluon distribution of the photon but appears to be a clean test for the underlying picture of quarkonium production as developed so far in the perturbative QCD sector.

Acknowledgements

R.M.G. wishes to acknowledge support from C.S.I.R. (India) under grant no. 03(0745)/94/EMR-II.

References

[1] P. Aurenche et al., $\gamma\gamma$ *Physics*, in: Proceedings of the Workshop *Physics with LEP2*, CERN Yellow report, CERN 96-01, G. Altarelli, T. Sjöstrand, F. Zwirner eds.

[2] M. Drees, M. Krämer, J. Zunft and P.M. Zerwas, Phys. Lett. **B306** (1993) 371.

[3] M. Drees and R.M. Godbole, in: Proceedings of the *Workshop on Physics and Experiments with Linear e^+e^- Colliders*, Waikaloa, Hawaii, April 1993, eds. F.A. Harris et al.

[4] O.J.P. Eboli, M.C. Gonzalez-Garcia, F. Halzen and S.F. Novaes, Phys. Rev. **D47** (1993) 1889

[5] M. Glück, E. Reya and A. Vogt, Phys. Rev. **D46** (1992) 1973.

[6] S. Frixione, M. Mangano, P. Nason and G. Ridolfi, Phys. Lett. **B319** (1993) 339.

[7] P. Chen, T. Barklow and M.E. Peskin, Phys. Rev. **D49** (1994) 3209.

[8] D. Schulte, private communication.

[9] M. Krämer and E. Laenen, CERN preprint CERN-TH/95-291 (hep-ph/9511358), to be published in Phys. Lett. B.

[10] B. Harris, M. Krämer and E. Laenen, in preparation.

[11] M. Cacciari, M. Greco, B. Kniehl, M. Krämer, G. Kramer and M. Spira, DESY preprint DESY 95-205 (hep-ph/9512246), to be published in Nucl. Phys. B.

[12] B. Mele and P. Nason, Nucl. Phys. **B361** (1991) 626; M. Cacciari and M. Greco, Nucl. Phys. **B421** (1994) 530.

[13] M. Cacciari and M. Greco, Z. Phys. **C69** (1996) 459; B. Kniehl, M. Krämer, G. Kramer and M. Spira, Phys. Lett. **B356** (1995) 539.

[14] E. Laenen, S. Riemersma, J. Smith and W.L. van Neerven, Phys. Rev. **D49** (1994) 5753.

[15] E. Laenen and S. Riemersma, preprint CERN-TH/95-324, DESY 95-240 (hep-ph/9602258), to be published in Phys. Lett. B.

[16] P. Aurenche, P. Chiapetta, M. Fontannaz, J.P. Guillet and E. Pilon, Z. Phys. **C56** (1992) 589; P. Aurenche, J.P. Guillet and M. Fontannaz, Z. Phys. **C64** (1994) 621.

[17] G.A. Schuler, CERN preprint CERN-TH.7170/94 (hep-ph/9403387), to be published in Phys. Rep.

[18] M. Drees and R.M. Godbole, Nucl. Phys. **B339** (1990) 355 and Z. Phys. **C59** (1993) 591.

[19] M. Krämer, J. Zunft, J. Steegborn and P.M. Zerwas, Phys. Lett. **B348** (1995) 657; M. Krämer, Nucl. Phys. **B459** (1996) 3.

[20] M. Drees and R.M. Godbole, J. Phys. G. Nucl. Part. Phys. **21** (1995) 1559.

[21] G.T. Bodwin, E. Braaten and G.P. Lepage, Phys. Rev. **D51** (1995) 1125.

[22] M. Cacciari and M. Greco, Phys. Rev. Lett. 73 (1994) 1586; E. Braaten, M.A. Doncheski, S. Fleming and M.L. Mangano, Phys. Lett. **B333** (1994) 548; D.P. Roy and K. Sridhar, Phys. Lett. **B339** (1994) 141; E. Braaten and S. Fleming, Phys. Rev. Lett. 74 (1995) 3327; M. Cacciari, M. Greco, M.L. Mangano and A. Petrelli, Phys. Lett. **B356** (1995) 560; P. Cho and A.K. Leibovich, Phys. Rev. **D53** (1996) 150 and CALT-68-2026 (hep-ph/9511315).

[23] M. Cacciari and M. Krämer, DESY preprint DESY 96-005 (hep-ph/9601276); J. Amundson, S. Fleming and I. Maksymyk, MADPH-95-914 (hep-ph/9601298); P. Ko, J. Lee and H.S. Song, SNUTP-95-116 (hep-ph/9602223).

σ [nb]	$m_c = 1.3$ GeV $\mu = m_c$	$m_c = 1.5$ GeV $\mu = \sqrt{2}\, m_c$	$m_c = 1.7$ GeV $\mu = 2m_c$
direct	6.88	5.68	4.78
1-res	6.69	3.72	2.92
2-res	0.21	0.12	0.07
total	13.8	9.52	7.77

Table 3: Total cross sections for $e^-e^- \to e^-e^- + c\bar{c}X$ at $\sqrt{s} = 500$ GeV. Input parameters as described in the text.

Q^2	x	Events			
range	range	c(WW)	b(WW)	c(Beam)	b(Beam)
100 - 320	$1.0 - 3.2 \cdot 10^{-2}$	1040	80	0	0
	$3.2 - 10.0 \cdot 10^{-3}$	3790	300	220	20
	$1.0 - 3.2 \cdot 10^{-2}$	6230	430	3150	200
	$3.2 - 10.0 \cdot 10^{-2}$	10,300	510	12,200	580
	$1.0 - 3.2 \cdot 10^{-1}$	21,700	830	34,700	1320
	$3.2 - 10.0 \cdot 10^{-1}$	43,300	730	73,800	1240
320 - 1000	$1.0 - 3.2 \cdot 10^{-2}$	1050	110	70	10
	$3.2 - 10.0 \cdot 10^{-2}$	2310	160	1230	80
	$1.0 - 3.2 \cdot 10^{-1}$	5610	260	6790	310
	$3.2 - 10.0 \cdot 10^{-1}$	13,300	400	21,200	620

Table 4: Event rates of $e\gamma$ collisions producing charm and bottom quarks at the NLC with a luminosity of 20 fb^{-1} and $\sqrt{S} = 500$ GeV.

Charm Mass	Q^2 range	x range	Events $\mu_f = Q/2$	$\mu_f = Q$	$\mu_f = 2Q$
1.3	32 - 100	$1.0 - 3.2 \cdot 10^{-3}$	2080	2140	2230
1.5			1880	1890	1930
1.7			1740	1750	1790
1.3	100 - 320	$1.0 - 3.2 \cdot 10^{-3}$	346	356	370
1.5			987	1024	1058
1.7			907	930	954
1.3	32 - 100	$1.0 - 3.2 \cdot 10^{-3}$	3770	4080	4500
1.5			3490	3740	4090
1.7			3240	3480	3810
1.3	100 - 320	$1.0 - 3.2 \cdot 10^{-3}$	478	509	561
1.5			774	854	943
1.7			716	777	847

Table 5: Event rates at small x at the NLC with a luminosity of 20 fb^{-1} and $\sqrt{S} = 500$ GeV. We used GRV [5] parton distributions in the $\overline{MS}$ scheme for the top half and ACFGP [16] for the bottom.

9 Gauge bosons production in polarized $\gamma\gamma$ collisions

M. Baillargeon[1], G. Bélanger[2], F. Boudjema[2], G. Jikia[3]

[1] *GTAE, Lisbon, Portugal* [2] *ENSLAPP-Annecy, France*
[3] *IHEP, Protvino, Russia*

A high-energy $\gamma\gamma$ collider, such as the one that can be obtained from backscattered laser beams could be a useful tool for probing the symmetry breaking mechanism which stands as one of the last open problem in the standard model. In models with a light Higgs particle, one unique opportunity for $\gamma\gamma$ colliders relates to the production of the Higgs on resonance and its ability to perform a direct measurement of the $H\gamma\gamma$ coupling[1,2]. Without the discovery of a Higgs at LEP2, LHC or the linear collider, the best alternative to study the symmetry breaking sector lies in the study of the self-couplings of the W. The large cross sections for processes involving W's give $\gamma\gamma$ colliders an advantage in probing the self couplings. These include either quartic couplings, probed in processes with W pair fusion or trilinear couplings. The former, which can also be sensitive to the presence of a heavy resonance is especially relevant for colliders with an energy above 1 TeV [3] while the latter can already be measured at more modest energies.

Here we report on the results of two analyses concerning anomalous trilinear couplings. The first which concerns $WW\gamma$ couplings in W pair production, extends previous studies in that it includes all 4 fermions final states. The information from the reconstructed density matrix allows an improvement over previous results and shows a sensitivity to anomalous couplings which could further constrain the region probed in $e^+e^- \to W^+W^-$[4]. A second analysis deals with probing the WWZ vertex through $\gamma\gamma \to WWZ$ production[5]. Only for a particular operator, that also induces parity violation, is the level of sensitivity comparable to what can be achieved in $e^+e^- \to W^+W^-$ or $e\gamma \to \nu WZ$[6].

Precision measurements that intend to uncover physics beyond the standard model must necessarily make use of the full standard model predictions including radiative corrections. We present a discussion of radiative corrections for $\gamma\gamma \to W^+W^-$ [7,8].

When discussing $\gamma\gamma$ colliders, an important issue relates to the choice of the photon spectrum. While it is possible to adjust the parameters of the laser to obtain a spectrum most suitable for gauge bosons production, one that is polarised and peaked at high energies, the shape of the predicted ideal spectrum[9] can be severely distorted. Indeed when one goes beyond the naive full conversion/single collision description, the nearly monochromatic spectrum acquires a long tail [10]. As detailed studies and choices of the optimal parameters have not been made, we have preferred to restrict our analysis to the case of monochromatic photons. As a worst case scenario, the effect of non-monochromaticity can be estimated with a luminosity in the peak that is ten times smaller.

9.1 $\gamma\gamma \to W^+W^-$ in the standard model

The reaction $\gamma\gamma \to W^+W^-$ will be the dominant source of W^+W^- at future linear colliders provided the photon-photon collider option, based on Compton backscattering is realized. Indeed the cross section for W^+W^- pair production in photon-photon collisions in the range $10^\circ < \Theta < 170^\circ$ is 60.7 pb at $\sqrt{s_{ee}} = 500$ GeV and 37.1 pb at 1 TeV[11]. Cross sections of W^+W^- pair production in e^+e^- collisions are an order of magnitude smaller: 6.6 pb at 500 GeV and 2.5 pb at 1 TeV. With more than a million WW pairs per year a photon-photon collider can be really considered as a W-factory and an ideal place to conduct precision tests on the anomalous couplings of the W bosons. However, such precision measurements rely on a very precise knowledge of the standard cross section, including radiative corrections.

Virtual radiative corrections to the process $\gamma\gamma \to W^+W^-$ were calculated recently [12] using the algebraic manipulation packages *FeynArts* and *FeynCalc*. Here we briefly report the main results of the complete $O(\alpha)$ calculation [7] taking into account electroweak virtual radiative corrections, soft and hard photon emission. The calculation is performed using symbolic manipulation program *FORM* and reproduces numerical results for the virtual corrections of Ref. [12].

9.1.1 Radiative corrections

On-mass-shell (OMS) renormalization scheme and 't Hooft-Feynman gauge are used to calculate loop corrections, i.e. α and the physical particle masses are used as basic parameters. Unless stated otherwise, values of $m_t = 174$ GeV and $m_H = 300$ GeV are used. It is important to note that electromagnetic coupling normalized at zero momentum transfer $\alpha(0)$ (and not $\alpha(M_Z)$) is relevant for WW production in photon-photon collisions, because incoming photons are on the mass shell. More technically, mass singularities coming from the light fermion contributions to the scalar loop integrals are cancelled out in the total unrenormalized amplitude as a consequence of the Kinoshita-Lee-Nauenberg (KLN) theorem. Singular terms present in the photon wave function renormalization constant are cancelled by the corresponding terms in the renormalization constant of the electric charge due to a Ward identity guaranteeing the universality of the electric charge. The width of the Higgs boson resonance is included in a gauge invariant manner, *e.g.* as described in Ref. [13].

Figure 1. *(a) photon energy distribution for the reaction $\gamma\gamma \to WW\gamma$. (b) relative fermionic corrections as a function of the scattering angle for various top-quark masses.*

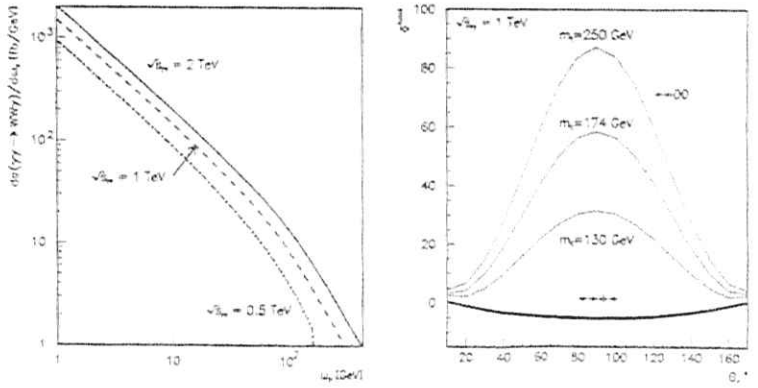

Fig. 1a presents the photon energy distribution for the process of real photon emission $\gamma\gamma \to W^+W^-\gamma$. The cross section is strongly peaked at small photon energies and it would be a hard task to discriminate a process of WW production from one accompanied by photon emission. Moreover, in realistic case the energy of the initial photons will not be fixed because of the quite wide spectrum of the Compton backscattered photons [9], and it will not be possible to require that W-bosons would be produced back-to-back to suppress real photon emission. So, in what follows no cuts are imposed on the photon angle and energy and the cross sections are integrated over the whole photon phase space.

Figure 2: *Born and corrected cross sections for WW production for various polarizations. Helicities denote the curves for the corrected cross sections. 0 stands for longitudinal.*

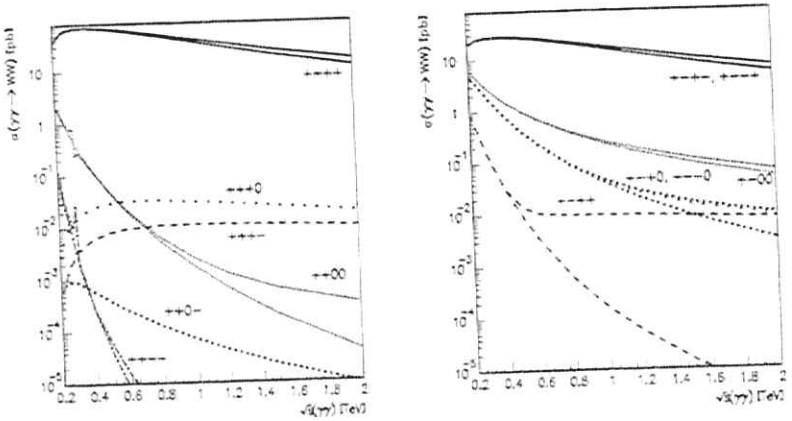

Fig. 2a,b shows the total cross section of WW pair production summed over both WW and $WW\gamma$ final states and integrated over $W^\pm$ scattering angles in the region $10^\circ < \Theta^\pm < 170^\circ$ as a function of energy for various polarizations. The bulk of the cross section originates from transverse W_TW_T pair production. Transverse W's are produced predominantly in the forward/backward direction and the amplitudes conserving helicities are dominating. Cross sections integrated over the whole phase space are non-decreasing with energy. For a finite angular cut $|\cos\Theta^\pm| < \cos\theta_c$ they do decrease as $1/s$, but still they are much larger than suppressed cross sections because transverse helicity conserving cross sections are still proportional to a large factor of $1/(1-\cos\theta_c)$. For such a case radiative corrections are negative and they rise with energy ranging from -3% at 500 GeV to -25% at 2 TeV. The cross section σ_{--LL}, which is the largest one after the dominating $\sigma_{-+++}, \sigma_{+---}$, is also decreasing as $1/s$ at tree level and corrections for it are also negative. For the other helicities radiative corrections are positive at high energies. Radiative corrections to cross sections σ_{--TL} which are decreasing at Born level as $1/s^2$ are positive and large. For the cross sections σ_{--LL} and σ_{+---} which are decreasing as $1/s^3$ for a finite angular cut corrections are even larger. The cross section σ_{+---} is decreasing at tree level as $1/s^5$ for a finite angular cut and is quite negligible at high energy. The

cross sections σ_{--LT} and σ_{----} vanish at the Born level, so only the process of $WW\gamma$ production contributes in Fig. 2a.

The cross section for longitudinal W_LW_L pair production is the one most sensitive to the mechanism of electroweak symmetry breaking. As an illustration, Fig. 1b presents a dependence of the fermionic corrections on the top quark mass at $\sqrt{s_{ee}} = 1$ TeV. Although the dependence is quite strong, the cross section σ_{--LL} itself is quite small in comparison to the cross section for transverse W_TW_T pair production and it will be very difficult to measure the top quark coupling with longitudinal weak bosons in this reaction.

Table 1. Total Born cross sections and relative corrections for various polarizations. When Born cross section is equal to zero cross sections of hard photon emission are given instead of relative corrections.

$\sqrt{s} = 500$ GeV						
$\lambda_1\lambda_2\lambda_3\lambda_4$	σ^{Born}, pb	δ^{hard}, %	δ^{soft}, %	δ^{bose}, %	δ^{fermi}, %	δ^{tot}, %
unpol	60.74	7.92	2.30	−13.0	−0.256	−3.04
$+-TT$	66.16	7.94	2.30	−13.0	−0.153	−2.92
$+-TL$	0	$6.04\cdot10^{-2}$ pb	0	0	0	-
$+-LL$	$4.909\cdot10^{-5}$	13.7	2.30	−22.3	9.68	5.00
$+--T$	52.61	7.69	2.30	−13.0	−0.318	−3.35
$+--L$	1.668	10.2	2.30	−12.6	−3.07	−3.18
$--LL$	0.9989	8.22	2.30	−12.6	0.467	−1.62
$\sqrt{s} = 1000$ GeV						
$\lambda_1\lambda_2\lambda_3\lambda_4$	σ^{Born}, pb	δ^{hard}, %	δ^{soft}, %	δ^{bose}, %	δ^{fermi}, %	δ^{tot}, %
unpol	37.06	13.4	3.11	−25.7	−1.29	−10.4
$+-TT$	40.09	13.5	3.11	−26.3	−1.31	−11.1
$+-TL$	0	$6.13\cdot10^{-2}$ pb	0	0	0	-
$+-LL$	$1.714\cdot10^{-3}$	64.2	3.11	−34.8	9.71	43.8
$+--T$	33.61	13.1	3.11	−25.0	−1.20	−10.0
$+--L$	0.1576	40.6	3.11	−21.9	−10.5	11.4
$--LL$	0.2510	14.2	3.11	−24.4	−2.77	−9.79
$\sqrt{s} = 2000$ GeV						
$\lambda_1\lambda_2\lambda_3\lambda_4$	σ^{Born}, pb	δ^{hard}, %	δ^{soft}, %	δ^{bose}, %	δ^{fermi}, %	δ^{tot}, %
unpol	14.14	20.1	3.49	−45.0	−3.00	−24.5
$+-TT$	15.17	20.1	3.49	−46.0	−3.05	−25.5
$+-TL$	0	$3.68\cdot10^{-2}$ pb	0	0	0	-
$+-LL$	$3.974\cdot10^{-5}$	748.	3.49	−84.8	32.7	704.
$+--T$	13.04	19.6	3.49	−44.0	−2.91	−23.8
$+--L$	$1.196\cdot10^{-2}$	248.	3.49	−29.8	−21.9	200.
$--LL$	$6.364\cdot10^{-2}$	21.0	3.49	−40.2	−7.40	−23.1

Finally, Tables 1 and 2 give Born cross sections and relative corrections for various polarizations and several scattering angles. Total corrections and corrections originating from virtual bosonic and fermionic contributions as well as from soft and hard photon emission are shown separately. A fictitious photon mass $\lambda = 10^{-2}$ GeV is used to regularize

infrared divergencies and a photon-energy cutoff $k_c = 0.1$ GeV discriminates between soft and hard bremsstrahlung. Looking at the Tables one concludes that bosonic corrections are dominating over fermionic ones. Corrections are larger in the central region. At high energies large cancellations occur between negative virtual corrections and positive corrections corresponding to real photon emission as one should expect. Indeed, the collinear singularities that give rise to the large corrections at high energies, should cancel out for the sum of virtual, soft and hard contributions as a consequence of KLN theorem.

Table 2. Differential Born cross sections and relative corrections.

$\sqrt{s} = 500$ GeV						
θ, °	$d\sigma^{Born}/d\cos\theta$, pb	δ^{hard}, %	δ^{soft}, %	δ^{bose}, %	δ^{fermi}, %	δ^{tot}, %
10.	435.3	7.62	2.30	-10.7	1.12	0.351
20.	163.6	7.94	2.30	-11.9	0.196	-1.44
60.	8.599	8.74	2.30	-16.5	-1.90	-7.38
90.	4.551	8.93	2.30	-17.4	-2.33	-8.49
$\sqrt{s} = 1000$ GeV						
θ, °	$d\sigma^{Born}/d\cos\theta$, pb	δ^{hard}, %	δ^{soft}, %	δ^{bose}, %	δ^{fermi}, %	δ^{tot}, %
10.	657.0	13.2	3.11	-20.2	0.216	-3.70
20.	98.09	14.2	3.11	-25.4	-1.21	-9.35
60.	2.416	15.8	3.11	-38.8	-4.75	-24.6
90.	1.212	16.2	3.11	-41.0	-5.39	-27.0
$\sqrt{s} = 2000$ GeV						
θ, °	$d\sigma^{Born}/d\cos\theta$, pb	δ^{hard}, %	δ^{soft}, %	δ^{bose}, %	δ^{fermi}, %	δ^{tot}, %
10.	384.7	20.3	3.49	-35.7	-1.17	-13.1
20.	32.44	22.0	3.49	-47.7	-3.53	-25.7
60.	0.6218	24.5	3.49	-69.0	-7.59	-46.6
90.	0.3078	25.0	3.49	-72.2	-8.31	-52.0

9.1.2 Discussion

In summary, electroweak radiative corrections are large but still under control at least for energies below 1 TeV. Taking them into account for precise measurements of the anomalous couplings is absolutely necessary but is not expected to affect dramatically the results that will be presented next. As one-loop correction for the total cross section is as large as -25% at 2 TeV (and even -50% at 90°) a relevant question is how about higher loops? The structure of leading corrections at $s \gg M_W^2$, $t \sim M_W^2$ is known to have Regge form. So, one can imagine that at very high energies it would be possible to experimentally study the reggeization properties of massive weak bosons which are a unique feature of non-abelian spontaneously broken gauge theory.

It is worth mentioning that WW production in photon-photon collisions should also qualify as a good $\gamma\gamma$ luminosity monitor. In fact, one can imagine that this reaction could be used both to uncover new physics and to calibrate luminosity. Indeed, anomalies would affect longitudinal and central W's, while to measure luminosity one would use most copiously produced transverse and forward/backward W's[14]. Table 2 shows that radiative corrections for forward W scattering are quite small even at 2 TeV.

9.2 $\gamma\gamma \to W^+W^- \to f_1\bar{f}_2f_3\bar{f}_4$ and anomalous couplings

Production of W pairs can probe the symmetry breaking sector through precision measurements of the $WW\gamma$ vertex. Although very little is known about the precise form of the symmetry breaking, chiral Lagrangians provide a formalism to describe models without a light Higgs scalar. An effective Lagrangian governing the interaction of the W can be written with only a small number of undetermined parameters. In particular, the $WW\gamma$ vertex is described by only one operator $L_9 = L_{9L} - L_{9R}$[4], which is expected to be $\mathcal{O}(1)$.

Rather than restricting ourselves to W pair production, we include the full set of four-fermions diagrams in the semileptonic channel, $jjl\nu$. Although a complete analysis of the effects of new physics on standard processes should include radiative corrections within the standard model, to get a first estimate of the level of accuracy achievable, a discussion at the tree-level is sufficient. Furthermore the radiative corrections for the four-fermions process are not available. These are not been calculated even for e^+e^- .

As the main contribution from four-fermions arises from the resonant diagrams, we first discuss the standard model and the anomalous couplings in the WW channel only. Note that the anomalous cross section, is dominated by the term linear in the anomalous coupling. The contribution of different helicity amplitudes to the total cross section in the SM were displayed in Fig. 2. The total cross section is completely dominated by transverse W's, especially at high energies. Although the anomalous couplings give rise to amplitudes that grow as s for the production of W_LW_L in the $J_Z = 0$ state, the corresponding $J_Z = 0$ production of W_LW_L in the SM decreases as $1/s$. As a net effect in the anomalous cross section, both W_TW_T and W_LW_L in either $J_Z = 0, 2$ have the same energy behaviour[1]. Therefore if one could interfere the anomalous LL amplitude and the standard TT amplitude, the contribution of the anomalous would be enhanced. This is precisely what can be achieved by performing a fit to the full four-fermions distributions, including angular variables characterizing the decay of the W. This procedures gives access to non-diagonal elements of the density matrix.

The $\gamma\gamma \to jjl\nu$ cross section was computed using MADGRAPH properly modified to include the anomalous couplings, at fixed center-of-mass energy. To obtain he following numerical results, we have taken $M_W = 80.1$ GeV, $M_Z = 91.187$ GeV, $\sin^2\theta_W = 0.23$, $\alpha(0) = 1/137$ and $\alpha(M_Z) = 1/128$. We assign $\alpha(0)$ ($\alpha(M_Z)$) to $WW\gamma$ (WWZ) vertices. The W width is taken to be the experimental width $\Gamma_w = 2.08$ GeV.

In order to compare different methods and make the connexion to previous analyses which relied only on a fit to either the total cross section or the angular distribution of the W's, we present the results of three different methods. The first is a simple comparison of the total number of events observed with the expected standard model rate. The second is a χ^2 fit on the θ_{jj} distribution, θ_{jj} being the angle of the jj system with the beam pipe, which corresponds to the angle of the W in the center of mass frame. Finally, we evaluate the accuracy that a full event by event maximum likelihood fit reaches. We base this analysis on all the 7 variables describing the kinematic: the polar and azimuthal angles of the jj and $l\nu$ pairs in the frame of the decaying "W's", the polar angle of the "W" pairs in the center-of-mass of the colliding beams and the invariant mass of the jj and $l\nu$ pairs (that are most of the time very close to M_W). The 3σ limits obtained on $|L_9|$ from the different fitting methods are presented in Table 3 for either unpolarized or polarized beams. The luminosity is assumed to be $\mathcal{L}_0 = 20(.4/\sqrt{s}(TeV))^2$. In all cases, we impose

angular cuts on all final particles with the beam $\cos\theta_{j,l_e} < .98$, we require the electron to be away from the jet, $\cos\theta_{jl_e} < .9$ and we impose a cut on the energy of the fermions, $E_{j,l_e} > 5(\sqrt{s}/400GeV)$.

As the standard cross section, with this set of cuts, decreases slowly with energy while the anomalous one stays constant, one expects only a mild improvement of the limits as the energy increases, once the effect of the increased luminosity has been taken into account. These expectations are borned out by the limits extracted from the total number of events shown in Table 3. Basically no improvement is obtained from a fit on the $\cos\theta_{jj}$ distribution since both standard and anomalous terms have similar distributions. On the other hand a full ML fit gives startling results, especially so at high energies. Note however that one suffers from not being able to identify the charge of the jet ($j - \bar{j}$). As mentioned above, the main improvement using this method occurs in the $J_Z = 0$ channel where the interference between the anomalous term which favours $W_L W_L$ and the standard one which favours $W_T W_T$ grows as s. As the fraction of W_L is much larger in the central region, we would expect that an angular cut on the W angle should bring even further improvement with the $J_z = 0$ state. While the limits obtained from the total cross section are degraded due to a loss in statistics, the improvement brought by the ML is indeed more noticeable after a cut on $|\cos\theta_W| < .8$ has been applied. This is especially so at the highest energy. If the efficiency for reconstructing W's is significantly better in the central region, it could be advantageous to impose this type of cut despite the loss in statistics.

Table 3. 3σ upper limits on $|L_9|$ obtained from a total cross section measurement and from ML fits to $\gamma\gamma \to jjl\nu$. For the case $j \neq \bar{j}$, an average over the two initial polarizations that form $J_z = 0$ or 2 is performed.

	$\sqrt{s} = 400$ GeV ($\mathcal{L} = 20 fb^{-1}$)						
	$\lvert\cos\theta_W\rvert \leq 1.$				$\lvert\cos\theta_W\rvert \leq 0.8$		
Polar	σ (pb)	total	ML $j \neq \bar{j}$	ML $j - \bar{j}$	σ (pb)	total	ML $j - \bar{j}$
unp	25.1	1.6	1.3	1.4	8.9	2.4	2.2
++	27.0	1.6	1.0	1.4	11.2	2.5	2.0
+-	23.2	1.5	1.4	1.4	6.7	2.2	2.1
	$\sqrt{s} = 800$ GeV ($\mathcal{L} = 80 fb^{-1}$)						
unp	13.8	1.1	.52	.80	2.9	2.2	1.2
++	15.2	1.1	.32	.61	3.9	2.3	0.8
+-	12.5	1.0	.91	.88	1.9	2.0	1.4
	$\sqrt{s} = 1600$ GeV ($\mathcal{L} = 320 fb^{-1}$)						
unp	4.6	.91	.14	.30	.78	2.2	.36
++	5.0	.92	.08	.19	1.07	2.2	.21
+-	4.1	.87	.62	.56	.49	2.0	.85

With the results using only the $jjl\nu$ channel, W pair production in $\gamma\gamma$ can test the electroweak symmetry breaking mechanism already at 400 GeV since it probes $L_9 \approx 1$. However one has to keep in mind that the luminosity spectrum has not been included. Since the limits on L_9 scale as $\mathcal{L}^{-1/2}$ the loss in precision occurring from a reduced luminosity in the peak is easy to estimate. As concerns the presence of a long tail in the

spectrum[10], the effect would be insignificant at 400GeV, since it lies for the most part below the threshold for pair production. At higher energies, again the crucial factor to extract a good bound on the anomalous coupling is the luminosity near the maximum energy. Provided the spectrum is precisely known, there is apparently no disadvantage at having also a large number of lower energy photon pairs.

9.3 $\gamma\gamma \to W^+W^-Z$ and W self-interactions

As the presence of anomalous WWZ couplings, might hint to a different scenario of symmetry breaking than those that affect the $WW\gamma$, it is interesting to investigate whether these can also be probed at the photon-photon collider. The most direct way of doing so is through WWZ production. Although this is a three-body final state process, its production rate turns out to be rather large [15], $\sigma = 1.4$ pb at 1 TeV centre-of-mass energy. This should be sufficient to provide a precise test of the tri-linear couplings.

In the effective chiral Lagrangian description of Higgsless models, the anomalous tri-linear couplings invoke, in addition to the two operators considered before, L_{9L} and L_{9R}, one C and P violating operator L_C[16]. The latter operator also breaks custodial $SU(2)_c$ and affects only ZWW and γZWW interactions. The $SU(2)_c$ conserving operators are expected to be $\mathcal{O}(1)$ while the non-conserving one might be further suppressed.

The explicit form of the C/P violating operator, is given in the notation of Ref. [16]

$$\mathcal{L}_c = g\frac{L_C}{16\pi^2}\left(Tr(\widetilde{W}^{\mu\nu}V_\nu)\right)\left(Tr(XV_\nu)\right) \quad ; \quad \widetilde{W}^{\mu\nu} = \frac{1}{2}\epsilon^{\mu\nu\alpha\beta}W_{\alpha\beta}. \tag{1}$$

where W, X and V are constructed from the Goldstone bosons and gauge fields.

In the last section we have shown that W pair production in $\gamma\gamma$ reactions can probe the electromagnetic W interaction to a very high accuracy which means a stringent bound on the combination $L_{9L} - L_{9R}$. One goal of the analysis of triple vector boson production is to separate the individual contributions coming from L_{9L}, L_{9R}. In addition, this is the lowest order process in $\gamma\gamma$ that can probe L_C, which contribute only to vertices involving a Z. Considering the different C and P properties of these two classes of operators they will be treated separately. In all cases, the helicity amplitudes for $\gamma\gamma \to W^+W^-Z$ were evaluated with FORM in both the unitary gauge and a modified non-linear gauge [5].

9.3.1 L_{9L} and L_{9R}

The effect of non standard operators such as L_{9L} and L_{9R} should appear mostly in the production of longitudinal gauge bosons. Indeed the amplitudes where three vector bosons are longitudinal are significantly enhanced over the standard model. However, we are considering only the term linear in the anomalous coupling. As a result of the interference with the standard amplitude containing a dismal amount of $W_L W_L Z_L$ [15], the contribution to the total cross section from this amplitude remains very small. Without a reconstruction of the polarizations of the vector bosons, the effect of anomalous couplings is significant only in those amplitudes where at most one vector boson is longitudinal. In that case, we find that all distributions are very similar to the standard one. The effect of the L_{9L}, L_{9R} operators is then restricted to a single observable, the total cross section.

The total cross section and the associated 3σ bound on L_{9L} and L_{9R} at fixed photon energy are shown in Table 4 for a luminosity $\mathcal{L}_0$ and a branching fraction $B = 89\%$ which

Figure 3: *L_{9L} and L_{9R} bounds coming from $\gamma\gamma \to W^+W^-Z$ (wide band) and $\gamma\gamma \to jjl\nu$ (narrow band). For each energy, the solid lines are obtained with a luminosity $\mathcal{L}_0$ and the dashed lines with $\mathcal{L}_0/10$.*

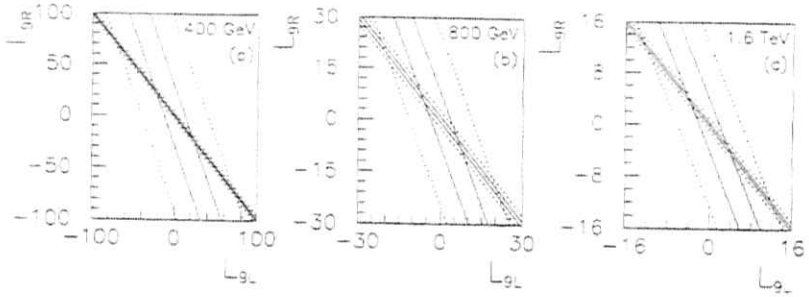

corresponds to all events containing less than three neutrinos. The angles between all particle pairs and between all vector bosons and the beams were restricted to $\cos\theta < 0.9$

Table 4: Cross sections and bounds on the operators L_{9L}, L_{9R} from $\gamma\gamma \to WWZ$. A branching fraction of $B = 89\%$ is included.

$\sqrt{s_{ee}}$ (GeV)	$\mathcal{L}$(fb^{-1})	σ (fb)	3σ bound
400	20	$95.4 - 0.55L_{9L} + 0.24L_{9R}$	$L_{9L} + 0.44L_{9R} < 13$
800	80	$276.3 - 1.65L_{9L} - 0.76L_{9R}$	$L_{9L} + 0.46L_{9R} < 3.6$
1600	320	$203.8 + 1.29L_{9L} + 0.64L_{9R}$	$L_{9L} - 0.50L_{9R} < 2.0$

While the $L_{9L} - L_{9R}$ combinations one can probe do not vary much with energy, increasing the energy from 400 GeV to 800 GeV improves very much the bound as the cross section at 400 GeV is still suppressed by a lack of phase space for the three massive particles. Going much higher in energy (1.6 TeV) brings further improvement only because of an expected higher luminosity; the visible cross section at this energy is less than at 800 GeV as it suffers more from the cut of events with a particle close to the beam pipe.

The bounds on L_{9L},L_{9R} are not nearly as good as the ones obtained previously with pair production, as shown in Fig. 3. However the pair production processes (in $\gamma\gamma$ and e^+e^-) have been analysed in much greater depth, in particular including full correlations between the decay products of the vector bosons. In light of the results obtained in the previous section for W pair production we also expect that a maximum likelihood fit allowing to retain some of the precious information from the density matrix elements sensitive to the interference between the mostly longitudinal anomalous amplitudes and the large standard amplitudes could significantly improve these limits.

9.3.2 Charge and Parity violating operator, L_C

As other anomalous operators, L_C will contribute predominantly to the production of longitudinal vector bosons. However it favours Z_L rather than W_L. Contrary to what happened for the L_9 operators, higher order terms, in particular those in L_C^2 cannot be

Figure 4: *Comparison of the L_C^2 distributions (dashed line) with the SM(full line).*

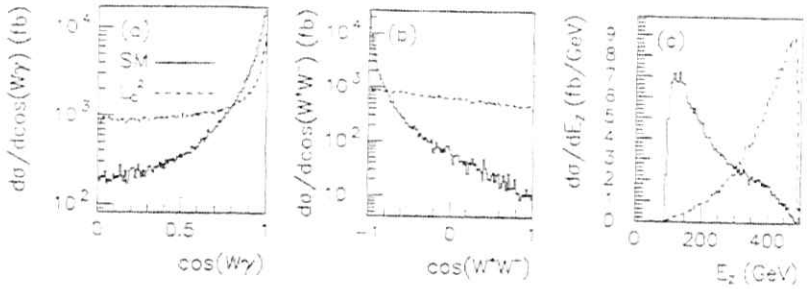

ignored. This is obviously so for observables that do not depend on the polarization of either the initial or final states. For such observables, terms linear in L_C vanish due to the C and P violating nature of this operator. Even for specific polarizations, quadratic terms in the anomalous coupling are not always negligible due to the specific structure of this coupling. This of course poses a conceptual problem as the contribution from L_C^2 corresponds in fact to a higher order operator in the energy expansion of the effective Lagrangian. For the sake of simplicity, we will neglect all other sub-leading operators whose interference with the standard model is of the same order as L_C^2.

In Fig. 4, comparisons between the standard model and purely anomalous distributions are displayed. Since the photons are not polarized, the latter correspond to the term in L_C^2. The distributions have been normalized such that the total cross sections without cuts are identical. Perhaps the most striking difference is in the energy of the Z. The standard Z's are mostly soft, as a purely infrared phenomena explains the unexpectedly large number of Z_L in the standard model. On the other hand, the anomalous interaction favours very energetic Z's. As is typical of processes involving longitudinal vector bosons, the anomalous interaction contributes to the production of a large number of W's and Z's in the central region relative to the standard model. Furthermore anomalous interactions produce W pairs that are evenly distributed over phase space while they are almost perfectly back-to-back in the standard model.

Upper limits on the operator L_C can be obtained from the total cross section or from asymmetries that are explicitly P violating[5]. However, the use of a ML method which takes advantage of the difference between the standard and anomalous distributions, provides better results already at the level of vector boson production. Evidently, further improvement are expected once the decay of the massive vector bosons is included, as this procedure allows for the possibility of reconstruction of the full density matrix.

The results of the ML fit are displayed in Table 5. The fit on L_C requires the identification of all final particles, which is provided only by the $W^+W^-Z = jjl\nu ll, l\nu jjll, l\nu l\nu jj$ and $l\nu l\nu ll$ channels, giving a small branching fraction of 12.6%. As the L_C^2 fit does not require knowing the charge of the W's, we can add to the above two more channels: $jjjjll$ and $jjjj\nu\nu$, giving a branching fraction of 26.5%. Although the limits coming from the linear term are not nearly as good, they are very useful to characterise the anomalous coupling once a signal in the total cross section or distribution has been observed. How-

ever, one needs to go beyond 1 TeV to probe the region where one expects new physics to appear.

Table 5. 3σ limits on L_C using a maximum likelihood fit.

Energy (TeV)	$\mathcal{L}$ fb^{-1}	Pol.	L_C			
			linear		quadratic	
			$B=1$	$B=0.126$	$B=1$	$B=0.265$
0.4	20	$++$	178	500	80	110
		$+-$	47	132	71	100
		unp	-	-	80	110
0.8	80	$++$	45	127	8.1	11
		$+-$	11	31	15	21
		unp	-	-	9.8	14
1.6	320	$++$	18	51	0.95	1.3
		$+-$	2.2	6.2	2.1	2.9
		unp	-	-	1.1	1.5

9.4 Conclusion

The predictions for W pair production, including radiative corrections in the standard model are known with very little theoretical uncertainty at least for energies below 1 TeV. This process can possibly be used both for luminosity monitoring and precision measurements of the W properties.

Four-fermion production in the $jj l\nu$ channel provide a sensitive test of alternative symmetry breaking mechanism via the measurement of anomalous couplings and this already at 400 GeV. For this process, the advantages of a maximum likelihood fit to the full angular distributions were illustrated. Such methods have not yet been used for $WWZ \to 6$ fermions, but the results from triple vector bosons production indicate that this process can provide meaningful constraint on WWZ anomalous couplings at colliders of energy greater than 1 TeV.

Acknowledgements

G.J. is grateful to the organizers of the workshop for financial support and kind hospitality. The work of G.J. was supported in part by the International Science Foundation grant NJR000 as well as in part by the joint ISF-RFBR grant NJR300, and in part by the INTAS grant 93-1180.

References

1. More details and references can be found in M. Baillargeon, G. Bélanger and F. Boudjema, *Proc. of Two-photon Physics from DAΦNE to LEP200 and Beyond*, eds. F. Kapusta and J. Parisi, World Scientific, (1994) 267.
2. G. Bélanger to appear in *Proc. of Photon'95*, Sheffield, England, april 1995.
3. G. V. Jikia, *Nucl. Instrum. Methods* **A355** (1995) 84, *Nucl. Phys.* **B437** (1995) 520; K. Cheung, *Phys. Rev.* **D50** (1994) 4290.

4. M. Baillargeon *et. al.*, contribution to the Electroweak Gauge Bosons report in this volume.
5. M. Baillargeon, G. Bélanger, F. Boudjema, G. Couture, preprint ENSLAPP-A-563, FISIST/17-95/CFIF, dec. 1995; O. Eboli, M. Magro and P. Mercadante, *Phys. Rev.* **D52** (1995) 3836.
6. K. Cheung, S. Dawson, T. Han and G. Valencia, *Phys. Rev.* **D51** (1995) 5.
7. G. Jikia, to be published.
8. See also A. Denner, S. Dittmaier and R. Schuster, contribution to the Electroweak Gauge Bosons report in this volume.
9. I.F. Ginzburg, G.L. Kotkin, V.G. Serbo and V.I. Telnov, *Pis'ma ZhETF* **34** (1981) 514; *Nucl. Instr. and Meth.* **205** (1983) 47; I.F. Ginzburg, G.L. Kotkin, S.L. Panfil, V.G. Serbo and V.I. Telnov, *Nucl. Instr. and Meth.* **219** (1984) 5.
10. D. Schulte, in this report.
11. The values for the cross sections without cuts are given for example by I. F. Ginzburg in this report.
12. A. Denner, S. Dittmaier, and R. Schuster, *Nucl. Phys.* **B452** (1995) 80.
13. R.G. Stuart, *Phys. Lett.* **B272** (1991) 353.
14. G. Bélanger and F. Boudjema, *Phys. Lett.* **B288** (1992) 210; Y. Yasui, I. Watanabe, J. Kodaira and I. Endo, *Nucl. Instr. Meth.* **A335** (1993) 385.
15. M. Baillargeon and F. Boudjema, *Phys. Lett.* **B317** (1993) 371; F. T. Brandt *et al.*, *Phys. Rev.* **D50** (1994) 5591.
16. F. Boudjema, Proceedings of *Workshop on Physics and Experiments with Linear e^+e^- Colliders*, eds. F.A. Harris *et al.* (World Scientific, 1994) 712.

10 Light Neutral Higgs at a Low Energy $\gamma\gamma$ Collider

Debajyoti Choudhury[1], Maria Krawczyk[2]

[1] *Max-Planck-Institut für Physik, München, Germany*
[2] *Institute of Theoretical Physics, Warsaw, Poland*

While the Standard Model (SM) Higgs scalar has been constrained by LEP1 data to be heavier than 65.2 GeV, minimal extensions like the general two Higgs doublet model (2HDM) may yet have a very light ($\lesssim 40\ GeV$) scalar (h) or a pseudoscalar (A) as long as $M_h + M_A > M_Z$ [1]. To probe the interesting regime ($\sim$ few GeV) in current or planned experiments is however a difficult task, both experimentally and theoretically [2,3,4]. In this context, the $\gamma\gamma$ option at the Next Linear Collider, seems to provide an unique opportunity [3]. We focus here on the resonant production of *very light Higgs particle* at the low energy $\gamma\gamma$ collider, suggested as a test machine for the NLC [7].

The general 2HDM is characterized by five masses and two angles: α and β [5]. We consider the phenomenologically appealing version, where the doublets $\phi_{1,2}$ (with vacuum expectation values $v_{1,2}$) couple exclusively to the $I_3 = \pm 1/2$ fermion fields. A large ratio $\tan\beta \equiv v_2/v_1 \sim m_t/m_b \gg 1$ then appears naturally. Concentrating on the very light scalar[*] h with the assumption $M_A > M_Z - M_h$, we note that LEP1 data constrains [1b] $\alpha \simeq \beta$. Assuming this to be an exact equality[†] we further restrict ourselves to the scenario with a large $\tan\beta$ thus enhancing the coupling to down-type quarks as well as charged leptons. Note that this parameter is not limited by LEP1 data for $M_h < 10\ GeV$ [4][‡]. In Fig.1*a*, we present the partial widths of h for $\tan\beta = 20$.

We consider the resonant production of very light Higgs scalar at e^+e^- NLC collider with energy $\sqrt{s_{ee}}$=10 GeV [7]. The cross section for the basic process $\gamma\gamma \to h \to f\bar{f}$ (where we specify f to be τ or μ) is given by

$$\sigma_{\gamma\gamma} = \frac{8\pi\Gamma(h\to\gamma\gamma)\Gamma(h\to f\bar{f})}{(s_{\gamma\gamma} - M_h^2)^2 + \Gamma_h^2 M_h^2}\,(1 + \lambda_1\lambda_2) \qquad (1)$$

where λ_i are the mean helicities of the photon beams and the rest of the symbols carry their usual meaning. In order to calculate the total cross section $\sigma^h_{ee}(f\bar{f})$, we need to fold the above with the photon spectrum resulting from Compton backscattering electrons on an intense laser light. The latter depends, apart from the momentum fraction of the initial electron carried by the photon ($z_{1,2}$), also on the helicity of the initial electrons λ_e, initial laser beam circular polarization P_c and other machine parameters [6]. To maximize the photon energy, we choose $x = 4.82$, and thus $\sqrt{s^{max}_{\gamma\gamma}} \simeq 0.83\sqrt{s_{ee}} = 8.3\ GeV$. Following ref. [6], we assume the 'broad' spectrum of photons with $2\lambda_e P_c = +1$. This has an advantage that it is rather flat over $\sqrt{s_{ee}}$ and favors the $J_Z = 0$ state, the polarization state of Higgs scalar.

[*] The opposite case, with very light A, leads to very similar signatures and will be discussed elsewhere [3].
[†] Note that this kills the coupling of h to W/Z bosons.
[‡] Also other data like those on the anomalous magnetic moment for muon, still allows $\tan\beta \sim 20$ or higher for $M_h \gtrsim$ 2-3 GeV [2,3].

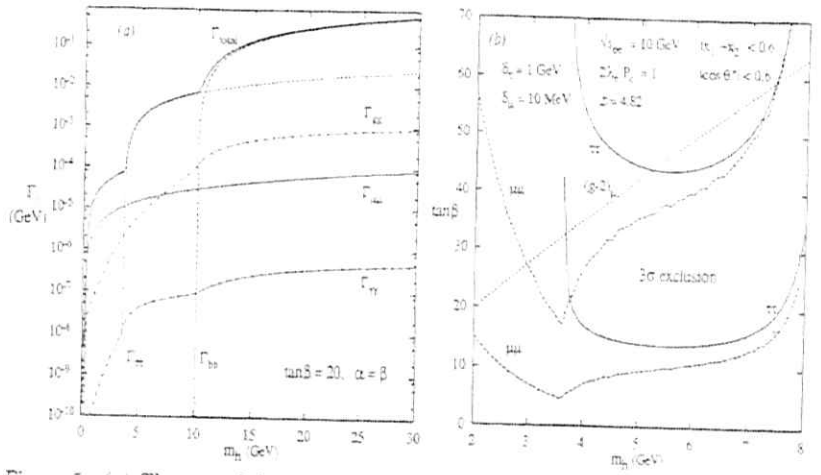

Figure 5: *(a) The partial decay widths for h for $\tan\beta = 20$ ($\alpha = \beta$). (b) The exclusion plots that may be achieved at NLC$\gamma\gamma$ from either $\mu\mu$ or $\tau\tau$ channels. The parameter space above the curves can be ruled out at 3σ. The upper and lower sets are for integrated luminosity of 100 pb^{-1} and 10 fb^{-1} respectively. Also shown is the limit "derivable" in the event of 10^{-9} accuracy in present $(g-2)_\mu$ measurement.*

To a very good approximation, $\sigma^h_{ee}(f\bar{f}) \propto \tan^2\beta$. For $\tan\beta = 20$, this cross section for M_h above the corresponding thresholds and below 8 GeV varies for $\tau\tau$ ($\mu\mu$) final state between 0.1–7.3 pb (0.5 fb–.6 pb). The (orders of magnitude larger) background is mainly due to direct $f\bar{f}$ pair production, since at such low energy the resolved photon contributions are negligible. While the predominant contribution ($J_z = 2$) is already reduced significantly by the choice for the spectrum, the forward/backward peaked $J = 0$ contribution is reduced by imposing a cut ($-0.6 < \cos\theta^* < 0.6$) on the CM scattering angle. Further improvements in the signal to background ratio can be made by restricting the total boost of the $f\bar{f}$ system, here we put $|x_1 - x_2| < 0.6$.

Since Γ_h is tiny (see Fig.1*a*), in the event of infinite resolution in the invariant mass, the signal would be striking indeed! We adopt, though, a more realistic approach and choose, for the experimental resolutions, $\delta M_{f\bar{f}} = 2\delta_f$, with δ_μ=0.01 GeV and δ_τ=2 GeV. The 3σ exclusion plots in the $\tan\beta$–M_h plane that may then be obtained using the $\mu\mu$ and $\tau\tau$ final states are displayed in Fig.1*b*. To be specific, we have adopted two representaive values for the integrated luminosity : 100 pb^{-1} and 10 fb^{-1}. It is interesting that though the $\tau^+\tau^-$ cross sections are typically larger, yet better limits are obtained from the muonic channel. The situation would be reversed if δ_τ could be improved. Note that the above results are not expected to have large theoretical uncertainties in contrast to e.g. $\Upsilon \to h\gamma$ process[2a,5].

To summarize, we consider the physics potential of high luminosity, low energy NLC$\gamma\gamma$ in the context of a possible light Higgs scalar in the general 2HDM. While the limits obtainable with an integrated luminosity of 100 pb^{-1} are better (for $3 < M_h < 7\ GeV$) than the existing limits from $(g-2)_\mu$, a luminosity of the order 10 fb^{-1}/y would lead to

bounds much more stringent even than those expected from a ten-fold improvement in $(g-2)_\mu$ measurement [2b]. Photon polarization is crucial though.

Acknowledgements

MK would like to thank F. Boudjema and G. Bélanger for the important suggestion which led to these calculations. This research is supported in part by grants from the Polish Committee for Scientific Research and the EC grant under the contract CHRX-CT92-0004.

References

1. *a*) EPS Conference, Brussels 1995; *b*) ALEPH Coll., D. Buskulic et al., Z. Phys. C 62 (1994) 539; DELPHI Collab., P. Abreu et al., Zeit. Phys. C 67 (1995) 69; L3 Collab., M. Acciarri et al., Z. Phys. C 62 (1994) 551; OPAL Collab. R. Akers et al., Z. Phys. C 61 (1994) 19; A. Sopczak, Int. Workshop "Physics from Planck Scale to Electro-Weak Scale", Warsaw, Poland, Sept. 1994
2. *a*) Crystal Ball Collab., D. Antresyan et al., Phys. Lett. B251(1990)204; Cleo Coll. R. Balest et al., CLEO 94-19; P.Franzini et al.Phys.Rev.D 35(87)2883; *b*) E. Carlson, S. Glashow, U. Sarid, Nucl.Phys. B 309 (1988)597, J. Ellis, M. Karliner, M. Samuel, Slac-Pub-6670, hep-ph/9409376)
3. D. Choudhury and M. Krawczyk, in preparation.
4. *a*) A. C. Bawa, M. Krawczyk, Phys. Lett. B357 (1995) 637; *b*) M. Krawczyk, Warsaw University IFT preprint 20/95, talk at Kazimierz Symposium (May 1995,Ames, USA); *c*) J. Kalinowski, M. Krawczyk, Phys. Lett. B361 (1995) 66; preprint IFT 96-03(hep-ph 9602292).
5. J. F. Gunion at al. The Higgs Hunter's Guide (Addison-Wesley,1990).
6. *a*) V.I.Telnov, Nucl.Inst.Methods Phys.Research A294(1990)72; *b*)J. Gunion, H. Haber, Phys.Rev. 48 (1993) 5109; D.Borden, D. Bauer, D. Caldwell , Phys. Rev. D 48 (1993) 4018; *c*) M. Baillargeon, G. Belanger, F. Boudjema, Phys. Rev. D 51 (1995) 4712.
7. D. L. Borden, NLC Workshop, Hawaii 1993, p 323; E.L.Saldin et al, Nucl. Instr. Methods Phys.Research A355(1995)171.

An Update to the Experimentation Discussion *

D. Schulte
DESY, Deutsches Elektronen-Synchrotron, Notkestraße 85, D-22603 Hamburg, Germany.
E-mail: schulted@x4u2.desy.de

R. Settles †
Max-Planck-Institut für Physik, Föhringer Ring 6, D-80805 München, Germany.
E-mail: settles@mppmu.mpg.de

1. Introduction

Extensive R&D efforts at the leading particle-physics laboratories are forming the basis of machine culture needed to construct and operate the future linear collider. This work is surveyed by an interregional collaboration[1], which in 1995 appointed a Technical Review Committee (TRC) to prepare a report on the status of the different machine designs and of the related R&D work[2]. This was the first report in a series which is to converge to a common conceptual design in three years. The TRC working groups covered injection systems, damping and compression systems, linac technology, beam dynamics, beam delivery, and experimentation, as well as each of the machine proposals.

Preceeding these recent developments, extensive groundwork was laid at workshops for the physics – La Thuile[3], SLAC[4], Snowmass[5], Japan[6, 16], Europe[7, 11, 12, 14], Finland[8], the USA[9, 13], Hawaii[10], among others, – and the machine – LC88 at SLAC, LC90 at KEK, LC91 in Protvino, LC92[17] in Garmisch-Partenkirchen, LC93[18] at SLAC, and LC95 at KEK[19].

Since completion of the 1995 TRC Report, there have been improvements in the machine designs, and the present series of workshops[14] led to more work on experimentation issues[15]. The present paper includes these updates along with a summary of the TRC experimentation report[2, 20] for completeness.

After a brief overview of the physics potential of a linear collider in Section 2, the experimental programme is highlighted in Section 3. Some main e^+e^- physics topics and their requirements on machine and detector are expanded upon in Section 4. Section 5 gives examples of adapting machine operation to physics questions arising from discoveries. Section 6 compares how the different machine designs affect the experiments. In Section 7, an overview of detector concepts is followed by an example for designing its performance. Some conclusions are drawn in Section 8.

*G. Cairnet/LAPP-Annecy, R. Settles/MPI-Munich, and A. Wagner/DESY-Hamburg were conveners of the experimentation working group for the present workshops.

†Chairman of the 1995 TRC Experimentation working group with the following members: T. Markiewicz/SLAC, S. Bertolucci/INFN Frascati, S. Kawabata/KEK, D. Miller/UC London, R. Orava/SEFT Helsinki, F. Richard/LAL Orsay, T. Tauchi/KEK, A. Wagner/DESY. Much material from their report[2, 20] is included here.

2. Overview

A few examples of e^+e^- experiments at $\sqrt{s}$ from 0.2 to 2 TeV with requirements on detector and machine are given in Tables 1 and 2 which result from the workshops cited above. The e^+e^- physics programme is well balanced between (1) a programme of discovery physics, such as search for the Higgs boson and for physics beyond the standard model ($\mathcal{SM}$), for example supersymmetry ($\mathcal{SUSY}$), and (2) a rich programme of standard "bread and butter" physics, such as new measurements in poorly mapped regions of the $\mathcal{SM}$, top quark properties and trilinear gauge couplings, and familiar measurements to further the understanding of QCD. This programme, the e^-e^-, $\gamma\gamma$, and $e^-\gamma$ collider options, and the possibility of improving on the precision measurements at Z^0 peak, create a collider facility with a new magnitude of potential for decades of frontier particle physics.

The main goal of next-generation colliders is to understand the origin of electroweak symmetry breaking ($\mathcal{ESB}$). The mechanism for $\mathcal{ESB}$ is most probably operating in the energy regime [13] of $\sqrt{s} \simeq \mathcal{O}(1\ \mathrm{TeV})$ or below, and the linear collider has the flexibility to answer all of the relevant questions in that range.

3. The Experimental Programme

In the following, the experimentation *phases* refer to the energies at which the machine could run for carrying out its experimental programme, and the machine *stages* refer to the construction work which has been realized. In present planning[21], designs for the first stage of the machine allow $\sqrt{s} \simeq 0.8$-1.0 TeV to be reached with an "adiabatic upgrade" of machine technology without having to build new tunnel, and the second stage would then go beyond 1 TeV. This approach has been successfully applied to the operation of LEP – LEP1→LEP1.5/1.8→LEP2 – with hardware upgrades and exciting new physics at each stage.

3.1. Experimentation Phases

1 – At the international workshops much work centered around a starting phase at $\sqrt{s} \simeq 0.5$ TeV which yields a physics programme with healthy complementary to that of LHC. The following are presently identifiable milestones for running the machine at lower energies:

–At $\sqrt{s} \simeq 0.3$ TeV with $1\mathrm{fb}^{-1}$ of data, any discovery gap that might exist between LEP2 and LHC could be closed, a definitive test of the $\mathcal{SUSY}$-Higgs scenarios could be made since in those models the lightest Higgs has $M_h \leq 150\ \mathrm{GeV}/c^2$ and would be discovered. Many standard analyses could be performed, for example the trilinear gauge couplings ($WW\gamma, WWZ^0$) measured twice as precisely as at LEP2. Already at

$\sqrt{s} \simeq 0.3$ TeV, the e^-e^- linear collider is unique in being able to cover all presently known $SUSY$ Higgs models and some theories involving multi-Higgs doublets and singlets.

-At $\sqrt{s} \simeq 0.4$ TeV, the top threshold could be found with a binary scan involving 0.5fb^{-1}of data at each of ~6 energies, or with a 2-3fb^{-1} run above threshold, to yield M_{top} to about ± 2 GeV/c^2. The trilinear-gauge-coupling precision would improve by a factor of four relative to LEP2. The top threshold scan with 5fb^{-1}per point at 10 energy points, which could follow straight away or be delayed until later, would determine M_{top} to ± 0.2 GeV/c^2. Now that the top quark has been discovered, $\sqrt{s} \simeq 0.4$ TeV is also be viable as first-phase energy of the machine.

-Many workshop studies were done assuming 10-100fb^{-1} of data at $\sqrt{s} \simeq 0.5$ TeV: precision measurements would look for new physics in properties the top quark such as evidence for its substructure, the trilinear gauge couplings would be measured to about $\pm 0.2\%$, and the Higgs bosons with masses up to ~350 GeV/c^2 could be discovered. If light supersymmetry exists, depending on how it is realized in nature, this first stage could find and study some of the lighter supersymmetric particles ($\tilde{\chi}_1^{\pm}$, $\tilde{\chi}_1^0$, $\tilde{l}$).

-Thus the pattern is clear for the first stage: there are physics questions to be answered at low energies, and the successive increase in machine energy and luminosity would continue, with ~100-200fb^{-1} of data to be taken at appropriate energies up to $\sqrt{s} \simeq 0.8$-1.0 TeV. The goal at higher energies of the first stage would be to search for heavier Higgses and/or supersymmetric particles. The SM Higgs can be discovered up to a mass of $M_{H_{SM}} \simeq$ 600-700 GeV/c^2. If $SUSY$ has been found earlier, the search for the heavier Higgs states (H^0 and A^0, produced in association, and $H^{\pm}$, produced in pairs) and the colored superpartners ($\tilde{g}$, $\tilde{q}$), which are heavy in most models, will follow.

? – The second stage uncovers the new and standard physics that lie at higher energies. Increasing the length and/or gradient of the machine would allow ~100-200fb^{-1} of data to be taken up to $\sqrt{s} \simeq 2$ TeV, opening the search for even heavier Higgses and supersymmetric particles. If the Higgs turns out to be heavier than ~800 GeV/c^2, it no longer behaves like particle as the Higgs sector is strongly interacting. The programme for studying the mechanism of electroweak symmetry breaking would pass to e.g. precision measurements of gauge boson production – the $W_L W_L$ scattering experiment at the highest energy which should be at least ~1.5 TeV. At this stage, the e^-e^- linear collider will be the best place to measure new phenomena which may exist at such energies. Examples are the direct or indirect evidence for an extended-gauge Z', or the production of new heavy fermions if their masses are within the energy range of the collider.

? – The e^-e^-, $e^-\gamma$, and $\gamma\gamma$ collider modes allow complementary measurements to those of the e^-e^- collider[51, 53, 54, 58]. For example, the reactions $e^-e^- \to e^-W^-\nu$, $e^-\gamma \to W^-\nu$, and $\gamma\gamma \to W^-W^-$provide alternate ways of measuring the trilinear gauge couplings and thus yield sensitive tests of the SM, and all three collider modes offer alternate ways of producing supersymmetric particles, e.g., $e^-e^- \to \tilde{e}\tilde{e}$, $e^-\gamma \to \tilde{e}\tilde{\nu}$, $\gamma\gamma \to \tilde{l}\tilde{l}$.

The e^-e^- collider gives access to possible exotic doubly charged objects, higgses or

Table 2. Some e^-e^- experiments and the corresponding performance needed for the machine. Quality key: from'-'not important, to'$\star\star\star$'very important.

PHYSICS	MACHINE[a]			
	$\int \mathcal{L}dt$	$\sqrt{s}$	Narrow	Pol.
	fb^{-1}/y	TeV	$\mathcal{L}(\sqrt{s})$	beams
•HIGGS				
Light Higgs	1-10	.2		
SM/Susy B.R	100	to	$\star\star$[b]	
Interm. Higgs	200	~1		
•ELECTROWEAK GAUGE BOSONS				
WWV-coupl.	10	.3		
Unfold γ, Z-coupl.	50	to	$\star\star\star$	$\star\star$
$W_L W_L$-scatt.	200	~1.5		
•EXTENDED GAUGE				
New particles	200	~2		$\star$
•SUSY				
$\tilde{\chi}_1^{\pm}, \tilde{\chi}_1^0, \tilde{l}$	10	.2		
Susy spectroscopy	20	to		$\star$[c]
$\tilde{q}, \tilde{g}$	100	~1-2		
•TOP QUARK				
Thr. scan	10	~.35	$\star\star\star$	
g-2,helanal.,V−A	50	.4		
Rare decays	50	to		$\star\star$
Yukawa coupl.	100	1		
•QCD				
Hadronization	1	All		
$\alpha_s(s)$	10	$\sqrt{s}$		
•(Virtual) $\gamma\gamma$				
Minijets, heavy flavors	1			
$F_2^{\gamma}(x, Q^2)$	10		$\star$	
Overall			$\star\star\star$	$\star\star$[c]

[a]Narrow c.m.s. energy spread arising from machine and beamstrahlung effects. $\star\star\star$ means the energy spread from the machine must be small ($\sigma \simeq \mathcal{O}(0.2\%)$), the luminosity spectrum must be well-measured (to the $\pm 0.1\%$ level), the last row of Table 2 gives the performance of the detector for measuring the luminosity spectrum.
[b]If $M_{H_{SM}} \simeq M_{Z^0}$, upgrade to $\star\star\star$.
[c]If supersymmetry is discovered, upgrade to $\star\star\star$.

Table 2. Some e^+e^- experiments and the corresponding performance needed for the detector. Quality key: from '-' not important, to '***' very important (LEP/SLC detectors ~ ***)

PHYSICS	DETECTOR [a]						
	Hermeticity	Tracking	Calorimetry	3-Dim. Granul.	Lepton I.D.	Vertex Tag	μ/K I.D.
•HIGGS							
Light Higgs							
SM/Susy B.R.	***	***	***	**	**	***	*
interm. Higgs							
•ELECTROWEAK GAUGE BOSONS							
WWV-coupl.							
Unfold^, Z-coupl.	***	***	**	***	***	-	-
$W_L W_L$-scatt.							
•EXTENDED GAUGE							
New particles	***	***	**	***	**	**	
•SUSY							
$\tilde{\chi}_i^{\pm}, \tilde{\chi}_i^0, \tilde{\ell}$							
Susy spectroscopy	***	***	**	***	**	-	-
$\tilde{q}, \tilde{g}$							
•TOP QUARK							
Thr. scan	**	**	**	**	**	***	*
g-2,helanal.,V+A							
Rare decays	***	**	**	***	**	***	**
Yukawa coupl.							
•QCD							
Hadronization							
$\alpha_s(s')$	**	**	**	*	*	**	*
• Virtual $\gamma\gamma$							
Minijets, heavy flavors							
$F_2^{\gamma}(x, Q^2)$	***	**	**	***	***	*	*
Overall	***	***	**	***	**	***	**
$\mathcal{L}(\sqrt{s})$ Det.[b]	**	***	**	**	**	-	-

[a] The last row of the Table gives the performance of the detector for measuring the luminosity spectrum for experiments in which the c.m.s. energy spread must be well measured.
[b] "Tracking", "Calorimetry" refer to measuring accuracy for momentum, energy, respectively.
[c] Small angle tagger would allow low-x studies and high Q^2.

dileptonic boson, and to possible discovery of a heavy Majorana neutrino. Since the e^+e^- collider requires only minor changes to the hardware of the e^+e^- machine and detector, its programme could be pursued during the first phase of the facility. The e^+e^- collider is the best conceivable machine for measuring the quark and gluon structure of the photon. For the $\gamma\gamma$ collider, a most important experiment, which should be a benchmark for feasibility studies, is the direct production of the higgs boson, which proceeds via loops with contributions from new particles as well as from $t\bar{t}$ and W^+W^-. Thus a precision measurement of $\Gamma_{\gamma\gamma\to H_{SM}}$ gives indirect access to new physics.

Σ – Running on the Z^0 peak with polarized beams could measure $\sin^2\theta_W$ to greater accuracy than at LEP/SLC and provide the indirect $M_{H_{SM}}$ determination to test the $S\mathcal{M}$ framework[6, 60]. The luminosity requirement is $\sim 5 \times 10^{31}\mathrm{cm}^{-2}\mathrm{s}^{-1}$, and both beams should be polarized to reduce the error on $\sin^2\theta_W$ to well below ± 0.0001[59]. For experiments measuring CP violation in the b-quark sector or B_s^0 oscillations, a luminosity of $\sim 10^{33}\mathrm{cm}^{-2}\mathrm{s}^{-1}$ would be needed[6, 61].

Finally, a technical remark. The Z^0 -peak running is important for calibrating the detectors and measuring the absolute energy scale. The luminosity requirement, $\sim 10^{31}\mathrm{cm}^{-2}\mathrm{s}^{-1}$, is modest.

3.2. Complementarity of Hadron and e^-e^- Colliders

It has been emphasized at the international workshops that the pp and e^+e^- physics programmes are complementary, and what is found at the LHC will influence the experimental programme at the e^-e^- collider and vice-versa. Examples of comparison of the physics potential of e^-e^- and pp colliders are found elsewhere[13, 22, 23, 24]. These studies show that the complementarity of the e^-e^- machine to LHC is already necessary and sufficient to justify its first-phase operation at $\sqrt{s} \simeq 0.3$-0.5 TeV, which is the first technological step on the way to the higher energies, where the complementarity shifts to other physics measurements. For example, the properties of a light Higgs would be measured at the first phase of the machine running at the peak of the Higgs production cross section, whereas an intermediate-mass Higgs would be measured at a second phase of the machine running at the appropriate energy. Most top quark properties will be derived from running at the peak of the $t\bar{t}$ cross section around 0.4 TeV. Similarly, for pinning down the properties of the supersymmetric particles and for mapping out $\mathcal{SUSY}$ parameter space, beam energy and polarization would be tailored to the measurement in question, as will be shown with examples in Section 5 below. If the Higgs as particle does not exist, the mechanism for $\mathcal{ESB}$ would be studied in W^+W^+ production at a second-stage energy of 1.5 TeV and in precision measurements with polarized beams at lower energies.

Hence, it is the capability to optimize different measurements by running at the desired energies with or without polarized beams that gives the e^+e^- collider its full physics potential and full complementarity to the hadron colliders. It is well understood[22] that the discovery reach of the LHC is matched by e^+e^- around 1 TeV. But the experiments at lower energy are an essential part of the entire programme, so that starting at $\sqrt{s} \simeq 0.4$ TeV is justified.

4. Experimentation: Machine–Detector–Physics

4.1. Machine

The global machine aspects of interest listed in Table 1 are: luminosity, $\sqrt{s}\equiv$ c.m.s. energy, $\mathcal{L}(\sqrt{s})$ spread, and beam polarization. Narrow $\mathcal{L}(\sqrt{s})$ means the energy spread from the machine must be small ($\sim \mathcal{O}(0.2\%)$) and the luminosity spectrum well-measured (to the $\sim$0.1% level, see Table 2). Table 1 makes it clear that there is important physics in the high luminosity and that the polarization of the beams will enrich the physics potential.

The luminosity spectrum is affected by the beam-energy spread, beamstrahlung, and initial state radiation (i.s.r.). While i.s.r. can be calculated to high precision, the first and second effects have to be measured. The beam-energy spread is mainly due to beam dynamics in the damping ring and accelerating structure. The beamstrahlung however induces an average loss in beam energy δ_B which is related to the luminosity, as $\mathcal{L} \propto \sqrt{\delta_B}$. The machine could thus achieve a better luminosity spectrum as far as beamstrahlung is concerned by compromising the luminosity, if it were to turn out for a given measurement that the overall systematic⊕statistical error is reduced.

4.2. Detector

The detector perfomance has the following general breakdown in Table 2: hermetic coverage, tracking, calorimetry and energy flow, 3-D granularity of the subdetectors, charged lepton identification (and sign determination), vertex tagging, and π/K identification. This way of categorizing detector performance emphasizes the measuring performance of various subsystems. If the breakdown is to according to analysis performance, the items would be: missing-energy measurement, energy-flow measurement, jet reconstruction, jet-jet resolution, lepton reconstruction, lepton-lepton resolution, b/τ-tagging efficiency, and measurement in the forward-backward direction. The subdivision according to subdetectors would be: vertex detector, inner tracker, central tracker, electromagnetic calorimeter, hadron calorimeter, the coil, muon chambers, luminosity and end-cap trackers/calorimeters, data-acquisition system, the trigger system, and, last-but-not-least, the computer farm for online reconstruction of the data. Table 3 shows the correlation between different breakdowns.

4.3. Physics

The ⋆-ratings in Tables 1 and 2 are based on examples from the international workshops[6, 25, 26, 27, 55, 29, 30, 31, 32, 33, 34, 35, 36, 37, 38, 39, 40, 41, 44, 45, 46, 47, 48, 52]:

- The Higgs boson

Discovery of and exploration of Higgs bosons (via Higgs-strahlung and gauge-boson-fusion) and of associated production in the minimal SUSY model (MSSM); measurement of the spin-parity quantum numbers and of the branching ratios to test the theory (e.g., to distinguish between SM and MSSM Higgses).

In the minimal $\mathcal{SM}$ there is a single CP-even scalar boson $H_{\mathcal{SM}}$. In the $\mathcal{MSSM}$ the physical spectrum consists of three neutral bosons, the CP-even h^0 and H^0 and the CP-odd A^0, and a pair of charged bosons $H^\pm$. The searches for these particles have been simulated in some detail using the performance of existing detectors [26, 30, 36, 39, 44, 56], and the discovery with such detectors is straightforward in the light-Higgs scenarios studied up to now (i.e., for Higgs masses up to about 350 GeV/c^2 at $\sqrt{s}$ up to 0.5 TeV). Vertex tagging improves the significance of the signals considerably and is thus rated highly, in particular if $M_{H_{\mathcal{SM}}} \simeq M_{Z^0}$[36]. Excellent tracking improves the $M_{H_{\mathcal{SM}}}$ measurement[6]. Hermeticity is needed to identify decays with large missing energy, since the $\mathcal{MSSM}$ Higgses can possibly decay invisibly. While light Higgses can be discovered with detectors of performance similar to LEP/SLC detectors, finding and studying a heavier Higgs at higher $\sqrt{s}$ puts more demands on the detector.

The summary in terms of detector performance desired is shown in Table 2; in terms of analysis performance, b/τ-tagging, jet-jet and lepton-lepton invariant mass resolution, and hermeticity are important to very important for the detector.

For the machine, high luminosity is needed to measure the Higgs branching ratios[39]. A higher c.m.s. energy and luminosity are required in case the $\mathcal{SM}$ Higgs is heavy[40]; the $H_{\mathcal{SM}}$ can be discovered up to a mass of $M_{H_{\mathcal{SM}}} \simeq$ 600-700 GeV/c^2 in the first stage of the machine. For $M_{H_{\mathcal{SM}}} \geq$ 800 GeV/c^2, the second stage is needed for the $W_L W_L$

Table 3. Correlation between different ways of looking at the detector

	Detector Performance						
Analysis Performance	Hermeticity	Tracking	Calorimetry	3-Dim. Granul.	Lepton I.D.	Vertex Tag	π/K I.D.
Missing-Energy Measurement	x	x	x	x	x		
Energy-Flow Measurement		x	x	x	x		
Jet Reconstruction	x	x	x	x			
Jet-Jet Resolution		x	x	x			
Lepton Reconstruction		x	x	x	x		
b/τ-Tagging		x	x	x	x	x	
Forward-Backward Direction	x	x	x				
Subdetector System							
Vertex Detector		x		x	x	x	
Inner Tracker	x	x		x	x	x	
Central Tracker	x	x		x	x	x	x
Electromagnetic Calorimeter	x		x	x	x		
Hadron Calorimeter	x		x	x	x		
Muon Chambers	x	x	x	x	x		
Lum. and End-Cap Devices	x	x	x	x	x		

scattering experiment (see below).

Higher luminosity and $\sqrt{s}$ will be required if the world is supersymmetric, since then the Higgs masses range from light (h^0) to possibly very heavy (H^0,A^0) and the charged Higgs ($H^\pm$) may also be heavy. In addition to Higgs-strahlung, the neutral $\mathcal{SUSY}$ Higgses are produced in association, and the charged Higgs is pair-produced.

• The electroweak gauge bosons

Measurement of the trilinear couplings, of the quadrilinear couplings; unfolding the γ and Z^0 couplings with polarized-beam experiments.

The golden channel for the measurement of trilinear $W^\pm$ couplings ($WWV, V = \gamma, Z^0$) [32, 28, 35, 47] is $e^-e^- \to W^-W^- \to \ell\nu\bar{q}q'$. Detector aspects for the measurement of the couplings are discussed in detail in Section 7. Hermeticity is important for yielding a good missing-energy measurement because of the energetic neutrino in the final state. The LEP/SLC-type detectors are adequate for extracting the couplings at $\sqrt{s} \simeq 0.5$ TeV[32], but detectors as studied for JLC[6] and for 1 TeV [48] improve the forward-angle performance, which is valuable due to the forward-peaking of the production angular distribution. These detectors allow good energy-flow measurement down to $|\cos\theta| < 0.98$ for the helicity analyses. At higher energies, the improved performance in jet reconstruction, lepton reconstruction, and jet-jet resolution for $W^\pm$ reconstruction are necessary. This bread-and-butter experiment of the physics programme puts strong demands on machine and detector[45], as seen in Table 2. Thus it will be used in Section 7 below as an example for studying the detector resolution.

A well-measured luminosity spectrum, polarized beams, high luminosity and higher energy are important machine aspects. The error in measuring the trilinear gauge couplings decreases roughly as $1/s$, so that higher energies will improve[32] this measurement. Beam polarization is necessary for disentangling the γ and Z^0 couplings.

• $W_L W_L$ scattering

In the heavy Higgs scenario, study the mechanism for $\mathcal{ESB}$ through measurement of $W_L W_L$-scattering at the highest energy if no light Higgs is found.

If $M_{H_{SM}}$is larger than ~800 GeV/c^2, the Higgs becomes strongly interacting, very broad, and no longer discoverable as particle, and the programme for understanding the mechanism of electroweak spontaneous symmetry breaking would consist of precision measurements of gauge boson production, the $W_L W_L$-scattering experiment[32, 47] at the second stage of the machine, which should encompass at least $\sqrt{s} \simeq 1.5$ TeV for this case.

• Extended gauge models

Discovery limits for new gauge bosons and new matter particles.

Extended gauge models require higher energies, higher luminosities, and therewith the best possible detectors. If a Z' exists, or new heavy fermions, the linear collider is ideally suited to investigate these objects. For these studies the highest energy of the second-stage e^-e^- collider should be realized, $\sqrt{s} \simeq 2$ TeV, and the discovery reach of the LHC will be exceeded by virtual Z' production in e^-e^-[13]. Beam polarization would then help in studying its production, and the detector would have to measure its final states: b/τ-tagging, $W^\pm/Z^0$ -reconstruction, and missing-energy resolution are

very important.

• Supersymmetry

Search for signals of charginos, neutralinos, sleptons, as well as of squarks and gluinos, if discovered, extraction of the mass spectrum, the widths and the couplings; measurement of the $\mathcal{SUSY}$-model parameters to understand the mechanism for supersymmetry breaking.

The lightest supersymmetric particle (LSP) is often assumed to be the lightest neutralino $\tilde{\chi}_1^0$ and stable. It is weakly interacting and frequently an end-product in reactions producing supersymmetric particles. Thus topologies involving $\mathcal{SUSY}$ particles are often characterized by missing energy, so that hermeticity of the detector is essential for these measurements. On the machine side, beam polarization will help for the searches, since for example *slepton* production is enhanced while the W^+W^- background is suppressed. If $\mathcal{SUSY}$ is discovered, the examples discussed in the following Section 6 show that beam polarization becomes a valuable tool for extracting its properties[37]. Very good three-dimensional granularity in the tracking and calorimetry in the detector translate into very good jet and lepton reconstruction and two-jet resolution, which make the studies of the complicated final states more tractable. In many $\mathcal{SUSY}$ models, the non-colored states (chargino $\tilde{\chi}_1^\pm$, neutralino $\tilde{\chi}_1^0$, slepton $\tilde{l}$) are light and might be produced at the 0.5 TeV phase of the machine (see Section 6), while the colored states (squark $\tilde{q}$, gluino $\tilde{g}$) tend to be heavy in most models so that higher energies would be needed to study them.

• The top quark

Measurement of M_{top} at and above threshold, of the top quark magnetic and electric dipole moments, of its decay properties, of the Yukawa coupling, and of rare decays.

The study of the top quark is one of the central research topics at the linear collider[34]. A precise determination of its mass will sharpen the sensitivity of the electroweak radiative corrections to the Higgs mass[60]. Precision measurements of top quark properties will be made at the threshold region and above, and the comparison between the two will give important cross-checks to the $\mathcal{SM}$. The above-threshold measurements can happen together with the search for discoveries at the highest available $\sqrt{s}$ at that time.

The measurement of the top mass in the *threshold region* will be an important part of the early programme of the collider's first phase. To achieve an accuracy of $\pm$500 MeV/c^2 for the top mass from a 10 fb^{-1} threshold scan[27], or $\pm$200 MeV/c^2 from a 50 fb^{-1} threshold scan[55], a precision measurement of the luminosity spectrum $\mathcal{L}(\sqrt{s})$ to $\pm 10^{-2}$ is needed. This requires good tracking in the endcap region of the detector[25], as indicated in the last row of Table 2. A detailed quantative study of the effect that the luminosity-spectrum measurement has on the precision measurements remains to be done. Assuming the spectrum to be known with infinite precision, a reduction of the beamstrahlung to achieve a better spectrum does not pay off, as the reduction in total luminosity reduces the precision of the scan for a given running time [64].

For top-quark studies *above threshold*, where $t\bar{t}$ events will be produced at about the same rate as $\mu^+\mu^-$ events, the collider can operate in its highest luminosity mode,

producing of the order of 10,000 well reconstructed $t\bar{t}$ events per year for analysis of angular distributions and decay-modes, allowing new precision measurements of parameters of the $\mathcal{SM}$ and opening new windows on its possible breakdown or extension. Examples listed in Tables 1 and 2 are the measurements of the top anomalous magnetic $(g-2)$ and electric dipole moments, of its decay $(V \pm A)$ structure, of searches for rare decay modes such as $t \rightarrow H^+ b$ and $t \rightarrow c\tilde{\chi}_1^0$, and of the Yukawa coupling. The measurements tend to require higher luminosity and energy and also beam polarization for those involving the analysis of helicity states.

A LEP/SLC-sized detector could do many of these measurements[27, 55, 29, 34]. The majority of $t\bar{t}$ events will have six jets or four jets and a hard lepton and missing energy coming from the prompt decay of each t-quark into a b-quark and a $W^{\pm}$-boson, so that jet resolution, missing-energy resolution, $W^{\pm}$- reconstruction, and b-tagging are very important, so that improved detectors are desirable. Hermetic coverage down to $|\cos\theta| < 0.98$ would ameliorate forward-backward measurements related to the the helicity structure and detecting rare decays involving the $\tilde{\chi}_1^0$. Good lepton reconstruction is essential for studying the leptonic decays of top, for the p_{top} measurement during the threshold scan, for the helicity analyses and for the study of rare decays $t \rightarrow H^+ b$, $H^+ \rightarrow \tau^+ \nu$. The latter reaction also calls for good vertex detection. For the calorimetry/energy-flow measurement, the calibration error must be below 1% to enable an uncertainty in the M_{top} measurement to less than ± 500 MeV/c^2[34].

• QCD

Measurement of $\alpha_s(s)$, many studies of the hadronic final state.

In general $e^+e^- \rightarrow (Z^*, \gamma^*) \rightarrow q\bar{q}g$, as well as $e^+e^- \rightarrow W^+W^-$, $e^+e^- \rightarrow t\bar{t}$, etc., all involve QCD, and careful measurements have to be performed at each phase of the machine to make sure that the $\mathcal{SM}$ is evolving properly with $\sqrt{s}$.

The measurement of the energy dependence of the strong coupling constant is an important ingredient of the $\mathcal{SM}$, and requires the machine energy to be varied over a broad range[43]. Further understanding of QCD requires continued measurement of the general properties of hadronic final states, because the theory also continues to evolve. Mainly the tracking and calorimetry of the detector should be good but they do not have to be excellent for these studies, and the lower luminosity, e.g., as expected in the early operating phase of the machine, is sufficient.

• Two-photon physics

Systematic study of QPM-QCD phenomenology, of the photon structure function $F_2^{\gamma}(x, Q^2)$, and of inclusive resonances and heavy-flavor production.

Even at an e^+e^- collider there are useful event rates both from virtual photon collisions and from beamstrahlung collisions with virtual photons. The higher energy and luminosity of the linear collider will significantly enhance the precision physics done at TRISTAN and LEP - particularly studies of heavy flavour production and the determination[42] of the quark and gluon structure of the photon by measurement of hadronic $\gamma\gamma$ events with and without an observed final state electron.

5. Machine—Physics

A big advantage of the linear-collider facility comes from the flexibility to orchestrate specialized experiments to answer questions arising from new physics being discovered. In the following are some examples from the $\mathcal{SUSY}$ world.

There has been much progress recently in understanding how to perform precision measurements to map out the spectroscopy of the *sparticle* masses and use their properties to measure the $\mathcal{SUSY}$ parameters[37]. An example from the study is seen in Fig.1, the results of a measurement of *slepton* production, specifically $e^+e^- \rightarrow \tilde{\mu}_R\tilde{\mu}_R \rightarrow \mu\tilde{\chi}_1^0\mu\tilde{\chi}_1^0$. The beam energy is chosen at enhanced production cross section, and beam polarization is used to eliminate the W background. The acoplanar-pair search is straight-forward, and the energy distribution of the muons is seen in Fig.1. The end-points depend on the masses $M_{\tilde{\mu}_R}$ and $M_{\tilde{\chi}_1^0}$. The result of a fit for the two masses gives the *smuon* mass and the LSP mass to ± 1.5 GeV and ± 1.0 GeV, respectively.

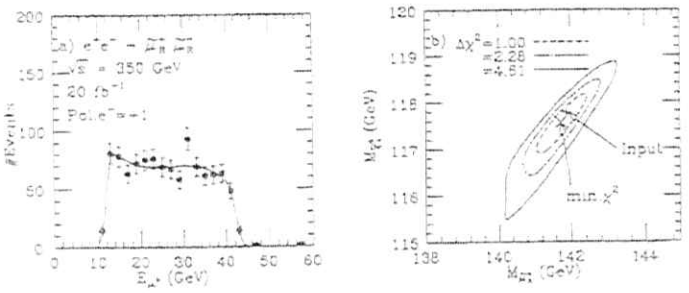

Fig. 1 (a) The energy distribution of the muons from $\tilde{\mu}_R\tilde{\mu}_R$ decays with the fit result shown by the solid curve. (b) χ^2-contours in the $M_{\tilde{\mu}_R}$ - $M_{\tilde{\chi}_1^0}$ plane obtained by fitting the muon energy spectrum.[37]

Beam polarization is thus an important tool for these measurements. For example, *charginos* $\tilde{\chi}_1^{\pm}$ are a mixture of charged *wino* and *higgsino* states. By measuring the production of *charginos* for left- and right-handed e^- polarization, the angular distribution changes as the rate of *higgsino* production changes, while the t-channel production of *winos* is turned off using right-handed electrons. Thus it is possible to decompose the states and deduce the mixing angles of *winos* and *higgsinos* in the *chargino*. A similar game can be played with the *neutralino* $\tilde{\chi}_1^0$, which is a mixture of *neutral wino*, *bino*, and *higgsino* states. In each of these experiments, $\sqrt{s}$ would be optimized to maximize the production of $\tilde{\chi}_1^{\pm}$ or $\tilde{\chi}_1^0$, the masses of which have been measured in earlier experiments similar to the one described above.

Further, the masses and production cross sections of the superpartners depend in a

redundant way on the $MSSM$ parameters m_0, M_1, M_2, μ, $\tan\beta$, ..[37]. By combining the measurements of many channels, it is possible to deduce these parameters and to have cross-checks on their universality. For example, *slepton* and *gaugino* production experiments giving $M_{\tilde{f}}$ and $M_{\tilde{\chi}}$ and the subsequent determination of the *chargino* and *neutralino* mixing angles fix these parameters, which can then be used to test the unification assumption $\frac{M_1}{\alpha_1} = \frac{M_2}{\alpha_2} = \frac{M_3}{\alpha_3} = \frac{m_{1/2}}{\alpha_{GUT}}$, as seen in Fig. 2. Also shown is the test of a mass relation between *slepton* and *wino* masses predicted by a specific model for the masses of the superpartners.

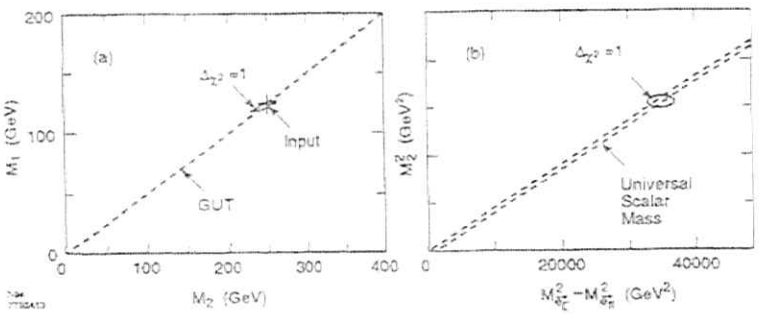

Fig. 2 Tests of $MSSM$ at the 500 GeV linear collider. (a) The χ^2-contour obtained by fitting the parameters $M_{\tilde{e}_R}$, μ, M_1, M_2, and $\tan\beta$ to the measurements of $M_{\tilde{e}_R}$, $M_{\tilde{\chi}_1^0}$, $M_{\tilde{\chi}_1^\pm}$, $\sigma_R(\tilde{\chi}_1^+\tilde{\chi}_1^-)$, and $\sigma_R(\tilde{e}_R\tilde{e}_R)$; the dotted line shows the grand unification relation between the $SU(2)$ and $U(1)$ gauge boson superpartners. (b) test of the mass relation involving the $SU(2)$ gauge boson superpartner and the electron superpartner. The χ^2 contours include reconstruction efficiencies and standard model backgrounds.[37, 22]

6. Machine–Detector

Here the different machine designs are compared. Some of the issues for which the machine and detector closely interact are listed first, and some quantities derived from machine parameters affecting the detector design are compared in Tables 4 and 5, the numbers for which were calculated by one of the authors (D. Schulte). This is an update to the TRC report[2], as the machine parameters for S-Band, Tesla, and NLC have evolved since then.

Backgrounds. The sources of background are from beam-beam effects, synchrotron radiation and debris from the final quads, and muon backgrounds arising from upstream sources. The main backgrounds are due to beam-beam effects: the creation of electron-positron pairs that make their way into the detector and of hadrons from two-photon processes. The pairs are created chiefly via $ee \to eee^+e^-$, $e\gamma \to ee^+e^-$, and $\gamma\gamma \to e^+e^-$,

where the γs are due to beamstrahlung. The total energy in the pairs per bunch crossing can be a few hundred times the c.m.s. energy. Nevertheless, this background can be suppressed since the trajectories of the particles have either small angles with respect to the beam axis or small transverse momenta. The first type is trapped by conical masks at the endcaps of the detector; the second type is constrained to stay close the the beam axis by the strong solenoidal magnetic field of the detector. The mask creates the "dead cone" of Table 4, row 12, to which the detector is blind. Due to the pairs, detector components inside the mask will experience high radiation levels, as will the vertex detector at small radii.

Vibration. All machine designs, whether at 0.5 or 1.0 TeV, require beam stability at the sub-10 nm level to achieve their design luminosities. Ground vibration, of either seismic or cultural origin, must be controlled to well below this level at the final focus.

Beam diagnostics near the IP. It is important to be able to measure the beam parameters at the interaction point (IP) separately for each beam at the full beam intensity. R&D to produce such devices and locate them within 20% of the distance from the IP to the first quad, will require close cooperation between detector and machine physicists.

Extracted beam diagnostics. Experience from the SLC/SLD tell us that these entail an energy spectrometer, a compton polarimeter, and beamstrahlung photon monitor.

$\gamma\gamma$-collider implications

The laser photons must be transported to within a few centimeters of the IP for Compton backscattering and the electrons must be extracted without creating too much background. The interaction among these devices, the vertex detector, the other beam monitoring equipment, and the masks is sufficiently complicated so as to require the design of a dedicated detector for the $\gamma\gamma$ experiments at a dedicated interaction region (IR). Conceptual engineering solutions have not yet begun to address these issues.

Detector timing

The bunch time structure of the various designs varies from 0.67 ns (CLIC) to 705 ns (TESLA), as seen in Table 4, row 8. Through the beam-beam interaction, each bunch crossing occuring within the time resolution of the detector may produce particles that can partially obscure a real physics event triggered by a different bunch in the train. Thus, the time resolution of the detector and the maximum tolerable trigger rate become potentially important parameters in deciding between competing machine designs. If sub-nanosecond timing were trivial and computing power large, fast, and cheap enough, any machine bunch structure could be considered. Unfortunately, such is not the case. Table 5, row 10 gives a measure of the probability of having stiff particles from underlying hadronic events in a good physics event for a typical subdetector with a timing resolution of 100 ns.

Trigger rate and Data volume

At the SLC/SLD the trigger rate and data volume can vary enormously from pulse-to-pulse. Overall trigger rates under poor conditions are much larger than can be explained by physics or simulated backgrounds. While one hopes that any future collider will be immune to such problems, it is prudent to design the trigger and data

aquisition with sufficient dynamic range to ride out these disturbances. In addition the detector often provides some of the most useful diagnostics for the accelerator, so that the ability to easily correlate its data with that of the machine should be a design consideration.

All the machine designs except VLEPP incorporate multibunch operation. When the interbunch spacing is long enough to allow for a trigger decision, one can imagine schemes where the rate of the first-level trigger would be the product of the average bunch-crossing rate (Table 5, row 11) and the probability for a hadronic background event from the beam-beam interaction (Table 5, row 6). The resulting trigger rates (Table 5, row 12) are quite tolerable but, for example, two orders of magnitude larger than the LEP first-level triggers.

When the interbunch spacing is very short, another possiblity is to consider a simple bunch train crossing as first level trigger[6]. This would be followed by a software trigger that analyzed all data buffered into memory during the bunch train. In this model, the maximum trigger rate would be the machine repetition rate, as tabulated in Table 4 row 7. For comparison, Table 5 row 13 shows the rate for useful physics events, assuming 20pb as the rough total for interesting-physics cross sections.

Finally, a guess at the data volume can be made: a good event (Table 5 row 13) will contain a few megabytes of information[6].

7. Detector Options

Here some global performance figures of detectors used in simulations for the international workshops[6, 8, 25, 26, 27, 55, 31, 32, 33, 44, 45, 46, 36, 39, 34, 41, 47, 48, 52] are listed, in Table 6. Earlier studies have shown that the performance of existing e^+e^- detectors would be good enough to do much of the physics in the early phase of the machine at low energy. Typical performance figures are shown in the first two columns of Table 6. For higher luminosities and/or higher energies, high performance detectors are needed, and such detectors are the subject of the last two columns. Examples given are the "JLC Detector" [6] which is being designed at KEK and a "1 TeV Detector" [48] which has been discussed in Europe. Both detectors are large and give good performance at $\sqrt{s}$ = 1-2 TeV. The JLC Detector is being designed to have good hermeticity over the fullest possible solid angle, to have jet invariant mass resolution comparable with the natural widths of the $W^{\pm}$ and the Z^0, and give a lepton pair recoil mass resolution for $e^+e^- \to Z^0 H_{SM}$ comparable with the beam energy spread of ~200 MeV. A "European" detector[49] is under study with the demands on performance listed in Tables 1, 2, and 3 in mind. Another alternative is a small high-field detector[41], which is one of the options for the "American" detector[50] being considered in view of NLC tolerances.

Table 4. Table of some machine parameters related to IR and detector design

	TESLA	SBLC	JLC(S)	JLC(C)	JLC(X)	NLC	VLEPP	CLIC
	DESY		KEK			SLAC	INP	CERN
[Units in brackets]	Upper numbers for 0.5 TeV$\equiv\sqrt{s_0}$ machine version Lower numbers for 1.0 TeV$\equiv\sqrt{s_0}$ machine version							
1)Accel. freq. [GHz]	1.3	3	3	6	11	11	14	30
2)$\mathcal{L}$ (with pinch)	5.9	5.2	4.6	9.3	5.1	5.8	6.7	1.0-4.5
$[10^{33}cm^{-2}s^{-1}]$	9.3	10.7		21.1	9.6	10.5		2.2-9.7
3)$\int \mathcal{L}dt/y=10^7s$	19	17	15	31	17	19	32	3-15
$\times$33%eff.$[fb^{-1}]$	31	35		70	32	35		7-32
4)δ_B (due to beamstr.)	2.5	2.7	6.2	4.9	3.0	2.9	10.0	3.6
[avg.beam en.loss in %]	5.4	7.9		8.0	7.5	9.9		7.3
5)$\mathcal{L}$ ($\sqrt{s}>0.99\sqrt{s_0}$)	3.6	3.1	1.7	4.4	3.2	3.5	1.4	0.5-2.4
$[10^{33}cm^{-2}s^{-1}]$	3.6	7.2		7.7	4.4	4.1		0.8-3.6
6)Bunches/train	1135	333	50	72	85	90	1	1-10
	1135	125		72	85	90		1-10
7)Trains/sec	5	50	50	150	150	180	300	2530-1210
	3	50		150	150	120		4000-1800
8)Interbunch spacing	705ns	6ns	5.6ns	2.8ns	1.4ns	1.4ns	3.3ns	0.67ns
	705ns	4ns		2.8ns	1.4ns	1.4ns		0.67ns
9)σ_x/σ_y-spot size	845/18.9	335/15.1	260/3.0	260/3.0	260/3.0	286/4.5	2000/4	250/7.5
[nm]	665/9.5	357/5.8		372/2.2	101/2.2	226/3.6		200/6.0
10)σ_z-spot size	700	300	120	120	90	100	750	200
$[\mu m]$	700	300		120	51	125		200
11)Crossing angle	0	3	6.4	6.0	6.1	20	5	1
[mrad]	0	3		6.0	3.0	20		1
12)Dead cone[mrad]	79	63	120	97	85	82	134	66
(2T,0.5m to mask)	82	84		116	89	94		70
13)l^* (drift to Q01)	3.0	2.0	2.5	2.5	2.5	2.0		1.45
[m]								

Table 5 Table of some machine parameters related to backgrounds.

	TESLA	SBLC	JLC(S)	JLC(C)	JLC(X)	NLC	VLEPP	CLIC
[Units in brackets]	Upper numbers for 0.5 TeV machine version Lower numbers for 1.0 TeV machine version							
1)$N_{e^\pm}$ per bunch	3.6	1.1	1.44	1.0	.63	.65	20	8
$[10^{10}]$	3.6	1.69		1.44	.62	0.95		8
2)$\gamma\epsilon_x$ / $\gamma\epsilon_y$	14./0.25	5./.25	3.3/.045	3.3/.045	3.3/.045	5./.08	20./.075	3./.15
$[10^{-6}$m rad]	14.0/1	5./.1		3.3/.048	3.3/.045	5./.1		3.9/.2
3)$N_{beamstr.\gamma}$ per $e^\pm$	2.0	1.4	1.8	1.3	.9	.8	4.7	1.4
	2.5	2.0		1.4	1.1	1.2		1.7
4)$\langle E_{beamstr.\gamma}\rangle$	3.0	4.7	11.3	9.3	8.6	7.3	5.3	6.3
[GeV]	8.5	19.5		28.	33.	29.		22.
Backgrounds/bunch								
5)$N_{beamstr.e^\pm}$/bunch	31	7	37	15	6	6	1219	7
θ>150mrad,p_T>20MeV/c	72	34		29	10	20		10
6)Hadr.ev./bunch	.13	04	.48	.14	.05	.04	11.0	.04
$E_{vis-c.m.s.} \geq 5$GeV	.70	0.53		.62	.19	.38		.16
7)Minijet ev./bunch$[10^{-2}]$	.30/.016	.10/.005	1.9/.10	.52/.03	.16/.009	.11/.007	28./1.4	15/.009
p_T^{min}/GeV/c= 3.2 / 8	2.4/.13	2.8/0.13		5.2/.26	2.0/.10	2.7/.14		1.2/.063
Backgrounds/100ns								
8)$N_{beamstr.e^\pm}$/100ns	31	117	661	536	429	429	1219	7-70
θ>150mrad,p_T>20MeV/c	72	850		1036	714	1500		10-100
9)Hadr.ev./100ns/unit lumi	.022	11	1.6	.50	.53	.35	.93	.04-.09
$[10^{33}cm^{-2}s^{-1}]$	.075	1.2		.83	1.2	1.4		.06-.13
10)Minijet ev./100ns	.003	.016	.33	.18	.11	.09	28.	.002-.015
p_T^{min}=3.2GeV/c	.024	70		1.9	1.4	2.2		.013-.12
Rates								
11)(Bunch crossing rate)	5.68	16.25	2.5	10.8	12.75	16.2	.3	2.53-12.1
[kHz]	3.41	6.25		10.8	12.75	10.8		4.-18.
12)(Hadr.ev. rate) [kHz]	0.74	.67	1.0	1.4	.5	.65	2.6	.09-.5
$E_{vis-c.m.s.} \geq 5$GeV	2.4	3.3		5.3	2.0	4.1		.5-2.3
13)1 event /20pb rate	.12	12	.09	18	11	12	.19	.02-.09
[Hz]	.19	.21		.42	.19	.21		.04-.19

Table 6. Examples of detector performances used in physics studies.

	ee500 '91,'93	LEP/SLC Style[a]	JLC Detector	1 TeV Detector	Units
Tracking					
$\frac{\delta p_t}{p_t^2} = C$					
$C =$	5-100	8	1	2	$\times 10^{-4}(\frac{GeV}{c})^{-1}$
E-M Calorimeter					
$\frac{\delta E}{\sqrt{E}} =$	0.02-0.15	0.2	0.15	0.10	$\sqrt{\frac{GeV}{c^2}}$
Hadronic Calorimeter					
$\frac{\delta E}{\sqrt{E}} =$	0.3-1.0	0.9	0.40	0.65	$\sqrt{\frac{GeV}{c^2}}$
Energy Flow					
$\frac{\delta E}{E} =$	0.3-0.8	0.65	0.3	0.4	$\sqrt{\frac{GeV}{c^2}}$
Vertexing					
$\delta(IP) = A \oplus \frac{B}{p}$					
$A =$	5-20	25	11	10	μm
$B =$	50-100	100	28	30	$\mu m \frac{GeV}{c}$
Hermetic coverage					
$\cos\theta \mid <$	0.70-0.99	0.96	0.98	0.98	

[a]Aleph

7.1. An Example for Detector Optimization

The measurement of trilinear $W^\pm$ couplings ($WWV, V = \gamma, Z^0$) [32, 28, 35, 47] is used as a benchmark reaction to study the detector performance. This is a continuation and update to the excercise started earlier [45]. The golden channel was recognized early on [62, 63] to be $e^+e^- \to W^+W^- \to q\bar{q}'\ell\bar{\nu}_\ell(\ell = \mu, e)$. The sign of the charge of the decaying W's is identified by that of the lepton, the production angle is given by the thrust axis of the hadronic system, and the decay angles are derived from the reconstructed quark and lepton four-momenta. The trilinear W-boson couplings arise from s-channel diagrams involving γ^*, Z^* exchange and measure the structure of the W (e.m. and weak magnetic and electric moments). They determine and are measured using the angular distributions of longitudinally-polarized W_L and transversally-polarized W_T. The W_L and W_T components are extracted statistically using the W-decay angular distribution. The W_L is the physically interesting component since it is related to the Higgs degrees of freedom used to expedite $\mathcal{ESB}$ and the massive gauge bosons. The dominant production in the W sector, however, is of W_T via the t-channel ν-exchange, which contains no information about the trilinear couplings, is thus a background for the measurement over all $\cos\theta$ and must be statistically subtracted. The W_T produced

via the t-channel are strongly forward-peaked, while trilinear couplings are sensitive to the W_L and W_T components prominent in the central-to-backward $\cos\theta$ region. The t-channel W_T background is still an order of magnitude larger than the signal at backward $\cos\theta$ for unpolarized beams. A polarized electron beam turns off the t-channel (for 100% polarization) background and changes the γ^*, Z^* mixture, which enables disentangling the γ, Z components of the anomalous couplings, so that it is very important for this experiment. But the beam polarization will not be a perfect 100%, so that it will always be necessary to subtract the background.

Many theoretical scenarios for fitting combinations of the parameters κ_γ, κ_Z, λ_γ, λ_Z, and g_{ZWW} which describe the structure and couplings of the W boson were tried out for different observables: the total cross-section σ, the production angular distribution $\frac{d\sigma}{d\cos\theta_{W^-}}$, and the production and decay angular distributions $\frac{d^5\sigma}{d\cos\theta_{W^-}d\phi_{W^-}d\cos\theta^*_{W^-}d\phi^*_{W^-}d\cos\theta^*_{W^+}d\phi^*_{W^+}}$. Table 7 lists the detector and machine aspects which were to be rated with regard to importance for the different experiments.

Table 7. Detector and machine aspects for which good performance is important for the measurement of the trilinear couplings. Quality keys: from '-' not important, to '***' very important. LEP/SLC detector ~ *. $\mathcal{L}(\sqrt{s})$ stands for a precision measurement of the luminosity spectrum.

Detector	σ	$\frac{d^5\sigma}{d\cos\theta_{W^-}d\phi_{W^-}d\cos\theta^*_{W^-}d\phi^*_{W^-}d\cos\theta^*_{W^+}d\phi^*_{W^+}}$ at $\sqrt{s}$= 0.5 TeV	$\frac{d^5\sigma}{d\cos\theta_{W^-}d\phi_{W^-}d\cos\theta^*_{W^-}d\phi^*_{W^-}d\cos\theta^*_{W^+}d\phi^*_{W^+}}$ at $\sqrt{s}$= 1.0 TeV
Hermetic Coverage	*	**	***
Tracking	*	**	***
Calorimetry	*	**	**
3-D Granularity	*	**	***
Lepton I.D. (including charge)	*	**	***
Vertex Tagging	-	-	-
π/K Separation	-	-	-
Detector+Machine			
$\mathcal{L}(\sqrt{s})$	*	**	***
Beam Polarization	-	**	***

The performance of the "LEP/SLC-style" detector in Table 6 is good enough for the couplings' measurements at $\sqrt{s}$= 0.5 TeV, but improved tracking of electrons and muons at small polar angles will allow more precise measurements for a given luminosity. This is the example used here to discuss detector optimization.

The tracking accuracy listed in Table 6 are for tracks in the central ($|\cos\theta| < 0.7$) region of the angular distribution. For "dipping" tracks in a solenoidal magnetic field, the formula should read

$$\frac{\delta p_t}{p_t^2} = C \text{ for } |\tan\theta| > \frac{R_O}{L}$$

$$\frac{\delta p_t}{p_t^2} = C \times G^2 \times \sqrt{\frac{N-5}{\frac{L}{C}-5}} \text{ for } |\tan\theta| < \frac{R_O}{L},$$

where C is the number in the "Tracking" row of Table 6. G is a geometrical factor

$$G = \frac{R_O - R_I}{L\tan\theta - R_I},$$

where R_O and R_I are the outer and inner radii of the tracking detectors, $2 \times L$ is the length (along the beam) of the central tracking detector and N is the maximum number of measured points of charged particles by the tracking detectors. For the discussion which follows, $C = 6$, $R_O = 1.8m$, $R_I = 0.1m$, $L = 2.2m$ and $N = 35$ have been used for the "LEP/SLC-style" detector (vertex information included).[2]

For 200 GeV electrons occuring in the events at $\sqrt{s} = 500$GeV, the energy measured by end-cap calorimetry is still good to a few percent even at small angles, until one runs out of calorimeter at angles below $|\cos\theta| \simeq 0.98$. For 200 GeV muons the momentum error from the curvature measurement by the tracking detectors becomes severe at small angles: e.g., $\frac{\delta p_t}{p_t} > 50\%$ for $|\cos\theta| > 0.96$, using the above formula and the "LEP/SLC-style" detector. However, the curvature measurement for the *electron* is important at small angles as well as for the muon, in order to reliably determine the sign of its charge, for knowing the charge of the corresponding $W^\pm$. Since the angular distribution is strongly peaked in the forward direction due to the t-channel, a wrong determination of the charge would put the event in the wrong hemisphere and bias the measurement in the backward direction, a sensitive region for the couplings. This bias can be corrected using Monte Carlo, but the smaller the correction, the smaller the systematic error.

Assuming that a 33% error on the curvature measurement is safe for determining the charge (3σ from zero, 6σ from the wrong sign), then the "LEP/SLC-style" detector can measure down to $|\cos\theta| \simeq 0.94$. One could live with this, but due to the forward-peaking of $\cos\theta$, one gains rapidly in statistics at smaller angles: the gain is a factor of two [28] in going from $|\cos\theta| = 0.95$ to $|\cos\theta| = 0.985$.

This performance is achieved at $\sqrt{s}$ =500 GeV with a detector that has been laid out to handle $\sqrt{s} \simeq 1000$ GeV[46]. The performance figures for such a detector are seen in Table 6, and the main improvement is in the tracking, which can be attained by increasing N to 300 and B to 2T. For this detector, the sign of charge of a 200 GeV track can be measured with 3σ significance relative to zero to $|\cos\theta| \simeq 0.98$. This is nearly the same performance as a "LEP/SLC-style" detector for measuring an 80 GeV track.

Thus, although this still must be verified by detailed simulation, the 1000GeV detector could be expected to have a similar performance for measuring the couplings at

[2] The value of the magnetic field B is contained in C; it is 1.5T for Aleph.

$\sqrt{s}$= 500 GeV, as a "LEP/SLC-style" detector at $\sqrt{s} = 200$ GeV. This statement only refers to the the effect of detector acceptance and smearing. The effects of initial state radiation and beamstrahlung are of course more severe at the high energy. The earlier studies at 500 GeV using various detectors gave selection efficiencies ranging from 59% (due to detector acceptance ($|\cos\theta| < 0.985$) but without radiative effects [28]) to 36% (with i.s.r., beamstrahlung and detector acceptance but no detector smearing [35]) to as low as 6% (with everything included: i.s.r., beamstrahlung, detector acceptance=$|\cos\theta| < 0.8$, and smearing [32]). In this case it is clear that effort should go into improving detector acceptance and reducing the smearing effects.

This has been one example to show that tracking at small angles, or more generally detector performance in the forward direction, should be considered carefully. For other channels which can be used for the couplings' measurements that involve t-channel gauge boson fusion[35], $e^+e^- \to e\nu W$, $e^-e^- \to \nu\bar{\nu}\gamma$, $e^+e^- \to \nu\bar{\nu}Z$ and $e^+e^- \to eeWW$, the performance at small angles is even more important. There is much work left to be done on understanding event selection, background subtraction, data correction and corrections for radiative effects.

8. Conclusions

One summarizes from Tables 1, 2, and the discussion that:
⊙ – the lowest energy of the machine should overlap with the highest energy of LEP so that no e^+e^- "discovery/measurement gap" exists;
⊙ – the starting energy for the experiments should be $\sqrt{s} \simeq 0.4$ TeV, which opens much of the physics potential listed in Tables 1 and 2, allows precision measurements of the $\mathcal{SM}$ and perhaps discovery of the Higgs and/or $\mathcal{SUSY}$;
⊙ – a first stage energy for the collider of $\sqrt{s} \simeq 0.8$-1.0 TeV provides a physics programme complementary to hadron colliders and with competitive discovery reach in many areas;
⊙ – the machine design should include an upgrade path to the second stage at $\sqrt{s} \simeq$ 1.5-2 TeV in order to match fully the discovery reach of LHC, to discover/measure any new physics in this energy regime, and to study $\mathcal{ESB}$ in the heavy Higgs case;
⊙ – the luminosity required $\int \mathcal{L}dt$ varies from about 1fb^{-1}/year for early commissioning (and discovery) runs and later up to 100fb^{-1}/year for precision measurements;
⊙ – polarized beams open new physics windows and are necessary: polarized e^- are essential, polarized e^+ improve the power of this technique;
⊙ – improved detector performance buys effective luminosity.

The series of physics milestones between LEP energies and $\sqrt{s} \simeq 1$ TeV show that a convincing physics case can be made for commissioning the machine at lower luminosity (10^{33}cm^{-2}s^{-1}) and a c.m.s. energy of 0.3 to 0.4 TeV before reaching the first stage energy of $\sqrt{s} \simeq 0.8$ to 1.0 TeV. The combination of experiments with polarized beams and attainment of the design luminosity (a few $\times$ 10^{33}cm^{-2}s^{-1}) would round out a programme that would span decade of physics at least. The second stage will continue with a step-wise energy increase up to $\sqrt{s} \simeq 1.5$-2 TeV. Both stages contain important ingredients of the complementarity and competition to the hadron colliders.

More details about the e^-e^-, $\gamma\gamma$, and $e^-\gamma$ options as well as that of running in the e^+e^- mode at the Z^0 peak may be found in the TRC report[2], and the reader is referred to the relevant contributions to this workshop.

9. References

1. D.Burke, "Status of the Interregional Collaboration", Opening Session at the *Fifth International Workshop on Next-Generation Linear Colliders*, (LC93, SLAC, October 13-21, 1993), SLAC-436 (1993).
2. *International Linear Collider Technical Review Committee Report 1995*, (Stanford Linear Accelerator Center Technical Publications Department, order number SLAC-R-95-471), G. Loew/SLAC(Chair) and T. Weiland/TH Darmstadt(Secreteriat).
3. *Proceedings of the Workshop on Physics at Future Accelerators* (La Thuile 1987), ed. J.H. Mulvey, CERN 87-07 (1987).
4. C. Ahn et al.,*Opportunities and Requirements for Experimentation at a Very High Energy e^+e^- Collider*, SLAC-Report-329 (1988).
5. *Proceedings of the Summer Study on High Energy Physics in the 1990s* (Snowmass, 1988), ed. S. Jensen (World Scientific, Singapore, 1989).
6. Three Workshops on the Japan Linear Collider (1989,1990,1992) resulting in: JLC Group, *JLC-I*, KEK Report 92-16 (1992).
   The latest workshop took place in 1995.
7. *e^+e^--Collisions at 500 GeV: The Physics Potential, Parts A and B* (Workshops at Munich, Annecy, Hamburg, 1991), ed. P.M. Zerwas, DESY 92-123A&B (1992).
8. *Physics and Experiments with Linear Colliders, Vols. I and II*, eds. R. Orava, P. Eerola and M. Nordberg (World Scientific, Singapore, 1992).
9. *Proceedings of the 1992 Workshops on High-Energy Physics with Colliding Beams* (Trilogy of Workshops at Yale, Wisconsin, Santa Cruz, 1992), ed. J. Rogers, SLAC-428 (1993).
10. *Workshop on Physics and Experiments with Linear e^+e^- Colliders, Vols.I and II* (Waikoloa, Hawaii, 1993), eds. F.A. Harris, S.L. Olsen, S. Pakvasa and X. Tata (World Scientific, Singapore, 1993).
11. *e^+e^--Collisions at 500 GeV: The Physics Potential, Part C* (Workshops at Munich, Annecy, Hamburg, 1992-1993), ed. P.M. Zerwas, DESY 93-123C (1993).
12. *Proceedings of the Zeuthen Workshop on Elementary Particle Theory - Physics at LEP200 and Beyond* (Teupitz/Brandenburg, Germany, April 1994), eds. T. Riemann and J. Blümlein, Nucl. Phys. B (Proc. Suppl.) 37B(1994).
13. The proceedings of the studies in the USA by "DPF Long Range Planning" working groups (DPF is the Division of Particles and Fields of the American Physical Society), available on the World Wide Web under http://www.pha.jhu.edu/cltp/.
14. These proceedings: *Physics with e^+e^- Linear Colliders, Part D* (Workshops

at Annecy, Gran Sasso, Hamburg, 1995), ed. P.M. Zerwas, to be published as DESY 96-123D.
15. Members of the LC2000 working group on experimentation were: P. Bambade, W. Bartel, T. Benke, G. Blair, T. Bolognese, A. Bonissent, R. Brinkmann, J. Bürger, O. Callot, G. Coignet, P. Comas, G. Cowan, M. Danilov, P.-G. Denis, E. Eisen, M. Grünewald, D. Haidt, J.D. Hansen, J. Harton, P. Hüntemeyer, L. Jönsson, F. Kapusta, S. Katsanevas, D. Kisielewska, U. Kötz, S. Komamiya, A. Lebedev, M. Leenen, B. Löhr, K. Long, P. Mättig, J. Meyer, D. Miller, J. Milewski, R. Miquel, A. Olshevski, K. Piotrzkowski, M. Pohl, F. Richard, A. Rousarie, E. Rulikowska, H.-G. Sander, M. Schmelling, M. Schmitt, U. Schneekloth, H.-J. Schreiber, S. Schreiber, D. Schulte, R. Settles, S. Shuvalov, A. Sopczak, P. Steffen, H. Steiner, L. Suszycki, T. Tauchi, J. Thompson, I. Typakin, A. Venturi, H. Videau, A. Wagner, R. Walczak, and G.W. Wilson.
16. *Proceedings of LCWS95, the 1995 International Linear Collider Workshop at Morioka-Appi* (Sept. 8-12, 1995), (World Scientific, to be published).
17. *Proceedings of LC92, the ECFA Workshop on e^+e^- Linear Colliders, Vols. I and II*, ed. R. Settles, MPI-PhE/93-14, ECFA 93-154 (1993).
18. *Proceedings of the Fifth International Workshop on Next-Generation Linear Colliders* (LC93, SLAC, October 13-21, 1993), SLAC-436 (1993).
19. *Proceedings of the Sixth International Workshop on Linear Colliders* (LC95, KEK, March 26-31, 1995), KEK Proceedings 95-5.
20. R. Settles, et al., *Experimentation at the Linear Collider*, in Ref.[16], to be published.
21. "Zeroth Design Report for NLC", SLAC (March 1996).
"Linear Collider Design Report", DESY, to be published (December 1996).
22. Michael E. Peskin, *Complementarity of e^+e^- and pp Colliders for the Exploration of Electroweak Symmetry Breaking*, SLAC-PUB-6582 (August 1994).
23. S.L. Glashow, *Proceedings of the LEP Summer Study*, CERN 79-01, Vol.1, p.285.
24. P. Zerwas, *Phys. Bl.* 49(1993)187.
25. M.N. Frary and D.J. Miller, in Ref.[7], p.379.
26. P. Janot, in Ref.[7], p.107.
27. G. Bagliesi, et.al., in Ref.[7], p.327.
28. M. Frank, P. Mättig, R. Settles and W. Zeuner, ibid., Part A, p. 223.
29. K. Fujii, in Ref.[8], p.203.
30. S. Komamiya, in Ref.[8], p.277.
31. J.-F. Grivaz, in Ref.[8], p.353.
32. T. Barklow, in Ref.[8], p.423.
33. David Burke, in Ref.[17], Vol. II, p.557.
34. P. Igo-Kemenes, in Ref.[10], p.95.
35. A. Miyamoto, in Ref.[10], p.141.
36. P. Janot, in Ref.[10], p.192.
37. S. Orito, in Ref.[10], p. 230.

T. Tsukamoto, in Ref.[10], p. 814.
T. Tsukamoto, K. Fujii, H. Murayama, M. Yamaguchi, and Y. Okada, KEK-Preprint-93-146 (1993).
38. D.L. Borden, in Ref.[10], p.323.
39. M.D. Hildreth, in Ref.[10], p.535.
40. JLC Study Group (Y. Kurihara), Ref.[6], p.73. and KEK Proceedings 91-10 (Nov. 1991), p.293.
41. P. Grosse-Wiessmann, contribution to Hawaii Workshop; cf. William W. Ash, in Ref.[10], p.402.
42. D.J. Miller, B.W. Kennedy, J.J. Ward, and J.R. Forshaw, in Ref.[10], p.577.
43. S. Bethke, in Ref.[10], p.687.
44. A. Sopczak, in Ref.[11], p.121.
45. R.W. Forty, J.B. Hansen, J.D. Hansen and R. Settles, in Ref.[11], p.235.
46. R. Settles, for the ee500 Experimentation Working Group (G. Coignet, P. Colas, J.D. Hansen, D. Miller and R. Settles) in Ref.[11], p.591.
47. T. Barklow, SLAC-PUB-6618 (1994).
48. R. Settles, in Ref.[12], p.316.
49. "ECFA/DESY Study of Physics and Detector for a Linear Collider", in progress, http://info.desy.de/conferences/ecfa-desy-lc96.html, to be published as DESY 96-123E.
50. A parallel study in progress in the USA to the one above[49], http://nlc.physics.upenn.edu/lc/lc.html, to be published.
51. *Proceedings of the Gamma-Gamma Collider Workshop* (Berkeley, March 28-31, 1994), ed. A. Sessler, NIM A355(1995).
52. F. Richard, Conventional Detectors for a Photon-Photon Collider, LAL 94-45 (June 1994).
53. G. Jikia, in Ref.[51], p. 84.
54. *Proceedings of the Santa Cruz Workshop on e^-e^- Collisions* (Sept. 4-5, 1995), ed. C. Heusch, to be published.
55. R. Miquel, et.al., in Ref.[14], these proceedings.
56. P. Igo-Kemenes, in Ref.[14], these proceedings.
57. D. Cline, UCLA, private communication.
58. D. Miller, in Ref.[16], to be published.
59. K. Flöttmann, DESY 95-064;
K. Fujii and T. Omori, KEK Preprint 95-127.
60. F. Richard, LAL 95-25;
P. Renton, private communication.
61. H.-G. Moser, NIM A295(1990)435.
62. G. Barbiellini, et. al., *Physics at LEP, Vols. 1 and 2*, CERN 86-02, p. 1, Vol. 2.
63. A. Blondel, et. al., *Proceedings of the ECFA Workshop on LEP200, Vols. I and II*, CERN 87-08, ECFA 87/108 (1987), p. 120.
64. D. Schulte, Ph.D. Thesis, U. Hamburg (1996), to be published.